James P. Denier
Matthew D. Finn *Editors*

Mechanics Down Under

Proceedings of the 22nd International Congress of Theoretical and Applied Mechanics, held in Adelaide, Australia, 24–29 August 2008

Springer

Mechanics Down Under

James P. Denier · Matthew D. Finn
Editors

Mechanics Down Under

Proceedings of the 22nd International Congress of Theoretical and Applied Mechanics, held in Adelaide, Australia, 24–29 August 2008

Springer

Editors

Prof. James P. Denier
Department of Engineering Science
The University of Auckland
Auckland
New Zealand

Dr. Matthew D. Finn
School of Mathematical Sciences
The University of Adelaide
South Australia
Australia

Additional material to this book can be downloaded from http://extras.springer.com

ISBN 978-94-007-5967-1 e-ISBN 978-94-007-5968-8
DOI 10.1007/978-94-007-5968-8
Springer Dordrecht Heidelberg New York London

Library of Congress Control Number: 2012953386

Printed on acid-free paper

Springer is part of Springer Science+Business Media (www.springer.com)

Preface

The International Congress of Theoretical and Applied Mechanics, held in Adelaide, Australia in 2008 was the twenty-second ICTAM. The idea of holding regular congresses devoted to the field of mechanics can be traced back to a conference on problems of fluid mechanics, held in Innsbruck, in 1922, and organized by four of the founding fathers of modern fluid dynamics, C.W. Oseen, T. Levi-Civita, T. von Karman, and L. Prandtl. Although it attracted only thirty people, this conference provided the spark that led to the first ICTAM held in Delft in 1924 and organised by J.M. Burgers and C.B. Biezeno. This conference was so fruitful that the organisers decided to arrange similar meetings in the future, every four years, and to extend the scope of the future meetings to include solid mechanics.

The organisation of successive congresses was placed in the hands of a Congress Committee. During the sixth congress, held in Paris, the idea arose of a more permanent organization to look out for the world interests in the mechanical sciences. Thus IUTAM, the International Union of Theoretical and Applied Mechanics, was formed on 26 September 1946. In 1947, IUTAM became a member of ICSU, the International Council of Scientific Unions, itself founded in 1931. The highest authority of IUTAM is the General Assembly, with delegates from the Adhering Organizations, each of which is affiliated with a national learned society or academy in a given country.

Contemporary mechanics incorporates fundamental problems from pure science and has strong links into modern technology. It pervades many areas of scientific endeavour, including oceanography, physical chemistry, biology, medicine, geophysics and astrophysics. The International Congress of Theoretical and Applied Mechanics continues to spread the ever-expanding pool of knowledge in the mechanical sciences and continues to contribute to the advancement of mutual human understanding.

The 22nd International Congress of Theoretical and Applied Mechanics comes to Adelaide, Australia at the invitation of the Australian Academy of Science, in conjunction with the University of Adelaide and the Flinders University of South Australia. The journey that was ICTAM2008, the first

IUTAM Congress to be held in the Southern Hemisphere, began in the middle of 2001 when discussions within the Australian and New Zealand mechanics communities explored the feasibility of putting forward a bid to IUTAM to host the 2008 International Congress of Theoretical and Applied Mechanics. The bid, which proved successful, was greatly facilitated by the support of the the Adelaide Convention Bureau and the support of many local and national organisations. This volume is the culmination of that journey and presents selection papers from the sectional lectures as well as details of all papers presented during the congress.

The scientific program consisted of plenary opening and closing lectures, sectional lectures, prize lectures, mini-symposia, and contributed papers presented in lecture and seminar presentation sessions. These cover all aspects of mechanics. It also showcased the research of the inaugural winners of the Batchelor Prize in Fluid Mechanics Howard Stone and the Rodney Hill Prize in Solid Mechanics Ortiz.

All contributed papers presented at the Congress were peer reviewed. Recommendations were received from Pre-selection Committees of the National Committees of nine countries: Canada, France, Germany, Japan, China, Poland, Russia, UK and USA. Moreover, recommendations were received from the Chairs of the Mini-Symposia and of the Pre-nominated Sessions. Finally, the International Papers Committee (IPC) reviewed each short paper, paying careful attention to the recommendations of the pre-selection committees. Accordingly, of the 1517 eligible submissions only 1322 contributions were invited by the IPC to be presented at the Congress.

Jim Denier

The 22nd International Congress of Theoretical and Applied Mechanics

President and Chairman of the Local Organising Committee

Ernie Tuck

Secretary-General

Jim Denier

Members of the Local Organising Committee

Rich Clarke (Auckland)
Bassam Dally (Adelaide)
Matt Finn (Adelaide)
Raj Huilgol (Flinders)
Richard Kelso (Adelaide)
Trent Mattner (Adelaide)
Gus Nathan (Adelaide)
Dzuy Nguyen (Adelaide)

Members of the Australasian Steering Committee

Ross Griffiths (ANU)
Kerry Hourigan (Monash)
Peter Jackson (Auckland)
Ernie Tuck (Adelaide)
Roger Tanner (Sydney)
Graham Baker (Southern Queensland)
Mark Bush (Western Australia)
Ian Collins (Auckland)
Yiu-Wang Mai (Sydney)
Francis Rose (DSTO)

Members of the IUTAM Congress Committee

Hassan Aref (USA)
member of XCCC
Nadine Aubry (USA)
Dominique Barthès-Biesel (France)
Martin Bendsøe (Denmark)
member of XCCC
representative of ISSMO
Dimitri Beskos (Greece)
Dick van Campen (Netherlands)
Alberto Carpinteri (Italy)
Gengdong Cheng (China)
David Durban (Israel)
Fernand Ellyin (Canada)
representative of ICM
Ben Freund (USA)
President of XCCC
Irina Goryacheva (Russia)
Peter Gudmundson (Sweden)
Michael Hayes (Ireland)
representative of ISIMM
Carl Herakovich (USA)
Tsutomu Kambe (Japan)
Bhushan Karihaloo (UK)
representative of ICF
Alfred Kluwick (Austria)
Tomasz Kowalewski (Poland)
member of XCCC
Edwin Kreuzer (Germany)
Stelios Kyriakides (USA)
Pierre Ladevèze (France)
Gary Leal (USA)
representative of ICR
Jean-Baptiste Leblond (France)
Fernando Lund (Chile)
Peter Monkewitz (Switzerland)
Nikita Morozov (Russia)
Nigel Peake (UK)
Timothy Pedley (UK)
Secretary of XCCC
Bernhard Schrefler (Italy)
member of XCCC
representative of CISM
André Thess (Germany)
Ernie Tuck (Australia)
Viggo Tvergaard (Denmark)
Manuel Velarde (Spain)
Genki Yagawa (Japan)

Acknowledgments

We would like to express our thanks to all our colleagues within the IUTAM community, in particular those within the IUTAM Congress Committee and the members of the International Papers Committee. Their ongoing support and advice allowed us to overcome many of the problems typically encountered by the organisers of large international meetings.

A specials thanks go to the chairs responsible for the mini-symposia and pre-nominated sessions. Their dedication in organising these sessions, and encouraging their colleagues to contribute, was a large contributing factor in the success of the congress. We must also thank the members of the nine national committees for the valuable and timely reviewing of submissions in their respective countries.

There are many people who contributed to an outstanding successful meeting and it my pleasure to formally acknowledge their contributions. First and foremost I must thank the local organising committee without whose efforts ICTAM2008 would not have been the success that it was. Thanks should also go to our Australasian Steering Committee whose support was fundamental in allowing the Australasian mechanics community to put forward such a compelling bid to IUTAM. Financial support for the Congress was provided by the Australian Mathematical Society, ANZIAM and the University of Adelaide. We are grateful for their support.

Many people contributed to the success of the congress and particular thanks go to our colleagues who contributed to the work of the local organising committee and without whose efforts ICTAM2008 would not have been the success it was. Thanks also go to members of the Australasian steering committee for their ongoing support. The journey that was ICTAM2008 began in the middle of 2001 when discussions within the Australian and New Zealand mechanics community first began as to the feasibility of putting forward a bid to IUTAM to host the 2008 International Congress of Theoretical and Applied Mechanics. This volume is the culmination of that journey. It presents selected papers from the sectional lectures as well as details of all papers presented at the meeting.

As with all large congresses the work behind the scenes, although vital for the smooth running of the conference, goes largely unheralded. In the case of ICTAM2008 much of this work was accomplished by Dr. Matt Finn who wrote all the support packages, including the website and the scheduling software, and introduced many innovations that have now become common at major international meetings.

Finally, it is with sadness that I thank and acknowledge the Congress President, Ernie Tuck who passed away in March 2009. This volume is dedicated to his memory.

Jim Denier

Congress Statistics

All contributed papers were peer reviewed. Recommendations had been received from Pre-selection Committees of the National Committees of the nine countries: Canada, France, Germany, Japan, PR China, Poland, Russia, UK and USA. Moreover, recommendations had been received from the Chairs of the Mini-Symposia and of the Pre-nominated Sessions. Finally, the International Papers Committee paid careful attention to the above recommendations. Accordingly, of the 1517 eligible submissions 1323 (87%) contributions were invited by the IPC for presentation at the Congress. Finally 901 contributed papers and 39 invited talks were given in Adelaide.

Fluid Mechanics was a subject of 550 presentations, Solid Mechanics was selected as a subject of 611 presentations, and 112 contributions aimed to cover problems involving both areas of mechanics and education in mechanics. The total number of participants, accepted papers and presentations for the past six congresses are shown in table 1. Despite the tyranny of distance often felt in Australasia attendance at ICTAM2008 was comparable to these most recent congresses. Table 2 displays country statistics of the presentations and table 3 details the number of presentations, both lecture and seminar, in each of the designated sessions at ICTAM2008.

Table 1 Comparison of the last 6 Congresses

ICTAM	Submitted Papers	Papers Presented	Participants
Grenoble 1988	1262	573	951
Haifa 1992	1183	420	525
Kyoto 1996	1642	703	936
Chicago 2000	1953	1126	1430
Warsaw 2004	2245	1273	1515
Adelaide 2008	1517	901	1176

Table 2 ICTAM2008 country statistics

	Country	Participants	Presentations	Invited Lectures
1	USA	143	126	8
2	Australia	141	110	1
3	China	110	96	0
4	France	86	79	2
5	Japan	81	73	0
6	Germany	68	61	0
7	UK	64	56	3
8	Russia	37	36	0
9	Poland	34	31	0
10	Taiwan	29	24	0
11	Denmark	25	20	0
12	Netherlands	25	23	0
13	India	21	21	1
14	South Korea	19	12	0
15	Italy	18	17	2
16	Canada	14	13	0
17	Sweden	13	10	0
18	Switzerland	11	9	0
19	Czech Republic	9	8	0
20	Israel	9	9	1
21	South Africa	9	7	0
22	Austria	8	7	0
23	Belgium	6	5	0
24	Brazil	6	5	0
25	New Zealand	6	5	0
26	Finland	5	4	0
27	Portugal	5	5	0
28	Spain	5	5	0
29	Ukraine	5	3	0
30	Estonia	4	4	0
31	Greece	4	3	0
32	Hong Kong	4	4	0
33	Hungary	4	4	0
34	Malaysia	4	3	0
35	Singapore	4	4	0
36	Georgia	2	1	0
37	Ireland	2	1	0
38	Kazakhstan	2	0	0
39	Latvia	2	2	0
40	Norway	2	2	0
41	Romania	2	0	0
42	Slovenia	2	2	0
43	Yugoslavia	2	2	0
44	Armenia	1	1	0
45	Belarus	1	0	0
46	Cyprus	1	1	0
47	Egypt	1	1	0
48	Iran	1	1	0
49	Jordan	1	1	0
50	Lebanon	1	1	0
51	Macau	1	1	0
52	Mexico	1	1	0
53	Thailand	1	1	0
54	Turkey	1	1	0
55	US MOI*	1	1	0
	TOTAL	1064	923	18

* US Minor Outlying Islands

Table 3 Session Statistics

Session	Lectures	Seminars	Total
Acoustics	8	1	9
Biomechanics	30	11	41
Boundary layers	12	7	19
Chaos and pattern formation in fluid and solid mechanics	7	3	10
Classical and quantum vortex rings	8	2	10
Cohesive zone models of fracture and failure	13	4	17
Combustion and flames	7	3	10
Complex and smart fluids	4	2	6
Compressible flow	7	2	9
Computational fluid dynamics	4	12	16
Computational solid mechanics	14	10	24
Contact and friction mechanics	7	7	14
Control of structures	6	2	8
Convection	8	6	14
Damage mechanics and fatigue	8	3	11
Drops, bubbles and multiphase flows	19	21	40
Education in mechanics	7	0	7
Elasticity	19	13	32
Experimental methods in solid mechanics	10	7	17
Flow control	6	2	8
Flow in thin films	14	1	15
Flow instability and transition	25	11	36
Fluid dynamics of animal swimming and flying	10	7	17
Fluid-structure interactions	12	13	25
Foams	6	0	6
Fracture and crack mechanics	20	11	31
Geophysical and environmental fluid dynamics	20	7	27
Geophysics and geomechanics	12	4	16
Granular materials and flows	14	0	14
Impact and wave propagation	15	18	33
Low-Reynolds-number flow	13	4	17
Magnetohydrodynamics	6	3	9
Material Instabilities	0	7	7
Mechanics of colloidal systems	10	3	13
Mechanics of composites	14	9	23
Mechanics of material processing	5	0	5
Mechanics of phase transitions	9	2	11

Table 3 *(continued)*

Mechatronics	6	3	9
Microfluidics	8	5	13
Microgravity fluid mechanics	6	5	11
Multi-component materials, modelling on different scales	17	7	24
Multibody and vehicle dynamics	20	7	27
Nanostructures and MEMS	7	10	17
Plasticity and viscoplasticity	17	2	19
Porous media	7	3	10
Solidification and crystal growth	5	3	8
Stability of structures	7	7	14
Stirring and mixing	10	0	10
Structural optimization	10	3	13
Structural vibrations	12	13	25
Turbulence	11	12	23
Viscoelasticity and creep	0	2	2
Waves	25	3	28

The IUTAM Bureau Prizes

As has been the tradition since the 1988 Congress in Grenoble the IUTAM Bureau selected 3 outstanding young scientists for Buerau prizes, based upon their papers, and their presentations at the Congress. The recipients of the prizes at ICTAM2008 were

Mr. Wim van Hoeve of the University of Twente, The Netherlands, for his paper entitled

Microbubble pinch-off in flow-focussing devices

presented during a Lecture (fluid mechanics)

Ms. Katia Bertoldi of Massachusetts Institute of Technology, USA, for her paper entitled

Mechanically-triggered transformations of pattern and phononic band gaps in periodic elastomeric structures

presented during a Lecture (solid mechanics)

Mr. Kazuya Shimizu of the The University of Tokyo, Japan, for his paper entitled

Study on the occurrence of the liquid yet and the bubble breakup in a convergent divergent channel flow

presented during a Seminar.

The Scientific Program

The following pages provide details of the content of the scientific program of the Congress. The program consists of plenary opening and closing lectures, sectional lectures, six mini symposia, and the predominated sessions devoted to all aspects of mechanics. Included in the program for this first time at ICTAM 2008 were the Batchelor Prize Lecture and the Rodney Hill Prize Lecture.

OL	Opening Lecture
CL	Closing Lecture
BL	Batchelor Prize Lecture
HL	Rodney Hill Prize Lecture
FL	Fluid Mechanics Sectional Lectures
SL	Solid Mechanics Sectional Lectures
FSL	Fluids and Solids Sectional Lectures

Mini Symposia

MS01	Cohesive zone models of fracture and failure
MS02	Multi-component materials, modelling on different scales
MS03	Mechatronics
MS04	Mechanics of colloidal systems
MS05	Classical and quantum vortex rings
MS06	Fluid dynamics of animal swimming and flying

Pre-Nominated Sessions on Fluid Mechanics

FM01	Boundary layers
FM02	Combustion and flames
FM03	Complex and smart fluids

FM04	Compressible flow
FM05	Computational fluid dynamics
FM06	Convection
FM07	Drops, bubbles and multiphase flows
FM08	Experimental methods in fluid mechanics
FM09	Flow control
FM10	Flow instability and transition
FM11	Flow in thin films
FM12	Geophysical and environmental fluid dynamics
FM13	Low-Reynolds-number flow
FM14	Magnetohydrodynamics
FM15	Microfluidics
FM16	Microgravity fluid mechanics
FM17	Solidification and crystal growth
FM18	Stirring and mixing
FM19	Turbulence
FM20	Waves

Pre-Nominated Sessions on Solid Mechanics

SM01	Computational solid mechanics
SM02	Contact and friction mechanics
SM03	Control of structures
SM04	Damage mechanics and fatigue
SM05	Elasticity
SM06	Experimental methods in solid mechanics
SM07	Fracture and crack mechanics
SM08	Geophysics and geomechanics
SM09	Impact and wave propagation
SM10	Material instabilities
SM11	Mechanics of composites
SM12	Mechanics of phase transitions
SM14	Multibody and vehicle dynamics
SM15	Nanostructures and MEMS
SM16	Plasticity and viscoplasticity
SM17	Stability of structures
SM18	Structural optimization
SM19	Structural vibrations
SM20	Viscoelasticity and creep

Topics Involving Both Fluid and Solid Mechanics

FSM01	Acoustics
FSM02	Biomechanics
FSM03	Chaos and pattern formation in fluid and solid mechanics
FSM04	Fluid-structure interactions
FSM05	Granular materials and flows
FSM06	Mechanics of material processing
FSM07	Porous media
FSM08	Education in mechanics
FSM09	Foams

The description of the session consists of the session ID, a descriptive name of the session (e.g. 'Chaos and pattern formation in fluid and solid mechanics') and the list chair (or co-chairs) of the session. The list of contributions then follows and are ordered as in the congress program.

OL :: Opening Lecture

Chair: Viggo Tvergaard (Denmark)

The role of mechanics in advancing thermal barrier coatings **10307**
John Hutchinson
Harvard University, USA

CL :: Closing Lecture

Chair: Ernest Tuck (Australia)

Physical limnology: advances and future challenges **10308**
Jorg Imberger
University of Western Australia, Australia

BL :: Batchelor Prize Lecture

Chair: Timothy Pedley (UK)

Interfaces: in fluid mechanics and across disciplines **12103**
Howard Stone
Harvard University, USA

HL :: Rodney Hill Prize Lecture

Chair: Bernhard Schrefler (Italy)

Nonconvex plasticity and deformation microstructures **12042**
Michael Ortiz
California Institute of Technology, USA

FL :: Fluid Mechanics Sectional Lectures

Chairs: Eberhard Bodenschatz (Germany), Jacques Magnaudet (France), Jean-Marc Vanden-Broeck (UK), Ross Griffiths (Australia) and André Thess (Germany)

Nonlinear transient growth on a vortex column **10310**
Fazle Hussain[†] and Dhoorjaty Pradeep
University of Houston, USA[†]

Bubbles in micro- and nano-fluidics **10311**
Detlef Lohse
University of Twente, Netherlands

Capillary constructions **10315**
David Quere
Ecole Supérieure Physique et de Chimi Industrielles, France

Indian Ocean Dipole and its possible link with climate modes **11053**
Toshio Yamagata
Japan Agency for Marine-Earth Science and Technology, Japan

Onset of oscillatory thermocapillary convection **10309**
Wenrui Hu
Chinese Academy of Sciences, China

The aerodynamics of wind turbines **10312**
Jens Sørensen
Technical University of Denmark, Denmark

FSL :: Fluids and Solids Sectional Lectures

Chairs: Dominique Barthès-Biesel (France), Tom Mullin (UK), Gary Leal (USA), Kaushik Bhattacharya (USA) and Patrick Huerre (France)

From dry granular flows to submarine avalanches **10017**
Olivier Pouliquen
Polytech Marseille, France

Biomechanical aspects in human reproduction **10471**
David Elad
Tel Aviv University, Israel

Material instabilities in elastic and plastic solids **10014**
Davide Bigoni
University of Trento, Italy

Cellular matter: interfacial mechanics and geometry **10015**
Sascha Hilgenfeldt
Northwestern University, USA

Instabilities of flows through deformable tubes and channels **10016**
Oliver Jensen
University of Nottingham, UK

SL :: Solid Mechanics Sectional Lectures

Chairs: Carl Herakovich (USA), Hans Muhlhaus (Australia), Nikita Morozov (Russia), Robert McMeeking (USA), Graham Weir (New Zealand) and Werner Schiehlen (Germany)

Self-healing materials systems: where mechanics meets chemistry **10319**
Nancy Sottos
University of Illinois at Urbana-Champaign, USA

Characterization of heterogeneous materials by multi-scale simulations **10061**
Peter Wriggers
University of Hannover, Germany

Failure of rocks in the laboratory and the Earth **10318**
John Rudnicki
Northwestern University, USA

Plasto-mechanics of large deformation under impact loading **10317**
Narinder Gupta
Indian Institute of Technology, Delhi, India

Maximal information systems **10013**
Hugh Durrant-Whyte
University of Sydney, Australia

Micro-architectured solids: from blast resistant structures to morphing wings **10316**
Norman Fleck
University of Cambridge, UK

FSL :: Fluids and Solids Sectional Lectures

Chairs: Dominique Barthès-Biesel (France), Tom Mullin (UK), Gary Leal (USA), Kaushik Bhattacharya (USA) and Patrick Huerre (France)

From dry granular flows to submarine avalanches **10017**
Olivier Pouliquen
Polytech Marseille, France

Biomechanical aspects in human reproduction **10471**
David Elad
Tel Aviv University, Israel

Material instabilities in elastic and plastic solids **10014**
Davide Bigoni
University of Trento, Italy

Cellular matter: interfacial mechanics and geometry **10015**
Sascha Hilgenfeldt
Northwestern University, USA

Instabilities of flows through deformable tubes and channels **10016**
Oliver Jensen
University of Nottingham, UK

MS01 :: Cohesive zone models of fracture and failure

Chairs: Thomas Siegmund (USA) and Alberto Carpinteri (Italy)

Modelling of bone failure by cohesive zone models: nano- and microscale **10081**
Thomas Siegmund
Purdue University, USA

Bridged and cohesive crack models for fracture in composite material systems **10123**
Roberta Massabò
University of Genova, Italy

Modelling strain localization by cohesive/overlapping zones in tension/compression: brittleness size effects and scaling in material properties **10511**
Alberto Carpinteri† and Marco Paggi
Politecnico di Torino, Italy†

Cohesive-zone modelling of adhesive joints **12034**
Michael Thouless
University of Michigan, USA

Fracture in confined thin films: a discrete dislocation study **11212**
Audrey Chng† and William Curtin
Institute of High Performance Computing, Singapore†

Length-scale dependency of crack tip fields under mode I loading **11985**
Lars Mikkelsen† and Stergios Goutianos
Technical University of Denmark, Denmark†

Direct extraction of rate-dependent traction-separations laws for polyurea/steel interfaces **10818**
Kenneth Liechti,† Krishnaswamy Ravi-Chandar and Yong Zhu
University of Texas at Austin, USA†

Micromechanics of elasto-damaging cohesive materials **10921**
Bernhard Pichler† and Luc Dormieux
LMSGC/ENPC/ParisTech and TU Wien, Austria†

A cohesive model coupling friction and adhesion for interfaces and fractures and applications **11327**
Michel Raous,† Yann Monerie, Mohamed Karray, Mathieu Schryve and Carole Henninger
Laboratory of Mechanics and Acoustics, CNRS, France†

General method for micromechanical based derivation of separation laws **11328**
Ingo Scheider
GKSS Research Centre, Germany

Simulation of delamination growth under high-cycle fatigue using cohezive-zone models **12185**
Albert Turon,† Pedro Camanho and Josep Costa
University of Girona, Spain†

Element-free Galerkin modelling of cohesive crack propagation in composite laminates **12134**
Brian Falzon,† Irene Guiamatsia and Glyn Davies
Monash University, Australia†

On measurement and modeling of interfacial behaviors between thin films and substrates using peel test **11330**
Yueguang Wei† and Haifeng Zhao
Chinese Academy of Sciences, China†

A mixed-mode constitutive damage model for multi-scale fracture analysis of composite structures **11279**
Anders Hansen† and Erik Lund
Aalborg University, Denmark†

A slip band based cohesive zone model for simulations of fatigue crack growth at sub-micron level **11291**
Xiaobo Yu,† Callum Wright and Manfred Heller
Defence Science and Technology Organisation, Australia†

Cohesive zone model for intergranular stress corrosion cracking in ceramics **11558**
Marc de la Osa,† Rafael Estevez, Christian Olagnon, Jérôme Chevalier, Christophe Tallaron and Lionel Vignoud
Université de Lyon, France†

Solution strategy for large three-dimensional composite structures with geometric and material instability under mixed-mode loading **11943**
Lars Overgaard,† Pedro Camanho and Erik Lund
Aalborg University, Denmark†

MS02 :: Multi-component materials, modelling on different scales

Chairs: Henryk Petryk (Poland) and Francis Rose (Australia)

Multi-scale analysis of polycristalline metals and composites **11332**
Jean-Louis Chaboche
ONERA, Châtillon, France

Modelling multi-scale damage evolution in composite materials **11727**
Brian Cox
Teledyne Scientific, USA

Instabilities across the scales **12133**
Hans Muhlhaus† and Louis Moresi
The University of Queensland, Australia†

Chemically driven inelastic deformation in materials with non-ideal sources and sinks for vacancies **10629**
Franz Fischer† and Jiri Svoboda
Montanuniversität Leoben, Austria†

An analysis of textile reinforced concrete structures on the micro, meso and macro scale **11164**
Bernd Zastrau,† Ingolf Lepenies and Mike Richter
Technische Universität Dresden, Germany†

Multiscale computing of CNTS fracture based on quasicontinuum/density functional theory hybridization **11753**
Jong Park,† Ki-Jeong Kong, Hyun Chang, Chan Park and Seyoung Im
Korean Advanced Institute of Science and Technology, South Korea†

Micromechanics of deformation of persulfonated polytetrafluoroethylene (Nafion) proton exchange membranes **11657**
Meredith Silberstein† and Mary Boyce
Massachusetts Institute of Technology, USA†

Constitutive description of plastic strain induced phenomena at cryogenic temperatures **10404**
Blazej Skoczen
Cracow University of Technology, Poland

Stresses in topologically interlocking structures: two scale approach **10134**
Arcady Dyskin,† Yuri Estrin, Elena Pasternak and David Yong
University of Western Australia, Australia†

Nonlinear dynamic response and self-sensing of functionally graded piezoelectric transducers **10429**
Fumio Narita,† Jun Nakagawa and Yasuhide Shindo
Tohoku University, Japan†

Evolution of the bonding mechanism of ZnO under isotropic compression: a first-principles study **11214**
Jinbin Wang,† Gongcheng Zhou, Lizhong Sun and Yichun Zhou
Xiangtan University, China†

Response of solids under electrical, magnetic, and mechanical loads **11292**
Su Hao,† Qian Wang, Leon Keer and John Ketterson
Northwestern University, USA†

Implicit constitutive modeling based on the energy principle **11427**
Hou Man,† Tomonari Furukawa and David Kellermann
University of New South Wales, Australia†

Crystal microstructure design of piezoelectric materials by multiscale finite element analysis **11444**
Yasutomo Uetsuji
Osaka Institute of Technology, Japan

Constitutive model of discontinuous plastic flow at cryogenic temperatures **11188**
Jan Bielski† and Blazej Skoczen
Cracow University of Technology, Poland†

Optimization and identification of multi-component materials in modelling on different scales **11881**
Tadeusz Burczynski† and Waclaw Kus
Silesian University of Technology, Poland†

Propagating modes of nano-scale periodic layers of solid-fluid composites **11071**
Chien-Cheng Chang† and Ying-Hong Liu
Academia Sinica, Taiwan†

A multiscale model for the sintering of air-plasma sprayed thermal barrier coatings **10568**
Alan Cocks† and Norman Fleck
University of Oxford, UK†

Multi-scale modeling of stress-induced microstructures in shape memory alloys **10509**
Henryk Petryk† and Stanislaw Stupkiewicz
Institute of Fundamental Technological Research, Poland†

Parametric study of strain hardening behaviour of glassy polymers using molecular simulations **12062**
Sumit Basu† and Dhiraj Mahajan
Indian Institute of Technology, Kanpur, India†

Ductile damage evolution in two-phase metallic materials applied at cryogenic temperatures. **10717**
Halina Egner† and Blazej Skoczen
Cracow University of Technology, Poland†

Multiscale models for multi-component structural energetic materials **11630**
Sathya Hanagud,† Rusi Zaharieva and Xia Lu
Georgia Institute of Technology, USA†

Inverse modelling to identify fibre hygroexpansion coefficient from experimental results of wood-fibre composites swelling **11458**
Karin Almgren,† Fredrik Berthold, Janis Varna and Kristofer Gamstedt
STFI-Packforsk AB, Sweden†

Constitutive model of plastic strain induced FCC–BCC phase transformation at cryogenic temperatures **11230**
Adam Wroblewski† and Blazej Skoczen
Cracow University of Technology, Poland†

MS03 :: Mechatronics

Chairs: Karl Hedrick (USA) and Heinz Ulbrich (Germany)

Trajectory planning for linearly-actuated elastic robots using flatness based control theory **10329**
Mathias Bachmayer† and Heinz Ulbrich
Technische Universität München, Germany†

Design and control of a novel type hybrid micromanipulator with piezoelectic actuators and vision feedback system **10756**
Daniel Prusak† and Tadeusz Uhl
AGH University of Science and Technology, Poland†

Classical mechanics and electromagnetism: a covariant view **11343**
Markus Schöberl† and Kurt Schlacher
Johannes Kepler University, Austria†

Friction discs: torsional slip control and radial dynamics **11806**
Alexander Fidlin
LuK GmbH & Co. oHG, Germany

Adaptive LQ controller for position control of machine tool axis **10993**
Petr Strakos,† Michael Valasek and Josef Bohm
Czech Technical University, Prague, Czech Republic†

New active mounting of machine tool feed drives **11380**
Jiri Sveda,† Michael Valasek and Zbynek Sika
Czech Technical University in Prague, Czech Republic†

Representation of hysteresis in discrete electro-magneto-mechanical systems **10682**
Andreas Mueller
Institut of Mechatronics, Germany

Analysis of with lower limb orthosis at sit to stand state **10777**
Dein Shaw,† Chi Huang and Li Huang
National Tsing Hua University, Taiwan†

Deformation and fracture behavior of ceramic-polymer ferroelectric nanocomposite film under uniaxial tension **11692**
Fei Fang,† Wang Zhe, Zhang Mingzhi and Yang Wei
Tsinghua University, China†

MS04 :: Mechanics of colloidal systems

Chairs: Dominique Langevin (France) and Peter Pusey (UK)

Single particle motion in colloids: from microrheology to osmotic propulsion **12131**
John Brady
California Institute of Technology, USA

Colloidal chemo-mechanics of engineering materials: clays, earth and cement **12123**
Henri Van Damme
Ecole Supérieure Physique et de Chimi Industrielles, France

Colloids and microfluidics **12122**
David Weitz
Harvard University, USA

The hydrodynamics of self-propelled suspensions **12125**
Sriram Ramaswamy
Indian Institute of Science, India

Liquid crystalline elastomers and magnetic gels: similarities and differences in their physical properties **11803**
Harald Pleiner,† Stefan Bohlius, Andreas Menzel, Helmut Brand and Philippe Martinoty
Max Planck Institute for Polymer Research, Germany†

On the origin of the remarkable stability of aqueous foams **10513**
Dominique Langevin,† Alfredo Martinez, Emmanuelle Rio, Giles Delon, Arnaud Jalmes and Bernard Binks
Université Paris Sud, France†

Self-assembly of particles for 2D lattices with adaptable spacing **10531**
Nadine Aubry,† Sai Nudurupati, Mohammad Janjua and Pushpendra Singh
Carnegie Mellon University, USA†

Microfluidic colloidal island self-assembly and erasure induced by surface acoustic waves: I. experiments **10648**
Leslie Yeo,† James Friend and Haiyan Li
Monash University, Australia†

Cross-stream migration of colloidal particles in confined flows **11718**
Peter Daivis,† Tanya Kairn and Ian Snook
RMIT University, Australia†

Hydrodynamic crystals: collective dynamics of regular arrays of spherical particles in a parallel-wall channel **11418**
Eligiusz Wajnryb† and Jerzy Blawzdziewicz
Institute of Fundamental Technological Research, PAS, Poland†

Consolidation of colloidal particles during drying **11660**
Arijit Sarkar,† Raj Rajagopalan and Mahesh Tirumkudulu
Indian Institute of Technology, Bombay, India†

Memories in paste of flow and vibration: their visualizations as crack patterns **10415**
Akio Nakahara† and Yousuke Matsuo
Nihon University, Japan†

Microfluidic colloidal island self-assembly and erasure induced by surface acoustic waves: II. dynamic analysis **10671**
James Friend,† Leslie Yeo and Haiyan Li
Monash University, Australia†

The effect of temperature on strain wave superstructures on two-dimensional colloidal crystals with confinement: a Monte Carlo study **10909**
David Chui,† Surajit Sengupta and Kurt Binder
Johannes-Gutenberg University of Mainz, Germany†

MS05 :: Classical and quantum vortex rings

Chairs: Hassan Aref (Denmark) and Carlo Barenghi (UK)

Classical vortex rings, with and without swirl **10736**
Keith Moffatt
Cambridge University, UK

Vortices in quantum fluids **10149**
Natalia Berloff
University of Cambridge, UK

Quantum fluid questions suggested by phenomena in classical fluids **10139**
Karim Shariff
NASA Ames Research Center, USA

Vortex rings and their use **10152**
Carlo Barenghi
University of Newcastle, UK

Relative equilibria of point vortices **10034**
Hassan Aref† and Rasmus Hansen
Danish Technical University, Denmark†

Alignment of strain and vorticity in vortex interactions **11159**
Robert Kerr† and Miguel Bustamante
University of Warwick, UK†

Motion of vortex rings with and without magnetic field **11581**
Yasuhide Fukumoto,† Keith Moffatt and Satoshi Ooshiro
Kyushu University, Japan†

Curvature instability of a vortex ring and a helical vortex tube **11696**
Yuji Hattori† and Yasuhide Fukumoto
Kyushu Institute of Technology, Japan†

Vortex ring chain due to the periodic motion of a sphere **11004**
Viatcheslav Meleshko,† Russell Donnelly, Diogo Bolster and Alexandre Gourjii
Kiev National University, Ukraine†

The effect of a uniform cross-flow on the circulation of vortex rings **11269**
Eyad Hassan,† Richard Kelso and Peter Lanspeary
The University of Adelaide, Australia†

Global time evolution of an axisymmetric vortex ring at small Reynolds numbers **10655**
Felix Kaplanski† and Yasuhide Fukumoto
Tallinn University of Technology, Estonia†

MS06 :: Fluid dynamics of animal swimming and flying

Chairs: John Blake (UK) and Jane Wang (USA)

How insects fly **10516**
Jane Wang
Cornell University, USA

Fish swimming dynamics: knowns and unknowns **11744**
Daniel Weihs
Technion, Israel

Understanding swimming at low Reynolds numbers: successes and challenges **12106**
Lisa Fauci
Tulane University, USA

The effect of body cross-sectional shape on glide force production in 'flying' snakes **11862**
John Socha,† Michael LaBarbera and Kevin Miklasz
Virginia Tech, USA†

Fluid-dynamic effects of both rigid and free boundaries on the swimming of singly flagellated bacteria **11370**
Tomonobu Goto,† Tonau Nakai, Masayuki Kikuda and Yuichiro Kuroda
Tottori University, Japan†

Instability of uniform suspensions of swimming micro-organisms **10330**
Timothy Pedley
University of Cambridge, UK

Scaling of wake energy and propulsive efficiency of two representative jellyfish species: Aurelia and Mastigias **10901**
Kakani Katija† and John Dabiri
California Institute of Technology, USA†

Optimal flexibility of a flapping appendage at high Reynolds number **11133**
Silas Alben
Georgia Institute of Technology, USA

Fluid dynamic simulation of human sperm accumulation near to surfaces **10517**
John Blake,† Jackson Kirkman-Brown, Eamonn Gaffney and David Smith
University of Birmingham, UK†

Linked bodies swimming through a free surface **11092**
Jules Kajtar† and Joe Monaghan
Monash University, Australia†

The upstream wake of swimming and flying animals and its correlation with propulsive efficiency **11675**
Jifeng Peng† and John Dabiri
California Institute of Technology, USA†

Analysis of ciliary gliding in freshwater planarians **10078**
Takeshi Sugimoto
Kanagawa University, Japan

Experimental comparison of a steady and unsteady self-propelled swimmer **11087**
Lydia Trevino† and John Dabiri
California Institute of Technology, USA†

A force element theory with applications to insect flight **11396**
Chin-Chou Chu,† Chien-Cheng Chang and Cheng-Ta Hsieh
National Taiwan University, Taiwan†

A biomimetic figure-of-eight flapping induced by flexible wings **11473**
Lung-Jieh Yang† and Cheng-Kuei Hsu
Tamkang University, Taiwan†

Robustness of an insect's hovering: a transition of flapping free-flight **11474**
Makoto Iima
Hokkaido University, Japan

The fluid mechanical basis of jellyfish feeding and the effects of prey size and escape forces **12129**
Madeline Miller,† Jifeng Peng and John Dabiri
California Institute of Technology, USA†

The dynamics of a fish inspired unsteady hydrofoil **11018**
Timothy Lau† and Richard Kelso
The University of Adelaide, Australia†

Intermittency in marine organisms swimming behaviour **12006**
Laurent Seuront
Flinders University, Australia

FM01 :: Boundary layers

Chairs: Kevin Cassel (USA) and Alfred Kluwick (Austria)

Characterising hairpin vortex packets in a low Reynolds number turbulent boundary layer **10072**
Chong Wong,† Shuo Li and Julio Soria
CSIRO, Australia†

Wind-tunnel studies on global unsteadiness of laminar separation bubbles **10746**
Alexander Dovgal,† Alexander Sorokin and Victor Kozlov
Institute of Theoretical and Applied Mechanics SB RAS, Russia†

Experimental investigation of coherent structure dynamics in the outer layer of a turbulent boundary layer **11223**
Gerrit Elsinga,† Fulvio Scarano, Andreas Schroeder, Reinhard Geisler, Christian Poelma and Jerry Westerweel
Delft University of Technology, Netherlands†

Bursting phenomena of boundary layer induced by 2D vortex patch **11232**
Henryk Kudela† and Ziemowit Malecha
Wroclaw University of Technology, Poland†

Mixed convection boundary layer flow from a vertical stretching sheet in a thermally stratified micropolar fluid **11263**
Roslinda Nazar,† Anuar Ishak and Ioan Pop
National University of Malaysia, Malaysia†

A comparison of internal and external turbulent boundary layers **11667**
Nicholas Hutchins,† Ivan Marusic, Min Chong and Jason Monty
University of Melbourne, Australia†

Series solution of non-similarity boundary-layer flows of non-Newtonian fluids **11104**
Shijun Liao,† Xiangchen You and Hang Xu
Shanghai Jiao Tong University, China†

Influence of dimpled surfaces on drag reduction in turbulent channel flows **11793**
Ahmed Al-Salaymeh† and Franz Durst
German Jordanian University, Jordan†

Bifurcation phenomena in incompressible laminar ramp flow **10484**
Alfred Kluwick,† Rene Szeywerth and Stefan Braun
Vienna University of Technology, Austria†

Boundary-layer breakdown in a rotating, fluid-filled torus **10446**
Richard Clarke,† Richard Hewitt, Carlos del Pino, Jim Denier and Tom Mullin
University of Auckland, New Zealand†

On unsteady boundary-layer separation in supersonic flow **11822**
Anatoly Ruban
The University of Manchester, UK

Transient growth induced by surface roughness in a Blasius boundary layer **12158**
Philippe Lavoie,† Jonathan Morrison and Ahmed Naguib
University of Toronto, Canada†

The turbulent shear stress in zero pressure gradient boundary layers **11041**
Peter Monkewitz,† Kapil Chauhan and Hassan Nagib
Swiss Federal Institute of Technology, Switzerland†

Boundary-layer separation and vortex generation in a suddenly blocked pipe **10028**
Jim Denier† and Nathaniel Jewell
The University of Adelaide, Australia†

On the relationship between large- and small-scale motions in turbulent boundary layers **11734**
Romain Mathis,† Nicholas Hutchins and Ivan Marusic
University of Melbourne, Australia†

A high Reynolds number turbulent boundary layer with regular roughness **11746**
Jason Monty,† James Allen and Min Chong
The University of Melbourne, Australia†

Non-universality of overlap region in turbulent pipe and channel flows **10437**
Hassan Nagib,† Peter Monkewitz and Kapil Chauhan
Illinois Institute of Technology, USA†

Sub-optimal control of unsteady boundary-layer separation in a channel with suction **10482**
Kevin Cassel† and Chetan Sardesai
Illinois Institute of Technology, USA†

Towards simulations of high-Reynolds number turbulent boundary layers **11282**
Philipp Schlatter,† Dan Henningson, Arne Johansson, Geert Brethouwer and Qiang Li
KTH Royal Institute of Technology, Stockholm, Sweden†

Pipe flow turbulence in the presence of roughness **10729**
Alexander Smits,† Marcus Hultmark, Sean Bailey, Michael Schultz and Richard Pepe
Princeton University, USA†

FM02 :: Combustion and flames

Chairs: Sebastien Candel (France) and Ishwar Puri (USA)

A mechanistic model for the catalytic growth of carbon nanotubes and their combustion synthesis **10486**
Ishwar Puri† and Sayangdev Naha
Virginia Tech, USA†

Characteristics of flow behaviors behind rifled nozzles **11740**
Kuo-Ching San† and Hong-Jzen Hsu
Air Force Institute of Technology, Taiwan†

Thermal structures and combustion efficiency of non-premixed reacting rifled nozzles **11743**
Shun-Chang Yen† and Hong-Jzen Hsu
National Taiwan Ocean University, Taiwan†

OH-PLIF visualisation of radical farming supersonic combustion flows **12031**
Russell Boyce
University of Queensland, Australia

The response of inverted flames to equivalence ratio modulations **10485**
Sebastien Candel,† Sebastien Ducruix, Anne-Laure Birbaud and Daniel Durox
Ecole Centrale Paris, France†

The effects of turbulence, hot spots, and stochasticity on the deflagration-to-detonation transition **10997**
Elaine Oran,† Vadim Gamezo and Takanobu Ogawa
US Naval Research Laboratory, USA†

Detonation structure for chain-branching kinetics: an analysis in the small initiation rate Limit **11090**
Luc Bauwens,† Josue Meguizo-Gavilanes and Laurie Bedard-Tremblay
University of Calgary, Canada†

Temporally resolved pseudo-3D measurements of turbulent flame interactions using orthogonal-plane cinema-stereoscopic PIV **11599**
Adam Steinberg,† James Driscoll and Steven Ceccio
University of Michigan, USA†

Behaviour of stability limits of non-premixed jet flames in a co-flowing air stream **12121**
Teresa Leung† and Ida Wierzba
University of Calgary, Canada†

Numerical optimization of shock to detonation transition by using shaped tubes **10222**
Ilya Semenov,† Vladimir Markov, Ildar Ahmedyanov and Pavel Utkin
Institute for Computer Aided Design, RAS, Russia†

FM03 :: Complex and smart fluids

Chairs: Alexander Yarin (USA) and Oliver Harlen (UK)

Coarse-graining hydrodynamic interactions in isolated polymer molecules in solution **10524**
Prabhakar Ranganathan
Monash University, Australia

Turbulence structures in turbulent boundary layer flows of cationic and non-ionic surfactant solutions **11752**
Motoyuki Itoh,† Shinji Tamano, Katsuo Kato and Kazuhiko Yokota
Nagoya Institute of Technology, Japan†

Yielding behaviour without an explicit yield stress for soft materials **10230**
Roger Tanner
University of Sydney, Australia

Jet breakup of polymeric fluids **10365**
Oliver Harlen† and Srinivas Yarlanki
University of Leeds, UK†

Drop impact of yield-stress fluids **10849**
Li-Hua Luu† and Yoël Forterre
University of Provence, France†

The dynamics of visco-elastic bridges in drop coalescence **10955**
Aleksey Rozhkov,† Theo Theofanous and Vladimir Mitkin
Institute for Problems in Mechanics, RAS, Russia†

FM04 :: Compressible flow

Chairs: Piotr Doerffer (Poland) and Holger Babinsky (UK)

Schlieren visualisation of rocket nozzle exhaust flow **11354**
Yvette McPhail,† Neil Mudford, Sean O'Byrne, Harald Kleine, Andrew Neely, Eddie Leonardi and Tracie Barber
University of New South Wales, Australia†

The aerodynamics of aerofoils and wings in transonic ground effect **11529**
Graham Doig,† Tracie Barber, Andrew Neely and Eddie Leonardi
University of New South Wales, Australia†

The von Neumann paradox for strong shock reflection **10691**
Susumu Kobayashi,† Takashi Adachi and Tateyuki Suzuki
Saitama Institute of Technology, Japan†

Experimental investigation of tripping between regular and Mach reflection in the dual-solution domain **10855**
Hans Hornung† and Christopher Mouton
California Institute of Technology, USA†

Shock regularisation in dense gases by viscous inviscid interaction **10889**
Georg Meyer† and Alfred Kluwick
Vienna University of Technology, Austria†

Shock wave reflection from curved surfaces **11180**
Beric Skews,† Harald Kleine, Christiaan Bode and Sebastian Gruber
University of the Witwatersrand, South Africa†

Low frequency unsteadiness in shock induced separated flows **11242**
Sébastien Piponniau,† Jean-François Debiève, Jean-Paul Dussauge and Pierre Dupont
Université de Provence, France†

Experiments on supersonic cavity flows with passive control **11792**
Sudhir Gai,† Pierre Naviaux and Harald Kleine
University of New South Wales, Australia†

European research on unsteady effects of shock wave induced separation: UFAST project **12120**
Jean-Paul Dussauge
France

FM05 :: Computational fluid dynamics

Chairs: John Kim (USA) and Wolfgang Schröder (Germany)

ALE-multigrid fictitious boundary method for Navier–Stokes equations with free moving solid boundaries **10213**
Decheng Wan
Shanghai Jiao Tong University, China

Numerical simulation of ice accretion on airfoils **10411**
Yihua Cao,† John Sheridan and Qiang Zhang
Beijing University of Aeronautics and Astronautics, China†

RANS prediction of free surface effects on the drag coefficient of an underwater hull form **10742**
Jagadeesh Putta
The University of Western Australia, Australia

Operator-splitting scheme for a Bingham fluid in a cavity flow **11353**
Zhenjiang You† and Raja Huilgol
Flinders University, Australia†

Adaptive finite element simulation of self-patterning phase decomposition **11871**
Roy Stogner† and Graham Carey
University of Texas at Austin, USA†

Laminar displacement of viscoplastic fluids in eccentric annuli: numerical simulation and experimental validations **11524**
Dzuy Nguyen,† Jeffery Liew, Thana Deawwanich, Wilson Chin, Peng Tonmukayakul and Mark Savery
The University of Adelaide, Australia†

DES simulations of the unsteady flow field around the Stratospheric Observatory for Infrared Astronomy **11088**
Sven Schmid,† Thorsten Lutz and Ewald Krämer
University of Stuttgart, USA†

Consistency in symmetry for numerical schemes **11143**
Marx Chhay,† Aziz Hamdouni and Pierre Sagaut
La Rochelle University, France†

Effect of inverted aerofoil geometry on aerodynamic performance in ground effect **11294**
Jonathan Vogt,† Eddie Leonardi and Tracie Barber
The University of New South Wales, Australia†

Shear viscosity along the freezing line of Weeks–Chandler–Andersen fluid **11415**
Alauddin Ahmed† and Richard Sadus
Swinburne University of Technology, Australia†

Inverse radiative problem with natural convection phenomenon **11298**
Yun Hong† and Seung Baek
Korea Advanced Institute of Science and Technology, South Korea†

A material interface transition algorithm for multiphase flow simulation **10079**
Marianne Francois,† Edward Dendy and Robert Lowrie
Los Alamos National Laboratory, USA†

Molecular simulation of shearing dense hyperbranched polymer fluids **10983**
Tu Le,† Alfred Uhlherr, Peter Daivis and Billy Todd
Swinburne University of Technology, Australia†

Simulation of atomizing jets with OCT-tree adaptive mesh refinement **11848**
Stephane Zaleski,† Anne Bagué, Daniel Fuster, Luis Lemoyne and Stéphane Popinet
Universite Pierre & Marie Curie, France†

A dynamic wall model constrained by external Reynolds stress **11879**
Krishnan Mahesh† and Noma Park
University of Minnesota, USA†

Modelling the wall roughness for RANS and LES using the discrete element method **11484**
Franco Magagnato,† Stefan Bühler and Martin Gabi
University of Karlsruhe, Germany†

FM06 :: Convection

Chairs: John Patterson (Australia) and André Thess (Germany)

Boundary layer structure in highly turbulent Rayleigh–Bénard convection **10834**
Ronald du Puits,† Christian Resagk and André Thess
Ilmenau University of Technology, Germany†

Scaling of the local convective heat flux in turbulent Rayleigh–Bénard convection **10938**
Penger Tong,† Ke-Qing Xia and Xiao-dong Shang
Hong Kong University of Science & Technology, Hong Kong†

Stability of buoyancy and surface-tension driven convection in a horizontal double-diffusive layer **10418**
Chuan Chen† and Cho Chan
University of Arizona, USA†

On thermal plumes in convective turbulence **10007**
Ke-Qing Xia,† Chao Sun and Quan Zhou
The Chinese University of Hong Kong, Hong Kong†

Heat and mass transfer features in magneto-polarized colloids **11362**
Alexandra Bozhko,† Gennady Putin and Yury Bratukhin
Perm State University, Russia†

Effect of the magnetic field on the flow inside droplet on a substrate **10764**
Masayuki Kaneda,† Toshio Tagawa and Jun Fukai
Kyushu University, Japan†

Direct numerical simulation of forced convection heat transfer from two staggered circular cylinders **10462**
Sirod Sirisup† and Saifhon Tomkratoke
National Electronics and Computer Technology Center, Thailand†

Two-dimensional thermal convection in a parallelogram-shaped cavity with tilted sidewalls **10819**
Yoshinari Fukazawa† and Mitsuaki Funakoshi
Kyoto University, Japan†

Temperature derivatives and thermal dissipation in turbulent Rayleigh–Bénard convection **11072**
Joerg Schumacher† and Mohammad Emran
Technische Universität Ilmenau, Germany†

Unsteady natural convection in a differentially heated partitioned cavity **11694**
Feng Xu,† John Patterson and Chengwang Lei
James Cook University, Australia†

Bifurcations in convection of incompressible fluid in a rotated square cylinder **10183**
Sergey Suslov† and Albert Sharifulin
University of Southern Queensland, Australia†

Viscous boundary layer measurement in turbulent thermal convection **11401**
Chao Sun,† Ke-Qing Xia and Yin-Har Cheung
University of Twente, Netherlands†

Unsteady natural convection in a reservoir model subject to periodic heating and cooling at the water surface **10773**
Tomasz Bednarz,† Chengwang Lei and John Patterson
James Cook University, Australia†

Unsteady jet impingement: a systematic study of its heat transfer performance **11200**
Heinz Herwig† and Georg Middelberg
Hamburg University of Technology, Germany†

Bounds for global stability of mixed convection in a channel **10264**
Saravanan Shanmugam† and Brindha Durairaj
Bharathiar University, India†

FM07 :: Drops, bubbles and multiphase flows

Chairs: Jacques Magnaudet (France) and Andrea Prosperetti (USA)

Turbulent sediment suspension and particle-fluid coupling in oscillating flows under ripple-bed conditions **11078**
Ken Kiger,† Philip Knowles, Alberto Scotti and Bong Chung
University of Maryland, USA†

Shock fluidization of solids and liquids **12142**
Vladimir Mitkin,† Theo Theofanous and Chee-Loon Ng
University of California, Santa Barbara, USA†

Particle spin in rotating and shearing flows **11456**
Johanna Bluemink,† Leen van Wijngaarden and Andrea Prosperetti
University of Twente, Netherlands†

Motion of bubbles in aqueous surfactant solutions **11481**
Yoichiro Matsumoto,† Masato Fukuta and Shu Takagi
The University of Tokyo, Japan†

Bubble resonance frequencies as a function of pressure **10159**
Richard Manasseh,† Ilija Sutalo, Andrew Ooi, Kurt Liffman, Suhith Illesinghe and Ben Aldham
CSIRO, Australia†

Rheological properties of suspensions of noncolloidal particles in yield stress fluids **10166**
Xavier Chateau,† Guillaume Ovarlez and Fabien Mahaut
Navier Institut, France†

Air cushioning and bubble entrapment in three dimensional droplet impact **11596**
Peter Hicks† and Richard Purvis
University of East Anglia, UK†

Interaction of gaseous bubbles under the action of radiation modified Bjerknes force **11140**
Yury Stepanyants† and Guan Yeoh
Australia Nuclear Science and Technology Organisation, Australia†

Towards efficient modeling of cavitation erosion potential in pumps **11144**
Patrik Zima,† Milan Sedlar and Frantisek Marsik
Academy of Sciences, Czech Republic†

Surface profiles of collapsing cavities of splash drops **11521**
Jong-Leng Liow† and David Cole
University of New South Wales Australian Defence Force Academy, Australia†

Dependence of saturated vapor pressure and surface tension coefficient on radius for an argon nano-droplet **11372**
Shigeo Fujikawa,† Hisao Yaguchi and Takeru Yano
Hokkaido University, Japan†

Oscillation frequency and deformation of levitated droplets **11526**
Tadashi Watanabe
Japan Atomic Energy Agency, Japan

An investigation of droplets impinging on liquid film **11536**
Jiahong Guo,† Hongxun Chen and Shiqiang Dai
Shanghai University, China†

The zipping wetting dynamics at the breakdown of superhydrophobicity **11561**
Peichun Tsai,† Mauro Sbragaglia, Christophe Pirat, Alisia Peters, Bram Borkent, Rob Lammertink, Matthias Wessling and Detlef Lohse
University of Twente, Netherlands†

Simulation of elastic objects in viscous fluid flows **11590**
Howard Hu
University of Pennsylvania, USA

A theoretical growth model for dynamic slugs in gas/liquid horizontal pipes **10385**
Usama Kadri,† Rene Oliemans and Robert Mudde
Delft University of Technology, Netherlands†

The effect of shear on the size distribution in concentrated vesicle suspensions **10882**
Gary Leal† and Arun Ramachandran
University of California, Santa Barbara, USA†

The impulsive generation of drops at a fluid-fluid interface **11168**
William Phillips† and Kuan-Khoon Tjan
Swinburne University of Technology, Australia†

Microbubble pinch-off in flow-focusing devices **11548**
Wim van Hoeve,† Benjamin Dollet, Chao Sun, Detlef Lohse and Michel Versluis
University of Twente, Netherlands†

Direct numerical simulation of interface turbulence interaction **10630**
Jean-Luc Estivalezes,† Pierre Trontin, Stephane Vincent and Jean-Paul Caltagirone
ONERA, France†

Study on the occurrence of the liquid jet and the bubble breakup in a convergent divergent channel flow **11797**
Kazuya Shimizu,† Kazuhiro Hashiguchi, Rie Tachibana, Shintaro Takeuchi, Shu Takagi and Yoichiro Matsumoto
The Univeristy of Tokyo, Japan†

Binary droplet collision at high impact **11902**
Kuo-Long Pan† and Ping-Chung Chou
National Taiwan University, Taiwan†

Effects of interfacial waves on turbulent mass transfer in a open channel flow **11953**
Yosuke Hasegawa† and Nobuhide Kasagi
The University of Tokyo, Japan†

Micromechanics of gas filled microballoons **11390**
Paulo Fernandes,† Andreas Fery, Rainer Fink and George Tzvetkov
Bayreuth University, Germany†

Inclined drop impact onto a curved surface **11874**
Ilia Roisman,† Shamit Bakshi and Cameron Tropea
Technische Universität Darmstadt, Germany†

Foam films of pure liquids **12201**
Satomi Onishi† and Vassili Yaminsky , *Australia*†

On the formation and cavity dynamics of big floating bubble by drop impact onto liquid pool **11818**
Chen-Chi Kuan,† An-Bang Wang and Fei-Yau Lu
National Taiwan University, Taiwan†

New types of a single bubble motions in dilute surfactant solution **11745**
Yoshiyuki Tagawa,† Yoichiro Matsumoto, Ami Funakubo and Shu Takagi *University of Tokyo, Japan*†

Submerged gas jet interface stability **11872**
Chris Weiland,† Jon Yagla and Pavlos Vlachos
Virginia Tech, USA†

Memory-encoding shape vibrations in a disconnecting air bubble **11645**
Wendy Zhang,† Sidney Nagel, Nathan Keim and Laura Schmidt
University of Chicago, USA†

Geometric confinement suppresses jet break-up in microfluidic channels **11445**
Katherine Humphry,† David Weitz, Howard Stone, Alberto Fernández-Nieves and Armand Ajdari
Harvard University, USA†

Discontinuous flow in the thinning process of viscoelastic filaments **11514**
Christian Wagner,† Rainer Sattler and Jens Eggers
Universitaet des Saarlandes, Germany†

Impact of drops of complex liquids on a small target **11579**
Michele Vignes-Adler,† Bernard Prunet-Foch and Aleksey Rozhkov
Université Paris Est, France†

Translational dynamics of an acoustically coupled microbubble pair in an ultrasound field **11658**
Michel Versluis,† Valeria Garbin, Benjamin Dollet, Leen van Wijngaarden, Nico de Jong and Detlef Lohse
University of Twente, Netherlands†

Bubble/microcantilever interactions in a confined channel **11668**
Ellen Longmire,† Matthew Stegmeir and Susan Mantell
University of Minnesota, USA†

Direct simulation of unsteady three-dimensional core-annular flows with high viscosity ratio **11857**
Jie Li
University of Cambridge, UK

Interaction of a shock wave with multiple gas bubbles in water **11627**
Stephen Shaw,† Omar Matar and Peter Spelt
Imperial College London, UK†

Liquid effects on the unsteady motion of a collision-dominant solid-liquid flow: experimental investigations and DEM simulations using a 'wet' collision model **11441**
Fu-Ling Yang,† Chen-Shan Chen, Shang-Hsien Hsieh and Wei-Tze Chang
National Taiwan University, Taiwan†

Evolution of neutral and charged drops in an electric field **11636**
Ultano Kindelan† and Marco Fontelos
Universidad Politécnica de Madrid, Spain†

Electrophoresis of gas bubbles **10954**
John Harper
Victoria University of Wellington, New Zealand

FM08 :: Experimental methods in fluid mechanics

Chairs: Cameron Tropea (Germany) and Jerry Westerweel (Netherlands)

Delta surface hot-wires as a means of measuring wall shear stresses at arbitrary flow directions **11757**
Christoph Dobriloff† and Wolfgang Nitsche
Berlin University of Technology, Germany†

Lorentz force velocimetry: theory and practice **10493**
André Thess,† Vitaly Minchenya, Yurii Kolesnikov and Christian Karcher
Ilmenau University of Technology, Germany†

Measurement of unsteady surface forces by means of pressure sensitive copolymer coatings **11609**
Jan Domhardt,† Wolfgang Nitsche, Inken Peltzer and Janin Leuckert
Berlin University of Technology, Germany†

Global Doppler imaging with near-resonant interferometry **10898**
Andrin Landolt† and Thomas Roesgen
ETH Zurich, Switzerland†

Control of the depth of correlation in micro-PIV using a novel post-processing method **11702**
Chuong Nguyen,† Josie Carberry and Andreas Foudras
Monash University, Australia†

Pressure and temperature measurements of supersonic microjet impingement **11923**
Chihyung Huang,† John Sullivan and James Gregory
Purdue University, USA†

Experimental study of lid driven cavity flow in the Lagrangian frame of reference **10591**
Reut Elfassi† and Alexander Liberzon
Tel Aviv University, Israel†

Optically interrogated MEMS pressure sensor array **11387**
Lukas Prochazka† and Thomas Roesgen
ETH Zuerich, Switzerland†

Planar imaging measurements of molecular transport effects in turbulent mixing **11840**
Lester Su† and Cody Brownell
Johns Hopkins University, USA†

An efficient correction for the finite-size effects of multihole pressure probes in velocity gradients **10383**
Valery Chernoray† and Johan Hjärne
Chalmers University of Technology, Sweden†

Measurements of the dynamic wall-shear stress distribution in turbulent flows using the micro-pillar sensor MPS^3 **10656**
Sebastian Grosse† and Wolfgang Schröder
RWTH Aachen University, Germany†

Heterodyne Doppler global velocimetry **11117**
Alexander Meier† and Thomas Rösgen
ETH Zurich, Switzerland†

Large spatial dynamic range measurements of a turbulent boundary layer and the velocity gradient tensor using tomographic PIV **12137**
Craig Dillon-Gibbons,† Callum Atkinson and Julio Soria
Monash University, Australia†

FM09 :: Flow control

Chairs: Avi Seifert (Israel) and Jonathan Morrison (UK)

Flow control by turbulence state modifications in the near-wall region **11064**
Bettina Frohnapfel,† Peter Lammers, Yosuke Hasagawa and Nobuhide Kasagi
The University of Tokyo, Japan†

Optimization of the dynamic properties of compliant coating **11969**
Inwon Lee,† Victor Kulik, Andrey Boiko and Ho Chun
Pusan National University, South Korea†

Estimation of the potential of a flow-control experiment by system identification **11787**
Fredrik Lundell
Linné Flow Centre, Sweden

Wake flow manipulation by means of blowing or suction **11810**
Jens Fransson† and Bengt Fallenius
Linné Flow Centre, Sweden†

Optimal control of vortex systems **11904**
Bartosz Protas
McMaster University, Canada

Active control of flow with trapped vortices **10399**
Owen Tutty,† Ruslan Kerimbekov and Eric Rogers
University of Southampton, UK†

Low-order estimation and modeling of transient growth in a laminar boundary layer **10498**
Jonathan Morrison† and Ahmed Naguib
Imperial College London, UK†

Synchronized force and PIV measurements on an electromagnetically forced separated flow **11600**
Christian Cierpka,† Tom Weier and Gunter Gerbeth
Forschungszentrum Dresden-Rossendorf, Germany†

FM10 :: Flow instability and transition

Chairs: Jean-Marc Chomaz (France) and Dan Henningson (Sweden)

The inviscid Rayleigh–Taylor instability **10772**
Larry Forbes
University of Tasmania, Australia

A new instability in thermal boundary layers **11260**
Jianjun Tao† and Friedrich Busse
Peking University, China†

Wake structures behind a rolling sphere on a wall **11352**
Bronwyn Stewart,† Thomas Leweke, Mark Thompson and Kerry Hourigan
Monash University, Australia†

Computation of convective instability in complex geometry flows **10291**
Hugh Blackburn,† Dwight Barkley and Spencer Sherwin
Monash University, Australia†

Effect of surface roughness on the laminar–turbulent transition in channel flow **10368**
Jerzy Floryan† and Masahito Asai
University of Western Ontario, Canada†

Secondary instability of variable-density jets **10499**
Jean-Marc Chomaz,† Joseph Nichols and Peter Schmid
Centre National de la Recherche Scientifique École Polytechnique, Palaiseau, France†

Convective and absolute instability of two miscible fluid core-annular flow **10372**
Dominique Salin,† Nicole Rakotomalala, Jerome Martin, Marguerite d'Olce and Laurent Talon
Universite Pierre & Marie Curie, France†

Transition to turbulence in a pipe *Tom Mullin* **10578**
University of Manchester, UK

Transitional plane Couette flow: an alternative to the low-dimensional dynamical system approach **10880**
Paul Manneville
Ecole Polytechnique, France

The strato-rotational instability with and without boundaries: application to Keplerian flows **11197**
Stéphane Le Dizès
Centre National de la Recherche Scientifique, France

Global low-frequency oscillations in a separated boundary layer **11226**
Francois Gallaire† and Uwe Ehrenstein
Laboratoire J.-A. Dieudonné, France†

Instability of steady and pulsatile flow in stenotic geometries **11717**
Martin Griffith,† Thomas Leweke, Mark Thompson and Kerry Hourigan *Monash University, Australia*†

Transition control in swept-wing boundary layers **11771**
William Saric,† Andrew Carpenter and Helen Reed
Texas A&M University, USA†

Symmetry breaking in two-dimensional, diverging-channel flow **11777**
Philip Haines,† Richard Hewitt and Andrew Hazel
The University of Manchester, UK†

Experiments on the elliptic instability in vortex pairs with axial core flow **10122**
Thomas Leweke,† Clément Roy, Thomas Leweke, Mark Thompson and Kerry Hourigan
Centre National de la Recherche Scientifique, France†

Interactions between wave motions and a spanwise array of streamwise streaks **10722**
Jonathan Watmuff
RMIT University, Australia

Sensitivity and forcing response in separated boundary-layer flow **10169**
Jean-Christophe Robinet,† Stefania Cherubini, Frédéric Alizard and Pietro De Palma
SINUMEF Laboratory, France†

Optimal perturbation in a channel flow: adjoint-based and Riccati-based control comparison **11629**
Patricia Cathalifaud,† Laia Moret-Gabarro and Christophe Airiau
Institut de Mécanique des Fluides, France†

Biglobal stability analysis of an unsteady separated flow with wall curvature **10276**
Julio Soria,† Vassili Kitsios, Vassilis Theofilis, Andrew Ooi and Daniel Rodriguez
Monash University, Australia†

On investigation of sinusoidal and varicose instabilities of streaks in boundary layers **10303**
Victor Kozlov,† Valery Chernoray and Lennart Loefdahl
Institute of Theoretical and Applied Mechanics, Russia†

An experimental and numerical study of the Faraday instability with miscible liquids **10505**
Sakir Amiroudine,† Ranga Narayanan and Farzam Zoueshtiagh
Ecole Nationale Supérieure d'Arts et Métiers, France†

Relaxation approach for stable PSE integration **11113**
Seung Park† and Bing Gao
Korea Advanced Institute of Science and Technology, South Korea†

Three-dimensional Richtmyer–Meshkov instability and turbulent mixing of a gas/liquid interface **11136**
Hong-Hui Shi† and Qi-Wei Zhuo
Zhejiang Sci-Tech University, China†

Low frequency instabilities in the initial merging zone of an annular jet **11237**
Maarten Vanierschot† and Eric van den Bulck
Katholieke Universiteit Leuven, Belgium†

Linear stability analysis of secondary instability of boundary layer flow on a two-dimensional airfoil **11538**
Takashi Atobe,† Jun Hiyama, Takahiro Sumi and Takuji Kurotaki
Japan Aerospace Exploration Agency, Japan†

Instabilities in bluff plate boundary layers **12117**
Mark Thompson† and Hemant Chaurasia
Monash University, Australia†

Electrohydrodynamic instability in a horizontal Poiseuille flow with an electrical conductivity gradient **11571**
Min-Hsing Chang,† An-Cheng Ruo, Falin Chen and Zhi-Wen Xiao
Tatung University, Taiwan†

Conditionally-sampled velocity in an oscillating-triangular-jet nozzle **11218**
Peter Lanspeary,† Soon-Kong Lee and Peter Kalt
The University of Adelaide, Australia†

Vortex structure in an oscillating-triangular-jet nozzle **11782**
Soon-Kong Lee,† Peter Lanspeary and Peter Kalt
The University of Adelaide, Australia†

Flow destabilization and chaotic mixing in the channel with transversely corrugated walls **11606**
Slawomir Blonski,† Tomasz Kowalewski and Jacek Szumbarski
Institute of Fundamental Technological Research, Poland†

Dynamics of a fluid inside a precessing cylinder **11817**
Romain Lagrange,† François Nadal, Christophe Eloy and Patrice Meunier *IRPHE, CNRS and Aix-Marseille Université, France*†

Primary and secondary instability of the boundary layer in a rotating annulus **11141**
Bertrand Viaud,† Jean-Marc Chomaz, Eric Serre and Bertrand Viaud
French Air Force, France†

Poincaré section analysis of an experimental frequency intermittency in an open cavity flow **11329**
François Lusseyran,† Christophe Letellier, Thierry Faure and Luc Pastur
LIMSI, CNRS, France†

Spatial optimal disturbances in swept attachment-line boundary layers **12061**
Patrick Huerre,† Peter Schmid and Alan Guegan
Ecole Polytechnique, France†

Spatial-temporal stability of mixed forced-free convection boundary layers **11569**
Eunice Mureithi† and Jim Denier
University of Pretoria, South Africa†

On the instability of vortices embedded in shear flows **11990**
Philip Hall
Imperial College London, UK

FM11 :: Flow in thin films

Chairs: Serafim Kalliadasis (UK) and Leonard Schwartz (USA)

Thin film flows over real surfaces **11851**
Yeaw Lee,† Philip Gaskell and Harvey Thompson
University of Leeds, UK†

Interfacial turbulence in falling liquid films **10518**
Serafim Kalliadasis,† Sergey Vlaskin, Eugene Kalaidin and Eugene Demekhin
Imperial College London, UK†

A general free surface rule for Stokes flow of fluid films over obstacles **11482**
Markus Scholle,† Nuri Aksel, Harvey Thompson, Mark Wilson and Philip Gaskell
University of Bayreuth, Germany†

Experimental and theoretical modelling of ice sheet–shelf grounding lines **11496**
Grae Worster,† Herbert Huppert and Rosalyn Robison
University of Cambridge, UK†

Structure of a pure-vapor–liquid contact line on a heated substrate: truncated adsorbed microfilms and the spreading coefficient **11955**
Alexey Rednikov† and Pierre Colinet
Université Libre de Bruxelles, Belgium†

Are outside corners more difficult to coat than inside ones? **10910**
Mathieu Sellier
University of Canterbury, New Zealand

Sliding drops of generalized Newtonian liquid **10519**
Leonard Schwartz,† Stephen O'Brien and Jean Charpin
University of Delaware, USA†

Stability of a thin radially moving liquid sheet in the presence of acoustic excitation **11956**
Mahesh Tirumkudulu,† Krishnaswami Ramamurthi and Aditya Mulmule
Indian Institute of Technology, Bombay, India†

Hydrodynamics of reactive thin films **11312**
Antonio Pereira,† Philip Trevelyan, Uwe Thiele and Serafim Kalliadasis
Imperial College London, UK†

Flow structure in free surface film and Couette flow over non-planar substrates **11321**
André Haas,† Harvey Thompson, Marc Wilson, Nuri Aksel, Markus Scholle and Philip Gaskell
University of Bayreuth, Germany†

3D waves on liquid films and rivulets flowing down vertical plate **12145**
Sergey Alekseenko,† Dmitriy Markovich, Sergey Kharlamov, Vladimir Guzanov and Aleksey Bobylev
Institute of Thermophysics, Russia†

Rupture of a current-carrying fluid cylinder **11807**
Jonathan Mestel,† Bill Ristenpart, Howard Stone and Tom Witelski
Imperial College London, UK†

Resonance of surface waves in gravity-driven films over undulated bottoms **11314**
Christian Heining,† Andreas Wierschem and Nuri Aksel
University of Bayreuth, Germany†

Centrifugally driven thin film flow over a fast rotating cone with arrays of micron sized holes **11812**
Paul Duineveld† and Theo Stolk
Philips Consumer Lifestyle, Netherlands†

Unsteady contact melting **10515**
Tim Myers,† Gift Muchatibaya and Sarah Mitchell
University of Cape Town, South Africa†

FM12 :: Geophysical and environmental fluid dynamics

Chairs: William Young (USA) and Jiachun Li (China)

Equilibrium states of quasi-geostrophic vortices **10503**
Takeshi Miyazaki,† Naoya Takahashi and Shintaro Hoshi
The University of Electro-Communications, Japan†

Investigating the formation of wind-formed dune fields based on discrete dynamics **10784**
Xiaojing Zheng† and Tianli Bo
Lanzhou University, China†

The effect of thermal diffusion on the stability of strongly tilted mantle plume tails **10891**
Ross Kerr† and Catherine Meriaux
The Australian National University, Australia†

Experimental study on propagation velocities of water surface ripples and turbulence in an open-channel flow **10963**
Hitoshi Miyamoto
Kobe University, Japan

Effects of upstream disturbances in a model of headland wakes **11134**
Melanie O'Byrne,† Ross Griffiths and Graham Hughes
The Australian National University, Australia†

Mixing in baroclinic exchange flows and its dependence on topography **11174**
Ross Griffiths,† Graham Hughes, Andrew Hogg and Tjipto Prastowo
Australian National University, Australia†

The viscous phase of horizontal gravity currents: how is the time evolution of the front selected? **11081**
Yannick Hallez† and Jacques Magnaudet
Institut de Mécanique des Fluides de Toulous, France†

Inertia-gravity wave generation: a geometric-optics approach **11337**
Jacques Vanneste† and Jonathan Aspden
University of Edinburgh, UK†

Forward energy cascade of geostrophic turbulence via near-boundary instabilities **11631**
William Dewar† and Andrew Hogg
Florida State University, USA†

Transcritical small disturbance theory for flow over topography **11513**
Ted Johnson,† Gavin Esler and Owen Rump
University College London, UK†

Solution of some vortical free boundary problems arising in ocean flows **10090**
Nicholas McDonald† and Ted Johnson *University College London, UK*†

The behaviour of dilute particle suspensions in waning flows **11114**
Robert Dorrell† and Andrew Hogg *Bristol University, UK*†

The large-scale effect of mesoscale ocean–atmosphere coupling **11706**
Andrew Hogg,† William Dewar, Pavel Berloff and Sergey Kravtsov
The Australian National University, Australia†

Adjustment processes in horizontal convection **11684**
Graham Hughes† and Ross Griffiths
The Australian National University, Australia†

Three-dimensionality in electromagnetically driven shallow flows **10737**
GertJan van Heijst,† Rinie Akkermans, Leon Kamp and Herman Clercx *Eindhoven University of Technology, Netherlands*†

Physics of the mesoscale atmospheric turbulence: laboratory experiments **11530**
Michael Shats,† Hua Xia, Horst Punzmann and Gregory Falkovich
The Australian National University, Australia†

Absence of small-scale fluctuations of high-Prandtl number scalars in stratified turbulence **10223**
Hideshi Hanazaki,† Kazuhiro Konishi and Takehiro Miyao
Kyoto University, Japan†

Some investigations into near surface wind and saltation intensity in mining area **10261**
Ning Huang,† Xiaojing Zheng and Feng Shi
Lanzhou University, China†

PIV measurements in the immediate wake of a cactus-shaped cylinder **11853**
Ghanem Oweis American University of Beirut, Lebanon

Experiment and simulation of unsteady sand mass flux in the near-surface layer **11055**
Ping Wang,† Xiaojing Zheng, Jinghong Zhang and Wenwen Hu
LanZhou University, China†

Hydraulic modeling of runoff yield in small watersheds **11142**
Qingquan Liu† and Yi An
Chinese Academy of Sciences, China†

Thermodynamics of irreversible transitions in the oceanic general circulation **11357**
Shinya Shimokawa† and Hisashi Ozawa
National Research Institute for Earth Science and Disaster Prevention, Japan†

New approach to mathematical modeling of admixture transport in free-surfaced streams **10970**
Konstantin Nadolin
Southern Federal University, Russia

Evidence of anisotropy of small scale turbulence in the laboratory model of an atmospheric cloud **11315**
Piotr Korczyk,† Szymon Malinowski and Tomasz Kowalewski
Instytut Podstawowych Problemów Techniki, Polska Akademia Nauk, Poland†

Particulate gravity currents along v-shaped valleys **11091**
Joe Monaghan,† John Mansour, Herbert Huppert and Catherine Meriaux
Monash University, Australia†

On numerical simulation of tropical atmospheric intraseasonal oscillation (MJO) **12157**
Jian Ling,† Chongyin Li and Jia Xiaolong
Institute of Atmospheric Physics, China†

Separating flow over two-dimensional rough hills **11617**
Juliana Loureiro,† Andre Monteiro, Fernando Pinho and Atila Silva-Freire
Federal University of Rio de Janeiro, Brazil†

FM13 :: Low-Reynolds-number flow

Chairs: Osamu Sano (Japan) and Elisabeth Guazzelli (France)

On the effects of atmospheric pressure, air concentration in a fluid, and the surface roughness on a solid-sphere motion along a wall **10919**
Alexander Prokunin
Moscow State University, Russia

A fast boundary element method for Stokes flow **11688**
Kian-Meng Lim,† Xuefei He and Siak-Piang Lim
National University of Singapore, Singapore†

Arbitrary oscillatory Stokes flow past a porous sphere: Faxen's laws **10793**
Raja Sekhar,† Mirela Kohr and Jai Prakash
Indian Institute of Technology, Kharagpur, India†

Eddy reversals in three dimensions **11228**
Christopher Hills
Dublin Institute of Technology, Ireland

Viscous flow past two spherical cavities in porous media: application to drug delivery system **10523**
Osamu Sano
Tokyo University of Agriculture and Technology, Japan

Three flow regimes of a viscous jet falling onto a moving surface **10713**
Andriy Hlod,† Mark Peletier, Fons van de Ven and Annemarie Aarts
Eindhoven University of Technology, Netherlands†

The irreversible effect of cavitation in near-contact region **10652**
Alan Graham,† Shihai Feng, Patrick Reardon, Cynthia Heath and Marc Ingber
Institute for Multiscale Materials Studies, USA†

Flow of microcapsules in small pores: a method for determining the elastic properties of the membrane **11309**
Dominique Barthès-Biesel,† Johann Walter, Yannick Lefebvre, Eric Leclerc and Florence Levy
Université de Compiègne, France†

Weak inertial effects associated with oscillating pressure in a 3D channel **11490**
Guibert Romain,† Alain Bergeon and Franck Plouraboué
University of Toulouse, France†

Stokeslet induced flows in the vicinity of a hybrid compound droplet **11949**
Devanayagam Palaniappan
Texas A&M University, USA

Periodic orbits of Stokesian dynamics **11682**
Maria Ekiel-Jezewska
Institute of Fundamental Technological Research, Polish Academy of Sciences, Poland

Large-scale simulations of emulsion flow through a granular material **11884**
Alexander Zinchenko† and Robert Davis
University of Colorado at Boulder, USA†

Low-Reynolds streaming in a cavity: an illustration of inviscid flow **10170**
Josue Sznitman† and Thomas Roesgen
University of Pennsylvania, USA†

Expanding volumes of channelized viscous gravity currents **10874**
Daisuke Takagi† and Herbert Huppert
University of Cambridge, UK†

Periodic fundamental solution of the two-dimensional Stokes flow **10380**
Hidenori Hasimoto
The University of Tokyo, Japan

Dynamics of the snail ball **10520**
William Young,† Neil Balmforth, John Bush and David Vener
Scripps Institution of Oceanography, USA†

Low Reynolds number swimming beneath a free surface **11123**
Darren Crowdy,† Anette Hosoi, Eric Lauga, Sungyon Lee and Ophir Samson
Imperial College London, UK†

FM14 :: Magnetohydrodynamics

Chairs: Sergey Surzhikov (Russia), Jean-François Pinton (France) and Rainer Hollerbach (UK)

Influence of magnetic and electrical fields on a thin layer of electrically conducting liquid **10391**
Hamid Abderrahmane† and Georgios Vatistas
Concordia University, Canada†

Importance of new magnetic field analysis for interface phenomena of ferromagnetic fluid **10727**
Yo Mizuta
Hokkaido University, Japan

Equilibrium and stability in relaxed magnetohydrodynamics of toroidal plasmas **10491**
Robert Dewar,† Matthew Hole, Mathew McGann, Ruth Mills and Stuart Hudson
The Australian National University, Australia†

Magnetic field reversals in nature, experiments and simulations **10869**
Andre Giesecke,† Gunter Gerbeth and Frank Stefani
Forschungszentrum Dresden, Germany†

Investigation of interface oscillations in liquid metals using magnetic field tomography **11227**
Christian Resagk,† Shouqiang Men, Hartmut Brauer and Marek Ziolskowski
Ilmenau University of Technology, Germany†

Dissipation bounds for dynamos **11824**
Thierry Alboussière
CNRS, LGIT Grenoble, France

The helical magnetorotational instability in cylindrical Taylor–Couette flow **11858**
Rainer Hollerbach,† Frank Stefani, Gunter Gerbeth, Thomas Gundrum and Gunther Rudiger
University of Leeds, UK†

The helicities and group velocities of unstable modes generated by tidal effects **11323**
Krzysztof Mizerski,† Konrad Bajer and Keith Moffatt
University of Leeds, UK†

Turbulent MHD channel flow with spanwise magnetic field **10715**
Thomas Boeck,† Dmitry Krasnov, Oleg Zikanov and Joerg Schumacher
Techniche Universität Ilmenau, Germany†

FM15 :: Microfluidics

Chairs: Carl Meinhart (USA) and Henrik Bruus (Denmark)

Semi-automated manipulation of crystals using acoustic fields and microfluidics in micromachined devices **10923**
Stefano Oberti,† Jürg Dual, Adrian Neild, Sascha Gutmann and Dirk Möller
Institute of Mechanical Systems - ETH Zurich, Switzerland†

Microflow induced by Opercularia Assymetrica: optical experimental investigations **11866**
Bogumila Zima-Kulisiewicz,† Antonio Delgado and Cornelia Rauh
Friedrich-Alexander University, Germany†

Computational study of a novel valve mechanism for synthetic jet actuator **11906**
Victoria Timchenko,† Chin Pang, Dan Li, Victoria Timchenko, John Reizes and Eddie Leonardi
The University of New South Wales, Australia†

Numerical studies of nonlinear kinetics in induced-charge electro-osmosis **10528**
Henrik Bruus,† Martin Bazant and Misha Gregersen
Technical University of Denmark, Denmark†

Non-local transport in nanofluids: k-space and real-space viscosity kernels **10794**
Ruslan Puscasu,† Peter Daivis and Billy Todd
Swinburne University of Technology, Australia†

The efficiency of the coupled electrode-membrane processes in hydrogen fuel cell: thermodynamic analysis **10158**
Frantisek Marsik† and Tomas Nemec
Institute of Thermomechanics CAS, Czech Republic†

Dewetting of nanometer thin films under an electric field **11287**
Guo-Hui Hu,† Ai-Jin Xu and Zhe-Wei Zhou
Shanghai Univeristy, China†

On penalty approaches for Navier-slip and other boundary conditions in viscous flow **11426**
Yvonne Stokes† and Graham Carey
The University of Adelaide, Australia†

Capillary driven flows: velocity dependent contact angles and chemically patterned walls **11701**
Mihail Popescu† and John Ralston
University of South Australia, Australia†

Hydrodynamic friction of a polymer adsorbed on a planar surface **11890**
Krzysztof Sadlej,† Maria Ekiel-Jezewska and Eligiusz Wajnryb
Polish Academy of Science, Poland†

Controlled cavitation and sonoporation in microfluidics **12209**
Pedro Quinto Su,† Claus-Dieter Ohl, Séverine Le Gac, Albert van den Berg, Ed Zwaan and Kinko Tsuji
Researcher, Singapore†

Free surface microfluidics for explosives detection **12199**
Brian Piorek,† Carl Meinhart, Seung Lee, Lisan Viel, Sanjoy Banerjee and Martin Moskovits
University of California, Santa Barbara, USA†

Fabrication of a nanofluidic field effect transistor for controlled cavitation in nanochannels **11932**
Egbert van der Wouden,† Johan Bomer, Jan Eijkel, Sumita Pennathur and Albert van den Berg
University of Twente, Netherlands†

FM16 :: Microgravity fluid mechanics

Chairs: Wenrui Hu (China) and Hans Rath (Germany)

Boiling heat transfer in microgravity **10803**
Jian-Fu Zhao† and Shi-Xin Wan
Chinese Academy of Sciences, China†

Vibration-induced Rayleigh instability in supercritical fluids under microgravity conditions **11201**
Daniel Beysens† and Sakir Amiroudine
Ecole Supérieure de Physique et de Chimie Industrielles, France†

Capillary channel flows **11302**
Michael Dreyer,† Joerg Klatte and Aleksander Grah
University of Bremen, Germany†

Experiments on aqueous foams in microgravity: a way to study poroelastic effects in soft wet cellular materials **11335**
Arnaud Saint-Jalmes,† Dominique Langevin and Sebastien Marze
Centre National de la Recherche Scientifique, France†

The capillary flow experiments aboard ISS: weakly 3D interior corner flows **11523**
Mark Weislogel† and Ryan Jenson
Portland State University, USA†

Reduced gravity testing and research capabilities at Queensland University of Technology's new 2.0 **second drop tower** **12008**
Ted Steinberg
Queensland University of Technology, Australia

Behaviour of drops and bubbles in non-uniform pulsational flows **10175**
Tatyana Lyubimova,† Alexandra Cherepanova and Dmitriy Lyubimov
Institute of Continuous Media Mechanics UB RAS, Russia†

Planar migration of two drops in a thermal gradient **10866**
Ren Sun
Shanghai Jiao Tong University, China

Numerical simulations of drop thermocapillary migration with variable viscosities **11435**
Zhaohua Yin,† Wenrui Hu and Peng Gao
Chinese Academy of Sciences, China†

Stability analysis of thermocapillary convections in liquid bridges with Prandtl number of 100 under microgravity **11733**
Qi-Sheng Chen† and Ya-Chao Liu
Chinese Academy of Sciences, China†

Mass transfer in supercritical carbon dioxide **11845**
Rainer Benning,† Özgür Ertunc and Antonio Delgado
University Erlangen-Nuremberg, Germany†

Effect of an eccentric rotation on the equilibrium shapes and stability of liquid bridges in a lateral gravity field **11621**
Ana Laverón,† Victoria Lapuerta, Angel Rodríguez and Jose Perales
Universidad Politécnica de Madrid, Spain†

FM17 :: Solidification and crystal growth

Chairs: Gustav Amberg (Sweden) and Grae Worster (UK)

Heterogenous nucleation and successive microstructure evolution during solidification **10245**
Heike Emmerich
RWTH Aachen, Germany

Asymptotic results for a Stefan problem with surface tension **10802**
Scott McCue,† Bisheng Wu and James Hill
Queensland University of Technology, Australia†

Steady-state solidification of aqueous solutions in a new directional solidification facility **11388**
Herbert Huppert,† Grae Worster and Stephen Peppin
University of Cambridge, UK†

Experimental compaction in a crystallizing mushy zone **11795**
Renaud Deguen,† Jean-Paul Masson, Patrick La Rizza, Daniel Brito and Thierry Alboussière
Université Joseph Fourier, France†

Modelling the growth and motion of a free dendrite under terrestrial conditions **11252**
Minh Do-Quang† and Gustav Amberg
Royal Institute of Technology, Sweden†

Analytical prediction of solidification in close-celled metal foams **12210**
Tongbeum Kim,† Tianjian Lu and Bin Zhang
Xi'an Jiaotong University, China†

Nano-scale solidification phenomena **10046**
Tomasz Kowalewski,† Justyna Czerwinska and Erwan Deriaz
Polish Academy of Sciences, Poland†

Phase-field simulation for the growth of boride (Fe2B) phase from austenite phase **10948**
Raden Ramdan,† Tomohiro Takaki and Yoshihiro Tomita
Kobe University, Japan†

FM18 :: Stirring and mixing

Chairs: Stephen Cox (UK) and Nadine Aubry (USA)

Stretching and mixing of chemically reactive chaotic flows **11662**
Paulo Arratia† and Jerry Gollub
University of Pennsylvania, USA†

Chaotic mixing in a helix-like pipe with periodic variations in curvature and torsion **10775**
Mitsuaki Funakoshi† and Bongkyun Jang
Kyoto University, Japan†

Topological chaos in flows on surfaces of arbitrary genus
Matthew Finn† and Jean-Luc Thiffeault **10000**
The University of Adelaide, Australia†

Tailoring chaotic mixing within a translating droplet by oscillatory rotation **11619**
Rodolphe Chabreyrie,† Pushpendra Singh, Cristel Chandre, Dmitri Vainchtein and Nadine Aubry
Carnegie Mellon University, USA†

Chaotic thermal mixing in a two rod mixer **11391**
Kamal El Omari† and Yves Le Guer
University of Pau, France†

Speeding up mixing with moving walls **11203**
Jean-Luc Thiffeault,† Emmanuelle Gouillart and Olivier Dauchot
University of Wisconsin—Madison, USA†

The prevalence of ghost rods in batch mixer designs **10481**
Stephen Cox† and Ben Binder
University of Nottingham, UK†

Advection of passive fluid by periodical injection from a two-dimensional flat chink **11003**
Alexandre Gourjii,† GertJan van Heijst, Viatcheslav Meleshko and Luca Zannetti
Institute of Hydromechanics, NASU, Ukraine†

Laminar mixing of fluids and scalars: a unified Hamiltonian approach **11461**
Michel Speetjens† and Viatcheslav Meleshko
Eindhoven University of Technology, Netherlands†

Mixing of polymer solution in curvilinear pipe **11374**
Shinji Tamano,† Motoyuki Itoh, Akira Sasakawa and Kazuhiko Yokota
Nagoya Institute of Technology, Japan†

Stirring with ghost rods in counter-rotating flows **10150**
Mark Stremler† and Jie Chen
Virginia Tech, USA†

FM19 :: Turbulence

Chairs: Fazle Hussain (USA) and Eberhard Bodenschatz (Germany)

A new look into re-effect on turbulent round jets **10206**
Jamie Mi
Peking University, China

Drag reduction of a deforming film covered with polysaccharide in turbulent water flow **11774**
Yoshimichi Hagiwara,† Kousuke Takashima and Katsutoshi Sakurai
Kyoto Institute of Technology, Japan†

Statistical theory of inhomogeneous turbulence based on the cross-independence closure hypothesis **10716**
Tomomasa Tatsumi
Kyoto University, Japan

The influence of turbulence on a columnar vortex with axial flow **10745**
Naoya Takahashi† and Takeshi Miyazaki
University of Electro-Communications, Japan†

Numerical and experimental study of stability of isothermal and hot round jet **11124**
Stanislaw Drobniak,† Andrzej Boguslawski and Artur Tyliszczaak
Czestochowa University of Technology, Poland†

CICLoPE: a new high Reynolds number pipe flow facility for detailed turbulence measurements **11400**
Jean-Daniel Rüedi,† Henrik Alfredsson, Hassan Nagib, Alessandro Talamelli and Peter Monkewitz
University of Bologna, Italy†

Direct numerical simulation of turbulence in a fully-developed channel flow with permeable boundaries **11420**
Satoshi Yokojima
Shizuoka University, Japan

Concentration of active nonlinear energy transfer in rolling-up vortices **11738**
Keisuke Araki† and Hideaki Miura
Okayama University of Science, Japan†

Investigation of Smagorinsky model in large-eddy simulation of periodic turbulent shear flows **11699**
Yihong Fang† and Dawei Guo
Tianjin University, China†

Intensive turbulent convection **11839**
Ilias Sibgatullin,† Semen Gertsenstein and Igor Palymsky
Moscow State University Lomonosov, Russia†

Turbulent flow past a rectangular cylinder confined in channel **12147**
Dong-Hyeog Yoon† and Kyung-Soo Yang
Inha University, South Korea†

Scale dependence of coarse-grained velocity gradient in turbulence **10532**
Eberhard Bodenschatz,† Alain Pumir and Haitao Xu
MPI Goettingen, Germany†

Multiscale geometrical analysis of vorticity and dissipation in homogeneous turbulence **11414**
Dale Pullin,† Kiyosi Horiuti and Ivan Bermejo-Moreno
California Institute of Technology, USA†

Turbulence suppression by self-generated and imposed large-scale flows **11520**
Hua Xia,† Michael Shats, David Byrne and Horst Punzmann
The Australian National Univeristy, Australia†

Deterministic wall turbulence and its applications **10626**
Yury Kachanov,† Vladimir Borodulin and Aleksej Roschektayev
Russian Academy of Sciences, Russia†

A bound for turbulent pair dispersion **11178**
Michael Borgas
CSIRO, Australia

Experimental measurement of acceleration correlations in turbulent flows of dilute polymer solutions **11402**
Haitao Xu† and Eberhard Bodenschatz
Max Planck Institute for Dynamics and Self-Organization, Germany†

Physical mechanism of the energy cascade in homogeneous turbulence **11889**
Susumu Goto
Kyoto University, Japan

On local cascade structures of turbulence **11963**
Zhen-Su She,† Jun Chen and Yu-Hui Cao
Peking University, China†

A study of subgrid models in lattice Boltzmann-based large eddy simulation **11443**
Yu-Hong Dong,† Simon Marie and Pierre Sagaut
Shanghai University, China†

Scaling regimes of the 2D Navier–Stokes equation with self-similar stirring **11915**
Paolo Muratore-Ginanneschi,† Andrea Mazzino and Stefano Musacchio
University of Helsinki, Finland†

Discussion on the rapid pressure–strain correlation in the rapid distortion limit **10598**
Song Fu† and Siyuan Huang
Tsinghua University, China†

Large eddy simulations of a self-similar mixing layer using the stretched-vortex subgrid model **10449**
Trent Mattner
The University of Adelaide, Australia

FM20 :: Waves

Chairs: Frederic Dias (France) and Kendall Melville (USA)

A practical forecast model for atmospheric internal waves produced by a mountain **10504**
James Rottman,† Dave Broutman and Stephen Eckermann
SAIC Naval Hydrodynamics, USA†

Internal solitary waves of very large amplitude subject to shear-instability **10576**
John Grue
University of Oslo, Norway

Nonlinear wave excitation of capillary waves in the presence of hydrocarbon films **11066**
Horst Punzmann† and Michael Shats
The Australian National University, Australia†

Open channel flow past a curved sluice gate **10661**
Ben Binder,† Jean-Marc Vanden-Broeck and Frederic Dias
University of Melbourne, Australia†

Wave-coherent tangential stress due to smaller scale breaking **11249**
William Peirson† and Andrew Garcia
Water Research Laboratory, Australia†

Surface gravity waves in Lagrangian description of motion **11868**
Didier Clamond
University of Nice, France

Nonlinear three-dimensional interfacial flows **10109**
Emilian Parau,† Jean-Marc Vanden-Broeck and Mark Cooker
University of East Anglia, UK†

Inertial estimates of surface wave dissipation due to breaking **10534**
Kendall Melville,† Luc Lenain and David Drazen
Scripps Institution of Oceanography, USA†

Spatial and temporal evolution of wave groups: experiments versus simulations **10744**
Lev Shemer,† Alexey Slunyaev and Boris Dorfman
Tel-Aviv University, Israel†

Short-crested gravity waves of large amplitude in deep water **10870**
Makoto Okamura
Kyushu University, Japan

Combined approach to the dynamics modelling of spatially nonlinear waves in shallow layers of viscous liquids **10790**
Georgy Khabakhpashev† and Dmitry Arkhipov
Institute of Thermophysics SB RAS, Russia†

Analyses on the flapping frequency of turbulent jets in a narrow channel **11905**
Jianhong Sun† and Chin-Tsau Hsu
Nanjing University of Aeronautics and Astronautics, China†

Dynamic wave impact simulation using an innovative particle-cluster scheme **10211**
André Baeten
LFK-Lenkflugkoerpersysteme GmbH, Germany

Nonlinear surface water waves over a random bottom **11047**
Walter Craig† and Catherine Sulem
McMaster University, Canada†

Impact of a heavy vertical jet on a horizontal wall **11146**
Paul Christodoulides† and Frederic Dias
Cyprus University of Technology, Cyprus†

Nonlinear surface waves in a square liquid tank under obliquely horizontal excitation **11736**
Takashi Ikeda† and Raouf Ibrahim
Shimane University, Japan†

Effect of surface stress on the propagation of solitary water waves **11768**
Paul Hammerton† and Andrew Bassom
University of East Anglia, UK†

Three-dimensional gravity capillary free surface flows **11786**
Jean-Marc Vanden-Broeck,† Emilian Parau and Mark Cooker
University College London, UK†

Adaptive direct numerical simulation of steep water waves **10397**
Stéphane Popinet
National Institute of Water and Atmospheric research, New Zealand

On the inclusion of arbitrary topography and bathymetry in the nonlinear shallow-water equations **11451**
Raphael Poncet† and Frederic Dias
École Normale Supérieure de Cachan, France†

Space-time measurements of breaking wave kinematics and void fraction in the surf zone **11622**
Olivier Kimmoun† and Hubert Branger
Aix-Marseille Université and Ecole Centrale Marseille, France†

Numerical study of breaking waves of different intensities **11809**
Alessandro Iafrati
INSEAN—Italian Ship Model Basin, Italy

The frequency and wavevector spectra of gravity wave turbulence in the laboratory flume **11375**
Sergei Lukaschuk,† Petr Denissenko and Sergey Nazarenko
The University of Hull, UK†

Airflow separation above wind waves **11808**
Fabrice Veron,† Marc Buckley and James Mueller
University of Delaware, USA†

On the self-similarity of short-wavelength incipient spilling breakers **11082**
James Diorio,† James Duncan and Xinan Liu
University of Maryland, USA†

Measurements of growth rates of wind-generated water waves **11058**
Dan Liberzon† and Lev Shemer
Tel Aviv University, Israel†

Drag on a ship and Michell's integral **11452**
Ernest Tuck† and Leo Lazauskas
The University of Adelaide, Australia†

Visco potential free-surface flows **10872**
Denys Dutykh
Ecole Normale Superieure de Cachan, France

FSM01 :: Acoustics

Chairs: Roger Ohayon (France) and Nigel Peake (UK)

Silent embedded boundaries for combustion noise simulation **10506**
Wolfgang Schröder† and Thanh Bui
Aerodynamisches Institut, Germany†

The effect of non-axisymmetric flow disturbances on the sound generation in the hole-tone feedback cycle **10414**
Mikael Langthjem† and Masami Nakano
Yamagata University, Japan†

Models for acoustic propagation through turbofan exhaust flows: lined ducts **10571**
Nigel Peake† and Ben Veitch
University of Cambridge, UK†

Sound generation in flows with steady heat communication **10728**
Nader Karimi,† William Moase, Michael Brear and Nader Karimi
University of Melbourne, Australia†

AGILD WMT ray-tracing interactive tomography **11215**
Jianhua Li,† Chien-Chang Lin, Ganquan Xie and Michael Oristaglio
GL Geophysical Laboratory, USA†

Wolf killing: the subtle problem of controlling cello string/body coupled resonances **11935**
Antunes Jose† and Octavio Inacio
Insituto Tecnologico e Nuclear, Portugal†

Acoustic properties of dry and saturated porous media **11161**
Pierre Adler,† Iryna Malinouskaya, Valeri Mourzenko, Igor Bogdanov and Jean-Francois Thovert
UPMC-Sisyphe, France†

Acoustics of streaming: a mechanism of noise generation in subsonic jets **11554**
Xuesong Wu† and Patrick Huerre
Imperial College London, UK†

The "two-phase sound" of cheering champagne glasses **11899**
Debut Vincent† and José Antunes
Institute of Nuclear Technology, Portugal†

FSM02 :: Biomechanics

Chairs: Stephen Cowin (USA) and Ross Ethier (UK)

Real-time simulation of non-linear tissues by model reduction techniques **10579**
Francisco Chinesta,† Siamak Niroomandi, Iciar Alfaro and Elias Cueto
LMSP-SERAM ENSAM, France†

Thin films of transversely isotropic fluid: applications to collagen gels **10808**
Edward Green† and Avner Friedman
The Ohio State University, USA†

Partitioned FEM/FVM coupling for cardiac fluid-structure interaction with a macroscopic composite approach **10844**
Sebastian Krittian,† Herbert Oertel and Torsten Schenkel
University of Karlsruhe, Germany†

Constitutive modeling of the stress–strain behavior of F-actin filament networks **10995**
Jeffrey Palmer† and Mary Boyce
Massachusetts Institute of Technology, USA†

Investigations of invariant based constitutive laws for modelling myocardial mechanics **11109**
Holger Schmid,† Yikan Wand, Jesse Ashton, Alexander Ehret, Sebastian Krittian, Martyn Nash, Peter Hunter and Mikhail Itskov
University of Aachen, Germany, Germany†

Resonance in the cochlea with wave packet pseudomodes **11125**
Dominik Obrist† and Peter Schmid
ETH Zurich, Switzerland†

Biomechanical models of epidermal wound closure in embryos **11126**
Alexander Sadovsky† and Frederic Wan
University of California, Irvine, USA†

Longterm prediction of bone remodelling effect around implant **11152**
Vaclav Klika,† Frantisek Marsik and Ivan Landor
Czech Academy of Sciences, Czech Republic†

Mechanics of memory and learning **11284**
Taher Saif,† Akira Chiba, Jie Sung, Scott Siechen and Shengyuan Yang
University of Illinois at Urbana-Champaign, USA†

Multiscale analysis of the human aortic valve **12000**
Mohammad Mofrad† and Eli Weinberg
University of California, Berkeley, USA†

The intervertebral disc as a saturated porous material **11320**
Nils Karajan† and Wolfgang Ehlers
University of Stuttgart, Germany†

Mechanics of traumatic brain injury at multiple length scales **11371**
Johannes van Dommelen,† Rudy Cloots, Matej Hrapko, Gerrit Peters, Jac Wismans and Marc Geers
Eindhoven University of Technology, Netherlands†

Microvascular-based multifunctional structural materials **11518**
Scott White,† Nancy Sottos, Jeff Moore, Jennifer Lewis and Ken Christensen
University of Illinois, USA†

Computational simulation of red blood cell motion in microvessels and bifurcations **11593**
Timothy Secomb,† Jared Barber, Jonathan Alberding and Juan Restrepo *University of Arizona, USA*†

Influence of endothelium monolayer unevenness on leukocyte deformation and migration **11697**
Pushpendra Singh,† Qian Jin, Claude Verdier, Nadine Aubry, Roxana Chotard-Ghodsnia and Alain Duperray
New Jersey Institute of Technology, USA†

Recent progress in the theoretical and computational modelling of flow in 3D collapsible tubes **10348**
Matthias Heil† and Jonathan Boyle *University of Manchester, UK*†

An actin-driven model for neuronal growth cone motility and axon guidance **10011**
Zhu Weiping
Shanghai University, China

The collective behavior of sarcomere ensembles: evolution of non-uniformities and insights on muscle function **10555**
Kaushik Bhattacharya† and Sefi Givli
California Institute of Technology, USA†

Russian doll poroelasticity; a model for fluid transport in tissues **10572**
Stephen Cowin† and Gaffar Gailani
City College of New York, USA†

Non-Newtonian fluid flow simulation in a progressively enlarged aneurysm model **11470**
Panagiotis Neofytou,† Sokrates Tsangaris and Michalis Kyriakidis
National Technical University of Athens, Greece†

Separatrices and basins of stability from time series data **11127**
Shane Ross† and Martin Tanaka
Virginia Tech, USA†

Computational design of novel stem cell based therapies for myocardial infarction **11345**
Ellen Kuhl,† Christopher Zarins, Oscar Abilez, Joe Ulerich and Serdar Goktepe *Stanford University, USA*†

Material characterization of biological membranes by inverse analysis **11386**
Martin Kroon† and Gerhard Holzapfel
Royal Institute of Technology, Sweden†

Cosserat theoretical modeling of single actin filament as a twisted elastic filament **11424**
Hidetaka Yamaoka† and Taiji Adachi
RIKEN, Japan†

Ionised media and fractures: application to cartilaginous tissues and oil industry **11951**
Jacques Huyghe,† Rene de Borst, Joris Remmers and Famke Kraaijeveld
Eindhoven University of Technology, Netherlands†

An anisotropic micro-sphere-based model for arterial tissue **12078**
Andreas Menzel,† Manuel Doblare, Miguel Martinez and Victor Alastrue *Technical University of Dortmund, Germany*†

Modeling skin wrinkling for reconstructive surgery: the effects of natural tension **11305**
Luigi Gambarotta,† Andrea Cavicchi and Roberta Massabò
University of Genova, Italy†

Liquid crystal model of vesicles under electromechanical fields **10933**
Xi-Qiao Feng,† Ling-Tian Gao and Huajian Gao
Tsinghua University, China†

The hysteretic large strain behavior of mussel byssal threads **11672**
Brian Greviskes
Massachusetts Institute of Technology, USA

Red blood cell deformation behavior in a high-shear flow **12181**
Shigeo Wada,† Masanori Nakamura and Sadao Bessho
Osaka University, Japan†

Peristalsis and hydrodynamic instabilities **11063**
Jerome Hoepffner† and Koji Fukagata
KEIO University, Japan†

Elementary mechanics of muscular exercise **10302**
Antonio DiCarlo Università Roma Tre, Italy

Simulation of migrating cell growth under limited nutrient supply based on a cellular automata model **10940**
Chih-Ang Chung† and Chih-Di Chen
National Central University, Taiwan†

Micro and macro shape deviations of the contact areas of the hip joint endoprosthesis **11297**
Vladimir Fuis,† Martin Houfek and Premysl Janicek
Brno University of Technology, Czech Republic†

Structure overload and structural anisotropy in human vertebral trabecular bone **11317**
Nicola Fazzalari,† Arash Badiei and Murk Bottema
The University of Adelaide, Australia†

Study on deformation of vesicle membrane based on evolution of topological defects **11450**
Akihiro Nakatani† and Yasuyuki Shobatake
Osaka University, Japan†

Investigation of the surface interactions of the implant-bone **11454**
Romuald Bedzinski
Wroclaw University of Technology, Poland

An elastica approximate for fibers and fibrous networks **11500**
Carlos Castro,† Matthew Lang and Mary Boyce
Massachusetts Institute of Technology, USA†

An inverse dynamic model of an arm via Kane's method: torque determination in smash activity **11633**
Azmin Rambely† and Fadiah Ariff
Universiti Kebangsaan Malaysia, Malaysia†

Forces on an adhering cell **11690**
Joseph Berry,† Mark Thompson, Josie Carberry and Shaun Jackson
Monash University, Australia†

Friction drag and pressure drag acting on an angled-wavy plate **11760**
Naoki Yoshitake,† Yoshimichi Hagiwara, Hui Zhang and Yoshihiko Ozaki
Kyoto Institute of Technology, Japan†

FSM03 :: Chaos and pattern formation in fluid and solid mechanics

Chairs: Tomasz Kapitaniak (Poland) and Edwin Kreuzer (Germany)

Misleading dye visualization near a 3D stagnation point with applications to the vortex breakdown bubble **10238**
Morten Brons,† Kerry Hourigan and Mark Thompson
Technical University of Denmark, Denmark†

Chaos thresholds in vibro-impact systems with heavy elastic elements **10574**
Tomasz Kapitaniak,† Barbara Blazejczyk-Okolewska and Krzysztof Czolczynski
Technical University of Lodz, Poland†

Experimental chaos in impact oscillator **11118**
Ekaterina Pavlovskaia,† Marian Wiercigroch, James Ing and Soumitro Banerjee
Aberdeen University, UK†

Chaos control by application of magnetorheological damping **11154**
Jerzy Warminski† and Krzysztof Kecik
Lublin University of Technology, Poland†

Nonsmooth mechanics: challenges and unsolved problems **11202**
John Hogan
University of Bristol, UK

Coexistence of synchronous states in chaotically driven mechanical oscillators **11563**
Andrzej Stefanski† and Przemyslaw Perlikowski
Technical University of Lodz, Poland†

Exploring extensive chaos in Rayleigh–Bénard convection using fractal and Karhunen-Loève dimensions **11635**
Andrew Duggleby† and Mark Paul
Texas A&M University, USA†

Acoustic chaos in sonic infrared imaging **10856**
Golam Newaz,† Robert Thomas, Lawrence Favro and Xiaoyan Han
Wayne State University, USA†

Normal forms of Hamiltonian systems via curvature line transformations **11031**
Xinhua Zhang
Xi'an Jiaotong University, China

Bifurcation and chaos in drive systems **11488**
Martin Houfek,† Vladimir Fuis and Ctirad Kratochvil
Brno University of Technology, Czech Republic†

FSM04 :: Fluid-structure interactions

Chairs: John Grue (Norway) and Michael Paidoussis (Canada)

Flow around a tethered neutrally-buoyant sphere **10871**
Kerry Hourigan,† Hyeok Lee and Mark Thompson
Monash University, Australia†

Energy transfer in fluid–structure interactions **10968**
Tatyana Krasnopolskaya,† Eugene Nikiforovich and Aleksandr Shvets
Institute of Hydromechanics, NASU, Ukraine†

Collective flutter of a parallel plate assembly **10084**
Lionel Schouveiler,† Christophe Eloy and Marcelo Abarca
Université Paul Cezanne, France†

Flow behind a cylinder forced by a combination of oscillatory translational and rotational motions **10684**
David Jacono,† Mehdi Nazarinia, Mark Thompson and John Sheridan
Monash University, Australia†

Hydroelastic analysis of multiple articulated floating elastic plates **10186**
Trilochan Sahoo,† Joydip Bhattacharjee and Debabrata Karmakar
Indian Institute of Technology, Kharagpur, India†

The effect of surface condition on the vortex-induced vibration response of cylindrical offshore structures **10231**
Brad Stappenbelt
University of Western Australia, Australia

Blast propagation in domains of changing topology
Leonid Antanovskii **10450**
Defence Science and Technology Organisation, Australia

Evaluation of added mass coefficients of a hull form using Landweber's method of conformal mapping **10836**
Hemlata Wadhwa† and Krish Thiagarajan
University of Western Australia, Australia†

Improvement of aircraft rolling performance using piezoelectric actuators **10947**
Min Li,† Weimin Chen and Ming-Chun Wang
Beijing University of Aeronautics and Astronautics, China†

Vortex-induced vibrations of a tethered sphere with neutral buoyancy **11299**
Hyeok Lee,† Kerry Hourigan and Mark Thompson
Monash University, Australia†

Nonlinear vibration of a curved pipe conveying fluid subjected to tip harmonic excitation tangential to the pipe center line **11348**
Ni Qiao† and Zhang Zilong
Huazhong University of Science and Technology, China†

DQM for solving stability of a tubular cantilever conveying fluid downwards immersed in a cylindrical container **11356**
Qian Qin† and Wang Lin
Huazhong University of Science and Technology, China†

Hydrodynamic behaviour characterization of vertical axis water turbine scale model **11376**
Nicolas Dellinger,† Jean-Luc Achard, Didier Imbault and Ali Tourabi
Laboratoire des Ecoulements Géophysiques et Industriels, France†

Simulation of unsteady hydrodynamic loadings and structural analysis of vertical axis water turbine **11379**
Jeronimo Zanette,† Cécile Münch and Ali Tourabi
Laboratoire Sols, Solides, Structures-Risques, France†

Impact of a spherical shell on a thin layer of the water **11778**
Tatiana Khabakhpasheva
Lavrentyev Institute of Hydrodynamic, Russia

Dynamics of fluid-conveying pipes: effects of velocity profiles **11821**
Stephanie Enz† and Jon Thomsen
Technical University of Denmark, Denmark†

Impinging jets on a plate with a degree of freedom in torsion **12109**
Yohann Nyirumulinga,† Clotilde Regardin, Frédéric Marmonier, Roger Ohayon and Edmond Szechenyi
Conservatoire National des Arts et Métiers, France†

Linear analysis of boundary layer flow interacting with a finite compliant surface **10689**
Mark Pitman† and Anthony Lucey
Curtin University of Technology, Australia†

The fluid–structure dynamics of a cantilevered-free flexible plate in a uniform flow **11217**
Anthony Lucey,† Richard Howell and Mark Pitman
Curtin University of Technology, Australia†

Nonlinear mixed-mode lateral vibration of a fluid-conveying cantilevered pipe with an end mass **11301**
Masatsugu Yoshizawa,† Kiyotaka Yamashita, Yuuki Hirose and Junji Ajiro *Keio University, Japan*†

Chaotic oscillation during vortex-induced vibration **11539**
Justin Leontini† and Mark Thompson
Monash University, Australia†

Oscillation onset in collapsible tubes by decreasing external pressure **11719**
Christopher Bertram,† Nicholas Truong and Stephen Hall
University of New South Wales, Australia†

Analytical model for the lift on a rotationally oscillating cylinder **11925**
Muhammad Hajj† and Isam Janajreh
Virginia Tech, USA†

Third-order effects in wave–body interaction **10478**
Bernard Molin,† Olivier Kimmoun and Fabien Remy
Ecole Centrale Marseille, France†

Phase shift effects for fluid conveying pipes with non-ideal supports **10725**
Jonas Dahl† and Jon Thomsen
Technical University of Denmark, Denmark†

FSM05 :: Granular materials and flows

Chairs: Detlef Lohse (Netherlands) and Tom Mullin (UK)

Ripple and undulation on vertically vibrated granular layers: dependence on material properties **11729**
Ataka Takei† and Osamu Sano
Tokyo University of Agriculture and Technology, Japan†

Highly nonlinear solitary waves in periodic granular media **11749**
Chiara Daraio,† Mason Porter, Eric Herbold, Ivan Szelengowicz and Panayotis Kevrekidis
California Institute of Technology, USA†

Crushing of granular media by a discrete numerical modeling **11813**
Mohamed Guessasma,† Jérôme Fortin, Patrice Coorevits and Adolphe Kimbonguila
Université de Picardie Jules Verne, France†

A constitutive model for unsaturated granular materials **10763**
Pierre-Yves Hicher† and Ching Chang
Ecole Centrale Nantes, France†

Influence of particle shape in the statistical mechanics of classical gases **10861**
Fernando Alonso-Marroquin† and Stefan Luding
The University of Queensland, Australia†

Computer modelling of doming phenomenon in flow of granular–cohesive material **11029**
Zdzislaw Wieckowski
Technical University of Lodz, Poland

Nonlinear stability of granular shear flow: Landau equation and shear-banding **10199**
Meheboob Alam† and Priyanka Shukla
Jawaharlal Nehru Center for Advanced Scientific Research, India†

Scaling the final deposits of dry cohesive granular columns after collapse and quasi-static fall **11285**
Catherine Meriaux† and Trent Triantafillou
Monash University, Australia†

Thermomicromechanical continuum theory for granular materials **12159**
Antoinette Tordesillas† and Maya Muthuswamy
, Australia†

Computer aided kinetic theory and granular matter **11642**
Isaac Goldhirsch
Tel-Aviv University, Israel

Realization of the Smoluchowski–Feynman ratchet in a granular gas **11476**
Devaraj van der Meer,† Peter Eshuis, Ko van der Weele and Detlef Lohse
University of Twente, Netherlands†

The numerical simulation for a hemisphere colliding into granular material **11466**
Lei Yang† and Caishan Liu
China Academy of Space Technology, China†

A multiscale methodology in granular matter physics **10705**
Qicheng Sun† and Guangqian Wang
Tsinghua University, China†

Pattern formation at a sand bed surface **10338**
Thomas Loiseleux,† Philippe Gondret, Delphine Doppler and Marc Rabaud
Lab FAST & ENSTA-ParisTech, France†

FSM06 :: Mechanics of material processing

Chairs: Francisco Chinesta (France) and Gabor Stepan (Hungary)

Apparent coexistence of multiple regimes of self-excited vibrations in deep drilling systems **11130**
Emmanuel Detournay† and Alexandre Depouhon
University of Minnesota, USA†

Bi-stable region estimations for metal cutting **10580**
Gabor Stepan,† Zoltan Dombovari and Eddie Wilson
Budapest University of Technology and Economics, Hungary†

A study of material behaviour at large plastic strains using plane-strain machining with a wedge indenter **11511**
Tejas Murthy,† Christopher Saldana, Ravi Shankar, Srinivasan Chandrasekar, Dale Compton and Kevin Trumble
Purdue University, USA†

Supercritical bifurcations in the state-dependent delay model of turning process **11550**
Tamás Insperger,† Gábor Stépán and David Barton
Budapest University of Technology and Economics, Hungary†

Numerical simulation of friction stir welding processes **11326**
Elias Cueto,† Arnaud Poitou, François Gratecap, Iciar Alfaro and Francisco Chinesta
University of Zaragoza, Spain†

FSM07 :: Porous media

Chairs: Wolfgang Ehlers (Germany) and Dominique Salin (France)

Simulation of carbonate matrix acidizing **10723**
Bulgakova Guzel,† Alexey Telin and Aygul Kamaltinova
Ufa State Aviation Technical University, Russia†

The tip of a fluid-driven fracture in a permeable elastic medium **10174**
Yevhen Kovalyshen† and Emmanuel Detournay
University of Minnesota, USA†

Swelling phenomena in chemically active hydrated materials **10333**
Wolfgang Ehlers,† Nils Karajan and Ayhan Acartürk
University of Stuttgart, Germany†

Stress measures in partially saturated porous media mechanics **11313**
Bernhard Schrefler,† Francesco Pesavento and William Gray
University of Padova, Italy†

Simulation, modelling and measurement of dispersive flow in bead packs **11410**
Howard Davis,† Kroll Daniel, Maier Robert, McCormick Alon and Vandre Eric
University of Minnesota, USA†

Effect of vibrations on stability of displacement front **11628**
Dmitriy Lyubimov,† Oleg Zikanov, Grigoriy Sedelnikov, Tatyana Lyubimova and Andrey Ivantsov
Perm State University, Russia†

A micromechanical modeling of poroplastic behaviour of saturated microcracked media **11880**
Djimédo Kondo,† Qizhi Zhu, Jian-Fu Shao and Vincent Monchiet
Laboratoire de Mécanique de Lille, France†

The three characteristic behaviours of dual-porosity media **11543**
Pascale Royer,† Jean-Louis Auriault and Claude Boutin
Laboratoire de Mécanique et Génie Civil, France†

Exact infiltration under concentration boundary conditions **10876**
Philip Broadbridge
University of Melbourne, Australia

Kinetic theory for suspension/colloid flow in porous media **10205**
Pavel Bedrikovetsky,† Oleg Dinariev and Luiz Rego
The University of Adelaide/PETROBRAS, Australia†

FSM08 :: Education in mechanics

Chairs: Igle Gledhill (South Africa) and Carl Herakovich (USA)

Practical study for vehicle dynamics **10781**
Yoshio Kano,† Takashi Kawaguchi and Masato Abe
Kanagawa Institute of Technology, Japan†

Design and use of supplementary software for an undergraduate program in engineering science and mechanics **10850**
Glenn Kraige,† Scott Hendricks and Don Morris
Virginia Tech, USA†

Photoelasticity as a teaching aid for the finite element method **10894**
Schalk Kok
University of Pretoria, South Africa

Teaching the modelling of structures **10979**
Juha Paavola† and Eero-Matti Salonen
Helsinki University of Technology, Finland†

Class participation experiments in mechanics: two-force members **11333**
Richard McNitt
The Pennsylvania State University, USA

The use of simplified strain gradient elasticity in structural analysis **11398**
Antonios Giannakopoulos† and Ioannis Vardoulakis
University of Thessaly, Greece†

Promoting education of applied mechanics by mechanics contest **11430**
Nelson Chen,† Ching Chen and Huei-Huang Lee
National Science and Technology Museum, Taiwan†

FSM09 :: Foams

Chairs: Stelios Kyriakides (USA) and Andrew Kraynik (USA)

Viscoelastic properties of open cell Kelvin foams **11224**
Heinz Pettermann,† Mathias Luxner, Jürgen Stampfl, Daniel Vallejo and Jaime Dominguez
Vienna University of Technology, Austria†

Structure and rheology of wet foams **11492**
Andrew Kraynik† and Douglas Reinelt
Sandia National Labs, USA†

On the crushing of metallic open-cell foams **10971**
Wen-Yea Jang† and Stelios Kyriakides
University of Texas at Austin, USA†

Investigation of the representative volume element size and analysis of the deformation mechanisms of open-cell foams **11205**
Anthony Burteau,† Jean-Dominique Bartout, Franck Nguyen, Samuel Forest, Yves Bienvenu, Shadi Saberi and Dirk Naumann
Mines de Paris—ParisTech, France†

Multi-scale modelling of fracture in metal foams **10059**
Patrick Onck† and Kodanda Mangipudi
University of Groningen, Netherlands†

Pressure-driven and free-rise foam flow **10621**
Lisa Mondy,† Rekha Rao, Christopher Brotherton, Christopher Bourdon, Mathias Celina, Anne Grillet and Sarah Leming
Sandia National Laboratories, USA†

SM01 :: Computational solid mechanics

Chairs: Jacob Fish (USA) and Wanxie Zhong (China)

Multiscale finite element simulation for crack propagation in heterogeneous media with microstructures **10130**
Seyoung Im,† Jae Lim and Dongwoo Sohn
Korean Advanced Institute of Science and Technology, South Korea†

Inverse analyses, artificial neural networks and dilatometric tests for damage and stress state assessment in concrete dams **11191**
Giulio Maier,† Tomasz Garbowski, Giorgio Novati and Ada Zirpoli
Politecnico di Milano, Italy†

Two-field and two-scale computational homogenization for coupled thermo-mechanical problems **10562**
Marc Geers,† Izzet Ozdemir and Marcel Brekelmans
Eindhoven University of Technology, Netherlands†

A generalized cosserat point element for isotropic nonlinear elastic materials including irregular 3D brick and thin structures **10732**
Miles Rubin† and Mahmood Jabareen
Technion - Israel Institute of Technology, Israel†

Model verification in dynamics through strict upper error bounds **11098**
Pierre Ladeveze† and Julien Waeytens
École Normale Supérieure de Cachan, France†

Natural boundary element method for mixed boundary problem of circular plate **10760**
Zhengzhu Dong,† Hui-ming Zhao and Wei-hong Peng
China University of Mining and Technology, China†

Exact solutions of frame structures **11017**
Haitao Ma† and Taicong Chen
South China University of Technology, China†

Gl mechanical and electromagnetic coupled field modeling and inversion **11259**
Ganquan Xie,† Lee Xie, Jianhua Li and Feng Xie
GL Geophysical Laboratory, USA†

A new rotation vector update for path-independent and strain-objective geometrically exact beam **11467**
Susanta Ghosh† and Debasish Roy
Indian Institute of Science, India†

Frequency dependent wave propagation in functionally graded materials **11615**
Laurent Aebi,† Jacqueline Vollmann, Juerg Bryner and Jürg Dual
ETH Zurich, Switzerland†

Multi-scale investigation of crystal plasticity **12074**
Zhuo Zhuang
Tsinghua University, China

Deformation simulation under constant volume condition using phase field crystal method **11741**
Tomoyuki Hirouchi,† Yoshihiro Tomita and Tomohiro Takaki
Kobe University, Japan†

Free vibration analysis of unsymmetric 6-noded element under mesh distortion **10252**
Senthilkumar Vaiyapuri† and Gangan Prathap
Centre for Mathematical Modelling And Computer Simulation, India†

Numerical solution of fractional derivative equations in mechanics: advances and problems **11290**
Wen Chen† and Hongguang Sun
Hohai University, China†

On the nonuniqueness of BIEM/BEM using SVD **11723**
Jeng-Tzong Chen
National Taiwan Ocean University, Taiwan

Vibration of thick plates under in-plane loading using finite strip-elements **11128**
Joe Petrolito† and Bruce Golley
La Trobe University, Australia†

Micropolar cohesive zone model for delamination failure in microsystem interconnects **11193**
Yan Zhang,† Johan Liu, Jing-yu Fan and Ragnar Larsson
Shanghai University, China†

Numerical simulation of glass fragmentation under impact using a coupled damage/decohesion model with the material point method **10912**
Luming Shen
Monash University, Australia

Neural networks for meshless and pufem approaches **10467**
Paolo Biagini† and Luca Facchini
Università di Firenze, Italy†

Deformability of flexibly jointed structure with negative Poisson's ratio **11463**
Hiro Tanaka† and Yoji Shibutani
Osaka University, Japan†

Nonlinear coupled FE-simulation of thermoelectromechanical processes in thin-walled structure **11485**
Ruediger Schmidt† and Sven Lentzen
RWTH Aachen University, Germany†

Morphology change in interfacial dislocation network by prismatic dislocation loop: discrete dislocation dynamics study **11726**
Kisaragi Yashiro,† Yoshihiro Tomita, Joy Pangetsu and Masaaki Konishi
Kobe university, Japan†

A new curved FE approach for analysis of masonry vaults **12144**
Antonio Tralli,† Enrico Milani and Gabriele Milani
University of Ferrara, Italy†

Nonconforming BETI/FETI method for time domain elastodynamics **10257**
Martin Schanz† and Thomas Rüberg
Graz University of Technology, Austria†

SM02 :: Contact and friction mechanics

Chairs: Irina Goryacheva (Russia) and Peter Wriggers (Germany)

A class of dynamic contact interaction problems in viscoelasticity **10227**
Marius Cocou,† Mathieu Schryve and Michel Raous
Laboratoire de Mecanique et d'Acoustique CNRS, France†

Effect of adhesion in sliding contact of rough bodies **10537**
Irina Goryacheva† and Yuliya Makhovskaya
Russian Academy of Sciences, Russia†

Contact analysis with non-linear elasticity and combined cone/spherical indenter **10750**
Pauli Pedersen
Technische Universität Denmark, Denmark

Influence of contact geometry on hardness values **10946**
Weimin Chen,† Che-Min Cheng, Yang-Tse Cheng and Min Li
Chinese Academy of Sciences, China†

Dynamic effects of a sliding tread block on concrete surfaces **10600**
Patrick Moldenhauer,† Matthias Kröger and Gunnar Gäbel
Technische Universität Bergakademie Freiberg, Germany†

Two smoothing methods in frictional beam-to-beam contact: a numerical comparison **10700**
Przemyslaw Litewka
Poznan University of Technology, Poland

Micro/nanoscale friction and its dependence on contact area **11673**
Sriram Sundararajan,† Kanaga Karuppiah and Angela Bruck
Iowa State University, USA†

A new contact width model for an automatic polishing process **12070**
Wei-Ling Kuo† and Ming Tsai
National Cheng Kung University, Taiwan†

Connected models of friction of rolling, sliding and whirling in problems of solids dynamics **10181**
Alexey Kireenkov
Institute for Problems in Mechanics, RAS, Russia

Analytical solution of the spherical indentation problem for a half-space with functionally graded elastic coating **10667**
Sergey Aizikovich,† Irina Trubchik, Leonid Krenev and Viktor Alexandrov
Don State Technical University, Russia†

On plane contact problems under partial reverse slip condition **11855**
Haradanahalli Murthy† and Naseem Hamza
Indian Institute of Technology, Madras, India†

Contact vibration analysis of an elastic-sphere oscillator and a semi-infinite viscoelastic cubic solid **10606**
Jiayong Tian† and Zhoumin Xie
Institute of Crustal Dynamics, China†

Friction mechanism of an elastomer sliding on smooth surface: influence of water squeeze film **10900**
Fabrice Deleau,† Koenen Alain and Mazuyer Denis
Laboratoire de Tribologie et Dynamique des Systmes, France†

SM03 :: Control of structures

Chairs: Felix Chernousko (Russia) and Andre Preumont (Belguim)

Design of resonant vibration absorbers with filtered feedback **10899**
Steen Krenk† and Jan Hogsberg
Technical University of Denmark, Denmark†

Controlled onset of low-velocity collisions in vibro-impacting systems with friction **11065**
Harry Dankowicz† and Fredrik Svahn
University of Illinois at Urbana-Champaign, USA†

A variational approach to 3D rod motion modeling and optimization **11464**
Georgy Kostin† and Vasily Saurin
Institute for Problems in Mechanics RAS, Russia†

Mobile systems controlled by internal moving masses **10538**
Felix Chernousko
Russian Academy of Sciences, Russia

Optimum control of thermal stress in a piezo-composite disk **11213**
Fumihiro Ashida,† Naotake Noda and Sei-ichiro Sakata
Shimane University, Japan†

Equilibrium stabilization via position and delayed position feedback **11052**
Haiyan Hu† and Bo Liu
Beijing Institute of Technology, China†

The adaptive spatial mobile robot-manipulator and way of diagnostics of physical and mechanical properties and the geometrical form of a surface of contact and trajectory of movement with his help **11555**
Sergey Sayapin† and Alexander Siniov
Mechanical Engineering Research Institute, Russia†

Distributed control of plate vibrations induced by in-plane time-dependent forces **10235**
Andrzej Tylikowski
Warsaw University of Technology, Poland

SM04 :: Damage mechanics and fatigue

Chairs: Nikita Morozov (Russia) and Romesh Batra (USA)

Life prediction based on crack growth analyses in different microstructures modeled by Voronoi-polygons under biaxial fatigue **10734**
Toshihiko Hoshide,† Atsushi Kasai and Naoya Takahashi
Kyoto University, Japan†

An analytical model for frictional load transfer in a clearance fit bolted joint **11033**
Ligieja Paletti,† Calvin Rans and Rinze Benedictus
Technische Universität Delft, Netherlands†

Phenomenological approach to the description of deformation and fracture of damaged solids **10619**
Evgeny Lomakin† and Tatiana Beliakova
Lomonosov Moscow State University, Russia†

Damage evolution in explosion of a particulate composite circular cylinder **10541**
Romesh Batra† and Anoop Varghese
Virginia Tech, USA†

Analytical correlations between the fatigue properties of engineering materials **10693**
Marco Paggi† and Alberto Carpinteri
Politecnico di Torino, Italy†

Evaluation of damage development in piezoelectric ceramics under repeated mechanical loading **10800**
Mamoru Mizuno,† Nozomi Odagiri and Mitsuhiro Okayasu
Akita Prefectural University, Japan†

Modelling progressive dynamic damage in advanced re-entry space transportation composite/hybrid structures **10792**
Javid Bayandor,† Bob Farahmand and Frank Abdi
Royal Melbourne Institute of Technology, Australia†

Residual strength based lifetime prediction of composite materials subjected to spectrum loading **10168**
Scott Case,† John Lesko, Jason Cain and Nathan Post
Virginia Tech, USA†

Modeling of hydrogen embrittlement of metals in wet H_2S containing environments **10421**
Vladimir Astafiev
Samara State University, Russia

Mean stress effect and bi-axial fatigue of structures from two scale damage model **10987**
Gregory Barbier,† Stephan Courtin, Alban du Tertre, Jean-Philippe Sermage, Bumedijen Raka and Rodrigue Desmorat
École Normale Supérieure de Cachan, France†

Finite element simulation and life prediction of thermal fatigue failure of the continuous casting tundish cover **11336**
Xia Zhou,† Zhanfei Tang and Guohui Qu
Dalian University of Technology, China†

SM05 :: Elasticity

Chairs: Reinhold Kienzler (Germany) and Gérard Maugin (France)

Nonlinear bulk strain waves in layered elastic waveguides with delamination: theory and experiments **11385**
Karima Khusnutdinova,† Galina Dreiden, Alexander Samsonov and Irina Semenova
Loughborough University, UK†

Plane waves in nonlinear anisotropic elasticity **11406**
Wlodzimierz Domanski
Polish Academy of Sciences, Poland

Propagation of magnetoelastic waves in a vortex field in a superconducting layer **10674**
Bogdan Maruszewski,† Andrzej Drzewiecki, Bogdan Maruszewski and Roman Starosta
Poznan University of Technology, Poland†

Reciprocity relations in Newtonian and Eshelbian mechanics **10542**
Reinhold Kienzler
University of Bremen, Germany

Numerical analysis of stress singularity in three-dimensional problems of elasticity theory **11384**
Valeriy Matveyenko,† Tatyana Nakaryakova and Natalya Sevodina
Institute of Continuous Media Mechanics, Russia†

Materials with Poisson's ratio near -1: properties and possible realisations **11982**
Elena Pasternak,† Arcady Dyskin and Elena Pasternak
The University of Western Australia, Australia†

The Flamant and Carothers type problems for cusped prismatic shells **10023**
George Jaiani
Ivane Javakhishvili Tbilisi State University, Georgia

Geometry, dynamics and fractals **10863**
Marcelo Barros,† Augusto Galeão and Luiz Bevilacqua
National Laboratory for Scientific Computing, Brazil†

Axisymmetric solution for a tetragonal medium **10988**
Marc Dahan
Université de Franche-Comté, France

Multi-field modelling of short wavelength deformations for Cosserat solids **10926**
Andrey Miroshnichenko† and Aleksey Vasiliev
Australian National University, Australia†

Elastic fields in quantum dot structures with arbitrary shapes and interface effects **11069**
Jianxiang Wang,† Haijian Chu, Huiling Duan and Bhushan Karihaloo
Peking University, China†

Size effect on probability of quasibrittle failure and lifetime: from atomistic to structural scale **11525**
Sze-Dai Pang,† Jia-Liang Le and Zdeněk Bažant
National University of Singapore, Singapore†

Intrinsic field tensors for strongly orthotropic continua **11677**
David Kellermann,† Tomonari Furukawa and Don Kelly
University of New South Wales, Australia†

Mechanics of nonlinear acoustoelasticity in fluid-saturated porous rocks **10590**
Jing Ba,† Jiong Liu, Huizhu Yang, Liyun Fu and Mengqiu Guo
Tsinghua University, China†

Analytical mechanics of bars, plates and shells on asymmetrical theory of elasticity **10679**
Samvel Sargsyan
Gyumri State Pedagogical Institute, Armenia

A multiscale projection method for fracturing solids in three dimensions **11378**
Stefan Loehnert,† Dana Mueller-Hoeppe and Peter Wriggers
Leibniz Universität Hannover, Germany†

Variational treatment of crack problems in plane micropolar elasticity **10649**
Stanislav Potapenko
University of Waterloo, Canada

Two-dimensional thermoelasticity problems for a rectangle **11000**
Yuriy Tokovyy,† Chien-Ching Ma and Viatcheslav Meleshko
National Taiwan University, Taiwan†

On the mechanical analysis of plates composed of functionally graded material **10195**
Holm Altenbach† and Victor Eremeev
Martin-Luther-Universität Halle-Wittenberg, Germany†

Time dependent mechanical response of the cell cytoskeleton **11663**
Robert McMeeking,† Anthony Evans, Vikram Deshpande, Zhensong Wei and Amit Pathak
University of California, Santa Barbara, CA, USA, USA†

The role of fiberwise constraints in the mechanics of linearly elastic shells **10989**
Paolo Podio-Guidugli
University of Rome Tor Vergata, Italy

Finite-amplitude Love waves in a pre-stressed neo-Hookean material **11110**
Elizabete Ferreira,† Philippe Boulanger and Michel Destrade
Universite Libre de Bruxelles, Belgium†

Effect of cubic elasticity on the distribution of stress in polycrystals **11392**
Maxime Sauzay
Commissariat à l'Énergie Atomique, France

On variational formulations for nonlocal elasticity **10294**
Francesco de Sciarra
Universita' di Napoli Federico II, Italy

New model for piezoelectric medium with initial porosity and analysis of ultrasonic piezoelectric devices **11819**
Andrey Nasedkin
Southern Federal University, Russia

Continuum dislocation theory and size effect **11844**
Khanh Le
Ruhr-Universität Bochum, Germany

Notes on stresses in chains **12051**
Marcelo Epstein† and Reuven Segev
University of Calgary, Canada†

Green's function for plane anisotropic elastic bimaterials with imperfect interface **11173**
Leszek Sudak
University of Calgary, Canada

Continuum modeling of elastic dielectric solids with defects, with application to barium strontium titanate thin films **10502**
John Clayton,† William Nothwang, Michael Grinfeld and Peter Chung
United States Army Research Laboratory, USA†

Mathematical modeling of linearly piezoelectric slender rods **11034**
Thibaut Weller† and Christian Licht
Centre National de la Recherche Scientifique, France†

Internal variables and microstructured materials **11079**
Juri Engelbrecht,† Arkadi Berezovski and Gerard Maugin
Tallinn University of Technology, Estonia†

Analysis of interfacial crack by means of hypersingular integro-differential equations **11350**
Noda Nao-Aki
Kyushu Institute of Technology, Japan

SM06 :: Experimental methods in solid mechanics

Chairs: Jacques Desrues (France) and Julia Greer (USA)

Recent developments and applications of the ISSR technique **11048**
Keyu Li
Oakland University, USA

Measurements of discontinuous displacement fields by extended 3D image correlation using X-ray tomography **10336**
Francois Hild,† Stéphane Roux, Julien Réthoré, Jean-Yves Buffière and Jean-Philippe Tinnes
LMT-Cachan, France†

In-situ investigation of nano-scale plasticity in FCC and BCC crystals via homogeneous deformation of nano-pillars **10545**
Julia Greer,† Steffen Brinckmann and Ju-Young Kim
California Institute of Technology, USA†

Characterization of the stress–strain relationships of ductile films using sharp indentation **11940**
Yyongli Huang,† Yanguo Liao and Yichun Zhou
Xiangtan University, China†

Evaluation of whole-field thin-film stress and strain by the biharmonic function **11157**
Wei-Chung Wang,† Kai-Hung Cheng and Chi-Hung Hwang
National Tsing Hua University, Taiwan†

Mechanical characterization of materials by micro-indentation and AFM scanning **10066**
Gabriella Bolzon,† Enzo Chiarullo and Massimiliano Bocciarelli
Politecnico di Milano, Italy†

Determination energy dissipation for aluminium deformed dynamically at modified Taylor impact test **10953**
Leopold Kruszka
Military University of Technology, Poland

3D volumetric DIC of X-ray microtomographic images to study localized deformation in a stiff clayey rock **10659**
Jacques Desrues,† Michel Bornert, Pierre Besuelle, Gioacchino Viggiani and Nicolas Lenoir
Grenoble University, France†

A new method for characterizing the surface periodic structure of photonic crystal and its application **10942**
Huimin Xie,† Fulong Dai, Satoshi Kishimoto and Qinghua Wang
Tsinghua University, China†

Measuring deformation of large vessels with innovative broken-ray videometrics **10984**
Yu Qifeng,† Fu Sihua, Jiang Guangwen and Shang Yang
National University of Defense Technology, China†

The research of measuring polymerization shrinkage of composite resins with ESPI **10662**
Guobiao Yang† and Zhang Zhang
Tongji University, China†

Development of an automated load and measurement device **10714**
Mohsen Javadi† and Bernd Behrens
Institute of Metal Forming and Metal-Forming Machines, Germany†

The optoelectronic method for measurement of small dynamic displacements **10740**
Michael Osipov,† Lydia Osipova and Maxim Popov
Samara State University, Russia†

Acoustic emission detection for damage evaluation of thermal barrier coatings under cyclic heating **11725**
Li Yang,† Yichun Zhou, Weiguo Mao and Qixing Liu
Xiangtan University, China†

A lattice unit model to evaluate interfacial residual stress in ferroelectric thin film **10966**
Xuejun Zheng,† Yichun Zhou and Qingyong Wu
Xiangtan University, China†

A novel magnetostrictive acoustic transducer for longitudinal guided wave inspection of steel strands **11449**
Zenghua Liu,† Bin Wu, Su Liu, Cunfu He and Yinong Zhang
Beijing University of Technology, China†

Development and performance study of a new apparatus for imparting lateral cyclic load on piles **10406**
Sudip Basack
Bengal Engineering & Science University, India

SM07 :: Fracture and crack mechanics

Chairs: Dietmar Gross (Germany) and Robert Goldstein (Russia)

A predictive model for chipping wear of hard coatings **11651**
Leon Keer† and Kun Zhou
Northwestern University, USA†

Structural-kinetic approach in dynamics of continuum: fracture, spalling, cavitation, electrical breakdown **11646**
Arseny Kashtanov† and Yuri Petrov
St Petersburg State University, Russia†

Dynamic fatigue behavior of cracked piezoelectric ceramics in three-point bending under electromechanical loading **11021**
Yasuhide Shindo,† Fumio Narita and Mitsuru Hirama
Tohoku University, Japan†

An extended Gurson model accounting for strain localization within thin planar layers **11334**
Jean-Baptiste Leblond† and Gérard Mottet
Universite Pierre et Marie Curie, France†

Condition for crack deviation in an anisotropic solid and its dependence on a crack model **11472**
Efim Shifrin† and Robert Goldstein
Institute for Problems in Mechanics RAS, Russia†

Exact solution of a penny-shaped crack in piezoelectric materials with electric saturation at the crack tip **10323**
Weiqiu Chen
Zhejiang University, China

Incubation time based fracture mechanics **11756**
Yuri Petrov
St Petersburg State University, Russia

The problem of co-linear twin cracks in elastic wave field **10398**
Bing-zheng Gai† and Cao Ning
Harbin Institute of Technology, China†

Multiscale energy momentum tensor and its application to fracture **10595**
Shaofan Li
University of California at Berkeley, USA

Thermal shock solution of a functionally graded material plate with arbitrary thermomechanical properties and a surface crack **10608**
Li-cheng Guo† and Naotake Noda
Harbin Institute of Technology, China†

Energy analysis of the brittle fracture of solid with cracks **11276**
Igor Dunaev† and Vladislav Dunaev
Kuban State Techology University, Russia†

Strain-energy criteria and fracture of plastic bodies in a neighborhood of strain concentrators **11318**
Anastasia Bukhanko† and Alexander Khromov
Samara State Aerospace University, Russia†

Support to rock excavations provided by adhesive liners
Herven Abelman† and David Mason **11776**
University of the Witwatersrand, Johannesburg, South Africa†

Research on mixed mode and mode II crack growth in orthotropic composites by caustics method **10892**
Zheng Li,† Kezhuang Gong and Kan Feng
Peking University, China†

3D interface crack in fully coupled electromagnetothermoelastic multiphase anisotropic composites **10614**
BoJing Zhu,† Shaohua Yu, Taiyan Qin and Yaolin Shi
Graduate University of Chinese Academy of Sciences, China†

Fracture simulation of concrete using fractal approach and lattice model: validation by AE study **10027**
Remalli Sagar† and Raghu Prasad
Indian Institute of Science, India†

Multiple cracking of an embedded concretion **10833**
Dominique Leguillon,† Daniel Quesada, Claude Putot and Eric Martin
Centre National de la Recherche Scientifique, France†

Spontaneous crack propagation in functionally graded materials **10145**
Dhirendra Kubair† and Sandip Haldar
Indian Institute of Science, Bangalore, India†

Crack bridging model for nanocomposites **10165**
Mikhail Perelmuter
Institute for Problems in Mechanics, Russia

Non-linear crack growth in short steel fibre reinforced concrete: modeling and experimental verification **10129**
Andrejs Krasnikovs,† Andrejs Pupurs and Olga Kononova
Riga Technical University, Latvia†

A computational method for three dimensional finite deformation fracture **11544**
Dana Mueller-Hoeppe,† Stefan Loehnert and Peter Wriggers
Leibniz Universitaet Hannover, Germany†

A computational approach for fatigue crack propagation in ship structures under random sequence of clustered loading **11551**
Yoichi Sumi† and Teppei Okawa
Yokohama National University, Japan†

Dominant mechanism for crack propagation in nonplanar interface **12063**
Abhijit Dasgupta,† Joseph Varghese and Koustav Sinha
University of Maryland, USA†

Simulation of crack propagation in functionally graded materials **10633**
Li Ma,† Zhi-Yong Wang and Lin-Zhi Wu
Harbin Institute of Technology, China†

Determination of the effective material properties of a linear elastic material with a randomly distributed microcracks by the three level finite element method **11208**
George Mejak
University of Ljubljana, Slovenia

Damage tolerance of a sandwich panel with square honeycomb core **11319**
Ignacio Alonso† and Norman Fleck
Cambridge University, UK†

Assessment on the structural integrity based on 3D crack growth simulations **10507**
Wilhelm Weber,† Paul Steinmann and Günther Kuhn
Institute of Applied Mechanics, Germany†

Pre-existing fluid driven fracture in permeable rock **11346**
David Mason† and Gideon Fareo
University of the Witwatersrand, South Africa†

Unidirectional 'DCB' and 'ENF' specimens: a comparative study between finite elements and higher order beam theories **11469**
Raghu Prasad† and Pavan Kumar
Indian Institute of Science, India†

Microstructural simulation on the brittle versus ductile transition of nanocrystalline metals **11916**
Wei Yang† and Fan Yang
Zhejiang University, China†

Mixed-mode fracture in viscoelastic orthotropic material **10645**
Rostand Pitti,† Octavion Pop and Frédéric Dubois
Universite de Limoges, France†

SM08 :: Geophysics and geomechanics

Chairs: Nadia Lapusta (USA) and Ioannis Vardoulakis (Greece)

Modelling high pressure shear using breakage mechanics **10201**
Itai Einav,† Giang Nguyen and Ioannis Vardoulakis
The University of Sydney, Australia†

Mechanical characteristics of seismic waves estimated from earthquake-induced structural failures **10628**
Koji Uenishi
Kobe University, Japan

Mechanisms of dynamic friction at slip rates appropriate for earthquake faulting **11931**
Yuri Fialko† and Kevin Brown
University of California, San Diego, USA†

3D modeling of dynamic and quasi-static fault slip: interaction of dynamic rupture with a stronger patch over several earthquake cycles **10548**
Nadia Lapusta† and Yi Liu
California Institute of Technology, USA†

Earthquake source mapping using strong motion array data **10706**
Narayana Iyengar† and Raghukanth Gudemella
Indian Institute of Science, India†

Fluid-driven fracture growth along an existing natural fracture **11132**
Xi Zhang† and Rob Jeffrey
Commonwealth Scientific and Research Organisation, Australia†

Predicting behavior in granular materials via multiscale computations **11206**
Jose Andrade
Northwestern University, USA

Laboratory experiments and theoretical studies of rupture modes and supershear transition **11522**
Xiao Lu,† Ares Rosakis and Nadia Lapusta
California Institute of Technology, USA†

Mathematical theory of plasticity for frictional materials **10358**
Kristian Krabbenhoft
University of Newcastle, Australia

Earthquake nucleation on geometrically complex faults **11917**
Guanshui Xu,† James Dieterich and Zijun Fang
University of California at Riverside, USA†

Spectral element simulations of dynamic rupture along non planar faults **11918**
Jean-Pierre Vilotte† and Gaetano Festa
Institut de Physique du Globe de Paris, France†

A multiscale modelling of damage and time dependent plastic behavior of cohesive rocks: formulation and numerical applications **11937**
Jian-Fu Shao,† Ariane Guery, Fabrice Cormery and Djimédo Kondo
Laboratoire de Mécanique de Lille, France†

Multi-phase coupled elasto-viscoplastic analysis of unsaturated soil slope during seepage flow **11436**
Fusao Oka,† Ryosuke Kato, Shinya Yamazaki and Sayuri Kimoto
Kyoto University, Japan†

Thermomechanics of faults **11604**
Emmanuil Veveakis,† Jean Sulem and Ioannis Vardoulakis
National Technical University of Athens, Greece†

Propagation of shear waves in an elastic layer with void pores **10851**
Prakash Pal
Indian School of Mines University, India

Non-Euclidean model of the zonal disintegration of rocks around an underground working **10847**
Mikhail Guzev
Russian Academy of Sciences, Far Eastern Branch, Russia

SM09 :: Impact and wave propagation

Chairs: Narinder Gupta (India) and Rod Clifton (USA)

Dynamic strain localization and fragmentation **11502**
Krishnaswamy Ravi-Chandar† and Haitao Zhang
The University of Texas at Austin, USA†

A substructure technique for impact-induced transient wave of discontinuous flexible system with wave geometric dispersion **11527**
Yunian Shen† and Xiaochun Yin
Nanjing University of Science and Technology, China†

Dynamic test of the main aircraft landing gear with failure **11865**
Wieslaw Krason,† Jerzy Malachowski and Rafal Kajka
Military University of Technology, Poland†

Modeling mechanical response and failure of ice submitted to high velocity impacts **12097**
Yann Chuzel-Marmot,† Alain Combescure and Roland Ortiz
INSA Lyon, France†

Bloch–Floquet flexural waves and localised defect modes in thin elastic plate structures **11404**
Natasha Movchan,† Ross McPhedran and Alexander Movchan
University of Liverpool, UK†

Modelling stress wave propagation under biaxial loading using SPH **10107**
Rajarshi Das† and Paul Cleary
CSIRO, Australia†

Emergence of soliton trains in microstructured materials **11311**
Andrus Salupere,† Merle Randrüüt and Kert Tamm
Tallinn University of Technology, Estonia†

Propagation of surface SH waves on a half space coated with a nonlinear thin layer **11373**
Ali Demirci,† Mevlut Teymur and Semra Ahmetolan
Istanbul Technical University, Turkey†

Guided elastodynamic waves in functionally graded cylindrical structures **11412**
Jacqueline Vollmann,† Laurent Aebi, Juerg Bryner, Nicolas Bochud and Jürg Dual
ETH Zurich, Switzerland†

High velocity penetration into ground media **11479**
Igor Simonov† and Yury Bivin
Institute for Problems in Mechanics, Russia†

Dispersive behavior of waves in pre-stressed imperfectly bonded compressible elastic layered composites **11567**
Anil Wijeyewickrema† and Sasikorn Leungvichcharoen
Tokyo Institute of Technology, Japan†

Thermoacoustic effect in thin plates with residual stresses **10020**
Ching-Chung Yin† and Shih-Ming Hsu
National Chiao Tung University, Taiwan†

An experimental study of plate wave diffraction tomography **11939**
Andrew Rohde† and Martin Veidt
Commonwealth Scientific and Research Organisation, Australia†

Energy dissipation study for drop test of landing gear **10124**
Jerzy Malachowski† and Wieslaw Krason
Military University of Technology, Poland†

Three-dimensional reflection and refraction of seismic waves in highly anisotropic media **10218**
Amares Chattopadhyay† and Pato Kumari
Indian School of Mines University, India†

Far-field solution of SH-wave by circular lining and linear crack **10796**
Hongliang Li† and Diankui Liu
Harbin Engineering University, China†

Calculation collisions by using inverse method **10021**
Janis Viba
Riga Technical University, Latvia

Asymptotic analysis of linear wave propagation in and free vibrations of elastic helical springs **10853**
Sergey Sorokin
Aalborg University, Denmark

Modelling of explosion damage tolerance in advanced space structures subject to hypervelocity impact in microgravity **11912**
Andrew Litchfield† and Javid Bayandor
Royal Melbourne Institute of Technology, Australia†

Plasticity-damage versus anisotropic damage for impact on concrete structures **11147**
Marion Chambart,† Rodrigue Desmorat, Fabrice Gatuingt, Daniel Guilbaud and Didier Combescure
École Normale Supérieure de Cachan, France†

The dynamics of pizza tossing **11175**
Kuang-Chen Liu,† James Friend and Leslie Yeo
Monash University, Australia†

On Hayes waves **11111**
Philippe Boulanger
Universite Libre de Bruxelles, Belgium

A new concept of dynamic biaxial plastic crushing of metallic thin-walled tubes **11086**
Akrum Abdul-Latif† and Rachid Baleh
Université Paris 8, IUT de Tremblay, France†

Surface waves in phononic crystals with large acoustic mismatch: band structure analysys by wavelet method **10687**
Yue-Sheng Wang,† Chuanzeng Zhang and Zhi-Zhong Yan
Beijing Jiaotong University, China†

Measurements of Lamb wave band gaps and guided waves in air/silicon phononic plates and channels **11099**
Tsung-Tsong Wu,† Wei-Chih Kuo and Jin-Chen Hsu
National Taiwan University, Taiwan†

Experimental study on negative effective mass in a 1D mass-spring system **11577**
Gengkai Hu,† Shanshan Yao and Xiaoming Zhou
Beijing Institute of Technology, China†

Use of magnesium for lightweight and crashworthy S-frame **10436**
Parisa Tehrani† and Mousa Nikahd
Iran University of Science and Technology, Iran†

The role of nonequilibrium in Hugoniot of a porous material **11131**
Anatoly Resnyansky
Defence Science and Technology Organisation, Australia

Repeated impact between two flexible rods **10789**
Ali Tian† and Xiaochun Yin
Nanjing University of Science and Technology, China†

Effects of micro-structures on the in-plane dynamic crushing of lattice materials **11220**
Ying Liu† and Xin-chun Zhang
Beijing Jiaotong University, China†

Study on the structure health monitoring based on AE and SMI technology **11179**
Ying Luo† and Ziping Wang
Jiangsu University, China†

Studies on the dynamic behavior of aluminum alloy foams **10463**
Hongwei Ma,† Guitong Yang, Longmao Zhao and Zhihua Wang
Jinan University, China†

Experimental analysis on lower clamp bolt of motorcycle front fork during frontal impact **12001**
Shaw Wong
Malaysian Institute of Road Safety Research, Malaysia

SM10 :: Material instabilities

Chairs: Ahmed Benallal (France) and Rene de Borst (Netherlands)

Effects of energy-providing components in 2D discrete structures **10172**
Yun-Che Wang
National Cheng Kung University, Taiwan

Material stability conditions for a class of inhomogeneous anisotropic media **10405**
Carlos Daros
University of Campinas, Brazil

Stability of an inverted spring pendulum driven by a periodic force **10730**
Moshe Gitterman
Bar-Ilan University, Israel

Numerical modelling of strain localization in glassy polymers recognising their intrinsic anisotropy **11613**
Huaxiang Li† and Paul Buckley
University of Oxford, UK†

Instability of compressible elastic materials at stretching stresses **10321**
Mikhail Karyakin
Southern Federal University, Russia

Mathematical theory of accreted solids and its applications **10470**
Alexander Manzhirov
Institute for Problems in Mechanics, Russia

Onset of cavitation in compressible, isotropic, hyperelastic solids **10721**
Oscar Lopez-Pamies
State University of New York, Stony Brook, USA

SM11 :: Mechanics of composites

Chairs: Peter Gudmundson (Sweden) and Donatus Oguamanam (Canada)

Buckling simulation of imperfect cylindrical composite shells using Reissner–Mindlin–von Karman type shell facet model **10341**
Petri Kere† and Mikko Lyly
Tampere University of Technology, Finland†

Effective properties of nonlinear power law elastic periodic composites **12175**
Vincent Monchiet† and Guy Bonnet
Universit Paris-Est Marne la Valle, France†

A coupled analytical model for hydrostatic response of 1-3 piezocomposites **10617**
Nimal Rajapakse† and Chen Yue
The University of British Columbia, Canada†

3D elastodynamics of an interface crack **10620**
Igor Guz,† Olexandr Menshykov and Maria Kashtalyan
University of Aberdeen, UK†

Analyses of a metallic rod bridging a unbonded interface **10902**
Brian Legarth
Technical University of Denmark, Denmark

Damage evolution during thermo-oxidation of polymeric matrix composites **10950**
Kishore Pochiraju,† Gyaneswar Tandon and Greg Schoeppner
Stevens Institute of Technology, USA†

Modeling of the degradation of laminates under impact: some key points **11245**
Olivier Allix,† Jean-Mathieu Guimard and Nicolas Feld
École Normale Supérieure de Cachan, France†

Delamination of compressed thin layers at corners **11325**
Johan Clausen,† Henrik Jensen and Kim Sørensen
Aalborg University, Denmark†

Multiple curved micro-beams model for in-plane mechanical properties of stitched composite laminates **11368**
Junqian Zhang† and Yuqing Wei
Shanghai University, China†

The characterization of interface adhesion of dissimilar elastic-plastic materials by a pressurized blister test modeling **11431**
Yichun Zhou† and Limei Jiang
Xiangtan University, China†

Transverse crack behavior in satin woven carbon fiber reinforced/epoxy composite laminates at cryogenic temperatures **11576**
Shinya Watanabe,† Yasuhide Shindo, Tomo Takeda and Fumio Narita
Tohoku University, Japan†

Micromechanics-based nonlocal modeling of elastic matrices containing aligned spheroidal inclusions **11409**
Ilaria Monetto† and Walter Drugan
University of Genoa, Italy†

The effect of interfaces on the plastic behavior of periodic composites **10642**
Martin Idiart† and Norman Fleck
University of Cambridge, UK†

Free edge effects of thermoplastic composite laminates **11183**
Min Shen,† Hongqi Li, Shibin Wang and Jingwei Tong
Tianjin University, China†

Continuum analysis for a unidirectional composite with a penny shaped crack **10893**
Michael Ryvkin† and Jacob Aboudi
Tel Aviv University, Israel†

On modelling reinforced composites exhibiting stochastic uncertainties on volume fraction: a stochastic micromechanical approach **10821**
Johann Guilleminot,† Christophe Binetruy, Djimédo Kondo and Christian Soize
Ecole des Mines de Douai, France†

Transient response of active constrained-layer damped FGM beams **11238**
Donatus Oguamanam† and Elena Miroshnichenko
Ryerson University, Canada†

Micromechanism of deformation in EMC laminates **10544**
Zhengdao Wang
Beijing Jiao-Tong University, China

Thermo-mechanical constitutive laws for particle-reinforced composites including multi-type ellipsoidal reinforcements **10704**
Yasser Shabana
El-Mataria, Masaken Elhelmia, Egypt

Meso-mechanical investigation on high temperature oxidation of thermal protective ceramics **11896**
Jun Liang,† Chao Wang and Yang Liu
Harbin Institute of Technology, China†

Influence of imperfect elastic contact condition on the effective properties of piezoelectric fibrous composites **11885**
Federico Sabina,† Reinaldo Rodriguez-Ramos, Juan Lopez-Realpozo, Raul Guinovart-Diaz and Julian Bravo-Castillero
Universidad Nacional Autonoma de Mexico, Mexico†

The influence of the dimension ratio and interfacial debonding on plastic flow of cylindrical SiC reinforced aluminum matrix composites **11835**
Ying Zhang† and Shaoxing Qu
Zhejiang University, China†

Accurate modelling of FRP composite sandwich plates having interlaminar slips **11275**
Anupam Chakrabarti
Indian Institute of Technology, Roorkee, India

SM12 :: Mechanics of phase transitions

Chairs: Kaushik Bhattacharya (USA) and Erik van der Giessen (Netherlands)

Multi-phase-field recrystallization simulation based on deformation microstructure **10636**
Tomohiro Takaki† and Yoshihiro Tomita
Kyoto Institute of Technology, Japan†

Nucleation and growth of stress-induced martensitic fine layered structures in shape memory alloys under uniaxial tension **11542**
Yongzhong Huo,† Cheng Peng and Yan Yan
Fudan University, China†

Elastoplastic phase-field simulation of cubic-tetragonal martensitic transformation in polycrystals **11528**
Akinori Yamanaka,† Yoshihiro Tomita and Tomohiro Takaki
Kobe University, Japan†

Electrical induced crack propagation and domain switching in ferroelectric single crystal **11093**
Daining Fang† and Ye-Jian Jiang
Tsinghua University, China†

Micromagnetic theory of ferromagnetic shape memory alloys **11676**
Jiangyu Li
University of Washington, USA

Thermomechanical properties of shape-memory polymer and composite **10703**
Hisaaki Tobushi,† Yoshiki Sugimoto, Yoshihiro Ejiri and Shunichi Hayashi
Aichi Institute of Technology, Japan†

Atomic-scale mechanism of crack-tip deformation: twinning and phase transformation **11020**
Ya-Fang Guo,† Wen-Ping Wu and Lei Liu
Beijing Jiaotong University, China†

Stress-induced martensitic phase transformation in Nitinol **10799**
Samantha Daly,† Kaushik Bhattacharya and Guruswami Ravichandran
University of Michigan, USA†

Guided phase pattern formation in monolayers **10816**
Wei Lu
University of Michigan, Ann Arbor, USA

An elastoplastic phase field model for microstructure evolution **10897**
San-Qiang Shi
The Hong Kong Polytechnic University, Hong Kong

Discrete dislocation-transformation model for austenitic single crystals **10914**
Sergio Turteltaub,† Erik van der Giessen and Jingyi Shi
Delft University of Technology, Netherlands†

SM14 :: Multibody and vehicle dynamics

Chairs: Jorge Ambrósio (Portugal) and Werner Schiehlen (Germany)

A fast iterative solution of the wheel-rail contact **11198**
Ingo Kaiser
German Aerospace Center, Germany

On the contact detection for contact analysis in multibody systems **11246**
Paulo Flores† and Jorge Ambrósio
University of Minho, Portugal†

Oscillation reduction of cranes by hoisting manipulation **10928**
Edwin Kreuzer† and Andreas Bockstedte
Hamburg University of Technology, Germany†

Planetary rover mobility performance on soft and uneven terrain **11243**
Bernd Schäfer,† Rainer Krenn and Andreas Gibbesch
German Aerospace Center, Germany†

Smoothing friction phenomena in railway dynamics **10099**
Werner Schiehlen,† Jens Koenig and Peter Meinke
University of Stuttgart, Germany†

Measurements and simulations of rail vehicle dynamics with respect to overturning risk **10456**
Dirk Thomas† and Mats Berg
Royal Institute of Technology, Sweden†

Environmental and track perturbations on multiple pantograph interactions with catenaries in high-speed trains **10559**
Jorge Ambrósio† and João Pombo
IDMEC/IST, Portugal†

Dynamic characteristics of pseudo-rigid bodies **11264**
Li-Sheng Wang,† Yih-Hsing Pao and Hsin-Min Peng
National Taiwan University, Taiwan†

Analytical and experimental analysis of a parallel leaf spring guidance **11310**
Jacob Meijaard,† Dannis Brouwer and Ben Jonker
University of Twente, Netherlands†

Numerical and experimental analysis of an automotive clutch disc **11377**
Samir Sfarni,† Matthieu Malley, Jérôme Fortin and Emmanuel Bellenger
Université de Picardie Jules Verne, France†

Dynamic analysis of rail vehicles and investigation of potential derailment caused by wheelflats **11533**
Wen-Fang Wu,† Sih-Li Chen and Yang-Tsai Fan
National Taiwan University, Taiwan†

Development of a dynamic analysis solver using an object-oriented programming method **11019**
Jiwon Yoon,† Sungpil Jung, Taewon Park and Jeongbeom Kim
Ajou University, South Korea†

Dynamics model and algorithm of floating raft with elastic limiters **11170**
Jianming Wen† and Qi Feng
Tongji University, China†

Symbolic tools for sensitivity analysis of multibody systems **11235**
Arnaud Sandel,† Philippe Boisse, Lionel Maiffredy and Michel Fayet
National Institute of Applied Sciences, Lyon, France†

Experimental analysis of the A-pillar vortex fluctuations **11632**
Benjamin Levy,† Pierre Brancher and André Giovannini
Institut de Mecanique des Fluides de Toulouse, France†

Modelling and simulating automobile hysteresis nonlinear dynamical system **11258**
Mingxia Fang† and Qi Feng
Tongji University, China†

On sensitivity methods for vehicle systems under stochastic crosswind-loads **11471**
Christian Wetzel† and Carsten Proppe
University of Karlsruhe, Germany†

The multi-impact dynamics in multibody systems **11070**
Caishan Liu,† Bernard Brogliato and Zhen Zhao
Peking University, China†

Analytical study of the improved seatbelt retractor **11531**
Chanseung Park,† Taewon Park, Sungpil Jung, Kwangyeil Cheong and Yosun Hong
Ajou University, South Korea†

The dynamic characteristic analysis of the bi-modal tram using the test platform of all wheel steering ECU **11535**
Sooho Lee,† Kijung Kim, Kyungho Moon, Sunghun Choi, Kabjin Jun and Taewon Park
Ajou University, South Korea†

Discrete time transfer matrix method for dynamics of multi-rigid-flexible-body system **10999**
Xiaoting Rui,† Bao Rong and Guoping Wang
Nanjing University of Science and technology, China†

Coupled simulation of dispersions in multibody systems **10751**
Peter Eberhard† and Florian Fleissner
University of Stuttgart, Germany†

Dynamics of a flexible body with rapid mass loss **10881**
Arun Banerjee† and Mark Lemak
Lockheed Martin Space Systems, USA†

Free vibration of vehicles with interconnected suspensions **11703**
Wade Smith,† Jeku Jeyakumaran and Nong Zhang
University of Technology, Sydney, Australia†

Motion of an inertially excited two-mass oscillator along a rough plane **11225**
Igor Zeidis,† Klaus Zimmermann, Mikhail Pivovarov and Nikolai Bolotnik
Technische Universitaet Ilmenau, Germany†

Helix beam finite element based on intrinsic spatial curvatures **10604**
Oleg Dmitrochenko† and Aki Mikkola
Lappeenranta University of Technology, Finland†

Roll-tracking control of an unmanned bicycle using fuzzy logic controller **11437**
Chih-Keng Chen† and Trung-Kien Dao
Dayeh University, Taiwan†

SM15 :: Nanostructures and MEMS

Chairs: Kyung-Suk Kim (USA) and Francesco de Bona (Italy)

Mechanics and physics of dislocation nucleation in nanostructured metals **11710**
Ting Zhu
Georgia Institute of Technology, USA

Thermo-elastic size-dependent properties of nano-composites with imperfect interfaces **10666**
Bhushan Karihaloo,† Jianxiang Wang and Huiling Duan
Cardiff University, UK†

Plectoneme formation in fluctuating DNA **10815**
Prashant Purohit
University of Pennsylvania, USA

On the ratio between surface tension and the bulk modulus of materials **10828**
Graham Weir
Industrial Research Ltd., New Zealand

Estimation of load-capacity of multi-layered porous nanofilters **10140**
Adam Kovacs,† Ulrich Mescheder and Andras Kovacs
Budapest University of Technology and Economics, Hungary†

Anisotropic polling and piezoelectric behaviors in rhombohedral ferroelectric single crystals **10445**
Ai-Kah Soh† and Yicheng Song
The University of Hong Kong, Hong Kong†

Nanomechanical deflection of DNA chips induced by hybridization exothermic effect **10811**
Neng-Hui Zhang,† Shu-Xiao Wan, Jian-Zhong Chen and Chang-Jun Cheng
Shanghai University, China†

Characterization of nanoimprinting polymers with laser ultrasonics **11001**
Juerg Bryner,† Timothy Kehoe, Jacqueline Vollmann, Laurent Aebi, Clivia Torres and Jürg Dual
ETH Zurich, Switzerland†

Elastic properties of nanostructures with the charged surfaces **11014**
Linli Zhu† and Xiaojing Zheng
Lanzhou University, China†

Influence of dislocation distribution density on interface relaxation stress in heteroepitaxial thin films with flexible substrate **11163**
Igor Dobovsek
University of Ljubljana, Slovenia

A coarse particle method for nanoimprinting process **11270**
Cheng-Da Wu,† Te-Hua Fang and Jen-Fin Lin
Cheng Kung University, Taiwan†

Tuning acoustic wave properties by mechanical resonators on a surface **11564**
Maria Dühring,† Vincent Laude and Abdelkrim Khelif
Technical University of Denmark, Denmark†

Theoretical analysis of three-point bending test of nanowires with surface effects **11591**
Xianwei Zeng,† Weifeng Wang and Jianping Ding
South China University of Technology, China†

On the modelling and decomposition of gradient enhanced electro-mechanically coupled deformation **11790**
Sebastian Skatulla,† Carlo Sansour and Arockiarajan Anrunachalakasi
University of Nottingham, UK†

Higher-order equations for quantum dot structures in thin solid films **10962**
Peter Evans,† Maciek Korzec, Andreas Münch and Barbara Wagner
Humboldt University of Berlin, Germany†

Application of molecular statistical thermodynamics to uniaxial tension of ZnO nanorods **11169**
Yilong Bai,† Pan Xiao, Fujiu Ke, Jun Wang and Mengfeng Xia
Chinese Academy of Sciences, China†

Theoretical analysis of adsorption-induced microcantilever bending **11419**
Shou-Wen Yu,† Ji-Qiao Zhang, Xi-Qiao Feng and Gang-Feng Wang
Tsinghua University, China†

SM16 :: Plasticity and viscoplasticity

Chairs: Marc Geers (Netherlands) and Christian Miehe (Germany)

A finite strain theory of gradient crystal plasticity **11296**
Mitsutoshi Kuroda† and Viggo Tvergaard
Yamagata University, Japan†

Thermodynamic coarse-graining of dislocation mechanics and the size-dependent continuum plasticity **11266**
Sinisa Mesarovic,† Raghuraman Baskaran, Sreekanth Akarapu and Hussein Zbib
Washington State University, USA†

Recent progress in the homogenization of elasto-plastic and elasto-viscoplastic inclusion-reinforced composites **11764**
Issam Doghri,† Koen Delaere, Nicolas Bilger, Laurent Adam, Laurent Delannay and Laurence Brassart
Université Catholique de Louvain, Belgium†

The effect of void shape on size-dependent void growth **11347**
Christian Niordson† and Viggo Tvergaard
Technical University of Denmark, Denmark†

Characterization of strain rate dependent deformation behavior of carbon-black filled rubber **10160**
Yoshihiro Tomita,† Masaki Kondou and Masato Naito
Graduate School of Engineering, Japan†

Incremental variational principles with application to the homogenization of nonlinear dissipative composites **10279**
Pierre Suquet† and Noel Lahellec
Centre National de la Recherche Scientifique, France†

On the link between discretization and higher order homogenization of elastic-plastic composites **10596**
Kenneth Runesson† and Fredrik Larsson
Chalmers University of Technology, Sweden†

Mesoscopic modeling of the relaxation of intrinsic stress in thin films by grain boundary diffusion and plasticity: a discrete dislocation dynamics approach **10556**
Erik van der Giessen† and Can Ayas
University of Groningen, Netherlands†

Simulation of deformation and fracture of metal/ceramic interfaces **11683**
Siegfried Schmauder† and Amir Siddiq
University of Stuttgart, Germany†

A canonical numerical formulation for wrinkling in elastoplastic membranes undergoing large deformations **11102**
Joern Mosler† and Fehmi Cirak
Ruhr University Bochum, Germany†

Computational challenges in finite plasticity from a mathematical view point **11958**
Carsten Carstensen† and Robert Huth
Humboldt University, Germany†

Grain size effect and intrinsic material length of a polycrystal **10047**
Ke-Shi Zhang
Guangxi University, China

Hardening and softening in micro and nanoplasticity **11497**
Carl Dahlberg† and Peter Gudmundson
Royal Institute of Technology, Sweden†

Discrete and continuum dislocations and plastic hardening of crystals **10886**
Pilar Ariza,† Ashwin Ramasubramaniam and Michael Ortiz
Universidad de Sevilla, Spain†

Ductile damage development in friction stir welded aluminum joints **10776**
Kim Nielsen
Technical University of Denmark, Denmark

Bauschinger effect in freestanding thin films modeled by discrete dislocation plasticity **11189**
Lucia Nicola,† Ranjeet Kumar and Erik van der Giessen
Delft University of Technology, Netherlands†

Viscoplasticity of ice single crystals loaded in torsion: experiments and discrete dislocation dynamics simulations **11181**
Marc Fivel,† Juliette Chevy and Paul Duval
SIMaP-GPM2, France†

Influence of die rotating speed on forward extrusion **11641**
Xiang Ma† and Matthew Barnett
SINTEF Materials and Chemistry, Norway†

An influence of torsional cycles on the uni-axial tension of selected materials **12118**
Zbigniew Kowalewski† and Tadeusz Szymczak
Motor Transport Institute, Poland†

The relationship between deformation-induced texture **10355**
Long Shiguo,† Ma Zengsheng, Pan Yong and Zhou Yichun
Xiangtan University, China†

SM17 :: Stability of structures

Chairs: Henrik Jensen (Denmark) and Nick Triantafyllidis (USA)

Structural and failure performance of load-carrying lattice structures **10996**
Hans Obrecht,† Ulf Reinicke and Marcel Walkowiak
Technische Universität Dortmund, Germany†

Buckling of single-crystal silicon nanolines under indentation **11162**
Rui Huang,† Bin Li, Min Kang and Paul Ho
University of Texas at Austin, USA†

Mechanically-triggered transformations of pattern and phononic band gaps in periodic elastomeric structures **11399**
Katia Bertoldi† and Mary Boyce
Massachusetts Institute of Technology, US Minor Outlying Islands†

Lüders bands induced localization and propagation of curvature in steel tubes under pure bending **10980**
Stelios Kyriakides,† Ali Ok and Edmundo Corona
University of Texas at Austin, USA†

Thermal post-buckling behavior of FG panels in supersonic airflows **10038**
Ji-Hwan Kim† and Ki-Ju Sohn
Seoul National University, South Korea†

Multi-bifurcation analysis for the multi-folding structures **10460**
Ichiro Ario† and Andrew Watson
Hiroshima University, Japan†

Wrinkling of thin rectangular plates under longitudinal tension **10758**
Barrie Fraser† and Charlie Macaskill
University of Sydney, Australia†

The computation of sensitivity analysis of stability problems of steel plane frames **10865**
Zdenek Kala,† Abayomi Omishore and Libor Puklicky
Brno University of Technology, Czech Republic†

Plastic buckling and post-buckling of rectangular plates, experiments and their simulation by FE computations **11037**
Suresh Shrivastava,† Kamal Berrada and Bing Liu
McGill University, Canada†

Analysis on aeroelastic dynamics of a rotating laminated disk with viscoelastic core layer **11367**
Xingzhe Wang† and Longfei Li
Lanzhou University, China†

Local lattice instability analysis on amorphous metals: effect of free surface **11686**
Masaomi Nishimura,† Yoshihiro Tomita and Kisaragi Yashiro
Kobe University, Japan†

Stress focusing in twisted thin elastic plates **11508**
Ciprian Coman† and Andrew Bassom
University of Glasgow, UK†

Large deformation and instability in hydrogels **11644**
Zhigang Suo,† Xuanhe Zhao and Wei Hong
Harvard University, USA†

The initiation of strain nonuniformity in thin-walled cylinders subjected to cyclic torsion analogous to internal buckling **11691**
Masami Kobayashi† and Koji Uetani
The University of Shiga Prefecture, Japan†

SM18 :: Structural optimization

Chairs: Mike Xie (Australia) and Byung Kwak (South Korea)

Topological design of isotropic composites **10326**
Vivien Challis,† Anthony Roberts and Andy Wilkins
University of Queensland, Australia†

Efficient optimization-based form finding of cable nets in uniform fluid flow **11049**
Michael Winther,† Niels Olhoff and Kurt Hansen
Aalborg University, Denmark†

Topology optimisation for micropolar elastic solids **11095**
Yutaka Arimitsu,† Zhiqiang Wu, Hiroto Kawano and Yuji Sogabe
Ehime University, Japan†

On optimization of involute gear teeth **11155**
Niels Pedersen
Technical University of Denmark, Denmark

Structural optimization using evolutionary algorithm and data mining **11176**
Ting-Yu Chen† and Yi Cheng
National Chung Hsing University, Taiwan†

Topology optimization of continuum by successive approximation **10214**
Sei-ichiro Sakata† and Fumihiro Ashida
Electronic Control Systems Engineering, Japan†

The optimum design of a rack and pinion gear using the Taguchi method **11440**
Sungpil Jung,† Sungmoon Park, Chanseung Park, Taewon Park and Taeckrim Song
Ajou University, South Korea†

Error estimate based remeshing strategy for shape optimization using radial basis functions **11825**
Daniel Wilke,† Albert Groenwold and Schalk Kok
University of Pretoria, South Africa†

Optimum material design of maximum structural seepage under compliance constraint **12088**
Gengdong Cheng† and Shengli Xu
Dalian University of Technology, China†

Topology optimization of optical band gap effects in slab structures modulated by periodic Rayleigh waves **12077**
Niels Aage,† Allan Gersborg and Ole Sigmund
Technical University of Denmark, Denmark†

Optimization of stepped beams and plates **11597**
Jaan Lellep,† Tiina Kraav and Julia Polikarpus
University of Tartu, Estonia†

Level set approach for structural optimization **11775**
Andrzej Myśliński
Systems Research Institute, Poland

Structural shape optimization by weight of NURBS with IGES file exchange **11363**
Geol Choi† and Byung Kwak
Korean Advanced Institute of Science and Technology, South Korea†

SM19 :: Structural vibrations

Chairs: Marian Wiercigroch (UK) and Pedro Ribeiro (Portugal)

Phenomenon of coupled structures of mechanical systems **11575**
Julijana Simonovic
University of Niš, Yugoslavia

Elastoplastic and geometrically non-linear vibrations of beams by the p-version finite element method **10366**
Pedro Ribeiro† and Gert van der Heijden
University of Porto, Portugal†

Nonlinear parametric vibration of axially accelerating beams **10384**
Li-Qun Chen† and Hu Ding
Shanghai University, China†

Gap waves propagating in layered piezoelectric material structures with initial stress **10860**
Jianke Du,† Xiaoying Jin and Ji Wang
Ningbo University, China†

Vibration and buckling behaviour of soft core sandwich plate using an improved higher order zigzag theory **11032**
Bhrigu Singh,† Mihir Pandit and Abdul Sheikh
Indian Institute of Technology, Kharagpur, India†

Vibration localization in disordered periodically stiffened double-leaf panels **11045**
Gui-Lan Yu,† Yue-Sheng Wang and Jian Lan
Beijing Jiaotong University, China†

Magnetic damping of resonant rotor-bearing vibrations **11077**
Wlodzimierz Kurnik† and Krzysztof Dziedzic
Warsaw University of Technology, Poland†

Difference resonances in a controlled van der Pol–Duffing oscillator **11129**
Jinchen Ji
University of Technology, Sydney, Australia

Chaotic vibrations of a post-buckled cantilevered beam constrained by a stretched string at the top end **11234**
Ken-ichi Nagai,† Shinichi Maruyama, Kota Muto and Takao Yamaguchi
Gunma University, Japan†

Nonlinear transient vibration of an axially moving string with an attached traveling oscillator under wind excitations **11295**
Yuefang Wang† and Lefeng Lü
Dalian University of Technology, China†

Stochastic data-based representation of uncertain complex non-linear systems **12071**
Sami Masri,† Miguel Hernandez-Garcia, Felipe Arrate and Roger Ghanem
University of Southern California, USA†

PDF solution to nonlinear oscillators excited by Gaussian and Poisson white noises **12104**
Hai Zhu,† Guo Er, Kun Kou and Vai Iu
University of Macau, Macau†

Normal vibration modes of a slender beam on elastic foundation with unilateral contact **10873**
Carlos Mazzilli† and Stefano Lenci
University of So Paulo, Brazil†

Forced response of waveguides from finite element analysis **10908**
Brian Mace,† Yoshiyuki Waki and Michael Brennan
University of Southampton, UK†

Nonlinear vibrations of an annular hyperelastic membrane **11196**
Paulo Gonçalves† and Renata Soares
Catholic University, PUC-Rio, Brazil†

Damage identification in multilayer composite structures using Lamb stress waves **10242**
Wieslaw Ostachowicz† and Pawel Kudela
Polish Academy of Sciences, Poland†

Dynamic analysis of an automatic transmission parking mechanism **10469**
Jeku Jeyakumaran† and Nong Zhang
University of Technology, Sydney, Australia†

Guided waves damage detection in beams utilising Bayesian artificial neural network model class selection **11257**
Ching Ng,† Martin Veidt and Chin Liew
The University of Queensland, Australia†

Bifurcation patterns of a whirling transported string **11389**
Gert van der Heijden† and Barrie Fraser
University College London, UK†

Experimental unfolding and reduced order model in the complex dynamics of a sagged cable **11411**
Giuseppe Rega† and Rocco Alaggio
Sapienza Università di Roma, Italy†

Subcritical flutter in the problems of acoustics of friction **10157**
Oleg Kirillov
Technische Universitaet Darmstadt, Germany

VIV of vertical offshore riser in lock-in: low-dimensional model **10567**
Marian Wiercigroch,† Narakorn Srinil and Marko Keber
University of Aberdeen, UK†

Phenomenological mapping method and mathematical analogy of hubrid system dynamics **10135**
Katica Hedrih
University of Nis, Yugoslavia

Amplitude reduction of self-excited micro-cantilever probe of atomic force microscope **10514**
Hiroshi Yabuno,† Masaharu Kuroda, Kiwamu Ashida and Takeshi Kobayashi
University of Tsukuba, Japan†

Proposals for visualising the evolution of approximate analytical solutions in engineering dynamics **11240**
Matthew Cartmell† and David Forehand
University of Glasgow, UK†

SM20 :: Viscoelasticity and creep

Chairs: Alan Cocks (UK) and George Voyiadjis (USA)

Bases and advances of the synthetic theory of irreversible deformation **11073**
Endre Ruszinko
Budapest Polytechnic, Hungary

An advanced rapid three-dimensional modeling technology for asphalt concrete **11856**
Xinhua Yang,† Yong Ye, Chuanyao Chen and Rui Xu
Huazhong University of Science and Technology, China†

Contents

Sectional Lectures and Mini-symposium Papers

Material Instabilities in Elastic and Plastic Solids: The Perturbative Approach 1
Davide Bigoni

Modelling Strain Localization by Cohesive (Overlapping) Zones in Tension (Compression): Brittleness Size Effects and Scaling in Material Properties 15
Alberto Carpinteri, Marco Paggi

Multi-scale Analysis of Polycristalline Metals and Composites 35
J.-L. Chaboche

Micro-architectured Solids: From Blast Resistant Structures to Morphing Wings 57
Norman A. Fleck

Plasto-Mechanics of Large Deformation under Impact Loading 67
N.K. Gupta

Onset of Oscillatory Thermocapillary Convection 85
W.R. Hu, Z.M. Tang

Instabilities of Flows through Deformable Tubes and Channels 101
O.E. Jensen

Surface Bubbles in Micro-and Nanofluidics 117
Bram Borkent, Detlef Lohse

Bridged and Cohesive Crack Models for Fracture in Composite Materials 135
Roberta Massabò

Relaxation to Steady Vortical Flows – And Knots in the Quark-Gluon Plasma 155
H.K. Moffatt

Instabilities across the Scales: Simple Models for Shear Banding, Plate Subduction and Mantle Convection in Geodynamics 165
Hans-Bernd Mühlhaus, Louis Moresi, Matt Davies, Klaus Gottschald, Alina Hale

From Dry Granular Flows to Submarine Avalanches 189
Mickael Pailha, Maxime Nicolas, Olivier Pouliquen

Failure of Rocks in the Laboratory and in the Earth 199
J.W. Rudnicki

Modeling of Bone Failure by Cohesive Zone Models 217
Thomas Siegmund, Matthew R. Allen, David B. Burr

The Aerodynamics of Wind Turbines 231
J.N. Sørensen, R. Mikkelsen, N. Troldborg, V.L. Okulov, W.Z. Shen

Cohesive-Zone Modeling of Adhesive Joints 249
M.D. Thouless

Author Index 257

Material Instabilities in Elastic and Plastic Solids: The Perturbative Approach

Davide Bigoni

Department of Mechanical and Structural Engineering, University of Trento,
via Mesiano 77, I-38050 Trento, Italy
bigoni@ing.unitn.it

The perturbative approach to material instabilities introduced by Bigoni and Capuani [2],[3] (in which a perturbing agent is superimposed to a uniformly stressed and strained infinite medium) is reviewed and applied to show how randomly-distributed dislocation-like defects can induce strain patterns in ductile metallic materials, prestressed near the border of ellipticity loss. These patterns result to be strongly focussed and organized into shear bands, evidencing a well-defined texture in the material.

1 Introduction

A *material instability* is usually identified with a localized loss of homogeneity of deformation occurring in a solid sample subject to a loading path compatible with continued uniform deformation and constrained on the whole boundary to prescribed displacements (or to smooth contact with a rigid wall [14]), Fig. 1. Since the stiff boundary constraint prevents development of 'global' (such as Euler-like buckling) or surface (such as necking) bifurcations, the loss of homogeneity occurring in the sample may be interpreted as a deformation mechanism 'alternative' to the homogeneous one, or, in other words, as a 'localized' bifurcation. Roughly speaking, this bifurcation results from a strongly nonlinear (nominal) stress versus (conventional) strain curve of the type sketched in Fig. 2 (referred to the experiment on drinking straw packaging reported in Fig. 3), exhibiting an initial linear response, followed by a nonlinear range, evidencing a peak and subsequent strain softening.[1]

[1] Note that in experiments of the type shown in Fig. 1, it is difficult to envisage by a purely visual inspection if the localization of deformation occurs just *before or after the peak* (in other words, whether softening is necessary to localization, or softening results from localization), but this is certainly already present during the softening response.

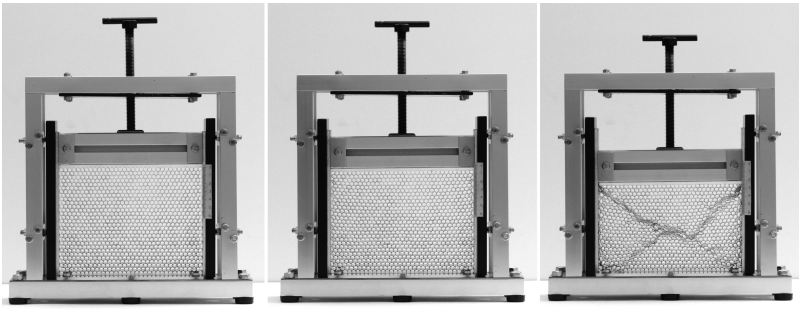

Fig. 1 Uniaxial deformation of a regular packaging of identical and parallel thin-walled cylinders (drinking straws), constrained within a rigid-wall box. The unloaded configuration is shown left and a configuration where deformation is still homogeneous is shown at the centre. While the strong confinement precludes diffuse bifurcations, strain localization can develop and is visible on the right (experiment inspired from [12] and performed at the University of Trento).

The softening may, as in Fig. 2, terminate at a certain strain level to give rise to a more or less pronounced strain hardening regime.

The strain localization visible in the experiment shown in Fig. 1 is only a 'strong and evident manifestation' that the material traverses an unstable state, beginning at a certain –sufficiently high – strain level, culminating with localization and (as in the case of the drinking straw packaging) continuing with an accumulation of deformation bands (or in other cases with intense deformation and damage within a single deformation band, [8]).

Since the 'standard' approach to material instability is limited to the determination of the *onset* of strain localization (identified with the loss of ellipticity of the incremental governing equations [13]), the unstable state previously traversed by the material is usually left unexplored. However, this state can efficaciously be investigated through the analysis of the material response to a *perturbation* applied at a certain level of deformation. For instance, we can perturb the sample in the experiment shown in Fig. 1, by applying a concentrated force when the deformation is still uniform, but the peak of the curve is approached (Fig. 3). As a result, the deformation induced by the perturbing force becomes highly focussed and localized, which would have not been the case if the perturbation were provided much before the peak of the stress/strain response. This experimental procedure has been rationalized by Bigoni and Capuani [2], who have defined a perturbation in terms of a concentrated force acting in an infinite prestressed continuum. In addition to the concentrated force, different perturbing agents have been envisaged, namely, a fracture, a rigid-thin inclusion, and a pre-existing shear band, so that the perturbative approach has been shown to be 'rich enough' to give evidence to phenomena involving dynamics of shear bands [3], strain pattern emergence for materials in flutter conditions [11], and interactions between shear bands and inclusions [4]–[7].

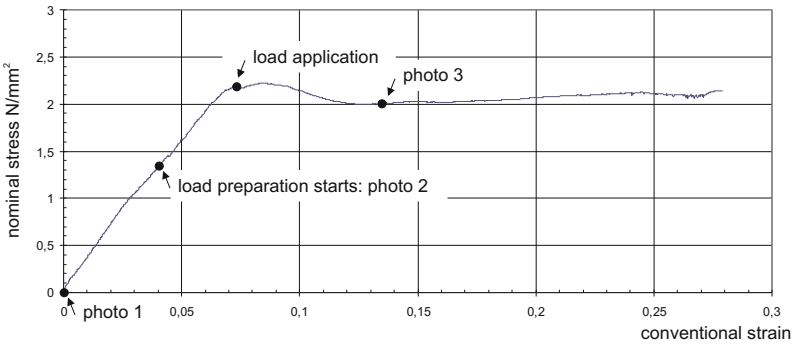

Fig. 2 Vertical nominal stress versus 'global' uniaxial conventional strain curve for a packaging of regularly disposed drinking straws obtained at a speed of the piston of 5mm/min. Note that, due to the lateral constraint, the state of stress in the test is not uniaxial. The indication of the photos refers to Fig. 3, where the application of a vertical concentrated load is visible. The velocity of the imposed vertical motion of the rigid piston has decreased from 5 mm/min to 1 mm/min when the concentrated load has applied.

We complement the above results in the present article with an analysis of the effects of a random distribution of dislocation-like defects on a prestressed, ductile material, showing that defects induce a well-oriented texture within a material, when prestressed near the elliptic border. To this purpose, we start introducing the infinite-body Green's function set for a prestressed, incompressible material, we continue showing analogies between force and dislocation dipoles (namely, for a special geometrical setting the far fields can be made to coincide for incompressible and isotropic elasticity) and, finally, we present results for random distributions of dipoles, simulating dislocation-like defects.

2 Infinite-Body, Quasi-Static Green's Function for an Incompressible, Prestressed Material

Green's functions for anisotropic prestressed materials have been found by Willis [15] and Bigoni and Capuani [2],[3]. We focus attention to two-dimensional Green's functions, considering the case of incompressible, anisotropic prestressed elasticity[2], solved by Bigoni and Capuani [2], whose incremental constitutive equations are written in terms of nominal stress increment $\dot{t}_{ij}$, functions of incremental displacement gradient $v_{i,j}$ and in-plane mean stress $\dot{p}$

[2] The case of compressible materials, including the loading branch of a generic elastoplastic constitutive operator, has been treated by Bertoldi et al. [1] for the quasi-static case and Piccoloraz et al. [11] for the dynamic case.

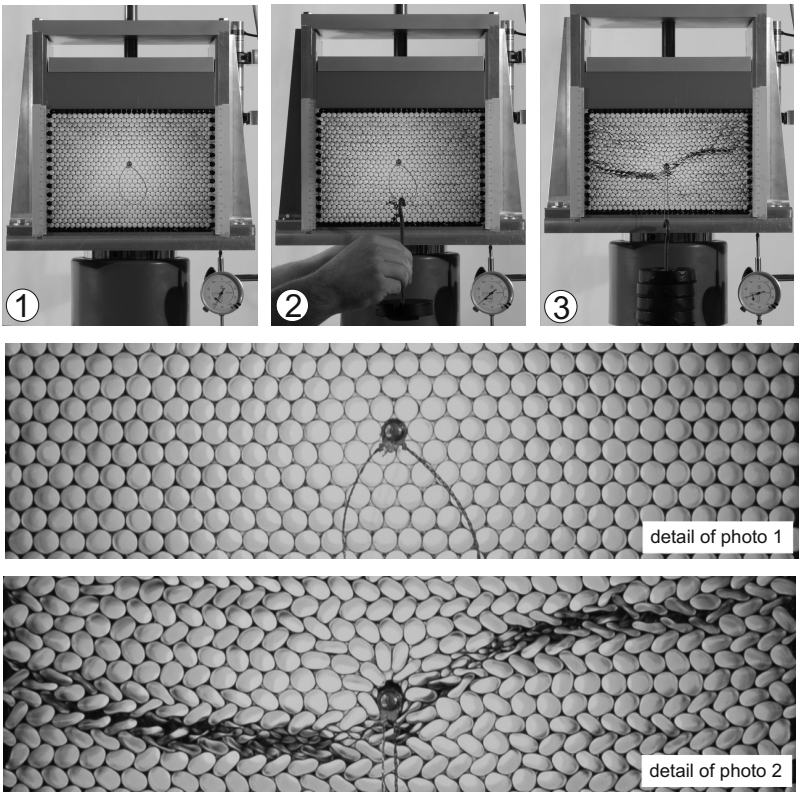

Fig. 3 Application of a concentrated load (50 N) during uniaxial deformation of a packaging of regularly disposed drinking straws. Photo 1 has been taken before the test start, while a vertical load has been applied at the instant when photo 2 has been taken. The shear bands emanating from the applied load are visible in photo 3. The two photos reported below are details of photo 1 (unloaded configuration) and 3 (strain localization already developed), where the device used to apply the concentrated load is visible.

$$\begin{aligned} \dot{t}_{11} &= \mu(2\xi - k - \eta)v_{1,1} + \dot{p}, & \dot{t}_{22} &= \mu(2\xi + k - \eta)v_{2,2} + \dot{p}, \\ \dot{t}_{12} &= \mu[(1+k)v_{2,1} + (1-\eta)v_{1,2}], & \dot{t}_{21} &= \mu[(1-\eta)v_{2,1} + (1-k)v_{1,2}], \end{aligned} \tag{1}$$

where the dimensionless parameters

$$\xi = \frac{\mu_*}{\mu}, \quad \eta = \frac{p}{\mu} = \frac{T_1 + T_2}{2\mu}, \quad k = \frac{T_1 - T_2}{2\mu}, \tag{2}$$

are functions of the current principal Cauchy stresses T_1, T_2 and of two incremental shear moduli, μ and μ_*.

Equilibrium equations expressed in terms of the stream function,

$$v_1^g = \psi^g_{,2}, \quad v_2^g = -\psi^g_{,1}, \tag{3}$$

can be written including a concentrated force of unit components, $\delta_{ig}\,\delta(\boldsymbol{x})$, as

$$(1+k)\psi^g_{,1111}+2(2\xi-1)\psi^g_{,1122}+(1-k)\psi^g_{,2222}+\frac{\delta_{1g}\delta_{,2}(\boldsymbol{x})-\delta_{2g}\delta_{,1}(\boldsymbol{x})}{\mu}=0. \tag{4}$$

Employing a plane wave expansion of the stream function ψ^g, which for a generic function h is written as

$$h(\boldsymbol{x}) = -\frac{1}{4\pi^2}\oint\limits_{|\boldsymbol{n}|=1} \tilde{h}(\boldsymbol{n}\cdot\boldsymbol{x})\mathrm{d}\boldsymbol{n}, \tag{5}$$

(where $\boldsymbol{n}$ is the radial unit vector centred at the origin of the position vector $\boldsymbol{x}$) and enjoying the following properties

$$\tilde{\delta}(\boldsymbol{n}\cdot\boldsymbol{x}) = \frac{1}{(\boldsymbol{n}\cdot\boldsymbol{x})^2}, \quad \nabla_{\boldsymbol{x}}\tilde{h}(\boldsymbol{n}\cdot\boldsymbol{x}) = \tilde{h}'(\boldsymbol{n}\cdot\boldsymbol{x})\,\boldsymbol{n}, \tag{6}$$

(where the prime denotes differentiation with respect to the argument $\boldsymbol{n}\cdot\boldsymbol{x}$), equation (4) becomes the ordinary differential equation

$$L(\boldsymbol{n})\left(\tilde{\psi}^g\right)'''' = 2\frac{\delta_{1g}n_2-\delta_{2g}n_1}{(\boldsymbol{n}\cdot\boldsymbol{x})^3}, \tag{7}$$

where the (strictly positive in the elliptic regime) function $L(\boldsymbol{n})$ has been introduced

$$L(\boldsymbol{n}) = \mu\, n_2^4\,(1+k)\left(\frac{n_1^2}{n_2^2}-\frac{1-k}{1+k}\Omega_2^2\right)\left(\frac{n_1^2}{n_2^2}-\frac{1-k}{1+k}\Omega_1^2\right) > 0, \tag{8}$$

in which Ω_i^2 are the squares of the roots of the homogeneous associated characteristic equation to (4).

A straightforward integration of (7) yields

$$\tilde{\psi}^g = \frac{\delta_{1g}n_2-\delta_{2g}n_1}{L(\boldsymbol{n})}(\boldsymbol{n}\cdot\boldsymbol{x})\left(\log|\boldsymbol{n}\cdot\hat{\boldsymbol{x}}|-1\right), \tag{9}$$

which, antitransformed, leads to the Green's stream function

$$\begin{aligned}\psi^g = -\frac{r}{2\pi^2\mu(1+k)}\Bigg[&(\log\hat{r}-1)\int_0^{\pi}\frac{\sin[\alpha+\theta+(1-g)\pi/2]\cos\alpha}{\Lambda(\alpha+\theta)}\,\mathrm{d}\alpha\\ &+\int_0^{\pi/2}\frac{\sin[\alpha+\theta+(1-g)\pi/2]\cos\alpha\log(\cos\alpha)}{\Lambda(\alpha+\theta)}\,\mathrm{d}\alpha\\ &-\int_0^{\pi/2}\frac{\cos[\alpha+\theta+(1-g)\pi/2]\sin\alpha\log(\sin\alpha)}{\Lambda(\alpha+\theta+\pi/2)}\,\mathrm{d}\alpha\Bigg],\end{aligned} \tag{10}$$

where

$$\Lambda(\alpha) = \sin^4\alpha\,\left(\cot^2\alpha - \gamma_1\right)\left(\cot^2\alpha - \gamma_2\right) > 0. \tag{11}$$

Employing now the definition of stream function (3) yields the Green's function for incremental displacements

$$v_j^g = \frac{1}{2\pi^2\mu(1+k)}\left\{\frac{\pi\,\delta_{jg}\,\log r}{[(2-j)\,\gamma_2 + 1 - j]\,\sqrt{-\gamma_1} + [(2-j)\,\gamma_1 + 1 - j]\,\sqrt{-\gamma_2}}\right.$$
$$\left. - \int_0^{\frac{\pi}{2}} \left[K_j^g(\alpha+\theta) + (3-2j)\,(3-2g)\,K_j^g(\alpha-\theta)\right]\log(\cos\alpha)\,\mathrm{d}\alpha\right\}, \tag{12}$$

where

$$K_j^g(\alpha) = \frac{\sin\left[\alpha + (j-1)\frac{\pi}{2}\right]\sin\left[\alpha + (g-1)\frac{\pi}{2}\right]}{\Lambda\,(\alpha)}, \tag{13}$$

The solution for the Green's function set for an incompressible material is not yet complete, since the knowledge of the velocity gradient does not allow determination of the Green's function for in-plane incremental mean stress $\dot{p}^g$. Therefore, we consider the rate equilibrium equations written for the Green's function set $\{v_i^g, \dot{p}^g\}$

$$\begin{aligned} \dot{p}_{,1}^g - \mu\,k v_{1,11}^g &= \mu[(1-2\xi)v_{1,11}^g - (1-k)v_{1,22}^g] - \delta_{1g}\delta(\boldsymbol{x}), \\ \dot{p}_{,2}^g - \mu\,k v_{1,12}^g &= \mu[(1-2\xi)v_{2,22}^g - (1+k)v_{2,11}^g] - \delta_{2g}\delta(\boldsymbol{x}). \end{aligned} \tag{14}$$

Introducing now the in-plane mean nominal stress

$$\dot{\pi} = \frac{\dot{t}_{11} + \dot{t}_{22}}{2} = \dot{p} - \mu\,k v_{1,1}, \tag{15}$$

differentiating eqn. (14a) with respect to x_1, eqn. (14b) with respect to x_2 and summing the resulting equations yields

$$\begin{aligned} \frac{\dot{\pi}_{,11} + \dot{\pi}_{,22}}{\mu} &= 2(1-\xi)\,(v_{1,111} + v_{2,222}) \\ &\quad + k\,(v_{1,111} - v_{2,222}) - \frac{\delta_{1g}\delta_{,1}(\boldsymbol{x}) + \delta_{2g}\delta_{,2}(\boldsymbol{x})}{\mu}, \end{aligned} \tag{16}$$

which in the transformed domain becomes the ordinary differential equation

$$\begin{aligned} \frac{(\tilde{\pi}^g)''}{\mu} &= 2(1-\xi)\left[n_1^3\,(\tilde{v}_1^g)''' + n_2^3\,(\tilde{v}_2^g)'''\right] \\ &\quad + k\left[n_1^3\,(\tilde{v}_1^g)''' - n_2^3\,(\tilde{v}_2^g)'''\right] + 2\frac{n_1\delta_{1g} + n_2\delta_{2g}}{\mu(\boldsymbol{n}\cdot\boldsymbol{x})^3}. \end{aligned} \tag{17}$$

Since $\tilde{v}_i^g$ and its derivatives are known from differentiation of equation (9), (17) can be integrated and antitransformed to give the Green's function for the in-plane mean nominal stress increment

$$\dot{\pi}^g = -\frac{1}{2\pi r}\left\{\cos\left[\theta-(g-1)\frac{\pi}{2}\right]+\frac{1}{\pi(1+k)}\int_0^\pi \frac{\tilde{K}_g\left(\alpha+\theta\right)}{\cos\alpha}\mathrm{d}\alpha\right\}, \tag{18}$$

where

$$\tilde{K}_g(\alpha)=K_g^g(\alpha)\left[2\left(\frac{\mu_*}{\mu}-1\right)\left(2\cos^2\alpha-1\right)-k\right]\cos\left[\alpha+\delta_{2g}\frac{\pi}{2}\right], \tag{19}$$

completing the infinite-body Green's function set. In particular, application of the constitutive equations (1)-(2) to the Green's velocity gradient and adding the Green's in-plane mean nominal stress (18) yields the Green's function for the incremental nominal stress

$$\begin{aligned} &\dot{t}^g_{11}=(2\mu_*-p)\,v^g_{1,1}+\dot{\pi}^g, && \dot{t}^g_{22}=(2\mu_*-p)\,v^g_{2,2}+\dot{\pi}^g,\\ &\dot{t}^g_{12}=(\mu-p)\,v^g_{1,2}+\left(\mu+\frac{\sigma}{2}\right)v^g_{2,1}, && \dot{t}^g_{21}=(\mu-p)\,v^g_{2,1}+\left(\mu-\frac{\sigma}{2}\right)v^g_{1,2}. \end{aligned} \tag{20}$$

3 Dipoles in an Infinite Medium

Superimposing the effects, the Green's function (12) can be used to investigate the response of a homogeneously prestressed infinite medium perturbed by a quasi-statically applied dipole (two equal and opposite concentrated forces placed at a distance, say, $2a$). The analysis of the resulting incremental displacement maps at different 'distances' from the border of ellipticity provides information on the behaviour of the material near a material instability [2].

An example is reported in Fig. 4, referred (as all other examples addressed in the following) to a material following the J_2–deformation theory of plasticity, namely, a nonlinear elastic law corresponding to the loading branch of von Mises plasticity, so that unloading is *a-priori* excluded [10]. The figure clearly indicates that, *while at null prestress the incremental deformation field does not evidence a particular structure* (Fig. 4 on the left), *a shear band pattern emerges as the response to the dipole perturbation at a prestress level near the boundary of (but still inside) ellipticity* (Fig. 4 on the right).

A quasi-static dipole represents the simplest 'zero-resultant-force' perturbation, so that many other possible perturbations can be invented to capture 'particular' effects. For instance, Bigoni and Capuani [3] have employed a time-harmonic pulsating dipole to obtain incremental displacements maps similar to that reported in Fig. 5 (referred to the same material considered in Fig. 4) and showing an interesting wave focussing, an effect which becomes critical to detect the so-called 'flutter instability' [11].

While other perturbing agents will be discussed later, our interest now is to analyze the effect of a random distribution of randomly oriented dipoles, a situation which may represent the presence of defects in a material and, in

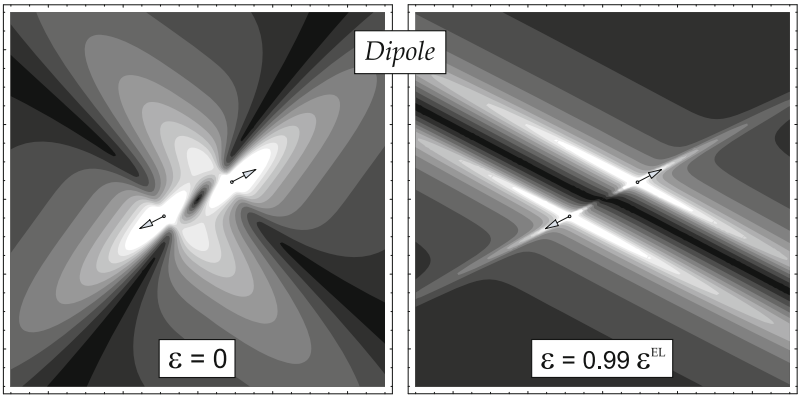

Fig. 4 Incremental displacement map resulting as the response of an unloaded (left) material and the same material prestrained close to the elliptic boundary (right) to a perturbing dipole (inclined at an angle of 27.367° with respect to the horizontal axis, corresponding to the shear band inclination at the elliptic boundary). A ductile metallic material (modelld through the J_2-deformation theory of plasticity) has been considered with an hardening exponent $N = 0.4$. Parameter ε denotes the logarithmic prestrain and ε^{EL} the value corresponding to ellipticity loss.

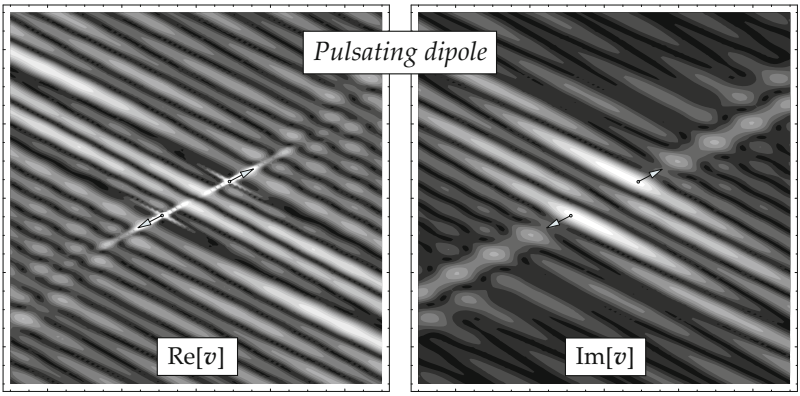

Fig. 5 A time-harmonic pulsating dipole is perturbing a ductile metallic (J_2-deformation theory) material near the elliptic border ($\varepsilon = 0.99\varepsilon^{EL}$), as in Fig. 4 on the right. Here the solution is the sum of a real (left) and imaginary (right) part. Note the focussing of the waves revealing formation of a complex shear band pattern.

particular, these defects can be representative of a dislocation distribution.[3] In fact, there are analogies between the solutions of a concentrated force and a dislocation in an elastic continuum and, we show below that *when the prestress is absent and for isotropic incompressible elasticity, the far-fields induced by a dislocation dipole on a single slip plane and a force dipole inclined at $\pi/4$ with respect to this plane are identical.*

In a x–y reference system, the in-plane stress field produced by *a single straight edge dislocation* in a linearly elastic, isotropic medium is [9]

$$\{\sigma_{xx}, \sigma_{yy}, \sigma_{xy}\} = \frac{b\,\mu}{2\pi(1-\nu)\,r^4}\left\{-y\left(3x^2+y^2\right),\ y\left(x^2-y^2\right),\ x\left(x^2-y^2\right)\right\}, \tag{21}$$

where b is the Burgers vector and μ and ν are the elastic shear modulus and the Poisson's ratio. The corresponding strain field follows from eqn. (21) in the form

$$\{\epsilon_{xx}, \epsilon_{yy}, \epsilon_{xy}\} = \frac{1}{\bar{E}}\left\{\sigma_{xx} - \bar{\nu}\sigma_{yy},\ \sigma_{yy} - \bar{\nu}\sigma_{xx},\ (1+\bar{\nu})\sigma_{xy}\right\}, \tag{22}$$

where $\bar{E}$ and $\bar{\nu}$ are the modified Young modulus and Poisson's ratio, while the displacement field can be written as

$$\begin{aligned} u_x &= \frac{b}{2\pi}\left[\arctan\frac{y}{x} + \frac{xy}{2(1-\nu)r^2}\right], \\ u_y &= -\frac{b}{8\pi\,(1-\nu)}\left[(1-2\nu)\log r^2 + \frac{x^2-y^2}{r^2}\right]. \end{aligned} \tag{23}$$

A dislocation dipole on a single glide plane consists of two parallel edge dislocations lying in the same slip plane at a distance $2d$ and having opposite sign (see Fig. 6 on the left for a sketch of the distortion induced in a crystal lattice and on the right for its graphical conventional representation). In quasi-static conditions, such a simple dislocation structure is not stable, so that the dislocations, unless pinned, 'attract' each other to reduce their total elastic energy. In this way they move toward each other until they combine and annihilate.

Leaving aside issues on stability, the stress field produced by the dislocation dipole can simply be obtained through superposition of solution (21), which can be used with reference to the local coordinates (Fig. 6 on the right)

$$x_i = x+(-1)^i d, \quad y_i = y, \quad r_i^2 = [x+(-1)^i d]^2+y^2 = r^2+(-1)^i xd+d^2, \tag{24}$$

where $i = 1, 2$.

At a large distance from the dislocation dipole the parameter d/r can be considered small and the stress fields can be expanded into a Taylor series, to obtain the far field approximation

[3] The analogy between dislocation and force dipoles has been suggested to me by Prof. A.B. Movchan (Liverpool University).

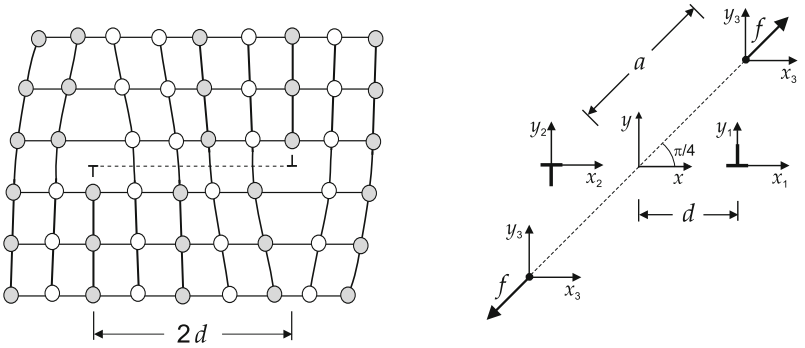

Fig. 6 Sketch of the lattice distortion induced by a dislocation dipole lying on a single slip plane (left) and its conventional representation (right), together with a force dipole (inclined at $\pi/4$ with respect to x–y system). In linear isotropic *incompressible* elasticity, the far-fields induced by the dislocation dipole and by the force dipole are identical.

$$\{\sigma_{xx}, \sigma_{yy}, \sigma_{xy}\} \sim \frac{\mu\, d\, b}{\pi(1-\nu)\, r^6} \left\{2xy\left(r^2-4x^2\right),\ 2xy\left(r^2-4y^2\right),\ r^4-8x^2y^2\right\}, \tag{25}$$

which satisfies equilibrium equations.

The far-field stress field for a force dipole in linear elasticity can be obtained by superimposing the solution (20) in the case of null prestress and isotropy as (for a force centered at the origin of a x–y reference system)

$$\left\{\sigma^g_{xx},\, \sigma^g_{yy},\, \sigma^g_{xy}\right\} = -\frac{g}{\pi\, r^4}\left\{x^2,\, y^2,\, xy\right\}, \tag{26}$$

where g, either equal to x or y, denotes the unit component of the applied force. Expressing (26) in the local coordinate systems shown in Fig. 6 on the right, so that

$$\begin{aligned} x_i &= x + (-1)^i a, \quad y_i = y + (-1)^i a \sin\alpha, \\ r_i^2 &= [x + (-1)^i a\cos\alpha]^2 + [y + (-1)^i a \sin\alpha]^2 \\ &= r^2 + (-1)^i a(x\cos\alpha + y\sin\alpha) + a^2, \end{aligned} \tag{27}$$

where $i = 3, 4$, the dipole solution can be easily obtained. At a large distance from the force dipole, the dimensionless parameter a/r becomes small, so that a Taylor series expansion of the stress fields gives again representation (25) with the correspondence

$$fa = 2db\mu, \tag{28}$$

where f is the modulus of the forces forming the dipole (inclined at $\pi/4$).

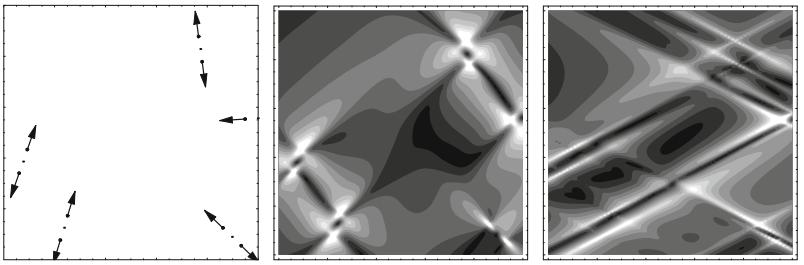

Fig. 7 Effects of prestrain on a ductile metallic (J_2–deformation theory) material (as in Fig. 4), revealed by a perturbation consisting of five randomly placed and oriented dipoles, representing dislocation-like defects (these are shown on the left, where the distance between dipole forces provides the bar scale of the representation). Maps of incremental displacements induced by the dipoles are shown on the centre at null prestrain ($\varepsilon = 0$) and on the right at a prestain near loss of ellipticity ($\varepsilon = 0.99\varepsilon^{EL}$).

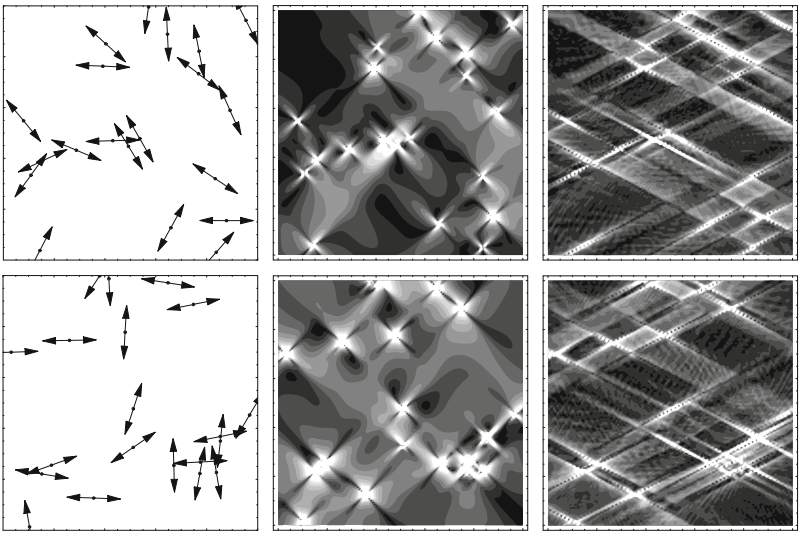

Fig. 8 As in Fig. 7, but now there are two different random distributions (upper and lower part) of twenty randomly oriented dipoles, representing dislocation-like defects

The effects of prestress have been explored by perturbing a uniform strain field with a random distribution of randomly oriented force dipoles (randomness has been obtained by using the pseudorandom real number generation function available in Mathematica© 5.2). In particular, a square window of material of edge $20a$ ($200a$) has been considered in Fig. 7 (Fig. 8), where a is the half distance between the forces forming the dipole. Inside this window

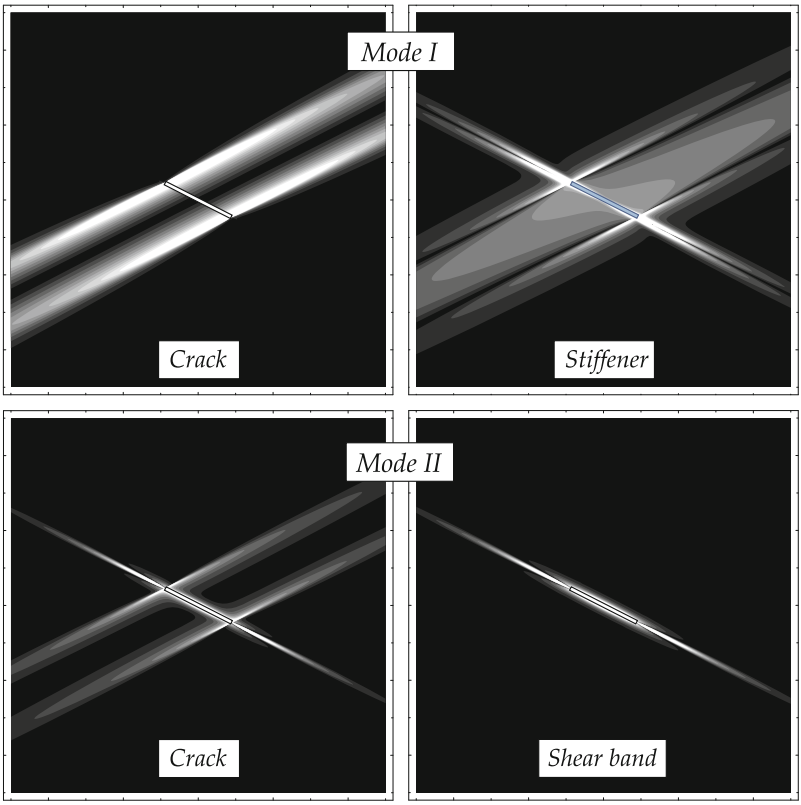

Fig. 9 Interactions between shear bands and a crack (upper part, left, see [4]), or a thin rigid inclusion (upper part, right, see [5], [6], [7]) –loaded under Mode I–, or a crack (lower part, left, see [4]), or a pre-existing shear band (lower part, right, see [4]) – loaded under Mode II. A ductile metallic (J_2–deformation theory) material is considered near the elliptic border, as in Fig. 4.

5 (20) dipoles have been randomly placed in Fig. 7 (Fig. 8), with random inclination of the forces (two random distributions have been reported in Fig. 8). The dipole distributions and inclinations are shown in Figs. 7 and 8 on the left, while the maps of modulus of displacements are shown on the centre for null prestrain ($\varepsilon = 0$, as in Fig. 4 on the left) and on the right for a prestrain near the boundary of loss of ellipticity ($\varepsilon = 0.99\varepsilon^{EL}$, as in Fig. 4 on the right).

The figures reveal that the effect of prestrain consists in *the emerging of a texture with privileged directions, corresponding to the shear band inclinations that can be calculated at the boundary of ellipticity loss.*

4 The Perturbative Approach: Conclusions and Perspectives

The conventional approach to material instability is confined to the analysis of failure of ellipticity for a uniformly deformed solid, yielding the threshold of the instability (in terms of a control parameter, for instance, the level of prestress, or the hardening) and the shear band inclinations [13]. Assuming that this conventional analysis can easily be performed and its results are available, the perturbative approach to material instability has been tailored to analyze the unstable state that is traversed by the material *before* ellipticity loss. In this way, features of this unstable state, otherwise remaining simply undetected, can be investigated. As an example, effects of a random distribution of dislocation-like defects acting in a ductile material prestressed near the elliptic boundary have been analyzed in the present article (Figs. 7 and 8). It has been found that these defects trigger incremental deformation patterns showing a well-defined texture, organized along shear bands. The obtained results fit coherently with previous findings concerning: (i) dynamical effects near the border of ellipticity (Fig. 5, see also [3]), or near the so-called 'flutter instability' [11]; (ii) interactions of a shear band with a thin rigid inclusion, or with a crack, or with a pre-existing shear band (see Fig. 9 containing a collection of results than can be compared to each other and to the previous figures). In all these problems, where defects incrementally perturb a prestressed solid, the resulting complex stress states (involving singularities and high stress concentrations) can be detailed through analytical solutions and employed to study incremental energy release rate and the associated tendency to defect growth or reduction, [4]–[7].

Acknowledgments. Financial support of MIUR–Prin 2007 (2007YZ3B24_002) is gratefully acknowledged.

References

1. Bertoldi, K., Brun, M., Bigoni, D.: Int. J. Numer. Meth. Eng. 64, 877–906 (2005)
2. Bigoni, D., Capuani, D.: J. Mech. Phys. Solids 50, 471–500 (2002)
3. Bigoni, D., Capuani, D.: J. Mech. Phys. Solids 53, 1163–1187 (2005)
4. Bigoni, D., Dal Corso, F.: Proc. R Soc. Lond. A 464, 2365–2390 (2008)
5. Bigoni, D., Dal Corso, F., Gei, M.: J. Mech. Phys. Solids 56, 839–857 (2008)
6. Dal Corso, F., Bigoni, D.: Proc. R Soc. Lond. A (2008) (in press)
7. Dal Corso, F., Bigoni, D., Gei, M.: J. Mech. Phys. Solids 56, 815–838 (2008)
8. Gajo, A., Bigoni, D., Muir Wood, D.: J. Mech. Phys. Solids 52, 2683–2724 (2004)
9. Hirth, J.P., Lothe, J.: Theory of dislocations. J. Wiley & Sons, New York (1968)
10. Hutchinson, J.W., Neale, K.W.: Finite strain J2-deformation theory. In: Carlson, D.E., Shield, R.T. (eds.) Proc. IUTAM Symp. on Finite Elasticity, Martinus Nijhoff, The Hague (1979)

11. Piccolroaz, A., Bigoni, D., Willis, J.R.: J. Mech. Phys. Solids 54, 2391–2417 (2006)
12. Poirier, C., Ammi, M., Bideau, D., Troadec, J.P.: Phys. Rev. Lett. 68, 216–219 (1992)
13. Rice, J.R.: The localization of plastic deformation. In: Koiter, W.T. (ed.) Theoretical and Applied Mechanics, North-Holland, Amsterdam (1977)
14. Ryzhak, E.I.: J. Mech. Phys. Solids 41, 1345–1356 (1993)
15. Willis, J.R.: Inclusions and cracks in constrained anisotropic media. In: Wu, J.J., Ting, T.C.T., Barnett, D.M. (eds.) Modern Theory of Anisotropic Elasticity and Applications. SIAM, Philadelphia (1991)

Modelling Strain Localization by Cohesive (Overlapping) Zones in Tension (Compression): Brittleness Size Effects and Scaling in Material Properties

Alberto Carpinteri and Marco Paggi

Politecnico di Torino, Department of Structural Engineering and Geotechnics, C.so Duca degli Abruzzi 24, 10129 Torino, Italy
{alberto.carpinteri,marco.paggi}@polito.it

The present paper is a state-of-the-art review of the research carried out at the Politecnico di Torino during the last two decades on the modelling of strain localization. Introducing the elementary cohesive/overlapping models in tension/compression, it will be shown that it is possible to get a deep insight into the ductile-to-brittle transition and into the scaling of the material properties usually detected when testing quasi-brittle material specimens or structures at different size-scales.

1 Introduction

Quasi-brittle materials in tension exhibit strain softening, i.e., a negative slope in the stress-deformation diagram, due to microcracking and localization of the deformation in a narrow band, where energy dissipation takes place.

From the Continuum Mechanics viewpoint, strain softening represents a violation of the Drucker's Postulate [1]. As a consequence, the following phenomena may occur: (i) loss of stability in the controlled load condition (snap-through); (ii) loss of stability in the controlled displacement condition (snap-back). From the historical point of view, such forms of instability were formerly recognized in the post-critical behaviour of shell buckling problems. In the pioneering papers by von Kármán and Tsien [2, 3], the initial geometrical imperfections were found to be responsible for the transition from snap-back to softening branches after the bifurcation point in the load-deflection curves of imperfection-sensitive axially compressed cylinders at large displacements.

The cohesive crack model is able to describe materials that exhibit a strain-softening type behaviour. Dugdale [4] firstly postulated the existence

of uniform tractions equal to the yield stress transmitted through a narrow yield zone in front of a crack in elastic-perfectly plastic materials. A detailed analysis of the spread of such a plastic zone was then proposed by Bilby, Cottrell and Swinden [5]. Independently, Barenblatt [6] proposed the concept of cohesive forces to model the effect of interatomic forces in polycrystals. It is also important to recall that Rice [7] devoted a section of his fundamental paper on the path independent integral to the analysis of the Barenblatt-Dugdale crack model. On the other hand, to the knowledge of the present authors, Smith [8] firstly used the terminology *Cohesive Zone Model* in 1974, which then received a great favour from the scientific Community.

Subsequently, Hillerborg and coworkers [9, 10] proposed the *Fictitious Crack Model* for the study of the nonlinear mechanical behaviour of concrete. More recently, the *Cohesive Crack Model* terminology was introduced by Carpinteri [11–15] when snap-back branches may be captured. This terminology has become very popular and has been used by a number of researchers (for instance, see [16, 17], among others).

The basic assumption underlying this model is the formation, as an extension of the real crack, of a fictitious crack, referred to also as the *process zone*, where the material, albeit damaged, is still able to transfer stresses. The crack is assumed to propagate when the stress at the crack tip reaches the tensile strength, σ_u. When the crack opens, the stress is not assumed to fall to zero at once, but to decrease gently with increasing crack width, w, until a critical displacement is reached and the interaction vanishes. The amount of energy absorbed per unit crack area is referred to as *fracture energy*, and represents the area under the stress-displacement curve. This modelling requires the use of a pair of constitutive laws: a stress-strain linear-elastic relationship for the undamaged material, and a softening stress-crack opening curve for the damaged material.

From the computational point of view, this approach has demonstrated to be very attractive, since it can be implemented in the finite element method eliminating the stress-singularity at the crack tip typical of Linear Elastic Fracture Mechanics (LEFM), and it permits to avoid the effects of mesh sensitivity [18]. Since 1984, Carpinteri and coworkers have shown that the cohesive crack model can be used for the analysis of stability of the mechanical response of quasi-brittle material specimens or structures, demonstrating that the brittle behaviour and the LEFM critical condition are represented by the occurrence of post-peak softening branches with positive slopes, leading to catastrophic snap-back instabilities under displacement control, in close analogy with the behaviour of shell buckling problems [11–15]. Such an indenting branch is not virtual only if the loading process is controlled by a monotonically increasing function of time, such as the crack length or the displacement discontinuity across the crack [18]. Moreover, a transition from snap-back to softening branches can be observed, leading to a size-scale effect on the brittleness or ductility. In particular, the specimen behaviour is brittle (snap-back) only for low fracture toughness, high tensile strength, and/or large structural sizes. More specifically, the combined effect of all of these

parameters can be investigated by using only one single parameter, the energy brittleness number s_E defined in [11].

In close analogy with the cohesive crack model for the description of strain localization in tension, the *Overlapping Crack Model* has recently been proposed in [19] for the description of the behaviour of quasi-brittle materials in compression. In this case, crushing takes place when the maximum stress in compression reaches the compressive strength, σ_c. After that, damage is described by a fictitious interpenetration of the two portions of the specimen and it represents the localization of the dissipated energy. As for the cohesive model in tension, larger is the interpenetration, also referred to as overlapping, lower are the compressive stresses transmitted by the damaged zone. Coupling of this elementary model with the cohesive one permits to realize a unified numerical algorithm able to describe both cracking and crushing growths during loading processes in reinforced concrete (RC) members in bending.

Moreover, in order to explain the size effects upon the parameters of the cohesive crack model (tensile strength, critical displacement, fracture energy), fractal geometry concepts can be applied to the description of the influence of the microstructural disorder [20, 21]. This led to an extension of the cohesive crack model, the so-called *Fractal Cohesive Crack Model* [22], which was proposed and applied to interpret the experimental tensile data from concrete specimens tested over a broad range of scales.

Finally, in the last few years, an extension of these studies has been carried out for the analysis of instability phenomena at the interfaces in heterogeneous materials [23, 24]. Using the finite element method, the following interface mechanical problems have been modelled: (i) debonding of particles in grained materials and study of the related scale effects depending on the grain size [25]; delamination of the reinforcement layer in retrofitted beams in bending [26], where the process of interface crack propagation results into severe snap-back instabilities; (iii) study of the delamination of layered beams with imperfect interfaces with multiple microdefects [27].

The present paper is organized as follows: in Section 2, an overview of the main features of the elementary Cohesive Crack Model are briefly presented and the numerical aspects are discussed. In Section 3, the Overlapping Crack Model is introduced and it will be shown that, using this model, it is possible to effectively capture the flexural behaviour of RC beams, by varying the reinforcement percentage and/or the beam size. Finally, Section 4 is devoted to the generalized Fractal (scale-invariant) Cohesive Crack Model, where the effect of microstructural disorder is taken into account according to fractal geometry.

2 Cohesive Crack Model

The Cohesive Crack Model is based on the following assumptions [9, 11]:

- The cohesive fracture zone (plastic or process zone) begins to develop when the maximum principal stress achieves the ultimate tensile strength, σ_u (see Fig.1a).

- The material in the process zone is partially damaged but still able to transfer stresses. Such stresses are dependent on the crack opening displacement w (see Fig.1b).

The energy necessary to produce a unit crack surface is given by the area under the $\sigma - w$ diagram in Fig.1b:

$$\mathcal{G}_F = \int_0^{w_{cr}^t} \sigma \mathrm{d}w = \frac{1}{2}\sigma_u w_{cr}^t. \tag{1}$$

Here, the superscript (t) refers to the material behaviour in tension. The real crack tip is defined as the point where the distance between the crack surfaces is equal to the critical value of the crack opening displacement, w_{cr}^t, and the normal stress vanishes. On the other hand, the fictitious crack tip is defined as the point where the normal stress attains the maximum value and the crack opening vanishes (Fig.1b).

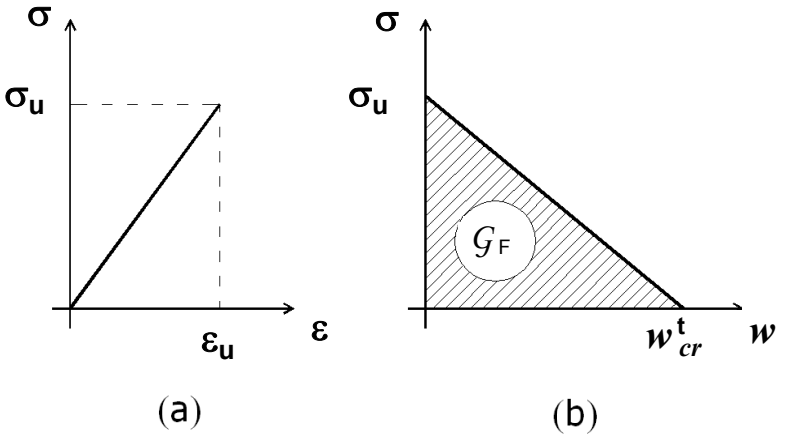

Fig. 1 Constitutive laws of the Cohesive Crack Model: (a) undamaged material, (b) process zone

Concerning the behaviour of plane concrete elements in Mode I conditions, such as the three point bending test, the crack trajectory is known *a priori* due to geometric symmetry. An extensive series of numerical analyses was carried out from 1984 to 1989 by Carpinteri and coworkers [11–15] based on the cohesive model implemented in the Finite Element Code FRANA (FRacture ANAlysis). A numerical procedure was considered to simulate a loading process where the parameter incremented step by step is the fictitious crack depth. Real (or stress-free) crack depth, external load, and deflection are obtained at each step after an iterative computation. Basically, the closing stresses acting on the crack surfaces are replaced by nodal forces (Fig.2).

The intensity of these forces depends on the opening of the fictitious crack, w, according to the $\sigma - w$ constitutive law of the material. When the tensile strength σ_u is achieved at the fictitious crack tip, the top node is opened and a cohesive force starts acting across the crack, while the fictitious crack tip moves to the next node.

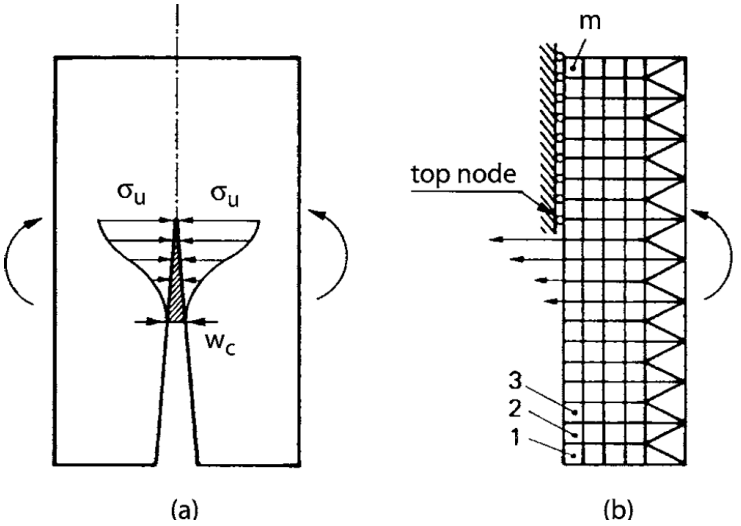

Fig. 2 (a) Stress distribution across the cohesive zone and (b) equivalent nodal forces in the finite element mesh

The coefficients of influence in terms of node openings and deflection are computed by a finite element analysis. At a generic step of the simulation, the crack opening displacements at the n fracture nodes may be expressed as follows:

$$\{w\} = [K]\{F\} + \{C\}P, \tag{2}$$

$\{w\}$ being the vector of the crack opening displacements, $[K]$ the matrix of the coefficients of influence (nodal forces), $\{F\}$ the vector of the nodal forces, $\{C\}$ the vector of the coefficients of influence (external load), and P the external load. The matrix equation (2) constitutes a set of n equation in $(2n + 1)$ unknowns, that is, the nodal displacements, the nodal forces and the external force. To solve the problem, $(n + 1)$ additional equations have to be considered. When a cohesive zone forms in front of the real crack tip, say between nodes j and l (see Fig.3), then we have:

$$F_i = 0, \qquad \text{for } i = 1, 2, \ldots, (j-1), \tag{3a}$$

$$F_i = F_u \left(1 - \frac{w_i}{w_{cr}^t}\right), \qquad \text{for } i = j, \ldots, l, \tag{3b}$$

$$w_i = 0, \qquad \text{for } i = l, \ldots, n, \tag{3c}$$

where F_u is the ultimate strength nodal force. Equations (2) and (3) constitute a linear algebraical system of $(2n+1)$ equations in $(2n+1)$ unknowns.

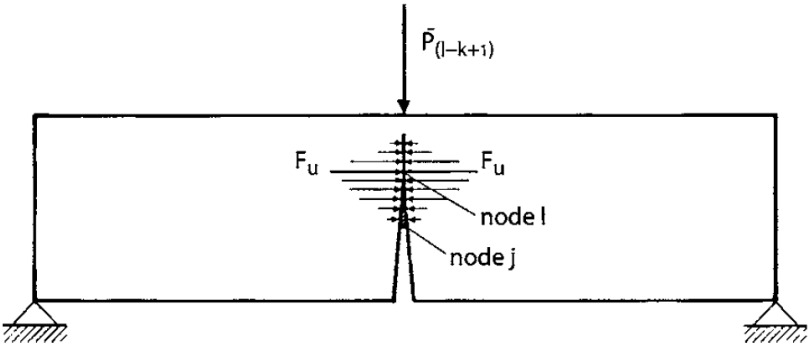

Fig. 3 Cohesive crack configurations at the $(l-k+1)$-th crack growth increment

If the load P and the vector $\{F\}$ are found, it is possible to compute the beam deflection, δ:

$$\delta = \{C\}^T \{F\} + D_P P, \tag{4}$$

where D_P is the coefficient of influence for the applied load. The present numerical algorithm simulates a loading process where the controlling parameter is the fictitious crack depth. On the other hand, real (or stress-free) crack depth, external load, and deflection are obtained at each step after an iterative procedure. The program stops with the untying of the node n and, consequently, with the determination of the last pair of values P_n and δ_n. In this way, the complete load-deflection curve is automatically plotted by the computer.

An example of the numerical simulations is shown in the dimensionless load-deflection diagram of Fig.4 for an unnotched beam made of concrete, $\varepsilon_u = 0.87 \times 10^{-4}$, $\nu = 0.1$, $t = h$, $l = 4h$, and by varying the energy brittleness number $s_E = \mathcal{G}_F / \sigma_u b$ [12, 13]. The specimen behaviour is brittle with the appearance of snap-back instabilities for low s_E numbers, i.e., for specimens with low fracture toughness, $\mathcal{G}_F$, high tensile strength, σ_u, and/or large sizes, h. For $s_E \lesssim 10.45 \times 10^{-5}$, the $P - \delta$ curve presents positive slope in the softening branch and a catastrophic event occurs if the loading process is deflection-controlled. Such indenting branch is not virtual only if the loading process is controlled by a monotonically increasing function of time [28, 29].

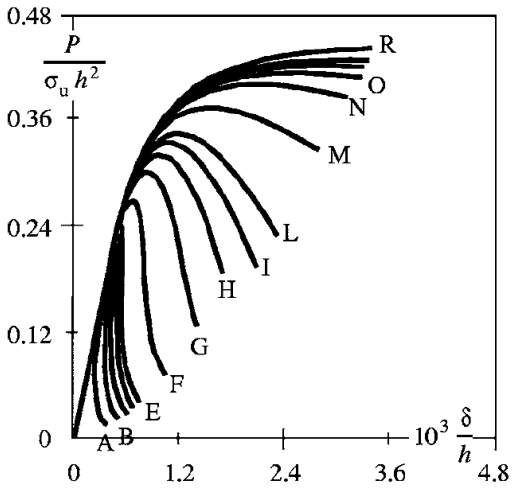

Fig. 4 Dimensionless load versus deflection diagrams by varying the brittleness number s_E, $a_0/h = 0.0$

Using this model, it is possible to investigate the size-scale effects on tensile strength and fracture toughness. Let us consider the ratio between P_{Cohes} and $P_{U.S.}$, where P_{Cohes} is the maximum loading capacity of initially uncracked specimens directly obtained from Fig. 3 and $P_{U.S.}$ is the maximum load of ultimate strength. The values of this ratio may also be regarded as the ratio of the apparent tensile strength, σ_f, given by the maximum load P_{Cohes}, to the true tensile strength, σ_u. It is evident from Fig.5 that the results of the cohesive crack model tend to those of the ultimate strength analysis for low s_E values. Therefore, only for comparatively large specimen sizes, the tensile strength σ_u can be obtained as $\sigma_u = \sigma_f$.

On the other hand, the values of the ratio $P_{Cohes}/P_{L.E.F.M.}$, where $P_{L.E.F.M}$ is the the maximum load of brittle fracture obtained from the LEFM relations, may also be regarded as the ratio of the fictitious fracture toughness, given by the maximum load P_{Cohes}, to the true fracture toughness considered as a material constant. This ratio is plotted in Fig.6 as a function of $1/s_E$, and it is evident that, for low s_E numbers, the results of the cohesive crack model tend to those of LEFM. Therefore, in this limit case, the maximum loading capacity can be predicted by applying the simple condition $K_I = K_{IC}$. This also provides an original interpretation to LEFM according to Catastrophe Theory [30], i.e., the Griffith instability for $s_E \to 0$ corresponds to the occurrence of a snap-back instability in the structural response.

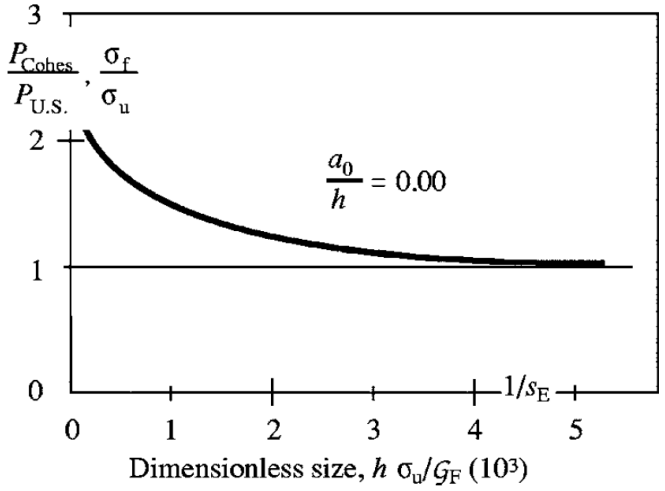

Fig. 5 Decrease in apparent strength by increasing the specimen size

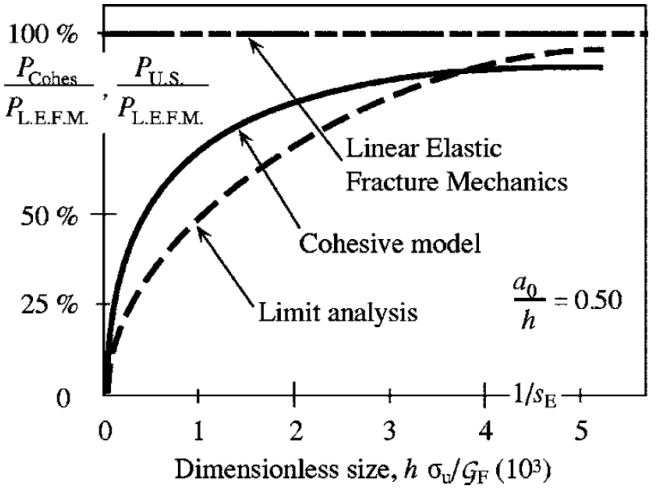

Fig. 6 Increase of fictitious fracture toughness by increasing the specimen size for notched specimens with $a_0/h = 0.50$.

3 Overlapping Crack Model

Also in compression, quasi-brittle materials show the phenomenon of strain localization when the elastic limit is overcome (see Fig.7).

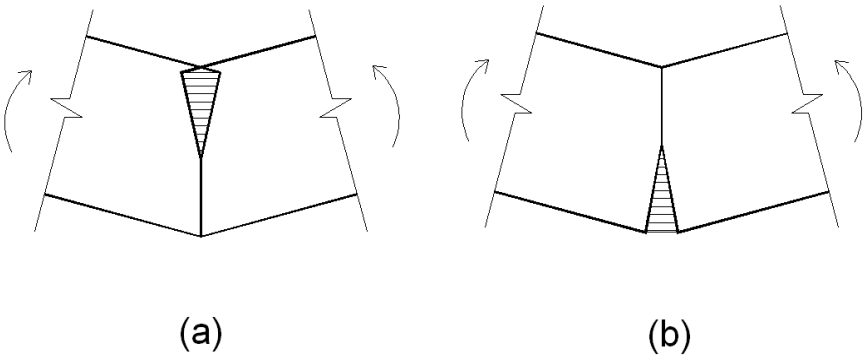

Fig. 7 (a) Compression crushing with overlapping; (b) tensile fracture with cohesive zone

In close analogy with the Cohesive Crack Model, we can define a pair of constitutive laws in compression. They consist of a linear elastic stress-strain relationship before the achievement of the compression strength, σ_c, and then a softening $\sigma - w$ diagram, where w is a measure of interpenetration (see Fig.8). The crushing energy (per unit surface), $\mathcal{G}_C$, is the area below the linear softening curve in the $\sigma - w$ diagram and it represents the counterpart of the fracture energy in tension.

The elementary Cohesive and Overlapping Crack Models can be merged into a more complex numerical algorithm for the study of the nonlinear behaviour of RC beams in bending. Following the approach outlined in Section 2, a discrete form of the elastic equations governing the mechanical response of the two half-beams can be introduced. The mid-span cross-section of the beam can be subdivided into finite elements by n nodes (see Fig.9).

In this scheme, cohesive and overlapping stresses are replaced by equivalent nodal forces, F_i, by integrating the corresponding tractions over each element size. Such nodal forces depend on the nodal opening or closing displacements according to the cohesive or overlapping softening laws. Using a mixed approach to deal with the contemporary presence of two crack tips, the vector of the horizontal nodal forces, $\{F\}$, can be computed as follows:

$$\{F\} = [K_w]\{w\} + \{K_M\}M, \tag{5}$$

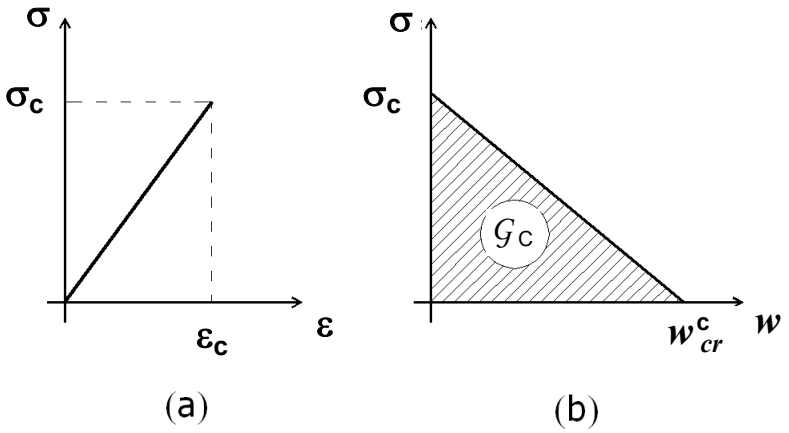

Fig. 8 Constitutive laws of the Overlapping Crack Model: (a) undamaged material, (b) crushing zone

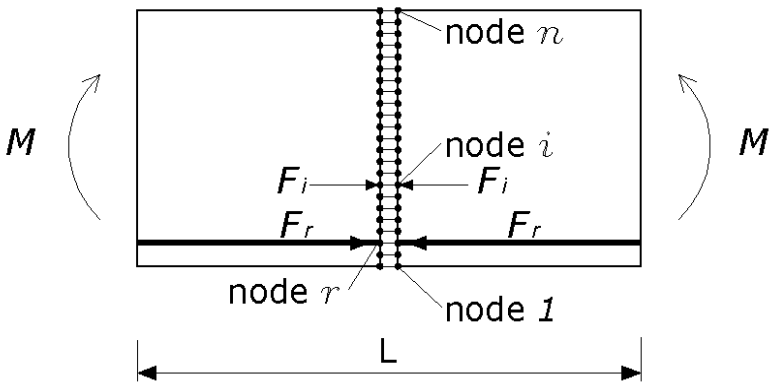

Fig. 9 Finite element nodes along the middle cross-section

where $[K_w]$ is the matrix of the coefficients of influence for the nodal displacements, $\{w\}$ is the vector of nodal displacements, $\{K_M\}$ is the vector of the coefficients of transmission for the applied moment and M is the applied moment. Equation (5) permits to analyse the fracturing and crushing process of the mid-span cross-section taking into account the elastic behaviour of the RC member. The reinforcement contribution is also included in the nodal force corresponding to the r-th node. In the generic situation shown in Fig.10, the following additional equations can be considered:

$$F_i = 0, \qquad \text{for } i = 1, 2, \ldots, (j-1);\ i \neq r, \tag{6a}$$

$$F_i = F_u \left(1 - \frac{w_i^t}{w_{cr}^t}\right), \qquad \text{for } i = j, \ldots, (m-1);\ i \neq r, \tag{6b}$$

$$w_i = 0, \qquad \text{for } i = m, \ldots, p, \tag{6c}$$

$$F_i = F_c \left(1 - \frac{w_i^c}{w_{cr}^c}\right), \qquad \text{for } i = (p+1), \ldots, n, \tag{6d}$$

$$F_r = f(w_r), \qquad \text{for } i = r. \tag{6e}$$

where the superscripts (t) and (c) stand for tension or compression, respectively, whereas F_u and F_c are the ultimate tensile and compresive nodal forces. The index j defines the position of the real crack tip, m the position of fictitious crack tip, p the position of the fictitious overlapping tip and r the node corresponding to the steel reinforcement. The relationship between the closing force exerted by the reinforcing steel and the crack opening at the reinforcement level, i.e., for $i = r$, can be determined on the basis of the bond-slip behaviour of concrete and steel. It is worth noting that, in this framework, it is possible to insert a reinforcement also in compression by introducing a suitable stress-displacement constitutive law in the corresponding node.

Equations (5) and (6) constitute a linear algebraic system of $(2n)$ equations in $(2n+1)$ unknowns, namely $\{F\}$, $\{w\}$ and M. A possible additional equation can be chosen: we can set either the force in the fictitious crack tip, m, equal to the ultimate tensile force, or the force in the fictitious crushing tip, p, equal to the ultimate compressive force. In the numerical scheme, we choose the situation which is closer to one of these two possible critical conditions. This criterion will ensure the uniqueness of the solution on the basis of physical arguments. The driving parameter of the process is the tip that in the considered step has reached the limit resistance. Only this tip is moved when passing to the next step. The two fictitious tips advance until

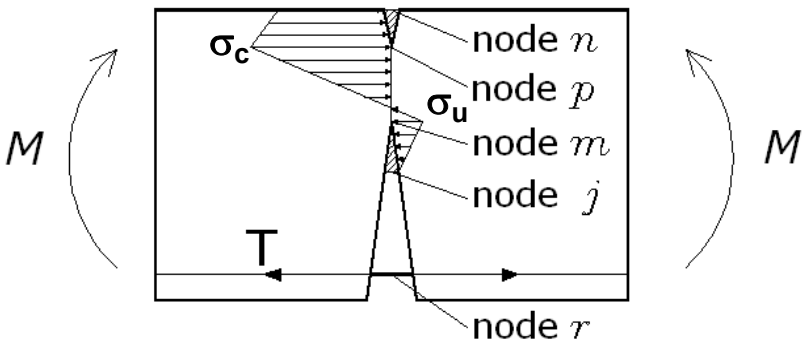

Fig. 10 Stress distribution with a cohesive crack in tension and crushing in compression

they converge to the same node. So forth, in order to describe the descending branch of the moment-rotation diagram, the two tips can move together towards the intrados of the beam. As a consequence, the crack in tension closes and the overlapping zone is allowed to extend towards the intrados. This situation is quite commonly observed in over-reinforced beams, where steel yielding does not take place. Finally, at each step of the algorithm, it is possible to calculate the beam rotation, ϑ, as follows:

$$\vartheta = \{D_w\}^{\mathrm{T}} \{w\} + D_M M, \tag{7}$$

where $\{D_w\}$ is the vector of coefficients of influence for the nodal displacements and D_M is the coefficient of influence for the applied moment.

An example of nondimensional moment-rotation diagram that can be obtained using this model is shown in Fig.11. Considering a reinforcement ratio $\rho = 1.0\%$, the beam depth, h, has been varied from 0.1 m to 2 m, keeping constant and equal to 0.9 the ratio between effective depth, d, and overall depth, h. The slenderness of the tested specimen has been set equal to unity. From the numerical results, it is evident that the structural behaviour becomes more and more brittle by increasing the beam depth. This is very well evidenced by a progressive reduction of the beam rotation at failure. It has to be emphasized that such size-scale effects are not considered in the actual design codes, whereas they have been found in several experimental programmes (see, e.g., [31], among others). Hence, the proposed model is expected to provide a deeper insight into the size-scale effects on the ductility of RC beams in bending.

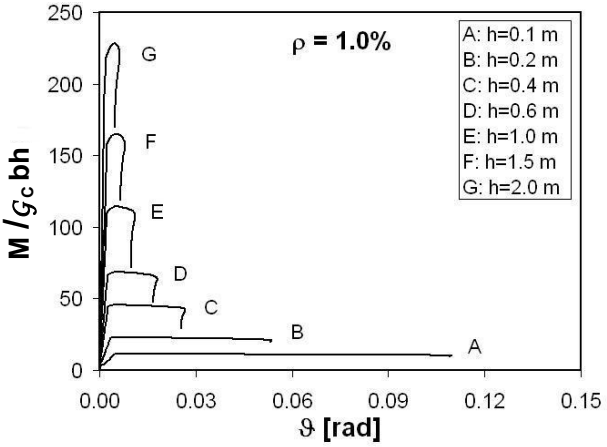

Fig. 11 Nondimensional moment vs. rotation diagrams by varying the beam depth

4 Fractal Cohesive Crack Model

In order to introduce the Fractal Cohesive Crack Model, we have to consider separately the size effects upon the three parameters characterizing the cohesive law (for more details, the readers are referred to [22]). Hence, let us consider the three fractal domains that are the cause of the size-scale effects on the nominal values of tensile strength, σ_u, critical deformation, ϵ_u, and fracture energy, $\mathcal{G}_F$ (see Fig.12).

Analyzing a concrete specimen subjected to tension, recent experimental results about porous concrete microstructure [32], as well as a stereological analysis of concrete flaws [33], led us to believe that a consistent modelling of damage in concrete can be achieved by assuming that the rarefied resisting sections in correspondence of the critical load can be represented by stochastic lacunar fractal sets with dimension $2 - d_\sigma$, with $d_\sigma \geq 0$ (see Fig.12a). From fractal geometry, we know that the area of lacunar sets is scale-dependent and tends to zero as the resolution increases; the tensile strength should be infinite, which is meaningless. Finite measures can be obtained only with noninteger (fractal) dimensions. The assumption of the Euclidean domain characterizing the classical continuum theory states that the maximum load F is given by the product of the strength σ_u times the nominal area $A_0 = b^2$. In this model, F equals the product of the Hausdorff fractal measure [34] $A^*_{res} \sim b^{2-d_\sigma}$ of the fractal, like the Sierpinski carpet in Fig.12a, times the fractal tensile strength σ^*_u [20]:

$$F = \sigma_u A_0 = \sigma^*_u A^*_{res}, \tag{8}$$

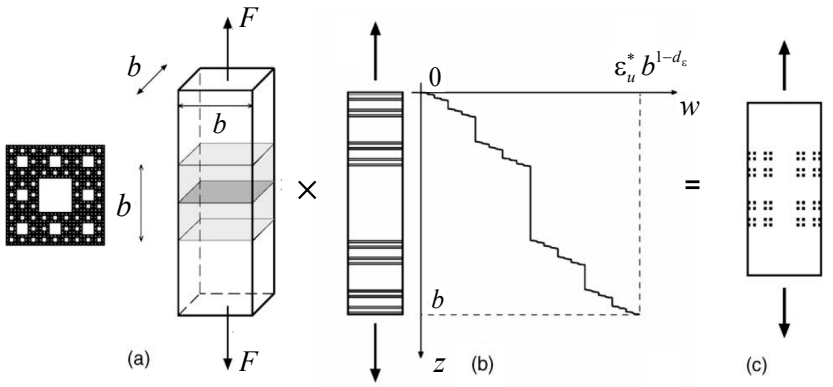

Fig. 12 (a) Fractal localization of the stress upon the resistant cross-section; (b) fractal localization of the strain along the bar length and (c) fractal energy dissipation inside the damage band

where σ^*_u presents the anomalous physical dimensions $[F][L]^{-(2-d_\sigma)}$. The fractal tensile strength is now a true material constant, i.e., it is scale-invariant. From Eq.(8) we obtain the scaling law for tensile strength:

$$\sigma_u = \sigma_u^* b^{-d_\sigma}, \tag{9}$$

i.e., a power law with negative exponent $-d_\sigma$.

Now, let us consider the deformation inside the zone where damage localizes, i.e., within the so-called damaged band. Again, it is possible to assume that the strain field presents fractal patterns. Thus, as representative of the damaged band, consider now a bar subjected to tension (Fig.12b), where, at the maximum load, dilation strain tends to concentrate into different softening regions, while the rest of the body undergoes elastic unloading. Here, all the quantities refer to tensile properties and therefore we omit the superscript (t) to lessen the notation. Let us assume, for instance, that the strain is localized at cross-sections whose projections onto the longitudinal axis are provided by the triadic Cantor set. The displacement function at rupture can be represented by a Cantor staircase graph, sometimes also called devils staircase (Fig.12b). The strain defined in the classical manner is meaningless in the singular points, as it diverges. This drawback can be overcome by introducing a fractal strain. Let us indicate with $1 - d_\epsilon$ (where $d_\epsilon \geq 0$) the fractal dimension of the lacunar projection of the damaged sections. According to the fractal measure of the damage line projection, the total elongation w_{cr} of the band at rupture must be given by the product of the Hausdorff measure $b^* \sim b^{1-d_\epsilon}$ of the Cantor set times the critical fractal strain ϵ_u^*, while in the classical continuum theory it equals the product of the length b times the critical strain ϵ_u:

$$w_{cr} = \epsilon_u b = \epsilon_u^* b^{(1-d_\epsilon)}, \tag{10a}$$

$$\epsilon_u = \epsilon_u^* b^{-d_\epsilon}, \tag{10b}$$

where ϵ_u^* has the anomalous physical dimension $[L]^{d_\epsilon}$. The fractal critical strain is the true material constant, i.e., it is the only scale-invariant parameter governing the kinematics of the damaged band. When d_ϵ varies from 0 to 1, the kinematical control parameter w_{cr}^* moves from the canonical critical strain ϵ_u, of dimension $[L]^0$, to the critical crack opening displacement w_{cr}, of dimension $[L]^1$.

Finally, this fractal approach can be applied to the work W necessary to break a concrete specimen of cross section b^2. This work is equal to the product of the fracture energy $\mathcal{G}_F$ times the nominal fracture area $A_0 = b^2$. On the other hand, due to the roughness of the crack surface, which can be modeled as a von Kock surface built on the square of side b, the area A_{dis} diverges as the measure resolution tends to infinity. Therefore, the fracture energy should be zero, which is meaningless. Finite values of the measure of the set where energy is dissipated can be achieved only via noninteger fractal dimension. The fractal dimension of the invasive domain will be $2 + d_\mathcal{G}$.

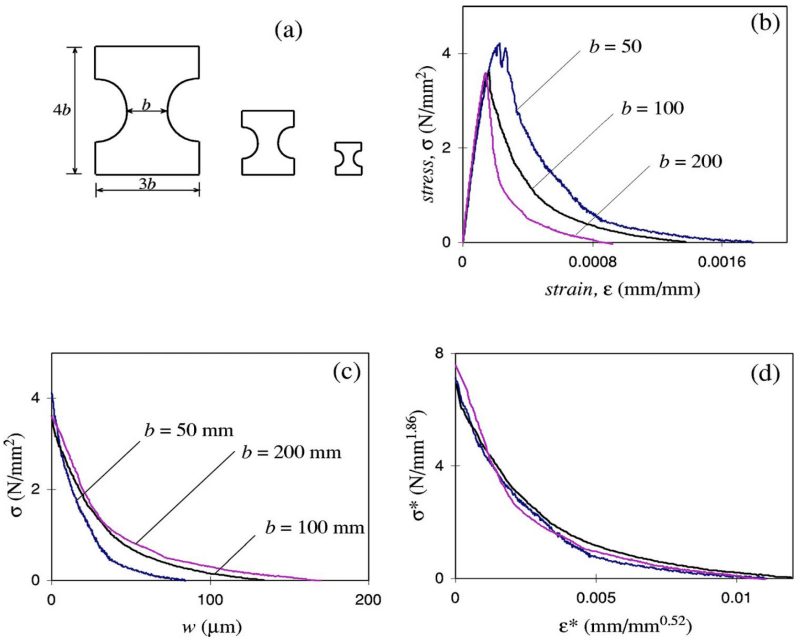

Fig. 13 (a) Tensile tests on dog-bone shaped concrete specimens [36]; (b) stress-strain diagrams; (c) cohesive law diagrams; (d) fractal cohesive law diagrams

In this framework, W equals the product of the fractal Hausdorff measure $A^*_{dis} \sim b^{2+d_\mathcal{G}}$ of the rough surface times the fractal fracture energy $\mathcal{G}^*_F$:

$$W = \mathcal{G}_F A_0 = \mathcal{G}^*_F A^*_{dis}, \tag{11a}$$

$$\mathcal{G}_F = \mathcal{G}^*_F b^{d_\mathcal{G}}, \tag{11b}$$

where $\mathcal{G}^*_F$ is the true scale invariant material parameter, whereas the nominal value $\mathcal{G}_F$ is subjected to a scale effect described by a power law with positive exponent.

The three size effect laws (9), (10b) and (11b) of the cohesive law parameters are not completely independent of each other. In fact, there is a relation among the scaling exponents that must be always satisfied. This means that, when two exponents are given, the third follows from the first two. In order to get this relation, let us suppose, for instance, to know d_σ and d_ϵ. Generalizing Eqs. (9) and (10b) to the whole softening regime, we get $\sigma = \sigma^* b^{-d_\sigma}$ and $w = \epsilon^* b^{(1-d_\epsilon)}$. These relationships can be considered as changes of variables and applied to the integral definition of the fracture energy:

$$\mathcal{G}_F = \int_0^{w_{cr}} \sigma \mathrm{d}w = b^{1-d_\epsilon-d_\sigma} \int_0^{\epsilon^*_u} \sigma^* \mathrm{d}\epsilon^* = \mathcal{G}^*_F b^{1-d_\epsilon-d_\sigma}. \tag{12}$$

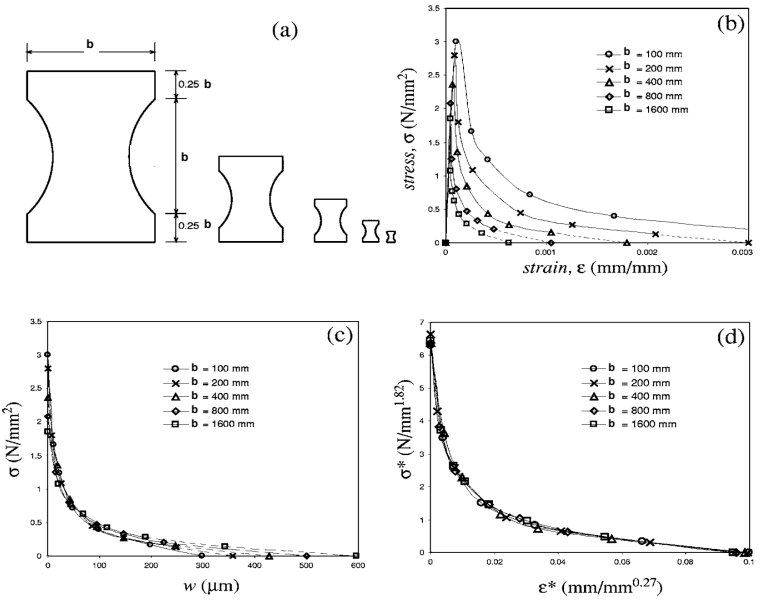

Fig. 14 (a) Tensile tests on dog-bone shaped concrete specimens [37]; (b) stress-strain diagrams; (c) cohesive law diagrams; (d) fractal cohesive law diagrams

Equation (12) highlights the effect of the structural size on the fracture energy, as Eq.(11b) does. Therefore, comparing Eqs.(12) and (11b), we get the relation among the exponents,

$$d_\sigma + d_\epsilon + d_\mathcal{G} = 1. \tag{13}$$

Note that, from a physical point of view, the geometrical relationship (12) states that, after the peak load, the energy is dissipated over the infinite lacunar sections where softening takes place inside the damaged band (Fig.12c).

The fractal fracture energy $\mathcal{G}_F^*$ can be obtained as the area below the fractal softening stress-strain diagram $\sigma^* - \epsilon^*$, according to Eq.(12). Hence, we call the $\sigma^* - \epsilon^*$ diagram the *scale-independent* or *fractal cohesive law*. Contrarily to the classical cohesive law, which is experimentally sensitive to the structural size, this curve should be an exclusive property of the material, being able to capture the fractal nature of the damage process.

This model has been applied to the data obtained from 1994 to 1998 by Carpinteri and Ferro [35, 36] for tensile tests on dog-bone shaped concrete specimens of various sizes under controlled boundary conditions (see Fig.13).

They interpreted the size effects on the tensile strength and the fracture energy by fractal geometry. Fitting the experimental results, they found the values $d_\sigma = 0.14$ and $d_\mathcal{G} = 0.38$. Some of the $\sigma - \epsilon$ (stress versus strain) and $\sigma - w$ diagrams are reported, respectively, in Figs.13b and 13c, where w is

the displacement localized in the damaged band, obtained by subtracting, from the total one, the displacement due to elastic and inelastic pre-peak deformation. Equation (13) yields $d_\epsilon = 0.48$, so that the fractal cohesive laws can be plotted in Fig.13d. As theoretically expected, all the curves related to the different sizes tend to merge in a unique, scale-independent cohesive law.

An analysis of the data obtained by van Mier and van Vliet [37] according to the fractal cohesive model was also performed in [22]. The results are shown in Fig.14 and, again, all the curves related to the different sizes tend to merge in a unique, scale-independent cohesive law.

Acknowledgements. The financial support of the European Union to the Leonardo da Vinci Project I/06/B/F/PP-154069 "Innovative Learning and Training on Fracture (ILTOF)" is gratefully acknowledged.

References

1. Drucker, D.C.: Some implications of work-hardening and ideal plasticity. Quart. Appl. Math. 7, 411–418 (1950)
2. von Kármán, T., Dunn, L.G., Tsien, H.S.: The influence of curvature on the buckling characteristics of structures. J. Aero. Sci. 7, 276–289 (1940)
3. von Kármán, T., Tsien, H.S.: The buckling of thin cylindrical shells under axial compression. J. Aero. Sci. 8, 303–312 (1941)
4. Dugdale, D.S.: Yielding of steel sheets containing slits. J. Mech. Phys. Solids 8, 100–114 (1960)
5. Bilby, B.A., Cottrell, A.H., Swinden, K.H.: The spread of plastic yield from a notch. Proc. R Soc. London A 272, 304–314 (1963)
6. Barenblatt, G.I.: The mathematical theory of equilibrium cracks in brittle fracture. Adv. App. Mech. 7, 55–129 (1962)
7. Rice, J.R.: A path independent integral and the approximate analysis of strain concentration by notches and cracks. J. Appl. Mech. 31, 379–386 (1968)
8. Smith, E.: The structure in the vicinity of a crack tip: a general theory based on the cohesive zone model. Engng. Fract. Mech. 6, 213–222 (1974)
9. Hillerborg, A., Modeer, M., Petersson, P.E.: Analysis of crack formation and crack growth in concrete by means of fracture mechanics and finite element. Cem. Concr. Res. 6, 773–782 (1976)
10. Petersson, P.: Crack growth and development of fracture zones in plain concrete and similar materials, Report TVBM-1006, Division of Building Materials, Lund Institute of Technology (1981)
11. Carpinteri, A.: Interpretation of the Griffith instability as a bifurcation of the global equilibrium. In: Shah, S.P. (ed.) Application of Fracture Mechanics to Cementitious Composites (Proc. of a NATO Advanced Research Workshop, Evanston, USA, 1984), pp. 284–316. Martinus Nijhoff Publishers, Dordrecht (1985)
12. Carpinteri, A.: Cusp catastrophe interpretation of fracture instability. J. Mech. Phys. Solids 37, 567–582 (1989)

13. Carpinteri, A.: Decrease of apparent tensile and bending strength with specimen size: two different explanations based on fracture mechanics. Int. J. Solids Struct. 25, 407–429 (1989)
14. Carpinteri, A.: Post-peak and post-bifurcation analysis on cohesive crack propagation. Engng. Fract. Mech. 32, 265–278 (1989)
15. Carpinteri, A.: Softening and snap-back instability in cohesive solids. Int. J. Num. Methods Engng. 28, 1521–1537 (1989)
16. Cen, Z., Maier, G.: Bifurcations and instabilities in fracture of cohesive-softening structures: a boundary elements analysis. Fatigue Fract. Engng. Mater. Struct. 15, 911–928 (1992)
17. Elices, M., Guinea, G.V., Planas, J.: Prediction of size-effect based on cohesive crack model. In: Carpinteri, A. (ed.) Size-Scale Effects in the Failure Mechanisms of Materials and Structures. E & FN Spon, pp. 309–324 (1996)
18. Carpinteri, A.: Size effects on strength, toughness and ductility. ASCE J. Engng. Mech. 115, 1375–1392 (1989)
19. Carpinteri, A., Corrado, M., Paggi, M., Mancini, G.: Cohesive versus overlapping crack model for a size effect analysis of RC elements in bending. In: Design, Assessment and Retrofitting of RC Structures. The Proceedings of the 6th Conference on Fracture Mechanics of Concrete and Concrete Structures (FraMCoS), vol. 2, pp. 655–663. Taylor & Francis, Catania (2007)
20. Carpinteri, A.: Fractal nature of material microstructure and size effects on apparent mechanical properties. Mech. Mater. 18, 89–101 (1994)
21. Carpinteri, A.: Scaling laws and renormalization groups for strength and toughness of disordered materials. Int. J. Solids Struct. 31, 291–302 (1994)
22. Carpinteri, A., Chiaia, B., Cornetti, P.: A scale-invariant cohesive crack model for quasi-brittle materials. Engng. Fract. Mech. 69, 207–217 (2002)
23. Paggi, M.: Interface Mechanical Problems in Heterogeneous Materials. Ph.D. Thesis, Politecnico di Torino (2005)
24. Paggi, M., Carpinteri, A., Zavarise, G.: A Unified Interface Constitutive Law for the Study of Fracture and Contact Problems in Heterogeneous Materials. In: Wriggers, P., Nackenhorst, U. (eds.) Analysis and Simulation of Contact Problems. LNACM, vol. 27, pp. 297–304. Springer, Berlin (2006)
25. Carpinteri, A., Paggi, M., Zavarise, G.: Snap-back instability in micro-structured composites and its connection with superplasticity. Strength, Fracture and Complexity 3, 61–72 (2005)
26. Carpinteri, A., Lacidogna, G., Paggi, M.: Acoustic emission monitoring and numerical modelling of FRP delamination in RC beams with non-rectangular cross-section. RILEM Mat. Struct. 40, 553–566 (2007)
27. Carpinteri, A., Paggi, M., Zavarise, G.: The effect of contact on the decohesion of laminated beams with multiple microcracks. Int. J. Solids Struct. 45, 129–143 (2008)
28. Fairhurst, C., Hudson, J.A., Brown, E.T.: Optimizing the control of rock failure in servo-controlled laboratory test. Rock Mech. 3, 217–224 (1971)
29. Rokugo, K., Ohno, K., Koyanagi, W.: Automatical measuring system of load-displacement curves including postfailure region of concrete specimen. In: Fracture Toughness and Fracture Energy of Concrete International Conference of Fracture Mechanics of Concrete, Lausanne, Switzerland (1986)
30. Thom, R.: Structural Stability and Morphogenesis, Benjamin, Reading, Massachusetts (1975)

31. Bosco, C., Debernardi, P.G.: Experimental investigation on the ultimate rotational capacity of R.C. beams. Report No. 36, Atti del Dipartimento, Politecnico di Torino, Ingegneria Strutturale (1992)
32. Carpinteri, A., Chiaia, B., Invernizzi, S.: Three dimensional fractal analysis of concrete fracture at the mesolevel. Theor. Appl. Fract. Mech. 31, 163–172 (1999)
33. Carpinteri, A., Cornetti, P.: Size effects on concrete tensile fracture properties: an interpretation of the fractal approach based on the aggregate grading. J. Mech. Behav. Mater. 13, 233–246 (2002)
34. Falconer, K.: Fractal Geometry: Mathematical Foundations and Applications, 2nd edn. John Wiley, Chichester (2003)
35. Carpinteri, A., Ferro, G.: Size effects on tensile fracture properties: A unified explanation based on disorder and fractality of concrete microstructure. Mater. Struct. 27, 563–571 (1994)
36. Carpinteri, A., Ferro, G.: Scaling behaviour and dual renormalization of experimental tensile softening responses. Mater. Struct. 31, 303–309 (1998)
37. van Mier, J.G.M., van Vliet, M.R.A.: Effect of strain gradients on the size effect of concrete in uniaxial tension. Int. J. Fract. 94, 195–219 (1999)

Multi-scale Analysis of Polycristalline Metals and Composites

J.-L. Chaboche[1,2]

[1] ONERA, 29 av. de la Division Leclerc, 92320 Châtillon, France
Jean-Louis.Chaboche@onera.fr
[2] LASMIS, Troyes University of Technology

1 Introduction

Multi-scale methods for the inelastic modelling of materials were already developed since a long time. We will concentrate here on the highest scales, for metals and alloys and for some composites, considering scale changes from the crystal plasticity level in polycrystals to the level of the structural component analysis. Lower scales, involving methods like discrete dislocation dynamics, molecular dynamics or atomistic simulations are out of the scope of the present discussion. We also limit the considered area to the context of elasto-plasticity and viscoplasticity, at moderate strains.

In this context of multi-scale analysis in mechanics of materials, we would like to distinguish two levels of application of scale change methods or homogenisation techniques:

- what we could call a *sequential multi-scale method*, in which the scale change, or the micro-to-macro transition method, is developed with the objective to convey information at the higher scale from more physical constitutive assumptions at the lower one. This is often realised with the objective to help to build up macroscopic constitutive relations for a representative volume element. In that case, simulations are used as virtual tests, giving additional information to the experimental tests, but the structural component analysis is made in a subsequent and independent way, after having fixed the macroscopic constitutive relations of the considered material.
- what we call an *integrated multi-scale method* (or a true multi-scale analysis), when the lower scale is permanently present inside the structural component analysis, through the scale change. There is no more use of a macroscopic constitutive relation (most often degrading or restricting the behaviour modelling capabilities), because the material point (elementary volume) inelastic response in the component is obtained, in real

time, from a localisation/homogenisation procedure and involves only local (microscale) constitutive properties and microstructural descriptions.

Another way to class various kinds of methods will be used, considering the following ones, that will correspond to the three main parts of the present paper :

- In section 2, we consider *numerical approaches*, essentially based on periodic homogenisation theory. Examples will be given for non-linear composites, treated either by Fast Fourier Transform (FFT) or by finite element (FE) techniques. The example of an integrated multi-scale approach to component analysis will be presented with the so called FE^2 technique, with imbricated FE, in the case of elasto(visco)plasticity;
- *mean-field approaches* are discussed in section 3, as more or less analytical methods. A version of the elastic localisation rule, called TFA (Transformation Field Analysis) is recalled, together with tangent localisation rules. They are compared with FE simulations in case of a non-linear composite. It is shown that tangent approaches still deliver too stiff stress-strain responses when applied with their correct anisotropic formulation;
- Section 4 presents some *intermediate approaches*, like TFA with multiple sub-volumes or NTFA (Non Uniform TFA). Moreover, macroscopic constitutive equations directly based on the local behaviours of phases, are briefly summarised that use two specific approximations, a corrected TFA method and a Generalised Eigenstrain Model.

2 Numerical Methods

2.1 Basic Formulation of Periodic Homogenisation

Also called asymptotic homogenisation, this is the basic method to obtain, from the numerical treatment of a so-called RVE (Representative Volume Element), both the homogenised responses to any macroscopic loading and corresponding local fields. The local problem writes as:

$$\underset{\sim}{\sigma}(x) = \mathcal{F}\left(x, \underset{\sim}{\varepsilon}(x), \dot{\underset{\sim}{\varepsilon}}(x)\right) \tag{1}$$

$$\underset{\sim}{\varepsilon} = \frac{1}{2}\left(\nabla \underline{\mathbf{u}} + (\nabla \underline{\mathbf{u}})^T\right) \tag{2}$$

$$div\ \underset{\sim}{\sigma} = 0 \tag{3}$$

$$\underline{\mathbf{u}}^* = \underline{\mathbf{u}} - \overline{\underset{\sim}{\varepsilon}}.x \qquad \text{periodic} \tag{4}$$

$$\underset{\sim}{\sigma}.\underline{\mathbf{n}} \qquad \text{anti-periodic} \tag{5}$$

The constitutive equation (1) of phases in the RVE is local in nature. Compatibility (2) and equilibrium (3) are non local in the sense they induce coupling between material points. $\underline{\mathbf{u}}^*$ in (4) is the periodic part of the displacement field and the tractions are anti-periodic on the boundaries with (5). The RVE is loaded by the average strain $\underset{\sim}{\overline{\varepsilon}}$.

Under an homogenised macroscopic loading, for a known and periodic microstructure, the method can be considered as exact provided the solution is obtained with a sufficiently fine discretisation (in space and time). Under non-uniform loads, as inside a component analysis, the method is valid only if the characteristic length of the microstructure is sufficiently small compared to the component size and the wavelength of the macroscopic fields.

2.2 Solutions by FFT Techniques

Periodic conditions allow an easy use of Fast Fourier Transform based numerical techniques. References [1], [2] are important contributions. We follow the presentation by Moulinec & Suquet [3], very briefly summarised. The constitutive equation is written as:

$$\underset{\sim}{\sigma}(x) = \underset{\approx}{\mathbf{L}} : (\underset{\sim}{\varepsilon}(u(x)) - \underset{\sim}{\varepsilon}^p(x)) = \underset{\approx}{\mathbf{L}}^0 : \underset{\sim}{\varepsilon}(u(x)) + \underset{\sim}{\tau}(x) \tag{6}$$

In the second form, we use the stiffness tensor $\underset{\approx}{\mathbf{L}}^0$ of the homogeneous reference medium and $\underset{\sim}{\tau}(x)$ is the transformation stress, or eigenstress, or polarisation stress. Obviously:

$$\underset{\sim}{\tau}(x) = \left(\underset{\approx}{\mathbf{L}} - \underset{\approx}{\mathbf{L}}^0\right) : \underset{\sim}{\varepsilon}(u(x)) - \underset{\approx}{\mathbf{L}} : \underset{\sim}{\varepsilon}^p(x) \tag{7}$$

Evolution equations for plastic strain and any associated internal variables have a totally free rate form, but are not indicated here.

Taking into account equilibrium and compatibility equations leads to the Lippman-Schwinger equation, an integral equation, in which $\underset{\approx}{\mathbf{\Gamma}}^0$ is the Green operator for the reference medium $\underset{\approx}{\mathbf{L}}^0$ and $*$ indicates the spatial convolution product :

$$\underset{\sim}{\varepsilon}(u) = \underset{\sim}{\overline{\varepsilon}} - \underset{\approx}{\mathbf{\Gamma}}^0 * \underset{\sim}{\tau} \tag{8}$$

From (7) we immediately obtain:

$$\underset{\sim}{\varepsilon}(u) = \underset{\sim}{\overline{\varepsilon}} - \underset{\approx}{\mathbf{\Gamma}}^0 * \left[\left(\underset{\approx}{\mathbf{L}} - \underset{\approx}{\mathbf{L}}^0\right) : \underset{\sim}{\varepsilon}(u(x)) - \underset{\approx}{\mathbf{L}} : \underset{\sim}{\varepsilon}^p(x)\right] \tag{9}$$

Solution of such an integral equation, for which the unknown u appears in the two sides, can be solved in an iterative way :

$$\underset{\sim}{\varepsilon}^{i+1} = \underset{\sim}{\overline{\varepsilon}} - \underset{\approx}{\mathbf{\Gamma}}^0 * \left[\left(\underset{\approx}{\mathbf{L}} - \underset{\approx}{\mathbf{L}}^0\right) : \underset{\sim}{\varepsilon}^i - \underset{\approx}{\mathbf{L}} : \underset{\sim}{\varepsilon}^{pi}\right] \tag{10}$$

which can be shown to be equivalent with:

$$\underset{\sim}{\sigma}^i = \underset{\approx}{\mathbf{L}} : \left(\underset{\sim}{\varepsilon}^i - \underset{\sim}{\varepsilon}^{pi}\right) \qquad \underset{\sim}{\varepsilon}^{i+1} = \underset{\sim}{\varepsilon}^i - \underset{\approx}{\mathbf{\Gamma}}^0 * \underset{\sim}{\sigma}^i \tag{11}$$

because a property of $\underset{\approx}{\mathbf{\Gamma}}^0$ is to be a projector on the compatible strain field of zero average, i.e. $\underset{\approx}{\mathbf{\Gamma}}^0 * (\underset{\sim}{\varepsilon}(u)) = \underset{\sim}{\varepsilon}(u) - \overline{\underset{\sim}{\varepsilon}}$. Equation (11-a) is local in the actual space. Equation (11-b) is non-local in the actual space but it becomes local in Fourier's space, which writes:

$$\underset{\sim}{\sigma}^i(x) = \underset{\approx}{\mathbf{L}}(x) : \left(\underset{\sim}{\varepsilon}^i(x) - \underset{\sim}{\varepsilon}^{pi}(x)\right) \qquad \hat{\underset{\sim}{\varepsilon}}^{i+1}(\xi) = \hat{\underset{\sim}{\varepsilon}}^i(\xi) - \hat{\underset{\approx}{\mathbf{\Gamma}}}^0(\xi) : \hat{\underset{\sim}{\sigma}}^i(\xi) \tag{12}$$

Now the algorithm, for a given time increment is as follows:

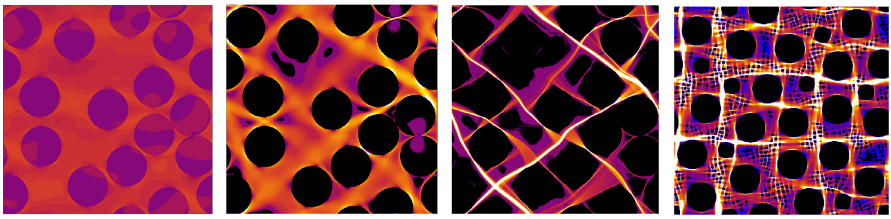

Fig. 1 FFT results with 2D non-linear composites : a - elastic matrix; b - plastic matrix with linear hardening; c - perfectly plastic matrix; d - matrix with power law (exponent 10) with 3 fibre diameter sizes

- Let us call $\underset{\sim}{\sigma}^i$, $\underset{\sim}{\varepsilon}^i$, $\underset{\sim}{\varepsilon}^{pi}$ the solution at the end of the time increment, for the i^{th} iteration
- by applying FFT to $\underset{\sim}{\sigma}^i$ and $\underset{\sim}{\varepsilon}^i$, we obtain their transforms $\hat{\underset{\sim}{\sigma}}^i(\xi)$ and $\hat{\underset{\sim}{\varepsilon}}^i(\xi)$
- using (12-b) we obtain $\hat{\underset{\sim}{\varepsilon}}^{i+1}(\xi)$ and $\hat{\underset{\sim}{\varepsilon}}^{i+1}(0) = \overline{\underset{\sim}{\varepsilon}}$
- through the inverse FFT is obtained $\underset{\sim}{\varepsilon}^{i+1}(x)$
- this serves as an input to the constitutive equation integrator (from the beginning to the end of the current time increment), which delivers $\underset{\sim}{\varepsilon}^{pi+1}(x)$ and $\underset{\sim}{\sigma}^{i+1}(x) = \underset{\approx}{\mathbf{L}}(x) : \left(\underset{\sim}{\varepsilon}^{i+1}(x) - \underset{\sim}{\varepsilon}^{pi+1}(x)\right)$.

The method has been shown to converge quite rapidly, and to induce a very low CPU cost, thanks to the performance of FFT. There are also many specific improvements that have been made during the last ten years [4].

Examples of Figure 1 are taken from [5] for a 2D composite, with a random repartition of elastic fibres and an elastoplastic matrix. The figure represents the obtained local fields of equivalent plastic strain. On the left is the linear elastic case, with a quasi-uniform strain field; then, for the matrix with a linear hardening, it is much less uniform. For the perfectly plastic matrix,

extremely severe strain localisations are obtained, showing a great heterogeneity of plastic strain in the matrix (case c). In that case, it is shown that effective properties of the composite are not depending too much on the fibre volume fraction but more on the tortuosity of channels in the matrix. On the right is shown another example [6], under pure shear, with three different fibre diameters, and a power law for the matrix. It shows both the localisation and the capability of the method to represent very complex fields in cases involving several scales together. Many other applications have been made, in various contexts, on composites as well as on polycristals or multiphase materials. The method has also been used in 3D in the context of an elastoplastic matrix and randomly distributed elastic inclusions.

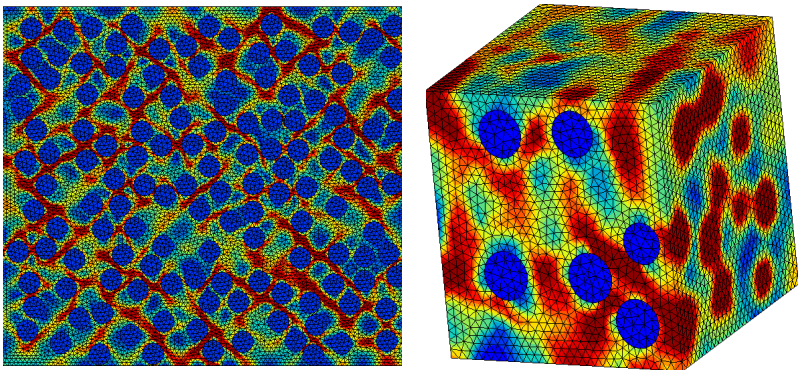

Fig. 2 Illustration of local accumulated plastic strain fields obtained by finite elements for random repartitions of fibres or inclusions

2.3 Solutions by FE Techniques

Similar periodic homogenisation based analysis can also be realised using finite element techniques, even if more costly. Figure 2 illustrates 2D and 3D cases, using random repartitions of elastic fibres or inclusions. The metal matrix is treated by incremental plasticity, with a power law. The corresponding macroscopic stress-strain responses will be used in section 3.3, as references for mean-field approaches.

In order to illustrate so-called integrated multi-scale analysis, we give here a few details on the FE^2 approach, used in the context of a MMC structure, in elasto-viscoplasticity with damage [7], [8]. Similar approaches have been developed earlier, like in [9], [10]. The principle is quite simple. At the level of the macroscopic component inelastic analysis, at each time (or loading) increment, each Gauss point in the composite part needs the use of a constitutive equation. In place of using a macroscopic one, the local constitutive response is delivered by an in-situ microscale analysis made by periodic homogenisation and a FE unit cell (for each GP).

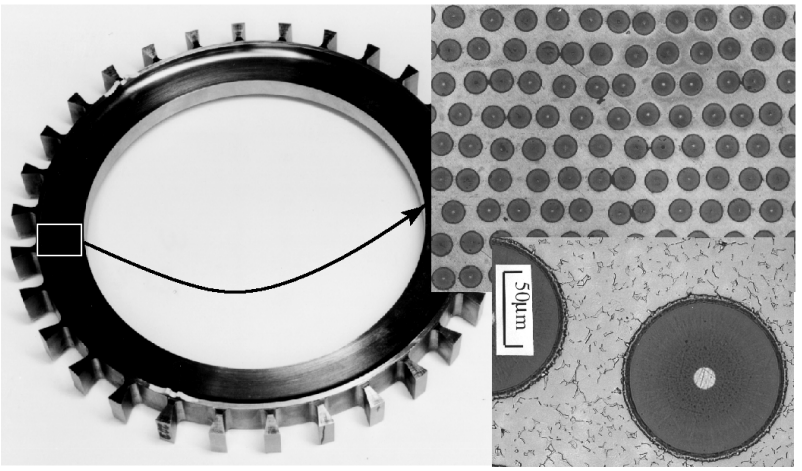

Fig. 3 The principle of the bladed ring with a SiC-Ti composite insert, as considered for future aero-engine designs

The example given here [7] concerns a bling, bladed ring, type of structure planed to replace the compressor discs, in which the ring is reinforced by a circumferential (unidirectional) composite (Figure 3). Fibres (105 to 150 μm diameter) are very well periodically arranged and the Titanium matrix is the same as the metal around the composite insert and in the blades. Knowing all internal variables, stress and strain states in the problem at instant t_n, at the beginning of the current time increment, the solution at t_{n+1} is searched iteratively by the standard Newton-Raphson approach. At each iteration j, the macroscopic strain $\overline{\underset{\sim}{\varepsilon}}^{j}_{n+1}$ serves as an input for the constitutive response. It is applied on the unit cell as the average macroscopic strain. The local periodic FE solution delivers strain, plastic strain and stress fields $\underset{\sim}{\varepsilon}^{j}_{n+1}(x)$, $\underset{\sim}{\varepsilon}^{p}_{n+1}{}^{j}(x)$, $\underset{\sim}{\sigma}^{j}_{n+1}(x)$. The average stress $\overline{\underset{\sim}{\sigma}}^{j}_{n+1}$ is then returned to the global solver (as for standard constitutive equations). In FE^2 method [11], solution of the unit cell is also obtained by standard FE techniques, with periodic boundary conditions and using the Newton-Raphson technique to solve the non-linear problem (for time increment (t_n, t_{n+1}). At this stage the solver of the local constitutive equations delivers the consistent tangent matrix at each material point in unit cell. This one is then assembled in such a way (a key point in the method) to become the local tangent stiffness operator for the macroscopic material point.

The method has been applied in 2D, with elastic fibres and a viscoplastic matrix, which constitutive equation is a classical elasto-viscoplastic model with two back-stresses. It was also applied including damaging events by means of cohesive models at the interface (in fact interphase) between matrix and fibres. Figure 4 shows results obtained simultaneously at the two

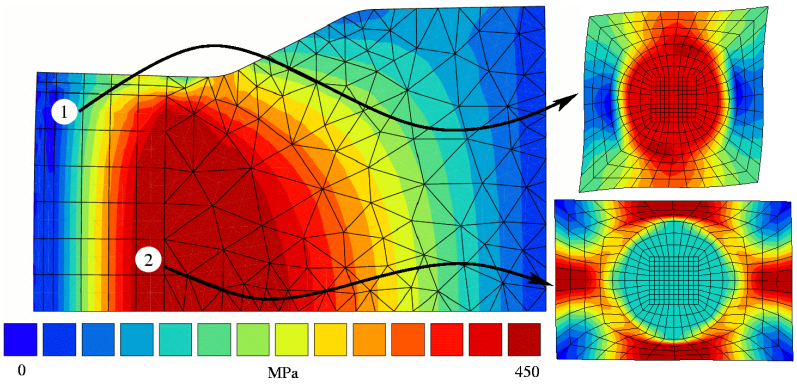

Fig. 4 Results obtained at the two scales at the maximum rotation speed. left: radial stress at the macroscale; right: radial strain in two local cells (the amplification factor for displacements is 10)

scales [7], at the maximum rotation speed. On the right, strain responses are shown for two typical unit cells, including one in a region where shear is predominant.

Let us note that FE^2 method allows an easy relocalisation at the lower scale of the obtained macroscopic fields, in critical regions of interest for a subsequent damage or fracture analysis [12]. Microstructural fields in each unit cell may be considered as internal variables at the macroscopic level, then easily reinterpolated with the standard post-treatment of the FE code, at the level of the structural component. This technique has been shown to deliver well defined continuous local fields (stress, strain, plastic strain...), even when an exaggerated diameter size was given to the fibres.

Other new developments were made in the literature, using similar methodologhies, for example in [13], [14], [15]. Let us mention the analysis of the bling component [16], in which the constitutive equation of the matrix material (inside the composite as well as in the non-reinforced part) is obtained through a second scale change by means of a mean-field approach. In the context of ITER, the future thermo-nuclear experimental reactor, it has been generalised in [17] as an FE^3 method, incorporating two successive (but integrated) scale changes by periodic homogenisation. It was done in elastoplasticity but with simplified responses (J_2 plasticity with isotropic hardening).

Higher order methods were also developed in the context of FE^2 [18], in which the periodic homogenisation method is enriched with higher order strain gradients, in order to build a generalised continuum at the macroscale. Such a generalisation is useful when the size of the microstructure is significant compared with component size.

3 Analytical Mean-Field Approaches

These methods are essentially based on, the Eshelby solution [19], given for an infinite elastic medium of stiffness $\underset{\sim}{\mathbf{L}}^0$, containing an ellipsoidal inclusion of stiffness $\underset{\sim}{\mathbf{L}}^I$. In case of the elastic inclusion, the strain $\underset{\sim}{\varepsilon}^I$ in the inclusion (uniform for the isotropic medium) depends linearly on the average strain $\overline{\underset{\sim}{\varepsilon}}$ (or strain at infinity) :

$$\underset{\sim}{\varepsilon}^I = \left[\underset{\sim}{\mathbf{I}} + \underset{\sim}{\mathbf{S}}^0 : \left(\underset{\sim}{\mathbf{L}}^0\right)^{-1} : \left(\underset{\sim}{\mathbf{L}}^I - \underset{\sim}{\mathbf{L}}^0\right)\right]^{-1} : \overline{\underset{\sim}{\varepsilon}} \tag{13}$$

in which $\underset{\sim}{\mathbf{S}}^0$ is Eshelby's tensor, depending upon ellipsoid geometry and on $\underset{\sim}{\mathbf{L}}^0$. Generalisation to elasto-plasticity can be done by different methods that depend on the choice made for the linear comparison material. Some of them are briefly presented now.

3.1 The Elastic Localisation Rule

Called TFA (Transformation Field Analysis [20]), it considers the true elastic Hooke law for the accommodation process, together with the plastic strain treated as an eigenstrain, exactly the same way as a thermal expansion (or a transformation strain):

$$\underset{\sim}{\sigma}(x) = \underset{\sim}{\mathbf{L}}(x) : \left(\underset{\sim}{\varepsilon}(x) - \underset{\sim}{\varepsilon}^T(x)\right) \qquad \underset{\sim}{\varepsilon}^T(x) = \underset{\sim}{\varepsilon}^p(x) + \underset{\sim}{\varepsilon}^{th}(x) \tag{14}$$

With the approximation of uniform eigenstrain $\underset{\sim}{\varepsilon}^T_s$ in each phase (or in each sub-volume), Lippman-Schwinger's equation (9) can be solved, leading for the average strain $\underset{\sim}{\varepsilon}_s$ in each sub-volume :

$$\underset{\sim}{\varepsilon}_s = \underset{\sim}{\mathbf{A}}_s : \underset{\sim}{\mathbf{E}} + \sum_r \underset{\sim}{\mathbf{D}}_{sr} : \underset{\sim}{\varepsilon}^T_r \tag{15}$$

where $\underset{\sim}{\mathbf{E}}$ is the average macroscopic strain on the RVE. $\underset{\sim}{\mathbf{A}}_s$ and $\underset{\sim}{\mathbf{D}}_{sr}$ are respectively the localisation (or concentration) tensor and influence tensors. An equivalent dual expression, not written here, does exist in terms of stress localisation. This theory generalises Kröner's approach [21] to cases where the phases obey non-isotropic elasticity and the overall stiffness

$$\underset{\sim}{\mathbf{L}} = \sum_s c_c \underset{\sim}{\mathbf{A}}_s : \underset{\sim}{\mathbf{L}}_s \tag{16}$$

is non-isotropic (c_s is the volume fraction of sub-volume s).

TFA method is interesting by its simplicity. With 2 phases, and 2 sub-volumes only, tensors $\underset{\sim}{\mathbf{A}}_s$ and $\underset{\sim}{\mathbf{D}}_{sr}$ are obtained in closed form from Eshelby's tensor (see [22]). When using sub-discretisation in sub-volumes, these tensors can be determined by a set of preliminary elastic analyses made by FE [23], [24] or by FFT, but they are constant tensors during the whole inelastic analysis.

3.2 Secant and Tangent Methods

They are used in order to soften the accommodation behaviour between phases when important plasticity takes place in some of them. In the **secant method**, not detailed here, the stiffness of the linear comparison material is directly defined from the current average total strain in each phase. It is isotropic in nature [25]. One version of this approach is the Berveiller-Zaoui model [26].

Incremental tangent method was proposed by Hill [27], using a rate form for the instantaneous stress-strain relation and the corresponding localisation rule:

$$\dot{\underset{\sim}{\sigma}}_s = \underset{\approx}{\mathcal{L}}_s(\underset{\sim}{\varepsilon}_s) : \dot{\underset{\sim}{\varepsilon}}_s \qquad\qquad \dot{\underset{\sim}{\varepsilon}}_s = \underset{\approx}{\mathcal{A}}_s(\underset{\sim}{\varepsilon}_s) : \dot{\underset{\sim}{\mathbf{E}}} \tag{17}$$

where $\underset{\approx}{\mathcal{L}}_s$ and $\underset{\approx}{\mathcal{A}}_s$ are respectively the tangent stiffness tensor (associated with the average strain in phase s) and the tangent localisation tensor:

$$\underset{\approx}{\mathcal{L}}_s = \underset{\approx}{\mathbf{L}}_s - \frac{1}{h_s}\underset{\approx}{\mathbf{L}}_s : \left(\underset{\sim}{\mathbf{n}}_s \otimes \underset{\sim}{\mathbf{n}}_s\right) : \underset{\approx}{\mathbf{L}}_s \qquad \underset{\approx}{\mathcal{A}}_s = \underset{\approx}{\mathbf{I}} + \underset{\approx}{\mathcal{P}}^0 : \left(\underset{\approx}{\mathcal{L}}_s(\underset{\sim}{\varepsilon}_s) - \underset{\approx}{\mathcal{L}}^0\right) \tag{18}$$

in which h_s and $\underset{\sim}{\mathbf{n}}_s$ are instantaneous tangent modulus and direction of plastic flow in phase s respectively, though $\underset{\approx}{\mathcal{P}}^0$ is Hill's polarisation tensor that will be discussed below. In the self-consistent version, the reference (tangent) medium is taken as the one for the overall macroscopic behaviour $\underset{\approx}{\mathcal{L}}$, with :

$$\dot{\underset{\sim}{\Sigma}} = \underset{\approx}{\mathcal{L}}_s : \dot{\underset{\sim}{\mathbf{E}}} \qquad\qquad \underset{\approx}{\mathcal{L}} = \sum_s c_s \underset{\approx}{\mathcal{A}}_s : \underset{\approx}{\mathcal{L}}_s \tag{19}$$

Affine method is a more recent version, proposed by Zaoui and Masson [28], as a generalisation of a tangent method proposed in [29]. Using the same tangent stiffness and replacing the rate form (17) by an eigenstrain, with :

$$\underset{\sim}{\sigma}_s = \underset{\approx}{\mathcal{L}}_s(\underset{\sim}{\varepsilon}_s) : \left(\underset{\sim}{\varepsilon}_s - \underset{\sim}{\eta}_s\right) \qquad \dot{\underset{\sim}{\varepsilon}}_s = \underset{\approx}{\mathcal{A}}_s(\underset{\sim}{\varepsilon}_s) : \dot{\underset{\sim}{\mathbf{E}}} + \sum_r \underset{\approx}{\mathcal{D}}_{sr}(\underset{\sim}{\varepsilon}_s) : \dot{\underset{\sim}{\eta}}_r \tag{20}$$

in which (18) still apply. Equation (20-b) ressembles TFA equation (15). Eigenstrain $\underset{\sim}{\eta}_r$ replaces $\underset{\sim}{\varepsilon}^p_r$ and is determined from the equality $\underset{\approx}{\mathcal{L}}_s : (\underset{\sim}{\varepsilon}_s - \underset{\sim}{\eta}_s) = \underset{\approx}{\mathbf{L}}_s : (\underset{\sim}{\varepsilon}_s - \underset{\sim}{\varepsilon}^p_s)$ obtained by combining (14-a) and (20-a). As for TFA, $\underset{\approx}{\mathcal{D}}_{sr}$ expresses in closed form from $\underset{\approx}{\mathcal{L}}_s$ and $\underset{\approx}{\mathcal{A}}_s$.

Isotropisation of the stiffness for the localisation rule. Either using $\underset{\approx}{\mathcal{L}}^0 = \underset{\approx}{\mathcal{L}}$ (self-consistent) or $\underset{\approx}{\mathcal{L}}^0 = \underset{\approx}{\mathcal{L}}_1$ (Mori-Tanaka [30]), with $\underset{\approx}{\mathcal{L}}_1$ being the tangent stiffness in the matrix (for composites), the anisotropy of $\underset{\approx}{\mathcal{L}}^0$ leads to an anisotropic Hill polarisation tensor $\underset{\approx}{\mathcal{P}}^0$, that can only be obtained by

the numerical integration over the inclusion of an expression involving Green's operator associated with $\underset{\approx}{\underset{\approx}{\mathcal{L}}}^0$.

Very often, in order to simplify, users of the tangent method implicitely consider the isotropized form of $\underset{\approx}{\underset{\approx}{\mathcal{L}}}^0$ together with the isotropic Eshelby expression:

$$\underset{\approx}{\underset{\approx}{\mathcal{P}}}^0 = \underset{\approx}{\underset{\approx}{\mathcal{S}}}^0 : \left(\underset{\approx}{\underset{\approx}{\mathcal{L}}}^0\right)^{-1} \tag{21}$$

As shown in [31], the isotropisation can be justified (to some extent) because it does not change the actual local flow response in the direction of plastic flow (in strain space). However it lowers the stiffness in transverse directions. Therefore, there are two ways of applying tangent methods :

- either using the correct anisotropic $\underset{\approx}{\underset{\approx}{\mathcal{P}}}^0$, obtained numerically at each time step;
- or using the approximate isotropic $\underset{\approx}{\underset{\approx}{\mathcal{P}}}^0$, obtained analytically by (21).

Next section demonstrates the great differences between these two ways. More details can be found in [32] and [31].

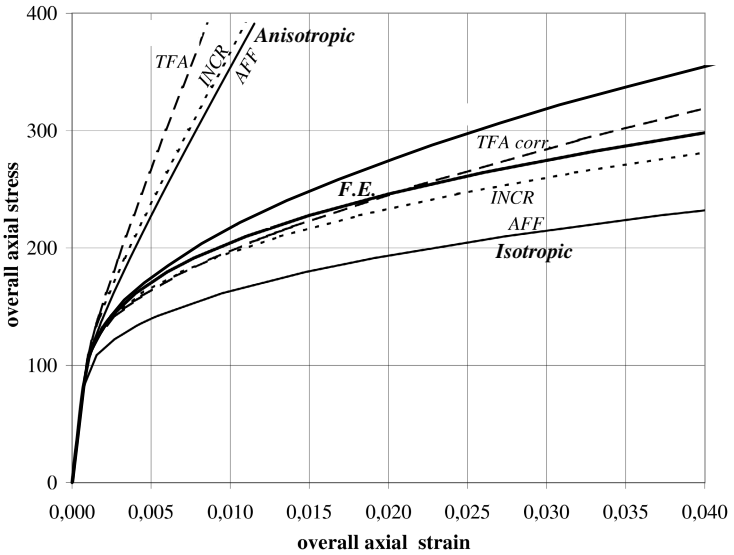

Fig. 5 Comparison of mean-field approaches for a non linear 2D composite

3.3 Methods Comparison

We use here a composite example due to Suquet [33], with elastic spherical inclusions (volume fraction 0.3, $E = 400$ GPa, $\nu = 0.2$) in a metallic matrix that obeys incremental elastoplasticity ($E = 75$ GPa, $\nu = 0.3$) with

isotropic hardening as a power law $\sigma_{eq} = 75 + 416\, p^{0.3895}$. Two reference curves, obtained by finite elements, are given on Figure 5 (thick solid lines). The lowest one is for a regular repartition of inclusions (square-hexagonal), the one used by Suquet. The higher one is for a random repartition (the highest obtained from several numerical simulations shown in section 2.3). As expected, TFA method with the elastic accommodation rule, delivers a much too stiff macroscopic stress-strain response. A result that is less known is that tangent methods (INCR and AFF) also deliver a much too stiff response. They give softer results than TFA, especially affine method, but still with an unacceptable overestimated tangent stiffness.

Contrarily, the approximate isotropized form of tangent methods give better results, but they are even too soft compared with reference simulations, especially for affine method. On the figure is also shown a *corrected TFA* method, with a better agreement, method that will be defined in section 4.2.

Similar results have been shown in [34] and [35]. In the last work il was also considered the use of the algorithmic tangent stiffness in place of the constitutive one. However, better results obtained with the isotropized form are difficult to justify theoretically and, as shown above, they can deliver too soft responses. Other methods, taking into account strain fluctuations in the phases have been proposed, like in [36], [37], [38], but their use is limited to materials with one potential for their constitutive equation, i.e. non-linear elasticity or deformation theory of plasticity. Incremental variational principles offer very interesting perspectives of improvements, for instance in the work by Lahellec and Suquet [39].

4 Intermediate Approaches

In this context, numerical methods are simplified in such a way to give them a quasi-analytical structure. A first example of such method consists in using *TFA with multiple sub-volumes* [23], [24]. It leads then to an analytical set of equations, that will be developed further in section 4.2.

A significantly different version of such an elastic accommodation based method is the *Generalised Method of Cells* developed by Aboudi and coworkers [40], [41], including its improvements like the *High Fidelity GMC* [42]. In this approach, the continuity of the tractions and displacements between adjacent sub-cells is defined in an average surface sense. To some extent, it ressembles to a mixed formulation of the FE method, with the advantage of delivering softer responses than TFA for identical discretisations.

A slightly different method, called *Finite Volume Direct Averaging Method*, was developed recently [43], using an additional parametric mapping between rectangular and quadrilateral sub-cells, that allows much better local fields in plasticity [44].

4.1 Non-uniform Tranformation Field Analysis

We develop with little more details this method initiated by Suquet and co-workers [45], [46].

The plastic strain is decomposed on a finite set of plastic modes that can present large deviations from uniformity:

$$\underset{\sim}{\varepsilon}^p(x) = \sum_k \varepsilon_k^p \, \underset{\sim}{\mu}^k(x) \tag{22}$$

The ε_k^p are now coefficients of the decomposition (that may depend on time) and the $\underset{\sim}{\mu}^k(x)$ are the non-uniform transformation fields, defined independently on each phase. These modes $\underset{\sim}{\mu}^k$ are non uniform (not even piecewise uniform) and are meant to capture the salient features of the plastic flow modes. They are determined once (most often by solving specific numerical problems on given unit cells) and are normalised with $\left\langle \underset{\sim}{\mu}_{eq}^k \right\rangle = 1$ in order for ε_k^p to be homogeneous to a plastic strain. The constitutive relations are expressed in terms of scalar projections on the modes (there is a direct analogy with crystal plasticity):

$$\tau_k = \left\langle \underset{\sim}{\sigma} : \underset{\sim}{\mu}^k \right\rangle \qquad e_k = \left\langle \underset{\sim}{\varepsilon} : \underset{\sim}{\mu}^k \right\rangle \qquad e_k^p = \left\langle \underset{\sim}{\varepsilon}^p : \underset{\sim}{\mu}^k \right\rangle \tag{23}$$

The NTFA localisation rule becomes then:

$$\underset{\sim}{\varepsilon}(x) = \underset{\approx}{\mathbf{A}}(x) : \overline{\underset{\sim}{\varepsilon}} + \sum_l \left\langle \underset{\approx}{\mathbf{D}} * \underset{\sim}{\mu}^k \right\rangle (x) \; \varepsilon_l^p \tag{24}$$

that can be rewritten, after multiplication by $\underset{\sim}{\mu}^k$ and averaging over V:

$$e_k = \underset{\approx}{\mathbf{a}}_k : \overline{\underset{\sim}{\varepsilon}} + \sum_l D_{kl} \varepsilon_l^p \tag{25}$$

where the second order tensor $\underset{\approx}{\mathbf{a}}_k$ and the influence factor D_{kl} are defined as:

$$\underset{\approx}{\mathbf{a}}_k = \left\langle \underset{\approx}{\mathbf{A}}^T : \underset{\sim}{\mu}^k \right\rangle \qquad D_{kl} = \left\langle \underset{\sim}{\mu}^k \left(\underset{\approx}{\mathbf{D}} * \underset{\sim}{\mu}^l \right) \right\rangle \tag{26}$$

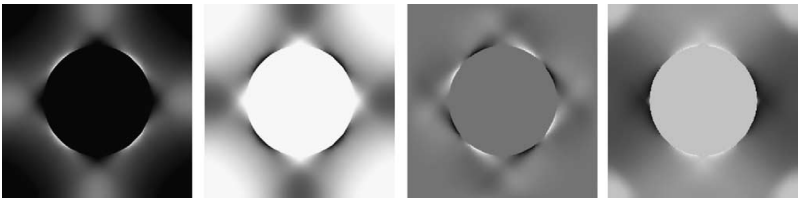

Fig. 6 Plastic mode, with its 4 components (with permission of P. Suquet)

Having assumed that all phases are elastically isotropic, characterized by a bulk modulus κ_k and a shear modulus G_k, the "resolved shear stress" is given by:

$$\tau_k = 2G_k\,(e_k - e_k^p) \tag{27}$$

A constitutive model is then written on a phenomenological basis to relate scalar variable ε_k^p to the resolved shear stress. It assumes a Generalised Standard Material format (GSM) [47] for the local constitutive laws in the phases. A coupling assumption is made for the different modes supported by the same phase :

$$\tau_{eq}^r = \left(\sum_{k=1}^{M(r)} |\tau_k|^2 \right)^{1/2} \tag{28}$$

The constitutive equation itself does mimic for parameter ε_k^p the ones of the corresponding phases (recall that modes k are attached independently to the various phases). For instance, using the viscoplastic potential $\psi^{(r)}$, it writes :

$$\dot{e}_k^p = \frac{\partial \psi^{(r)}}{\partial \tau_k}(\tau_{eq}^r) = \frac{\partial \psi^{(r)}}{\partial \tau_{eq}^r}\frac{3}{2}\frac{\tau_k}{\tau_{eq}^r} = \dot{p}_r \frac{3}{2}\frac{\tau_k}{\tau_{eq}^r} \tag{29}$$

Similar expressions can be used when introducing additional kinematic hardening variables for each phase (see [48]).

An example is given here, taken from Michel and Suquet [46], for a plane strain unit cell (square periodicity), with a cylindrical elastic fibre (matrix power law given in section 3.3). There are 3 modes introduced, corresponding to 3 independent monotonous inelastic analyses with the same constitutive behaviour (made by FFT or by FE), uniaxial tension in directions 1 and 2, as well as pure shear. Figure 6 shows the plastic mode $\underset{\sim}{\mu}^1$, with its 4 components μ_{11}^1, μ_{22}^1, μ_{12}^1, μ_{33}^1. Figure 7 indicates the results for uniaxial (1) and shear (2) loadings for the reference calculations (very fine mesh), for TFA (with 1 sub-volume by phase), for NTFA. Very clearly TFA delivers a much too stiff macroscopic response, though NTFA correlates very well with the reference solution.

The advantage of NTFA over classical TFA is evident, from the above example and others. However, there are still some limitations, like:

- the need for a number of initial numerical elasto-plastic solutions and the corresponding selection of the relevant modes for a given situation.
- the situations where cyclic conditions or non proportional loading conditions are taking place, or non-isothermal ones, which was not the case in the shown example;
- the GSM format that is needed, which limits the possible flexibility of the local constitutive behaviour (non-linear kinematic hardening, static recovery, aging,...).

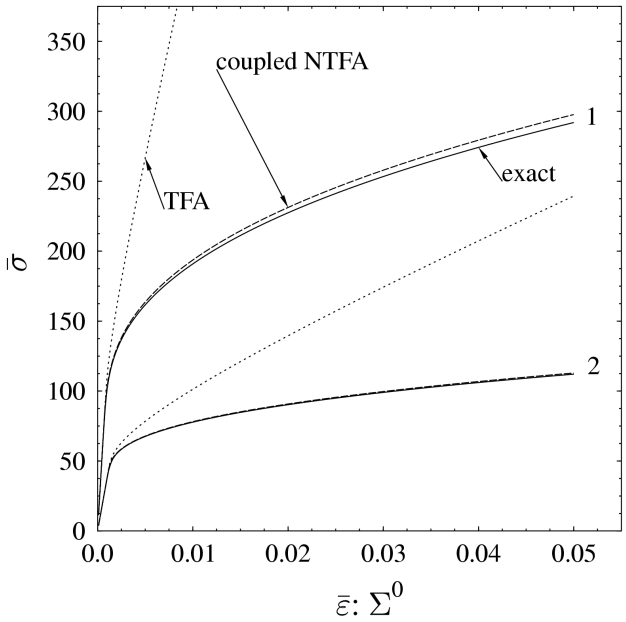

Fig. 7 Comparisons between TFA, NTFA and the reference computation for 5 loading conditions (with permission of P. Suquet)

Another advantage of the NTFA method is its ability to easily recover the local fields, in a natural way, after the solution of the overall structural boundary value problem. Such a capability is illustrated by examples given in Michel and Suquet [48].

4.2 A Macroscopic Constitutive Equation Defined by the Scale Transition Model

In this section, we summarise a macroscopic constitutive model entirely based on the constitutive equiations written at the level of each phase in the RVE. They use TFA as a scale change method, including two additional approximate methods, which are presented first.

A Corrected TFA Method

With the objective to reduce the stiffness of the macroscopic response when using an insufficient subdiscretisation, it consists in correcting the plastic strain when defining the eigenstrain in phase r, in equation (15), with:

$$\underset{\sim}{\varepsilon}_r^T = \underset{\approx}{\mathbf{K}}_r : \underset{\sim}{\varepsilon}_r^p + \underset{\sim}{\varepsilon}_r^{th} \tag{30}$$

The corrector $\underset{\sim}{\mathbf{K}}_r$ is determined by a preliminary analysis based on the use of an asymptotic tangent stiffness for large strains (as a phase constitutive parameter). It defines then an asymptotic tangent stiffness $\underset{\sim}{\underset{\sim}{\mathcal{L}}}_s^{\infty}$. By identifying for these asymptotic conditions the derivative of the TFA localisation equation (15) with the localisation rule (17-b) in the incremental tangent method, one obtain a linear system [49]:

$$\sum_r \underset{\sim}{\underset{\sim}{\mathbf{D}}}_{sr}\, \underset{\sim}{\underset{\sim}{\mathbf{K}}}_r \left(\underset{\sim}{\underset{\sim}{\mathcal{L}}}_r{}^{-1} - \underset{\sim}{\underset{\sim}{\mathbf{L}}}_r{}^{-1} \right) \underset{\sim}{\underset{\sim}{\mathcal{L}}}_r \underset{\sim}{\underset{\sim}{\mathcal{A}}}_r = \underset{\sim}{\underset{\sim}{\mathcal{A}}}_s - \underset{\sim}{\underset{\sim}{\mathbf{A}}}_s \tag{31}$$

Its solution gives the tensors $\underset{\sim}{\underset{\sim}{\mathbf{K}}}_r$. Let us note that $\underset{\sim}{\underset{\sim}{\mathcal{L}}}_s^{\infty}$ defined this way is isotropic by definition, because the direction of plastic flow in the phases is not known in advance. Figure 8, reproduced from [49], shows the clear improvement on the overall stress-strain response when using this corrected TFA method in place of standard TFA. It corresponds to the example of transverse traction, at different strain rates, for a long fibres SiC/Ti composite.

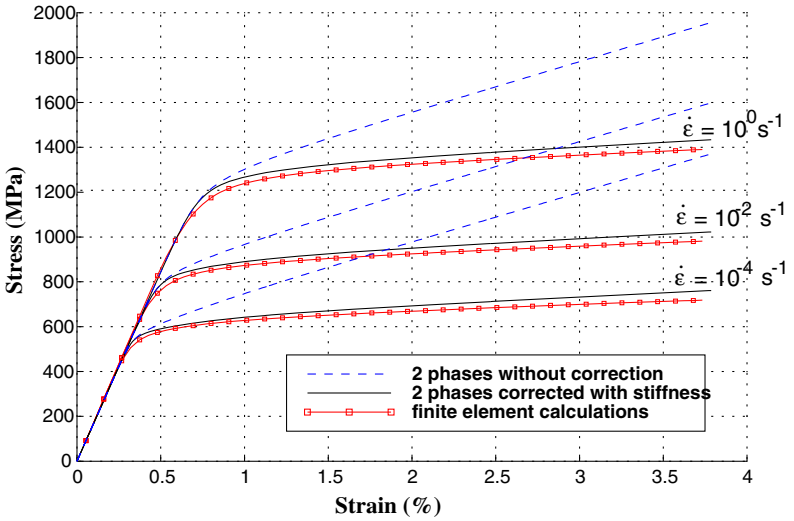

Fig. 8 Correction with the asymptotic tangent stiffness for various macroscopic strain rates (volume fraction 35%)

Generalised Eigenstrain Model

When elastic stiffness of the phases is varying, either by varying temperature or due to the effect of some damage, the direct application of TFA is based on localisation and influence tensors $\underset{\sim}{\underset{\sim}{\tilde{\mathbf{A}}}}_s$ and $\underset{\sim}{\underset{\sim}{\tilde{\mathbf{D}}}}_{sr}$, different from the initial ones:

$$\underset{\sim}{\sigma}_s = \underset{\sim}{\underset{\sim}{\tilde{\mathbf{L}}}}_s : \left(\underset{\sim}{\varepsilon}_s - \underset{\sim}{\varepsilon}_s^p - \underset{\sim}{\varepsilon}_s^{th} \right) \qquad \underset{\sim}{\varepsilon}_s = \underset{\sim}{\underset{\sim}{\tilde{\mathbf{A}}}}_s : \underset{\sim}{\mathbf{E}} + \sum_r \underset{\sim}{\underset{\sim}{\tilde{\mathbf{D}}}}_{sr} : \left(\underset{\sim}{\varepsilon}_r^p + \underset{\sim}{\varepsilon}_r^{th} \right) \tag{32}$$

In order to have an analytical model, even for cases with multiple sub-volumes, it was proposed in [49] to use the so-called generalised eigenstrain together with the constant initial elastic behaviour, with:

$$\underset{\sim}{\sigma}_s = \underset{\approx}{\mathbf{L}}_s : \left(\underset{\sim}{\varepsilon}_s - \underset{\sim}{\varepsilon}_s^{GE}\right) \qquad \underset{\sim}{\varepsilon}_s = \underset{\approx}{\mathbf{A}}_s : \underset{\sim}{\mathbf{E}} + \sum_r \underset{\approx}{\mathbf{D}}_{sr} : \underset{\sim}{\varepsilon}_r^{GE} \tag{33}$$

Identification of (32-a) and (33-a) immediately gives :

$$\underset{\sim}{\varepsilon}_s^{GE} = \left(\underset{\approx}{\mathbf{I}} - \underset{\approx}{\mathbf{L}}_s^{-1} : \underset{\approx}{\tilde{\mathbf{L}}}_s\right) : \underset{\sim}{\varepsilon}_s + \underset{\approx}{\mathbf{L}}_s^{-1} : \underset{\approx}{\tilde{\mathbf{L}}}_s : \left(\underset{\sim}{\varepsilon}_s^{p} + \underset{\sim}{\varepsilon}_s^{th}\right) \tag{34}$$

Figure 9 shows the prediction of elastic properties of the same composite as above, as a function of temperature. The present method, using the generalised eigenstrain, reproduces quite well the direct method, that should be considered as the correct reference. Other examples, given in [50] have shown similar good results, including damage effects.

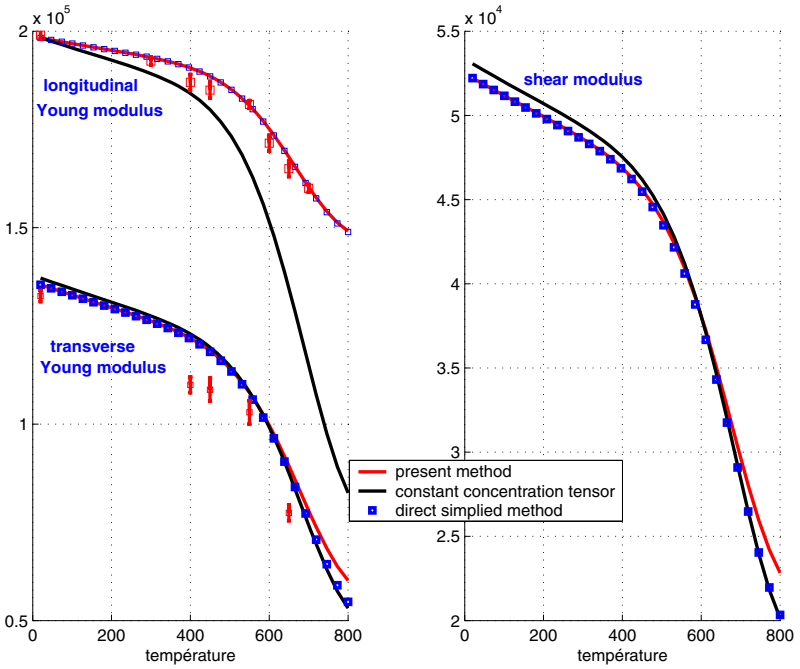

Fig. 9 Prediction of elastic properties evolution with temperature for the SiC/Ti composite

A Macroscopic Model in the Unified Viscoplastic Framework

It is shown here that corrected TFA scale change allows to transfer locally defined constitutive equations (in phases) to macroscopic ones that can be written in closed form. We limit the presentation to the case without damage induced and temperature changes on elasticity properties of constituents. We write equations in the context of corrected TFA with as many phases (or sub-phases) as needed. Damage effects and temperature effects were also considered in [50].

The local elastic constitutive equation in phase r (or sub-domain) is :

$$\underset{\sim}{\sigma}_r = \underset{\approx}{\mathbf{L}}_r : \left(\underset{\sim}{\varepsilon}_r - \underset{\sim}{\varepsilon}_r^{th} - \underset{\sim}{\varepsilon}_r^{p}\right) \qquad \underset{\sim}{\varepsilon}_r^{th} = \underset{\sim}{\alpha}_r \theta \tag{35}$$

The yield surface is defined by von Mises criterion and viscoplasticity by normality rule and a power law (as an example) :

$$f_r = \left|\left|\underset{\sim}{\sigma}_r - \underset{\sim}{\chi}_r\right|\right| - \sigma_y \qquad ||\underset{\sim}{\mathbf{a}}|| = \left(\frac{3}{2}\underset{\sim}{\mathbf{a}} : \underset{\approx}{\mathbf{I}}^d : \underset{\sim}{\mathbf{a}}\right)^{1/2} \tag{36}$$

$$\dot{\underset{\sim}{\varepsilon}}_r^p = \left\langle \frac{f_r}{K} \right\rangle^n \frac{\partial f_r}{\partial \underset{\sim}{\sigma}_r} \tag{37}$$

Moreover, we consider a multi-kinematic non linear hardening rule [51]:

$$\underset{\sim}{\chi}_r = \sum_q \underset{\sim}{\chi}_r^q \qquad \dot{\underset{\sim}{\chi}}_r^q = \underset{\approx}{\mathbf{C}}^q : \dot{\underset{\sim}{\varepsilon}}_r^p - \underset{\approx}{\mathbf{\Gamma}}^q : \underset{\sim}{\chi}_r^q \, ||\dot{\underset{\sim}{\varepsilon}}_r^p|| \tag{38}$$

Isotropic hardening can also be introduced without difficulty (not considered here). σ_y, n, K are material coefficients of the local phase r, eventually depending on temperature. $\underset{\approx}{\mathbf{C}}^q$ and $\underset{\approx}{\mathbf{\Gamma}}^q$, $q = 1, 2, ...$, are hardening and dynamic recovery tensors (reduced to isotropic forms in the applications).

With such a local constitutive behaviour at every point in the matrix, and using TFA methodology, it is possible to build up a purely macroscopic model, as shown in the works of El Mayas [52], Suquet [33], Pottier [53]. Corrected TFA approach is used with its dual form, as a stress localisation :

$$\underset{\sim}{\sigma}_s = \underset{\approx}{\mathbf{B}}_s : \underset{\approx}{\mathbf{\Sigma}} - \sum_r \underset{\approx}{\mathbf{F}}_{sr} : \underset{\approx}{\mathbf{L}}_r : \left(\underset{\approx}{\mathbf{K}}_r : \underset{\sim}{\varepsilon}_r^p + \underset{\sim}{\varepsilon}_r^{th}\right) \tag{39}$$

in which $\underset{\approx}{\mathbf{B}}_s$ and $\underset{\approx}{\mathbf{F}}_{sr}$ are the stress concentration tensors and the influence tensors. Both of them are analytically related with $\underset{\approx}{\mathbf{A}}_s$ and $\underset{\approx}{\mathbf{D}}_{sr}$ [20].

The present generalisation is demonstrated in details in [16]. The key here is to consider the following overall plastic strain decomposition :

$$\underset{\sim}{\mathbf{E}}^p = \sum_r \underset{\sim}{\mathbf{E}}_r^p \qquad \underset{\sim}{\mathbf{E}}_r^p = c_r \underset{\approx}{\mathbf{B}}_r^T : \underset{\sim}{\varepsilon}_r^p \tag{40}$$

The resulting model writes as a multi-mechanism model:

$$f_r = \left|\left|\underset{\sim}{\Sigma} - \underset{\sim}{X}_r\right|\right|_{H_r} - \sigma_y \qquad \left|\left|\underset{\sim}{a}\right|\right|_H = \left(\underset{\sim}{a} : \underset{\sim}{\underset{\sim}{H}} : \underset{\sim}{a}\right)^{1/2} \tag{41}$$

$$\dot{\underset{\sim}{E}}{}_r^p = c_r \left\langle \frac{f_r}{K} \right\rangle^n \frac{\underset{\sim}{\underset{\sim}{H}}_r : \left(\underset{\sim}{\Sigma} - \underset{\sim}{X}_r\right)}{\left|\left|\underset{\sim}{\Sigma} - \underset{\sim}{X}_r\right|\right|_{H_r}} \qquad \dot{\underset{\sim}{E}}{}^p = \sum_r \dot{\underset{\sim}{E}}{}_r^p \tag{42}$$

$$\underset{\sim}{\underset{\sim}{H}}_r = \frac{3}{2}\underset{\sim}{\underset{\sim}{B}}_r^T : \underset{\sim}{\underset{\sim}{I}}^d : \underset{\sim}{\underset{\sim}{B}}_r \qquad \underset{\sim}{b}_r = \sum_k \underset{\sim}{\underset{\sim}{F}}_{rk} : \underset{\sim}{\underset{\sim}{L}}_k : \underset{\sim}{m}_k \tag{43}$$

$$\underset{\sim}{X}_r = \sum_k \underset{\sim}{X}_r^k + \underset{\sim}{X}_r^\theta + \underset{\sim}{\chi}_r^* \tag{44}$$

The first and second terms in (44) are respectively the "composite" hardening effect and the residual stresses due to thermal expansion mismatch:

$$\underset{\sim}{X}_r^k = \frac{1}{c_k}\underset{\sim}{\underset{\sim}{B}}_r^{-1} : \underset{\sim}{\underset{\sim}{F}}_{rk} : \underset{\sim}{\underset{\sim}{L}}_k : \underset{\sim}{\underset{\sim}{K}}_k : \underset{\sim}{\underset{\sim}{B}}_k^{-T} : \underset{\sim}{\underset{\sim}{E}}_k^p \qquad \underset{\sim}{X}_r^\theta = \underset{\sim}{\underset{\sim}{B}}_r^{-1} : \underset{\sim}{b}_r\theta \tag{45}$$

The last term is driven by the kinematic hardening of the matrix. It can be demonstrated that it obeys also a multikinematic hardening rule:

$$\underset{\sim}{\chi}_r^* = \sum_q \underset{\sim}{\chi}_r^{*q} \qquad \dot{\underset{\sim}{\chi}}_r^{*q} = \underset{\sim}{\underset{\sim}{C}}_r^{*q} : \dot{\underset{\sim}{E}}_r^p - \underset{\sim}{\underset{\sim}{\Gamma}}_r^{*q} : \underset{\sim}{\chi}_r^{*q} \left|\left|\dot{\underset{\sim}{E}}_r^p\right|\right|_{H_r^{-1}} \tag{46}$$

$$\text{with} \quad \underset{\sim}{\underset{\sim}{C}}_r^{*q} = \frac{1}{c_k}\underset{\sim}{\underset{\sim}{B}}_r^{-1} : \underset{\sim}{\underset{\sim}{C}}^q : \underset{\sim}{\underset{\sim}{B}}_r^{-T} \qquad \underset{\sim}{\underset{\sim}{\Gamma}}_r^{*q} = \frac{1}{c_k}\underset{\sim}{\underset{\sim}{B}}_r^{-1} : \underset{\sim}{\underset{\sim}{\Gamma}}^q : \underset{\sim}{\underset{\sim}{B}}_r^{-T} \tag{47}$$

The set of macroscopic variables in this analytical model appears to be defined by the average stress $\underset{\sim}{\Sigma}$ and strain $\underset{\sim}{E}$, the individual plastic strains $\underset{\sim}{E}_r^p$ and the individual back-stresses $\underset{\sim}{\chi}_r^{*q}$ (or their strain counterpart).

5 Concluding Remarks

The present review paper was mainly concerned with the multi-scale analysis of non-linear mechanical behaviour of materials and structural components. More or less arbitrarily we have separated multi-scale methodologies into three different categories. In each of them were presented various kinds of developments, including some of them made at Onera.

Such a short review is necessarily limited, and cannot pretend to be exhaustive. There are certainly many other similar or different excellent contributions, that were not described and even not mentioned.

From this rapid overview, it appears that many developments are still open questions, both at a theoretical level and in the context of practical applications. Among them, we may mention more specifically:

- the development of analytical methodologies that could take into account local strain fluctuations in the phases but with theories able to apply to general local constitutive equations;
- the further development and application of "integrated multi-scale" methods and the associated necessary numerical improvements, that should offer the capability to bypass any use of a macroscopic and restrictive constitutive framework.

References

1. Walker, K.P., Jordan, E.H., Freed, A.D.: Equivalence of Green's function and the fourier series representation of composites with periodic microstructures. In: Weng, G., Taya, M., Abe, H. (eds.) Micromechanics and Inhomogeneity, San Francisco, pp. 535–558. Springer (1990)
2. Fotiu, P.A., Nemat-Nasser, S.: Overall properties of elastic–viscoplastic periodic composites. Int. J. of Plasticity 12(2), 163–190 (1996)
3. Moulinec, H., Suquet, P.: A FFT-based numerical method for computing the mechanical properties of composites from images of their microstructure. In: Pyrz, R. (ed.) Microstructure Property Interactions in Composite Materials, pp. 235–246. Kluwer Academic Pub. (1995)
4. Michel, J.-C., Moulinec, H., Suquet, P.: A computational method based on augmented lagrangians and fast fourier transforms for composites with high contrast. Comput. Modeling Eng. Sci. 1(2), 79 (2000)
5. Moulinec, H., Suquet, P.: A numerical method for computing the overall response of non-linear composites with complex microstructure. Computer Methods in Applied Mechanics and Engineering 157, 69–94 (1998)
6. Moulinec, H., Suquet, P.: Intraphase fluctuations in nonlinear composites: a computational approach. Eur. J. Mech., A/Solids 22, 751–770 (2003)
7. Feyel, F.: Application du calcul parallèle aux modèles à grand nombre de variables internes. Thèse de doctorat, École Nationale Supérieure des Mines de Paris (1998)
8. Feyel, F., Chaboche, J.L.: FE^2 multiscale approach for modelling the elastoviscoplastic behaviour of long fibre SiC/Ti composite materials. Computer Methods in Applied Mechanics and Engineering 183, 309–330 (2000)
9. Terada, K., Kikuchi, N.: Nonlinear homogenization method for practical applications. In: Ghosh, S., Ostoja-Starzewski, M. (eds.) Computational Methods in Micromechanics. ASME, vol. AMD - 212 (1995)
10. Smit, R.J.M., Brekelmans, W.A.M., Meijer, H.E.H.: Prediction of the mechanical behavior of non-linear heterogeneous systems by multi-level finite element modelling. Computer Methods in Applied Mechanics and Engineering 155, 181–192 (1998)
11. Feyel, F.: Multiscale FE^2 elastoviscoplastic analysis of composite structures. Computational Materials Science 16, 344–354 (1999)
12. Feyel, F., Chaboche, J.L.: Multi-scale non linear FE^2 analysis of co mposite structures : damage and fiber size effects. Revue Européenne des Éléments Finis 10(2-3-4), 449–472 (2001)

13. Miehe, C., Schröder, J., Schotte, J.: Computational homogenization analysis in finite plasticity. Computer Methods in Applied Mechanics and Engineering 171, 317–418 (1999)
14. Terada, K., Kikuchi, N.: A class of general algorithms for multi-scale analysis of heterogeneous media. Computer Methods in Applied Mechanics and Engineering 190, 5427–5464 (2001)
15. Monteiro, E., Yvonnet, J., He, Q.C.: Computational homogenization for nonlinear conduction in heterogeneous materials using model reduction. Computational Materials Science 42, 704–712 (2008)
16. Carrère, N.: Sur l'analyse multiéchelle des matériaux composites à matrice métallique : application au calcul de structure. Doctorat de l'ecole Polytechnique, Ecole Polytechnique (2001)
17. Boso, D.P., Lefik, M., Schrefler, B.A.: A multilevel homogenised model for superconducting strands thermomechanics. Cryogenics 45(4), 259–271 (2005)
18. Kouznetsova, V., Brekelmans, W.A., Baaijens, F.T.: An approach to micro-macro modelling of heterogeneous materials. Comput. Mech. 27, 37–48 (2001)
19. Eshelby, J.D.: The determination of the elastic field of an ellipsoidal inclusion and related problems. Proc. Royal Soc. London, A 241, 376–396 (1957)
20. Dvorak, G.: Transformation Field Analysis of inelastic composite materials. Proc. Royal Soc. London, A 437, 311–327 (1992)
21. Kröner, E.: Zur plastischen verformung des vielkristalls. Acta. Metall. Mater. 9, 155–161 (1961)
22. Dvorak, G., Benveniste, Y.: On transformation strains and uniform fields in multiphase elastic media. Proc. Royal Soc. London, A 437, 291–310 (1992)
23. Dvorak, G., Bahei-El-Din, Y., Wafa, A.: Implementation of the Transformation Field Analysis for inelastic composite materials. Comput. Mech. 14, 201–228 (1994)
24. Carrère, N., Feyel, F., Kanouté, P.: A comparison between an embedded FE^2 approach and a tfa-like model. Int. J. for Multi. Comp. Eng. 2(4), 20–38 (2004)
25. Gilormini, P.: A critical evaluation of various nonlinear extensions of the self-consistent model. In: Pineau, A., Zaoui, A. (eds.) Micromechanics of Plasticity and Damage of Multiphase Materials, pp. 67–74. Kluwer Acad. Publ. (1996)
26. Berveiller, M., Zaoui, A.: An extension of the self–consistent scheme to plastically flowing polycrystal. J. Mech. Phys. Solids 6, 325–344 (1979)
27. Hill, R.: A self-consistent mechanics of composite materials. J. Mech. Phys. Solids 13, 213–222 (1965)
28. Zaoui, A., Masson, R.: Modelling stress-dependent transformation strains of heterogeneous materials. In: Transformation Problems in Composite and Active Materials IUTAM Symposium, pp. 3–15. Kluwer Academic Pub., Cairo (1998)
29. Molinari, A., Canova, G.R., Ahzi, S.: A self–consistent approach to the large deformation polycrystal viscoplasticity. Acta. Metall. Mater. 35, 2983–2994 (1987)
30. Mori, T., Tanaka, K.: Average stress in matrix and average elastic energy of materials with misfitting inclusions. Acta. Metallurgica et Materialia 21, 597–629 (1973)
31. Chaboche, J.L., Kanouté, P., Roos, A.: On the capabilities of mean-field approaches for the description of plasticity in metal matrix composites. Int. J. of Plasticity 21, 1409–1434 (2005)

32. Chaboche, J.L., Kanouté, P.: Sur les approximations "isotrope" et "anisotrope" de l'opérateur tangent pour les méthodes tangentes incrémentales et affine. C. R. Acad. Sci. Paris, 857–864 (2003)
33. Suquet, P.: Effective properties of nonlinear composites. In: Suquet, P. (ed.) Continuum Micromechanics. CISM Lecture Notes, vol. 377, pp. 197–264. Springer (1997)
34. González, C., Llorca, J.: A self-consistent approach to the elasto-plastic behaviour of two-phase materials including damage. J. Mech. Phys. Solids 48, 675–692 (2000)
35. Doghri, I., Ouaar, A.: Homogenization of two-phase elasto-plastic composite materials and structures. study of tangent operators, cyclic plasticity and numerical algorithms. Int. J. Solids Structures 40, 1681–1712 (2003)
36. Ponte Castañeda, P.: New variational principles in plasticity and their application to composite materials. J. Mech. Phys. Solids 40, 1757–1788 (1992)
37. Suquet, P.: Overall properties of nonlinear composites : a modified secant moduli theory and its link with Ponte Castañeda's nonlinear variational procedure. C.R. Acad. Sc. Paris 320, 563–571 (1995)
38. Ponte Castañeda, P.: Second-order homogenization estimates for nonlinear composites incorporating field fluctuations: I - theory. J. Mech. Phys. Solids 50, 737–757 (2002)
39. Lahellec, N., Suquet, P.: On the effective behavior of nonlinear elasto-viscoplastic composites: I. Incremental variational principles. J. Mech. Phys. Solids 55(9), 1932–1963 (2007)
40. Aboudi, J.: Mechanics of composite materials - A unified micromechanical approach. Elsevier, Amsterdam (1991)
41. Arnold, S.M., Pindera, M.J., Wilt, T.E.: Influence of fiber architecture on the inelastic response of metal matrix composites. Int. J. of Plasticity 12(4), 507–545 (1996)
42. Aboudi, J., Pindera, M.J., Arnold, S.M.: Higher-order theory for periodic multiphase materials with inelastic phases. Int. J. of Plasticity 19, 805–847 (2003)
43. Bansal, Y., Pindera, M.J.: Finite-volume direct averaging micromechanics of heterogeneous materials with elastic-plastic phases. Int. J. of Plasticity 22(5), 775–825 (2006)
44. Khatam, H., Pindera, M.J.: Parametric finite-volume micromechanics of periodic materials with elastoplastic phases. Accepted for IJP (2008)
45. Michel, J.C., Galvanetto, U., Suquet, P.: Constitutive relations involving internal variables based on a micromechanical analysis. In: Drouot, R., Maugin, G.A., Sidoroff, F. (eds.) Continuum Thermomechanics, pp. 301–312. Kluwer Academic Publishers, The Netherlands (2000)
46. Michel, J.C., Suquet, P.: Nonuniform transformation field analysis. Int. J. Solids Structures 40, 6937–6955 (2003)
47. Halphen, B., Nguyen, Q.S.: Sur les matériaux standards généralisés. J. de Mécanique 14(1), 39–63 (1975)
48. Michel, J.C., Suquet, P.: Computational analysis of nonlinear composite structures using the nonuniform transformation field analysis. Computer Methods in Applied Mechanics and Engineering 193, 5477–5502 (2004)
49. Chaboche, J.L., Kruch, S., Maire, J.F., Pottier, T.: Towards a micromechanics based inelastic and damage modeling of composites. Int. J. of Plasticity 17, 411–439 (2001)

50. Chaboche, J.L., Carrère, N.: Multiscale structural analyses incorporating damage mechanics at the meso- or micro-scales. In: Skrzypek, J.J., Ganczarski, W. (eds.) Anisotropic Behavior of Damaged Materials, pp. 35–74. Springer (2003)
51. Chaboche, J.L., Rousselier, G.: On the plastic and viscoplastic constitutive equations, parts I and II. Int. J. Pressure Vessel & Piping 105, 153–158, 159–164 (1983)
52. El Mayas, N.: Modélisation microscopique et macroscopique du comportement d'un composite à matrice métallique. Thèse de doctorat, ENPC (1994)
53. Pottier, T.: Modélisation multiéchelle du comportement et de l'endommagement de composites à matrice métallique. Doctorat d'Université, Ecole Nationale des Ponts et Chaussées (1998)

Micro-architectured Solids: From Blast Resistant Structures to Morphing Wings

Norman A. Fleck

Cambridge University Engineering Department
Trumpington Street, Cambridge CB2 1PZ, UK
NAF1@eng.cam.ac.uk

Abstract. Classes of lattice material are reviewed, and their fracture response is explored in the context of the core of a sandwich panel. Attention is focussed on the strength of a sandwich plate with centre-cracked core made from an elastic-brittle square lattice. Predictions are summarised for the unnotched strength of the sandwiched core and for the fracture toughness of the lattice under remote tension, remote compression or remote shear. It is assumed that the lattice fails when the local stress in the cell walls attains the tensile or compressive strength of the solid, or when local buckling occurs. The local failure mechanism that dictates the unnotched strength may be different from that dictating the fracture toughness. Fracture mechanism maps are generated in order to reveal the dominant local failure mechanism for any given cell wall material.

1 Introduction

Cellular solids with a periodic microstructure are increasingly used in applications where severe mechanical loads and operating conditions lead to material damage, see Figure 1. Examples include catalytic converters for automobiles, filters for liquid metal, absorbers for solar receivers, supports for space mirrors, and orthopaedic implants for bone repair. Recently, their potential has been explored as the cores of sandwich panels in ship hulls in order to withstand water blast and air blast. The advantage derives from the fact that sandwich construction enhances bending stiffness, while thin face sheets promotes earlier cavitation of the water and thereby to a reduced level of transmitted impulse. Lattice materials also have application for morphing application. For example, a sub-class of lattice materials can be stiff, stretching-type structures when subjected to external loads, yet undergo large changes in shape with only a small internal energy penalty when one

or more of its bars are extended; in order to possess this favourable property the lattice material needs to be statically and kinematically determinate in the pin-jointed state.

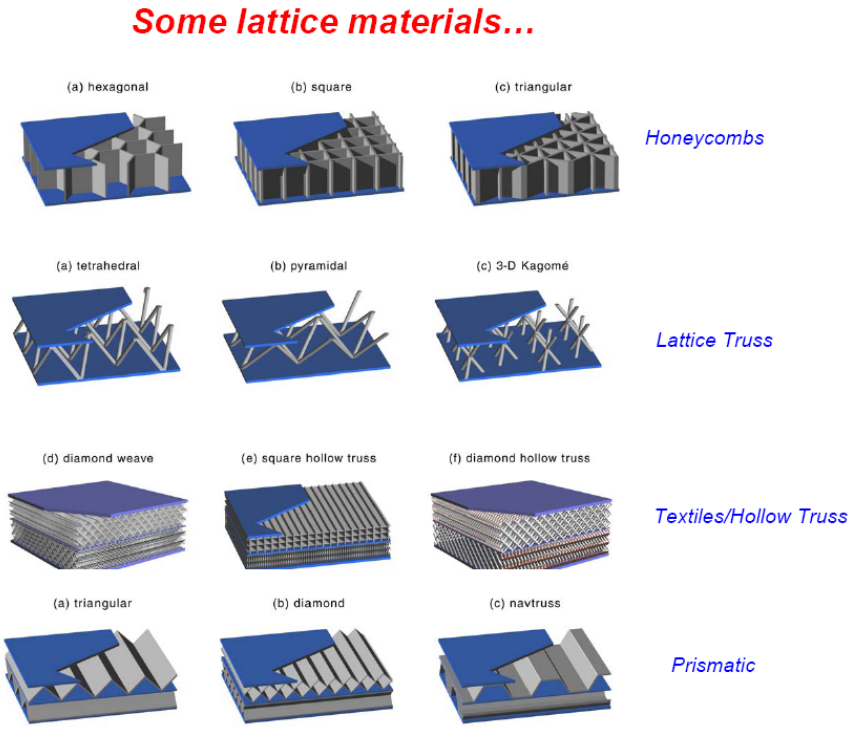

Fig. 1. Examples of periodic lattice materials

2 The Damage Tolerance of the Diamond-Celled Lattice

Cracks can exist in a lattice material and cause a significant decrease of its fracture strength. Frequently, the lattice is loaded in a sandwich panel configuration with stiff and strong face-sheets. The damage tolerance of these structures is of concern and motivates the present study. The damage tolerance can be quantified by two strength parameters for the lattice material: the unnotched strength and the fracture toughness. At short crack lengths, the unnotched strength governs the response, whereas at large crack lengths, a K-field exists near the crack tip and the fracture toughness dictates the response.

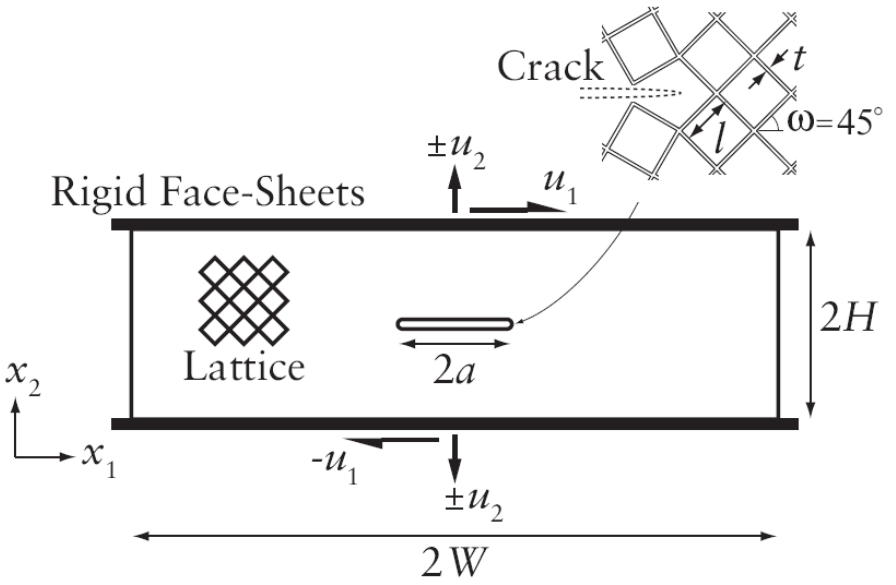

Fig. 2. Sandwich panel comprising a cracked diamond-celled lattice core

Consider, as a representative example, a centre-cracked sandwich panel with an elastic-brittle diamond-celled lattice core (Figure 2). The sandwich panel has rigid face-sheets and a diamond-celled lattice core of cell size l , cell thickness t , and core angle 45°, as sketched in Figure 2. The panel is of height $2H$ and width $2W$, and the core contains a central crack of length $2a$. Simple analytical models can be used to determine the strength of the cracked sandwich panel. Three types of loading are considered in turn: tension, compression and shear.

3 Unnotched Strength of the Core

In the absence of a crack, the strength of the sandwich geometry shown in Figure 2 is determined by classical beam theory. First, consider the case where the sandwich panel is loaded in tension by applying prescribed tensile displacements to the face-sheets. Failure occurs when the maximum tensile stress in the elastic lattice attains the tensile fracture strength of the solid material σ_{TS}. Dimensional analysis tells us that the normalised net-section strength σ_{net}/σ_{TS} is a function of the four geometric non-dimensional groups: $(t/l, a/l, H/l, H/W)$. We limit attention to practical geometries where $H/W \ll 1$.

For the case of remote tension, local failure within the cell walls is always tensile in nature. In contrast, for remote compression and shear, local failure

Table 1. Unnotched strength of the $\pm 45^\circ$ square core. The superscripts T, C, and B denote the relevant local failure criterion: tensile, compressive, and buckling, respectively.

Loading	*Failure Criterion*	*Unnotched Strength*
Tension	Tensile	$\sigma_u = \dfrac{t/l}{1+3t/l}\sigma_{TS}$
Compression	Compressive	$\sigma_u^C = \dfrac{t/l}{1+3t/l}\sigma_{CS}$
	Tensile	-
	Buckling	$\sigma_u^B = 0.82\,(t/l)^3\,E_S$
Shear	Compressive	$\tau_u^C = \dfrac{t/l}{1+3t/2l}\sigma_{CS}$
	Tensile	$\tau_u^T = \dfrac{t/l}{1+3t/2l}\sigma_{TS}$
	Buckling	$\tau_u^B = 1.88\,(t/l)^3\,E_S$

can be tensile, compressive, or can be due to elastic buckling. Consequently, the normalised net-section compressive strength and shear strength depend upon the geometric non-dimensional groups $t/l, a/l, H/l$; *and* upon the material groups σ_{CS}/σ_{TS}, σ_{CS}/E_s, where E_s is the Young's modulus and σ_{CS} is the compressive strength of the solid. The sensitivity of the unnotched fracture strength to the above non-dimensional groups is reported below.

Expressions for the unnotched strength of the panel under remote tension, compression, and shear are listed in Table 1. The formulae take into account both stretching and bending of the cell walls, and have been validated by FE calculations [2].

4 Fracture Toughness of the Lattice

Numerical predictions of the fracture toughness of the diamond-celled lattice can be obtained by using the finite element method to solve the boundary layer problem sketched in Figure 3. On the outer boundary, the applied displacements $\underset{\sim}{u}$ are derived from a K-field in an equivalent orthotropic continuum [6].

This configuration, referred to as boundary layer analysis, simulates the near-tip conditions associated to a K-field. The deformation field in the orthotropic lattice is characterised by narrow zones of intense bending emanating from the crack tip along the $\pm 45^\circ$ directions (Figure 2). The length of

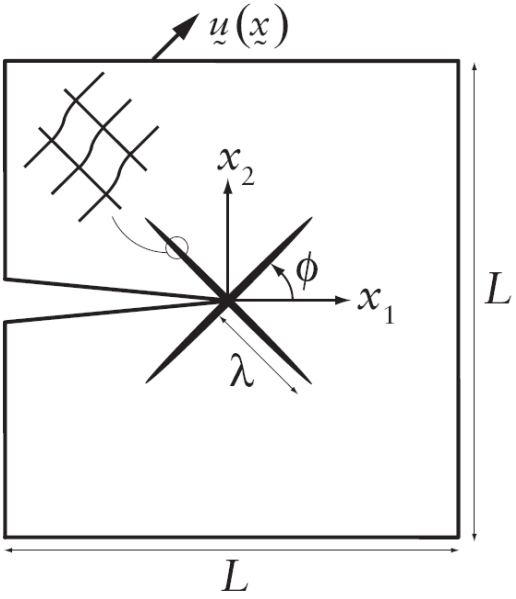

Fig. 3. The finite element mesh used in the fracture toughness predictions. The crack tip is at the centre of the mesh. Shear bands form at $\phi = \pm 45°$.

these bands is of order $\lambda \equiv l^2/t$, and must be small relative to the size of the model ($\lambda \ll L$) in order for the boundary layer analysis to be valid.

Linear elastic calculations are performed for varying stockiness t/l of the lattice. The fracture toughness for local tensile failure (K_{IC}^T for mode I and K_{IIC}^T for mode II) is calculated by equating the maximum tensile stress at any point in the lattice to the tensile strength σ_{TS} of the solid. Similarly, for local compressive failure the minimum compressive stress in the lattice is equated to the compressive strength σ_{CS} of the solid to obtain K_{IC}^C and K_{IIC}^C for modes I and II respectively. Power law fits to the predicted values are given in Table 2.

An eigenvalue extraction is used in the FE calculations in order to determine the bifurcation loads for buckling. The so-obtained buckling fracture toughness (Table 2) has been validated by full non-linear elastic simulations with small initial geometric imperfections [2]. In the post-buckling regime, a significant elevation of strain near the crack tip was observed, confirming the relevance of the buckling fracture toughnesses, K_{IC}^C and K_{IIC}^C, as useful parameters.

Analytical models of the fracture toughness can be found in the recent literature [7, 8, 9]. These models relate the crack tip elastic fields of an equivalent continuum to the stress state within the lattice. The estimates obtained have the correct functional form and are in close agreement with the numerical predictions of Table 2.

Table 2. Fracture toughness of the $\pm 45^\circ$ square lattice. The superscripts T, C, and B denote the relevant local failure criterion: tensile, compressive, and buckling, respectively.

Mode	*Failure Criterion*	*Fracture Toughness*
Mode I Crack opening	Tensile	$K_{IC} = 0.44\,(t/l)\,\sigma_{TS}\sqrt{l}$
Mode I Crack closing	Compressive	$K_{IC}^{C} = 0.44\,(t/l)\,\sigma_{CS}\sqrt{l}$
	Tensile	$K_{IC}^{T} = 0.74\,(t/l)\,\sigma_{TS}\sqrt{l}$
	Buckling	$K_{IC}^{B} = 2\,(t/l)^3\,E_S\sqrt{l}$
Mode II	Compressive	$K_{IIC}^{C} = 0.44\,(t/l)\,\sigma_{CS}\sqrt{l}$
	Tensile	$K_{IIC}^{T} = 0.44\,(t/l)\,\sigma_{TS}\sqrt{l}$
	Buckling	$K_{IIC}^{B} = 2.75\,(t/l)^3\,E_S\sqrt{l}$

5 The Competition between Local Failure Mechanisms for the Case of Macroscopic Shear Loading of a Sandwich Panel

The core of a sandwich panel is primarily designed to resist shear loads. In this section, we examine the failure mechanisms of a cracked sandwich panel subjected to shear. The mode II fracture toughness K_{IIC} of the diamond-celled lattice equals $\min(K_{IIC}^{C}, K_{IIC}^{T}, K_{IIC}^{B})$. It depends upon the lattice geometry and upon the cell wall properties. Likewise, the unnotched shear strength τ_u of the sandwich panel equals $\min(K_{IIC}^{C}, K_{IIC}^{T}, K_{IIC}^{B})$. We limit attention to solids which satisfy $\sigma_{CS}/\sigma_{TS} > 1$, so that compressive local failure of the unnotched lattice and of the cracked lattice never occur. This is not a severe restriction on material choice: almost all engineering solids have the characteristic that $\sigma_{CS}/\sigma_{TS} > 1$.

Note from Table 1 that the unnotched strength is buckling-governed when $\tau_u^B/\tau_u^T = 1.88t^2E_S/(l^2\sigma_{TS}) < 1$. Similarly, from Table 2, the fracture toughness is buckling-governed when $K_{IIC}^{B}/K_{IIC}^{T} \equiv 6.25t^2E_S/(l^2\sigma_{TS}) < 1$. Thus, the value of the single non-dimensional group

$$\Pi \equiv \frac{\sigma_{TS}}{E_S}\left(\frac{l}{t}\right)^2 \tag{1}$$

dictates whether the unnotched strength and the fracture toughness are due to buckling or tensile local failure. This competition of local failure criteria is summarised in Table 3.

Table 3. Competition of local failure criteria for shear loading of a cracked sandwich panel. Unnotched strength τ_u and mode II fracture toughness K_{IIC} are controlled by local cell-wall buckling or by local tensile failure. The weakest mode of local failure is dictated by the value of Π. The transition Ht/l^2 between Regimes I and II is also set by Π.

$\Pi \equiv \sigma_{TS} l^2/E_S t^2$	τ_u	K_{IIC}	$\left(Ht/l^2\right)_{trans}$
< 1.88	Tensile	Tensile	0.07
$\times$	Tensile	Buckling	Not viable
$1.88 - 6.25$	Buckling	Tensile	$0.02\ \Pi^2$
> 6.25	Buckling	Buckling	0.76

We emphasise that the expressions in Tables 1 and 2 for τ_u and K_{IIC} depend upon the active failure mechanisms, as dictated by the value of Π. Recall that the competition between cell wall buckling and local tensile failure is determined by the value of Π, as summarised in Table 3. Π scales with the material index σ_{TS}/E_S and with $(l/t)^2$.

5.1 Application to Engineering Solids

A material-property chart is now presented to show the active failure mechanisms for a wide range of engineering materials when manufactured into a lattice core and loaded in shear. The active mechanisms are presented for both the unnotched shear strength τ_u of the lattice core and for the mode II fracture toughness K_{IIC}.

Recall that the competition between cell wall buckling and local tensile failure is dictated by the value of Π, as summarised in Table 3. Π scales with the material index σ_{TS}/E_S and with $(l/t)^2$. Thus, the value of Π is dependent upon material choice, for any given t/l. This competition of local failure criteria is explored through a material-property chart in Figure 4. Plots of the tensile strength σ_{TS} versus the Young's modulus E_S have been generated for engineering materials using the CES [10] software (Figure 4). We limit materials to those which are elastic-brittle. Data for a given class of materials (e.g. technical ceramics) are enclosed in property-envelopes.

For the unnotched strength (dotted lines in Figure 4), the contour $\Pi = 1.88$ marks the transition from local buckling to local tensile failure. Likewise, for the fracture toughness (dash-dot in Figure 4), the contour of $\Pi = 6.25$

delimits this transition. These boundaries have been added to the charts for selected values of t/l.

For stocky lattices with $t/l = 0.1$, almost all materials possess a value of Π which is much less than 1.88 (they lie to the right of the transition boundaries). Consequently, the unnotched strength and the fracture toughness are governed by local tensile failure. In contrast, for more slender lattices, $t/l = 0.01$, the lines of constant $\Pi = 1.88$ and 6.25 cut through the body of the data: there is an active competition between buckling and local tensile failure of the cell walls, and the dominant failure mechanism is material-dependent. We conclude that for the same material, the local failure mechanism may be different in an unnotched lattice core than in a cracked one. For example, a glassy lattice core of $t/l = 0.01$ possesses a value of Π between 1.88 and 6.25 (see Figure 4). Hence, it would collapse by local buckling in an unnotched strength test, but it would fail by the attainment of the tensile strength of the cell wall material in a fracture toughness test.

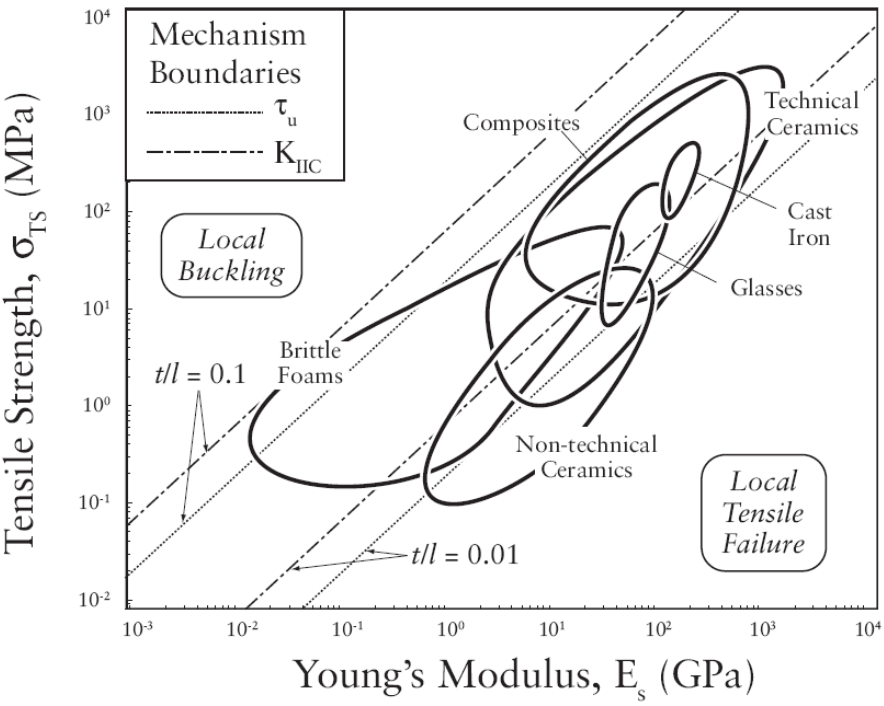

Fig. 4. Material-property chart for failure mechanisms dictating the unnotched shear strength of lattice core and the mode II fracture toughness of the $\pm 45^\circ$ square lattice

6 Concluding Remarks

Microstructural imperfections such as wavy struts and displaced joints are expected to have a knock-down effect upon the fracture properties of elastic-brittle lattices. The sensitivity of fracture toughness to imperfections in the form of displaced joints has been explored by Romijn and Fleck [9]. Their analysis indicates that the fracture toughness of the square topology is imperfection-sensitive. Their results can be used to modify the strength predictions of the cracked sandwich panel with imperfections present at the cell wall level.

Acknowledgements. The author is grateful to Dr. Quintana-Alonso for help in preparation of this manuscript.

References

1. Quintana-Alonso, I., Fleck, N.A.: The Damage Tolerance of a Sandwich Panel Containing a Cracked Honeycomb Core. Journal of Applied Mechanics (2007) (in press)
2. Quintana-Alonso, I., Fleck, N.A.: The Compressive Response of a Sandwich Panel with a Cracked Honeycomb Core. To appear in Journal of Mechanics and Physics of Solids (2008)
3. Wicks, N., Guest, S.D.: Single Member Actuation in Large Repetitive Truss Structures. International Journal of Solids and Structures 41(3-4), 965–978 (2004)
4. Timoshenko, S.P., Gere, J.M.: Theory of Elastic Stability, 2nd edn. McGraw-Hill, New York (1961)
5. Newmark, N.M.: A Simple Approximate Formula for Effective End-Fixity of Columns. Journal of the Aeronautical Sciences 16, 116 (1949)
6. Sih, G.C., Paris, P.C., Irwin, G.R.: On Cracks in Rectilinearly Anisot-ropic Bodies. International Journal of Fracture Mechanics 1(13), 189–203 (1965)
7. Gibson, L.J., Ashby, M.F.: Cellular Solids: Structure and Properties, 2nd edn. Pergamon Press, Oxford (1999)
8. Quintana Alonso, I., Fleck, N.A.: Damage Tolerance of an Elastic-Brittle Diamond-Celled Honeycomb. Scripta Materialia 56(8), 693–696 (2007)
9. Romijn, N.E.R., Fleck, N.A.: The Fracture Toughness of Planar Lattices: Imperfection Sensitivity. Journal of Mechanics and Physics of Solids 55(12), 2538–2564 (2007)
10. EduPack, C.E.S.: The Cambridge Engineering Selector, Granta Design, Rustat House, 62 Clifton Road, Cambridge CB1 7EG, UK (2007)
11. Huang, J.S., Lin, J.Y.: Fatigue of Cellular Materials. Acta Mater. 44(1), 289–296 (1996)
12. Olurin, O.B., McCullough, K.Y.G., Fleck, N.A., Ashby, M.F.: Fatigue Crack Propagation in Aluminium Alloy Foams. Int. J. Fatigue 23(5), 375–382 (2001)
13. Burman, M., Zenkert, D.: Fatigue of Foam Core Sandwich Beams. Int. J. Fatigue 19(7), 551–578 (1997)

Plasto-Mechanics of Large Deformation under Impact Loading

N.K. Gupta

Department of Applied Mechanics,
Indian Institute of Technology Delhi,
Hauz Khas, New Delhi – 110016 India

Abstract. Plasto-mechanics of large deformation is inherently complex. There is a lack of understanding of the phenomenon and its dependence on various parameters like strain rate, inertia, history of loading, annealing and thermal processes and geometry. Mechanics of large deformation in relation to absorption of kinetic energy of external impact loading has been studied over the years through several experimental, analytical and numerical researches. Many problems relating to deformation modes and their dependence on various parameters, however, are yet to be resolved. Structured experiments are of help to study the phenomenon and provide plausible explanations, assumptions and parameters needed for its realistic analysis. In this sectional lecture, I share some of the observations made in studies carried out to help in understanding the phenomenon and its dependence on different parameters.

1 Introduction

Mechanics of large inelastic deformation and failure of structures subjected to impact loading is inherently a complex phenomenon. What makes it more complex is its dependence on various parameters like strain rate, inertia, history of loading, annealing and thermal processes, and geometry. Motivated by the needs of defence, desire for better safety against unforeseen accidents or disasters, industrial applications, and academic interests, great improvements have been made in analytical, numerical, and experimental methods to study the phenomenon in its varied aspects and to propose simple realistic analysis based on the mechanics observed for the solution of such problems. Several studies have appeared in literature in recent years which present formulations that describe large deformations and attempt to bring together various facets affecting the deformation. However, many problems relating to the deformation modes and their dependence on various parameters remain unresolved. In what follows, an overview of observations in some large deformation studies, which are of interest, involving thin walled structures of varying geometry and size and subjected to drop hammer, projectile or

blast loading, are presented in a hope that plausible explanation for these having been found, would help in understanding of the large deformation phenomenon under impact loading.

1.1 Constitutive Relation and Fracture Criterion

In analysis with and without finite elements for the realistic description of the mechanical response of engineering structures subjected to impact loading, constitutive relationships accounting for large strains, high strain rates and temperature softening are essential. In many cases it is also important that damage and fracture may be included in the structural model. The strain rate phenomenon is one major factor to be incorporated in the simulation of the deformation process. The *Cowper-Symonds* material model [1] is one of the commonly used models used to describe strain rate effects; the essence of this model is in the calculation of the yield stress scaled by the strain rate dependent factor to determine the yield surface, Y;

$$Y = (\sigma_0 + B\varepsilon_{pl}^n)\left[1 + \left[\frac{\dot{\varepsilon}_{pl}}{D}\right]^{1/q}\right] \tag{1}$$

Where parameters σ_0 is the initial strain rate and ε_{pl}^n is the effective plastic strain and B is the strain hardening coefficient which incorporates the contributing parameter choosing the isotropic or kinematic analysis and E_{p}, the plastic hardening coefficient $(E_{\tan} - E)/(E - E_{\tan})$, the material constants D and q are specific to material type. For steel general values giving stable results are $D = 40.4, q = 5$. [1] It is important that the constitutive behavior matches experiments when deformation begins to be large. Some modifications have been proposed [2] in the past to take into account relative softening that accompanies large deformation and subsequent failure. Such material behavior is well described by Johnson Cook plasticity and failure models. Numerical solutions of plastic strain rate is associated with spurious oscillations which can be avoided by adopting damping by 1st order visco-plastic correction which is shown in the *Johnson-Cook* model [3]. This model is often used in problems involving intense impulsive loading due to high velocity impact and explosive detonation such as UNDEX loading. The temperature and annealing effects play an important role in altering the response pattern and subsequent failure behavior of metals. This important phenomenon may be incorporated in the numerical model by the factor homologous temperature T_{H} in the J-C equation giving radius of the Von-Mises stress envelope as:

$$Y = \left[A + B\varepsilon_p^n\right]\left[1 + C\ln\varepsilon_p^*\right]\left[1 - T_H^m\right] \tag{2}$$

Where, ε_{p} is the effective plastic strain, $\varepsilon_{\mathrm{p}}^*$ is normalized effective plastic strain rate, T_{H} is homologous temperature given by $(T - Troom)/(Tmelt - Troom)$

and A, B, C, n & m are material constants. The *Johnson Cook* failure model is in the form of a damage parameter (Ω) defined as:

$$\Omega = \sum \frac{\Delta \overline{\varepsilon}^{pl}}{\overline{\varepsilon}_f^{pl}} \quad \overline{\varepsilon}_f^{pl} \tag{3}$$

Where, $\overline{\varepsilon}^{pl}$ is an increment of the equivalent plastic strain, is the strain at failure, and the summation is performed over all increments in the analysis. The material failure is assumed to occur when the damage parameter exceeds "1". In this model the cumulative value of equivalent plastic strain at element integration points employed to compute progressive damage and failure of materials. This model is used in conjunction with the *Johnson-Cook* plasticity model, which is suitable for materials under high strain rate such as typically in high velocity impact and UNDEX loads.

2 Collapse of Thin Metallic Shells

The plasto-mechanics of structural elements like tubes of circular and non-circular cross-sections, spherical shells, and conical frusta, have received considerable attention during the last four decades. Their application in the design of devices for absorbing kinetic energy in situations of a crash or an accident is common. Various factors that determine the efficiency of performance of the energy absorbers, and their selection criteria have been discussed in detail in [4]. Several experiments on such structures [5–7] have shown that their modes of deformation are insensitive to the strain rates and methods of plasticity are useful in their analysis in most cases. Here we present some experimental observations, which are of interest.

2.1 Axial Crushing of Round Tubes

Axially crushed thin-walled tubes are perhaps the most investigated structural elements. Their progressive collapse is either axisymmetric due to local axial and radial buckling or diamond due to local circumferential buckling. They provide an efficient way of absorbing the kinetic energy of impact. Therefore, study of plasto-mechanics of their post-collapse deformation has received considerable attention. Most of the solutions available in literature pertain to the concertina mode of collapse and the analysis for diamond mode of collapse is almost non-existent. The analytical approaches of analysis of tubes and frusta for axisymmetric folding have so far been by either considering straight folds or curved folds of circular curvature or their combination. In many of these studies, the folding has been assumed to be either total outside or total inside. It has, however, been observed in experiments that the folds are partly inside and partly outside. Plausible factors contributing

to such folding include consideration of the influence of variation in tube thickness along the fold length, and stress–strain behaviour of the material in tension and compression [8]. The problem in these modelling techniques is in the estimation of the peak load at which the folding starts. The average load obtained analytically on the basis of the formation of independent folds cannot be compared with the experimental results because the folds do not form independently. In most of the analytical studies, only two modes of deformation viz. bending and circumferential deformations have been incorporated. Experiments on round tubes of materials like aluminium and mild steel of different sizes and aspect ratios have shown that their modes of deformation remains quite insensitive when tested under quasi-static or drop hammer loading. It is however seen [9] that the progressive collapse mode is concertina, diamond, or mixed depending on their state of work hardening, subsequent annealing process and the geometry of the tube. For tubes of d/t ratios between 10 and 40, it is found that as-received strain-hardened steel tubes deform in concertina mode and on annealing, they deform in diamond mode, see Fig.1.Their respective stress strain curves are shown in Fig 2.

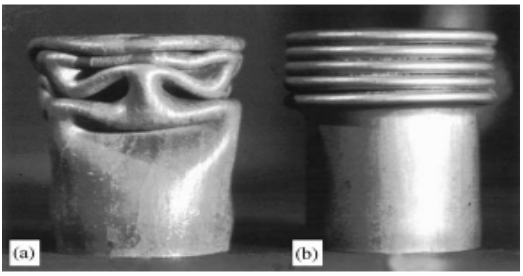

Fig. 1. Deformed shape of the 52.6mm diameter steel tube in (a) annealed; and (b) as-received state

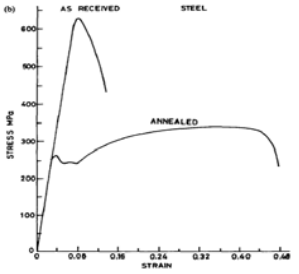

Fig. 2. Stress-strain curve for mild steel

2.1.1 Tube Imperfections – Aluminum Tubes

The influence of wall thickness eccentricity on the mode of deformation was investigated with 50.8mm dia tube. Eccentricity $e = 0.5$mm, was introduced around the circumference of the tube through off center machining. The load compression curves of as received tube and the one with thickness eccentricity at axial compression of 40mm are shown in Fig 3. As received tube was seen to deform in concertina mode and the wall thickness eccentricity of 0.5mm caused the transition to primarily a diamond mode of collapse. In numerical modeling of thickness eccentricity e= 0.5mm, one half of the tube is modeled with a constant tube thickness and other half is modeled with a gradual reduction in thickness as:

$$t = t_0 - e \sin \theta \tag{4}$$

where t is thickness of the tube wall at a given θ, t_0 is the max wall thickness and, e, the tube wall thickness eccentricity around the tube circumference, is $tmax--tmin$. There is no variation in thickness along the length of the tube. The discussed global geometric imperfection is parametrised as a function of the specified 'e' in the finite element model of the tube. The required variation in the thickness around circumference is incorporated into the discretised domain by unchecking the FE mesh from the solid model and updating the nodal coordinates as given by 't'. The thickness eccentricity modeled in the FE simulation gives results which match well with the experimental transition from concertina to diamond collapse mode. Good correlation is observed between the experimental collapse mode and the numerical model.

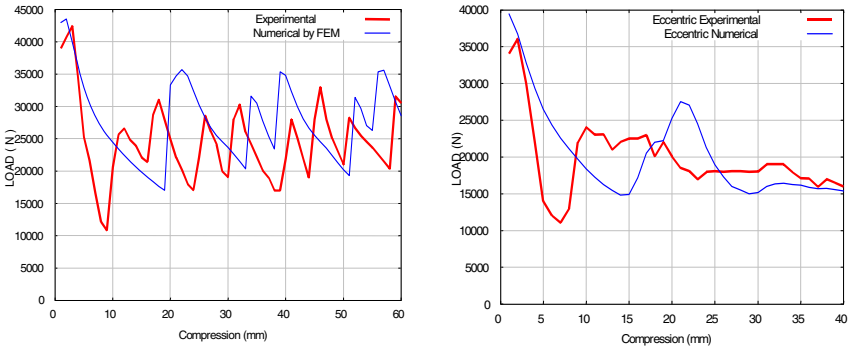

Fig. 3. Experimental and numerical load compression curves of (a) the tube in as received condition and (b) of tube with 0.5mm thickness eccentricity

2.1.2 Collapse Mode Sensitivity to e/t Ratio (Thickness Eccentricity to Wall Thickness) Ratio with Axisymmetric Tube End Conditions

The sensitivity of the collapse mode shape to increasing wall thickness eccentricity over 180 degree sector for the 50.8mm diameter aluminum tube with $L/D = 1.4$ was studied numerically. The eccentricities were varied as 0.03mm, 0.1mm, 0.2 mm, 0.3mm, 0.4mm and 0.5mm for a wall thickness of 1.74mm. One end of the tube was restrained against rotation and inplane radial and circumferential displacement and the other end was prescribed small incremental displacements. A bilinear isotropic material model was incorporated in the non-linear FE analysis. The deformed profiles and collapse modes of the tubes under axial compression with increasing wall thickness eccentricity are shown in Fig 4. Both peak load and and mean collapse load decrease linearly with increasing wall thickness eccentricity in the studied range as shown in Fig 5.

2.1.3 Collapse Mode Variations with Equal Spaced Wall Thickness Eccentricities around the Circumference

Different configurations investigated in addition to the single eccentricity are 2, 3 and 4 sine wave equally spaced wall thickness eccentricities around the tube circumference. The tube wall thickness at any point around the circumference is modeled with a reduction in maximum thickness , as a function of its polar coordinates given by :

$$t = t_0 - e \sin \theta(n/2) \tag{5}$$

where, n, is the number of sine waves around the tube circumference. The discussed global geometric imperfection is parameterised as a function of the specified, $e = 0.4$mm in the finite element model of the tube. Variation in thickness around the tube circumference is incorporated into the discretised domain by unchecking the FE mesh from the solid model and updating the nodal coordinates given by 't' in equation (5).

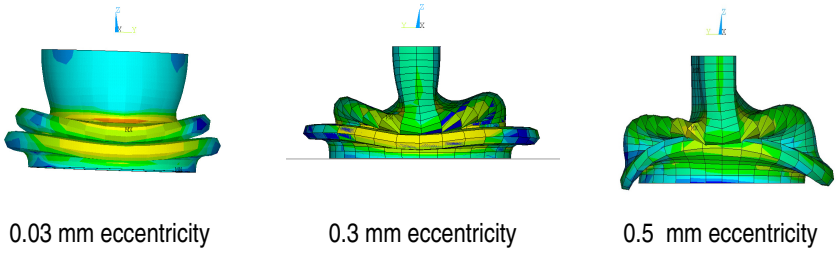

Fig. 4. Computed collapse modes and deformed profiles of tubes with 0.03mm, 0.3mm 0.5mm wall thickness eccentricity. The tube end conditions are axisymmetric.

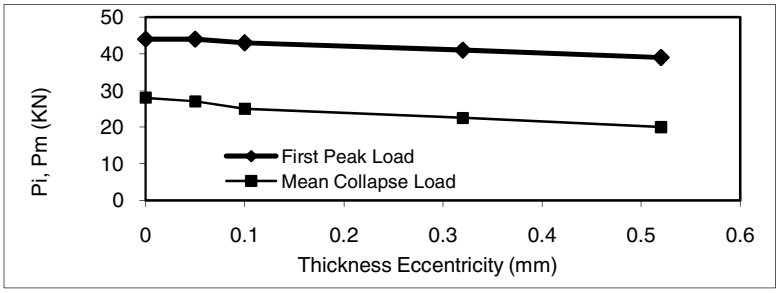

Fig. 5. Variation of First peak load (Pi) and Mean Load (Pm) with increasing wall thickness eccentricity for the aluminum tube

2.1.3.1 End Rotation and Inplane Displacement Fully Constrained (Axisymmetric Boundary Condition)

Aluminum tube of 50mm diameter with $L/D = 2$ and thickness = 2.0mm has been studied numerically. The configurations in 1 , 2 , 3 and 4 sine wave thickness eccentricities around the circumference have been studied. The boundary conditions in these computations were axi symmetric.

Computed deformed shapes of these tubes are shown in Fig 6. The results reveal that without eccentricities the tube collapses in concertina mode. With one and two sine wave eccentricities the tube collapses in a mixed mode of concertina and diamond mode while, with three and four sine wave eccentricities these collapse in a concertina mode.

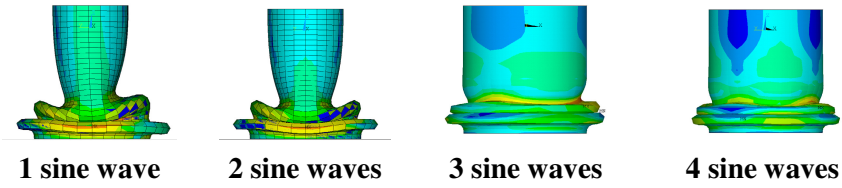

Fig. 6. Collapse modes and deformation profiles with 1, 2, 3 and 4 sine wave wall thickness eccentricity around circumference at 40mm axial compression

2.1.3.2 Inplane Radial Displacement Constrained over 180 Deg.

The collapse mode shows a strong sensitivity to the tube end conditions particularly the inplane displacement constraints. It is seen that these tubes collapse in a diamond mode. Tube end conditions with deviations from the axi symmetric inplane constraints have a strong influence on the collapse mode shapes. The computed deformed profiles of the tubes with in plane radial displacements constrained over 180 degrees are shown in Fig 7.

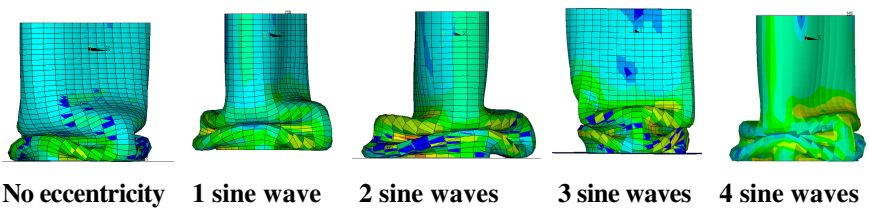

Fig. 7. Deformed profiles of tubes without and with 1, 2, 3 and 4 sine wave wall thickness eccentricities around circumference at 40mm axial compression

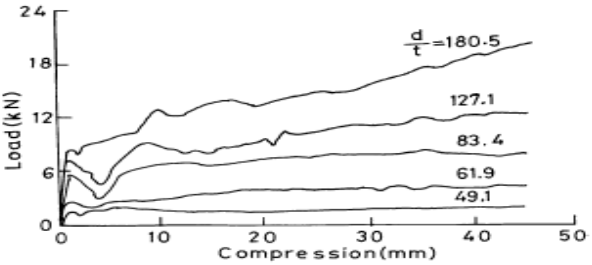

Fig. 8. Load–compression curves of frusta collapsing due to the movement of rolling plastic hinge

2.2 Axial Crushing of Frusta

One of the major advantages in using a frustum as compared to a cylindrical tube as energy absorbing device is that it minimizes the chances of collapse by buckling in Euler mode. Another significant feature of a frustum is its increasing collapse load with progression of crushing excepting for large semi-apical angles (>60 Deg) for which reverse bending takes place at some later stages of collapse and that causes fall in load. In experiments, frusta have been found to normally fail by diamond mode excepting those of very low and very high semi-apical angles. As the frusta of low semi-apical angles may fail in concertina mode that is perhaps why many of the studies available in literature seem to be for frusta of low semi-apical angles. The frusta of semi-apical angles up to about 30 Deg are found to begin yielding with an axisymmetric ring, and thereafter these collapse progressively by multilobe diamond fold mechanism [10]. In case of frusta of semi-apical angles about 45 Deg and above, plastic buckling is initiated at the smaller end by a rolling plastic hinge resulting in the formation of an inverted frusta. Some typical load–deformation curves of frusta collapsing due to the movement of rolling plastic hinge are shown in Fig. 8, wherein it is seen that the structural component shows the ability to sustain the load at the maximum level with the progress of compression. Fig. 9 (a) and (b) show deformed shapes of the frusta of semi-apical angles 30 Deg and 45 Deg, respectively. The former collapse in diamond mode, while the latter collapse by the movement of rolling plastic hinge. Similarity of the collapse mode of the large angle frusta with that of hemispherical shells under axial loading [11] can easily be seen; collapse in these is initiated by inward dimpling and it progresses with the formation of the rolling hinge.

In case of these frusta with low t/d values, in the later stages of compression, stationary plastic hinges are also formed. In all the cases of frusta of semi-apical angles 65 Deg, at a certain stage of compression, a reverse bending occurs from the larger end associated with a rolling plastic hinge.

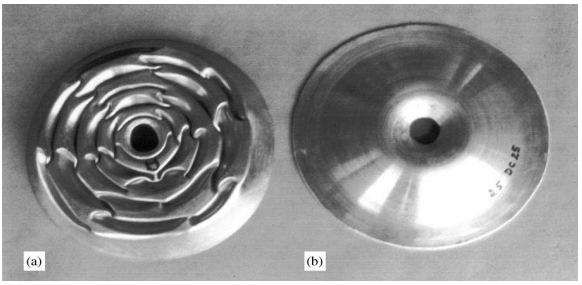

Fig. 9. Deformed shapes of frusta of semi-apical angle (a) 301, and (b) 451

3 Impact of Projectile on Plates

Comprehensive surveys of the mechanics of penetration and perforation of projectiles into the targets have been published by Backman and Goldsmith [12], Zukas [13], and Corbett et al. [14] covering the major experimental and analytical works done in the field. The first formulae to be developed predicted the penetration depths into semi-infinite targets when struck normally by a projectile. The advent of battleship armour in the 19th century led to the development of equations predicting the depth of penetration of finite thickness armour plating. Even to this day these formulae and others like them are being used extensively by impact engineers. In recent years appreciable advances have been made in the analytical approach to the problem of impact with the models gradually becoming more and more sophisticated and more accurate. However, these too have relied heavily, and indeed still do, on experimental data to justify certain assumptions made and to supply various parameters for the models. A commonly used measure of a target's ability to withstand projectile impact is its "Ballistic Limit Velocity (BLV)" simply known as "Ballistic Limit" and much work has been carried out by researchers to enable estimates of this parameter. Another useful term is "Ballistic Limit Thickness (BLT)" [15], which is the minimum thickness of plate required for a projectile of known weight and velocity to prevent any perforation. Fig. 10(a) shows a typical residual velocity variation for the impact of projectiles on plates of different materials and thicknesses for 820 m/s incident velocity. The relationship between the velocity drop and the angle of obliquity is shown in Fig 10(b) for MS plates of various thicknesses. Armour steels although the oldest of armour material are still considered satisfactory material in dealing with ballistic protection.

A basic requirement of armour steel is that it should have high hardness; but it seems that there is no simple correlation between hardness and resistance to perforation, as measured by a structure's ballistic limit. It has been noted that an efficient combination is a hard front face to break up the projectile and a ductile rear face to absorb the projectile's kinetic energy.

Thick targets offer better ballistic protection, however increasing thickness of the monolithic homogenous armour beyond a limit begins to present constraints of weight, manufacture, and cost. This has led to the consideration of possible targets made of layered plates of metals, nonmetals and their combinations for improving the efficiency of the armour as well as achieving the required thickness conveniently. Need for lightweight protective armours and shields have necessitated optimal use of thinner targets. Studying the mechanism of energy absorption and failure of different configurations of thin targets thus becomes relevant. Experiments have been conducted to study the effects of target thickness, target strength (material), layers (number, spacing and order) and obliquity as the target parameters, and impact velocity, mass and geometry (nose shape and L/D ratio) as the projectile parameters.

Single and layered configurations of thin aluminium targets of thicknesses 0.5, 0.71, 1.0, 1.5, 2.0, 2.5 and 3 were impacted by projectiles of 10mm, 15mm, 19mm, 22mm at impact angles of 0^0, 15^0, 30^0, 45^0 and 60^0 [18–20]. Penetration resistance was found to be highest for single aluminium plates, followed by layered (contact) and layered (spaced) plates upto a thickness of 2mm. The dishing of single plates is more compared to layered (incontact) aluminium plates which in turn is more than the dishing of layered (spaced) plates. The residual velocity decreases with increase in the angle of impact at a given impact velocity. The velocity drop and absorbed energy increases with increase in the angle of obliquity at a given impact velocity. The bending of the plate decreases with increase in the angle of impact. Ballistic limit (BL) of plates upto 30^0 obliquity remains almost the same as in case of normal impact and increase beyond 45^0 obliquity. Interestingly, BL of the plate at 15^0 obliquity is even lesser than BL of plate in normal impact. Ricochet was observed for 1.5 and 2mm thick plates at 60^0 at impact velocity of about 80m/s. Ogive nosed projectiles were found to be the most efficient penetrator

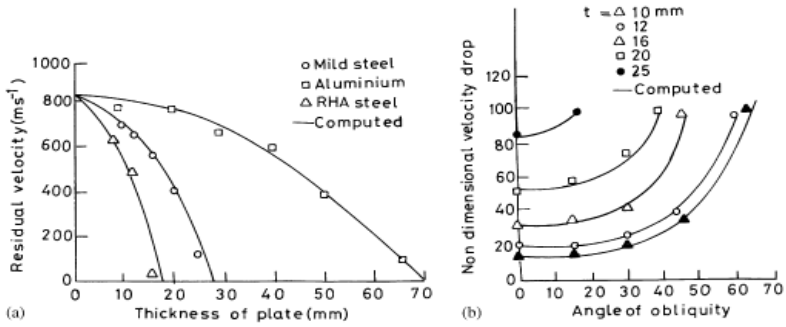

Fig. 10. (a) Residual velocity variation for the impact of projectiles on plates of different materials, and (b) velocity drop with the angle of obliquity for MS plates. Incident velocity is 820 m/s.

for the case of plates of thicknesses 0.5, 0.71, 1.0 and 1.5mm. For the case of plates of thicknesses 2.0, 2.5 and 3.0mm however, blunt nosed projectiles required least energy to perforate the target plates. The ballistic limit velocity of hemispherical nosed projectiles was found to be highest as compared to the other two projectiles.

In thick plate regime, single and layered mild steel, aluminium and RHA (rolled homogeneous armour) targets of thicknesses 8 to 40mm were impacted at about 820m/s at various impact angles in Armour Piercing projectiles [16]. The impact angles were varied until ricochet occurred. In normal impact, all the tested plates were perforated. The diameter of the crater was larger at the entry point than at the exit point, and the plates showed the formation of petals on their front side and a bulge on the rear side, Fig 13. For two layered targets of MS, when the total thickness is greater than t^* (The ballistic limit thickness) and the thickness of each layer is less than t^*; the projectile gets embedded when the front layer is thinner than the rear layer.

However, when the front layer is thicker, one encounters an interesting phenomenon; the projectile penetrates up to a certain depth and then rebounds back, presumably due to a stress wave effect. For relatively thick plates (plates with thickness> one fourth of ballistic limit thickness $t*$) in two layers, the residual velocities are comparable to the single plates of equal thickness. For thinner plates, the layered combination in contact absorbs lesser energy. When a projectile perforates a target at an oblique angle of incidence, it is observed in experiments that it does not come out of the rear side in the same straight path, but tends to turn towards or away from the normal to the plate. This deviation depends on the angle at which it strikes the plate, its material, and the thickness of the plate. When the projectile is fired at an angle greater than the angle for the ballistic limit, a stage comes when the projectile penetrates the plate and comes out of it from the impacted side itself.

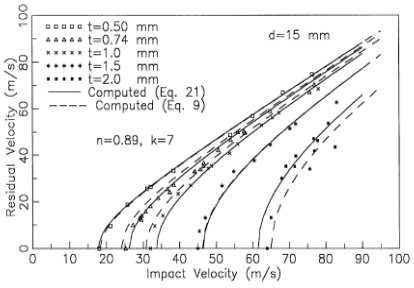

Fig. 11. Experimental results of residual velocities versus impact velocities for aluminium plates of different thicknesses [17]

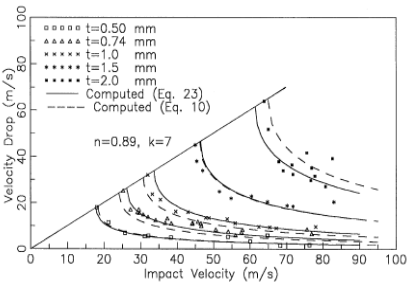

Fig. 12. Comparison of experimental velocity drop for aluminium plates of different thicknesses

Fig. 13. (a) Front and (b) rear crater damages in Mild Steel plate [16]

Spaced targets gave even higher residual velocities. In oblique impact, the angle of exit is smaller or greater than the angle of incidence depending on the plate thickness and material hardness. The difference between angles of obliquity for the ballistic limit and critical ricochet increase with the increase in plate thickness.

The experimental results were used to validate the numerical simulations for impact of projectiles on flat plates. The FE model essentially incorporated controls like surface to surface contact definitions and adaptive meshing at the impact region. The JC model for defining material plasticity and fracture was incorporated.

4 Explosive Loading on Plates

Explosive loading may be broadly classified with regard to the medium of surrounding environment as in-air explosions and underwater. An explosion is associated rapid breakdown of an exited unstable molecule into stable solids and gases and is associated with release of high amount of heat and energy. The underwater explosion event involves nonlinearities in fluid medium in the form of cavitation at the fluid solid surface interface, and causing geometric as well as material nonlinearities in solids. The need to incorporate these nonlinearities in a numerical model becomes necessary to predict the response of structures to UNDEX loads. Apart from the factors just discussed above one has to take to account another important phenomenon which is the combined effect of fluid and structure as a continuum, also known as the fluid-structure interaction (FSI), FSI model proposed by Geers, [18, 19] known as Doubly-Asymptotic Approximation (DAA) is often be efficiently incorporated in the FEM. The criteria for damage, such as maximum strain criteria, rupture strain, equivalent plastic work and damage models, have earlier been used towards simulation of tear phenomenon in plates under shock loads. The various modes of failure observed in plates due to explosive loading are as given below.

Mode I: large plastic deformation: It was observed by Gupta *et al.*, Jones *et al.*, Nurick *et al.*, [20, 21] that this is the first of failure modes where in the material has reached plastic deformation stage of deformation.

Mode II: tensile tearing: The mode I failure would be predominant till the material reaches the fracture strain. With the increase in intensity of shock measured as shock factor (SF) the mode II failure starts which has the characteristic of tensile tearing at the supports. The mode II failure has further been subdivided into phases namely mode II* - partial tearing, mode IIa - partial tearing with increased midpoint deformation and mode IIb - partial tearing with decreased midpoint deformation. [22, 23]

Mode III: shear tearing failure: A localized early stage response of the plate is seen as mode III failure or the shear failure at supports this failure has much interaction with mode II failure, Gupta et al, Jones N *et al.*, Yu TX, Chen FL [24] treated this failure mode as a plastic shear sliding failure which is done by calculating a shear sliding parameter which is a function of fracture strain off the plate material, plate thickness and width of the shear band and the shear failure is said to occur when the shear sliding value reached a critical value at the strain equals the fracture strain of the material.

Validated numerical experiments were carried out on plates and the following inferences were drawn on the behavior of plates subjected to air and underwater explosions, the numerical analysis incorporated the strain rate hardening of the material by the use of Cowper-Symonds material model and the material failure was modeled using a progressive damage phenomenon using the Johnson cook plasticity and failure.

4.1 In-Air Explosions

For comparison of the established numerical model results in Mode I failure, experiments reported by Nurick et al. [22] for 1.6mm thick circular plate of 120mm diameter with clamped edges subjected to close proximity blast loads have been used. The analysis was carried out for increasing impulses from 4 to 28Ns. The results of midpoint deflection versus impulse have been shown in Fig. 1.0. It is observed that the midpoint deflection increases with impulse in Mode I failure. The plate responds to large deformations almost linearly with time, reaches a maximum and then undergoes a small magnitude of elastic vibrations. The influence of strain rate through its effect on yield stress is highly significant. The results indicate that for a specific impulse, the midpoint deflection is larger for plates with smaller radii. As seen from the comparative plots between the experimental results and the numerical ones in Fig. 14 and Fig. 15, a good correlation has been obtained which validates the set up numerical scheme for Mode I failure. Modes II*, II and III failure modes have been incorporated in the numerical scheme using suitable criteria as discussed earlier.

Experiments reported by Teeling-Smith and Nurick [1] for 1.6-mm-thick circular plates of 100mm diameter with clamped edges subjected to close proximity blast loads have been used to validate the numerical scheme. The analysis was carried out for a sequence of impulses from 5 to 50Ns. For the purpose of numerical convergence and accuracy, several numerical simulations were carried out using varying mesh density and load step size. The results of midpoint deflection versus impulse for the 100mm diameter and 1.6mm thickness plates have been plotted in comparison to the experimental values and observed failure modes with increasing impulse magnitude as shown in Fig. 18.

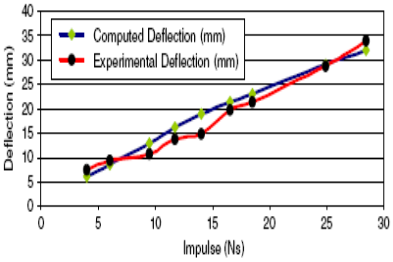

Fig. 14. Comparative plots of computed and experimental values of the central deflection of 60mm radius plate for Mode I failure with increasing impulse

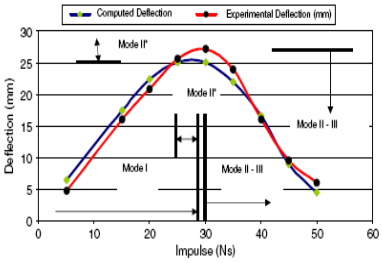

Fig. 15. Comparative plots of computed and experimental values of the central deflection of 50mm radius plate for Modes I, II and II–III failure with increasing impulse

4.2 Underwater Explosions

Underwater explosions unlike air explosions are complex involving nonlinearities in structure and fluid (water in this case). The underwater shock wave has a characteristic exponential decay with transient and spatial variation as shown in Fig 17. A validated FE procedure was adopted in which a plate was subjected to an exponentially decaying shock pulse. We observed that the numerical analysis results match closely with experimental values, as seen in Fig 16 below. The load profile on the plate which has a transient and spatial variation was adopted. The numerical study was conducted on stiffened and un-stiffened plate configurations. As the weight of the charge was increased and the distance of standoff was reduced it was observed that the central deformation in the plate reduced.

This trend is as shown in Fig 18, we observe in the central deformation vs. SF plot for the case of a 2mm plate thickness, the humps at 0.8 SF and 1.605 SF was due to the fact that the weight of charge and stand-off distance considered for a shock factor of 0.8 was 125 gm and 0.20 m, these values when

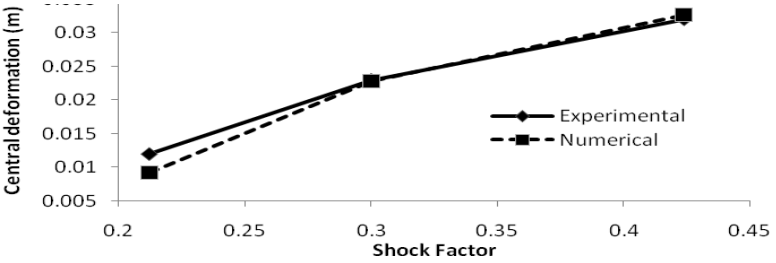

Fig. 16. Plot of central deformation validated results for high strength steel plates

compared with either side of the hump that is at a shock factor of 0.7 (55gm at 0.15 m) and a shock factor 0.9 (40gm at 0.1 m) we observe that at 0.8 SF the charge is farther away from the plate as compared to charges in the 0.7 and 0.8 shock factors hence one can conclude with this observation that the central deformation in the plate reduces when the charge is placed close to the structure, which modifies the behavior of the plate to display modes of failure higher than the Mode I (Large deformation failure) when the charge is near the structure. This behavior pattern is also seen at shock factors 1.605 (790gm at 0.25 m) and 1.7 (135gm at 0.1 m) where there exists a hump at 1.605 SF.

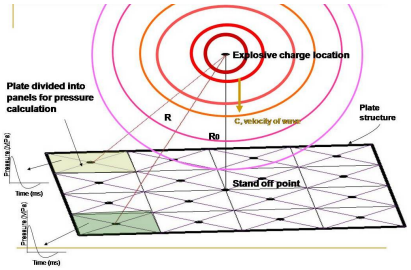

Fig. 17. Transient and spatial variation of UNDEX loads on plate

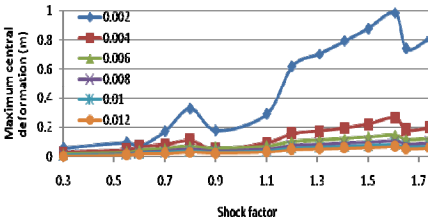

Fig. 18. Maximum central deformation of 2,4,6,8,10 & 12mm thick unstiffened plates for various shock factors

4.3 Tearing of Plates Subjected to Underwater Explosions

The mode II failure was defined earlier as tearing of plate at the centre of the supports and progressively moving to the corners at the clamped edges. This phenomenon has been numerically simulated as described in this section; the tearing phenomenon is brought about by Johnson-Cook failure criterion. An FE scheme was adopted using Johnson-Cook failure criterion calculating the

equivalent plastic strain at the element integration points and computing the resulting damage parameter, Ω. A progressive damage feature is then adopted to delete the elements which attain the damage parameter equals to "1" symbolizing the damage/tearing of the plate at that element, this procedure is continued till the response time of the UNDEX load is completed hence tracing the damage process in the plate. The Mode II failure pattern on a 2mm, 0.25x0.3m WELDOX 460E is shown in Fig 19(a) – 19(d) below, the plates shown are only quarter model.

The fracture of the plate is predicted by computation of the damage ratio i.e. the plate is said to have ruptured when the plastic strain increment equals the rupture strain. When the condition of damage in the plate is met at the elements the material properties of the particular element are nullified so that they do not contribute any stiffness for further analysis. This process is continued till the complete decay of the blast load profile hence, plotting the initiation and progression of damage in plates subjected to decaying underwater blast loads. The plots in Fig 19(a)–19(d) below show the variation of Von-Mises stress contour with time.

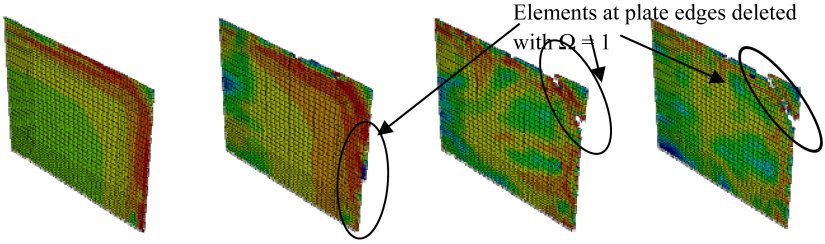

Fig. 19(a). Mises stress plot 2mm quarter plate at $2e^{-4}$ seconds

Fig. 19(b). Mises stress plot 2mm quarter plate at $3e^{-4}$ seconds

Fig. 19(c). Mises stress plot 2mm quarter plate at $4e^{-4}$ seconds

Fig. 19(d). Mises stress plot 2mm quarter plate at $4.37e^{-4}$ seconds

5 Conclusion

I have presented above some examples of experimental observations along with validated numerical results in an attempt to draw attention to the basic complexities of the large deformation phenomena. I have tried not to obscure these by theory or mathematics. There are, however many issues concerning the understanding of the mechanics of large deformations and delineation of deformation modes under various loading and boundary conditions, numerical methods and analytical solutions for their description and material constitutive behavior, which need attention.

References

1. Teeling-smith, R.G., Nurick, G.N.: The deformation and tearing of thin circular plates subjected to impulsive loads (1990)
2. Jones, N.: Role of plasticity methods in protection and safety. In: Bruhns, O.T., Meyers, A. (eds.) Implast 2007. University Press Bochum (2007)
3. Johnson, G.R., Cook, W.H.: A constitutive model and data for metals subjected to large strains, high strain rates and high temperatures. In: Proceedings of the Seventh International Symposium on Ballistics. The Hague (1983)
4. Johnson, W., Reid, S.R.: Applied Mechanics Reviews 31, 277 (1978)
5. Alexander, J.M., Reid, S.R.: Q. J. Mech. Appl. Math. 13, 10 (1960)
6. Abramowicz, W., Jones, N.: Dynamic axial crushing of circular plate. International Journal of Impact Engineering 2, 263 (1984)
7. Gupta, N.K., Velmurugan, R.: Consideration of internal folding and nonsymmetrical folding in axisymmetric axial collapse of round tubes. International Journal of Solids and Structures 34, 2611 (1997)
8. Gupta, N.K., Abbas, H.: Some aspects in axial crushing of cylindrical tubes. Int. J. Impact Engg. 25, 331–344 (2001)
9. Gupta, N.K., Gupta, S.K.: Effect of annealing, size and cut-outs on axial collapse behaviour of circular tubes. Mech. Sci. 35, 597–613 (1993)
10. Gupta, N.K., Prasad, G.L.E., Gupta, S.K.: Plastic collapse of metallic conical frusta of large semiepical angles. Int. J. Crash 2, 349–366 (1997)
11. Gupta, N.K., Prasad, G.L.E., Gupta, S.K.: Axial compression of metallic spherical shells between rigid plates. Thin. Walled Str. 34, 21–41 (1999)
12. Backman, M.E., Goldsmith, W.: The mechanics of penetration of projectiles into targets. Int. J. Eng. Sci. 16, 1–99 (1978)
13. Zukas, J.A.: High velocity dynamics. Wiley, New York (1990)
14. Corbett, G.G., Reid, S.R., Johnson, W.: Impact loading of plates and shells by free-flying projectiles: a review. Int. J. Impact Eng. 18, 141–230 (1996)
15. Gupta, N.K., Madhu, V.: An experimental study of normal and oblique impact of a hard core projectile on single and layered plates. Int. J. Eng. 19, 395–414 (1987)
16. Gupta, N.K., Madhu, V.: Experimental study of normal and oblique impact of hard core projectiles on single and layered plated. International Journal of Impact Engineering 19, 395–414 (1997)
17. Gupta, N.K., Ansari, R., Gupta, S.K.: Normal impact of ogive nosed projectiles on thin plates. International Journal of Impact Engineering 25, 641–660 (2001)
18. Geers, T.L.: Doubly asymptotic approximation for transient motions of submerged structures. J. Acoustic. Soc. Am. 64(5), 1500–1508 (1978)
19. Geers, T.L., Felippa, C.A.: Doubly asymptotic approximation for vibration of submerged structures. J. Acoust. Soc. Am. 73(4), 1152–1159 (1983)
20. Nurick, G.N., Gelman, M.E., Marshall, N.S.: Tearing of blast loaded plates with clamped boundary conditions. International Journal of Impact Engineering 18, 803–827 (1996)
21. Gupta, N.K., Nagesh: Deformation and tearing of circular plates with varying support conditions under uniform impulsive loads. International Journal of Impact Engineering 34, 42–59 (2007)

22. Nurick, G.N., Shave, G.C.: The deformation and tearing of thin square plates subjected to impulsive loads-an experimental study. International Journal of Impact Engineering 18, 99–116 (1995)
23. Rudrapatna, N.S., Vaziri, R., Olson, M.D.: Deformation and failure of blast loaded square plates. International Journal of Impact Engineering 22, 449–467 (1999)
24. Yu, T.X., Chen, F.L.: The large deflection dynamic plastic response of rectangular plates. International Journal of Impact Engineering 12(4), 603–616 (1992)

Onset of Oscillatory Thermocapillary Convection

W.R. Hu and Z.M. Tang

National Microgravity Laboratory, Institute of Mechanics,
Chinese Academy of Sciences, Beijing 100080, China
{wrhu,zmtang}@imech.ac.cn

Thermocapillary convection is an important subject of nature convection in the microgravity environment, and dominates many processes in the space materials processing and space biotechnologies. The onset of oscillatory convection relates to the bifurcation transition of fluid system. The microgravity experiments of larger scale in space and the simulation experiments of small scale on the ground are summarized to search the critical parameters for onset of oscillatory thermocapillary convection. The theoretical models are analyzed for discussion of the mechanisms. The results show that, the subject is still open for future research, and several space experiments are arranged to be performed in the near future.

1 Introduction

The natural convection in microgravity environment is driven by the variation of surface tension on the free surface but not by the buoyancy, and main research interesting on such natural convection is concentrated in the bifurcation transition, especially the onset of oscillatory convection. Pearson published a pioneer paper in 1958 on the Marangoni convection induced by surface tension [1], which fluid system consisted of a liquid layer bounded by a lower solid wall of higher temperature and a upper free surface of lower temperature was similar to the Benard-Rayleigh convection induced by buoyancy. In this case named as Marangoni convection, the applied temperature difference is perpendicular to the free surface. In another case named as thermocapillary convection, the applied temperature difference is parallel to the free surface, and the usual models are the liquid bridge of floating zone, the liquid between two cylinders, and the liquid layer in a rectangular container. Most studies have been done for a floating half zone.

The model of floating half zone was suggested from half of a floating full zone, and the liquid bridge was floated between two solid boundaries with different temperatures. The model was studied firstly by Chun and Wuest [2],

and Schwabe et al [3] in 1978. Then, there are many books and review papers, for example [4] – [7]. The thermocapillary convection in the liquid bridge of a floating half zone in the microgravity environment is a typical subject of the microgravity sciences related to the fluid physics and the materials science. From the view point of fluid physics, it is a new system of fluid mechanics, which controls many processes in the microgravity environment and is not easy to be studied on the ground. From the view point of materials science, the floating zone technique is attracted for high quality crystal growth, and to understand the mechanism of thermocapillary convection is helpful for materials processing in the microgravity environment and also on the ground.

In the present paper, the review will concentrate in the experiments of floating half zone, theoretical models, critical parameters, and discussions respectively in the following sections.

2 Experiments of Floating Half Zone

2.1 Small Bond Number Simulation

Simulation of small Bond number, which is defined as follows, is the basis of ground experiments

$$B_o = \frac{\rho g \ell^2}{\sigma} \quad or \quad B_d = \frac{\rho g \ell^2}{|\sigma_T'|\, \Delta T}, \tag{1}$$

where ρ, σ, g, l, σ_T' and ΔT are the liquid density, surface tension, gravitation, typical scale, gradient of surface tension and typical temperature difference respectively. B_o and B_d are named the static Bond number and dynamic Bond number respectively. The case of small Bond number means the important effect of surface tension in comparison with the effect of gravity, and small Bond number may be realized by small gravity level or small typical scale. Mostly, the Bond number is small than 1 if the typical scale of a system is centimeter in order of magnitude in the microgravity environment. It seems that the microgravity phenomena may be simulated on the ground by reducing the typical scale in a few of millimeter to satisfy the condition of small Bond number.

However, the experimental results show that it is much stable in the microgravity environment of lower g level and larger scale than on the ground of earth's gravity and small scale. If the flow region in a floating half zone is divided into two regions of boundary layer near the rods and a core region connected with the two region of boundary layer, and the flow in two regions of boundary layer will be more important relative to the flow in the core region in case of small Bond number with small typical scale on the ground than in case of small Bond number with larger typical scale in the microgravity environment. In addition, the configuration of free surface is symmetric to

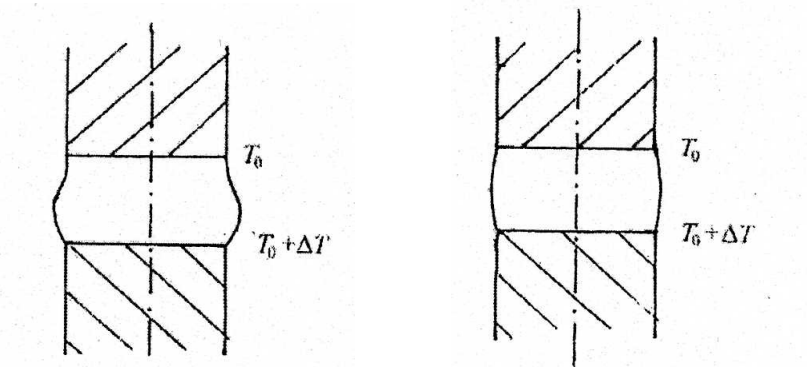

Fig. 1 Free surface configurations on the ground (left) and in microgravity environment (right)

middle vertical plane in the microgravity environment, and is a part of calabash which is different on the ground due to the influence of earth's gravity, as shown in Fig. 1. Difference of free surface deformation relates to difference of momentum equilibrium on the free surface and then the different flow features. Therefore, the experiments in microgravity environment are essentially important.

2.2 Preliminary Experiments

Preliminary model of a floating half zone on the ground consisted of a liquid bridge confined by two co-axial cylindrical copper rods with different temperatures T_o and $T_o+\Delta T$ respectively as shown in Fig. 2, and is benefit to study the transparent liquid medium of larger Prandtl number [2, 3]. The ground experiments require a small typical scale of a few of millimeters for small Bond number, and the boundaries of rods are planar. The temperature at a position in the liquid bridge may be measured by a thermal couple inserted in the liquid bridge. The flow field in a vertical cross-section may be measured by the PIV method via a sheet light passed through the cross-section, and the flow pattern changes from an axis-symmetric to an asymmetric pattern when the applied temperature difference is larger than a critical value $(\Delta T)_c$ as shown in Fig 3. In the same time, the temperature distribution at a position measured by a thermal couple inserted in a liquid bridge changes from a smooth to an oscillatory distribution. Usually, onset of the oscillation is characterized by a non-dimensional parameter, the critical Marangoni number $(Ma)_c$ related to the critical temperature difference $(\Delta T)_c$, and the Marangoni number is defined as follows.

$$Ma = \frac{|\sigma_T'|\,\Delta T \ell}{\rho \nu \kappa}, \tag{2}$$

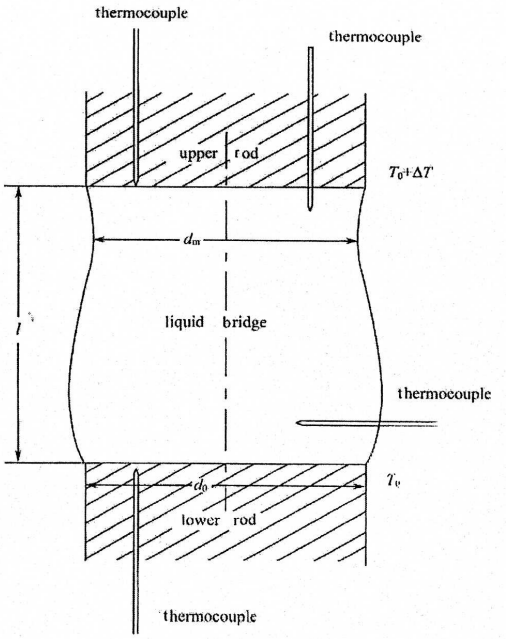

Fig. 2 The schematic diagram of a floating half zone

where ν and κ are respectively the viscous coefficient and thermal diffusion coefficient of liquid. Onset of oscillatory thermocapillary convection is an important subject in the microgravity fluid physics. It should be noted that the transition process of a floating half zone is a non-linear process in principle, because the velocity deviation has same order of magnitude as the average velocity. This experimental result implies that the theoretical conclusion based on the linear analyses should be with care [8].

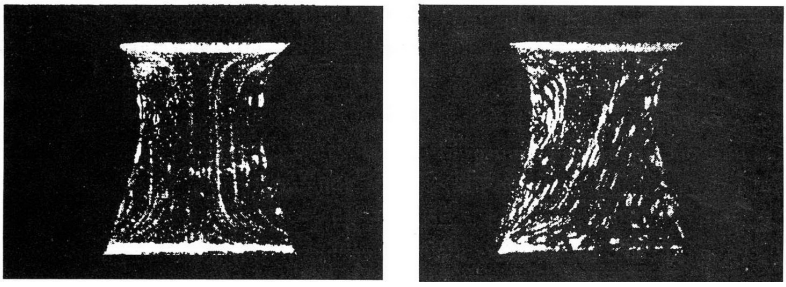

Fig. 3 Flow field in a quasi-steady state (left) and oscillatory state (right) in a vertical cross-section

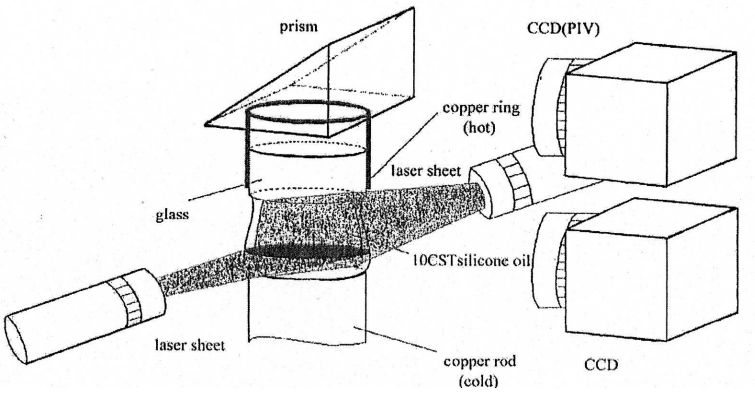

Fig. 4 The PIV measurement system in two cross-sections of a floating half zone

2.3 Observing Flow Field in a Horizontal Cross-Section

Hirata et al (1997) suggested that using a rod of transparent materials such as sapphire or glass covered by a metal ring to replace one of the copper rods as shown in Fig. 4, and this suggestion is an important improvement of experimental facility of floating half zone [9]. Velocity fields in both a vertical cross-section and a horizontal cross-section could be measured in the new experimental facility, and are more beneficial to know the whole flow field and to compare the experimental results with the theoretical results. As an example, Fig. 5 shows the flow patterns in a horizontal cross-section in one period of the oscillatory thermocapillatory convection in a floating half zone. It should be noted that the temperature boundary condition at the transparent rod is not a constant, and could be determined by direct measurement [10].

2.4 Space Experiments

Most experiments of thermocapillary convection have been performed on the ground in the liquid bridge or liquid layer of small scale to emphasize the effect of surface tension in comparison with the effect of earth's gravity. Several microgravity experiments have been completed by using the sounding rocket and the drop shift facility. The space experiments of longer microgravity period are extremely important for discovering the essential of thermocapillary convection because of longer experimental period and larger scale of the liquid system. Monti and his team completed successfully the first space experiment of floating half zone in D2 missions on board the Space Shuttle [11]. The floating half zones were cylinders of 30, 45 and 60 mm in diameters

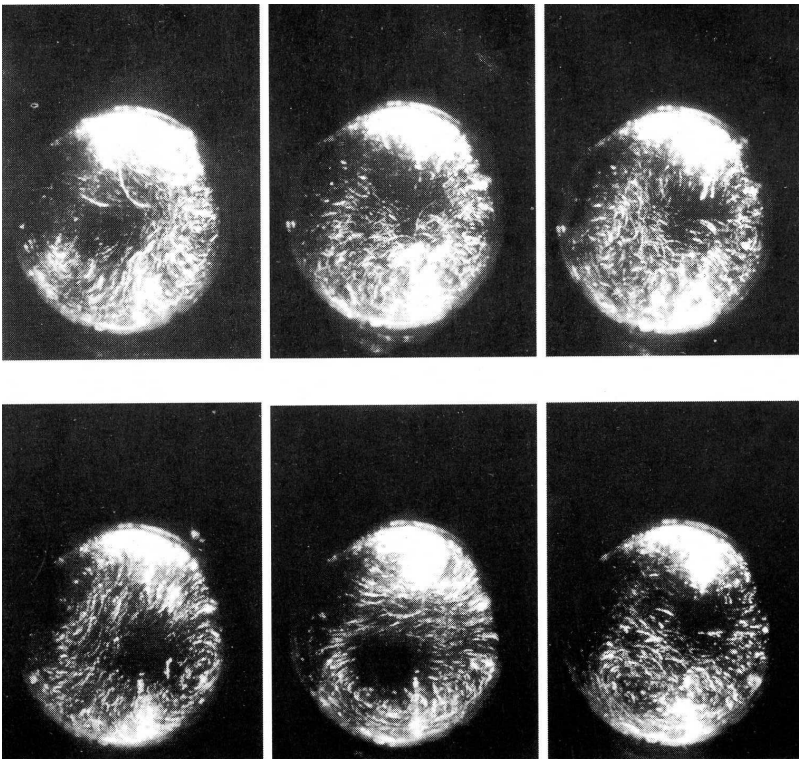

Fig. 5 Flow field patterns in one oscillatory period in a horizontal cross-section

respectively. The experimental results showed that the critical Marangoni number and the critical frequency of space experiments were respectively one order of magnitude larger and one order of magnitude smaller than the ones of experiments on the ground. Furthermore, the critical Marangoni numbers were increased with the increasing aspect ratio A = l/d, and d was rod diameter of floating half zone. Different conclusions of space experiments and ground experiments require the theoretical exploration in addition to more space experiments, which are arranged in the ISS Japanese program in the near future.

2.5 Measurements of Free Surface Waves

Free surface wave is an interesting subject in the fluid mechanics, especially a new fluid system. It is difficult to observe the free surface wave in a fluid system of thermocapillary convection, where the small typical scale is only a few of millimeters. The optical diagnostic methods were applied to observe the one-dimensional [12], two-dimensional [13], and three-dimensional free surface

wave respectively [14]. The experiments showed that, the free surface wave of oscillatory thermocapillary convection is an oblique traveling wave with same frequency of temperature and velocity oscillations, and the amplitude of free surface wave is only a few of micrometer, much small than the typical scale of liquid bridge. Fig. 6 shows the evolution of free surface wave in one period of oscillatory thermocapillary convection.

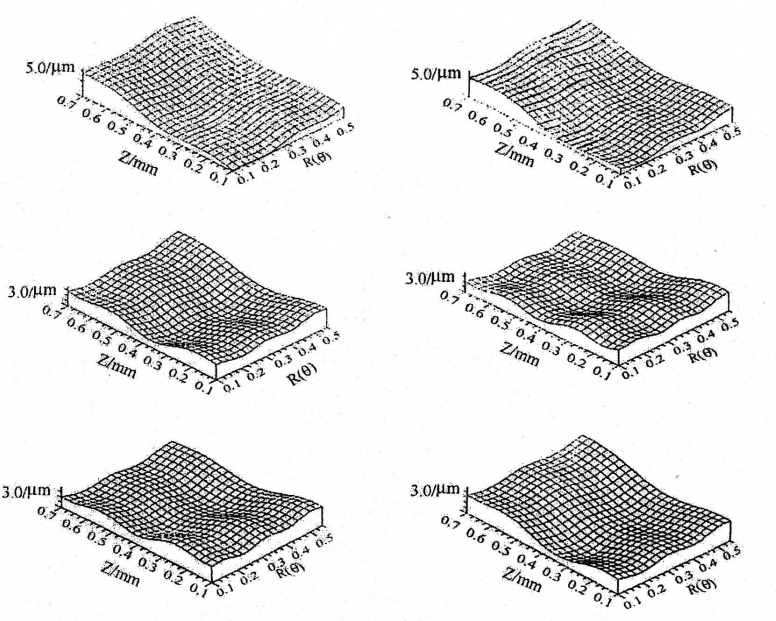

Fig. 6 Free surface wave patterns in one period of oscillatory thermocapillary convection [14]

2.6 Experiments of Small Prandtl Number

The liquids of floating zone technique are melts of metals or alloys of small Prandtl number $\mathrm{Pr} = \nu/\kappa$ ¡¡ 1. These melts are non-transparent of light, and it is difficult to measure directly the onset of oscillation, especially in small scale. Materials scientists believe that the appearance of striation during the solidification of material processing relates to the appearance of oscillatory flow in the liquid bridge, and the critical Marangoni number in a floating full zone can be determined when the striations appear in the crystal during the increasing of applied temperature difference. In addition to several experiments of melt floating full zones on the ground, Croll et al performed the microgravity experiments of GaSb melt based on the appearance of striation [15] and summarized the experimental results of small Prandtl number as

$$(Ma)_c = 2.2x10^4 Pr^{1.32}. \tag{3}$$

Han et al suggested a non-contacted optical diagnostic method to measure directly the onset of oscillatory thermocapillary convection in a slender mercury liquid bridge of 3mm in height and A = 0.6, and the critical Marangoni number and critical frequency were respectively $(\mathrm{Ma})_c$ ¡ 900 and f_c = 5 Hz [16]. Furthermore, Yang and Kou performed the experiment of Tin liquid bridge of 4 mm in height and A = 1, and the experimental results given by temperature measurement were $(\mathrm{Ma})_c = 194 \pm 14$ and $\mathrm{f}_c = 1.1 \pm 0.1$ Hz [17]. Takagi et al completed a similar experiment of Tin liquid bridge of 2.97 mm in height and 3mm in diameter, and the experimental results given by non-contact temperature measurement were $(\mathrm{Ma})_c = 43.3$ and $\mathrm{f}_c = 0.08$Hz [18]. It can be seen that two critical frequencies of the Tin liquid bridges are different in one order of magnitude, and the results mean that two experiments may be worked in different characteristic regions.

3 Theoretical Models

3.1 Theoretical Problem

Onset of oscillatory convection is a problem of transition from steady flow to oscillatory flow in incompressible fluid mechanics, and the basic equations are Navier-Stokes under Boussinesq approximation, that is

$$\nabla \cdot \mathbf{V} = 0, \tag{4}$$

$$\frac{\partial V}{\partial t} + V \bullet \nabla V = -\frac{1}{\rho}\nabla p + \nu \Delta V + f, \tag{5}$$

$$\frac{\partial T}{\partial t} + V \bullet \nabla T = \kappa \Delta T, \tag{6}$$

Where **V**, T, p are the vector velocity, temperature and pressure of fluid respectively, f is the vector body force, and $\Delta$is the Laplace operator.

The boundary conditions of a floating half zone as shown in Fig. 2 are written as follows.

$$z = 0 : \mathbf{V} = 0, T = T_o + \Delta T; \tag{7}$$

$$z = l : \mathbf{V} = 0, T = T_o; \tag{8}$$

$$r = R(z) : T \cdot \mathbf{e}_n = 0, \tag{9}$$

$$\mathbf{V} \cdot \mathbf{e}_n = 0, \tag{10}$$

$$\tau \cdot \mathbf{e}_n \cdot \mathbf{e}_s = (\mathbf{e}_s \cdot)\sigma, \tag{11}$$

$$\tau \cdot \mathbf{e}_n \cdot \mathbf{e}_\theta = (\mathbf{e}_\theta \cdot)\sigma, \tag{12}$$

where τ is the viscosity stress tensor, ($\mathbf{e}_n$, $\mathbf{e}_\theta$, $\mathbf{e}_s$) is unit vector on the free surface, which is described by r = R(z). The onset of oscillatory thermocapillary convection in theory is to solve equation (1) – (3) under boundary condition (7) - (12) for special problem.

Usually, the theoretical problem can be solved by the methods of linear instability analysis, energy instability analysis, and three-dimensional numerical simulation. It should be noted that the theoretical models based on the perturbation analyses give only the small deviations from a steady state, and have no information on the non-linear development of large deviation, which can be described by the three-dimensional numerical simulation.

3.2 Hydrothermal Wave Instability

Smith and Davis analyzed a liquid layer of infinite extension limited by a solid boundary and free surface with a constant temperature graduate, and the linear instability analysis showed a perturbed traveling wave, named the hydrothermal wave of oscillatory thermocapillary convection [17]. Such theoretical model is different from the usual model of floating half zone at least in two points. At first, this theoretical model has no boundary layers near the rods, which are important especially for liquid bridge of small scale. Secondly, the constant temperature graduate on the free surface is a strong assumption for onset of oscillation. Therefore, the critical Marangoni number in a liquid layer of rectangular container given by [17] is quite difficult from the one given by the model of floating half zone.

Numerical studies show that, the hydrothermal wave is existed in the oscillatory thermocapillary convection in a rectangular container of larger extension, and all fluctuated quantities are much small in order of magnitude in comparison with the average quantities, see for example [18]. Therefore, the onset of oscillatory thermocapillary convection is in principle a linear problem in a rectangular container discussed in [19], and the problem of floating half zone is a strong non-linear process. Many experiments on the ground had performed to check existence of the hydrothermal wave, but were not success until the one given by Riley and Neitzel (1998), who completed the experiment in a thick layer of 1.2 mm related to a small Bond number B_d ¡ 0.2 [21].

3.3 Hydrodynamic Instability

Levenstam and Amberg (1995) studied the thermocapillary convection in a floating half zone of small Prandtl number Pr = 0.01 by numerical simulation,

and found two bifurcation transitions: from steady and axis-symmetric state to steady and asymmetric state with first critical Marangoni number $(\mathrm{Ma})_c = 19.60$ at first, and then to oscillatory state with second critical number $(\mathrm{Ma})_c = 62.50$ [22]. The process was explained by the mechanism of hydrodynamic instability. The numerical simulation results of different calculating programs by different research groups for case of $\mathrm{Pr} = 0.01$ were compared together as benchmark of numerical solution and summarized in [23]. It should be noted that the experimental results of small Prandtl number can give only the second Marangoni number at present time.

Similar studies have been extended to cases of larger Prandtl number by the numerical simulation [24] and the experiments on the ground [25]. The results show that two bifurcation transitions exist in the thermocapillary convection of floating half zone with larger Prandtl number in cases of fat liquid bridge with small aspect ratio, otherwise, there is one bifurcation transition from steady and axis-symmetric thermocapillary convection to the oscillatory thermocapillary convection.

3.4 Other Models

Ostrach et al suggested a mechanism based on the free surface oscillatory [26], and performed space experiments in a cylindrical container with a horizontal free surface heated in the surface center [27]. The amplitude of free surface wave is about 10 micrometers, and is much small than the typical scale of the fluid system. This means that the energy of free surface oscillation is much small than the fluctuated internal energy for example.

Three-dimensional numerical simulation is a better method for studying of the non-linear problem, including the thermocapillary convection in a floating half zone. Many numerical simulations have been applied to study the onset of oscillatory thermocapillary convection in liquid bridge of large Prandtl number, see for example [28]. These studies are helpful to discover the essential of transition process, especially the critical parameters for onset of oscillation.

4 Critical Parameters

Experimental results, especially the space experiments, are essential for understanding of the bifurcation transitions of thermocapillary convection, and the most important point is to search the influence of critical parameters.

The Marangoni number related to the applied temperature difference is a basic critical parameter for onset of oscillatory thermocapillary convection. There are two critical Marangoni numbers $(\mathrm{Ma})_{c1}$ and $(\mathrm{Ma})_{c2}$ related to the process of two bifurcation transitions in cases of small Prandtl number or some cases of large Prandtl number. The first critical Marangoni number in

cases of small Prandtl number has not been observed yet by any experiment at present time.

The Prandtl number depending on the property of liquid medium is another critical parameter for onset of oscillatory thermocapillary convection. Heat transfer in the cases of small Prandtl numbers are much serious than the ones of large Prandtl numbers, and theoretical research shows that there are two bifurcation transitions in case of small Prandtl number, although the experimental studies can give only the second critical Marangoni number. The theoretical results show that the distribution of critical Marangoni number depending on Prandtl number is a bit complex near the region of Pr 1 [29].

The geometric parameter of aspect ratio A = l/d is a critical parameter. Results of experiments on the ground gave by Schwabe et al [30] showed that the critical Marangoni numbers $(\mathrm{Ma})_c$ decrease with the increasing aspect ratios A for a tetracosane liquid bridge of Pr = 49. However, the space experiments of D2 give an opposite conclusion for a liquid bridge of 5 sct silicon oil of Pr = 74, that is, the critical Marangoni numbers increase with the increasing aspect ratios [11]. Recent experiments on the ground by Ay et al (2008) observed that the critical Marangoni numbers increase firstly and then decrease with the increasing aspect ratio as shown in Fig. 7 as an example [31], and the numerical simulation give the similar conclusion (Tang et al, 2008).

Another sensitive critical geometrical parameter is the liquid bridge volume. The results of both numerical simulation and experiments on the ground showed that the margin instability curve for onset the oscillatory thermocapillary convection was divided into two branches: the slender liquid and fat

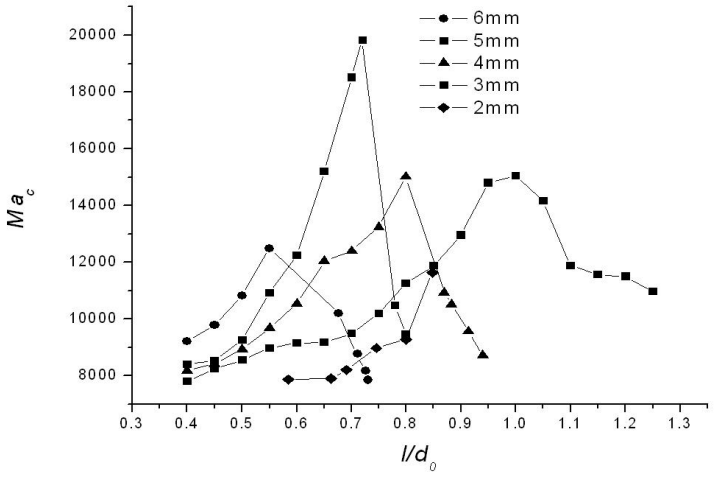

Fig. 7 Critical Marangoni number depending on the aspect ratio in a liquid bridge of 10 sct silicon oil

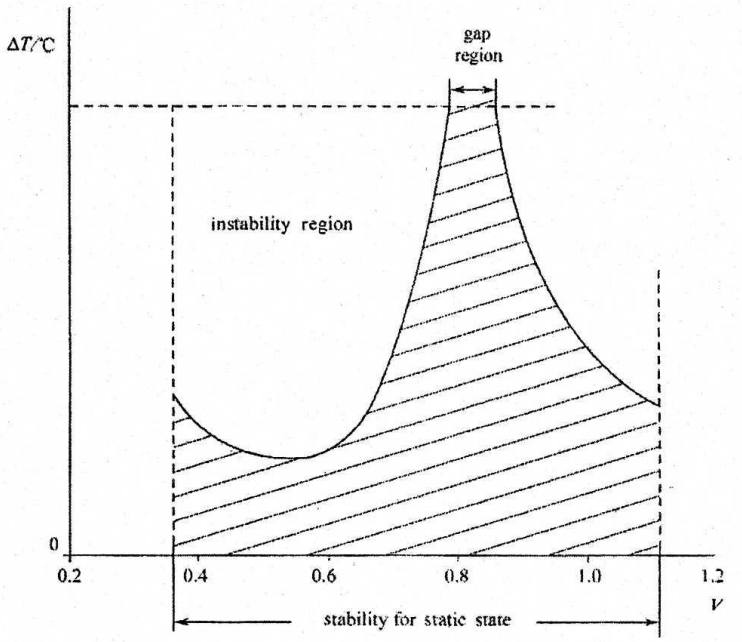

Fig. 8 Critical Marangoni number depending on liquid bridge volume

liquid bridge as shown by Fig. 8, and two branches connected at a peak of maximum critical Marangoni number. These results imply that the experimental results should be given by a specified liquid bridge volume, because the critical Marangoni numbers are changed greatly for same aspect ratio but different liquid bridge volume.

The critical Marangoni numbers of space experiments of several centimeter in diameter are 10^5 in order of magnitude, which is one order of magnitude larger than the one of experiments with a few of millimeter in diameter on the ground. Monti suggested that the dimensional scale l is also a critical member [32]. If the difference is due to the boundary layer near the rod, and a non-dimensional critical geometric parameter may probably be introduced as the ratio of thickness of boundary layers to the height of liquid bridge.

It was believed that the heat transfer from the boundary of free surface could stabilize the onset of oscillatory thermocopillary convection, in fact, the situation is more complex, see for example [32]. The Boit number, described the heat transfer from free surface, is a critical parameter.

The bifurcation transition of thermocapillary convections are physical phenomena, and need to be observed at first as details as possible by the experiments and to search clearly the critical parameters for describing the

process. Based on the present knowledge, the bifurcation transition should be described in a function, such as

$$F(Ma, Pr, A, V/V_o, l, Bi, \ldots.) = 0, \tag{13}$$

where V and V_o are respectively the liquid bridge volume and the volume of a cylinder liquid bridge with same height and diameter. To clear the function relationship is an important subject in the future.

5 Discussion

The microgravity environment supports excellent opportunity for studying many phenomena including the thermocapillary convection which is difficult to be studied on the ground due to the dominated effect of earth's gravity. There are many attracted subjects of thermocapillary convection such as the bifurcation transitions for onset of oscillatory oscillation, chaotic features of oscillatory thermocapillary convection, transition to turbulence etc, in addition to the applied studies on the materials processing.

Onset of oscillatory thermocapillary convection is a strong non-linear phenomenon in the liquid bridge of a floating half zone where the fluctuation velocity has same order of magnitude as the average velocity, but a linear phenomenon in liquid layer of a rectangular container where all the perturbed quantities are small in order of magnitude than the averaged ones. In general, features of the non-linear process may be quite different from the ones of the linear process, although both convections may be driven by the graduate of surface tension on the free surface. It should be carefully to apply the linear features, which have not been proved especially by a microgravity experiment, to explain the non-linear process.

The experiments, especially the space experiments of larger typical scale, are essential for studies of thermocapillary convection. Most experiments limit to the ones of larger Prandtl number, because the experiments of small Prandtl number are difficult to be diagnostic even on the ground of small typical scale. The sensitive critical parameters are the bases for understanding of the bifurcation transitions and also for the theoretical explanations. Many basic features of the floating half zone convection are still waiting for explanation although the studies have been continued in the last 30 years, such as the different critical Marangoni numbers given by the space experiment and the ones on the ground, how to explain the feature of margin instability curve depending on the liquid bridge volume, what is the dependence between the critical Marangoni number and aspect ratio, if there is another critical geometric parameter in addition to the aspect ratio and liquid bridge volume, and etc. More space experiments will be performed in the next years, and they will discover more features in the near future.

Acknowledgements. This research was supported by the National natural Science Foundation of China (Contract No. 10432060) and the Knowledge Innovation Program of CAS.

References

1. Pearson, J.R.A.: J. Fluid Mechanics 4, 489–500 (1958)
2. Chun, C.H., Wuest, W.: Acta. Astronaut. 5, 681-686 (1978)
3. Schwabe, D., Scharmann, A., Preisser, F., Oeder, R.: J. Crystal Growth 43, 305–312 (1978)
4. Kuhlmann, H.C.: Thermocapillary convection in model of crystal growth. Springer, New York (1999)
5. Hu, W.R., Tang, Z.M.: Floating zone convection. Science Press, Beijing (2003)
6. Schatz, M.F., Neitzel, G.P.: Ann. Rev. Fluid Mechanics 33, 93–129 (2001)
7. Hu, W.R., Tang, Z.M., Li, K.: Applied Mechanics Review 61(1-15), 10803 (2008)
8. Hu, W.R., Tang, Z.M.: Microgravity and Space State Utilization 1, 23–30 (2000)
9. Hirata, A., Sakurai, M., Ohishi, N., Koyama, M.: J. Japan Soc. Microgravity Appl. 14, 137–143 (1997)
10. Han, J.H., Zhou, Y.R., Hu, W.R.: Intl. J. Heat and Mass Transfer 40, 2671–2677 (1997)
11. Albanese, C., Cerotenuto, L., Castagnolo, D., Celia, E., Monti, R.: First results from onset experiment during D2 space mission. In: Sahm, P.R., Keller, M.H., Schiewe, B. (eds.) Scientific Results of German Spacelab Mission D-2, vol. 2, pp. 247–258. DARA, Bonn (1995)
12. Cao, Z.H., You, H.T., Tang, Z.M., Hu, W.R.: Adv. Space Research 11(7), 232–236 (1991)
13. Hu, W.R., You, H.T., Cao, Z.H.: Scientia Sinica A 35, 1101–1107 (1992)
14. Shu, J.Z., Yoa, Y.L., Hu, W.R.: Scientia Sinica A 36, 326–332 (1993)
15. Croll, A., Kaiser, T., Schweizer, A., Danilewsky, A.N., Lauer, S., Tegetmeier, A., Benz, K.W.: J. Crystal Growth 191, 365–376 (1998)
16. Han, J.H., Sun, Z.W., Dai, L.R., Xie, J.C., Hu, W.R.: J. Crystal Growth 169, 129–135 (1996)
17. Yang, Y.K., Kou, S.: J. Crystal Growth 222, pp. 135–143 (2001)
18. Takaji, K., Otaka, M., Natsui, H., Arai, T., Yoda, S., Yuan, Z.F., Mukai, K., Yasuhiro, S., Imaishi, N.: J. Crystal Growth 233, 399–407 (2001)
19. Smith, M.K., Davis, S.H.: J. Fluid Mech. 132, 119–131 (1983)
20. Tang, Z.M., Hu, W.R.: Microgravity Sci. Tech. 16, 253–258 (2005)
21. Riley, R.J., Neitzel, G.P.: J. Fluid Mech. 359, 143–164 (1998)
22. Levenstam, M., Amberg, G.: J. Fluid Mech. 297, 357–372 (1995)
23. Shevtosova, V.: J. Crystal Growth 280, 632–651 (2005)
24. Hu, W.R., Tang, Z.M.: Cryst. Res. Tech. 38, 627–634 (2003)
25. Aa, Y., Cao, Z.H., Tang, Z.M., Hu, W.R.: Microgravity Sci. Tech. 17(4), 5–12 (2005)
26. Ostrach, S., Kamotani, Y., Lai, C.L.: PCH Physico-Chemical Hydrodynamics 6(5/6), 585–599 (1985)
27. Kamotoni, Y., Ostrach, S.: Int. J. Heat Mass Transfer 42, 555–564 (1999)
28. Tang, Z.M., Hu, W.R.: J. Crystal Growth 207, 239–246 (1999)

29. Levenstam, M., Amberg, G., Wimkler, C.: Phys. Fluids 13, pp. 807–816 (2001)
30. Velten, R., Schwabe, D., Scharmann, A.: Physics Fluids A3, pp. 267–227 (1991)
31. Ay, Y., Cao, Z.H., Li, K., Hu, W.R., (2008) (submitted)
32. Monti, R.: Acta Astronautica 15(8), 557–560 (1987)
33. Kamotani, Y., Wang, L., Hatta, S., Wang, A., Yoda, S.: Int. J. Heat Mass Transfer 46, 3211–3220 (2003)

Instabilities of Flows through Deformable Tubes and Channels

O.E. Jensen

School of Mathematical Sciences, University of Nottingham, University Park, Nottingham NG7 2RD, UK
Oliver.Jensen@nottingham.ac.uk

Flow driven through a segment of flexible tube, supported between rigid pipes and enclosed in a pressurized chamber, is susceptible to a variety of self-excited oscillations. This paper provides a brief review of recent modelling efforts aimed at understanding some of the underlying mechanisms of instability in this system. In particular, it is shown how a family of spatially one-, two- and three-dimensional models have been used to investigate a global instability arising at high frequencies, whereby axial sloshing motions driven by transverse wall oscillations are able to sustain themselves by extracting kinetic energy from the underlying mean flow.

1 Introduction

Fluids are distributed around the human body via networks of flexible tubes, and accordingly flow-structure interaction plays an important role in a number of biomedical transport phenomena. Flow limitation, for example, is well known to clinicians: collapse of veins above the heart (because of reduced hydrostatic pressure in an upright individual) limits return of blood to the heart — a particular concern for giraffes [1] — and flow-induced collapse of asthmatic airways inhibits expiration from the lung. Collapse of an elastic tube such as a vein or airway is likely to involve a buckling instability. Under positive transmural (interior minus exterior) pressure, the tube is circular in cross section and strongly resists area change; however under negative transmural pressure, the tube buckles (for example to an elliptical cross section) and becomes much more compliant. In the buckled state, there is potential for significant interaction between internal fluid flows and the elastic wall, and instabilities are commonplace. In the body, these are manifested for example as Korotkoff sounds (oscillations of the collapsed brachial artery underneath a blood-pressure cuff inflated around the upper arm) and wheezing during forced expiration [2, 3].

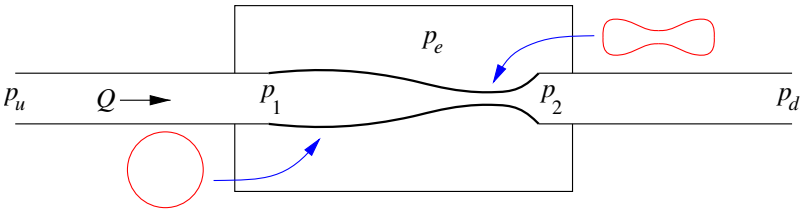

Fig. 1 The Starling Resistor. A flux Q is driven from left to right by a pressure drop between inlet and outlet (at pressures p_u and p_d respectively). The collapsible segment of tube is subject to external pressure p_e and may buckle to a non-axisymmetric cross-section when collapsed, as indicated.

The Starling Resistor [4] is a bench-top device that has been used to illustrate these phenomena to medical students for many years, and which has inspired and challenged researchers in biofluid-mechanics since the 1960s. A segment of elastic tube is mounted between two rigid tubes (Fig. 1). Flow is driven through the system either under a fixed pressure drop $p_u - p_d$, or with fixed volume flux Q. A chamber enclosing the flexible segment is raised to pressure p_e, causing collapse of the tube. When carrying a flow, the viscous pressure drop along the flexible segment causes the tube to collapse first towards its downstream end as p_e is increased. The pressures at the upstream and downstream ends of the flexible segment (p_1, p_2) are typically recorded experimentally. The steady flow properties of the system are strongly nonlinear: sucking on the downstream end of the tube (increasing $p_1 - p_2$ for fixed $p_1 - p_e$) leads to flow limitation, i.e. a maximum possible flux Q; blowing on the upstream end of the tube (increasing Q while holding $p_2 - p_e$ fixed) leads to saturation of the pressure drop $p_1 - p_2$. Self-excited oscillations arise during these manoeuvres in many regions of parameter space, even at modest Reynolds numbers (e.g. 300-500) if the tube wall is sufficiently thin. The oscillations fall into distinct frequency bands, exhibit a variety of characteristic nonlinear waveforms and depend strongly on the properties of the rigid parts of system (such as the lengths of the upstream and downstream rigid segments). The dynamics of the system have been carefully characterised experimentally by Bertram and co-workers [5, 6].

The present paper provides a review of some recent theoretical developments aimed at understanding the possible mechanisms of self-excited oscillation. The discussion is confined to a specific parameter regime in which the internal flow is below Reynolds numbers at which there is transition to turbulence, and for which fluid inertia dominates wall inertia (high-frequency flutter modes associated with wall inertia are not considered). The primary mechanical ingredients in all models discussed below are wall elasticity, fluid inertia (throughout the entire system) and viscous dissipation. The problem illustrates the value — and limitations — of relatively elementary models

in informing more sophisticated approaches. Accordingly, the discussion progresses from spatially one-dimensional (1D) models, which are useful in exploring the relationship between local and global instabilities and in providing an overview of parameter space (§3), through 2D models, in which oscillation thresholds can be predicted using high Reynolds-number asymptotics (§4), through to recent developments in 3D (§5). Comprehensive reviews of earlier studies and a more general account of relevant biomedical applications are provided in [2, 3, 7].

2 Models of Flow in the Starling Resistor

It is helpful to put the discussion to follow into context by taking a brief overview of the different modelling approaches that have been used to address flow in the Starling Resistor.

Initial zero-dimensional (lumped-parameter) models described the system using a small set of time-dependent variables, incorporating approximate statements of mass and momentum conservation and a simple 'tube law' to model wall elasticity. By incorporating the basic mechanical ingredients mentioned above, Bertram & Pedley [8] for example were able to reproduce self-excited oscillations, and later models were shown to exhibit nontrivial dynamics [9]. However the inability to capture wave propagation is a fundamental limitation of this approach, and motivated the development of 1D models. These involve two coupled PDEs in the tube area $\alpha(x,t)$, cross-sectionally averaged axial velocity $u(x,t)$ and internal pressure $p(x,t)$ [10, 11]. However in this framework there is (inevitably) an *ad hoc* representation of viscous dissipation (either distributed along the tube [12] or associated with a separated internal jet [11]) and of the tube elasticity, for which a modified tube law of the form $p - p_e = P(\alpha) - T\alpha_{xx}$ is commonly used, where T represents axial tension and P is a nonlinear function capturing the dependence of compliance on the degree of tube collapse. 1D models predict multiple steady tube configurations in the presence of axial flow [13] and distinct oscillatory modes (numbered $2, 3, 4, \ldots$ according to the number of area extrema) arising in overlapping regions of parameter space, appearing in distinct frequency bands [14].

Given the inherent complexity of the Starling Resistor, involving as it does non-axisymmetric tube buckling coupled to unsteady separating 3D internal flow, much attention has focussed on a simpler 2D problem, first addressed by Pedley [15]. This involves a finite-length channel, one wall of which contains a segment of flexible membrane (see Fig. 2 below). While the device has yet to be realised in any physical experiment, because of the difficulty of constructing genuinely 2D flow conditions, it has nevertheless been investigated fruitfully by both asymptotic and numerical modelling approaches. Guneratne & Pedley [16] explored steady flow at high Reynolds numbers, using interactive boundary-layer theory, which captures weak flow reversal beyond

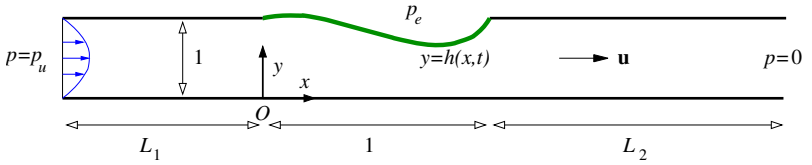

Fig. 2 The 2D analogue of the Starling Resistor. Flow is driven by a fixed pressure drop p_u through a finite-length channel, one wall of which contains a flexible membrane under external pressure $p_e(x)$. Distances x and y along and across the channel are scaled on the length of the flexible segment and the channel width.

constrictions. They demonstrated multiple static solutions in modes 1, 2, etc., bifurcating from the uniform state via transcritical bifurcations or through saddle-node bifurcations when the symmetry of the base state was perturbed by non-zero external pressure. The model revealed regions of parameter space in which no steady state could exist. Unsteady flows in the 2D analogue of the Starling Resistor have been captured in a series of papers using finite-element methods by Luo, Pedley and co-workers [17, 18]. Here oscillatory modes 2, 3, 4 have again been identified in overlapping regions ('tongues') of parameter space, arising in distinct frequency bands, associated with which are transverse wavelike displacements of the internal core flow downstream of the oscillating membrane; these are low frequency, long wavelength Tollmien–Schlichting (TS) waves, often referred to in this context as vorticity waves. While distinct oscillatory modes were captured also in 1D [14], it is clearly not possible to describe TS waves in a 1D framework and their role in the underlying instability mechanism remains to be fully understood.

Improvements in computational power in the last decade, plus the development of algorithms in which fluid and solid mechanics problems are solved in a fully coupled (monolithic) manner [19], have recently allowed 3D simulations of the Starling Resistor to become feasible. Finite-element simulations coupling geometrically nonlinear shell theory to a steady Navier–Stokes solver were reported by Hazel & Heil [20]; there has also been success in simulating steady flow solutions using a commercial package [21]. Something of a milestone in the history of this problem was passed at the XXII ICTAM with the first report of fully unsteady 3D simulations of self-excited oscillations in the Starling Resistor [22], which involve transitions between distinct buckled states (illustrated schematically in Fig. 5(b) below).

A parallel strand of research has addressed instabilities of flows in homogeneous flexible channels. Here, wave-like solutions of the linearized Navier–Stokes equations are sought, satisfying boundary conditions capturing properties of a deformable wall (bending stiffness, tension, springs, damping, inertia, etc.). Multiple modes of local instability have been identified, and it is useful to consider how they may be related to the global instabilities arising in the Starling Resistor. Briefly, the local modes are classified into four

major groups [23, 24, 25]: static divergence (SD); TS waves; travelling-wave flutter (TWF); and interactive modes. A global SD instability is responsible for the multiple static modes seen in 1D [13] and 2D [16] analyses of finite-length collapsible tube or channel flows: SD can arise through both viscous and inertial mechanisms. TS waves (evident in 2D simulations [17]) arise of course in rigid-walled channels but in the presence of a flexible wall they can be destabilized by wall damping. In contrast, TWF is stabilized by wall damping (requiring energy to be transferred from the flow to the wall).

Connections between local and global modes of instability in the context of a 1D model are now explored further, and energy methods are used to distinguish between distinct mechanisms of global instability in the Starling Resistor.

3 A One-Dimensional Model

A recent study [26] of a 1D model of flow in a 2D collapsible channel (Fig. 2) has revealed a number of significant features of self-excited oscillations, which we review briefly here. Consider the flow driven by a prescribed pressure drop through the 2D analogue of the Starling Resistor (Fig. 2). An external pressure distribution is prescribed that exactly matches the linear pressure drop that would arise if the channel were uniform. This enables the system to support the uniform flow state as a steady solution. The membrane is held under longitudinal tension. The 2D Navier–Stokes equations describing the flow through the channel are reduced to the boundary-layer equations by making a long-wavelength approximation. A further reduction to a 1D system is achieved by making a von Kármán–Pohlhausen approximation, whereby a prescribed parabolic velocity profile is assumed, enabling the mass and momentum equations to be integrated across the channel. The resulting model equations expressing mass and momentum conservation are, in dimensionless form [26],

$$h_t + q_x = 0, \tag{1a}$$

$$q_t + \frac{6}{5}\left(\frac{q^2}{h}\right)_x = Thh_{xxx} + \frac{12}{R}\left(h - \frac{q}{h^2}\right) \tag{1b}$$

along the length of the flexible segement of channel in $0 < x < 1$. Here $h(x,t)$ is the channel width and $q(x,t)$ the axial volume flux. The rigid segment of channel upstream has relative length L_1 and that downstream L_2. Attention is focused on the case $L_1 < L_2$, for reasons explained below. Additional dimensionless parameters are a Reynolds number R and a membrane tension parameter T; the term $12h/R$ arises from the choice of external pressure distribution. The model is expected to be reliable for $R \lesssim 1$, when viscous effects are dominant, but potentially unreliable for $R \gg 1$ or for high frequency motion. Equations (1a,b) are solved subject to boundary conditions

$$h = 1, \qquad Th_{xx} = L_1 \left[\frac{12}{R}(q-1) + q_t \right] \qquad (x = 0), \tag{1c}$$

$$h = 1, \qquad Th_{xx} = -L_2 \left[\frac{12}{R}(q-1) + q_t \right] \qquad (x = 1), \tag{1d}$$

which account for the pressure drop associated with viscous dissipation and unsteady inertia in the upstream and downstream rigid channel segments. Eqs (1a-d) admit the uniform steady solution $h = 1$, $q = 1$, enabling straightforward linear stability analysis of this state.

It is useful first to consider the dispersion relation for small-amplitude wavelike disturbances of wavenumber k and frequency ω arising in the flexible segment of the channel, satisfying the linearised form of Eqs (1a,b). This is

$$\omega^2 + \frac{6}{5}\left(k^2 - 2\omega k\right) - Tk^4 - \frac{12i}{R}(3k - \omega) = 0. \tag{2}$$

Analysis of Eq. (2) in the complex k and ω planes using the Briggs–Bers condition reveals that any unstable disturbances are convectively, but not absolutely unstable, with the large-time response to point forcing arising through an interaction of an evanescent upstream SD mode and an unstable downstream TWF mode [26]. Thus any instabilities that arise in the finite-length system cannot involve absolute instability of these modes.

In order to account for boundary conditions, a global linear stability analysis is necessary. Looking for small disturbances to the uniform state with time dependence $e^{\sigma t}$, a fourth-order eigenvalue problem must be solved. This reveals multiple modes of static and dynamic instability. Neutral curves in the (R, T)-plane are identified across which static modes arise through transcritical bifurcations (where $\sigma = 0$) and oscillatory modes arise through Hopf bifurcations (where $\mathrm{Re}(\sigma) = 0$). Following the convention mentioned previously, modes are labelled by the number of extrema in h. The uniform state is linearly stable for high tension and low Reynolds number. If T is reduced for fixed low R, the uniform state becomes unstable to static mode 1 and mode 2 instabilities, through a global viscous SD instability. Alternatively, if R is increased for fixed $T \gg 1$, the uniform state becomes unstable to an oscillatory mode 1 instability, which has high frequency because of the large membrane tension.

Although this 1D model is not expected to be quantitatively reliable for high-frequency motion, the oscillatory mode 1 instability arising for $T \gg 1$ turns out to be worthy of analysis. An asymptotic approximation can be constructed by expanding variables in powers of $T^{-1/2}$. At leading order, the flux perturbation $Q_0(x)$ satisfies a fourth-order self-adjoint eigenvalue problem parameterized only by L_1 and L_2, involving a balance between unsteady inertia and membrane tension. This reveals a normal mode of the system, in which transverse oscillations of the wall drive an axial oscillatory sloshing motion of the fluid within the entire channel. This is independent of the imposed mean flow to this order. Because $L_1 < L_2$, the amplitude of sloshing is larger

in the upstream rigid segment than downstream (i.e. $|Q_0(0)| > |Q_0(1)|$). At the following order in $T^{-1/2}$, the mean flow, convective inertia and viscous effects enter the problem. A solvability condition enables a critical Reynolds number to be identified

$$R_1 = \frac{10\left[L_1 Q_0^2(0) + L_2 Q_0^2(1) + \int_0^1 Q_0^2 \,\mathrm{d}x\right]}{Q_0^2(0) - Q_0^2(1)}. \tag{3}$$

This can be interpreted as a ratio of viscous dissipation to kinetic energy flux. Critically, the asymmetry of the system ($L_1 < L_2$) induces asymmetry in the eigenmode; more vigorous sloshing at the upstream end of the channel allows the instability to extract more energy from the mean flow entering the flexible segment of channel than is swept out of its downstream end. The system can therefore be destabilized by increasing the ratio L_2/L_1, which might be achieved by prescribing the downstream flux (setting $L_2 \to \infty$) or minimising upstream inertance. In systems for which the upstream flux is prescribed ($L_1 \to \infty$), instability of the uniform state is not expected to arise through this mechanism. The asymptotic estimate Eq. (3) for $T \gg 1$ agrees well with predictions of the full stability calculation [26].

Further analysis [26] shows that the mode 1 instability contains four independent components (two TWF modes and two SD modes, with one of each type propagating upstream and downstream), and that global instability can arise when all four component modes are convectively stable. Analysis of the history of a disturbance as it propagates upstream, reflects from the rigid segment at $x = 0$, propagates downstream and reflects from $x = 1$ (following [27]) confirms that growth arises from reflections at the boundaries of the flexible segment of channel.

A further notable feature of the mode-1 instability is that, as its amplitude grows, the unsteady sloshing induces a steady pressure gradient along the flexible segment of channel through the action of Reynolds stresses (via the nonlinear q^2/h term in Eq. (1b)). As the pressure drop across the channel is assumed fixed, the effect is to induce an adjustment to the mean flux of the form [26]

$$\overline{q} = 1 + \frac{7RA^2}{240(1 + L_1 + L_2)}\left[Q_0^2(0) - Q_0^2(1)\right], \tag{4}$$

where A is the amplitude of the oscillation. Thus the mode 1 oscillation acts as a pump, increasing the mean flux. As a consequence, mode 1 can arise through a subcritical Hopf bifurcation.

Finally, it is instructive to examine the energy budget of the mode 1 instability. Integrating the energy transport equation over the domain, and averaging over a period of a neutrally stable oscillation, yields an equation of the form

$$\overline{\mathcal{F}} + \overline{\mathcal{P}} = \overline{\mathcal{D}} \tag{5}$$

where $\overline{\mathcal{F}}$ is the net kinetic energy flux, $\overline{\mathcal{P}} = \frac{6}{5} p_u \overline{q}$ is the net work-rate by the upstream pressure, and $\overline{\mathcal{D}}$ is the net viscous dissipation rate. The choice of

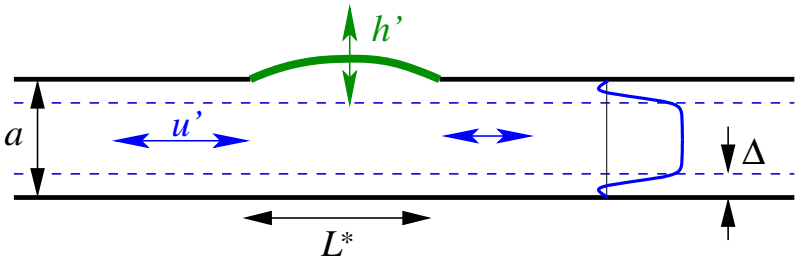

Fig. 3 Sloshing in a 2D channel: the membrane length L^* exceeds the channel width a; transverse wall motions of amplitude h' drive axial flows of magnitude u'; at high frequencies, Stokes layers of width Δ are thin compared to the channel width

wall model implies that zero net work is done on the flexible wall over an oscillation. The denominator in Eq. (3) is proportional to $\overline{\mathcal{F}}$, which must be positive in order to sustain the mode 1 instability. Significantly, numerical simulations of Eqs (1) for an oscillatory mode 2 instability (a secondary instability of a static mode 2 state, arising at lower T) exhibit $\overline{\mathcal{F}} < 0$, indicating that work done by the upstream pressure $\overline{\mathcal{P}}$ provides the source of energy in this case. This mechanism is a likely candidate for the instabilities observed in 2D simulations with prescribed upstream flux [17, 18].

In summary, the 1D model shows that high-frequency mode 1 oscillations arise through wave reflections, not local instability. Asymmetric boundary conditions ($L_1 < L_2$) allow energy to be extracted from the mean flow via kinetic energy fluxes. However, this mechanism is not universal, and other modes may, for example, rely on work done by the upstream pressure as the source of energy.

4 A Two-Dimensional Model

The 1D approach is attractive as analysis is relatively straightforward. However the model described above is predicated on an assumption about the velocity profile that is not uniformly valid across parameter space. In particular, at high frequencies, oscillatory viscous boundary layers (Stokes layers) can be expected to form on the walls of the channel, which were not resolved within the 1D approach. It is therefore desirable to revisit the 2D problem illustrated in Fig. 2 within a fully 2D framework, avoiding any *ad hoc* assumptions. This approach was adopted by Jensen & Heil [28], in a study combining high Reynolds number asymptotics and full simulation of the 2D system, assuming uniform external pressure.

The mode 1 oscillatory instability in a 2D channel is described asymptotically by assuming disturbances are of long wavelength compared to the

channel width, and of sufficiently high frequency for viscous effects to be confined to Stokes layers. The leading-order inviscid 'sloshing' behaviour identified in the 1D model carries over directly to 2D. It is helpful to revisit the scaling argument that captures the primary physical balances, using the dimensional variables illustrated in Fig. 3. Neutrally stable unsteady sloshing at frequency ω involves a balance between unsteady inertia and an axial pressure gradient (i.e. $\rho u_t \sim p_x$, where '$\sim$' denotes 'scales like' and ρ is density) giving a balance $\rho\omega u' \sim p'/L^*$; the pressure is proportional to the curvature of the membrane ($p \sim T^* h_{xx}$) but the high tension ensures deflections are small ($p' \sim T^* h'/L^{*2}$); because the channel is slender, axial flows are larger than transverse ones ($u_x \sim v_y$ implies $v' \sim au'/L^*$); transverse fluid velocities balance wall motion ($v \sim h_t$ implies $v' \sim \omega h'$). Combining these relations yields the frequency estimate $\omega^2 \sim T^* a/\rho L^{*4}$. An energy balance (following Eq. 5) determines the conditions necessary for neutral stability. Viscous dissipation takes place in Stokes layers, of thickness $\Delta \sim (\mu/\rho\omega)^{1/2} \ll a$. For $L_2 > L_1$, the rate of dissipation must balance the net kinetic energy flux into the flexible segment ($\rho U_0 u'^2 a \sim \mu\overline{(u'^2/\Delta^2)}\Delta L^*$), which yields a critical Reynolds number

$$Re = \frac{\rho U_0 a}{\mu} \sim \left(\frac{\rho T^* a}{\mu^2}\right)^{1/4}. \tag{6}$$

This scaling differs from the predictions of the 1D model, because the 1D model used an inconsistent description of viscous dissipation. Detailed analysis is required to determine the coefficient in Eq. (6), which must also be validated against direct numerical simulation [28].

The analysis is pursued in a distinguished limit involving a single small parameter $\delta \ll 1$, whereby the channel length scales like $\delta^{-1/2}$, Reynolds number like $\delta^{-3/2}$ and membrane tension like δ^{-3}. The Navier–Stokes and membrane equations (with uniform p_e) then reduce with error $O(\delta^3)$ to

$$\begin{aligned}
u_x + v_y &= 0 \\
u_t + \delta(\mathbf{u}\cdot\nabla)u &= -p_x + \delta^2 r^{-2} u_{yy} \\
\lambda\delta[v_t + \delta(\mathbf{u}\cdot\nabla)v] &= -p_y \\
u = 0,\ v = h_t,\ p &= p_e - h_{xx} && (y = 1 + \delta h) \\
u &= v = 0 && (y = 0) \\
p &= 12\delta^2 r^{-2}(1 + L_1 + L_2) && (x = -L_1) \\
p &= 0 && (x = 1 + L_2)
\end{aligned}$$

with λ, r, L_1 and L_2 treated as $O(1)$ parameters as $\delta \to 0$. An expansion is constructed, setting $\mathbf{u} = \mathbf{u}_0 + \delta\mathbf{u}_1 + \delta^2\mathbf{u}_2 + \ldots$, with

$$\begin{aligned}
u_0 &= u_{00} + u_{01}e^{i\beta t} + \bar{u}_{01}e^{-i\beta t} \\
u_1 &= u_{10} + u_{11}e^{i\beta t} + \bar{u}_{11}e^{-i\beta t} + u_{12}e^{2i\beta t} + \bar{u}_{12}e^{-2i\beta t} \\
u_2 &= u_{20} + \ldots
\end{aligned}$$

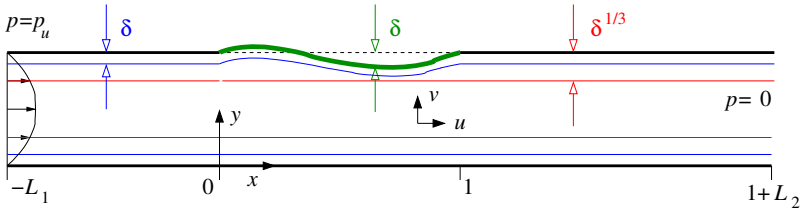

Fig. 4 The asymptotic structure of sloshing flows in a 2D channel. Stokes layers have dimensionless thickness $\delta \ll 1$; membrane displacements are $O(\delta)$; steady streaming boundary layers have thickness $\delta^{1/3}$.

for some $O(1)$ frequency β to be determined, with bars denoting complex conjugates and coefficients depending on slow timescales $t_1 = \delta t$, $t_2 = \delta^2 t$, etc.

The physical structure of the asymptotic problem is illustrated in Fig. 4. In problem 00, the membrane is deflected slightly by the mean pressure ($h_{00} = -\frac{1}{2}p_e x(1-x)$) and the mean flux is uniform Poiseuille flow ($u_{00} = 6q_{00}y(1-y)$, $v_{00} = 0$, $p_{00} = 0$), but with the flux q_{00} undetermined to this order. Stokes layers of thickness $O(\delta)$ appear in problems 01, 11; a Prandtl transformation is used to wrap the upper Stokes layer onto the membrane (Fig. 4). Steady-streaming boundary layers of thickness $O(\delta^{1/3})$ appear in problems 10 and 20. The inviscid sloshing mode appears in problem 01. The leading-order eigenmode $h_{01} = A(t_1)\phi_{01}(x)$, where A is a slowly varying amplitude, is determined exactly as in the 1D model (Sec. 3). Interaction between the mean flow and the sloshing motion arises in problem 11, where again a solvability condition is imposed to determine a condition for neutral stability in terms of the rescaled Reynolds number

$$r = \frac{(2\beta)^{\frac{1}{2}}}{q_{00}} \frac{\int_0^1 \phi_{01x}^2 \,\mathrm{d}x}{\phi_{01x}^2(1) - \phi_{01x}^2(0)}, \tag{7}$$

which is positive for $L_2 > L_1$. This expression provides the coefficient in (6). However the mean flux q_{00} remains undetermined to this order. To determine q_{00}, it is necessary to consider the time-averaged Reynolds stresses $\overline{(\mathbf{u}_0 \cdot \nabla)u_0}$, which create a steady pressure gradient in the core to which q_{00} must adjust (the analogue of Eq. (4)). Further contributions to the mean flow come from steady streaming driven by Stokes layers and by deflection due to indentation of the membrane by p_e.

The energy budget for the neutral oscillation is again given by Eq. (5), where the dissipation rate can be partitioned into a contribution from the Stokes layers $\overline{\mathcal{D}_S}$ plus that in the core $\overline{\mathcal{D}_P}$. Accounting for mean flow adjustment, this partition turns out to be in a precise 2:1 ratio, with $\overline{\mathcal{D}_S} = \frac{2}{3}\overline{\mathcal{F}} > 0$, $\overline{\mathcal{D}_P} = \overline{\mathcal{P}} + \frac{1}{3}\overline{\mathcal{F}}$.

The asymptotic prediction Eq. (7) with $q_{00} = 1$ was tested against simulations conducted using a finite-element method in which the Navier–Stokes

and membrane equations were fully coupled [28]. The initial-value problem was solved following a jump in p_e. For $\delta = 0.3$ — not a particularly small value — the predicted transitional Reynolds number (around 400) differed from that determined by simulation by less than 10%; predicted frequencies and growth rates were more accurately predicted for smaller δ. Thus the mechanism of mode 1 oscillation identified (albeit qualitatively) in the 1D model therefore carries through to 2D, where it can be described using rational validated asymptotics.

5 Towards a Three-Dimensional Model

Having identified a mechanism of instability in a flexible channel using an approximate 1D approach (Sec. 3), and produced a refined asymptotic description of its operation in 2D (Sec. 4), the next obvious step is to ask how this mechanism might operate in a more realistic 3D tube.

Heil & Waters [29] addressed this problem theoretically by considering axial sloshing flows generated in a circular tube. They prescribed periodic wall motions with azimuthal mode number 2 (resembling elliptical post-buckled configurations) of small ($O(\epsilon)$) amplitude, high frequency and long wavelength. Because the base state they examined was axisymmetric, the area change during an oscillation was small and the induced sloshing was of magnitude $O(\epsilon^2)$, with transverse oscillations being decoupled from the axial flow. While such weak sloshing inhibits energy transfer from the mean flow via kinetic energy fluxes, the decoupling made it feasible to study the transverse flow-structure interaction, with wall bending balancing unsteady fluid inertia, and viscous dissipation (in Stokes layers and the core) determining the decay rate of oscillatory modes. The imposed symmetry of the computations accommodated buckled states symmetric about orthogonal axes, with the primary buckling being either horizontal or vertical (cross-sections are illustrated schematically in Fig. 5(a)). Large-amplitude oscillations decayed first by switching between these two states during each period (motion denoted as 'Type I' in [29]), before jumping to one of the two states (becoming a 'Type II' oscillation) and then decaying towards the corresponding equilibrium buckled configuration. The dynamics is reminiscent of a Duffing oscillator, and is illustrated in a schematic phase plane in Fig. 5(a). The switch from Type I to Type II can then be interpreted as the passage of a trajectory in phase space past a saddle point corresponding to the unbuckled equilibrium state. It is notable that recently reported 3D simulations of self-excited oscillations [19, 22] exhibit sustained Type-I oscillations, illustrated schematically by the limit cycle in Fig. 5(b). This in turns suggests the likelihood of homoclinic bifurcations arising from the collision of limit cycles with fixed points, reported in this context in [9].

To ensure that transverse wall motion would generate a strong axial sloshing flow, Heil & Waters [30] then computed the unsteady 3D flow through

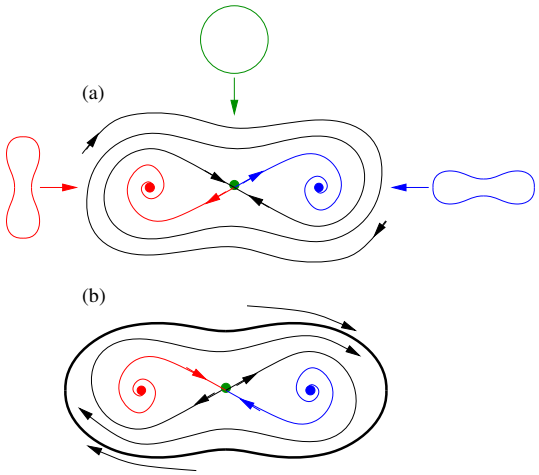

Fig. 5 (a) A phase portrait of a Duffing oscillator, which captures the dominant dynamics of decaying oscillations in an elastic ring, reported in [29]. Initial large-amplitude Type-I oscillations that flip between vertically and horizontally buckled states ultimately decay to smaller-amplitude Type-II oscillations in one of the two states. Cross-sections at fixed points are illustrated. (b) A stabe limit cycle of Type I.

a non-axisymmetric tube, a segment of which underwent prescribed small-amplitude wall motion of frequency ω. This motion was formulated as a set of Fourier modes in axial and azimuthal coordinates for which the tube perimeter was preserved. The non-axisymmetric base state, combined with area-changing perturbations of $O(\epsilon)$ amplitude, ensured $O(\epsilon)$ sloshing. The flux at the downstream end of the tube was prescribed, a condition expected to promote kinetic energy transfer from the mean flow (as explained following Eq. 3). Simulations showed how energy could indeed be transferred to the wall, provided α/St exceeded a threshold (where $\alpha = a(\rho\omega/\mu)^{1/2}$ is the Womersley number, $St = a\omega/\mathcal{U}$ the Strouhal number, a an effective tube radius and $\mathcal{U}$ a measure of the imposed axial flow), again reflecting a balance of kinetic energy flux with dissipation in Stokes layers.

This finding has been generalised in a recent study by Whittaker et al. [31] in which the necessary asymptotic conditions for prescribed wall motion to extract energy from the mean flow have been identified. Here flow through a tube is considered in which the shape of the cross-section is arbitrary except that it varies slowly in the axial direction and exhibits small-amplitude temporal oscillations. The tube centreline is straight and lies on $0 < z < L$. Oscillations about the base state are prescribed, and a flow is driven through the tube under fixed flux or under prescribed pressure drop. The tube kinematics can be characterized using just a handful of quantities: the perimeter

$\mathbb{P}(\check{z})$ and cross-sectional area $A_0(\check{z})$ of the base state (as a function of axial distance $\check{z} = z/L$); the oscillatory area change in each cross-section $\mathbb{A}(\check{z})$; and the volume variation along the tube $\mathbb{V}(\check{z})$ arising from the axially integrated area changes. The flow is characterized by Strouhal and Womersley numbers (St and α, as defined above), tube length $\ell = L/a$ and oscillation amplitude Λ. Once again, a distinguished limit is considered in which the kinetic energy flux balances dissipation in Stokes layers, and wall motions are assumed to be long wave and small amplitude, i.e.

$$1 \ll \alpha \sim \ell St \sim \ell^2 \ll \frac{1}{\Lambda}. \tag{8}$$

The asymptotic approach to this problem follows that outlined in Secs 3 and 4, but inevitably is more involved. Variables are decomposed into steady, period-1 and period 2 or greater, in the core and in Stokes layers, and the Navier–Stokes equations are decomposed accordingly. The system is expanded in powers of the small amplitude, with the core and boundary-layer problems being treated separately. The leading-order inviscid sloshing problem is governed by a Poisson problem; associated Stokes layers eject flux into the core. Sloshing generates Reynolds stresses, the steady component of which adjusts the dimensionless mean flux $\mathbb{Q}$ (under prescribed pressure conditions) or the net pressure drop (when the flux is prescribed). The energy budget for small amplitude periodic oscillations, integrated over the flow domain, is expressed as

$$\mathcal{E} = \mathcal{F} + \mathcal{P} - \mathcal{D}, \tag{9}$$

where $\mathcal{E}$ is the work done on the wall by the fluid, $\mathcal{F}$ is the kinetic energy flux, $\mathcal{P}$ is the work done by the upstream pressure and $\mathcal{D}$ the dissipation. Decomposition of Eq. (9) into steady and oscillatory components allows the former to be studied independently. As for the 2D problem (Sec. 4), there is a remarkably precise partition of energy, with 2/3 of the kinetic energy flux due to sloshing being available to do work on the walls and the remaining 1/3 being dissipated in the mean flow or doing work against pressure at the tube ends. The condition that there is zero energy transfer to the wall over a period (Eq. (5)) yields a simple condition on the inverse Strouhal number (or equivalently a critical Reynolds number α^2/St_c) that resembles Eqs (3) and (7) in being the ratio of viscous dissipation to kinetic energy flux, this ratio being expressed in the form [31]

$$\frac{\alpha}{\ell St_c} \sim C(\mathbb{Q}; \mathbb{V}, A_0, \mathbb{P}) \tag{10}$$

where C is a functional of the kinematic variables. Eq. (10) has been validated against 3D simulations in an elliptical tube with prescribed wall motion [31], showing good agreement across a range of α and ℓ for both prescribed flux and prescribed pressure boundary conditions. Further work is required to test this stability prediction when the prescribed wall displacement is replaced by a normal mode of the tube, accounting for fully unsteady 3D flow-structure interaction.

6 Discussion

This brief review has hopefully demonstrated the usefulness of using a hierarchy of models to understand instabilities of flows in the Starling Resistor. In particular, low-dimensional approximations have provided valuable signposts for more elaborate asymptotic and computational models. Stability thresholds of increasing accuracy ((3), (7) and (10)) have been used to characterise a potential mechanism of high-frequency self-excited oscillation. Further steps are needed to establish a definitive connection between this mechanism and what happens in the real experimental device: in particular, unsteady simulations of the 3D problem must be analysed to establish the nature of energy budgets, and the simulations must themselves be validated against experiment. It is important to recognise also that the 'sloshing' mechanism described above is not generic: the 1D model shows how oscillations with a quite distinct energy signature can arise [26] where the dominant energy source is work done by the upstream pressure, from which oscillations may be able to sustain themselves by increasing the mean flux. Simulations in 2D highlight a potential role for internal hydrodynamic modes [17, 18], and recent 3D simulations demonstrate the dominant role of buckling instabilities [20, 22].

The distinguished physiologist Ernest Starling [4] will not have appreciated how much he contributed to the study of flow-structure interaction by inventing his Resistor.

Acknowledgements. Jonathan Boyle, Matthias Heil, Peter Stewart, Sarah Waters and Robert Whittaker have contributed to many of the developments reported above. Support from the Royal Society is gratefully acknowledged. This article is dedicated to the memory of Peter W. Carpenter (1942–2008), who made lasting and profound contributions to the study of flows interacting with compliant surfaces.

References

1. Pedley, T.J., Brook, B.S., Seymour, R.S.: Blood pressure and flow rate in the giraffe jugular vein. Phil. Trans. Roy. Soc. B 351, 855–866 (1996)
2. Heil, M., Jensen, O.E.: Flows in deformable tubes and channels - Theoretical models and biological applications. In: Carpenter, P.W., Pedley, T.J. (eds.) Flow Past Highly Compliant Boundaries and in Collapsible Tubes, IUTAM Proceedings, vol. 72. Springer (2003)
3. Grotberg, J.B., Jensen, O.E.: Biofluidmechanics of flexible tubes. Ann. Rev. Fluid Mech. 36, 121–147 (2004)
4. Knowlton, F.P., Starling, E.H.: The influence of variations in temperature and blood-pressure on the performance of the isolated mammalian heart. J. Physiol. London 44, 206–219 (1912)
5. Bertram, C.D., Raymond, C.J., Pedley, T.J.: Mapping of instabilities for flow through collapsed tubes of differing length. J. Fluids Struct. 4, 125–153 (1990)

6. Bertram, C.D., Tscherry, J.: The onset of flow-rate limitation and flow-induced oscillations in collapsible tubes. J. Fluids Struct. 22, 1029–1045 (2006)
7. Pedley, T.J., Luo, X.Y.: Modelling flow and oscillations in collapsible tubes. Theor. Comput. Fluid. Dyn. 10, 277–294 (1998)
8. Bertram, C.D., Pedley, T.J.: A mathematical model of collapsible tube behaviour. J. Biomech. 15, 39–50 (1982)
9. Armitstead, J., Bertram, C.D., Jensen, O.E.: A study of the bifurcation behaviour of a model of flow through a collapsible tube. Bull. Math. Biol. 58, 611–641 (1996)
10. Shapiro, A.H.: Steady flow in collapsible tubes. J. Biomech. Engng. 99, 126–147 (1977)
11. Cancelli, C., Pedley, T.J.: A separated-flow model for collapsible-tube oscillations. J. Fluid Mech. 157, 375–404 (1985)
12. Hayashi, S., Hayase, T., Kawamura, H.: Numerical analysis for stability and self-excited oscillation in collapsible tube flow. J. Biomech. Engng. 120, 468–475 (1998)
13. Jensen, O.E., Pedley, T.J.: The existence of steady flow in a collapsed tube. J. Fluid Mech. 206, 339–374 (1989)
14. Jensen, O.E.: Instabilities of flow in a collapsed tube. J. Fluid Mech. 220, 623–659 (1990)
15. Pedley, T.J.: Longitudinal tension variation in collapsible channels: a new mechanism for the breakdown of steady flow. J. Biomech. Engng. 114, 60–67 (1992)
16. Guneratne, J., Pedley, T.J.: High Reynolds number steady flow in a collapsible channel. J. Fluid Mech. 569, 151–184 (2006)
17. Luo, X.Y., Pedley, T.J.: A numerical simulation of unsteady flow in a two-dimensional collapsible channel. J. Fluid Mech. 314, 191–225 (1996)
18. Luo, X.Y., Cai, Z.X., Li, W.G., Pedley, T.J.: The cascade structure of linear instability in collapsible channel flows. J. Fluid Mech. 600, 45–76 (2008)
19. Heil, M., Hazel, A.L., Boyle, J.: Solvers for large-displacement fluid-structure interaction problems: segregated versus monolithic approaches. Comput. Mech. 43, 91–101 (2008)
20. Hazel, A.L., Heil, M.: Steady finite Reynolds number flows in three-dimensional collapsible tubes. J. Fluid Mech. 486, 79–103 (2003)
21. Marzo, A., Luo, X.Y., Bertram, C.D.: Three-dimensional collapse and steady flow in thick-walled flexible tubes. J. Fluids Struct. 20, 817–835 (2005)
22. Heil, M., Boyle, J.: Recent progress in the theoretical and computational modelling of flow in 3D collapsible tubes. XXII ICTAM, Adelaide, Australia (2008)
23. Benjamin, T.B.: The threefold classificion of unstable disturbances in flexible surface bounding inviscid flows. J. Fluid Mech. 16, 436–450 (1963)
24. Landahl, M.: On the stability of a laminar incompressible boundary layer over a flexible surface. J. Fluid Mech. 13, 609–632 (1962)
25. Davies, C., Carpenter, P.W.: Instabilities in plane channel flow between compliant walls. J. Fluid Mech. 352, 205–243 (1997)
26. Stewart, P.S., Waters, S.L., Jensen, O.E.: Local and global instabilities of flow in a flexible-walled channel (2008) (submitted)
27. Doaré, O., de Langre, E.: The role of boundary conditions in the instability of one-dimensional systems. Eur. J. Mech. B 25, 948–959 (2006)
28. Jensen, O.E., Heil, M.: High-frequency self-excited oscillations in a collapsible-channel flow. J. Fluid Mech. 481, 235–268 (2003)

29. Heil, M., Waters, S.L.: Transverse flows in rapidly oscillating elastic cylindrical shells. J. Fluid Mech. 547, 185–214 (2006)
30. Heil, M., Waters, S.L.: How rapidly oscillating collapsible tubes extract energy from a viscous mean flow. J. Fluid Mech. 601, 199–227 (2008)
31. Whittaker, R.J., Waters, S.L., Jensen, O.E., Boyle, J., Heil, M.: The energetics of flow through a rapidly oscillating tube. Part I: general theory. Part II: application to an elliptical tube (preprint) (2008)

Surface Bubbles in Micro- and Nanofluidics

Bram Borkent and Detlef Lohse

Physics of Fluids, Faculty of Science and Technology,
J.M. Burgers Centre for Fluid Dynamics, and MESA$^+$ and Impact Institutes,
University of Twente, P.O. Box 217, 7500 AE Enschede, The Netherlands
d.lohse@utwente.nl

Abstract. In this Proceeding we review and summarize recent findings of the Twente Physics of Fluids group on controlled cavitation of surface microbubbles [1–4] and surface nanobubbles [5] and in addition give some overview on the Twente findings on surface nanobubbles [6–9]. – Gas accumulation at liquid-solid interfaces can occur in the form of bubbles, for instance at a surface defect. The resulting micro- and nanoscale air pockets can act as nucleation sites in shockwave-induced cavitation experiments, leading to the random nature of cavitation, both in space and time. However, by controlling the size and the position of the defects, Bremond et al. [2; 3] succeeded to make cavitation perfectly reproducible both in time and space. This technique made it possible to study the dynamics of individual bubbles, bubble pairs, and bubble clusters emerging from the defects in an extremely reproducible fashion. In addition, by further minaturizing the pits down to diameters of 100nm, Borkent et al. [4] could measure the pressure at which these bubbles start to nucleate, giving results in perfect agreement with the theory by Atchley and Prosperetti [10]. In contrast, so-called surface nanobubbles, though comparible in size and volume to the bubbles in the nanopits, do not act as nucleation sites in cavitation experiments [5]. Finally, we report on some typical properties of surface nanobubbles [6] and report that they can be created in a reproducible and controllable way by electrolysis [8]. That suggests that these surface nanobubbles are in a dynamic equilibrium, i.e., gas in- and outflux are balanced. Such a dynamic stabilization has also been suggested for standard surface nanobubbles [11].

1 Introduction

Water in contact with (in particular hydrophobic) solid surfaces can contain submicroscopic air bubbles at the solid interface. The bubbles are stabilized by surface defects and/or impurities and generally they are not visible with the naked eye. An example is provided by the daily life situation of freshly

drawn tap water in a glass beaker. Since the water is slightly oversaturated once it comes out of the pipe system, the water gets rid off its excess gas through diffusion and bubbles - which were initially not visible - suddenly appear at the glass interface. These growing surface bubbles originated on much smaller length scales, where they started from microscopic gas bubbles trapped in tiny surface imperfections. In general, surface bubbles may become important in micro- and nanofluidic environments, since - depending on the shape, stability, and number densities of the bubbles - they may alter hydrodynamic boundary conditions, form nucleation sites in boiling and cavitating liquids, or affect chemical surface reactions. A detailed understanding of surface bubbles on these small length scales will therefore be of great potential value for various applications like Lab-on-a-Chip devices, inkjet printing, megasonic cleaning, boiling, and sonochemistry.

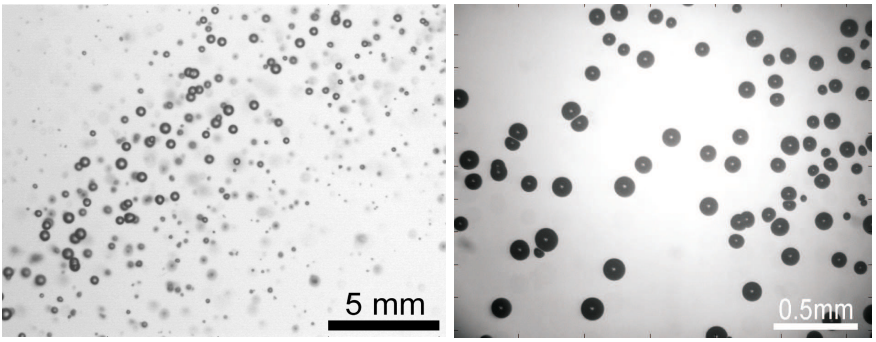

Fig. 1 Cloud cavitation at particles in suspension (left, taken from [12]) and randomly distributed cavitating bubbles on a surface (right)

2 Controlled Surface Bubble Cavitation

Cavitation is a well-known phenomenon which occurs undesirably around ship propellers, rudders, and in water turbines [13]. The noise emitted by the collapsing bubbles can be a nuisance, while the destructive nature of aspherical bubble collapses is even more problematic, since it can lead to surface erosion. The destructive power of cavitation bubbles, however, can also be beneficial, e.g. for cleaning jewelry, glasses, or semiconductor surfaces or for a snapping shrimp when killing prey animal through a cavitating bubble [14]. In all these cases, the rapid growth of vapor bubbles occurs due to a local stress in the liquid, which can be applied either by hydrodynamic or acoustic means [13]. One of the main issues in cavitation research is: Where do the bubbles originate exactly? It has been postulated that the bubbles are nucleated from microscopic gas pockets, trapped at surface defects [15], such as walls or suspended particles. Indeed, in many practical applications

surfaces are not completely smooth and the water is not entirely free from tiny particles, and as a result cavitation clouds of all kinds can occur [1; 12; 16; 17] (see Fig. 1). How can one control these cavitation nuclei? Once the bubbles emerge from their nucleation sites, another issue arises too: how to describe the bubble-bubble dynamics? For sure the bubbles will interact with each other, but how can one measure and describe this quantitatively?

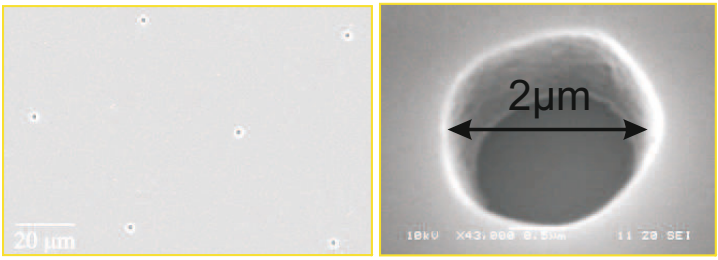

Fig. 2 Microholes positioned on a silicon surface, shown on two different scales. Figure taken from [2].

2.1 Experimental Setup

A way to tackle both problems in one experiment is by controlling the surface defects down to the microscopic level and by positioning them very precisely on a two-dimensional surface (Bremond et al. [1–3]). Standard lithography techniques allow to etch cylindrical pits of uniform sizes (typically $2, \mu$m) into pieces of silicon and to put the pits on predefined locations (Fig. 2). After coating the surface with a monolayer of hydrophobic molecules, the pits will entrap air once the surface is submerged in water.

To nucleate bubbles Bremond et al. used a commercially available lithotripter, which consists of a focused array of piezoelectric elements at the bottom of a liquid bath, which is filled with gas-saturated ultrapure MilliQ water (Fig. 3). This technique made it possible to generate shock waves in water, which typically look like the pulse depicted in Fig. 3: The pressure first rose and after a few μs it droped and became negative down to values of ~ -15 bar or more. After some small reflections the pressure got restored to its atmospheric value. The bubbles could be recorded in reflection mode through either high-speed video imaging or simply by taking single snapshots. Since the resulting bubble dynamics turned out to be extremely reproducible, Bremond et al. chose the latter option and recorded images with a high resolution CCD camera. By shifting the trigger of the shock wave source in repeated experiments they could obtain high-resolution stroboscopic videos, from which the bubble sizes could be extracted.

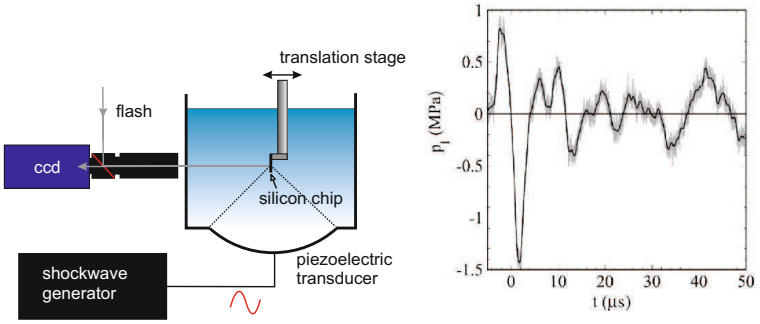

Fig. 3 Experimental setup (left) and employed pressure wave (right) employed in the controlled cavitation experiments of Bremond et al. [2]

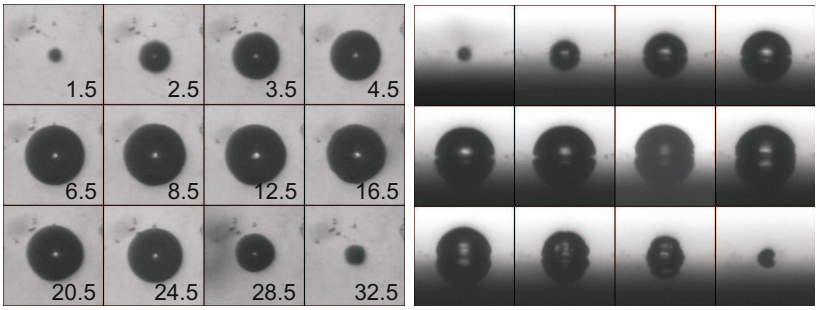

Fig. 4 Top and side view of the dynamics of a single cavitating surface microbubble. The numbers represent the time (in microseconds) after inception. At maximum, the bubble is around 150μm in radius. Figure taken from [3].

2.2 Single Bubble

The simplest scenario to study is the case of a single bubble. Figure 4 depicts the resulting images both from top and side view for a single bubble subjected to a minimum negative pressure of $p_m = -2\,\mathrm{MPa}$. The bubble grows rapidly in the first microseconds and then collapses at around $32.5\,\mu$s. The bubble radius R can be extracted from the top view images. The side view shows that the bubble is essentially hemi-spherical in shape during the majority of its lifetime. The hemi-spherical bubble together with its hemi-spherical image bubbles can be interpreted as spherical bubble, (neglecting viscous effects directly at the wall). The situation is thus equivalent to that of a spherically symmetric bubble and the standard Rayleigh-Plesset equation can be applied,

$$R\ddot{R} + \frac{3}{2}\dot{R}^2 = \frac{1}{\rho}\left(p_v + p_g - p_\infty - \frac{2\sigma}{R} - 4\mu\frac{\dot{R}}{R}\right). \tag{1}$$

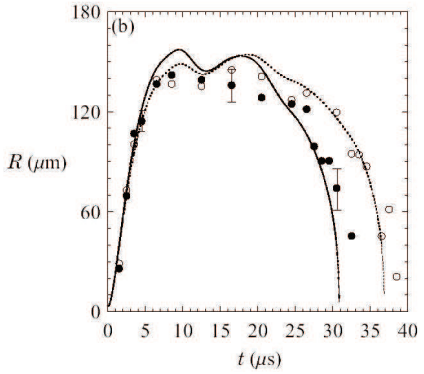

Fig. 5 Bubble radius as function of time for one isolated surface microbubble (solid circles) and two neighboring surface microbubbles (open circles; the initial distance is $d = 400\mu$m). The correspondingly theoretical curves are also shown. Figure taken from [3].

Here p_v and p_g are the pressure of the gas and vapor in the bubble, p_∞ the liquid pressure far away, and σ and μ the liquid surface tension and dynamic viscosity, respectively. Integration of Eq. 1 using the measured pressure profile $p_\infty(t)$ gives a theoretical prediction of the radial bubble dynamics. Comparing this result with the experimental observations gives a perfect match, as shown in Fig. 5.

2.3 Two Bubbles

In the case of two bubbles the situation becomes more complex since the bubbles will interact with each other through acoustic coupling. Typical experimental results of two bubbles subjected to $p_m = -2\,$MPa, but with different interdistances d, are shown in Fig. 6. In the left case ($d = 400\,\mu$m), both bubbles remain essentially spherical during their whole lifetime (so-called "weak interaction regime"). However, the stage of bubble collapse happens a few microseconds later than in the single bubble case, thanks to mutual shielding of the bubbles. This effect can be embodied into the Rayleigh-Plesset equation by adding the sound emission of the neighboring bubble, leading to

$$R\ddot{R} + \frac{3}{2}\dot{R}^2 = \frac{1}{\rho}\left(p_v + p_g - p_\infty - \rho\frac{R}{d}(R\ddot{R} + 2\dot{R}^2) - \frac{2\sigma}{R} - 4\mu\frac{\dot{R}}{R}\right). \qquad (2)$$

Indeed, the $R(t)$ curve resulting from this extended Rayleigh-Plesset equation (2) leads to a delayed bubble collapse for the two bubble case, see figure 5, in good quantitative agreement with the measurements, despite the fact that the bubbles feel an anisotropic pressure field around their surface, especially

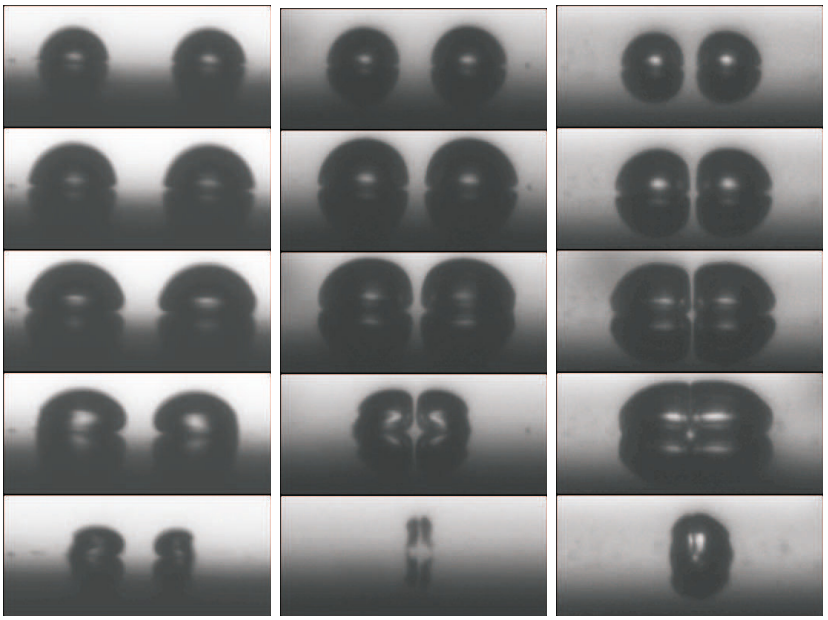

Fig. 6 Dynamics of the interaction of two surface microbubbles with initial distance of $d = 400\,\mu$m, $d = 300\,\mu$m, and $200\,\mu$m, respectively (left to right). At maximum, the bubbles are about 150μm in radius. Figure taken from [3].

in the last stage of their collapse. When the bubbles come closer to each other (middle and right column of Fig. 6, with $d = 300\,\mu$m and $200\,\mu$m resp.), the bubbles loose their hemi-spherical symmetry much earlier ("strong interaction regime") and Eq. 2 cannot be applied anymore. Instead, the dynamics of the interacting collapsing bubbles and the film thinning in between the bubbles can be described with boundary integral methods [3].

2.4 Bubbles in a Row and a Bubble Matrix

The next step is to extent the number of bubbles to three or even more, in order to study multiple bubble interactions, as again done by Bremond et al. [3]. The bubbles were either aligned in a row (Fig. 7) or ordered in a hexagonal structure (Fig. 8), with in both cases $d = 200\mu$m and $p_m = -1.4\,$MPa. In Fig. 7 (left column) the three inner bubbles are 'shielded' from the surrounding liquid by the outer bubbles and collapse much later. Since the bubbles strongly deform, their dynamics cannot be described by Eq. 2. Fortunately, two plains of symmetry are present (wall and z-axis), which makes it possible to employ an axisymmetrical boundary integral code to describe the bubble dynamics. The features of the numerical scheme were based on a method de-

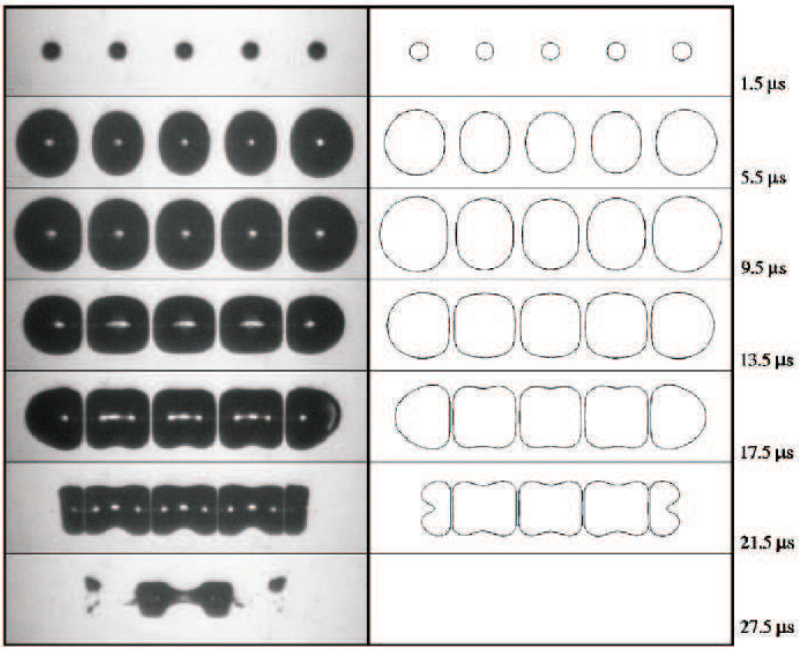

Fig. 7 Dynamics of five cavitating surface microbubbles with initial distance of $d = 200\mu$m in a row: experiment (left) and boundary integral simulation (right). Figure taken from [3].

veloped by Oğuz and Prosperetti [18], and were validated for the single and two-bubble cases. The result of the simulations (Fig. 7, right column) could be directly compared with experimental top views (left column), with nice agreement between the two. The screening effect, as visible in the previous example, is even more pronounced for the bubbles located in an hexagonal array (Fig. 8). The center bubble is now shielded from all sides and clearly collapses at last. In addition, wall-normal jets directed towards the centre of the bubble cluster become nicely visible during the collapse phases of the outer bubbles. These jets develop due to an asymmetry in the liquid phase surrounding the bubble. They are similar to wall-normal jets for single bubbles close to a wall. Since the bubbles in this example stayed hemi-spherical during the majority of their lifetimes, Eq. 2 could be applied with good success [2].

2.5 Cavitation from Nano-sized Pits

The perfect reproducibility of the experiment and the spatial control of nuclei were two important ingredients for the experiment of Borkent et al. [4]. These

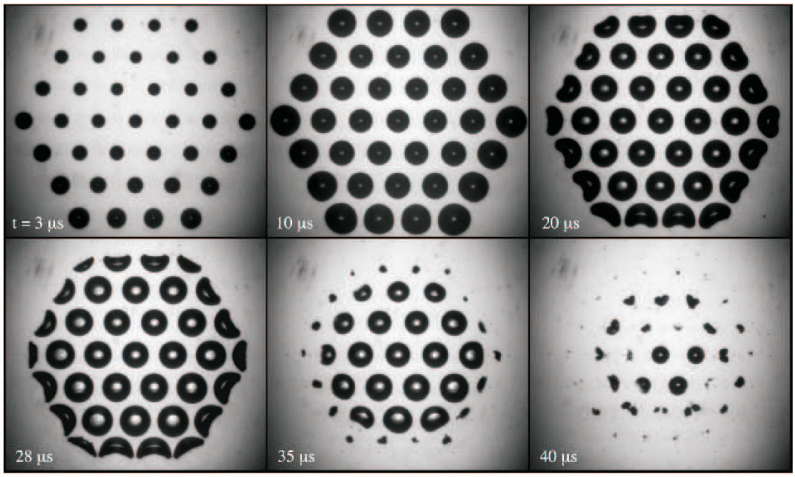

Fig. 8 Dynamics of cavitating surface microbubbles with initial distance of $d = 200\mu$m. Figure taken from [2].

authors verified the theoretical nucleation threshold of surface bubbles, as developed by Atchley and Prosperetti in 1989 [10]. According to this theory, the minimum liquid pressure p_m needed to nucleate a bubble trapped in a cylindrical pit with radius r_c and depth d_c, is

$$p_m = p_v + \frac{3p_{g,0}}{3 + (r_c/d_c)g(\theta_R)/\sin^3\theta_R} - \frac{2\sigma\sin\theta_R}{r_c} \quad . \tag{3}$$

Here θ_R is the receding liquid contact angle on the plain surface and $g(\theta_R)$ a geometrical factor. For small pits the third term on the righthand side of Eq. 3 is dominant and thus p_m inversely proportional to r_c. Therefore one needs very small cavities to measure large differences in p_m. For this purpose, Borkent et al. have produced three samples with square arrays containing uniformly sized pits with diameters of 900 nm, 500 nm, and 100 nm resp. (Fig. 9).

For each array, Borkent et al. decreased the minimum pressure of the shockwave applied to the liquid, until all bubbles of the array were nucleated

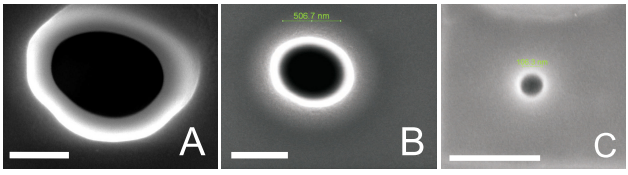

Fig. 9 SEM picture of nanopits with diameters of 900 nm, 500 nm, and 100 nm respectively. Figure taken from [4].

(as observed by the camera). The bubble patterns are shown in Fig. 10 and the resulting nucleation phase diagram is shown in Fig. 11. In this plot, the line is the theoretical prediction according to Eq. 3. It perfectly matches the experimental results. The results of Borkent et al. [4] were the first demonstration that nucleation of surface bubbles down to nanometer length scales can be fully controlled and quantitatively understood.

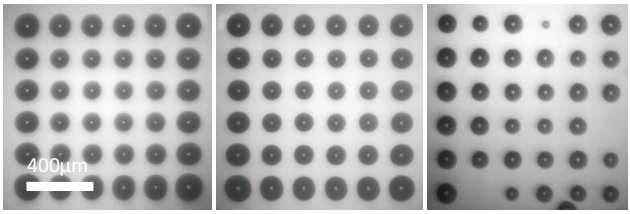

Fig. 10 Cavitation bubbles nucleated from cylindrical pits with radius $r_c = 495\,\text{nm}$ (left), $r_c = 246\,\text{nm}$ (middle) and $r_c = 53\,\text{nm}$ (right), and depth $d_c = 2r_c$ for a pressure pulse with $p_m = -3.2\,\text{MPa}$. Figure taken from [4].

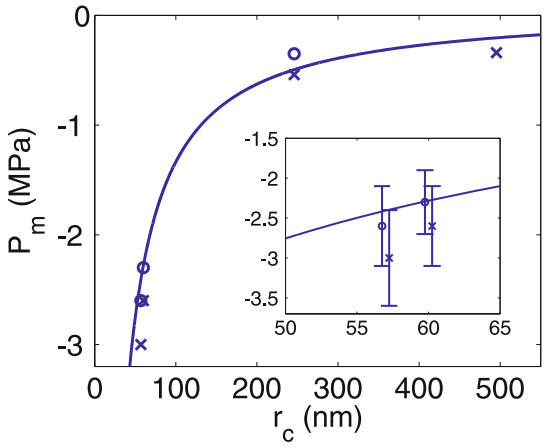

Fig. 11 Nucleation threshold as function of the pit radius for both theory (line) and experiment (symbols, crosses: nucleation, circles: no nucleation). The inset shows a zoom in with errorbars. For visibility overlapping points are shifted $\pm 0.25\,\text{nm}$ with respect to each other. Figure taken from [4].

3 Surface Nanobubbles

In this review we up to now dealt with surface micro- and nanobubbles in artifically produced surface pits. These bubbles served as cavitation nuclei.

One wonders whether also naturally formed surface bubbles can serve as such nuclei. A good candidate would be so-called surface nanobubbles. Before we will address this question in subsection 4.2, we will first summarize some of their properties.

3.1 What Are Surface Nanobubbles?

Surface nanobubbles are spherically cap-shaped objects residing at atomically smooth hydrophobic surfaces (hydrophobized Si, graphite, etc.) [19; 20]. The features are typically $\sim 10\,\text{nm}$ in height and $\sim 100\,\text{nm}$ in diameter, are able to merge together [21; 22], disappear in degassed water [23] and re-appear when the water is gas-oversaturated [5–7; 24–26]. Hence, they are believed to consist of gas. As they are not visible with normal light, Atomic Force Microscopy in tapping mode is employed to image the bubbles. Here, the oscillations of a vibrating cantilever (with a sharp tip) are measured and are kept constant with a feedback mechanism. Once the tip of the cantilever comes close to a surface, the amplitude of the vibration becomes smaller and the system tracks the surface structure. In this way, topography images of a solid-liquid interface can be obtained. With this technique, surface nanobubbles have been imaged successfully, and it is found that they are surprisingly stable. Since the bubbles have a radius of curvature R_c on the order of $\sim 100\,\text{nm}$, the Laplace excess pressure $2\sigma/R_c$ is several bars and should lead to rapid dissolution of the bubbles within milliseconds [27; 28]. This is not observed: in experiments the bubbles are stable for hours, or even days [26].

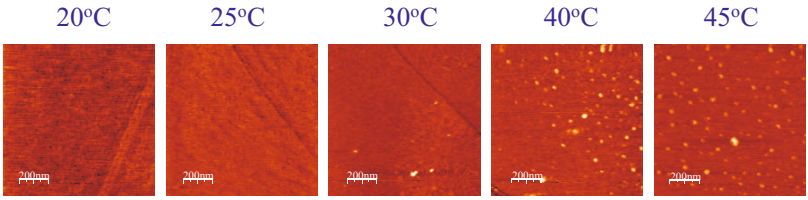

Fig. 12 Surface nanobubble formation on a silanated Si surface with increasing temperature. Figure taken from [6].

One example of a series of AFM images is shown in Fig. 12. Here, the temperature of a water droplet is increased before deposition on a piece of hydrophobized silicon wafer [6]. The topography of the solid-liquid interface shows a rapid increase in number density of nanobubbles for increasing temperature. This observation can be understood as follows: The gas solubility of water decreases with increasing temperature. If the water is heated quickly, the excess amount of gas has not enough time to escape to the environment.

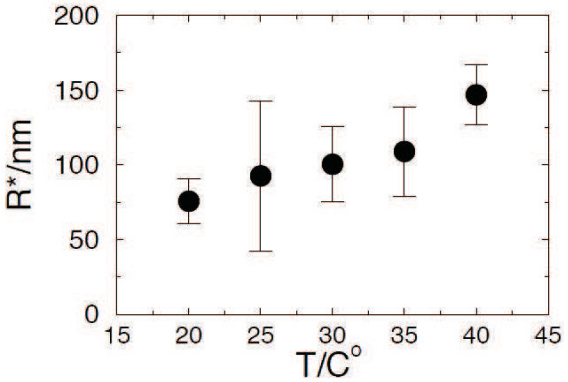

Fig. 13 Preferred surface nanobubble radius of the nanobubbles of figure 12. The error bar represents one standard deviation.

As a result, the water becomes slightly oversaturated with gas, which stimulates the formation of interfacial air bubbles. The bubbles become larger as well: A statistical analysis on the radius of the nanobubles present in Fig. 12 and in a number of repeated experiments (not shown) shows that the nanobubble radius increases as a function of temperature, see Fig. 13.

3.2 Surface Nanobubbles Subjected to Extreme Stresses

As surface nanobubbles have sizes similar to the nanopits used in the previous experiment, Borkent et al. [4] asked whether it is possible to nucleate surface nanobubbles to visible sizes. According to Eq. 3, or alternatively Eq. 1, this should be possible. If one could nucleate these nanobubbles, this would disclose a new type of nucleation sites, while in addition this would provide a relatively easy method to check whether surface nanobubbles are present on a surface. In the experiment Borkent et al. used hydrophobized silicon samples without any surface defects. First, they check with AFM that surface nanobubbles were densely present on these surfaces, after having submerged the sample in clean water (Fig. 14, top right). However, when Borkent et al. subjected the same sample to a negative pressure, which was ten times stronger than according to Eq. 3 would be needed, they saw hardly any cavitation (Fig. 14 top left). Only occasionally one or two bubbles are visible, presumably from a small bubble trapped by some surface contamination (note the difference in scales between the left and the right pictures). By applying a forced-oversaturation (flushing ethanol away with water), larger surface nanobubbles could be created in a reproducible way. Strikingly, this did not help at all: not a single nanobubble was nucleated to visible size in the cavitation experiment (Fig. 14 down left). To check whether the nanobubbles had

been removed by the strong shock wave, Borkent et al. took the very same surface, kept it immersed in water, and measured the solid-liquid interface with AFM. Remarkably, they found that the surface was still covered with hundreds of large surface nanobubbles (Fig. 14 down right)! The experiments by Borkent et al. have thus revealed that surface nanobubbles are no suitable nucleation sites in shock-wave induced cavitation experiments, in contrast to nanobubbles trapped in pits of similar sizes, see Fig. 15. Remarkably, surface nanobubbles are able to survive huge pressure sweeps. Borkent et al. denoted this property as "superstability" of surface nanobubbles.

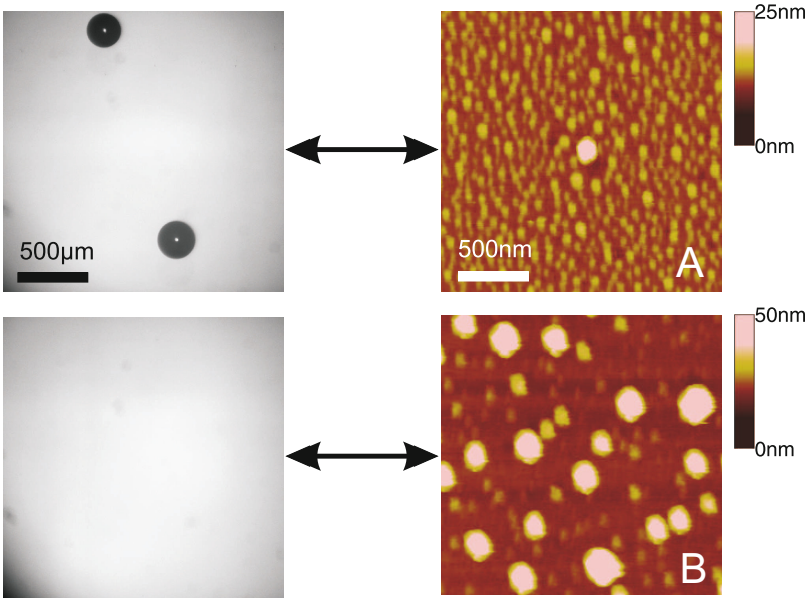

Fig. 14 In spite of high nanobubble concentration (right) there is hardly any cavitation activity (left). Note that the scale on the left is a factor 1000 larger than on the right. Figure taken from [5].

3.3 Preference in Size

The AFM pictures shown in Fig. 14 show dense populations of surface nanobubbles of roughly similar sizes within each picture (case A and B, resp.). Therefore one may ask whether nanobubbles have a preferred radius. The answer was found by Borkent et al. [9] through a statistically analysis of the nanobubble diameters. The result is shown in Fig. 16. Indeed, Borkent et al. observed a single preferred size in case A, while in case B two maxima show up. Notice that in case B the liquid was oversaturated temporally to stimulate nanobubble formation. Possibly, this led to the formation of the larger set

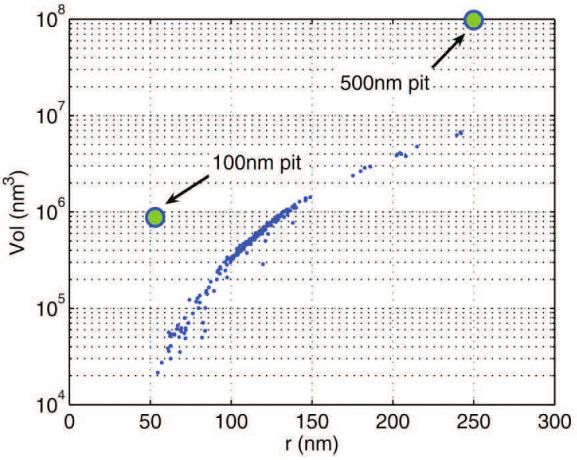

Fig. 15 Volume vs radius of artifical (green) and natural (blue) surface nanobubbles. While the former do cavitate for large enough pressure reduction, the latter do not, though they are of similar size and volume.

of nanobubbles (right peak). The left peak in figure 16 is representing small nanobubbles, which were still present in between the larger ones and similar in size as those in case A. Presumably, this set of smaller bubbles formed once the oversaturation had disappeared. The results of Borkent et al. [9] suggest that, indeed, nanobubbles in dense populations have a tendency towards an equilibrium radius, which increases when the liquid becomes oversaturated.

3.4 Electrolysis: A Controlled and Reproducible Way to Create Surface Nanobubbles

A well-known method to produce gas at solid-liquid interfaces is through electrolysis. What happens here at the nano-scale? Yang et al. [8] could monitor the growth of gaseous surface nanobubbles in real time using AFM [8], when the sample surface acted as of the hydrogen-producing electrode. A typical result of that experiment, at 1 V, is shown in Fig. 17.

Although the bubble grew in time, after some tens of seconds a stable situation set in and the bubble maintained a constant shape. This observation was reproduced by the further experiment, in which Yang et al. [8] measured the electrical current as a function of time (Fig. 18) at constant voltage: in the first $\sim$ 20s the current decreased exponentially, but then it saturated and became constant. One would have expected that surface nanobubbles would constantly accumulate gas on the electrode surfaces and therefore grow without bounds, especially since the current is non-zero. However, Yang et al.'s AFM images showed stationary nanobubbles of certain sizes. These observations therefore suggest that electrolytically generated nanobubbles are in a

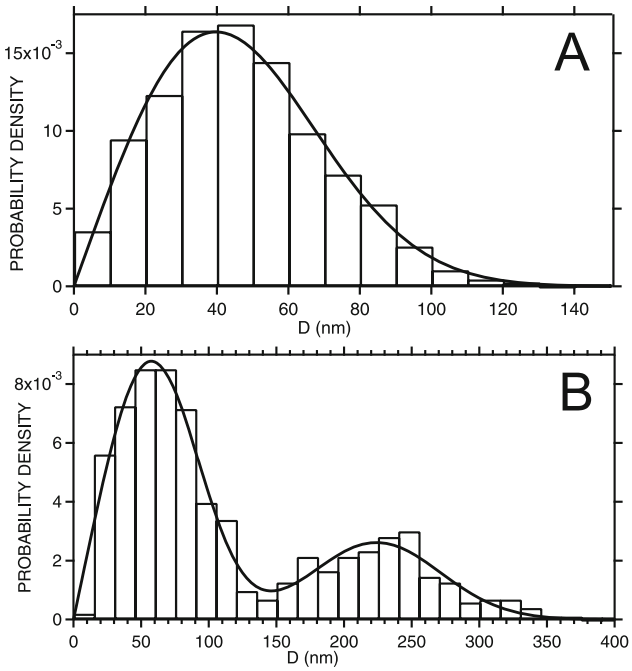

Fig. 16 Probability distribution functions for the nanobubble diameter for two different experimental procedures for the nanobubble creation (see text). Figure taken from [9].

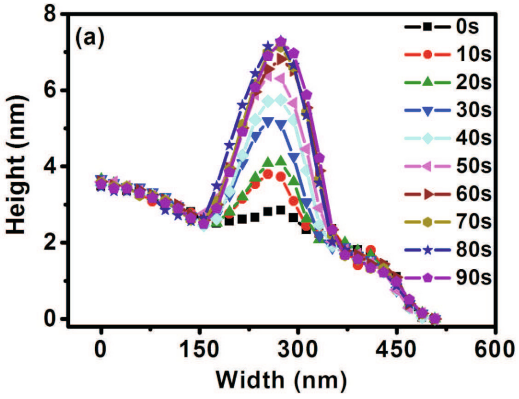

Fig. 17 Time evolution of the cross-section height profile of a electrolytically generated hydrogen surface nanobubble (1V). Figure taken from [8].

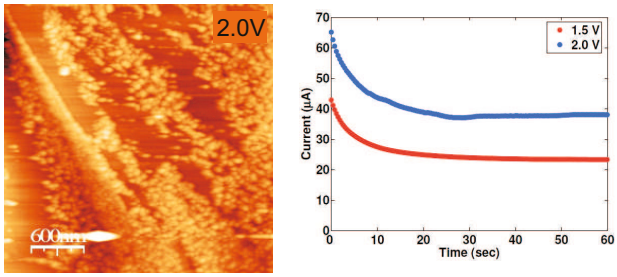

Fig. 18 Electrolytically generated hydrogen surface nanobubbles (left) and the time evolution of the current towards that situation at 1.5V and 2.0V (right). Figures taken from [8].

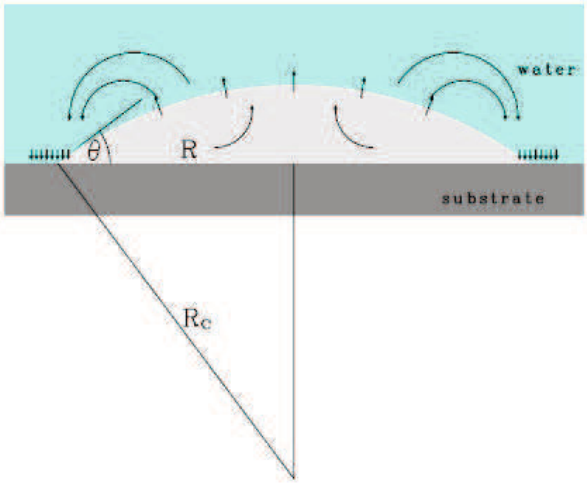

Fig. 19 Sketch of the dynamic equilibrium of surface nanobubbles. Figure taken from [11].

dynamic equilibrium state: gas flows into the bubble, but simultaneously this is balanced by a gas outflow, presumably thanks to the Laplace pressure.

3.5 Another Conjecture Why Surface Nanobubbles Do Not Dissolve

Brenner and Lohse [11] suggested that such a dynamic equilibrium may also stabilize standard nanobubbles. On one hand the Laplace pressure $2\sigma/R_c$

creates an overpressure in the bubble, which leads to a gas outflux. On the other hand, a gas influx, similar to that in the electrolysis-experiments, could compensate for the outflux. It is known from experiments, but also from MD simulations [29], that hydrophobic surfaces attract gas molecules. Brenner and Lohse [11] suggested that these accumulated gas molecules are able to enter the nanobubble at the contact line, resulting in a gas influx, see the sketch in Fig. 19 (though it is unclear what drives this mechanism in the long term). They calculated the effective gas in- and outflux and found that these effects are of similar order of magnitude and could balance each other at a particular stable equilibrium radius R^*. Brenner and Lohse's theory would therefore indeed explain the observation that nanobubbles show a preferred radius (figures 13 and 16), but various other bubble stabilization mechanisms may be possible, too.

4 Conclusions

In summary, this overview article discussed two types of micro- and nanoscopic surface bubbles. The first type - gas entrapped in controlled surface defects - serves as nucleation sites in cavitation experiments. For these bubbles cavitation inception and the resulting bubble dynamics can be controlled and understood perfectly, by tuning the size and positions of the respective cavitation nuclei and the strength of the pressure wave. The second type, i.e. surface nanobubbles, is presently much less understood and needs more experimental and theoretical work, in particular to better understand their stability under various circumstances.

Acknowledgements. Most of the results presented here were obtained by PhD students and postdocs associated with the Twente Physics of Fluids group. In particular, we thank Nicolas Bremond for his pioneering work on controlled cavitation from micropits and Shangjiong Yang for his work on nanobubbles. Furthermore, we thank Manish Arora, Michael Brenner, G. Le Caër, Stefan Dammer, Benjamin Dollet, Stephan Gekle, Stefan Kooij, Claus-Dieter Ohl, Bene Poelsema, Andrea Prosperetti, Holger Schönherr, Peichun Tsai, Julius Vancso, and Harold Zandvliet, who all contributed significantly to the research results presented here. We also thank FOM and STW for financial support.

References

[1] Bremond, N., Arora, M., Ohl, C.D., Lohse, D.: Cavitation on surfaces. J. Phys.: Condens. Matter 17, 3603–3608 (2005)
[2] Bremond, N., Arora, M., Ohl, C.D., Lohse, D.: Controlled multibubble surface cavitation. Phys. Rev. Lett. 96, 224501 (2006)
[3] Bremond, N., Arora, M., Dammer, S.M., Lohse, D.: Interaction of cavitation bubbles on a wall. Phys. Fluids 18, 121505 (2006)

[4] Borkent, B.M., Gekle, S., Prosperetti, A., Lohse, D.: Nucleation threshold and deactivation mechanisms of nanoscopic cavitation nuclei. Phys. Fluids (2009)
[5] Borkent, B.M., Dammer, S.M., Schönherr, H., Vancso, G.J., Lohse, D.: Superstability of surface nanobubbles. Phys. Rev. Lett. 98, 204502 (2007)
[6] Yang, S., Dammer, S.M., Bremond, N., Zandvliet, H.J.W., Kooij, E.S., Lohse, D.: Characterization of nanobubbles on hydrophobic surfaces in water. Langmuir 23, 7072–7077 (2007)
[7] Yang, S., Kooij, E.S., Poelsema, B., Lohse, D., Zandvliet, H.J.W.: Correlation between geometry and nanobubble distribution on hopg surface. EPL 81, 64006 (2008)
[8] Yang, S., Tsai, P., Kooij, E.S., Prosperetti, A., Zandvliet, H.J.W., Lohse, D.: Electrolytically generated nanobubbles on highly orientated pyrolytic graphite surface. Langmuir 25, 1466–1474 (2009)
[9] Borkent, B.M., Schönherr, H., Le Caër, G., Dollet, B., Lohse, D.: Preferred sizes and ordering in surface nanobubble populations. Phys. Rev. E (2009)
[10] Atchley, A.A., Prosperetti, A.: The crevice model of bubble nucleation. J. Acoust. Soc. Am. 86(3), 1065–1084 (1989)
[11] Brenner, M.P., Lohse, D.: Dynamic equilibrium mechanism for surface nanobubble stabilization. Phys. Rev. Lett. 101, 214505 (2008)
[12] Borkent, B.M., Arora, M., Ohl, C.D.: Reproducible cavitation activity in water-particle suspensions. J. Acoust. Soc. Am. 121, 1406–1412 (2007)
[13] Brennen, C.E.: Cavitation and Bubble Dynamics. Oxford University Press, New York (1995)
[14] Versluis, M., von der Heydt, A., Schmitz, B., Lohse, D.: How snapping shrimp snap: through cavitating bubbles. Science 289, 2114–2117 (2000)
[15] Harvey, E.N., Barnes, D.K., McElroy, W.D., Whiteley, A.H., Pease, D.C., Cooper, K.W.: Bubble formation in animals. J. Cell. Comp. Physiol. 24, 1–22 (1944)
[16] Arora, M., Junge, L., Ohl, C.D.: Cavitation cluster dynamics in shockwave lithotripsy: Part 1. free field. Ultrasound Med. Biol. 31(6), 827–839 (2005)
[17] Arora, M., Ohl, C.D., Lohse, D.: Effect of nuclei concentration on cavitation cluster dynamics. J. Acoust. Soc. Am. 121, 3432–3436 (2007)
[18] Oguz, H., Prosperetti, A.: Bubble entrainment by the impact of drops on liquid surfaces. J. Fluid Mech. 219, 143–179 (1990)
[19] Lou, S., Ouyang, Z., Zhang, Y., Li, X., Hu, J., Li, M., Yang, F.: Nanobubbles on solid surface imaged by atomic force microscopy. J. Vac. Sci. Technol. B 18, 2573–2575 (2000)
[20] Ishida, N., Inoue, T., Miyahara, M., Higashitani, K.: Nano bubbles on a hydrophobic surface in water observed by tapping-mode atomic force microscopy. Langmuir 16, 6377–6380 (2000)
[21] Simonsen, A.C., Hansen, P.L., Klösgen, B.: Nanobubbles give evidence of incomplete wetting at a hydrophobic interface. J. Colloid Interf. Sci. 273(1), 291–299 (2004)
[22] Zhang, L., Zhang, Y., Zhang, X., Li, Z., Shen, G., Ye, M., Fan, C., Fang, H., Hu, J.: Electrochemically controlled formation and growth of hydrogen nanobubbles. Langmuir 22, 8109–8113 (2006)
[23] Zhang, X.H., Li, G., Maeda, N., Hu, J.: Removal of induced nanobubbles from water/graphite interfaces by partial degassing. Langmuir 22, 9238–9243 (2006)

[24] Zhang, X.H., Maeda, N., Craig, V.S.J.: Physical properties of nanobubbles on hydrophobic surfaces in water and aqueous solutions. Langmuir 22, 5025–5035 (2006)
[25] Zhang, X.H., Khan, A., Ducker, W.A.: A nanoscale gas state. Phys. Rev. Lett. 98, 136101 (2007)
[26] Zhang, X.H., Quinn, A., Ducker, W.A.: Nanobubbles at the interface between water and a hydrophobic solid. Langmuir 24, 4756–4764 (2008)
[27] Epstein, P.S., Plesset, M.S.: On the stability of gas bubbles in liquidgas solutions. J. Chem. Phys. 18, 1505–1509 (1950)
[28] Ljunggren, S., Eriksson, J.C.: The lifetime of a colloid-sized gas bubble in water and the cause of the hydrophobic attraction. Phys. Rev. E 129-130, 151–155 (1997)
[29] Dammer, S.M., Lohse, D.: Gas enrichment at liquid-wall interfaces. Phys. Rev. Lett. 96, 206101 (2006)

Bridged and Cohesive Crack Models for Fracture in Composite Materials

Roberta Massabò

Department of Civil, Environmental and Architectural Engineering,
University of Genova,
Via Montallegro, 1, 16145 Genova, Italy
roberta.massabo@unige.it

Abstract. The presentation revisits work done by the author and her collaborators over the last decade on two fundamental approaches for studying fracture in composite material systems, the bridged- and cohesive-crack models. Characteristic length scales and dimensionless groups that control fracture characteristics in finite size members and slender bodies, including the stability of crack growth, scaling transitions in the mechanical response and modes of failure, are recalled and discussed. Applications to composite materials for civil, naval and aeronautical structures are presented to highlight the significance of the bridged-crack model in the design of and with advanced composites. Recent results on the problem of multiple dynamic delamination fracture in multilayered systems are used to show how controlled fracture via material/structure design can be exploited to improve mechanical performance.

1 Introduction

The cohesive- and bridged-crack models have been effectively used, since the early works of Barenblatt [1] and Dugdale [2], to model fracture in composite systems where nonlinear mechanisms arise along extended regions of the crack surfaces or ahead of pre-existing cracks (process zones) [3–6]. These mechanisms, which include the formation, coalescing and branching of microcracks, crazing, debonding, yielding, sliding and pulling-out of the reinforcing phases and frictional contact, can dissipate a considerable amount of energy so that additional external work is required for sustained growth of the macrocracks. Figure 1 highlights the bridging action developed by titanium short rods (z-pins) inserted to reinforce in the through-thickness direction a conventional carbon-epoxy laminate [7]. The pins oppose the relative mode I and mode II crack displacements so shielding the crack tip from the applied load. As a consequence, the intrinsic fracture toughness of the base material is increased.

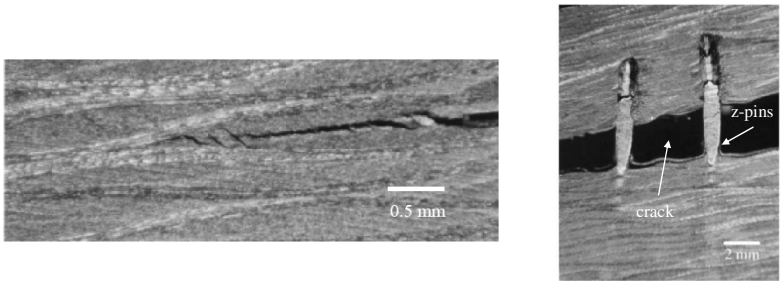

Fig. 1. (a) S-shaped microcracks ahead of the macrocrack in a carbon-epoxy laminate tested in mixed mode. (b) Titanium z-pins bridging a mixed mode crack in a carbon-epoxy laminate (adapted from [7]).

In these systems, fracture becomes a large scale bridging problem that cannot be described by Linear Elastic Fracture Mechanics (LEFM) or characterized by a single fracture parameter; LEFM gives a correct description of the response only in limiting configurations, where the length of the process zone is much smaller than the crack length or any other relevant lengths of the problem (e.g., the ligament size). The nonlinear crack processes must be represented explicitly in the models used to analyze fracture. The bridged- and cohesive-crack models replace the process zone by a fictitious crack ahead of the pre-existing traction free crack and represent the nonlinear mechanisms as a distribution of tractions that oppose the relative crack displacements (Figure 2, for mode I problems). The tractions are related to the relative crack displacement through bridging traction laws, which are generally nonlinear, and replace toughness and strength as the essential material properties (Figure 3 for mode I problems). The area beneath the laws define the energies supplied by the bridging or cohesive mechanisms. The bridging/cohesive traction laws can be deduced by micro- or macro-mechanics models or experiments [6, 8].

From a mathematical point of view, the difference between the bridged- and cohesive-crack models is in the form of the assumed crack tip stress field. In the bridged crack model this is singular and when the crack is at the onset of growth the singular field is measured by an intrinsic fracture toughness, $K_{\mathrm{I}} = K_{\mathrm{IC}}$, or fracture energy, $\mathcal{G}_{\mathrm{I}} = \mathcal{G}_{\mathrm{IC}} = K_{\mathrm{IC}}^2/E$, with E a representative Young's modulus (for mode I problems). In the cohesive crack model, the crack tip stress field is finite (non singular) and when the crack is at the onset of propagation the stress normal to the crack plane at the crack tip equals the value of the cohesive tractions at zero displacement (for mode I problems). In this sense the cohesive-crack model can be considered as a particularization of the bridged-crack model under the assumption of

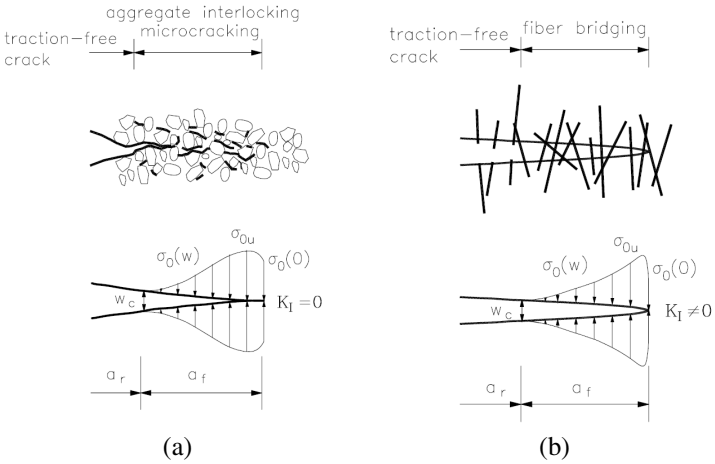

Fig. 2. Qualitative diagrams of bridging and process zones in brittle-matrix composites and quasi-brittle materials. (a) Schematic of a cohesive-crack (e.g. concrete). (b) Schematic of a crack bridged by uniformly distributed fibers (e.g. fiber-reinforced high-strength concrete, fiber reinforced ceramic matrix composite). (adapted from [5]).

a vanishing crack tip stress-intensity factor or a vanishing intrinsic fracture toughness, $K_{\mathrm{I}} = K_{\mathrm{IC}} = 0$. However, the two models are conceptually different as they presuppose different descriptions of the material leading to a different significance of the bridging tractions.

In the bridged-crack model, the composite is theoretically simulated as a biphase material and two distinct factors contribute to its global toughness: the toughness peculiar to the matrix, described by K_{IC} or $\mathcal{G}_{\mathrm{IC}}$ (for mode I problems), and the secondary phase toughening mechanism, which is represented by the shielding effect that the bridging tractions develop on the crack tip stress field and defined by $\mathcal{G}_{\mathrm{b}} = \int_0^{w_c} \sigma_0(w)dw$ in the LEFM limiting configuration (see Section 2). Crack growth is governed by the intrinsic toughness of the matrix and the bridging tractions, which control relative crack displacements, are governed by the properties of the reinforcing phase and by its interaction with the matrix. The bridged-crack model is then suitable for the description of separation processes that involve distinct physical phenomena (crack tip toughness + shielding), such as those of through-thickness reinforced laminates, fiber reinforced high strength concrete or reinforced concrete.

In the cohesive-crack model, the composite material is theoretically simulated as being homogeneous. Only the global toughening mechanism of the whole composite is defined, and it is represented by the shielding effect due

to the cohesive tractions. The toughening mechanism peculiar to the matrix and explicitly represented in the previous model by $\mathcal{G}_{\rm IC}$ is now merged with the toughening mechanisms developed in the process zone through the cohesive law and defined by $\mathcal{G}_{\rm b} = \int_0^{w_c} \sigma_0(w)dw$ in the LEFM configuration. The damage process producing the growth of the crack is the same as that governing the relative crack displacement along the process zone. The model is suitable to describe the separation process of materials characterized by a wide zone of microcracking, plastic deformation or crazing, when the matrix toughness is negligible compared to the energy dissipated in the nonlinear processes. The definition of appropriate cohesive laws (e.g. a two-part law, Fig. 3d) allows utilization of the cohesive-crack model also in the description of materials characterized by distinct mechanisms of crack control. However this modeling choice is computationally much more expensive since very fine discretizations are needed near the crack tip to properly reproduce the local fields. On the other hand, the bridged crack model has a number of limitations that should be highlighted: first it cannot be used to study materials in the absence of an initial crack; then, it has a limited range of applicability when used to describe real materials with matrices that are not perfectly brittle. An example application will presented later that highlights the mutual relations between the two models [5, 9].

The bridged crack problem is typically nonlinear and requires iterative, numerical solution procedures. However there are problems where the application of the bridged crack approach is direct and the solution can be obtained quite simply imposing equilibrium and kinematic compatibility. One such example is the problem shown in Fig. 4a, which represents a cracked beam with a brittle matrix and a single layer of ductile reinforcement loaded in flexure. This problem was solved originally by Carpinteri in [10] with a bridged crack model that was later extended in [11–13] to describe materials

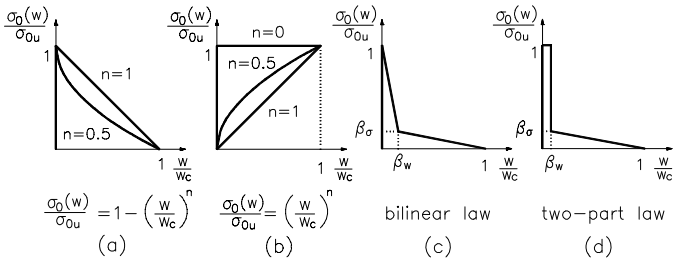

Fig. 3. Exemplary bridging and cohesive traction laws used to describe different nonlinear mechanisms: (a) pull out of short fibers or rods; (b) progressive debonding and yielding of continuous fibers; (c)–(d) cohesive mechanisms in concrete like materials and fiber reinforced concrete (adapted from [5])

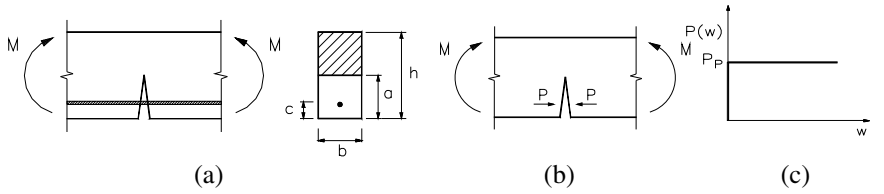

Fig. 4. (a) Cracked beam with a brittle matrix and a single layer of reinforcement loaded in flexure, (b) Bridged-crack modeling of problem (a) and (c) Bridging traction law (adapted from [12]).

with a larger number of discrete reinforcements and materials with continuously distributed reinforcements and arbitrary bridging traction laws.

Following the bridged crack model approach the action of the fiber is described by means of a pair of closing forces, P, opposing the crack opening displacement w, Fig. 4b. The bridging traction law is assumed as rigid perfectly plastic to describe progressive yielding or debonding of the continuous fiber, Fig. 4c. The crack tip field is singular and the matrix toughness defined by the critical stress intensity factor K_{IC}. This system can assume two different configurations. In the first the crack opening displacement is zero at the level of the fiber, $w = 0$. In this configuration the problem is statically indeterminate since the force P is unknown. By applying the superposition principle and Castigliano's theorem the crack tip opening at the level of the fiber can be defined as a function of the crack tip stress intensity factors produced by the applied moment K_{IM} and the unknown forces K_{IP}. The unknown forces are then obtained by imposing a kinematic compatibility condition stating that the crack displacement at the fiber level must be zero. In the second configuration the crack opening is non zero at the level of the fiber. In this case the forces P are known and given by the yielding or debonding values, $P = P_{\mathrm{P}}$ (Fig. 4c). Crack growth can then be studied and the critical load for crack propagation determined by imposing an equilibrium condition stating that at the onset of growth the crack tip stress intensity factor must be equal to the intrinsic matrix toughness.

Many problems, with different geometries, boundary conditions and arbitrary bridging traction laws can be solved by extending these basic concepts and using the weight function method (e.g. [9, 12, 13]). The weight functions for this type of problems are given by the stress intensity factors due to pair of unit forces acting along the crack faces. They can be found in fracture handbooks or in the recent literature. For instance, approximate weight functions for double cantilever beams loaded in mode I an mode II were derived by the author in [14, 15] in order to apply the approach presented above to study delamination fracture in slender bodies so overcoming the limitations of solutions based on beam theory approximations.

2 Characteristic Length Scales and Brittleness Numbers

Crack propagation in composite systems is typically a large scale bridging problem where the response is strongly influenced by the geometry of the body and the loading and boundary conditions and the length of the process zone and the toughness due to the bridging mechanisms are not constant or material properties and vary during crack growth. However, a bridged crack can approach during its growth some limiting configurations that can be derived analytically and define the characteristic length scales of the problem.

The first limit is the *small scale bridging limit* where the crack propagates with a process zone of constant size which is much smaller than all other characteristic dimensions of the body (Fig. 5a). In this limit the crack tip shielding provided by the bridging mechanisms becomes a material property independent of crack length and given by the area underneath the bridging traction law, $\mathcal{G}_{\rm b}$. The bridged crack model then becomes equivalent to Griffith theory and the fracture process is characterized by a single fracture parameter, the composite fracture energy, given by $\mathcal{G}_{\rm b} + \mathcal{G}_{\rm IC}$ and can be studied using LEFM (Fig. 5b).

The length of the process zone in the small scale bridging limit is a characteristic length scale of the problem and a material constant. Using the model parameters defined in Fig. 3, for a rectangular bridging or cohesive law ($\sigma_0(w)$=σ_{0u} for $w \leq w_c$ and $\sigma_0(w)$=0 for $w > w_c$), the length is given by:

$$l_{\rm SSB} = \frac{\pi}{8}\frac{w_{\rm c}E}{\sigma_{0\rm u}}, \tag{1}$$

for a cohesive crack with a vanishing intrinsic fracture toughness $\mathcal{G}_{\rm IC} = 0$ [16], and by

$$l_{\rm SSB} = \frac{\pi}{8}\frac{w_{\rm c}E}{\sigma_{0\rm u}}\left(\sqrt{1+\frac{\mathcal{G}_{\rm IC}}{\mathcal{G}_{\rm b}}} - \sqrt{\frac{\mathcal{G}_{\rm IC}}{\mathcal{G}_{\rm b}}}\right)^2, \tag{2}$$

for a bridged crack [17]. The factor $\pi/8$ changes on varying the shape of the cohesive/bridging law but it remains of order unity. The length of the process zone in the small scale bridging limit characterizes the *intrinsic brittleness of the material*; its order of magnitude is equal to 10^{-6} mm in glass, 10^{-3} mm in ceramic-matrix ceramic-fiber composites, $10^0 \div 10^1$ in conventional 2D laminates and $10^2 \div 10^3$ mm in concrete, fiber-reinforced cementitious materials and through-thickness reinforced laminates.

The size of the cohesive/bridged zone depends on the groups w_cE/σ_{0u} and $\mathcal{G}_{\rm IC}/\mathcal{G}_{\rm b}$. The dimensional group w_cE/σ_{0u}, which alone defines the process zone length in a cohesive crack model of the material, was first noted by Cottrell [18] as the material parameter correlating notch sensitivity of ultimate strength to notch size, and reconsidered by Hillerborg in its definition of the characteristic length, $l_{\rm ch}$, to describe concrete like materials [19]. The second dimensionless group, $\mathcal{G}_{\rm IC}/\mathcal{G}_{\rm b}$, is the ratio between the intrinsic

fracture energy and the energy supplied by the bridging mechanisms; it appears in the definition of the small scale bridging process zone length when a bridged-crack approach is used and indicates a progressive transition toward material brittleness when $\mathcal{G}_{\rm IC}/\mathcal{G}_{\rm b}$ increases. The length scale (1) defines an upper bound solution to the length of the process zone for $\mathcal{G}_{\rm IC}/\mathcal{G}_{\rm b} \to 0$.

In slender bodies, such as delamination beams (Fig. 5c), the length of the process zone in small scale bridging becomes a material/structure parameter that scales with the thickness $2t$ of the body and the scaling rule depends on the mode of fracture. The characteristic length scales for slender bodies have been derived in [20] and [21] and are given by:

$$l^{\rm I}_{\rm SSB} \approx (l_{\rm SSB})^{1/4} t^{3/4} \quad \text{(mode I)}, \tag{3}$$

$$l^{\rm II}_{\rm SSB} \approx (l_{\rm SSB}\, t)^{1/2} \quad \text{(mode II)}, \tag{4}$$

where $l_{\rm SSB}$ is given in (1) and (2). Since the thickness of these systems is usually quite small this result indicates that the length of the process zone in the small scale bridging limit can be much smaller than the length that

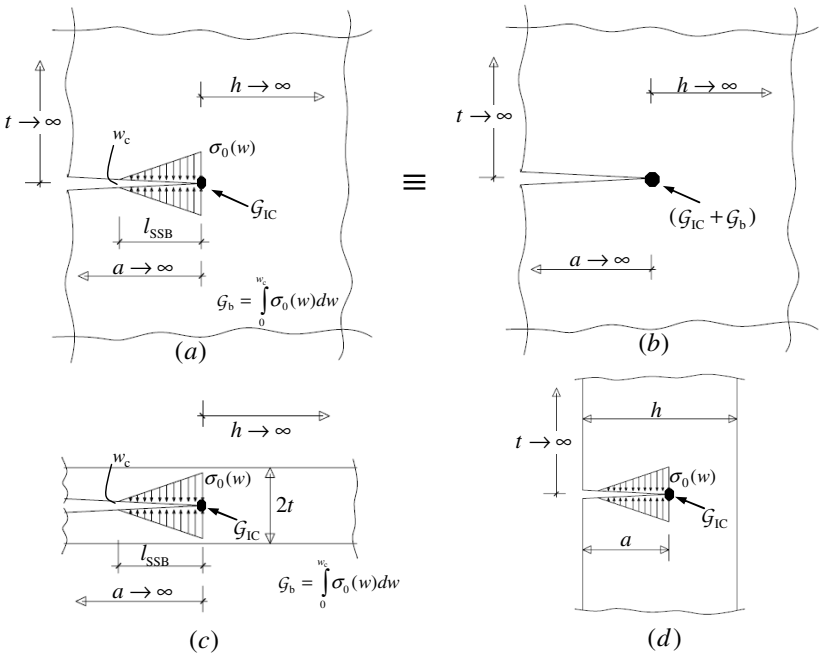

Fig. 5. Schematics of bridged cracks: (a) fracture process zone in *small scale bridging* conditions; (b) LEFM approximation of small scale bridging fracture; (c) small scale bridging limit in a slender body; (d) large scale bridging fracture in a member of finite size

would be predicted using formulas obtained for infinite media. This conclusion should be accounted for when the characteristic lengths are used to size the elements in numerical descriptions of the problem.

In members subjected to uniform loading conditions and when the bridging traction law is an increasing function of the relative crack displacement (at least over a certain interval), a second limiting configuration can be approached, the *ACK limit* (from the seminal work of Avenston, Cooper and Kelly [22]). In this limit, which is characterized by a long crack entirely bridged by intact ligaments and is typically reached after the crack has grown several time a non-catastrophic characteristic length scale, $l_{\rm ACK}$, the critical load for crack propagation becomes constant. The ACK characteristic length scales for infinite and slender bodies have been derived in [17] and [21]. For a prescribed mode I power bridging law, $\sigma_0(w_{\rm N}) = \beta(w_{\rm N}/2)^\alpha$, in an infinite body, $l_{\rm ACK}$is a material property given by:

$$l_{\rm ACK} = \frac{\pi E}{4}\left(\frac{1+\alpha}{2\alpha}\mathcal{G}_{\rm Ic}\right)^{\frac{1-\alpha}{1+\alpha}}\beta^{\frac{-2}{1+\alpha}}, \tag{5}$$

and for a centered mode II crack in a slender beam of half thickness t, with a power bridging law, $\tau_0(w_{\rm s}) = \beta(w_{\rm s}/2)^\alpha$, $l_{\rm ACK}$ is a material/structure property given by:

$$l^{\rm II}_{\rm ACK} \approx (l_{\rm ACK} t)^{1/2}, \tag{6}$$

Whether crack propagation across a long and unnotched member ($h \gg l_{\rm SSB}, l_{\rm ACK}$, Fig. 5a, c) will be noncatastrophic (no ligament failure - ACK limit attainable) or catastrophic (extensive ligament failure - small scale bridging limit approached) can be estimated by comparing the orders of magnitude of $l_{\rm SSB}$ and $l_{\rm ACK}$. If $l_{\rm ACK} \gg l_{\rm SSB}$, failure will be catastrophic; if $l_{\rm SSB} \gg l_{\rm ACK}$, noncatastrophic. The presence of a notch favours catastrophic cracking. If neither limit can be approached (e.g., $l_{\rm SSB} \approx l_{\rm ACK}$ or $h \approx l_{\rm ACK}$ or $h \approx l_{\rm SSB}$) then large-scale bridging conditions prevail and detailed calculations are required.

Figure 6 highlights failure transitions in a mode II delamination beam subject to uniformly distributed shear stresses, τ, acting along the crack surfaces. The assumed bridging law is linear and non proportional to describe bridging mechanisms developed by stitches loaded in mode II $\tau_0(w_{\rm S}) = \tau_0(0) + \beta w_{\rm S}/2$ with $\tau(0) = 2\sqrt{\mathcal{G}_{\rm IIC}\beta}$ and $\mathcal{G}_{\rm b}/\mathcal{G}_{\rm IIC} = 80$ [8]. The problem can be used to describe fracture in a stitched ENF specimen. The critical stress for crack propagation in the ACK limit is a material property, $\tau_{\rm ACK} = 3(\mathcal{G}_{\rm IIC}\beta)^{1/2}$, and the characteristic length scale $l_{\rm ACK}$ a material structure property $l_{\rm ACK} = [E/(4\beta)t]^{1/2}$ [21]. For the stitched laminate tested in [8] with $2t = 7$ mm, $E = 49$ GPa, $\tau_0(w_{\rm S}) = 12.7 + 51 w_{\rm S}$ MPa and $w_c = 1.0$ mm, $l_{\rm ACK} \approx 20$ mm and $l_{\rm SSB} \approx 40$ mm. The two length scales have similar magnitude; this indicates that crack propagation in laboratory specimens made of this material will be in large scale bridging conditions with neither of the two limiting configurations approached.

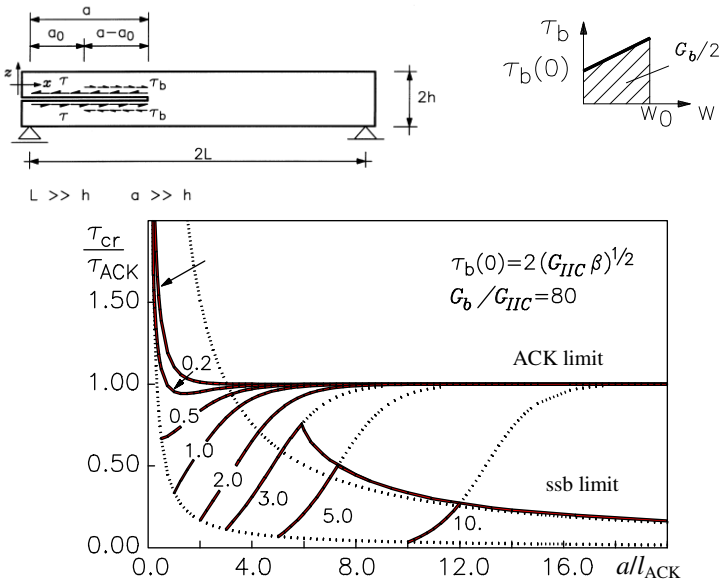

Fig. 6. Transition from noncatastrophic (ACK limit approached, $\tau = \tau_{\rm cr} = \tau_{\rm ACK}$) to catastrophic (small scale bridging limit approached) failure on varying the notch length, a_0, in thin beam loaded in mode II (adapted from [8])

In finite bodies, where the dimension of the ligament ahead of the crack is not infinite (Fig. 5d), a unitary description of the fracture behavior relies on parameters that account for this characteristic dimension. For cohesive cracks, characterized by a zero intrinsic fracture toughness $\mathcal{G}_{\rm IC} = 0$, dimensionless groups depending on the ratio between the small scale bridging characteristic length scale and the characteristic dimension h have been used in the literature, $l_{\rm SSB}/h$. The energy brittleness number defined by Carpinteri $s_{\rm E} = \dfrac{\mathcal{G}_{\rm b}}{\sigma_{0\rm u} h}$ [23] is one of such groups that will be used in one of the applications that follow. For a bridged crack, where two distinct toughening mechanisms are present in the material, the mechanical behaviors is described by two dimensionless group, $l_{\rm SSB}/h$ and the ratio $\mathcal{G}_{\rm IC}/\mathcal{G}_{\rm b}$ (an application will be presented in 3.3). There are then special problems, namely when the ratio $\mathcal{G}_{\rm IC}/\mathcal{G}_{\rm b} \to 0$, either because $\mathcal{G}_{\rm b}$ becomes very large (rigid-plastic bridging traction law) or because $\mathcal{G}_{\rm IC}$ becomes very small, where the response is again characterized by a single dimensionless parameter (an application will be presented in 3.1).

3 Scaling Transitions in the Mechanical Response of Composite Structures

Example applications are presented in the following sections to highlight scaling transitions in the mechanical response of different composite systems and to investigate mutual relations between the cohesive- and bridged-crack models.

3.1 Constitutive Flexural Response of a Brittle Matrix Composite with a Discrete Layer of Ductile Reinforcement

The diagrams presented in Fig. 7 describe the constitutive moment versus localized rotation response of the cracked beam of Fig. 4, which could represent a reinforced concrete beam. The diagrams have been obtained by applying the bridged-crack model presented in Section 1 and depict the response on varying the brittleness number $N_{\rm P} = \dfrac{\rho\sigma_{\rm u}h^{0.5}}{K_{\rm IC}}$, where $\rho\sigma_u = P_{\rm P}$ is the value of the bridging forces at the yielding or sliding limits (Fig. 4b, c), h is the height of the beam and $K_{\rm IC}$ the matrix fracture toughness $K_{\rm IC}$ [5, 12]. $N_{\rm P}$ is the single parameter that controls flexural failure and the transitions from ductile (for large values of $N_{\rm P}$) to brittle (for small values of $N_{\rm P}$) behavior in this system. In addition, the response of the system remains physically similar if the model parameters are varied while $N_{\rm P}$ is kept fixed. The bridged crack model also reproduces the local snap through instabilities that are typically observed in the response of reinforced concrete and other brittle matrix composite. Experiments performed on high-strength reinforced concrete beams confirm the theoretical predictions [24].

3.2 Constitutive Flexural Response of a Brittle Matrix Composite with Uniformly Distributed Discontinuous Reinforcements

The diagram in Fig. 8 shows the double brittle-ductile-brittle transition that occurs in the flexural response of a brittle-matrix composite reinforced with uniformly distributed discontinuous fibers on increasing the brittleness number $N_{\rm P}$. In this case the bridging traction law is assumed as rectangular, $\sigma_0(w) = \sigma_{0\rm u}$ for $w \le w_{\rm c}$; $\sigma_0(w) = 0$ for $w > w_{\rm c}$, with $w_{\rm c}$ the critical crack opening displacement beyond which the closing tractions vanish, in order to describe the response of short fibers with a high aspect ratio [5].

The dimensionless moment versus bending rotation constitutive response is controlled in this material by two dimensionless parameters: the brittleness

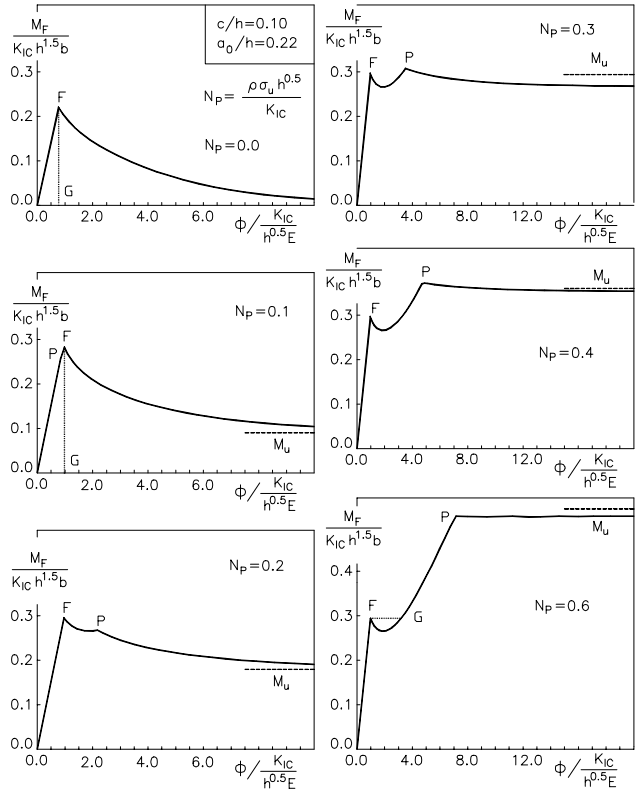

Fig. 7. Transitions in the constitutive flexural response of brittle matrix composites with a discrete layer of ductile reinforcement (Fig. 4a), e.g., a reinforced concrete (adapted from [5]).

number $N_{\mathrm{P}} = \sigma_{0\mathrm{u}} h^{0.5}/K_{\mathrm{IC}}$ and $\mathcal{G}_{\mathrm{b}}/\mathcal{G}_{\mathrm{IC}}$. For a cementitions material reinforced with steel fibers with K_{IC}= 50 N/mm$^{1.5}$, E = 40 GPa, $\sigma_{0\mathrm{u}}$= 4 MPa and w_{c}= 4 mm (leading to $\mathcal{G}_{\mathrm{b}}/\mathcal{G}_{\mathrm{IC}}$=256), the curves labeled C, F and M describe the response of beams with depths $h \sim 40$ mm, $h \sim 190$ mm and $h \sim 690$ mm, respectively. The depths of the first two beams are in the range normally covered by the laboratory specimens and in this range a brittle-ductile transition is typically observed when the beam depth increases [25]. However, in the steel fiber reinforced composite examined here, a new ductile-brittle transition is predicted when the beam depth further increases above the transitional value given by the curve F, and the largest beam (curve M), which could represent a real structural component, is characterized by an unstable response. For larger/smaller values of the ratio $\mathcal{G}_{\mathrm{b}}/\mathcal{G}_{\mathrm{IC}}$, the critical value of N_{P} beyond which the response changes from globally stable to globally unstable increases/decreases and the reversal is not present when the bridging

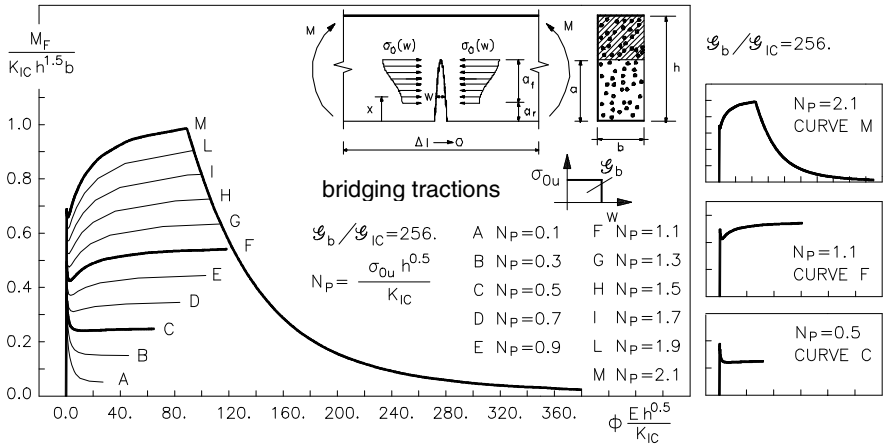

Fig. 8. Double brittle-ductile-brittle transition in the flexural response of a brittle-matrix composite reinforced with uniformly distributed discontinuous fibers (rectangular bridging law). (adapted from [12]).

traction law is rigid-perfectly plastic ($w_c \to \infty$), as in Fig. 7. The diagram has been obtained with the bridged-crack model formulated in [9, 12].

3.3 Bridged versus Cohesive Crack in the Flexural Behavior of Composites with Quasi-Brittle Matrices and Uniformly Distributed Reinforcements

In order to highlight important transitions in the flexural response of quasi-brittle matrix composites and the mutual relations between the bridged- and cohesive-crack models, the three point bending beam shown in Fig. 9a has been examined. The material is assumed to be a quasi-brittle matrix composite reinforced with short fibers, such as a high strength fiber reinforced concrete or a ceramic matrix composite. The response of this system can be studied using both modeling approaches. Within the bridged crack model, an intrinsic fracture energy $\mathcal{G}_{\rm IC}$ describes the toughness of the matrix and a linearly decreasing bridging traction law, with subtended area $\mathcal{G}_{\rm b}$, describes the bridging mechanisms developed by the fibers (Fig. 9b). The composite fracture energy in the LEFM limit is $\mathcal{G}_{\rm b} + \mathcal{G}_{\rm IC}$. Within the cohesive crack model, the response of the material is described by a two part cohesive law with an initial steep peak and a very long tail (Fig. 9c). This law has been inferred from tests on high strength fiber reinforced concrete [5]. The first part of the curve, with subtended area $\mathcal{G}_{\rm IC}$, describes the cohesive mechanisms proper of the quasi brittle matrix (microcracking, aggregate interlocking) while the

second part, with subtended area $\mathcal{G}_b$, describes the bridging mechanisms provided by the fibers. The area under the whole curve is the composite fracture energy in the LEFM limit, $\mathcal{G}_b + \mathcal{G}_{IC}$.

The flexural response of this material is described, as observed above, by two dimensionless parameters that can be chosen as the energy brittleness number $s_E = \dfrac{\mathcal{G}_b + \mathcal{G}_{IC}}{\sigma_{0u} h}$ and the ratio $\mathcal{G}_b/\mathcal{G}_{IC}$. The diagrams in Fig. 10 have been obtained for a fixed value of the ratio $\mathcal{G}_b/\mathcal{G}_{IC}$= 250 chosen to represent a composite with a brittle matrix, such as a high-strength fiber reinforced concrete. The two curves in each diagram describe the response predicted by the bridged- and cohesive-crack models; they essentially coincide in all diagrams but the last one, a behavior that will be explained later.

In the intermediate range of values of s_E, described by the diagrams (e), (d) and (c), the models predict a transition from a strain softening to a strain hardening response on decreasing s_E. This ductile-brittle transition characterises laboratory tests on fiber reinforced materials, such as fiber reinforced concrete or mortar [25], where variations in s_E can be obtained by varying the beam height or the fiber percentage. This result indicates that the two models are able to reproduce behaviors typically observed in the laboratories. However, the models give more information on the behavior of such structures since they also predict that if s_E is reduced further, as in the diagrams (b) and (a), for instance by increasing the height of the beam to values that could represent a real structural component, a second important transition in the response can be observed and the behavior goes back to brittle. For small values of s_E, diagram (a), the crack is propagating in *small scale bridging* conditions and the behavior is well described by LEFM with the fracture energy of the composite material given by $\mathcal{G}_b + \mathcal{G}_{IC}$. This theoretical prediction is quite important because it highlights a scaling transition that is not normally observed in laboratory experiments but could occur in real components.

A final comment on the diagrams in Fig. 10 relates to the diagrams for large values of s_E, diagram (f). For large values of s_E the model predictions differ. This behavior occurs when the crack propagates with crack opening displacements that are very small over its whole length so that the cohesive

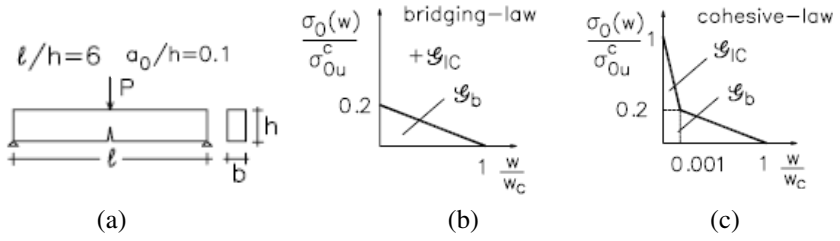

Fig. 9. (a) Schematic of a three-point bending beam, (b) Assumed bridging traction law and (c) Assumed cohesive traction law.

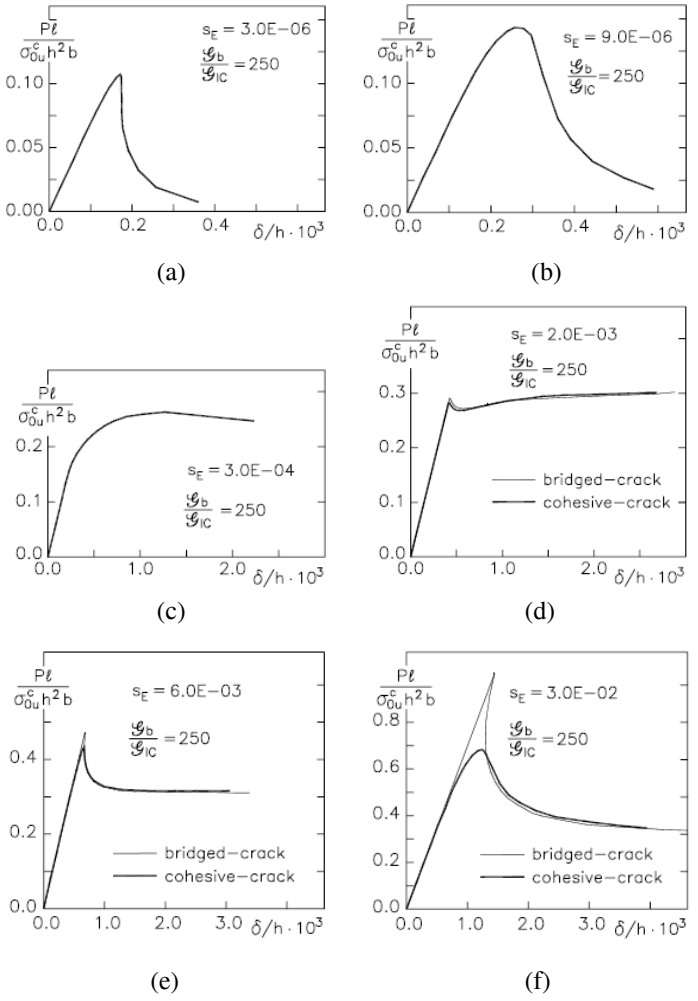

Fig. 10. Load versus deflection response of the three point bending beam of Fig. 9a on varying the energy brittleness number, (adapted from [5]).

tractions fall within the first branch of the cohesive law of Fig. 9c. Crack propagation is controlled only by the nonlinear mechanisms proper of the quasi-brittle matrix and the presence of the fibers is irrelevant. In this regime, the assumption of the bridged crack model, which lumps all matrix nonlinear mechanisms into an intrinsic fracture energy, is not correct any more and the cohesive mechanisms proper of the matrix must be properly modeled. The cohesive crack model then correctly predicts a new transition toward a more ductile response on increasing s_E, for instance by decreasing the beam height,

while the bridged crack model predicts an erroneous transition toward more brittle responses.

4 The Bridged Crack Model in the Optimal Design of Advanced Composites

The bridged- and cohesive-crack models have been used in the recent past by the author and her collaborators to study single and multiple delamination fracture under quasi-static and dynamic loading conditions in multilayered systems [6, 21, 26–34]. The importance of the bridged-crack model to design new advanced composites with improved mechanical properties (e.g. laminates reinforced with a through-thickness reinforcement such as stitching or z-pins) has already been noted in Section 1 where the diagram of Fig. 6 clearly highlights the necessity to abandon LEFM when dealing with large scale bridging conditions and the importance to know the asymptotic solutions of the problem and the associated characteristic length scales.

Complex behaviors that occur when multiple cracks or delaminations are present in a body, such as local instabilities in the macrostructural response, can only be explained and understood by theoretical models based on the concepts presented in this paper. The diagram in Fig. 11, for instance, shows the experimental results obtained by Robinson et al. [35] by testing a double cantilever beam with two implanted delaminations and the theoretical results obtained in [29]. The load versus load-point displacement curves shown in Fig. 11 presents an initial strain softening branch when the edge crack starts to propagate unstably at (A). At (B) the tip of the edge delamination reaches the left tip of the internal delamination and a snap-back instability occurs with a sudden drop in the critical load to point (C); this drop corresponds to a sharp and sudden change (amplification) in the energy release rate which is created by the interaction between the two delaminations. The edge crack then continues to propagate stably (with increasing applied load) until its tip reaches approximately the center of the internal delamination at (D) when also the energy release rate of the right tip of the internal crack becomes critical (amplification phenomena) and the internal delamination starts to propagate. Simultaneous propagation of the two cracks then continues for the remainder of the test.

The problem of multiple dynamic delamination fracture, which is the typical outcome of extreme dynamic loading conditions, such as high velocity impact and blast, has been examined in recent work of the writer [6, 26–34]. The effects of the interaction between delaminations and of nonlinear crack face mechanisms, including bridging by fibers and through-thickness reinforcements, contact and friction, on fracture characteristics, macrostructural response, damage and impact tolerance and energy absorption have been discussed and some interesting conclusions have been drawn. Damage/impact

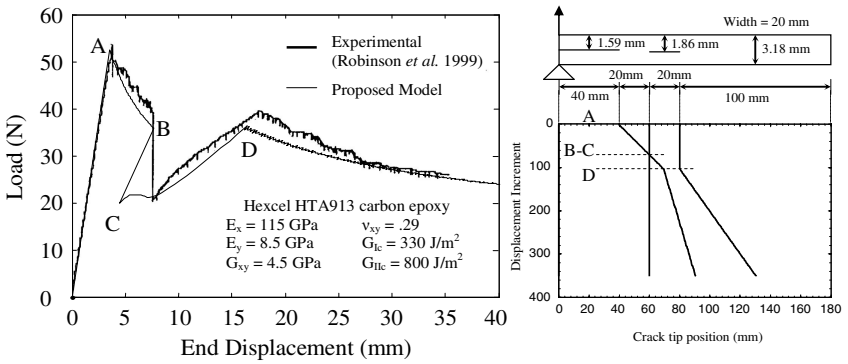

Fig. 11. Diagram of the critical reaction load for crack propagation versus load-point displacement in a double cantilever beam with two unequally spaced implanted delaminations tested by Robinson et al. [35]. The material is a carbon-epoxy laminate. The experimental results are compared with the theoretical results in [29] (crack growth criterion: $\mathcal{G}_{\rm I}/\mathcal{G}_{\rm Icr} + \mathcal{G}_{\rm II}/\mathcal{G}_{\rm IIcr} = 1$) (adapted from [29]).

tolerance can be substantially improved by adding a through-thickness reinforcement [6, 32, 34] and energy absorption through multiple delamination fracture can be optimized if the system is designed so that cracks will form at predefined spacing [30, 33, 34]. Figure 12 highlights these behaviors.

The figure depicts results on damage tolerance and energy absorption through multiple dynamic delamination fracture in homogeneous systems subject to out of plane loading (cohesive interface model formulated in [30]). Two delaminated clamped-clamped beams with equally and unequally spaced cracks have been loaded quasi-statically up to predefined values of the mid-span displacement $w_{\rm st}$ that ensure the input of a fixed value of the strain energy, $\mathcal{L}$, in the systems. Crack growth was prevented during the static loading. The cracks were then allowed to propagate dynamically through the specimens with the mid-span displacement kept fixed at $w_{\rm st}$ (fracture criterion: $\mathcal{G} \geq \mathcal{G}_{\rm cr}$, with $\mathcal{G}$ the energy release rate and $\mathcal{G}_{\rm cr}$ the intrinsic fracture energy of the base material). The strain energy introduced into the two systems is such that crack growth occurs in the regime of small to moderate crack speeds. Diagrams (b-c) refer to the unreinforced beams; diagrams (d–e) refer to the reinforced beams in the presence of large scale bridging mechanisms described by linear proportional bridging laws that could represent a stitched laminate (the bridging mechanisms act in the initially intact ligaments of the beams) [34].

The diagrams highlight important features of the response of these systems. In both the reinforced and the unreinforced systems, (b) and (d), the equally spaced cracks propagate together (at a speed of approximately $0.1c_{\rm L}$, with $c_{\rm L}$ the longitudinal wave speed); in the unequally spaced system only the lower crack propagates and in the unreinforced system single growth occurs at much higher speed (approximately $0.2c_{\rm L}$) and the crack quickly approaches

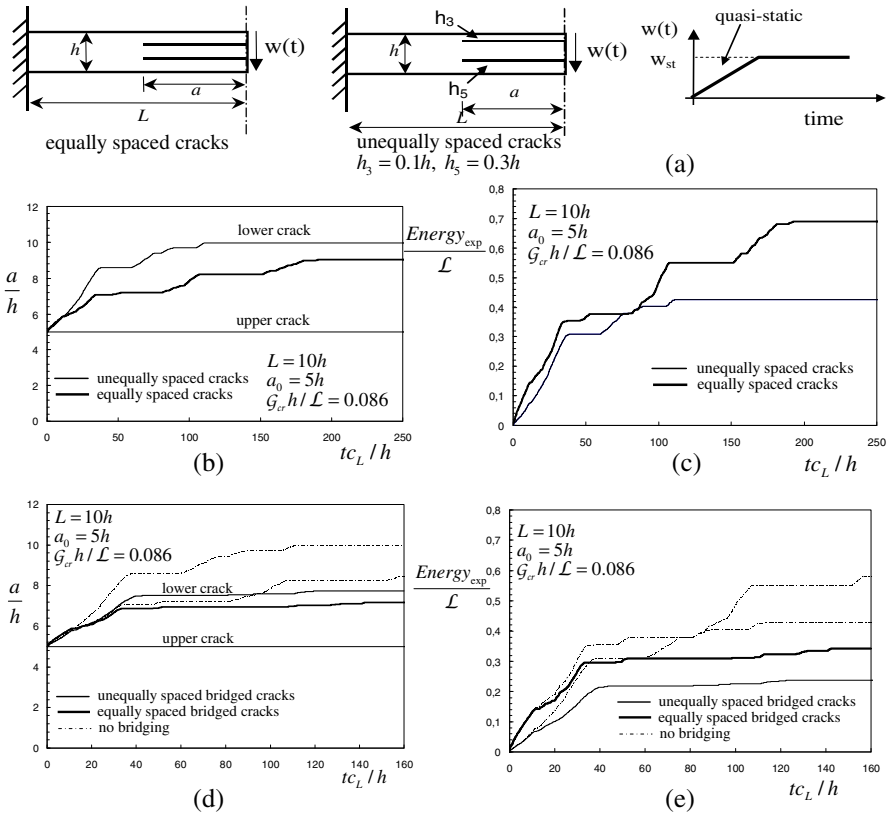

Fig. 12. (a) Delaminated clamped-clamped beams with equally and unequally spaced cracks loaded under displacement control (only half beam is shown). Crack growth is prevented during the quasi-static loading phase. (b–e) Time histories of crack length and energy expended into the creation of new fracture surfaces in beams with (d–e) and without (b–c) a through-thickness reinforcement.

the fixed boundary of the member. The large scale bridging mechanisms reduce crack speed in the unequally spaced system and, after a phase of growth at reduced speed, lead to crack arrest in both systems; this indicates that the damage and impact tolerance of the material can be substantially improved by a through-thickness reinforcement when crack growth occurs in the low to moderate crack speed regime [27]. In the unreinforced systems, the energy expended into the creation of new surfaces, (c), is much higher when both cracks propagate suggesting that if the beams were designed so that cracks will form at equal spacing, energy absorption through multiple delamination fracture could be optimized. The presence of large scale bridging conditions minimizes differences in the responses of the systems with equally and unequally spaced cracks.

5 Conclusions

The presentation reviews basic concepts of the theory of crack bridging and revisits the work done by the author and collaborators over the last decade. Focus has been on length scales and dimensionless groups that control fracture characteristics, size-scale transitions in the structural response and modes of failure of members of finite size and slender bodies. Recent results on static and dynamic, single and multiple delamination fracture have been presented that highlight the significance of the bridged-crack model in designing and optimizing new advanced composite materials and structures with improved mechanical properties.

Acknowledgments. The author would like to acknowledge support while writing this paper by the U.S. Office of Naval Research through contract no. N00014-05-1-0098, administered by Dr. Yapa D.S. Rajapakse, and by the MIUR Prin07 project 2007YZ3B24, Multi-scale problems with complex interactions in Structural Engineering.

References

[1] Barenblatt, G.I.: The formation of equilibrium cracks during brittle fracture. General ideas and hypotheses. Axially-symmetric cracks. J. Applied Mathematics and Mechanics 23, 622–636 (1959)
[2] Dugdale, D.S.: Yielding of steel sheets containing slits. J. Mechanics Physics Solids 8, 100–104 (1960)
[3] Bao, G., Suo, Z.: Remarks of crack-bridging concepts. Applied Mechanics Review 24, 355–366 (1992)
[4] Cox, B.N., Marshall, D.B.: Concepts for bridged cracks in fracture and fatigue. Acta. Metall. Mater. 42, 341–363 (1994)
[5] Massabò, R.: The bridged-crack model. In: Carpinteri, A., Gladwell, G. (eds.). Nonlinear Crack Models for Nonmetallic Materials. Solid Mechanics and its Applications Series, pp. 141–208. Kluwer Academic Publisher, Dordrecht (1999) ISBN 0-7023-5750-7
[6] Massabò, R.: Single and multiple delamination in the presence of nonlinear crack phase mechanisms. In: Delamination Behavior of Composites (Ed. Sridharan), pp. 514–558. Woodhead Publishing Ltd., Cambridge (2008) ISBN: 978-1-84569-244-5
[7] Rugg R.L, Cox B.N., Massabò R.: Mixed mode delamination of polymer composite laminates reinforced through the thickness by z-fibers. Composites, part A 33(2), 177–190 (2002)

[8] Massabò, R., Mumm, D., Cox, B.N.: Characterizing mode II de-lamination cracks in stitched composites. Int. Journal of Fracture 92(1), 1–38 (1998)
[9] Carpinteri, A., Massabò, R.: Bridged versus cohesive crack in the flexural behavior of brittle matrix composites. Int. Journal of Fracture 81, 125–145 (1996)
[10] Carpinteri, A.: Stability of fracturing process in r.c. beams. J. Structural Engineering 110, 544–558 (1984)
[11] Bosco, C., Carpinteri, A.: Discontinuous constitutive response of brittle matrix fibrous composites. J. Mechanics Physics Solids 43, 261–274 (1995)
[12] Carpinteri, A., Massabò, R.: Continuous versus discontinuous bridged crack model for fiber-reinforced materials in flexure. Int. Journal of Solids and Structures 34(18), 2321–2338 (1997)
[13] Carpinteri, A., Massabò, R.: Reversal in the failure scaling transition of brittle matrix fibrous composites. Journal of Engineering Mechanics (ASCE) 123(2), 107–114 (1997)
[14] Massabò, R., Brandinelli, L., Cox, B.N.: Mode I Weight Functions for an Orthotropic Double Cantilever Beam. International Journal of Engineering Science 41, 1497–1518 (2003)
[15] Brandinelli, L., Massabò, R.: Mode II Weight Functions for isotropic and orthotropic Double Cantilever Beams. Int. Journal of Fracture 139, 1–25 (2006)
[16] Bilby, B.A., Cottrell, A.H., Swinden, K.H.: The spread of plastic yield from a notch. Proceedings Royal Society London A 272, 304–314 (1963)
[17] Marshall, D.B., Cox, B.N., Evans, A.G.: The mechanics of matrix cracking in brittle-matrix fiber composites. Acta. Metal. Mater. 33, 2013–2021 (1985)
[18] Cottrell, A.H.: Mechanics of Fracture. In: Tewksbury Symposium of Fracture, pp. 1–27. University of Melbourne, Australia (1963)
[19] Hillerborg, A., Modeer, M., Petersson, P.E.: Analysis of crack formation and crack growth in concrete by means of fracture mechanics and finite elements. Cement and Concrete Research 6, 773–782 (1976)
[20] Suo, Z., Bao, G., Fan, B.: Delamination R-Curve phenomena due to damage. J. Mech. Phys. Solids 40, 1–16 (1992)
[21] Massabò, R., Cox, B.N.: Concepts for bridged mode II delamination cracks. Journal of the Mechanics and Physics of Solids 47(6), 1265–1300 (1999)
[22] Aveston, J., Cooper, G.A., Kelly, A.: Single and multiple fracture. In: The Properties of Fiber Composites, Conf. Proc., National Physical Laboratory, pp. 15–24. IPC Science and Technology Press Ltd. (1971)
[23] Carpinteri, A.: Cusp catastrophe interpretation of fracture instability. J. Mechanics Physics Solids 37, 567–582 (1989)
[24] Levi, F., Bosco, C., Debernardi, P.G.: Two aspects of the behavior of slightly reinforced structures. CEB Bulletin d'Information 185, 39–50 (1988)
[25] Jenq, Y.S., Shah, S.P.: Crack propagation in fiber-reinforced concrete. J. Structural Engineering 112, 19–34 (1986)
[26] Massabò, R., Cox, B.N.: Unusual characteristics of mixed mode delamination fracture in the presence of large scale bridging. Mechanics of Composite Materials and Structures 8(1), 61–80 (2001)
[27] Sridhar, N., Massabò, R., Cox, B.N., Beyerlein, I.: Delamination dynamics in through-thickness reinforced laminates with application to DCB specimen. International Journal of Fracture 118, 119–144 (2002)

[28] Andrews, M.G., Massabò, R., Cox, B.N.: Elastic interaction of multiple delaminations in plates subject to cylindrical bending. International Journal of Solids and Structures 43(5), 855–886 (2006)
[29] Andrews, M.G., Massabò, R.: Delamination in flat sheet geometries in the presence of material imperfections and thickness variations. Composites Part B 39, 139–150 (2008) (special issue on Marine Composites)
[30] Andrews, M.G., Massabò, R., Cavicchi, A., Cox, B.N.: Dynamic interaction effects of multiple delaminations in plates subject to cylindrical bending. Int. Journal of Solids and Structures 46, 1815–1833 (2009)
[31] Andrews, M.G.: The Static and Dynamic Interaction of Multiple Delaminations in Plates Subject to Cylindrical Bending, Dissertation. Ph.D. Degree, Northwestern University, Evanston, IL, U.S.A. (2005)
[32] Massabò, R., Cavicchi, A.: Influence of crack wake mechanisms on the dynamic fracture of multiply delaminated plates. In: Proceedings of the 16th Int. Conference on Composite Materials, ICCM 16, Kyoto, CDrom. Japan Society of Composite Materials, pp. 1–7 (July 2007)
[33] Massabò, R.: Dynamic interaction of multiple damage mechanisms in multilayered systems. In: Proceedings of the XVIII National Congress of the Italian Association of Theoretical and Applied Mechanics, AIMETA 2007, Brescia. CDROM, pp. 1–12 (September 2007)
[34] Massabò, R.: Interaction of multiple damage mechanisms in composite and sandwich structures. In: Daniels, et al. (eds.) Major Accomplishments in Composite Materials and Sandwich Structures – An Anthology of ONR Sponsored Research, pp. 133–168. Springer (2009) (in press)
[35] Robinson, P., Besant, T., Hitchings, D.: Delamination growth prediction using a finite element approach. In: 2nd ESIS TC4 Conference on Polymers and Composites, Les Diablerets, Switzerland (1999)

Relaxation to Steady Vortical Flows – And Knots in the Quark-Gluon Plasma

H.K. Moffatt

Trinity College, Cambridge, CB2 1TQ, UK

Abstract. The method of magnetic relaxation for the determination of solutions of the Euler equations representing steadily propagating vortical structures is reviewed, and compared with alternative artificial relaxation procedures that conserve the topology of the vorticity field. Attention is focussed first on axisymmetric vortex ring configurations, for which such relaxation techniques provide simple proofs of the existence of vortex rings of prescribed 'signature', the imprint of conserved topology. Relaxation of knotted and linked configurations are briefly considered, from which the concept of an energy spectrum of knots and links emerges in a natural way. Attention is drawn to recent work of Buniy & Kephart (2005), which seeks to identify such energy spectra with the spectrum of excitations (glueballs) in the quark-gluon plasma, in a spirit reminiscent of Kelvin's 'vortex theory of atoms' but here at the elementary particle level of quantum chromodynamics.

1 Introduction

I am grateful to the organisers of this Mini-Symposium on *Classical and Quantum Vortex Rings* for inviting me to give this introductory lecture. I shall talk mainly about the classical situation, but will also discuss briefly a novel manifestation of knotted quantum vortices in the quark-gluon plasma, the primitive state of matter in the Universe some microseconds after the Big Bang.

It is widely recognised that the vortex ring is a universal phenomenon. I mention here just three examples: (i) The vortices shed by the sweep of the oars in a rowing boat: these are in fact 'half vortex rings', semi-circular in form and intersecting the water surface. Each half ring propagates under its self-induced velocity in a direction opposite to that of the boat, carrying momentum equal and opposite to that imparted to the boat by the sweep of the oar. (ii) The spectacular ring vortices shed by the volcanic eruption of Mount Etna on 20 February 2000, and captured on film by Marco Fulle (see $\langle http://stromboli.net \rangle$); this is really a smoke ring, but there is little doubt

that it coincides with a (turbulent) vortex ring and rises due to a combination of buoyancy and self-induced velocity. (iii) The equally remarkable air-core vortices blown in water by dolphins as described and filmed by Don White (see $\langle http://earthtrust.org/delrings.html \rangle$). Dolphins evidently not only blow such rings, but then pursue them, play with them, and try to swim through them. The smoke rings that we humans used to blow when it was politically correct to do so are but pale shadows in comparison!

I wish to pay particular tribute in this lecture to William Thomson, Lord Kelvin, who died on 20 December 1907, just over 100 years ago. Kelvin was of course, with Helmholtz, one of the great pioneers of vortex dynamics. When he was a student at Cambridge in 1842-1844, he rowed as 'bow' for his College, Peterhouse. In this leading position in the boat, he was well placed to observe the vortices shed from the eight oars, and I like to think that this set him brooding on the mechanism of vortex ring propagation that he was to analyse some 20 years later. Kelvin (or Thomson as he then was) conceived his ill-fated theory of 'vortex atoms' in 1867 (Kelvin 1867, 1869), whereby he sought to explain the fundamental atomic structure of matter in terms of knotted vortices imbedded in the 'ether', imagined as an ideal incompressible fluid permeating the whole universe. Ill-fated it was, because over the subsequent 20 years or so, Kelvin was unable to find any nontrivial stable vortical structures as solutions of the steady Euler equations of fluid motion. I wish to demonstrate here that, if only he had been able to think in terms of magnetic flux tubes, rather than vortex tubes, his theory might have had more lasting impact.

2 Vortons

I use the word *vorton* to mean a localised blob of vorticity ω that propagates without change of structure, with constant velocity, $-\mathbf{U_0}$ say, relative to the fluid at ∞. In this respect, although in no other, it resembles a *soliton*, justifying the use of the term. [The word *vorton* has occasionally been used with a different meaning, and with less justification, to signify an artificial type of point singularity of vorticity. There should be no confusion with the meaning adopted here.] In a frame of reference moving with the vorton, the flow field $\mathbf{u}(\mathbf{x})$ is steady, and $\mathbf{u} \sim \mathbf{U_0}$ at ∞. The vorton carries with it a domain $\mathcal{D}$ of fluid, bounded by a surface $\partial\mathcal{D}$, which is fixed in the frame of the vorton. Outside $\mathcal{D}$, the streamlines all extend to infinity, and since the vorticity is zero at infinity, this means that $\omega \equiv \mathbf{0}$ outside $\mathcal{D}$. From this perspective, a vortex ring is simply an axisymmetric vorton, steady only insofar as viscous diffusion may be neglected. Although such rings will be our primary concern, it is instructive to consider the possibility of non-axisymmetric vortons also. The question of existence of steady solutions of the Euler equations of this type is then of central concern; and if they do exist, how are they to be classified?

Note that streamline topology (unlike vorticity topology) changes under Galilean transformation; thus for example, Hill's spherical vortex has closed streamlines inside a sphere in the frame of reference in which the flow is steady; but relative to a frame of reference moving with a sufficiently large velocity, the instantaneous streamlines are all perturbations of straight lines extending (both ways) to infinity.

A vorton is characterised by four properties that are invariants of Euler flows even under unsteady conditions: in the frame in which the velocity vanishes at infinity, these are the momentum $\mathbf{P}$, the angular momentum $\mathbf{M}$, the kinetic energy E, and the helicity $\mathcal{H}$, defined (for a fluid of unit density) by:

$$\mathbf{P} = \tfrac{1}{2}\int \mathbf{x}\times\omega\,\mathrm{d}V\,, \tag{1}$$

$$\mathbf{M} = \tfrac{1}{3}\int \mathbf{x}\times(\mathbf{x}\times\omega)\,\mathrm{d}V\,, \tag{2}$$

$$E = \tfrac{1}{2}\int \mathbf{A}\cdot\omega\,\mathrm{d}V\,, \tag{3}$$

$$\mathcal{H} = \int \mathbf{u}\cdot\omega\,\mathrm{d}V\,, \tag{4}$$

where $\mathbf{A}$ is a vector potential for $\mathbf{u}$; the gauge is arbitrary, but usually taken so that $\nabla\cdot\mathbf{A} = 0$. These integrals are deliberately written in terms of ω, and can be taken to be over the finite domain $\mathcal{D}$, since $\omega = 0$ outside $\mathcal{D}$. The helicity is a topological invariant, providing a measure of the degree of linkage of the vortex lines in $\mathcal{D}$ (Moffatt 1969), and is conserved whenever conditions are such the 'vortex lines are frozen in the fluid'. Actually the integral in this case may be taken over any volume inside a Lagrangian surface on which $\omega\cdot\mathbf{n} = 0$, a condition that persists under frozen field evolution.

Steady Euler flows satisfy the equations:

$$\mathbf{u}\times\omega = \nabla h\,,\quad \omega = \nabla\times\mathbf{u}\,,\quad \nabla\cdot\mathbf{u} = 0\,,\quad h = p + \tfrac{1}{2}\mathbf{u}^2\,, \tag{5}$$

where p is the pressure field, and h the 'total head'. It follows that $\mathbf{u}$-lines (i.e. streamlines) and ω-lines (i.e vortex lines) lie on surfaces $h = \text{const}$. The only way that the $\mathbf{u}$-lines can escape from this 'surface' constraint is if $\nabla h \equiv 0$, and $\mathbf{u} = \alpha\omega$, with $\alpha = \text{const.}$, (and of course then the vortex lines coincide with the streamlines). For this type of Beltrami flow, the streamlines need not lie on surfaces, and may be chaotic in sub-domains of $\mathcal{D}$. The 'ABC-flow' of Arnol'd (1966) is of this type, and the chaotic character of its streamlines (albeit in a periodic domain) was explored by Dombre et al (1986).

3 Existence of Vortons

To establish existence results, it is expedient to switch attention to an analogous problem: magnetostatics in a perfectly conducting fluid, described by

the equations:

$$\mathbf{j} \times \mathbf{B} = \nabla p\,, \quad \mathbf{j}(\mathbf{x}) = \nabla \times \mathbf{B}\,, \quad \nabla \cdot \mathbf{B} = 0\,. \tag{6}$$

Here, $\mathbf{B}$ is the magnetic field distribution in the fluid, $\mathbf{j}$ the corresponding current distribution, and $\mathbf{j} \times \mathbf{B}$ the associated Lorentz force. There is an exact analogy between the systems (5) and (6), the analogous pairs of variables being:

$$\{\mathbf{u}\,, \mathbf{B}\}\,, \quad \{\omega\,, \mathbf{j}\}\,, \quad \{h\,, p_0 - p\}\,, \tag{7}$$

where p_0 is a constant. Note the change of sign, the Lorentz force being $\mathbf{j} \times \mathbf{B}$, not $\mathbf{B} \times \mathbf{j}$!

In switching attention to the magnetostatic problem (6), it would appear that we have gained nothing: we have merely replaced one problem by another that is apparently identical. However, the magnetic problem lends itself to a physically natural *relaxation* procedure for the determination of *stable (minimum energy) equilibrium states*.

This invokes a *different* magnetic field analogy: under unsteady conditions, the magnetic field evolves according to the induction equation

$$\partial \mathbf{B}/\partial t = \nabla \times (\mathbf{v} \times \mathbf{B})\,, \tag{8}$$

where $\mathbf{v}$ is now the velocity field (and we deliberately use the symbol $\mathbf{v}$ here rather than $\mathbf{u}$.) This equation has the well-known consequence that the $\mathbf{B}$-lines are frozen in the fluid (like the vortex lines in unsteady Euler flow). However, $\mathbf{B}$ is not here constrained to be the curl of the convecting field $\mathbf{v}$, and equation (8) is linear if $\mathbf{v}$ is regarded as known. One consequence of (8) is conservation of *m*agnetic helicity

$$\mathcal{H}_M = \int \mathbf{A} \cdot \mathbf{B}\, \mathrm{d}V\,, \tag{9}$$

where now $\mathbf{A}$ is a vector potential for $\mathbf{B}$, and the integral is again taken over any volume inside a Lagrangian surface on which $\mathbf{B} \cdot \mathbf{n} = 0$. This result was first obtained by Woltjer (1958), albeit in more restricted form.

The magnetic helicity invariant provides an important lower bound on the magnetic energy $M = \frac{1}{2} \int \mathbf{B}^2\, dV$, namely

$$M \geq 2q\, |\mathcal{H}_M| \tag{10}$$

where q is a constant with the dimensions of (length)$^{-1}$, which depends only on the domain topology, geometry and scale (or the scale of the support of $\mathbf{B}$ if the fluid is unbounded) (Arnol'd 1974).

It is not difficult to construct a process whereby magnetic energy decreases monotonically to a minimum compatible with this lower bound, while conserving the 'frozen-in' character of the field, and therefore conserving its topology however complex this may be. In this process, the field-lines contract (due to Maxwell tension) as far as permitted by this topology. In the

asymptotic stable minimum energy state, the fluid is at rest, and the field satisfies the magnetostatic equilibrium equations (6), reflecting a balance between the Lorentz force and the pressure gradient.

Now we can exploit the Euler-magnetic (or $\{\mathbf{u}, \mathbf{B}\}$) analogy: to each solution of the magnetostatic problem, there corresponds via this analogy a solution of the steady Euler equations. Hence we have an amazing result: given an arbitrary solenoidal velocity field $\mathbf{U}(\mathbf{x})$, there apparently exists a steady Euler flow $\mathbf{u}(\mathbf{x})$ whose streamlines are obtained by continuous deformation (induced by the 'image' relaxation process) of the streamlines of $\mathbf{U}(\mathbf{x})$. Thus there is a huge family of steady Euler flows (e.g. given any knot K, there exists a steady Euler flow for which each streamline is closed and in the form of the knot K); and this result applies equally if the field $\mathbf{U}$ is uniform at infinity (care being needed in this case in handling the surface integrals). Detaile discussion and justification of these statements may be found in Moffatt(1985, 1986, 1988).

There are two immediate qualifications to this result. First, tangential discontinuities of $\mathbf{B}$ may appear asymptotically in the magnetic relaxation process (an important phenomenon in magnetohydrodynamics, believed to be responsible for flares and heating of the solar corona, Parker 1994); this means that the asymptotic state is not strictly topologically equivalent to the initial state. It may however be described as being *topologically accessible* from this initial state (Moffatt 1985). The analogue of the tangential discontinuity in the Euler flow is a vortex sheet, which may be expected to be subject to Kelvin-Helmholtz instability.

This leads naturally to the second qualification: whereas the magnetostatic solutions are stable, being minimum energy states under frozen field perturbations, in fully three-dimensional situations the analogous Euler flows are generally unstable with respect to isovortical perturbations for which the vorticity field is frozen in the fluid, as natural for the unsteady Euler equations (Rouchon 1991). Although the analogous steady equilibrium states (magnetostatic and Euler) are in effect identical, their stability properties are quite different. Kelvin's vortex atom theory was doomed because of the intrinsic instability of steady three-dimensional Euler flows! It is moreover this intrinsic instability that may be recognised as the primary cause of turbulence!

4 The Axisymmetric Situation

The same magnetic relaxation procedure may be carried out when the initial magnetic fields is axisymmetric and uniform ($\mathbf{B}_0$, say) at infinity. Obviously if all field lines extend to infinity, then the field can and will relax to the uniform field $\mathbf{B}_0$ everywhere. Only if there is a domain of closed $\mathbf{B}$-lines does the field relax to a non-trivial state. Let χ be the flux-function (the analogue of the Stokes streamfunction ψ) of the magnetic field. During relaxation the toroidal surfaces $\chi = \text{const.}$ move with the fluid, and, by virtue of incompressibility,

the volume $V(\chi)$ inside each such surface is conserved. So also is the flux $W(\chi)$ of field in the zonal direction inside each such torus, by virtue of the frozen field behaviour (and Alfvén's theorem). The pair of functions $S = \{V(\chi), W(\chi)\}$ constitutes a *signature* for the field, conserved, as a signature should be, during the relaxation process. The 'amazing' result here is that, for any initial field uniform at infinity and having a domain $\mathcal{D}$ of closed streamlines, and arbitrary signature S within $\mathcal{D}$, there exists a steady Euler flow with the same topology and the same signature S. These are vortex rings, and it is apparent from this argument that a very wide family of such rings exist. The function $W(\psi)$ corresponds to the distribution of swirl within the vortex around the axis of symmetry; of course, this W may be identically zero.

The domain $\mathcal{D}$ may have either spherical or toroidal topology. The former type of vortex ring is sometimes described as 'fat', the latter 'thin'. There is an important distinction here in that tangential discontinuities cannot form if the relaxing field has fat topology, for this would require infinite stretching of field lines on the osculating surfaces, and this is incompatible with monotonic decrease of magnetic energy to a minimum. Tangential discontinuities can however form for the thin topology, due to possible collapse of the field at the ring of saddle points on the inner part of $\partial\mathcal{D}$ (Moffatt 1988). Such collapse has been described for 2-dimensional field relaxation by Linardatos (1993), and the situation is similar here.

Hence it is only for fat rings that the magnetic relaxation process provides a family of rings with everywhere continuous velocity.

5 The Wind-Up Process of Vallis, Carnevale and Young

The magnetic relaxation process suffers from the disadvantage that it is the topology of the velocity field, rather than that of the vorticity field, that can be 'prescribed'. It would be far more useful to devise a relaxation process that conserves vorticity topology, because that is what is conserved by the unsteady Euler equations themselves.

One such procedure has been devised by Vallis et al (1989). This is potentially extremely useful for two-dimensional or axisymmetric situations, but fails for three-dimensional situations, for reasons indicated below. We suppose that a localised vorticity field evolves according to the equation

$$\partial\omega/\partial t = \nabla\times(\mathbf{v}\times\omega), \text{where } \omega = \nabla\times\mathbf{u},\ \mathbf{v} = \mathbf{u}+\alpha\partial\mathbf{u}/\partial t \text{ and } \nabla\cdot\mathbf{u} = 0\,. \quad (11)$$

This may be described as 'artificial dynamics', but it is a dynamical evolution for which the vorticity field is transported by $\mathbf{v}$, and so has conserved topology. The energy E is not however conserved: elementary manipulations give

$$dE/dt = -\alpha\int[\partial\mathbf{u}/\partial t]^2\ \mathrm{d}V, \quad (12)$$

so that E decreases or increases according as α is positive or negative. This result is useful only if a positive lower bound or a finite upper bound can be placed on E (since otherwise, E may relax to zero in the former case, or increase to infinity in the latter, and in neither case can a useful conclusion be drawn). Unfortunately, there is in general no lower bound on E analogous to (10). However, there is a finite *upper* bound in the axisymmetric situation without swirl, as may be proved using a combination of Schwartz and Poincaré inequalities coupled with the fact that $[\omega_\varphi / r \sin\theta]$ is a Lagrangian invariant of the flow $\mathbf{v}$ (Moffatt 1990b); this means that in this case, if we take α negative, so that E *increases* monotonically, it must tend to a limit not greater than this upper bound. This process is perhaps better described as a 'wind-up' rather than a 'relaxation' process, because of the increase of kinetic energy. Anyway, the important thing is that the process tends to a limit in which $\partial \mathbf{u}/\partial \mathbf{t} = 0$ everywhere; in this limit, $\mathbf{v} \equiv \mathbf{u}$, and we have a steady Euler flow, whose signature is that of the (arbitrary) initial field.

It had previously been asserted (Benjamin 1976) that vortex rings are steady solutions of the Euler equations of maximum energy with respect to 'rearrangement' of the vortex lines, or what amounts to the same thing, isovortical perturbations. The above 'wind-up' process has provided some justification for this assertion. Such solutions should also be stable with respect to axisymmetric isovortical perturbations, by arguments due to Arnol'd (1966), but the question of their stability with respect to non-axisymmetric perturbations remains open.

6 Energy of Knotted Flux Tubes

A flux tube of volume V, carrying magnetic flux Φ (the analogue of κ) and knotted in the form of a knot of type K , has magnetic helicity $\mathcal{H}_M = h\Phi^2$, where h is the conserved writhe-plus-twist of the tube (Moffatt & Ricca 1992). On dimensional grounds, the minimum energy of this knotted tube, in its fully relaxed state, is

$$M_{min} = m_K(h)\Phi^2 V^{-1/3}\,, \tag{13}$$

where $m_K(h)$ is a dimensionless function of h, determined solely by the knot type K (Moffatt 1990b). Moreover, this state, being stable, will be characterised by a spectrum of real frequencies ω_n, which, again on dimensional grounds, are given by

$$\omega_n = \Omega_{Kn}(h)\Phi V^{-1}\,. \tag{14}$$

This is just the sort of result that Kelvin needed as a basis for his 'vortex' atom theory! If he had been able to formulate his ideas in terms of magnetic flux tubes in an 'ideal' conducting fluid, instead of vortex tubes, then these ideas could really have taken root! Although all the ingredients of electromagnetism were by then available, another 75 years were to pass before

the marriage of electromagnetic theory and fluid dynamics was successfully consummated in the work of Alfvén (1942).

When the internal twist of a flux tube is small, minimum energy is achieved when the tube is contracted to minimum length (for prescribed volume in response to Maxwell tension); in this configuration, the tube is in a 'pulled-tight' state, making contact with itself on contact surfaces of tangential discontinuity.

This configuration is close to the 'ideal knot' concept of Stasiak et al(1998). One physically illuminating way to construct an ideal knot is as follows: take a unit volume of plasticine in the form of a 'standard' cylinder of circular cross-section whose height and diameter are equal, and roll this out so that it becomes a cylinder, still of circular cross-section, of length L. For large L, the work done in this process is roughly proportional to L, and it is reasonable to *define* the (dimensionless) energy of this rolled-out state as $E = L$. Now for a given knot K, we choose L to be the minimum length for which the tube can be tied in this knot, the ends being then joined together (the bending energy expended in this knotting process can be supposed negligible, and the cross-section can be assumed to remain circular and of constant radius). The result is the 'ideal' (or what I would prefer to call the 'pulled-tight') configuration of the knot K.

This differs from the magnetic flux tube in two minor respects: (i) the minimum energy knotted flux-tube does not have uniform circular cross-section (although this can be imposed as an additional constraint – see Chui & Moffatt 1995); and (ii) it does in general have internal twist, which is not present in the above plasticine construction (although it could be added). Nevertheless, the ideal knot may be recognised as a close relative of the minimum energy knotted flux tube.

The pulled-tight configurations of all prime knots of up to 8 crossings and their associated lengths have been computed by Stasiak *et al* (1998) (see also Flammini & Stasiak 2006). Thus the 'ground-state' energies of these knots may be regarded as known. As pointed out by Moffatt (1990b), higher energy states (corresponding to local energy minima) may be expected to exist also, and we should therefore allow for an 'energy spectrum' for each knot; it is the lowest, or ground state, energy that is of greatest potential interest.

7 Knots in the Quark-Gluon Plasma

These arcane considerations come to life in the extreme context of the 'quark-gluon' plasma, the hypothesised state of matter in the universe just microseconds after the Big Bang. Experiments in the Relativistic Heavy Ion Collider (Brookhaven National Laboratory) involving collision of gold nuclei produce a quark-gluon plasma that, remarkably, behaves like "a liquid of very low viscosity" [as described in *New Scientist*, 14 July 2007].

Gluons are the quantum chromodynamic (QCD) flux tubes that connect quarks allowing the transmission of force between them. It has been conjectured that 'glueballs' (solitonic solutions of the QCD equations) are knotted QCD tubes within such a plasma (Buniy & Kephart 2005); these are manifest as excitations in the plasma with an energy spectrum which is in principle measurable.

Bunyi & Kephart have found a remarkable correlation between the low-energy levels measured in these experiments, and the ground-state energies of knots of low crossing number: the two are linearly related up to knots of crossing number nine (as far as measurements are available). The suggestion that these fundamental excitations in matter in its most primitive form are knotted QCD flux tubes is quite compelling. Kelvin might have said "I told you so"! But of course here, the physical context is very different. Most importantly, the QCD tubes are quantised with universal cross-sectional radius on the quantum scale determined by the QCD force field, so relaxation to a minimum energy state conserves cross-section rather than volume. Nevertheless, the concept of knotted flux tubes in a minimum energy configuration returns to centre-stage!

8 Conclusions and Perspectives

I may perhaps be allowed to conclude with three philosophical, not to say, theological, remarks. First, the old 19th century concept of an ether (an ideal incompressible fluid permeating all space), so ardently embraced by Kelvin, is now replaced in this 21st century by the 'quark-gluon plasma', the most primitive manifestation of matter in the very early universe.

Second, as we have seen above, Kelvin's knotted vortices in the ether representing atoms (in his time the most fundamental building blocks of the material world) are now replaced by knotted chromo-magnetic flux tubes, i.e. glueballs, the most fundamental excitations in the quark-gluon plasma.

And third, God, that 'immortal, invisible' influence promoting the creation of matter and life as we know it, is replaced in current cosmology by 'Dark Energy', that equally intangible concept required to render astronomical observations compatible with currently-known fundamental principles of physics.

Plus ça change, plus c'est la même chose?

References

1. Alfvén, H.: On the existence of electromagnetic-hydromagnetic waves. Arkiv. F. Mat. Astron. Fysik 29B(2), 7 (1942)
2. Arnol'd, V.I.: Sur un principle variational pour les ecolements stationnaires des liquides parfaits et ses applications aux problemes de stabilité non-lineaires. J. Mec. 5, 29–43 (1966)

3. Arnol'd, V.I.: The asymptotic Hopf invariant and its applications. In: Proc. Summer School in Differential Equations, Erevan, Armenian SSR Acad. of Sc. (1974) [English translation: Sel. Math. Sov. 5, 327–345, 1986]
4. Benjamin, T.B.: The alliance of practical and analytical insights into the nonlinear problems of fluid mechanics. In: Germain, P., Nayroles, B. (eds.). Lecture Notes in Mathematics, vol. 503, pp. 8–29. Springer (1976)
5. Buniy, R.V., Kephart, T.W.: Glueballs and the universal energy spectrum of tight knots and links. Int. J. Mod. Phys. A 20, 1252–1259 (2005), doi:10.1142/S0217751X05024146
6. Chui, A.Y.K., Moffatt, H.K.: The energy and helicity of knotted magnetic flux tubes. Proc. Roy. Soc. Lond. A 451, 609–629 (1995)
7. Dombre, T., Frisch, U., Greene, J.M., Hénon, M., Mehr, A., Soward, A.M.: Chaotic streamlines in the ABC flow. J. Fluid Mech. 167, 353–391 (1986)
8. Flammini, A., Stasiak, A.: Natural classification of knots. Proc. Roy. Soc. Lond. A (2006), doi:10.1098/rspa.2006.1782
9. Kelvin, L.: On vortex attoms. Phil. Mag. 34, 15–24 (1867)
10. Kelvin, L.: On vortex motion. Trans. Roy. Soc. Edin. 25, 217–260 (1869)
11. Linardatos, D.: Determination of two-dimensional magnetostatic equilibria and analogous Euler flows. J. Fluid Mech. 246, 569–591 (1993)
12. Moffatt, H.K.: The degree of knottedness of tangled vortex lines. J. Fluid Mech. 36, 117–129 (1969)
13. Moffatt, H.K.: Magnetostatic equilibria and analogous Euler flows of arbitrarily complex topology Part I, Fundamentals. J. Fluid Mech. 159, 359–378 (1985)
14. Moffatt, H.K.: On the existence of localized rotational disturbances which propagate without change of structure in an inviscid fluid. J. Fluid Mech. 173, 289–302 (1986)
15. Moffatt, H.K.: Generalised vortex rings with and without swirl. Fluid Dynamics Research 3, 22–30 (1988)
16. Moffatt, H.K.: Structure and stability of solutions of the Euler equations: a Lagrangian approach. Phil. Trans. R. Soc. Lond. 333, 321–342 (1990a)
17. Moffatt, H.K.: The energy spectrum of knots and links. Nature 347, 367–369 (1990b)
18. Moffatt, H.K., Ricca, R.L.: Helicity and the Călugăreanu invariant. Proc. Roy. Soc. Lond. A 439, 411–429 (1992)
19. Rouchon, P.: On the Arnol'd stability criterion for steady-state flows of an ideal fluid. Eur. J. Mech. B/Fluids 10, 651–661 (1991)
20. Parker, E.N.: Spontaneous current sheets in magnetic fields. Oxford University Press (1994)
21. Stasiak, A., Dubochet, J., Katritch, V., Pieranski, P.: Ideal knots and their relation to the physics of real knots. In: Stasiak, A., Katritch, V., Kauffman, L.H. (eds.) Ideal Knots, pp. 1–19. World Scientific (1998)
22. Vallis, G.K., Carnevale, G.F., Young, W.R.: Extremal energy properties and construction of stable solutions of the Euler equations. J. Fluid Mech. 207, 133–152 (1989)
23. Woltjer, L.: A theorem on force-free magnetic fields. Proc. Nat. Acad. Sci. USA 44, 489–491 (1958)

Instabilities across the Scales: Simple Models for Shear Banding, Plate Subduction and Mantle Convection in Geodynamics

Hans-Bernd Mühlhaus[1,2], Louis Moresi[3], Matt Davies[1], Klaus Gottschald[1], and Alina Hale[4]

[1] Earth Systems Science Computational Centre (ESSCC), The University of Queensland, St Lucia, Queensland, Australia
muhlhaus@uq.edu
[2] CSIRO Division of Exploration and Mining, 26 Dick Perry Ave, Kensington, Western Australia, Australia
[3] School of Mathematical Sciences, Monash University, Clayton, Victoria, Australia
[4] School of Geosciences, University of Sydney, Sydney, Australia

Abstract. The Earth shows different modes of deformation in response to thermal or gravitational driving forces. The bulk mantle convects like a viscous fluid on the global scale, while the lithosphere is broken into several plates. They show little internal deformation, but change their shapes and relative positions. Oceanic plate material is generated at divergent margins and recycled into the mantle at subduction zones, on a regional scale. The buoyant continental crust resists subduction and develops meter-scale shear bands during deformation.

In this article we review Eulerian finite element (FE) schemes and a particle-in-cell (PIC) FE scheme [15]. Focussing initially on models of crustal deformation at a scale of a few tens of km, we choose a Mohr-Coulomb yield criterion based upon the idea that frictional slip occurs on whichever one of many randomly oriented planes happens to be favourably oriented with respect to the stress field. As coupled crust/mantle models become more sophisticated it is important to be able to use whichever failure model is appropriate to a given part of the system. We have therefore developed a way to represent Mohr-Coulomb failure within a mantle-convection fluid dynamics code.

With the modelling of lithosphere deformation we use an orthotropic viscous rheology (a different viscosity for pure shear to that for simple shear) to define a preferred plane for slip to occur given the local stress field. The simple-shear viscosity and the deformation can then be iterated to ensure

that the yield criterion is always satisfied. We again assume the Boussinesq approximation - neglecting any effect of dilatancy on the stress field.

Subduction is modelled as a Rayleigh-Taylor instability with dense oceanic lithosphere sinking into less dense sublithospheric mantle. We use a linear viscous rheology for the mantle in this case. Parts of the lithosphere are viscous, others brittle. The values of the dynamic viscosity are different for lithosphere and mantle. The brittle behaviour of parts of the lithosphere can be modelled in the continuum limit by using a viscoplastic rheology.

Turning to the largest planetary scale, we present an outline of the mechanics of unified models plate-mantle models and then show how computational solutions can be obtained for such models using Escript. The consequent results for different types of convection are presented and the stability of the observed flow patterns with respect to different initial conditions and computational resolutions is discussed.

1 Introduction

Heat loss from the Earth's deep interior occurs through a process of thermal convection in the solid mantle. The pattern of deep convection is not directly observable as it is strongly modified by the very non-linear response of the near-surface rocks in the cool thermal boundary layer (the lithosphere).

The ocean floor is made up of a dozen or so near-rigid "plates" which constitute the upper thermal boundary layer of this convection system. Consequently, the entire ocean floor is recycled with a characteristic time of 100-200 million years.

Tectonic plates on Earth are characterized by little internal deformation , but changing relative positions and shapes due to subduction, deformation in back-arc basins or collisional zones, and generation of oceanic lithosphere, all at different plate rim segments. This mode of convection is the primary means of cooling the mantle, mainly driven by the negative buoyancy of subducting slabs.

The entire ocean floor is recycled with a characteristic time of 100-200 million years. Continents do not participate in the active overturn of the mantle, largely because they contain a high percentage of granitic rock which is light relative to the olivine composition of the mantle. The continents have been able to resist being recycled completely for at least 4 billion years. In some areas ("cratons") have remained largely undeformed for this time, while other areas have undergone enormous deformation to form (and reform) mountain belts. The strong correlation between seismicity and plate boundaries (e.g. Barazangi and Dorman) makes it seem likely that plate motions are associated with localization of deformation occurring when stresses reach the yield strength of the lithosphere. In addition, close to the surface where temperatures are less than approximately 600° C it becomes necessary to consider the role of elasticity.

From a modelling point of view, it is necessary to consider the fluid convection of the mantle and the history-dependent viscoelastic/brittle behaviour of the continental crust as a single coupled system. The requirements for a geological simulation code are therefore an ability to track boundaries and interfaces through extremely large deformation, including fluid convection, of non-linear history dependent materials. The wide range of physical and temporal scales, and the many coupled physical processes also impose a need for computational efficiency. The code should also be very flexible in the rheological laws which it can treat.

In this paper we describe two flow models which accurately treat these difficulties at overlapping scales. In the first we describe an orthotropic plasticity model formulated from a fluid dynamics viewpoint which can model coupled mantle convection and crustal deformation. This model can also be used to model localized faulting in the crust. In the second example, we examine the role of the temperature-dependent viscosity and elasticity in planetary scale convection models with a yield criterion applied to the lithosphere.

1.1 Continuum Deformation and Fault Formation

The surface deformation of the Earth is dominated by the presence of faults on which a very large fraction of strain is accommodated in the long term (Dolan, *pers. comm.*). In the modeling of large scale deformation of the Earth in both the ocean basins and in the continents, there has been a strong philosophical divide between those who consider that these faults are dominant, fundamentally distinct, component of the system at every scale [28, 30, 29, 31, 32, 2], and those who believe that, on a lithospheric scale, the deformation on faults can be averaged within a continuum description more in tune with the underlying driving forces [7, 8].

The reason that such a debate is possible after many years of discussion is almost certainly due to the fact that each of these approaches captures something important, but different, about the way the Earth works. In models of actively deforming continents, a thin skin continuum representation of the mantle lithosphere and crust captures the large-scale deformation in a reliable, reproducible way [6, 7] but not capture important detail in the surface strain field associated with the largest faults. Thin skin models of the brittle layer in which known faults are explicitly included capture this fine detail [2, 14] but the fidelity of the model deformation is very reliant on accurate prior knowledge of the faults' distribution and their dips.

A "thick-skin" model of the continental lithosphere which also includes the major faults in the brittle regime is the appropriate way to bridge these two thin-skin approaches, but is significantly more challenging computationally. We describe an algorithm which can model both the frictional behaviour of localized faults, the non-linear rheology applicable to the broad scale where the faults are too small to resolve individually, and the fluid behaviour of active thermal convection in the mantle.

We use a linear viscous rheology for the mantle. Parts of the lithosphere are viscous, others brittle. The values of the dynamic viscosity are different for lithosphere and mantle. In regional subduction models, the brittle behaviour of parts of the lithosphere can be modelled in the continuum limit by using the viscoplastic rheology. Elastoviscoplastic deformation is a more suitable description for the small scale behaviour of the crust.

2 Constitutive Models

In geodynamics we commonly treat the Earth on a large scale as an incompressible, viscous fluid with infinite Prandtl number in which motions are driven by internal temperature variations. Elastic deformation is important only in the low-temperature part of the system and is therefore usually assumed to have a minor effect on the system at the largest (planetary) scale [26, 27]. The force term is a gravitational body force due to density changes. We assume that these arise, for any given material, through temperature effects so that:

$$\sigma_{ij,j} - p_{,i} = g\rho_0(1 - \alpha_T T)z_i \tag{1}$$

where g is the acceleration due to gravity, ρ_0 is material density at a reference temperature, α_T is the coefficient of thermal expansivity, and T is temperature. z_i is a unit vector in the vertical direction. We have also assumed that the variation in density only needs to be considered in the driving term (the Boussinesq approximation: Boussinesq, 1903).

Substituting a general viscous constitutive law

$$\sigma_{ij} = 2\eta_{ijkl}D_{kl}, \qquad D_{ij} = (v_{i,j} + v_{j,i})/2 \tag{2}$$

gives the equation of motion:

$$(\eta_{ijkl}D_{kl})_{,j} - p_{,i} = g\rho_0(1 - \alpha_T T)z_i \tag{3}$$

Motion is driven by the heat escaping from the interior. The energy equation governs the evolution of the temperature in response to advective transport of heat by the fluid and diffusion of heat through the fluid. For a given fluid element,

$$\dot{T} = \frac{\mathrm{D}T}{\mathrm{D}t} = -(\kappa T_{,i})_{,i} + Q(t) \tag{4}$$

where κ is the thermal diffusivity of the material, and $Q(t)$ is a source term attributed to decay of radioactive materials within the Earth.

2.1 Viscosity of Mantle Materials on Geological Timescales

The viscosity of the mantle at long timescale is known to be a strong function of temperature, pressure, stress, grain-size, composition (particularly water

content). Karato & Wu [12], give the following expression for the deformation of upper mantle material:

$$\eta = \frac{1}{2A}\left(\frac{\mu}{\tau}\right)^{n-1}\left(\frac{h}{b^*}\right)^{m} e^{\frac{E^*+PV^*}{RT}} \tag{5}$$

where A is a constant, μ is shear modulus, b^* is the Burgers vector, T is temperature, τ is the second invariant of the deviatoric stress tensor (i.e $\tau = \sqrt{\sigma_{ij}\sigma_{ij}/2}$ where σ_{ij} is the stress tensor and σ'_{ij} its deviator), E^* is an activation energy, V^* and activation volume, R is the gas constant, h is the grain size, n is a stress exponent, and m a grain-size exponent. Despite this complexity, the dominant effect on the viscosity from the point of view of the large-scale dynamics of the system is the effect of temperature (e.g. Solomatov [22]). Some anisotropy of material properties is observed in mantle materials due to crystallographic realignment during strain but the effect is not well characterized and may be more important in diagnosing strain than in influencing the deformation itself [20].

Fault Model Failure Criterion

An idealized picture of a geological fault is of a two dimensional discontinuity surface arbitrarily embedded in the unfractured rock. In all but the very near surface regions, it is appropriate to assume that the overburden pressure is sufficient to prevent the fault surfaces separating, and that deformation occurs by frictional sliding in the plane of the fault [1]. If we consider a small planar element of the fault with a normal, **n**, and mutually orthogonal vectors, **s** and **m**, lying in the fault plane. The traction resolved in each of these directions is given by:

$$\sigma_{nn} = n_i n_j \sigma_{ij} \tag{6}$$

$$\sigma_{sn} = s_i n_j \sigma_{ij} \tag{7}$$

$$\sigma_{nm} = n_i m_j \sigma_{ij} \tag{8}$$

If we assume that **s** was chosen parallel to the direction of maximum traction in the fault-plane, then the yield criterion for the fault segment is given by $f = 0$ in

$$f = |\sigma_{sn}| + \tan\varphi\sigma_{nn} - c \leq 0 \tag{9}$$

Where φ the friction angle and c is cohesion. It is possible to express the magnitude of the maximum shear traction in the fault plane as

$$\tau_s = |\sigma_{sn}| = \sqrt{\sigma_{ik}\sigma_{il}n_k n_l - \sigma_{nn}^2} \tag{10}$$

without explicitly calculating **s**. We note that $\tau_S$is invariant with respect to changes of the pressure p so that $\tau_S(\sigma_{ij}) = \tau_S(\sigma'_{ij})$, where σ'_{ij} is the deviatoric stress tensor.

Continuum Failure Criterion

The previous model applies to a fault which is already established independently of the prevailing stress field and has a length scale which is large with respect to the system as a whole. This description is only appropriate for the largest few faults in any system. We also assume that there are very many faults at smaller scales which can be represented by a continuum approximation. The continuum approximation rests upon the assumption that, at the small scale, all orientations of incipient faults are present. For any given stress field, we can then assume that there is at least one incipient fault within every element of the material which is oriented in such a way that it fails earlier than any other fault and begins to grow. For a point in the material we consider the plane which contains the minimum (here most compressive) and maximum principal stresses (σ_I and σ_{III}). Resolving the stress onto a fault oriented at an angle θ measured positive counterclockwise to the σ_{III} direction yields

$$\sigma_{nn} = \frac{1}{2}(\sigma_I + \sigma_{III}) + \frac{1}{2}(\sigma_I - \sigma_{III})\cos(2\theta) \tag{11}$$

$$\sigma_{sn} = \frac{1}{2}(\sigma_I - \sigma_{III})\sin(2\theta) \tag{12}$$

Substituting into the yield criterion (9) gives:

$$\sigma_I - \sigma_{III} = \frac{\tan\varphi \frac{\sigma_I + \sigma_{III}}{2} + c}{\sin(2\theta) - \tan\varphi\cos(2\theta)} \tag{13}$$

In the early theories of shear failure and shear banding it was assumed that failure takes place on spontaneously forming rupture planes or shear bands which are oriented such that the stress difference on the left hand side of (13) is a minimum (see Brady and Brown [3] for a derivation close to the spirit of Coulomb's (1776) derivation). It is then simple to compute $d(\sigma_I - \sigma_{III})/d\theta$ to find the value of θ_B which minimizes the differential stress required for failure to be

$$\theta_B = \pm \arctan(\tan^{-1}\varphi) = \mp(\frac{\pi}{4} + \frac{\varphi}{2}) \tag{14}$$

Replacing θ by θ_B in (13) gives

$$\frac{\sigma_I - \sigma_{III}}{2} = -\sin\varphi\frac{\sigma_I + \sigma_{III}}{2} + c\cos\varphi \tag{15}$$

In a pristine material we expect faults to form at an angle between 22.5° and 45° to the most compressive principal stress direction. In the Earth ($\tan\varphi \leq 1$) this means that we expect steep faults to form in extensional environments (**s** close to the direction of gravity) and shallow faults to form in compressive environments (**s** close to orthogonal to the direction of gravity). The orientations (14) can be used to define a curve-linear system of coordinates within the plastic zone of a boundary value problem. The coordinate

lines are the so called static characteristics (see Hill [10] for an outline of the method of characteristics). The static characteristics do not necessarily coincide the orientation of macroscopic shear bands (see the pioneering paper by Rudnicki and Rice [21] and Vardoulakis and Sulem [25] for an outline in the context of geomechanics including experiments).

Flow Rule for Plasticity Model

The yield criterion provides a limit on the acceptable stress states in the material. A corresponding flow rule is needed to determine the manner in which the material deforms when the yield stress is reached. The incompressible fluid assumption which we made in formulating the mantle convection problem is a severe constraint on the possible flow rules. In the theory of plasticity one assumes flow rules of the form

$$\mathbf{D}^p = \dot{\gamma}^p \frac{\partial g}{\partial \sigma} \tag{16}$$

Where $\dot{\gamma}^p$ is the equivalent plastic strain rate and g is the so called plastic potential and $\mathbf{D}^p$ is the plastic part of the stretching; here we assume that the total stretching can be decomposed into a viscous and a plastic part. Elastic strains are assumed as insignificant for the problems considered here. The incompressibility constrain is satisfied if g depends on the deviatoric stress only. Apart from that, g depends on the stress invariants according to the symmetry of the material and possibly on other state variables such as temperature. The standard choice for g in connection with a yield criterion of type (9) or (15) with $\theta = \pm\theta_B$ is $g = \tau_S(\theta = \pm\pi/4) = \sqrt{(\sigma_{11} - \sigma_{22})^2/4 + \sigma_{12}^2}$.

Closer to the implicitly made assumption that upon yielding, plastic deformation consists in frictional sliding on two, possibly simultaneously active sets of thin parallel bands [5] is the following choice of the flow rule:

$$\mathbf{D}^p = \dot{\gamma}_a^p \frac{\partial \tau_S^a}{\partial \sigma} + \dot{\gamma}_b^p \frac{\partial \tau_S^b}{\partial \sigma} \tag{17}$$

where $\tau_S^a = \tau_S(\theta = \pi/4 + \varphi/2)$ and $\tau_S^b = \tau_S(\theta = -\pi/4 - \varphi/2)$ and $\dot{\gamma}_a^p \geq 0$, $\dot{\gamma}_b^p \geq 0$.

We shall concentrate on shear banding processes on a scale involving the lithosphere as well as parts of the underlying asthenosphere. Shear banding may be triggered by the structural non-symmetry of the constitutive equations due to the simultaneous pressure sensitivity of the yield criterion and the assumed incompressibility and/or due to some form of strain softening. In the application we will consider softening of the friction angle and the cohesion. In these applications we adopt a simplified form of the constitutive model where we assume that only one of the two glide mechanisms is active. In this case upon continuing yielding the material deforms like a transversely anisotropic medium of the type proposed by Mühlhaus *et al* [19, 18].

To account for the anisotropic nature of the material, locally transverse-isotropic viscous material is characterised by two effective viscosities, η and η_S, where η is the conventional viscosity and η_S is introduced as a shear viscosity applicable for flow along a layer. The isotropic part of the stretching is then corrected by the Λ_{ijkl} tensor:

$$\sigma_{ij} = 2\eta D_{ij} + 2\,(\eta_S - \eta)\,\Lambda_{ijkl} D_{kl} - p\delta_{ij} \tag{18}$$

where

$$\Lambda_{ijkl} = {}^1\!/_2\,(n_i n_k \delta_{lj} + n_j n_k \delta_{il} + n_i n_l \delta_{kj} + n_j n_l \delta_{ik}) - 2 n_i n_j n_k n_l$$

and $\mathbf{n}$ is a normal surface vector defining the orientation of the material layering known as the *director*. The inverse form of the constitutive model (18) reads [18]:

$$D_{ij} = \frac{1}{2\eta}\sigma'_{ij} + (\frac{1}{2\eta_S} - \frac{1}{2\eta})\Lambda_{ijkl}\ \sigma'_{kl} \tag{19}$$

We also note the relationship:

$$\tau_S = \sqrt{1/2 \Lambda_{ijkl}\sigma_{ij}\sigma_{kl}} \tag{20}$$

Since we consider only one slip system we do not need subscripts anymore and designate the equivalent strain rate of the active glide system as $\dot{\gamma}^p$. Comparing (17) and (19) we find the following expression for the shear viscosity η_S:

$$2\eta_S = 2(\frac{1}{\eta} + \frac{\dot{\gamma}^p}{\tau_S})^{-1} = \frac{2\eta(\dot{\gamma} - F/\eta)}{\dot{\gamma}}, \qquad \dot{\gamma} = \frac{\partial \tau_S}{\partial \sigma_{ij}} D_{ij} \tag{21}$$

where

$$F = \Big(\frac{\partial \tau_S}{\partial \sigma_{ij}} + \tan\varphi \frac{\partial \sigma_{nn}}{\partial \sigma_{ij}}\Big)\sigma_{ij}^{\mathrm{vis}} - c, \qquad \sigma_{ij}^{\mathrm{vis}} = 2\eta D_{ij} - \delta_{ij} p \tag{22}$$

Thus:

$$2\eta_S = \frac{-\tan\varphi(2\eta n_k n_l D_{kl} - p) + c}{\dot{\gamma}} \tag{23}$$

The denominator of (23) is the total shear strain rate on the active glide system.

Failure History, Strain Softening and Healing

We now consider a possible history dependency of the mechanical parameters of the glide planes and the effect of deformation on the orientation of the failure planes; we also wish to consider the possibility of simple healing (annealing) of the glide planes or shear bands once de-activated.

Before addressing the above items we note that although our models bares some superficial similarities with the micromechanics based crystallographic

slip theories for metals [4], the present model is very different. We neglect elastic deformations, vacancies and interstitials, the main carriers of the viscous part of the deformation are assumed to diffuse freely through the lattice without affecting the plastic part of the deformation. An intermediate configuration as assumed in elasto-plasticity does not exist in the present case. The glide planes are considered either as shear fractures or in the plasticity case as macroscopic strain localizations usually encompassing multiple grains. Plasticity becomes relevant at greater depth below the top 30 kilometres at large pressures and high temperatures. In this case, the pressure sensitivity (angle of friction) usually disappears. If not, the formal description is analogous to that of fractures. The question then arises as to how the glide planes are affected by deformation and stress rotation. One possibility is to treat the glide planes as embedded in the plastic deformation as described by the history of the inelastic velocity gradient $\mathbf{L}^p$. However, experience with fixed smeared crack models demonstrates that these models tend to cause stress locking, i.e. an artificial build-up of shear stresses along the crack. In the smeared crack model the stress locking was overcome by co-rotating the cracks with the principal stress axes. This is very simple indeed and an analogous approach is adopted here. The glide planes are always oriented relative to the principal stress axes as defined by the mobilized angle of friction φ in relationship (14). In metal plasticity the orientation of the slip planes are constant with respect to the intermediate configuration.

We assume that strain hardening/softening and healing can be described by means of the following relative strain measure:

$$\gamma^p_{rel} = \int (\dot{\gamma}^p - \theta \frac{\tau_S}{\eta})\, \mathrm{d}t \quad , \quad \gamma^p_{rel} \geq 0 \tag{24}$$

In (24) $0 < \theta < 1$ is a dimensionless temperature-dependent healing parameter. Given that the most likely micro-structural features that give rise to shear bands are dislocations, the healing or annealing processes usually involve movement of vacancies (maybe interstitials) to these dislocations which will rearrange themselves into lower energy configurations such as sub-grain structures. The extent of this rearranging process depends on the density of dislocations and the temperature at which the "healing" occurs. The healing is usually considered at a two stage process involving (a) recovery and (b) re-crystallization. Since both processes may occur during deformation itself, the term dynamic can be applied to both processes. Details on the physics of recrystallisation and annealing can be found in Humphreys and Hatherly [11]. Another healing mechanism is associated with fluid flow along channels in grain boundaries and flow in microcracks; this mechanism is several orders of magnitude faster than having vacancies diffuse along such crystalline defect structures as dislocations, dislocation substructures and intact grain boundaries.

The relationship (24) is assumed to hold even if the shear band is not active, i.e. $\dot{\gamma}^p = 0$. The parameter γ^p_{rel} is not a state parameter but a measure

to quantify the relative effect of creation and annihilation of inelastic structures (e.g. shear bands) caused by plastic deformations chosen for heuristic reasons.

During the actual calculation, we iterate to determine the distribution of particles which are currently yielding, we consider first whether each particle has failed in a previous time step and test to see if it will fail given the updated stress distribution. In 3D, the slip direction is assumed to lie in the failure plane in the direction of maximum resolved shear stress. The friction coefficient and/or the cohesion for the material points which have failed weaken as relative slip (24) accumulates during yielding. If a material point has failed in the past but changes in the ambient stress field mean that it is no longer yielding, then the history parameter (24) decreases until $\gamma^p_{rel} = 0$.

The cohesion and/or friction coefficient are softened according to

$$c(\alpha) = \alpha c(0) + (1-\alpha)c(1) \quad \text{and} \tag{25}$$

$$\tan(\phi(\beta)) = \beta \tan(\phi(0) + (1-\beta)\tan(\phi(1)) \tag{26}$$

where $\alpha = \min(1, \gamma^p_{rel}/\gamma^c_0)$ and $\beta = \min(1, \gamma^p_{rel}/\gamma^\phi_0)$.

3 Numerical Strategies

3.1 Moving Integration Points

The constitutive model described above has been implemented into a Lagrangian integration point finite element code [15]. The method uses a standard mesh to discretize the domain into elements. The shape functions interpolate node points in the mesh in the usual fashion and are used to compute derivatives of nodal variables. Material property variations, and history variables such as failure plane orientation and failure history are stored on integration points which are also material points of the fluid. The problem is formulated through the usual FEM weak form to give an integral equation which can then be decomposed to a series of element integrals and through the usual Galerkin discretization procedure, give element stiffness matrices, $\mathbf{K}^E$:

$$\mathbf{K}^E = \int_{\Omega_E} \mathbf{B}^T(\mathbf{x})\mathbf{C}(\mathbf{x})\mathbf{B}(\mathbf{x})\,\mathrm{d}\Omega \tag{27}$$

We replace the continuous integral by a summation

$$\mathbf{K}^E = \sum_p w_p \mathbf{B}^T_p(\mathbf{x}_p)\mathbf{C}_p(\mathbf{x}_p)\mathbf{B}_p(\mathbf{x}_p) \tag{28}$$

Here the matrix $\mathbf{B}$ consists of the appropriate gradients of interpolation functions which transform nodal point velocity components to strain-rate

pseudo-vectors at any points in the element domain. $\mathbf{C}$, the constitutive operator corresponding to (18), is composed of two parts $\mathbf{C} = \mathbf{C}_{iso} + \mathbf{C}_{aniso}$. In standard finite elements, the positions of the sample points, $\mathbf{x}_p$, and the weighting, w_p are optimized in advance. In our scheme, the $\mathbf{x}_p$'s correspond precisely to the Lagrangian points embedded in the fluid, and w_p must be recalculated at the end of a timestep for the new configuration of particles.

3.2 Scripting of Boundary Value Problems

The toolkit *Escript* [9] has been applied to obtain the results relating to planetary scale mantle convection. *Escript* provides a scripting interface in which specific differential problems are stated to parallelised computational kernels, shielding the user from low-level parallel development. Of particular interest, the *"Finley"* FEM computational kernel has been used within *Escript* to solve the constitutive equations of section 2. A brief overview of *Finley* and its FEM implementation is presented in this section.

To use *Finley*, the Data module is used to transform an initial boundary value problem (IBVP) into a sequence of linear BVPs to be solved at each time step. The linear BVP can then be provided to *Finley* to assemble a stiffness matrix associated with a given unstructured domain using a discretisation based on the standard variational formulation appropriate for the supplied mesh and selected element type. The linear BVP is then provided to *Finley* to assemble a stiffness matrix associated with a given unstructured mesh using a discretisation based on the standard variational formulation.

For an unknown vector function u, the PDEs of a BVP are provided to *Finley* through the specification of the coefficients of the following templated form in tensorial notation:

$$-(A_{ijkl}u_{k,l})_{,j} - (B_{ijk}u_k)_{,j} + C_{ikl}u_{k,l} + D_{ik}u_k = -X_{ij,j} + Y_i \tag{29}$$

The tensorial coefficients A, B, C, D, X and Y are functions of their location in the physical domain. For example, to solve equation (3) for velocity, the identification of like terms with (29) reveals it is necessary to provide *Finley* with A, X, and Y only.

In a similar manner, *Finley* provides a system of implicit (natural) boundary conditions and explicit Dirichlet boundary conditions as given by the respective systems:

$$n_j(A_{ijkl}u_{k,l} + B_{ijk}u_k) + d_{ik}u_k = n_j X_{ij} + y_i \ \text{ on } \Gamma^N \tag{30}$$

$$u_i = r_i \ \text{ on } \Gamma^D \tag{31}$$

where n denotes the outer boundary normal, and A, B and X are as previously defined. Here, d and y are coefficients defined on the natural boundary Γ^N while r is a function defined on the Dirichlet boundary Γ^D. The linear BVP defined by equations (29)–(31) is referred to as the *Finley Boundary*

Value Template (FBVT). Finally, a general form of the FBVT for the case of a steady BVP with a single differential equation in a scalar unknown also exists.

4 The Level Set Method

We use the level set method to track the moving and deforming interface between lithosphere and mantle in subduction models. It is a part of Escript/Finley. This method is based upon an implicit representation of the interface by a smooth function . The function usually has the form of a signed distance to the interface, whereby the zero level curve or surface represents the actual interface between the fluids. The field equations are solved on an Eulerian mesh. The parameters are stored as tables, their value depending upon which side of the interface they are located. The distance function is updated during the simulation by solving the equation of motion using the velocity field calculated previously. The level set method is particularly well suited for two or three dimensional problems with strong topological changes such as breaking or merging as well as the formation of corners and cusps. The level set algorithm works as follows: A scalar function, ϕ is initialised on an Eulerian grid as a signed-distance function with respect to the interface. The values of the parameters are then calculated, depending upon the sign of ϕ. The governing equations can be solved using these parameters, resulting in a velocity field. At each time step, the function ϕ must be updated, according to the velocity field. This is done by solving the "advection equation":

$$\frac{\partial \phi}{\partial t} + \mathbf{v} \cdot \nabla \phi = 0 \tag{32}$$

where $\mathbf{v}$ is the velocity field. Special care must be taken when solving the advection equation and a two step method based on the Taylor-Galerkin procedure is used. For a detailed presentation of this method, we refer the reader to a previous publication by Bourgouin et al. (2006)

5 Examples

5.1 Shear Banding

We now consider the extension and compression of a brittle layer which lies above a viscous layer for a range of non-dimensionalised material properties and strain-softening parameters. In each case the deformation is driven by a boundary condition which uniformly stretches or compacts the background mesh (initial size 2.0×1.0) in the horizontal direction only with a velocity of 1.0. The evolving interface geometry and material history is recorded on the

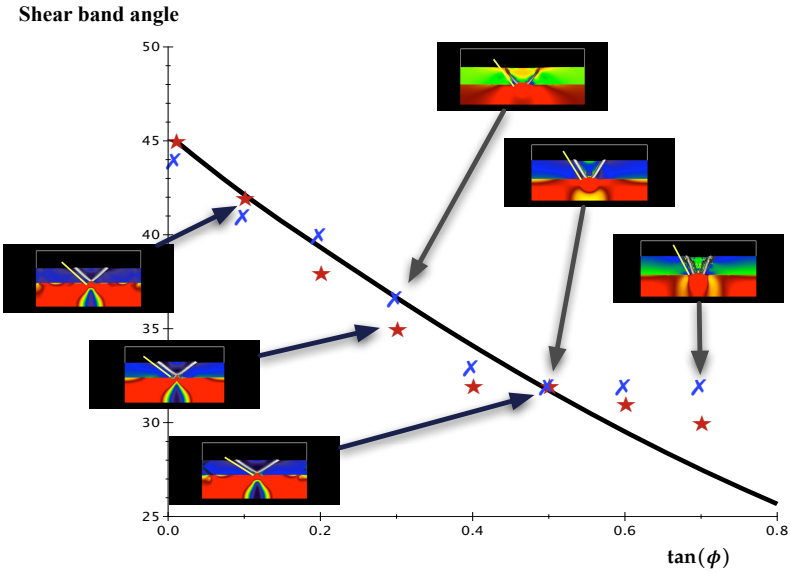

Fig. 1 Shear band formation in compression (stars) and extension (crosses) of a layer of length 2.0, thickness 0.35 with a small notch removed, viscosity $\eta = 10.0$, cohesion 4 (compression) and 15 (extension). The compression/extension velocity is 1.0; the lower layer viscosity is 1.0, the upper layer viscosity is 0.1 and this material is compressible. The ideal orientation of shear bands assuming the principle stress orientations are horizontal/vertical is indicated by the broad white lines on each image.

swarm of particles. A layer of low-viscosity, compressible material is always included in the calculation above the layers of interest to allow the volume change of the domain to be accommodated. In geological models the effect of gravity is always important so we have included this effect. The strength of gravitational acceleration is 10.0 and the density of the layers is 1.0. The shading in the figures represents the second invariant of the stress tensor plotted between 0 and 10 in the top layer and 0 and 1 in the lower layer.

In Figure 1, a brittle layer of thickness 0.35, viscosity 10.0, and cohesion 4 (compression), 15 (extension) lies above a purely viscous layer of viscosity 1.0. The strain softening parameter, γ was 0.1 for all six models shown, and the minimum value of the cohesion was 1.0 at this reference strain. A narrow notch of material in the brittle layer was removed (replaced by material of the lower layer) to provide an initial stress concentration which encourages shear band formation.

In this experiment, the layers were only deformed until the pair of shear bands had developed across the entire layer – total strain of between 2% and 5%. The orientation of these shear bands was then compared with the ideal orientation of the slip planes (assuming that the orientation of the principal

stress directions is not strongly influenced by the shear band formation) which is indicated in the diagram by the light coloured line. In compression the fit between the macroscopic shear band orientation and the microscopic material point slip orientation is very close. In extension the shear bands form at shallow angles for low values of the cohesion, steeper angles for higher values, but the agreement between the microscopic slip orientation and the shear bands is not as good. We attribute this to the fact that at shallow depths in the layer the gravitational loading is insufficient to keep the fault surfaces in contact during extension, so that our assumption that all failure occurs through pure frictional sliding is not valid. Our model does not allow the possibility of failure in tension and clips the second viscosity to slightly above zero whenever it would be zero or negative.

5.2 Large Deformation Model

Figure 2 shows the evolution of the deformation when the extension is comparatively large. In this model we account for gravitational loading of the crust. The dimensionless gravitational acceleration is 100, the cohesion is 1.0, and $\tan(\phi)$ is 0.5. The grid resolution was 300×150 elements and the total extension was 70%. We plotted the upper layer deformation using initially horizontal stripes of passive markers to indicate the total deformation. The instantaneous plastic deformation rate was plotted in bright white superimposed on the stripes in the background.

An initially large number of active shear bands in the upper part of the brittle layer reduced during the first 1-2% of extension as strain softening

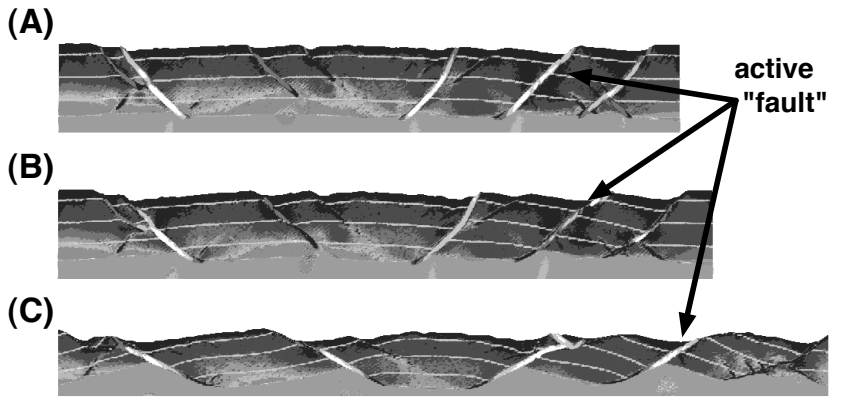

Fig. 2 A model crust with initial random orientations of damage was extended by 20% (A), 28% (B) and 70% (C). The horizontal stripes in the upper layer are passive strain markers. Current plastic strain rate is indicated by the intensity of the white colouring in the shear bands.

within the shear bands allowed them to compete. Throughout the deformation experiment, due to stress transfer from the lower, viscous layer, there are approximately five active shear bands which accumulate significant slip (from a visual inspection of the strain markers).

At the end of the experiment it is possible to see how resilient shear bands have rotated during extension. These are the shear bands which have accumulated significant slip and, consequently, are significantly weaker than surrounding material. This population of shear bands coexists with a second generation which have formed at steep angles in the less deformed blocks, and some old scars of shear bands which were active early in the experiment.

5.3 Subduction

Because of the required higher resolution and numerically more demanding rheology, it has not been possible to include subduction directly into global models. Some subgrid parameterization – like for the phase boundaries in the mantle – would be desirable for subduction. However, despite its importance for the thermal and tectonic evolution of the Earth, recent studies still deal with the fundamental controls of subduction. The current modelling strategy is to isolate specific aspects of subduction zone behaviour in models that are as simple as possible. The following example focuses on the effects of the tear resistance at the subduction zone edges (Hale et al., 2009). It is a geometrical consequence of finite subduction zone length and subduction hinge migration that some edges of subduction zones propagate through the subducting plate (Govers & Wortel, 2005). Continued subduction requires ongoing tearing of the lithosphere. Once established, tear faults are able to propagate as long as subduction continues and the lithospheric strength is less than the slab strength. Otherwise subduction may stall or the slab may break off. Tear propagation is dominated by shear stresses, acting parallel to the fault plane and parallel to the crack front. Such a tearing configuration is also known as Mode 3 Crack in fracture mechanics. The tear fault is most likely to propagate parallel to the direction of rollback, but might also follow pre-existing weak zones. Tearing of the lithosphere is a shallow process. Hence compressibility can be neglected. The density variations driving subduction are mainly due to cooling of the lithosphere. We impose an unstable density stratification as initial condition, rather than calculating it from the energy equation. Although thermal diffusion is present in real subduction, it acts on a longer timescale than advection. We use a simplified model setup (Fig. 3) to gain first-order understanding of resistance to tear propagation on the dynamics and morphology of subduction zones.

The results show the importance of tear resistance for the speed of trench migration and for shaping the final geometry of subduction systems. Figure 4 shows that slab tearing along a weak layer can result in a relatively straight slab hinge shape, while increasing the strength in the weak layer results in the curvature of the hinge increasing substantially. The rollback velocity of the

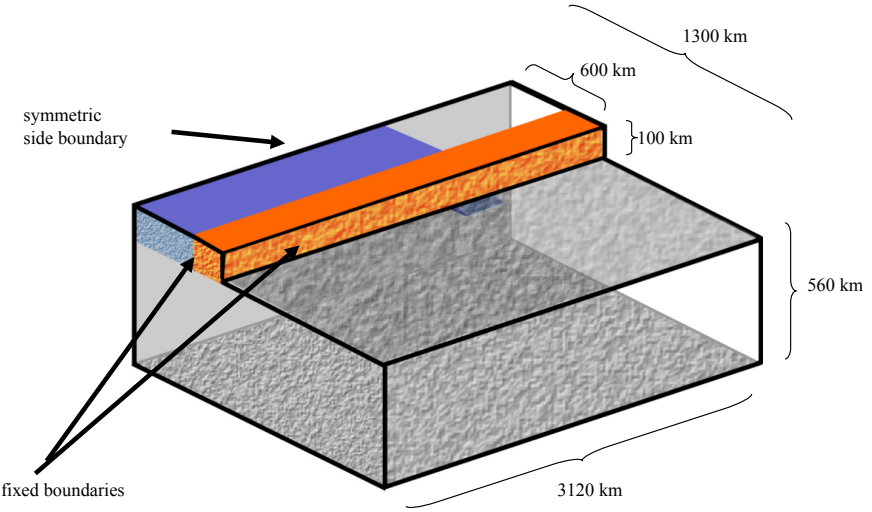

Fig. 3 Our modelling domain is a box, containing a part of a lithospheric plate, with a subducting slab (blue) and the underlying upper mantle. We prescribe a visco-plastic weak zone (orange) and vary its rheological parameters, i.e. the tear resistance.

simulated subduction zones is time-dependent. It reaches 2.5 cm/yr for the fixed weak zone (figure c) and more than 14 cm/yr for the free-slip weak zone. Those values are comparable to the observed range (Schellart et al., 2007). Rollback velocity controls the induced mantle flow, which is also deforming the sinking slabWe used the finite element code eScript/Finley and the level set method to describe the lithosphere to solve this fluid dynamics problem.

5.4 Mantle Convection

Turning to the longest planetary scale we use the temperature-dependent rheology (5) to explore the mechanical conditions underlying the 3 basic types of planetary convection modes, namely stagnant lid, episodic subduction and continuous (Earth-like) convection modes. Viscous deformation is described by a combined Newtonian and power law creep model. The power law viscosity includes a contribution from dislocation glide, a typical power law exponent ($n = 3$) and a contribution from von Mises plastic deformations with temperature independent coefficients and a large exponent ($n = 15$). The effective viscosity is given by:

$$\frac{1}{\eta_{eff}} = \frac{1}{\eta_N} + \frac{1}{\eta_N \left(\frac{\tau}{\tau_0}\right)^{1-n}} + \frac{1}{\eta_Y \left(\frac{\tau}{\tau_Y}\right)^{1-n_p}} \tag{33}$$

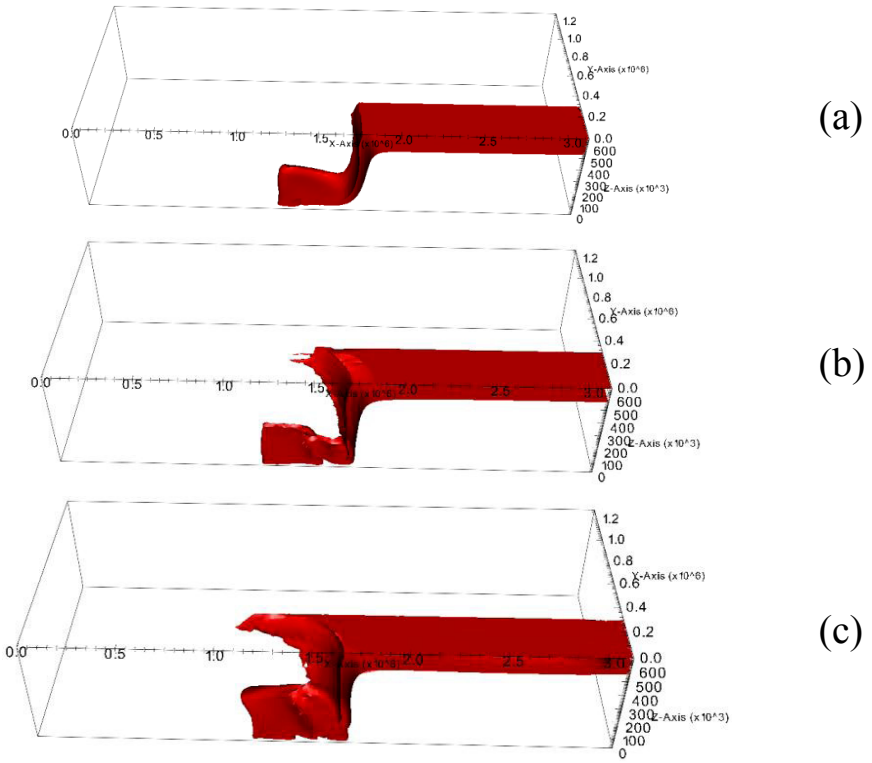

Fig. 4 Snapshots showing the subducting lithosphere after the slab hinge has rolled-back a distance of 500 km. All simulations have a yield strength of 100MPa for the plate and a density difference between plate and mantle of = 69 kg m^{-3} (a) Free slip in the weak zone (yield stress = 0 MPa);(b) Yield stress in the weak zone = 25 MPa (c) Fixed boundary in the weak zone.

where η_N is the temperature dependent Newtonian viscosity, η_Y is a reference viscosity for plastic deformation, τ is the second deviatoric stress invariant, τ_0 is the reference transition stress, and τ_Y is the reference yield stress invariant. For η_N we assume the Arrhenius relationship:

$$\eta_N = \eta_{N0} e^{\frac{AT_M}{T}} \tag{34}$$

where $AT_M = {}^{E^*+PV^*}/_R$, T_M is the pressure dependent melting temperature, A is a positive constant (distinct from that used in (5)) and η_{NO} is the viscosity as $T \to \infty$.

In the convection study of section 5.4 we ignore the pressure dependence of T_M in the Arrhenius relation. The main emphasis in the study will be on the role of elasticity, power law creep and plasticity on the emergence of different

styles of convection. In the dimensionless formulation we write the Arrhenius relationship of (34) as follows [23]:

$$\eta_{NO} e^{\frac{2\hat{A}}{3}} e^{\hat{A}\left(\frac{1}{1+T}-\frac{2}{3}\right)} = \eta_{ref} e^{\hat{A}\left(\frac{1}{1+T}-\frac{2}{3}\right)} \tag{35}$$

Here, η_{ref} is the reference viscosity used in the definition of the Rayleigh number. This corresponds to a Newtonian viscosity contrast of about 10^5 across the convection cell. In the applications we assume that $\hat{A} = 23$. In the absence of convection, the ratio of the Newtonian viscosity to η_{ref} varies slowly due to temperature change in the lower half of the cell, from 1 in the middle to 0.022 on the bottom and rapidly in the upper half from 1 to 2087 on the top.

In the formulation of the constitutive model we make the standard assumption that the symmetric part of the velocity gradient, the so called stretching, is the sum of elastic, and a visco-plastic part, i.e.:

$$D_{ij} = D^{\mathrm{e}}_{ij} + D^{\mathrm{vp}}_{ij} \tag{36}$$

We assume incompressible flow so that $D_{ii} = v_{i,i} = 0$. According to (33) the visco-plastic stretching is defined as:

$$D^{\mathrm{vp}}_{ij} = \frac{\sigma'_{ij}}{2\eta_{eff}} \tag{37}$$

and for the elastic part we assume:

$$D^{\mathrm{e}}_{ij} = \frac{\dot{\sigma}^{J\prime}{}_{ij}}{2\mu} \tag{38}$$

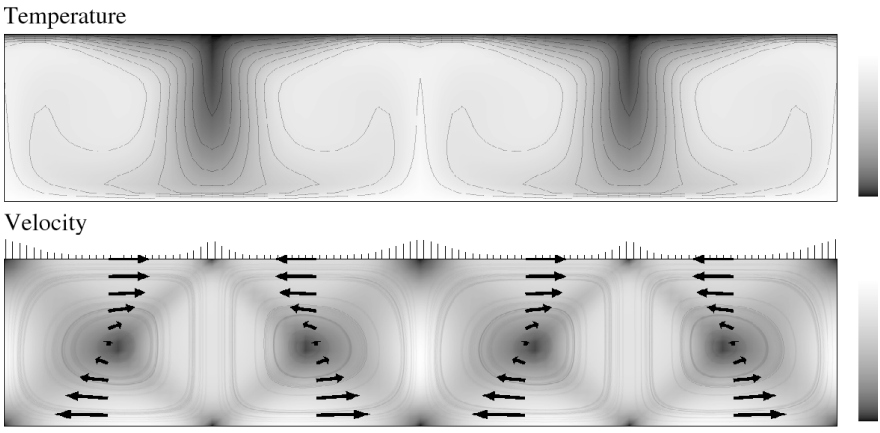

Fig. 5 Typical temperature and velocity distributions for episodic convection at a maximum of the Nusselt number (refer to Figure 8)

where μ is the elastic shear modulus and $\dot{\sigma^J}_{ij}$ is the Jaumann stress rate (see Kolymbas and Herle [13] and Mühlhaus and Regenauer-Lieb [17] for recent discussions and objective stress rate comparisons). The Jaumann stress rate is related to the material stress rate as:

$$\dot{\sigma^J}_{ij} = \sigma_{ij,t} + v_k \sigma_{ij,k} - W_{ik}\sigma_{kj} + \sigma_{ik}W_{kj} \tag{39}$$

where W_{ij} is the non-symmetric part of the velocity gradient.

The temperature dependence of the viscosity was given by (35), resulting in a viscosity ratio from the cold to the hot boundary of 10^5 due to temperature variation alone. More extreme viscosity contrasts can be easily considered in the present formulation because the upper limit for the effective dimensionless viscosity is set by the dimensionless elastic shear modulus and the time increment $\mu t_D \delta t/\eta^*$. We assume $Ra = 10^4$, $\tau_0 = 0.866 \times 10^{5/2}$, $\tau_Y = 3\tau_0$, ideal plasticity (τ_Y =constant) and $\mu t_D/\eta^* = 10^4$ In the simulations we use the power law plasticity model with $n_Y = 15$ and $\eta_Y = \eta_N O$. The initial temperature distribution was

$$T = \frac{1}{10}\sin(x_2\pi)\cos(x_1\pi) + (1 - x_2) \tag{40}$$

The basic modes of convection applicable to a cooling planet, such as stagnant lid, episodic resurfacing and mobile lid convection have been reproduced with the non-linear viscoelastic approach and are shown in figures 5, 6, and 7 respectively. The vertical spikes on top of the velocity streak-line plot in each of the subfigures represent the relative magnitudes of the horizontal cold boundary velocities: larger spikes represent lower velocities, and smaller spikes represent higher velocities. A comparison between the Nusselt numbers for the stagnant, episodic and mobile lid cases is shown in figure 8.

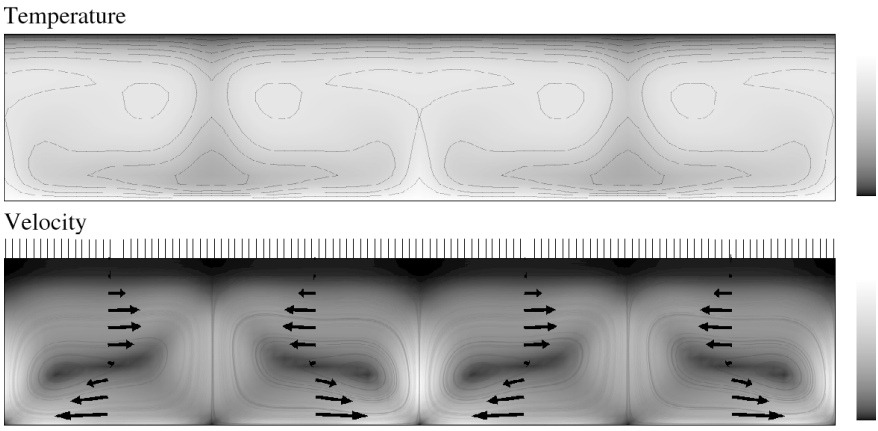

Fig. 6 Typical temperature and velocity distributions for episodic convection at a minimum of the Nusselt number (refer to Figure 8)

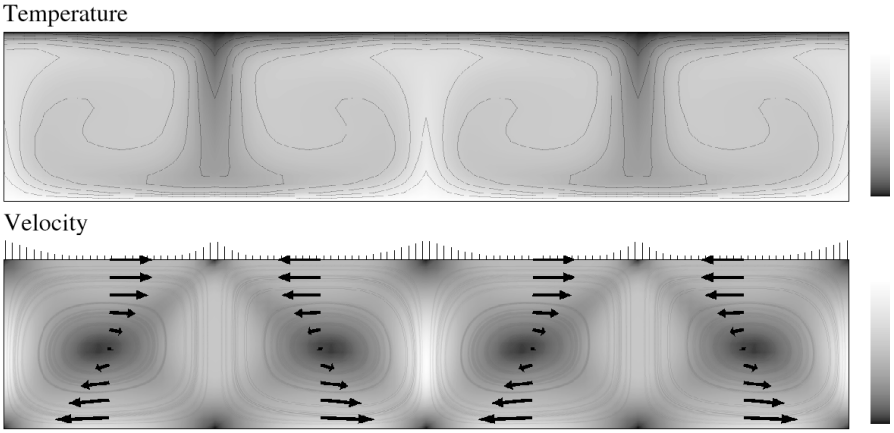

Fig. 7 Typical temperature and velocity distributions at steady state for mobile lid convection. For mobile lid convection, significant parts of the top layer move like rigid bodies.

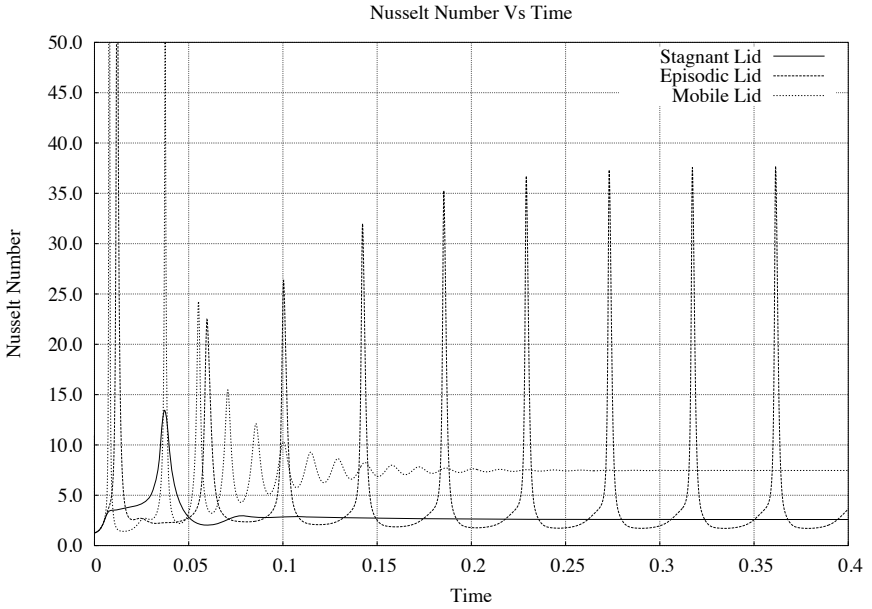

Fig. 8 A comparison of Nusselt numbers for stagnant-lid (lowest with steady state) episodic and mobile lid convection. Here the yield stress τ_y is respectively a factor of 3, 6 and 9 times the transition stress $\tau_0 = 0.866 \times 10^{25}$ (i.e. the transition from Newtonian-Power law creep). The dimensionless shear modulus is 10^4. An Arrhenius relation describes the temperature dependence of creep with a viscosity contrast across the layer of 10^5. The power law exponents are $n = 3$ and $n = 15$ (dislocation glide and plastic deformation respectively).

A slight but noticeable shift in parameter values and validity fields for cases including elasticity has been recorded. In addition, the buffering action of elasticity permits solutions to extreme viscosity variations and introduces long-range interactions. This results in an ordering and stabilization of patterns of convection at high Rayleigh numbers, replacing smaller-scale turbulence by larger planetary-scale re-mobilization.

6 Conclusions

The plasticity algorithm described in this paper addresses a prominent problem in geodynamics: how to model the brittle deformation of the uppermost lithosphere which occurs when mantle convection deforms the continents at the same time as modelling the underlying fluid convection which drives the surface deformation. The formulation has been developed from a mathematical description of fluid flow which is inherently capable of modelling thermally driven convection.

By locally satisfying the failure criterion for frictional sliding and adopting the assumption that deformation initially occurs along the static characteristics, we have generated macroscopic shear bands aligned with the static characteristics of the global stress field. A strain softening model based on the accumulated slip at failed material points is required for localization to occur.

In a simple extension experiment, the shear bands interact to generate geologically plausible patterns of deformation including rotated fault blocks and multiple generations of faults.

We have also outlined a formulation for visco-elastic convection based on a combined Newtonian and power law rheology; the effect of plastic yielding is considered by an additional power law term with a high ($n = 15$) power law coefficient (Equation (33)). The model is valid for studying the geodynamics of mantle convection amongst other problems. The nonlinear equations of motion are solved incrementally based on a consistent tangent formulation producing second order accurate results so that iterations within each time step are not necessary in most cases. In Moresi and Solomatov [16] and Tackley [24], plastic yielding is considered by introducing an upper limit to the viscosity given by the ratio of the yield stress and the equivalent viscous strain rate. Since the strain rate strain rate at the current time is unknown, an initial estimate has to be based on the strain rate from the last time step producing first order accurate results; hence a time consuming, iterative approach is necessary. The iterative approach is usually more time consuming than the present incremental approach with occasional iterative reduction of residuals. In the iterative approach the constitutive operator is more sparse than in the consistent incremental approach, which sometimes can be used to advantage.

The convection problem with strongly temperature dependent viscosity has some unique characteristics: the strains in much of the system are very

large, necessitating a fluid-dynamics formulation, yet the relaxation time in the cool thermal boundary layer is significant compared to the characteristic time associated with fluid flow. In the bulk of the fluid the relaxation time is small compared to the time taken for convective features to evolve due to the much lower viscosity of the warm fluid.

Because elastic stresses in the strongly convecting part of the system relax rapidly, the introduction of elasticity does not produce a qualitative change to the stagnant lid convection regime (see Solomatov [22]). In episodic and mobile lid regimes, there is a competition between the build-up of stresses in the cool lid, and the stress-limiting effect of the yield criterion. The introduction of elastic deformation does not quantitatively influence this balance either, although we do expect a difference in the distribution of stresses in the lid, which explains the variation in the onset of overturns and their increasing frequency which we observed as the elastic shear modulus was reduced.

The presence of an elastic deformation mechanism also allows significant deformation of the highly viscous lid with considerably lower viscous energy-dissipation rates. This is reflected in the lower energy dissipation during episodic overturns which we observed by integrating the system Nusselt number. In the Earth this effect may be important in subduction zones where prediction of dissipation rates due to slab bending is un-physically large. We observed a breakdown in the highly regular boundary layer overturn time when moving from a perfectly harmonic initial condition to a non-harmonic initial condition. This is similar to the results of Moresi and Solomatov [16], who noted for the purely viscous case that the regularity of the episodic regime was an artifact of the small convection domains. Once we break the perfect symmetry of the convection pattern, the evolution also becomes significantly more time-dependent.

We note, finally, keeping our goal of a unified planetary dynamics model in mind, that the two formulations can be merged as the orthotropic constitutive law can be inverted from the stress/strain-rate relationship of (18) to that of (19) and substituted into (37).

Acknowledgements. Support is gratefully acknowledged from the Australian Computational Earth Systems Simulator Major National Research Facility (ACcESS MNRF) and from AuScope which is funded under the National Collaborative Research Infrastructure Strategy (NCRIS) an Australian Commonwealth Government Programme.

References

[1] Barr, A.H.: Superquadrics and angle-preserving transformations. IEEE Computer Graphics and Applications 1(1), 11–23 (1981)

[2] Bird, P., Kong, X.: Computer simulations of california tectonics confirm very low strength of major faults. Geol. Soc. Am. Bull. 106, 159–174 (1994)

[3] Brady, B.H.G., Brown, E.T.: Rock Mechanics. George Allen and Unwin., London (1985)
[4] Bronkhorst, C.A., Kalidindi, S.R., Anand, L.: Polycrystalline plasticity and the evolution of crystallographic texture in fcc metals. Phil. Trans. Royal Soc. A 341, 443–477 (1992)
[5] de Josselin de Jong, G.: The double sliding free rotating model for granular assemblies. Geotechnique 21, 155–163 (1971)
[6] England, P., Houseman, G.: Role of lithospheric strength heterogeneities in the tectonics of tibet and neighbouring regions. Nature 315, 297–301 (1985)
[7] England, P., Houseman, G., Sonder, L.: Length scales for continental deformation in convergent, divergent and strike-slip environments: Analytical and approximate solutions for a thin viscous sheet model. J. Geophys. Res. 90, 3551–3557 (1985)
[8] England, P.C., Houseman, G.A.: The mechanics of the tibetan plateau. Philos. Trans. R. Soc. Lond. Ser. A-Math. Phys. Eng. Sci. 326, 301–320 (1988)
[9] Gross, L., Bourgouin, L., Hale, A.J., Muhlhaus, H.-B.: Interface modeling in incompressible media using level sets in escript. Physics of the Earth and Planetary Interiors 163, 23–34 (2007)
[10] Hill, R.: The Mathematical Theory of Plasticity. Oxford University Press, Oxford (1998)
[11] Humphreys, F.J., Hatherly, M.: Recrystallization and related annealing phenomena. Pergamon Press, U.K. (1995)
[12] Karato, S., Wu, P.: Rheology of the upper mantle - a synthesis. Science 260, 771–778 (1993)
[13] Kolymbas, D., Herle, I.: Shear and objective stress rates in hypoplasticity. Int. J. Numer. Anal. Methods Geomech. 27, 733–744 (2003)
[14] Kong, X., Bird, P.: Thin-shell finite- element models with faults. In: Yin, A., Harrison, T.M. (eds.) The Tectonic Evolution of Asia, pp. 18–34. Cambridge University Press (1996)
[15] Moresi, L., Dufour, F., Muhlhaus, H.B.: A lagrangian integration point finite element method for large deformation modeling of viscoelastic geomaterials. Journal of Computational Physics 184, 476–497 (2003)
[16] Moresi, L.N., Solomatov, V.S.: Mantle convection with a brittle lithosphere: thoughts on the global tectonic styles of the earth and venus. Geophysicical Journal International 133, 669–682 (1998)
[17] Muhlhaus, H.-B., Regenauer-Lieb, K.: Towards a self-consistent plate mantle model that includes elasticity: simple benchmarks and application to basic modes of convection. Geophys. J. Int. 163(2), 788–800 (2005)
[18] Muhlhaus, H.-B., Dufour, F., Moresi, L., Hobbs, B.: A director theory for viscoelastic folding instabilities in multilayered rock. Int. J. Solids Structures 39, 3675–3691 (2002)
[19] Muhlhaus, H.B., Moresi, L., Hobbs, B., Dufour, F.: Large amplitude folding in finely layered viscoelastic rock structures. Pure and Applied Geophysics 159, 2311–2333 (2002), doi:10.1007/s00024-002-8737-4
[20] Muhlhaus, H.B., Moresi, L., Cada, M.: Emergent anisotropy and flow alignment in viscous rock. Pure Appl. Geophys. 161, 2451–2463 (2004)
[21] Rudnicki, J.W., Rice, J.R.: Conditions for the localization of deformation in pressure sensitive dilatant materials. J. Mech. Phys. Solids 23, 371–394 (1975)
[22] Solomatov, V.S.: Scaling of temperature- and stress- dependent viscosity convection. Phys. Fluids 7, 266–274 (1995)

[23] Tackley, P.J.: Three-dimensional simulations of mantle convection with a thermo-chemical basal boundary layer: D"? Americal Geophysical Union (1998)
[24] Tackley, P.J.: Self-consistent generation of tectonic plates in threedimensional mantle convection. Earth Planet. Sci. Lett. 157, 9–22 (1998)
[25] Vardoulakis, I., Sulem, J.: Bifurcation Analysis in Geomechanics. Blackie Academics and Professional (1995)
[26] Watts, A.B., Bodine, J.H., Ribe, N.M.: Observations of flexure and the geological evolution of the pacific basin. Nature 283, 532–537 (1980)
[27] Watts, A.B., Bodine, J.H., Steckler, M.S.: Observation of flexure and the state of stress in the oceanic lithosphere. J. Geophys. Res. 85, 6369–6376 (1980a)
[28] Zhong, S.J., Gurnis, M.: Controls on trench topography from dynamic-models of subducted slabs. J. Geophys. Res.-Solid Earth 99, 15683–15695 (1994)
[29] Zhong, S.J., Gurnis, M.: Towards a realistic simulation of plate margins in mantle convection. Geophys. Res. Lett. 22, 981–984 (1995)
[30] Zhong, S.J., Gurnis, M.: Mantle convection with plates and mobile, faulted plate margins. Science 267, 838–843 (1995)
[31] Zhong, S.J., Gurnis, M.: Interaction of weak faults and non-newtonian rheology produces plate tectonics in a 3d model of mantle flow. Nature 383, 245–247 (1996)
[32] Zhong, S.J., Gurnis, M., Moresi, L.: Role of faults, nonlinear rheology, and viscosity structure in generating plates from instantaneous mantle flow models. J. Geophys. Res.-Solid Earth 103, 15255–15268 (1998)

From Dry Granular Flows to Submarine Avalanches

Mickael Pailha, Maxime Nicolas, and Olivier Pouliquen

IUSTI, CNRS UMR 6595, Aix-Marseille Université, France
olivier.pouliquen@univ-provence.fr

Granular materials like sugar or sand can behave macroscopically like a liquid and flow. However, the description of this peculiar fluid still represents a challenge due to the lack of constitutive laws able to describe the rich phenomenology observed. In a first part of the paper, we rapidly review the properties of dry granular flows and we discuss recent advances in our understanding of their rheological behaviour. In a second part we discuss the more complex case of mixture of grains and liquid, and we show how the recent progresses obtained in the dry case allow to better understand immersed granular flows such as those encountered in submarine avalanches.

1 Introduction

Flows of mixtures of grains and liquid are ubiquitous in industrial applications like food industry, mining industry, chemical engineering... In many catastrophic geophysical events such as landslides, debris flows or submarine avalanches, granular slurries are also involved [1]. The description of such multiphase media still represents a challenge and motivates a lot of studies. One difficulty is that many of these flows belong to a very dense regime, for which the concentration of grains in the mixture is high and contact interactions between grains are important [2]. In this regime, the use of rheological models developed for dilute suspensions and based solely on hydrodynamic interactions is certainly not legitimate. There is a need for wet granular rheological models [3, 4]. We discuss in this paper how recent advances in the rheology of dry granular flows can serve to model liquid-grains mixture.

A lot of effort has been devoted the last ten years to understand the rheology of dry granular materials, when the interstitial fluid plays no role. Flows in many different configurations have been studied, like flows on inclined planes, in rotating drums, in shear cells, in silos [5, 6]... A rich phenomenology has been observed, which is far from being understood. However, in the case of dense granular flows, a simple description in terms of a shear rate dependent friction law has been shown to capture many of the observed features

[7]. This result has led to the development of an empirical visco-plastic rheology, which represents a first step in a continuum description of granular flows [8]. Although the visco-plastic description presents serious limits, especially close to the flow threshold, it can serve as a starting point to develop more elaborate models. An improvement presented in this paper is the addition of the dilatant behaviour of granular material, the so-called Reynolds dilatancy.

When the grains are immersed in a liquid, they interact not only with their neighbours but also with the liquid through hydrodynamic interactions. A natural framework to describe such media is the two phase flow approach, in which each phase is described as a continuum [9]. The constitutive equations for each phase and the interaction forces have to be specified, the main difficulty being the choice of the granular phase rheology. In the very dense regime, when contacts between grains are predominant, the recent advances in our understanding of the dry granular rheology can be helpful. It has been shown that a modified version of the friction law proposed in the dry case can be relevant for the wet case in steady and fully developed regimes [10, 23]. We show in this paper that in the transient regime, when dilatancy effects play a crucial role, a two phase flow approach inspired by a modified dry granular rheology provides quantitative predictions for the problem of the initiation of submarine avalanches.

2 Dry Granular Flows

The term dry granular material refers to a collection of rigid non brownian particles, which interact only by contact interactions. We do not consider soft particles [11], for which the elastic deformation plays a major role, or cohesive materials for which other interaction forces exist [12]. Despite the apparent simplicity of the system, the dynamics of dry granular matter is rich and non trivial and has been the subject of an intense activity during the last 15 years. Many different configurations have been studied from the simple shear cell to more complex configurations [6]. Qualitatively, the behaviour of granular material is classified in three regimes: a solid, a liquid and a gaseous regime. The transition between solid and liquid is controlled by a friction criterion, stipulating that the material starts to flow when the shear stress reaches a critical value proportional to the normal stress. Above the yield stress, the material flows like a liquid and there are evidences of viscous effects and shear rate dependent behaviours. Finally, at high shear rate and low concentration, the particles interact through binary collisions and the medium looks like a gas. This last regime has been described using kinetic theory of granular gases [13].

This section is devoted to the dense liquid regime. We first recall the empirical rheological laws derived from simple arguments based on dimensional analysis. An extension of the rheology is then proposed to take into account the dilatant behaviour of granular media.

2.1 The Dry Visco-Plastic Model

Let us consider a granular material made of particles of diameter d and density ρ_p sheared at a uniform shear rate $\dot{\gamma}$, and submitted to a confining pressure p^p. This is for example achieved by confining a granular material in between two rough plates and by prescribing a constant load on the top plate. In the steady regime, when the equilibrium is reached, one can easily show that the shear stress τ_{eq} necessary to maintain the shear and the volume fraction ϕ_{eq} of the sample are given by the following rules:

$$\tau^p_{eq} = \mu(I)p^p, \tag{1}$$

$$\phi_{eq} = \phi_{eq}(I), \tag{2}$$

where

$$I = \frac{t_{micro}}{t_{macro}} = \frac{\dot{\gamma}d}{\sqrt{p^p/\rho_p}}$$

is a dimensionless number given by the ratio of two time scales: the time scale of rearrangement $t_{micro} = d(p^p/\rho_p)^{-1/2}$ and the macroscopic time scale $t_{macro} = 1/\dot{\gamma}$. These constitutive laws are derived from a simple dimensional argument: the inertial number I is the single dimensionless parameter of the problem [7, 6]. Numerical simulations using discrete element methods and experiments in various configurations show that the friction coefficient $\mu(I)$ is an increasing function of I starting at a value μ_s when I goes to zero, and that the volume fraction ϕ_{eq} is a decreasing function of the inertial number [5] (see Fig. 1).

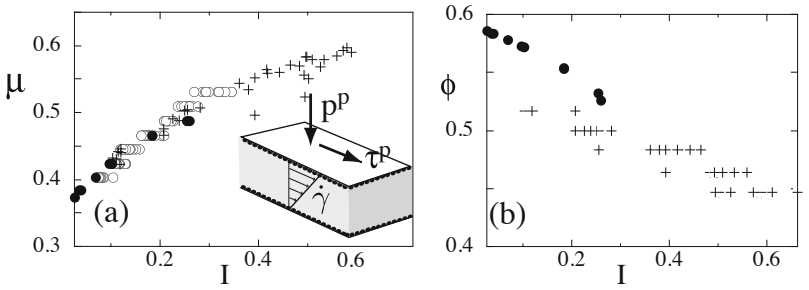

Fig. 1 (a) Friction coefficient as a function of the inertial number I for numerical simulations in plane shear or inclined plane, experiments on inclined plane. (b) volume fraction as a funciton of I for the same data. Figure from [5]

This scalar relation obtained in the simple shear configuration can be generalized to three dimensional flows in a tensorial form [8]. The rheology is then given by a visco-plastic formulation for the particle stress tensor:

$$\sigma_{ij}^p = -p^p \delta_{ij} + \tau_{ij}^p \tag{3}$$

where p^p is the isotropic pressure and

$$\tau_{ij}^p = \eta \dot{\gamma}_{ij} \qquad \text{with} \qquad \eta = \frac{\mu(I)P}{|\dot{\gamma}|}. \tag{4}$$

In this formulation $|\dot{\gamma}|$ is the second invariant of the tensor: $|\dot{\gamma}| = \sqrt{\frac{1}{2}\dot{\gamma}_{ij}\dot{\gamma}_{ij}}$.

This constitutive law has proven to be relevant to describe various configurations. Flows between rough walls [8], waves at the surface of a granular layer flowing down an inclined plane [14], and more recently the collapse of granular column on an horizontal plane [15] are examples of systems well described by the proposed rheology. The visco-plastic formulation then represents a first step to describe the viscous character of granular flows. However, serious limits exist, which appear when considering slow quasi-static flows. The first limit concerns the velocity profiles observed in quasi-static flows [5]. Shear bands often develop [16], which are not described by the model. Secondly, the flow threshold in the model is simply described as a coulomb criterion, whereas experiments show more complex behaviours with finite size effects and hysteresis [17]. Different approaches trying to take into account non local effects are under development to circumvent these limitations. A last limit of the model is that it does not take into account the influence of the preparation of the material. It is well know that the initiation of a dry granular flows strongly depends on its preparation. For example, the collapse of a column of grains initially compacted under vibration is dramatically different from the collapse of a loose column [18]. To capture this kind of effect, the visco-plastic model needs to be modified to take into account dilatant or contractant behaviours, which occur during the early deformation.

2.2 Taking into Account the Dilatancy

Critical state theories developed in soil mechanic are simple ways to describe the initial deformation of a granular sample under quasi-static deformations and to model the dilatancy or compaction [19]. The simplest model [20] consists in introducing an angle of dilatancy ψ, which relates the vertical motion experienced by one layer of particle relative to the other when a shear is applied (Fig. 2(a)), $\Delta Z = \tan\psi \Delta X$. A positive (resp. negative) dilatancy angle corresponds to a dilatant (resp. contractant) behavior. The dilatant-contractant character is known to depend on the volume fraction ϕ, and a first simple description consists in assuming a linear variation between ψ and ϕ. If ϕ is greater (resp. less) than a critical value ϕ_{eq}, ψ is positive (resp. negative) and dilatancy (resp. compaction) will occur. Meanwhile, due to the geometrical entanglement it is easy to show that the coefficient of friction is

greater (resp. lower) than the equilibrium coefficient of friction. The evolution of the material under a simple shear $\dot{\gamma}$ is then controlled by the following equations:

$$\frac{1}{\phi}\frac{d\phi}{dt} = \tan\psi\dot{\gamma} \tag{5}$$

$$\tau^p = \tan\psi p^p + \tau_{eq} \tag{6}$$

$$\tan\psi = K(\phi - \phi_{eq}) \tag{7}$$

where τ_{eq} and ϕ_{eq} are the stress and volume fraction obtained in the steady regime. The first equation is a rewriting of the kinematic condition $\Delta Z = \tan\psi\Delta X$ and stipulates how dilatation or contraction occurs depending on the value of the dilatancy angle. The second equation means that the change in volume fraction implies an additional stress contribution due to the geometrical entanglement. The last equation simply assumes that the dilatancy angle is proportional to the difference between the actual volume fraction and the critical volume fraction. Such a theory has been introduced initially for quasi-static deformations, in which τ_{eq} and ϕ_{eq} are constant. To generalize this approach to more rapid deformations and take into account shear rate dependence, we assume that τ_{eq} and ϕ_{eq} in equations (6) and (7) are given by the dense granular rheology controlled by the inertial number I eqs (1) and (2).

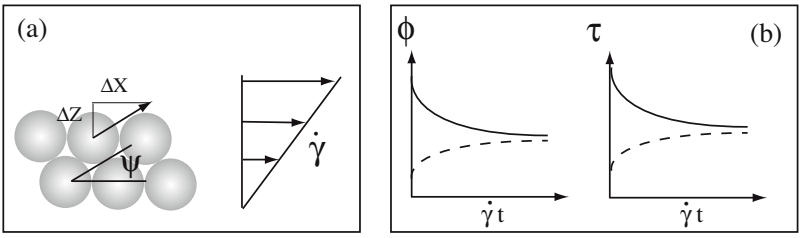

Fig. 2 (a) definition of the dilatancy angle ψ; (b) prediction of the simple critical state theory for the time evolution of the volume fraction and of the shear stress when the initial volume fraction is higher (solid line) or lower (doted line) than the critical value

This simple model predicts that a granular media initially at a volume fraction ϕ_0 and suddenly sheared at $\dot{\gamma}$ will relax to the steady state regime within a characteristic time $1/\phi_0\dot{\gamma}$, in agreement with observations. This model, which brings together a critical state theory with the rheology of dense granular materials, seems to contain the basic ingredient to capture the role of the initial preparation. More complex configurations need to be analyzed to confirm the validity of the approach.

3 Wet Granular Flows

The case of granular flows immersed in a liquid has been much less studied. However, some experiments exist for granular flows down inclined plane [10], flow in rotating drums [21, 22], flow on a pile [23]. Some of these experiments suggest that the visco-plastic approach developed in the dry case is relevant for the wet case.

3.1 A Wet Visco-Plastic Model

In the case of mixture of grains and fluid in the high concentration limit, flows are dominated by contact between particles. A simple assumption is that a rheology similar to the one proposed in the dry case still holds for the wet case, but with a rearrangement time scale t_{micro} introduced in the definition of the inertial number being modified by the presence of the fluid. An analysis of time scales of the fall of one grain in a liquid has been performed by Courrech du Pont et al [22] allowing to estimate t_{micro}. It can be shown that in the viscous regime $t_{micro} \propto \eta/p^p$, whereas in the inertial regime, $t_{micro} \propto d/\sqrt{p^p/\rho_p}$. Under this assumption the rheology of an immersed granular material is given by equations 1 and 2 with I depending on the flow regime and computed using the expression of microscopic timescales. Such a rheology gives predictions in agreement with experimental observations for submarine granular flows down inclined planes [10] and for flows on a pile [23]. However, both experiments are carried out in a steady and fully developed regime, in a situation where no relative motion between the fluid and the grains is present. If for some raison, the fluid and the granular skeleton do not move at the same velocity, additional stresses apply on the grains, which should be taken into account.

3.2 When a Relative Motion between Fluids and Grains Exists

A natural framework to model the interaction between a fluid phase and a granular medium is the two-phase flow approach. The particles and fluid are described as two continuum phases characterized by different velocities $\mathbf{u}^p$ and $\mathbf{u}^f$, by different stresses σ^p and σ^f, the two phases interacting through hydrodynamic forces $\mathbf{f}$. The mass conservation and momentum equations then write:

$$\frac{\partial \phi}{\partial t} + \nabla.(\mathbf{u}^p \phi) = 0 \tag{8}$$

$$\frac{\partial (1-\phi)}{\partial t} + \nabla.(\mathbf{u}^f (1-\phi)) = 0 \tag{9}$$

$$\rho_p \phi \left(\frac{\partial \mathbf{u}^p}{\partial t} + \mathbf{u}^p.\nabla \mathbf{u}^p \right) = \nabla.\sigma^p + \phi \nabla.\sigma^f + \mathbf{f} + \rho_p \phi \mathbf{g} \tag{10}$$

$$\rho_f(1-\phi)\left(\frac{\partial \mathbf{u}^f}{\partial t}+\mathbf{u}^f.\nabla\mathbf{u}^f\right)=(1-\phi)\nabla.\sigma^f-\mathbf{f}+\rho_f(1-\phi)\mathbf{g} \quad (11)$$

The term $\mathbf{f}$ includes the interaction forces between the two phases, beside the buoyancy $\phi\nabla.\sigma^f$. In the low Reynolds regime, one usually adopts the simple viscous drag formulation given by

$$\mathbf{f}=(1-\Phi)^2\beta(\mathbf{u}^f-\mathbf{u}^p)$$

with $\beta=\frac{\eta}{\alpha d^2}$, where αd^2 is the permeability of the porous media formed by the particles [24].

The major difficulty is the choice of the constitutive laws for each phase. For the fluid, different choices can be found in the literature. The first one consists in neglecting the viscous stress in the liquid phase, assuming that they are negligible compare to the granular stresses. The fluid stress then reduces to a simple isotropic pressure, the so-called pore pressure. Other choices are a simple newtonian viscosity, or an eddy viscosity in the case of a turbulent regime [25].

The rheology of the granular phase remains a subject of debate. However, we have seen in the previous section that in the limit of a very dense granular phase, new constitutive laws can be proposed. A simple choice is to use equation 1 to describe the granular stress. This is the choice made recently by Berzi and Jenkins [25] to theoretically study debris flows. They have shown that the visco-plastic granular rheology for the solid phase coupled with an eddy viscosity for the fluid phase allows to predict velocity profiles and density profiles observed experimentally by Armini et al [26].

However, in some geophysical situations like the initiation of landslides, the change in volume fraction, occurring during the initial deformation plays a crucial role [27]. In this case, the constitutive equations derived in section 2.2, taking into account the dilatancy seem appropriated. In the next section, we show an example of application to describe the initiation of submarine avalanches.

3.3 Crucial Role of the Dilatancy: An Example for the Initiation of Submarine Avalanches

The role of the initial volume fraction in the triggering of debris flows has been previously studied in large scale experiments by Iverson et al [27]. Recently, we have designed a small scale experiment, which captures the role of the initial volume fraction on the initiation of immersed granular flows [28].

The experiment consists in preparing a uniform layer of glass beads (160 μm in diameter) in a long box full of liquid by creating a suspension and by letting the particles sediment. The initial volume fraction of the layer can be precisely controlled by imposing successive taps on the box. The box is then suddenly inclined from horizontal. We measure the time evolution of

the granular free surface velocity (Fig. 3b). The avalanches can be classified in two categories. For an initial loose packing, a rapid acceleration first takes place and a transient velocity higher than the final velocity can be observed. For an initial dense packing, a first stage characterized by a very low velocity is observed which can last more than 3 minutes, before the velocity increases and reaches the steady state value (Fig. 3b). The higher the initial volume fraction, the longer the triggering time. The qualitative explanation of the phenomenon is given by the influence of the pore pressure on the granular skeleton. When the avalanche starts, the granular medium starts to deform and induces a variation of volume fraction (a dilatation if the sample is initially dense, a contraction otherwise). This change in volume fraction causes a variation of the pore pressure, which in turn changes the stresses on the granular skeleton. This mechanism has been called pore pressure feedback by Iverson [29].

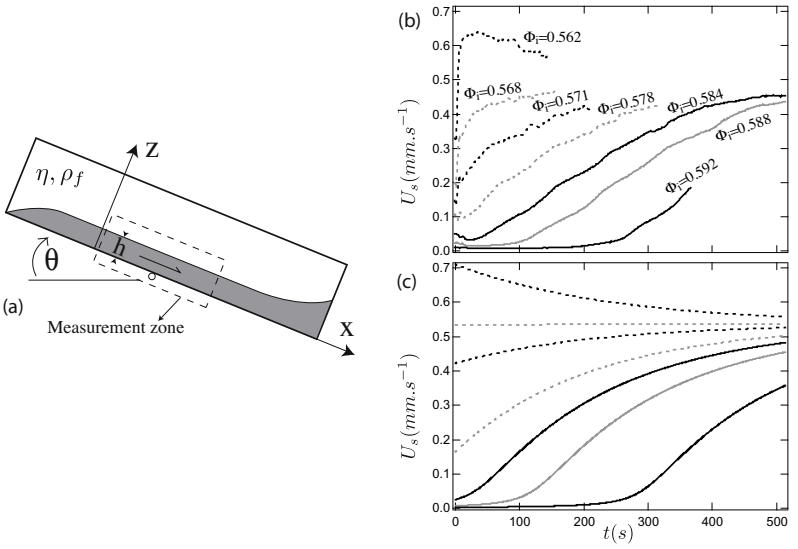

Fig. 3 (a) sketch of the experimental setup to study the role of the initial volume fraction on the initiation of submarine avalanches. (b) experimental measurements of the free surface velocity as a function of time for different initial volume fraction. (c) predictions of the theoretical two phase flow model under the same conditions.

To describe these observations, a complete theory should contain the coupling between the fluid and the granular phase, the dilatant behaviour of the granular phase, and a rheology capturing the long time evolution towards a steady state. The two phase flow equations together with the dilatant visco-plastic theory developed in section 2.2 represents a good candidate.

Using a depth averaged version of the two phase flow equations, we have shown that a semi-quantitative agreement is obtained between the model and the measurements for a large range of inclinations, different initial value fraction and different fluid viscosities [30]. An example of prediction is plotted in Fig. 3c, where the time evolution of the granular layer velocity is plotted for the same initial volume fraction as in the experiments.

4 Conclusion

In conclusion, we have shown that the recent advances in the phenomenology of the rheology of dry granular materials can help in developing theoretical models to address the problem of mixtures of grains and liquid. By taking into account the shear rate dependence of the friction coefficient and the dilatant behaviour of granular media in two phase flow equations, rich dynamics such as the one observed during the initiation of submarine avalanches can be described. This opens new perspectives to study configurations closer to real geophysical situations.

References

1. Iverson, R.M.: Review of Geophysics 35, 245–296 (1997)
2. Ancey, C., Coussot, P., Evesque, P.: J. Rheol. 43, 1673–1699 (1999)
3. Morris, J.F., Boulay, F.: J. Rheol. 43, 1213–1237 (1999)
4. Huang, N., Ovarlez, G., Bertrand, F., Rodts, S., Coussot, P., Bonn, D.: Phys. Rev. Lett. 94, 028301 (2005)
5. Forterre, Y., Pouliquen, O.: Ann. Rev. Fluid Mech. 40, 1–24 (2008)
6. GDR MiDi: Eur. Phys. J. E 14, 341–365 (2004)
7. Da Cruz, F., Emam, S., Prochnow, M., Roux, J.N., Chevoir, F.: Phys. Rev. E 72, 021309 (2005)
8. Jop, P., Forterre, Y., Pouliquen, O.: Nature 44, 727–730 (2006)
9. Jackson, R.: Ch. Eng. Sci. 52, 2457–2469 (1997)
10. Cassar, C., Nicolas, M., Pouliquen, O.: Phys. Fluids 17, 103301 (2005)
11. Campbell, C.S.: J. Fluid Mech. 465, 261–291 (2002)
12. Richefeu, V., El Youssoufi, M.S., Radjai, F.: Phys. Rev. E 73, 051304 (2006)
13. Goldhirsch, I.: Ann. Rev. Fluid Mech. 35, 267–293 (2003)
14. Forterre, Y.: J. Fluid Mech. 563, 123–132 (2006)
15. Lacaze, L., Kerswell, R.: To be published in Phys. Rev. Lett. (2008)
16. Mueth, D.M., Debregeas, G.F., Karczmar, G.S., Eng, P.J., Nagel, S.R., Jaeger, H.M.: Nature 406, 385–389 (2000)
17. Pouliquen, O.: Phys. Fluids 11, 542–548 (1999)
18. Daerr, A., Douady, S.: Europhys. Lett. 47, 324–330 (1999)
19. Schofield, A., Wroth, P.: Critical Soil Mechanics. McGraw-Hill (1968)
20. Roux, S., Radjai, F.: Texture -dependent rigid plastic behavior. In: Herrmann, H.J., et al. (eds.) Physics of Dry Granular Media, pp. 305–311. Kluwer, Dordrecht (1998)

21. Jain, N., Ottino, J.M., Lueptow, R.M.: J. Fluid Mech. 508, 23–44 (2004)
22. Courrech du Pont, S., Gondret, P., Perrin, B., Rabaud, M.: Phys. Rev. Lett. 90, 044301 (2003)
23. Doppler, D., Gondret, P., Loiseleux, T., Meyer, S., Rabaud, M.: J. Fluid Mech. 577, 161–181 (2007)
24. Ouriemi, M., Aussillous, P., Guazzelli, E.: J. Fluid Mech. (2008) (in press)
25. Berzi, D., Jenkins, J.T.: J. Fluid Mech. 608, 393–410 (2008)
26. Armanini, A., Capart, H., Fraccarollo, L., Larcher, M.: J. Fluid Mech. 532, 269–319 (2005)
27. Iverson, R.M., Reid, M.E., Iverson, N.R., Lahusen, R.G., Logan, M., Mann, J.E., Brien, D.L.: Science 290, 513–516 (2000)
28. Pailha, M., Nicolas, M., Pouliquen, O.: Triggering of submarine granular avalanches. To be published in Phys. Fluids (2008)
29. Iverson, R.M.: J. Geophys. Res. 110, F02015 (2005)
30. Pailha, M., Pouliquen, O.: Two phase flow description of submarine granular avalanches. Submitted to J. Fluid Mech (2008)

Failure of Rocks in the Laboratory and in the Earth

J.W. Rudnicki

Northwestern University, Evanston, IL USA
jwrudn@northwestern.edu

1 Introduction

Although rocks, at least some of them, are nearly as old as the Earth itself, their behaviour continues to play an important role in a variety of applications and phenomena of societal interest. These include natural disasters, such as landslides, volcanic eruptions and earthquakes. Rocks are widely used for building materials, foundations, tunnels and underground facilities. Most of the world's energy now, and for the foreseeable future, comes from the shallow crust and an understanding of rock behaviour is essential to efficient and safe production and storage. Moreover, many of the by-products of energy production are re-injected to the shallow crust. An increasingly important application is geological sequestration of carbon dioxide, injection into the earth to mitigate harmful effects on the climate [42]. Many of these problems involve not only mechanical behaviour but also its coupling with fluid flow, heat and chemistry.

The vast majority of tests performed on rocks to determine constitutive behaviour have been on cylindrical specimens loaded axially symmetrically. Of these, most have been in axisymmetric compression (largest magnitude principal stress is compressive). There are historical and technical reasons for the emphasis on this type of test and it does provide information on the dependence of the behaviour on the mean stress (or confining stress). Such tests, however, provide very limited information about the response for the range of deviatoric stress states. Information about the full range of deviatoric stress states is needed for applications, in which the stress is seldom axially symmetric, and for numerical simulations.

A particular issue is the role of the intermediate principal stress: In axisymmetric tests it is equal to either the most or least compressive principal stress. The Mohr-Coulomb condition (e.g., [14], [29]) posits behaviour depending only on the sum and difference of the largest and smallest principal stresses and, thus, is independent of the intermediate principal stress. Mogi ([20],[21],[22]) noted, however, that the difference in the behaviour observed in axially symmetric compression and extension indicated a dependence on

the intermediate principal stress. In seminal work intended to further explore the role of the intermediate principal stress, Mogi ([21], [22]) conducted experiments in a true triaxial apparatus in which a cubical specimen could be subjected to three different principal stresses. Despite their importance, few true triaxial tests have been conducted on rocks (though there are more on soils and concrete). Recently, however, Haimson ([9], [5], [10], [24]) has fabricated a true triaxial apparatus similar in design to that of Mogi and has conducted a series of true triaxial tests on several different rock types.

This paper uses the theoretical framework of shear localization as a bifurcation from homogeneous deformation ([33], [30], [3]) to interpret observations of the inclination of the failure plane in true triaxial tests on Westerly granite. Although this theory also yields a prediction of the failure stress, assumed to coincide with shear localization, in terms of a critical value of the slope of the stress strain curve, the emphasis here is on the orientation of the failure plane. One reason is that it is difficult to determine the precise point on the stress strain curve where localization occurs. Although the zone in which failure occurs is seldom precisely planar, it is often nearly so in the central portion of the specimen and, thus, is relatively easy to observe. Depending on the deviatoric stress state, the stress at localization is predicted to be from slightly before to well after a peak in the stress strain curve. Although there is some observational evidence for these predictions, failure tends to occur closer to peak than predicted for axially symmetric stress states. This discrepancy is thought to be due to the limitations of smooth yield surface models to capture adequately the response to abrupt changes in the pattern of deformation (as must occur for localization in axisymmetric states), but these limitations do not seem to significantly affect the failure angle.

Because the theory of shear localization is strongly dependent on the type of constitutive relation used, the paper first discusses the framework for rate-independent, elastic plastic models and, especially the form for a class that depends on all three stress invariants. A particular form of yield function dependent on three invariants is used to infer parameters of the function from data on Westerly granite and use them to predict the failure angle.

2 Form of Constitutive Relation

The constitutive relation is assumed to have the standard form for a rate-independent solid. Strain increments are the sum of elastic and inelastic parts

$$d\varepsilon_{ij} = d\varepsilon^e_{ij} + d\varepsilon^p_{ij} \tag{1}$$

(and attention is restricted to small strain). The elastic portion is related to the stress increment by

$$d\varepsilon^e_{ij} = C_{ijkl}\, d\sigma_{kl} \tag{2}$$

where C_{ijkl} is the elastic compliance tensor. For isotropy, this is given by

$$C_{ijkl} = \frac{1}{2G}\left\{\frac{1}{2}(\delta_{ik}\delta_{jl} + \delta_{il}\delta_{jk}) - \frac{\nu}{1+\nu}\delta_{ij}\delta_{kl}\right\} \tag{3}$$

where G is the shear modulus, ν is Poisson's ratio and $\delta_{ij} = 1$, if $i = j$, but $\delta_{ij} = 0$, if $i \neq j$. The inelastic strain increments have the form

$$d\varepsilon_{ij}^{p} = \frac{1}{H}P_{ij}Q_{kl}d\sigma_{kl} \tag{4}$$

where H is a hardening modulus, P_{ij} gives the direction of the inelastic strain increment (in stress space), and Q_{kl} is the direction of the normal to the yield surface. If the dependence of the yield surface on stress is given by

$$F(\sigma_{ij}) = 0 \tag{5}$$

where other parameters that keep track of the current state of inelastic deformation are suppressed, then

$$Q_{ij} = \partial F/\partial\sigma_{ij} \tag{6}$$

If a plastic potential exists and is of the form

$$G(\sigma_{ij}) = 0 \tag{7}$$

then

$$P_{ij} = \partial G/\partial\sigma_{ij} \tag{8}$$

If $P_{ij} = Q_{ij}$, then the inelastic strain increment is normal to the yield surface in stress space and the flow rule (or plastic potential) is said to be associated. For rocks (and soils and other geomaterials), observations generally indicate that the traces of P_{ij} and Q_{ij} are not equal, i.e., $P_{kk} \neq Q_{kk}$, and these macroscopic observations are supported by the nature of the microstructural mechanisms of inelasticity, such as frictional sliding and local tensile microcracking due to grain scale inhomogeneities. There appears, however, to be no evidence for deviations from normality in the deviatoric plane (Π - plane or planes in which σ_{kk} is constant). Because there is also no reason to expect such deviations on the basis of microstructural mechanisms, we assume here that $P'_{ij} = Q'_{ij}$, where the prime denotes the deviatoric part of the tensor.

3 Predictions for Two Invariant Model

If the yield function (5) and plastic potential (7) depend on only the first two invariants of the stress, taken to be $\sigma = \sigma_{kk}$ and

$$\tau = (s_{kl}s_{kl}/2)^{1/2} \tag{9}$$

where $s_{ij} = \sigma_{ij} - (\sigma_{kk}/3)\delta_{ij}$ is the deviatoric part of the stress, they can be written as

$$\tau = f(\sigma) \tag{10}$$

and

$$\tau = g(\sigma) \tag{11}$$

Then Q_{ij} (6)and P_{ij} (8) are given by

$$Q_{ij} = \frac{s_{ij}}{2\tau} + \frac{1}{3}\mu\delta_{ij} \tag{12}$$

and

$$P_{ij} = \frac{s_{ij}}{2\tau} + \frac{1}{3}\beta\delta_{ij} \tag{13}$$

where $\mu = -3f'(\sigma)$ is a friction coefficient and $\beta = -3g'(\sigma)$ is a dilatancy factor. For this case $P'_{ij} = Q'_{ij} = s_{ij}/2\tau$.

Extending seminal work by Hadamard [8], Thomas [39], Mandl [18] and Hill [12], Rudnicki and Rice [33] analyzed localization as a bifurcation from homogeneous deformation for the case of a constitutive relation having the form of (4) with (12) and (13). They show the prediction for the angle between normal to the band of localization and the least (most compressive) principal stress is ([33], eqn. (19))

$$\tan^2\theta_{RR} = \frac{\xi - (s_3/\tau)}{(s_1/\tau) - \xi} \tag{14}$$

where

$$\xi = \frac{1}{3}(1+\nu)(\beta+\mu) - (s_2/\tau)(1-\nu) \tag{15}$$

and $s_1 \geq s_2 \geq s_3$ are the largest, intermediate and smallest principal values of s_{ij} (Rudnicki and Rice [33] use $N_{\max}$, N and $N_{\min}$ for s_1/τ, s_2/τ and s_3/τ). Rudnicki and Olsson ([32], eqns. (10) and (11)) rewrite this result in the form

$$\theta_{RR} = \frac{\pi}{4} + \frac{1}{2}\arcsin\alpha \tag{16}$$

where

$$\alpha = \frac{(2/3)(1+\nu)(\beta+\mu) - (s_2/\tau)(1-2\nu)}{\sqrt{4 - 3(s_2/\tau)^2}} \tag{17}$$

For $\alpha \leq -1$, the plane of localization is perpendicular to the most compressive stress ($\theta_{RR} = 0$) and said to be a compaction band. For $\alpha \geq 1$, the plane of localization is perpendicular to the least compressive stress ($\theta_{RR} = \pi/2$) and said to be a dilation band. Observations of compaction bands in porous sandstones in the field ([36], [34]) and in the laboratory ([25], [1], [16], [38], [41], [40], [6], [26], [7]) have been reported recently. Understanding the conditions for their formation and evolution is of interest because they dramatically reduce the permeability for flow across them ([41], [13], [37], [35]). Consequently, their formation in porous subsurface reservoirs could significantly affect applications involving fluid injection or withdrawal. Du Bernard et al. [2] have reported an observation of dilation bands in the field, but they appear to be much less common.

4 Three Invariant Results

Rice [30] has given a more general localization analysis of the constitutive relation (4) without specific reference to the forms of P_{ij} and Q_{ij} and Ottosen and Runesson [28] have extended the analysis for a yield function and plastic potential that depend on all three stress invariants. The results for a three invariant model can, however, be obtained by appropriate replacements in the results of [33].

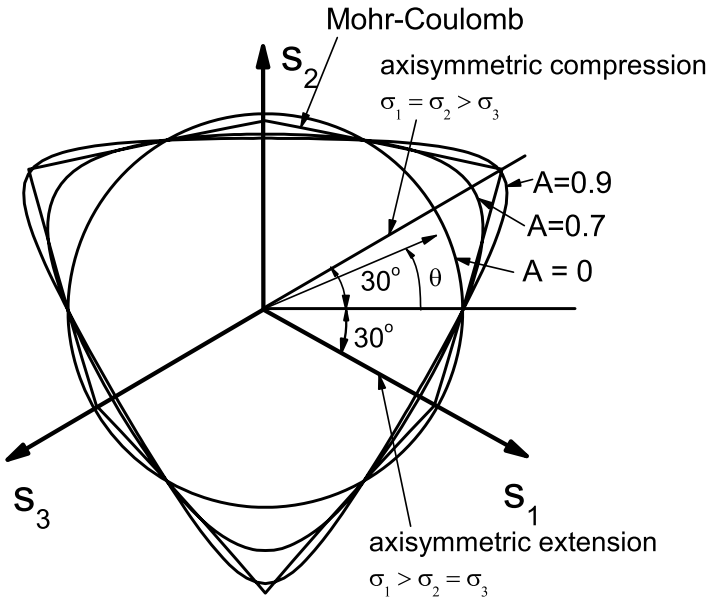

Fig. 1 The figure compares the shape (33) in a the deviatoric plane ($\sigma_{kk} = \text{constant}$) with the Mohr-Coulomb hexagon. Also shown is the angle θ defined by (18). The axes of the principal deviatoric stresses differ by angles of 120^o in this plane.

Two of the invariants are taken to be the trace of the stress $\sigma = \sigma_{kk}$, and the second invariant of the deviatoric stress (or Mises equivalent stress) (9). It is convenient to take the third invariant as the Lode angle [11]

$$\theta = -\frac{1}{3} \arcsin\left(\sqrt{\frac{27}{4}} \frac{J_3}{\tau^3}\right) \tag{18}$$

where $J_3 = \det(s_{ij})$ is the third invariant of the deviatoric stress. Geometrically, the angle (18) defines a 60^o sector in planes σ_{kk} =constant, $-\pi/6 \leq \theta \leq \pi/6$ (Figure 1). The limiting values correspond to axisymmetric extension ($\theta = -\pi/6$; $\sigma_1 > \sigma_2 = \sigma_3$) and axisymmetric compression

($\theta = \pi/6$; $\sigma_1 = \sigma_2 > \sigma_3$). Deviatoric pure shear ($\sigma_2 = (\sigma_1 + \sigma_3)/2$) corresponds to $\theta = 0$. Because this angle (18) is related to s_2/τ in (17) by

$$s_2/\tau = 2\sin\theta/\sqrt{3} \tag{19}$$

the result (17) does depend on the third invariant of stress although the yield function and plastic potential on which it is based do not. With this choice of invariants, the yield function and plastic potential have the forms

$$F(\tau, \sigma, \theta) = 0 \tag{20}$$

and

$$G(\tau, \sigma, \theta) = 0 \tag{21}$$

The normal to the yield surface (6) is

$$Q_{ij} = \frac{\partial G}{\partial \sigma_{ij}} = G_\tau \frac{\partial \tau}{\partial \sigma_{ij}} + G_\sigma \frac{\partial \sigma}{\partial \sigma_{ij}} + G_\theta \frac{\partial \theta}{\partial \sigma_{ij}} \tag{22}$$

where the subscript denotes the partial derviative of G with respect to that argument. The derivatives of the first two invariants with respect to stress are easily calculated as $\partial\tau/\partial\sigma_{ij} = s_{ij}/\tau$ and $\partial\sigma/\partial\sigma_{ij} = \delta_{ij}$ and the third is given by

$$\frac{\partial J_3}{\partial \sigma_{ij}} = t_{ij} = s_{ik}s_{kj} - (2/3)\delta_{ij}\tau^2 \tag{23}$$

The tensor t_{ij} is deviatoric ($t_{kk} = 0$) and has the same principal axes as s_{ij}. The result (23) can be used to shown that

$$\frac{\partial \theta}{\partial \sigma_{ij}} = -\frac{1}{\tau}\left\{ \frac{\sqrt{3}}{2\cos(3\theta)} \frac{t_{ij}}{\tau^2} + \tan(3\theta)\frac{s_{ij}}{2\tau} \right\} \tag{24}$$

and (22) can be rewritten as

$$Q_{ij} = F_\sigma \delta_{ij} + F_\tau \frac{s_{ij}}{2\tau} - F_\theta \frac{1}{\tau}\left\{ \frac{\sqrt{3}}{2\cos(3\theta)} \frac{t_{ij}}{\tau^2} + \tan(3\theta)\frac{s_{ij}}{2\tau} \right\} \tag{25}$$

where the last two terms give the deviatoric part. The direction of the inelastic strain increment is given by the same expression with F replaced by G. The assumption that the deviatoric parts of P_{ij} and Q_{ij} be equal, $Q'_{ij} = P'_{ij}$, requires that

$$F_\tau = G_\tau,\ F_\theta = G_\theta \tag{26}$$

Consequently, the yield function and plastic potential can differ only by a function of σ. Calculating $2Q'_{ij}Q'_{ij}$ yields

$$2Q'_{ij}Q'_{ij} = F_\tau^2 + (F_\theta/\tau)^2 \tag{27}$$

using the intermediate results

$$t_{ij}t_{ij} = 2\tau^4/3$$

and

$$t_{ij}s_{ij} = -2\tau^3 \sin(3\theta)/\sqrt{3}$$

5 Expression for the Band Angle

For the three invariant constitutive model and $P'_{ij} = Q'_{ij}$, the band angle is given by the same expressions, (14), (15), (16) and (17), with the replacements:

$$\beta \to \frac{1}{2}\frac{P_{kk}}{\sqrt{Q'_{ij}Q'_{ij}/2}}$$

$$\mu \to \frac{1}{2}\frac{Q_{kk}}{\sqrt{Q'_{ij}Q'_{ij}/2}}$$

$$N_{ij} = \frac{s_{ij}}{\tau} \to \frac{Q'_{ij}}{\sqrt{Q'_{kl}Q'_{kl}/2}}$$

Thus, the expression for α becomes

$$\alpha = \frac{(1/3)(1+\nu)(P_{kk}+Q_{kk}) - Q'_2(1-2\nu)}{\sqrt{2Q'_{kl}Q'_{kl} - 3(Q'_2)^2}} \tag{28}$$

Using (19), (23), (25) and (27) yields the following more compact result:

$$\alpha = \frac{\sqrt{3}(1+\nu)\cos\phi(F_\sigma + G_\sigma) - (1-2\nu)\sin(\phi+\theta)F_\tau}{\sqrt{3}F_\tau\cos(\phi+\theta)} \tag{29}$$

where ϕ, defined by

$$\tan\phi = \frac{F_\theta/\tau}{F_\tau} \tag{30}$$

is the angle between the normal to the yield surface in the deviatoric plane and a radial vector.

5.1 Mohr-Coulomb Result

A number of three invariant yield surfaces have been suggested for soils, rock and concrete (see, e.g., [27], [15], [4]). Of this class, the most familiar, at least in geomechanics, is the Mohr-Coulomb form. Although this condition is usually applied as a failure criterion ([14], [29]), it has also been used for yield (e.g., [23]). The Mohr-Columb condition has the form

$$F_{MC} = q + M(p) = 0 \tag{31}$$

where $q = (\sigma_1 - \sigma_3)/2$ and $p = (\sigma_1 + \sigma_3)/2$. Thus, it does not depend at all on the intermediate principal stress σ_2. Although (31) can be expressed in terms of σ, τ, and θ, it is more convenient to follow [28] and identify the principal values of Q_i directly. The denominator of (28) is unity and (28) reduces to

$$\alpha = (1+\nu)(P_{kk} + M')/3 + (1-2\nu)M'/3 \tag{32}$$

where M' denotes the derivative with respect to its argument. Assuming normality, $P_{kk} = Q_{kk} = M'$ reduces (32) to $\alpha = M'$. Thus, as noted by [28], (32) reduces to the usual Mohr-Coulumb prediction for a friction angle defined by $\arcsin(M')$. Although this result can be used to interpret data from axisymmetric compression, the absence of any dependence on σ_2 is at odds with observations in true triaxial tests ([21], [22], [9], [5], [10], [24]).

6 A Class of Three Invariant Yield Surfaces

A class of three invariant yield surfaces is defined by

$$F(\tau, \sigma, \theta) = -\sqrt{\frac{4}{27}} A \sin(3\theta) \left(\frac{\tau}{\tau_0}\right)^3 + \left(\frac{\tau}{\tau_0}\right)^2 - 1 = 0 \tag{33}$$

where $0 \leq A \leq 1$, and both A and τ_0 may depend on σ. For $A = 0$ and $\tau_0 = \tau_0(\sigma)$, (33) reduces to the form considered by [33] (10). For $A = 1$, the shape of the yield surface in the deviatoric plane is triangular, as for a Rankine material in which yield occurs at a particular value of the largest (least compressive) principal stress. For $\theta = 0$, the first term in (33) vanishes and the condition again reduces to $\tau = \tau_0(\sigma)$. Thus, $\tau_0(\sigma)$ is determined by the mean stress dependence in deviatoric pure shear.

The form (33) has the same shape in the deviatoric plane as the Lade-Duncan ([17], [4]) and Matsuoka-Nakai ([19], [4]) criteria but the mean stress dependence is not specific and can be adjusted by the forms of A and τ_0. In particular, taking

$$\tau_0 = -\frac{\sigma}{3}\sqrt{\frac{(k_{LD} - 27)}{k_{LD}}} \tag{34}$$

and $A = \sqrt{1 - 27/k_{LD}}$ gives the form of the Lade-Duncan criterion in which $k_{LD} > 27$. Taking

$$\tau_0 = -\frac{\sigma}{3}\sqrt{\frac{k_{MN} - 9}{k_{MN} - 3}} \tag{35}$$

and $A = \sqrt{3k_{MN}^2(k_{MN} - 9)/(k_{MN} - 3)^3}$ gives the form of the Matsuoka-Nakai criterion in which $k_{MN} > 9$. Because these two criteria and (33) have the identical shape in the deviatoric plane if normalized to agree in pure shear ($\theta = 0$), the demonstration of convexity by [15] for Lade-Duncan and Matsuoka-Nakai also applies to (33). An advantage of the form (33) is that the dependence of τ_0 and A on σ can be chosen to agree with particular data sets. Figure 1 compares the shape of Mohr Coulomb criterion in the deviatoric plane with the shape of (33) for $A = 0, 0.7$ and 0.9 with all normalized to agree in pure shear. The curve for $A = 0$ is identical with the Mises circle in this plane. For each criterion (except with $A = 0$) the yield stresses differ in axisymmetric compression ($\theta = 30^o$) and axisymmetric extension ($\theta = -30^o$) and the amount of the difference varies for each criterion.

7 Westerly Granite Data

In this section, (33) is used with (29) to model band angle data on Westerly granite. These data combine results of Mogi [20] for axially symmetric extension and compression with more recent true triaxial data of [10]. Rudnicki [31] has examined this data set using (16) and (17) but allowing the sum of $\mu + \beta$ to depend on the mean stress in a manner inferred from the results of axisymmetric compression. Although this analysis roughly captures some trends in the data, the quantitative agreement is not very good. As will be shown here, the use of the three invariant model (33) yields better agreement between data and predictions.

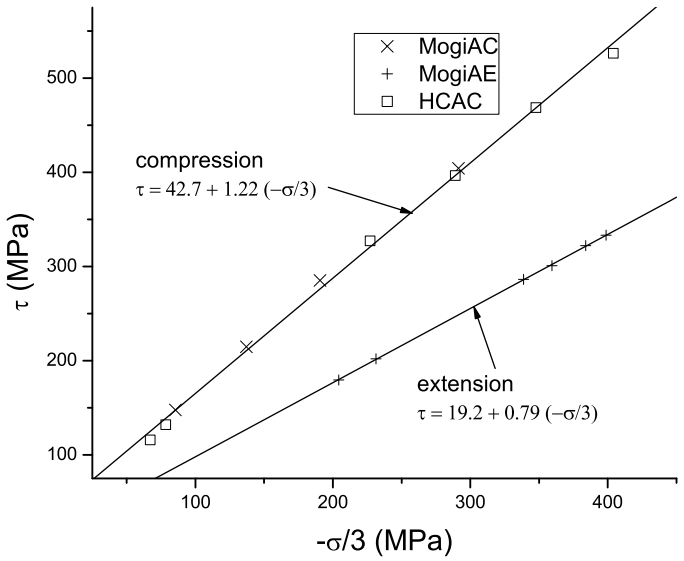

Fig. 2 A plot of τ (at failure) vs. mean normal stress $-\sigma/3$ for the axisymmetric compression and extension tests of [20] and the true triaxial tests of [10] loaded in axially symmetric compression. Also shown are lines fit to the results in compression and extension.

As mentioned earlier, data on the evolution of the yield surface is seldom available for rocks. The data used here are for "failure" which corresponds roughly to the development of a through going fault approximately at a peak in the stress vs. strain curve. As also noted earlier, the bifurcation analysis predicts that localization can occur slightly before peak, for deformation states near plane strain, or well after peak, for axisymmetric deformation states. Although there is some evidence consistent with these predictions [3], localization is typically observed to occur near peak stress. Whether it is

observed slightly before or after depends not only on the deformation state but on a variety of experimental factors such as effective stiffness of the loading machine, nominal deformation rate, precise alignment of the platens and degree of constraint imposed by the end conditions. In the absence of detailed information on yield, I assume the failure data approximately reflect variation of the yield surface. Figure 2 plots τ (at failure) vs. mean compressive stress, $-\sigma/3$, for the axisymmetric extension and compression tests of Mogi [20] on Westerly granite. Also shown are results of Haimson and Chang [10] in a true triaxial apparatus for axisymmetric compression stress states ($\sigma_1 = \sigma_2 > \sigma_3$). Agreement of the tests of [20] and [10] illustrates the consistency of results obtained using the different apparati. The results for both tests are well-modelled by the straight lines given on the graph. The different lines for compression and extension indicate a dependence on the Lode angle θ [31]. For axisymmetric compression, τ is given by $t_{AC}\tau_0(\sigma)$, where t_{AC} is the root of (33) for $\theta = \pi/6$. Similarly, for axisymmetric extension, $\tau = t_{AE}\tau_0(\sigma)$, where t_{AE} is the root of (33) for $\theta = -\pi/6$. The linear variations suggest that it suffices to take A as constant (not dependent on mean stress) and $\tau_0(\sigma)$ as linear:

$$\tau_0(\sigma) = \tau_{00} + \tau_{01}(-\sigma/3) \tag{36}$$

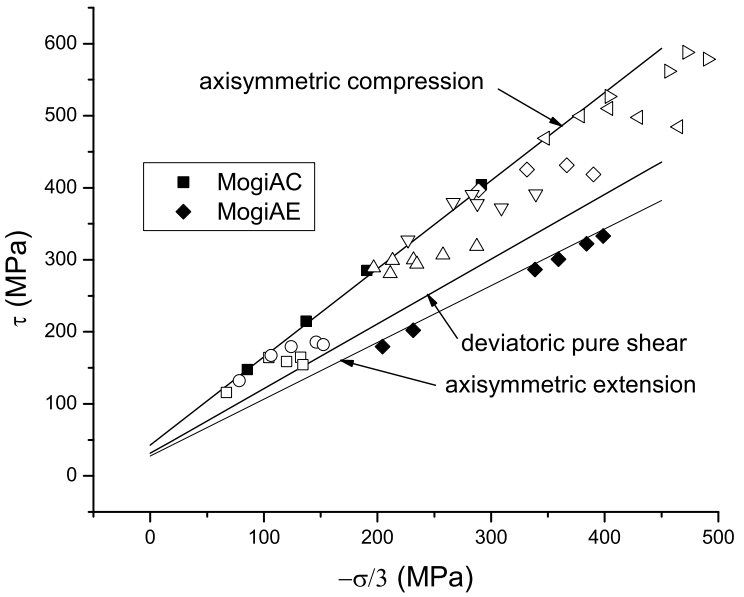

Fig. 3 Plot of τ vs. $-\sigma/3$ for axisymmetric compression and extension data of [20] and all the true triaxial data of [10]. Lines are predictions of (33) for $A = 0.88$ and $\theta = \pi/6$, 0, and $-\pi/6$.

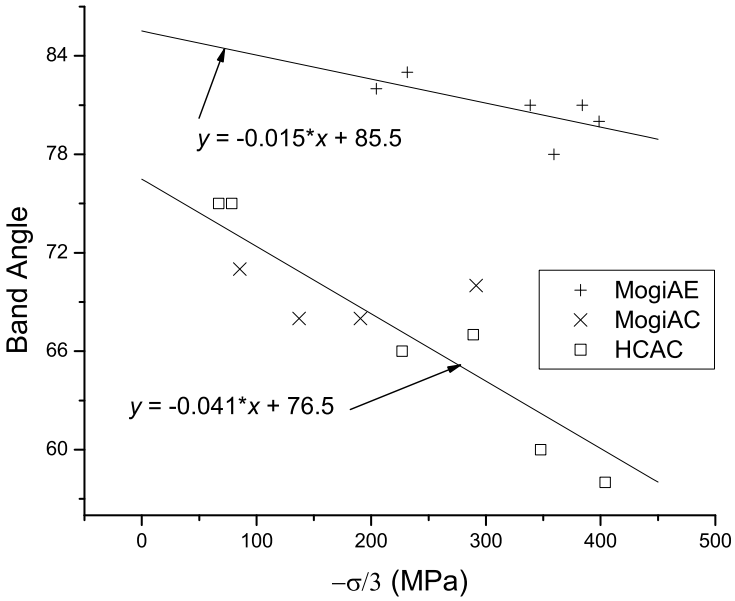

Fig. 4 Measured band angles for axisymmetric compression and extension versus the mean normal stress and straightline fits to the data

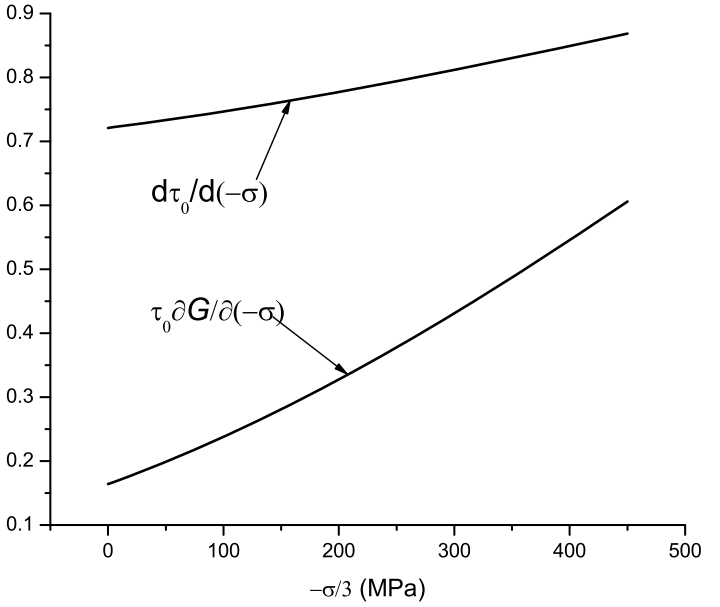

Fig. 5 Variations of $d\tau_0/d\sigma$ and $\tau_0 \partial G/\partial\sigma$ inferred from (29) applied to the linear variation of band angles in compression and extension (Figure 4). Vertical axis gives numerical values for both $d\tau_0/d\sigma$ and $\tau_0 \partial G/\partial\sigma$.

where τ_{00} and τ_{01} are the intercept and slope of the fit to the axisymmetric compression data in Figure 2 divided by t_{AC}. The value of $A = 0.88$ is chosen so that the ratio of t_{AC}/t_{AE} is equal to the ratio of slopes in Figure 2.

Figure 3 plots the data of [20] shown in Figure 2 along with all the true triaxial data of [10]. The true triaxial tests were conducted by loading the specimens in hydrostatic compression to the level of σ_1, then loading biaxially with $\sigma_2 = \sigma_3$ to a fixed value of σ_2, and finally increasing σ_3 to failure. Different symbols correspond to tests at different values of the least compressive stress (σ_1). From a conceptual point-of-view, it would be preferable to conduct tests at constant values of σ or θ, but both vary during these tests. The lines in Figure 3 show the resulting predictions for axisymmetric compression, axisymmetric extension and deviatoric pure shear from (33) with $A = 0.88$ and (36). Although $\tau_0(\sigma)$ (36) is fixed by the data for axisymmetric compression and A is chosen to give the observed ratio of slopes in compression and extension, the intercept for extension is only slightly larger than that given by the fit to the data; i.e., axisymmetric extension points lie slightly below the line in Figure 2. Furthermore, the values of θ for the true

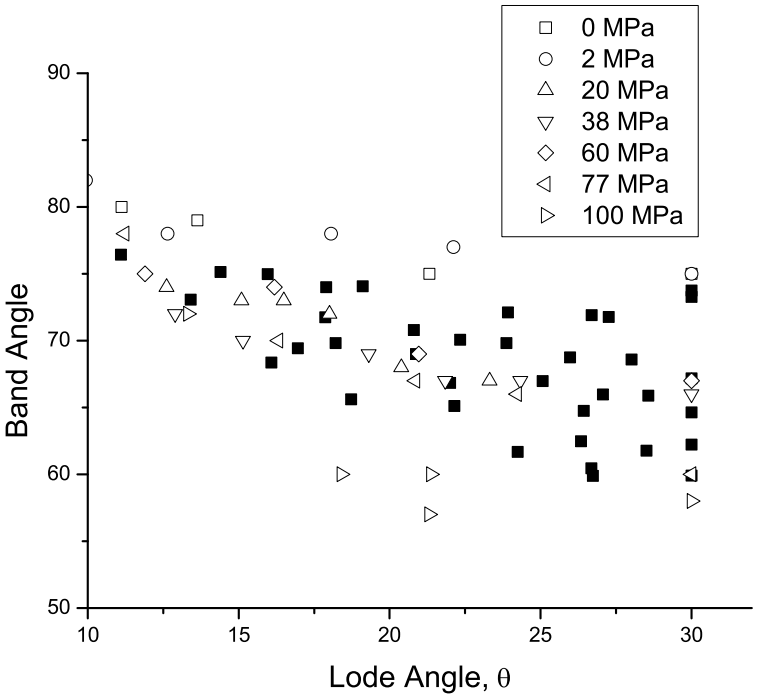

Fig. 6 Comparison of predicted (solid squares) and observed band angles (open symbols) as a function of the Lode angle θ. Different open symbols correspond to the value (shown in legend) of the fixed minimum compressive stress in the test.

triaxial tests lie between 0.0 and 30^o which is consistent with the position of the line for deviatoric pure shear. (See Figure 3 of [31] which shows data for the band angle plotted against $2\sin\theta$).

Figure 4 shows the measured band angles for axisymmetric compression and extension versus the mean normal stress and straightline fits to the data. The derivatives F_τ and F_θ that enter (29) and (30) can easily be calculated from (33). If A is a constant and only τ_0 depends on σ, then

$$F_\sigma = \frac{1}{\tau_0}\frac{d\tau_0}{d\sigma}\left[\left(\frac{\tau}{\tau_0}\right)^2 - 3\right] \tag{37}$$

where the ratio τ/τ_0 depends on θ for a given value of A. $G_\sigma$in (29) is unknown but can be determined along with $d\tau_0/d\sigma$ from the observed variations of the band angles in axisymmetric compression and extension. In other words, using the linear fits to the band angle data shown in Figure 4 in the expressions (16) with (29) and (30) evaluated for compression and extension yields two linear equations to determine G_σ and $d\tau_0/d\sigma$. The results are shown in Figure 5. The inferred dependence of $d\tau_0/d\sigma$ with σ is not consistent with the linear variation of $\tau_0(\sigma)$ shown in Figure 2. Nevertheless, the variation of $d\tau_0/d\sigma$ is small (0.72 to 0.87) and only slightly below the value used to plot the lines in Figure 2 (0.898). This discrepancy may be due to the issues discussed earlier

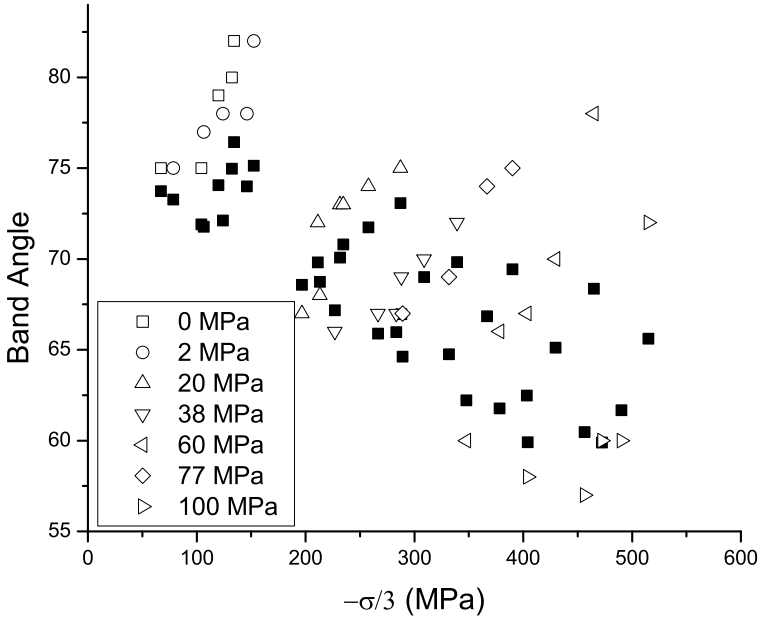

Fig. 7 Same as Figure 6 but plotted against the mean normal compressive stress $-\sigma/3$

about using failure data to approximate the variation of the yield surface. The data for stress at failure are, however, only used to estimate the value of A. Alternatively, the value of A could be chosen to improve the agreement between the predictions and observations of the band angle data.

Figure 6 compares the values of the predicted and observed band angles as a function of the Lode angle θ. The agreement is good and the correlation between the two data sets is 0.912. Figure 7 shows the comparison as a function of mean stress. Note that the predictions capture the roughly linear increase in band angle with increasing intermediate principal stress and the generally downward trend with increasing mean compressive stress.

8 Conclusion

Data from true triaxial tests provide an opportunity to investigate the form of three-dimensional constitutive relations for rocks. Tests at multiple mean stresses for axisymmetric compression and extension can be used to infer the behaviour for other deviatoric stress states and mean stresses. Use of the predictions for the band angle from bifurcation theory with a simple form of the yield function that depends on all three stress invariants yields results that are an improvement over those based on the two invariant model. The predictions are in reasonable agreement with the observations on Westerly granite and it will be interesting to see if similarly good agreement can be achieved with other rock types.

Acknowledgement. I am grateful to Bezalel Haimson for providing me with his experimental data and for many helpful discussions. I also greatly appreciate the many discussions with Florent Gimbert about three invariant constitutive models. Partial financial support for this work was provided by the US Department of Energy, Office of Science, Basic Energy Sciences, Geosciences program through grant DE-FG02-93ER14344/A016 to Northwestern University.

References

[1] Baud, P., Klein, E., Wong, T.-F.: Compaction localization in porous sandstones: Spatial evolution of damage and acoustic emission activity. Journal of Structural Geology 26, 603–624 (2004)

[2] Bernard, X.D., Eichhubl, P., Aydin, A.: Dilation bands: A new form of localized failure in granular media. Geophysical Research Letters 29(24), 2176 (2002), doi:10.1029/2002GL015966

[3] Bésuelle, P., Rudnicki, J.W.: Localization: Shear bands and compaction bands. In: Guéguen, Y., Boutéca, M. (eds.) Mechanics of Fluid Saturated Rocks. International Geophysics Series, vol. 89, pp. 219–321. Academic Press, London (2004)

[4] Borja, R.I., Sama, K.M., Sanz, P.F.: On the numerical integration of three-invariant elastoplastic constitutive models. Computer Methods in Applied Mechanics and Engineering 192, 1227–1258 (2003), doi:10.1016/S0045-7825(02)00620-5
[5] Chang, C., Haimson, B.: True triaxial stength and defomrability of the german continental deep drilling program (KTB) deep hole amphibolite. Journal of Geophysical Research 105(B8), 999–919 (2000)
[6] DiGiovanni, A.A., Fredrich, J.T., Holcomb, D.J., Olsson, W.A.: Micromechanics of compaction in an analogue reservoir sandstone. In: Girard, J., Liebman, M., Breeds, C., Doe, T. (eds.) Pacific Rocks 2000, Proceedings of the 4th North American Rock Mechanics Symposium, pp. 1153–1158. A. A. Balkema (2000)
[7] Fôrtin, J., Stanchits, S., Dresen, G., Guéguen, Y.: Acoustic emission and velocities associated with the formation of compaction bands in sandstone. Journal of Geophysical Research 111(B10203) (2006), doi:10.1029/2005JB003854
[8] Hadamard, J.: Leçons sur la Propagation de Ondes et Les Equations de L'Hydrodynamique, Paris (1903)
[9] Haimson, B.: True triaxial stresses and the brittle fracture of rock. Pure and Applied Geophysics 163, 1101–1130 (2006), doi: 10.007/s00024-006-0065-7
[10] Haimson, B., Chang, C.: A new true triaxial cell for testing mechanical properties of rock, and its use to determine rock strength and deformability of Westerly granite. International Journal of Rock Mechanics and Mining Science 37(1-2), 285–296 (2000)
[11] Hill, R.: The Mathematical Theory of Plasticity. Oxford Engineering Science Series, Oxford, London (1950)
[12] Hill, R.: Acceleration waves in solids. Journal of the Mechanics and Physics of Solids 10, 1–16 (1962)
[13] Holcomb, D.J., Olsson, W.A.: Compaction localization and fluid flow. Journal of Geophysical Research 108(B6, 2290) (2003), doi: 10.1029/2001JB000813
[14] Jaeger, J.C., Cook, N.G.W.: Fundamentals of Rock Mechanics. John Wiley and Sons, Inc., New York (1969)
[15] Jiang, J., Pietruszczak, S.: Convexity of yield loci for pressure sensitive materials. Computers and Geotechnics, 51–63 (1988)
[16] Klein, E., Baud, P., Reuschlé, T., Wong, T.-F.: Mechanical behaviour and failure mode of Bentheim sandstone under triaxial compression. Physics and Chemistry of the Earth (A) 26, 21–25 (2001)
[17] Lade, P.V., Duncan, J.M.: Elastoplastic stress-strain theory for cohesioness soil. J. Geotech. Engrg. Div., ASCE 101, 1037–1053 (1975)
[18] Mandel, J.: Conditions de stabilté et postulat de drucker. In: Kravtchenko, J., Sirieys, P.M. (eds.) Rheology and Soil Mechanics, pp. 58–68. Springer (1966)
[19] Matsuoka, H., Nakai, T.: Stress-deformation and strength characteristics of soil under three different principal stresses. Proc. Japan Soc. Civil Engn., 1037–1053 (1974)
[20] Mogi, K.: Effect of the intermediate principal stress on rock failure. Journal of Geophysical Research 72, 5117–5131 (1967)
[21] Mogi, K.: Effect of the triaxial stress system on the failure of dolomite and limstone. Tectonophysics 11, 111–127 (1971)
[22] Mogi, K.: Experimental Rock Mechanics. Geomechanics Research Series, vol. 3.Taylor & Francis (2007)

[23] Molenkamp, F.: Comparison of frictional material models with respect to shear band initiation. Géotechnique 35(2), 127–143 (1985)
[24] Oku, H., Haimson, B., Song, S.-R.: True triaxial strength and deformability of the siltstone overlying the chelungpu fault (chi-chi earthquake), taiwan. Geophysical Research Letters 34(L09306) (2007), doi:10.1029/2007GLO29601
[25] Olsson, W.A.: Theoretical and experimental investigation of compaction bands. Journal of Geophysical Research 104, 7219–7228 (1999)
[26] Olsson, W.A., Holcomb, D.J.: Compaction localization in porous rock. Geophysical Research Letters 27(21), 3537–3540 (2000)
[27] Ottosen, N.S.: Theoretical framework for modelling the behaviour of frictional materials. International Journal of Solids and Structures 22(11), 1325–1342 (1986)
[28] Ottosen, N.S., Runesson, K.: Properties of discontinuous bifurcation solutions in elasto-plasticity. International Journal of Solids and Structures 27, 401–421 (1991)
[29] Paterson, M.S., Wong, T.-F.: Experimental Rock Deformation - The Brittle Field, 2nd edn. Springer, Heidelberg (2005)
[30] Rice, J.R.: The localization of plastic deformation. In: Koiter, W.T. (ed.) Proceedings of the 14th International Congress on Theoretical and Applied Mechanics Theoretical and Applied Mechanics, pp. 207–220. North-Holland Publishing Company, Delft (1976)
[31] Rudnicki, J.W.: Localized Failure in Brittle Rock. In: Proceedings of the 3rd International Symposium GeoProc 2008, pp. 25–40. Wiley (2008)
[32] Rudnicki, J.W., Olsson, W.A.: Reexamination of fault angles predicted by shear localization theory. International Journal of Rock Mechanics and Mining Science 35, 512–513 (1998); extended abstract, full paper on CD Rom.
[33] Rudnicki, J.W., Rice, J.R.: Conditions for the localization of deformation in pressure-sensitive dilatant materials. Journal of the Mechanics and Physics of Solids 23, 371–394 (1975)
[34] Sternlof, K.R.: Structural geology, propagation mechanics and hydraulic effects of compaction bands in sandstone, Ph.D. thesis, Stanford University (2006)
[35] Sternlof, K.R., Chapin, J.R., Pollard, D.D., Durlofsky, L.J.: Permeability effects of deformation band arrays in sandstone. American Association of Petroleum Geologists Bulletin 88, 1315–1329 (2004)
[36] Sternlof, K.R., Rudnicki, J.W., Pollard, D.D.: Anti-crack inclusion model for compaction bands in sandstone. Journal of Geophysical Research 110(B11403) (2005), doi:10.1029/2005JB003764
[37] Sternlof, K.R., Karimi-Fard, M., Pollard, D.D., Durlofsky, L.J.: Flow effects of compaction bands in sandstone at scales relevant to aquifer and reservoir management. Water Resources Research 42(W07425) (2006), doi:10.1029/2005WR004664
[38] Tembe, S., Vajdova, V., Wong, T.-F., Zhu, W.: Initiation and propagation of strain localization in circumferentially notched samples of two porous sandstones. Journal of Geophysical Research 111(B02409) (2006), doi:10.1029/2005JB003611
[39] Thomas, T.Y.: Plastic Flow and Fracture in Solids. Academic Press (1961)

[40] Vajdova, V., Wong, T.-F.: Incremental propagation of discrete compaction bands and microstructural observations on circumferentially notched samples of Bentheim sandstone. Geophysical Research Letters 30(14), 1775 (2003), doi:10.1029/2003GL017750.
[41] Vajdova, V., Baud, P., Wong, T.-F.: Permeability evolution during localized deformation in Bentheim sandstone. Journal of Geophysical Research 109(B10406) (2004), doi:10.1029/2003JB002942
[42] Wawersik, W.R., et al.: Terrestrial sequestration of CO2: An assessment of research needs. In: Dmowska, R. (ed.) Advances in Geophysics, vol. 43, pp. 97–177. Academic Press (2001)

Modeling of Bone Failure by Cohesive Zone Models

Thomas Siegmund[1], Matthew R. Allen[2], and David B. Burr[2,3,4]

[1] School of Mechanical Engineering, Purdue University
[2] Department of Anatomy and Cell Biology, Indiana University School of Medicine
[3] Department of Orthopaedic Surgery, Indiana University School of Medicine
[4] Biomedical Engineering, Indiana University-Purdue University at Indianapolis

Abstract. Cohesive zone models are a powerful tool for investigations of non-linear deformation and failure processes. For the nanoscale, the use of cohesive zone models is particularly attractive as the ratio of interface to volume is high, and because locally acting bonds between material components can become relevant. The present paper demonstrates the relevance of cohesive zone modelling approaches to the development of a nano-mechanical composite model of the mineralized collagen fibril, a fundamental building block of bone. As difficulties exist in determining the independent biomechanical effects of collagen cross-linking using in vitro and in vivo experiments, computational modeling can provide insight into the nanoscale processes. Stress-strain curves for mineralized collagen fibrils were obtained under tensile loading for various collagen cross-linking conditions. Our model predicts that the elastic deformation mode, the yield response and the final failure of the mineralized collagen fibril may depend significantly on the state of collagen cross-linking.

1 Introduction

Cohesive zone models have emerged as an important tool in the modeling and simulation of the mechanical behavior of materials. These models capture the processes occurring during material separation as a constitutive model and describe the formation of a new defect or the extension of an already existing defect. The use of CZMs in the context of the finite element method (FEM) has drawn particular attention. The capability of the FEM to solve non-linear full field problems has enabled solutions to interesting problems related to failure of materials and structures. Studies of crack growth in a variety of material systems and load conditions have greatly benefited from this modeling approach (Hutchinson and Evans 2000). Thereby, the CZM approach

can be particularly useful if crack growth resistance emerges as a combination of creation of fracture surface and bulk dissipation, and if large strains need to be considered. In micromechanical investigations of failure of multiphase materials CZMs have been used to incorporate the phase-to-phase interface behavior (Needleman 1987) as well as particle fracture into the analysis. Such studies have highlighted the role of reinforcement particle mechanical properties, size and geometry on the composite response under uniaxial and multiaxial loading. More recently, CZMs have also attracted attention for the development of models for nano-composites (Tan *et al.* 2007). From these models, the importance of the the interplay between reinforcement size and interface bond conditions emerges.

We describe a nano-scale mechanical model for the mineralized collagen fibril (MCF) underlying bone, and demonstrate that the use of CZMs enable such efforts. In the past, several continuum mechanics-based models for the MCF were proposed, including the equivalent inclusion method (Hellmich *et al.* 2004, Fritsch and Hellmich 2007), shear-lag models (Jäger and Fratzl 2000, Kotha and Guzelsu 2003, Wang and Qian 2006), and numerical models based on a shear-lag type geometry (Ji and Gao 2004, Arnoux *et al.* 2002).

An extended continuum mechanistic model of a MCF is presented with detailed consideration of the potential deformation modes in collagen, the debonding between collagen and mineral, and fracture of the mineral. We consider two types of interactions between individual collagen helix domains in the overall collagen matrix. Weak and distributed interactions between collagen would occur due to hydrogen bonds, non-collageneous proteins, and electrostatic interaction, whereas strong and local interactions are due to enzymatic and non-enzymatic cross-linking. We hypothesize that the predicted stress-strain curves would exhibit significantly different characteristics as the state of collagen is changed, and that such differences would also be reflected in the distribution of strains and stresses in collagen and mineral.

The significance of the development of a model accounting for detailed features of the collagen structure arises from the need for a better understanding of deformation and failure behavior of bone, and ultimately its relationship to bone health. The mechanical behavior of bone is significantly influenced by bone mass, mineral density, and micro-architecture, but contributions of collagen to bone's pre- and post-yield properties are less well understood (Burr 2002). Collagen appears to play a major role on the bone nano-scale. While the mineral dictates much of the tissue stiffness, collagen has a profound effect on bone's post-yield properties (e.g. energy absorption) (Burr 2002). The effects of collagen depend largely on cross-linking (Knott and Bailey 1998, Viguet-Carrin *et al.* 2006a, Wang *et al.* 2003) which can occur either enzymatically or non-enzymatically (Bailey *et al.* 1998, Eyre *et al.* 1988, Viguet-Carrin *et al.* 2006a). Experiments in vitro (Vashishth *et al.* 2004, Wu *et al.* 2003, Catanese *et al.* 1999) and in vivo (Boxberger and Vashishth 2004, Tang *et al.* 2005), (Wang *et al.* 2002, Viguet-Carrin *et al.* 2006b, Allen *et al.* 2008) have documented that increases in collagen cross-linking are

associated with enhancement of some mechanical properties (strength and stiffness) and reductions of others (energy absorption). As these experimental data are limited in their ability to define the individual biomechanical effect of altered cross-linking as concomitant changes associated with aging (increased mineralization and increased microdamage) or pharmacological treatment also contribute to the mechanical properties (Allen and Burr 2007) modeling studies become of importance.

2 Model Description

Mineral and collagen are arrangements in the MCF follow the collagen packing model of (Petruska and Hodge 1964) with the mineral located in gaps of the collagen assembly (Lees 1987, Landis 1995) (Fig. 1a). The simplified packing model of (Jäger and Fratzl 2000) (Fig. 1b) enables an analysis with a periodic unit cell. Such unit cell contains two quarters of mineral phase embedded in a collagen matrix (Figs 1b,c), but can be reduced in size through antisymmetry boundary conditions (Fig. 1d). The present model represents the collagen as composed of individual collagen molecules aligned parallel to the main faces of the mineral platelets. Such subdivision of the collagen matrix appears as relevant only for the area between mineral platelets as shear deformation vanishes adjacent to the ends of mineral (Jäger and Fratzl 2000).

The interactions between the building blocks of the model are accounted for through cohesive zone models. Cohesion of the mineral-collagen interface

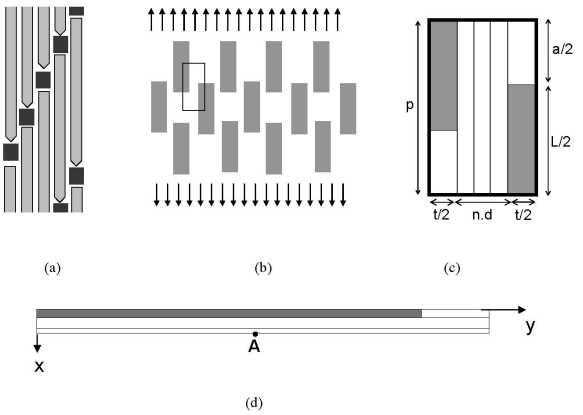

Fig. 1. Model definition: (a) Staggered array model for MCF, (b) Model with simplified periodicity of collagen (white) and mineral (gray), (c) unit cell dimensions, (d) computational unit cell with actual geometric proportions. Reprinted from J. Biomech. 41, Siegmund *et al.*, Failure of mineralized collagen fibrils: Modeling the role of collagen cross-linking, Copyright (2009), with permission from Elsevier.

is thought to be due to a layer of structural water (Wilson *et al.* 2005). Weak and distributed interactions between collagen occur due to hydrogen bonds, non-collageneous proteins, and electrostatic interaction. Furthermore, collagen cross-links provide strong, local interactions between collagen molecules. *Enzymatic* cross-links are located specifically at the collagen overlap position (Eyre and Wu 2005), and are thus placed beyond the end faces of mineral platelets. *Non-enzymatic* cross-links appear to possess no specific spatial arrangement. In the model five non-enzymatic cross-links are placed randomly between collagen domains. A potential fracture site is introduced at the center of the mineral platelet ($y = 0$). The plate-shape geometry of the mineral motivates the use of a plane strain model corresponding to the mid-plane of the mineral platelet – collagen assembly. The model is characterized by periodicity p (Jäger and Fratzl 2000), $p = (L + a)/2 = 67$ nm, L the mineral platelet length, a the distance between the short faces of the mineral platelets, and t the mineral thickness. The distance between the long faces of the mineral, b, is a multiple of the diameter of a collagen helix $b = nd$. The mineral volume fraction is $V_V^m = Lt/[(L + a)(b + t)]$. Given V_V^m, phase arrangements can be constructed choosing two of the parameters t, L, a, b. We assume $V_V^m = 0.3$ (Currey 1984, Fritsch and Hellmich 2007), $t = 2.5$nm (Gourrier *et al.* 2007), $b = 3d = 3 \cdot 1.5$ nm $= 4.5$ nm (three collagen domains between mineral platelets), such that $L = 113.9$ nm and $a = 20.1$ nm.

Uniaxial tensile loading along the fibril axis is considered. One half of the unit cell of Fig. 1c is analyzed. Starting from the analysis of the $^1/_2$ unit cell, Fig. 1d, an adjacent $^1/_2$ unit cell is identical to the base analysis domain but rotated by 180°about the midpoint (A) of the collagen-only edge (Tvergaard 1990). The structure in the deformed state can be reconstructed by employing symmetry conditions at $x = 0$ and $y = 0$, and periodicity boundary conditions along the remaining edges of the unit cell. Consequently, one obtains boundary conditions as:

$$\begin{aligned} y = 0: &\qquad u_y = -\frac{U_y}{2} \quad \text{and} \quad \Sigma T_x = 0 \\ y = p: &\qquad u_y = +\frac{U_y}{2} \quad \text{and} \quad \Sigma T_x = 0 \\ x = 0: &\qquad u_x = 0 \quad \text{and} \quad \Sigma T_y = 0 \\ x = \frac{b+t}{2}: &\; u_x(y) = u_x\left(\frac{p}{2} - y\right) \end{aligned} \tag{1}$$

with U_y the applied displacement, and T_x and T_y tractions on the respective boundaries. The fourth boundary condition in (1) is introduced such that the cross-sectional area is independent of the location along the y-axis. For the plane strain model with depth "1" the average nominal stress in the loading direction is $\Sigma_y = (\Sigma T_y)/[\text{"1"} \cdot (b + t)/2]$, and the average strain in that direction is $\varepsilon_y = U_y/p$.

The model volume $V$is comprised of mineral V_V^m and multiple collagen domains $V_V^{C,i}$ connected by interfaces S_{int}. The equilibrium equations include contribution of the cohesive zones as integral over internal surfaces S_{int}, and lead to the principle of virtual work:

$$\int_V \mathbf{s}{:}\delta\mathbf{F}\ \mathrm{d}V - \int_{S_{int}} \mathbf{T}_{\mathrm{CZ}} \cdot \delta\Delta\ \mathrm{d}S = \int_{S_{ext}} \mathbf{T}_e \cdot \delta\mathbf{u}\ \mathrm{d}S \tag{2}$$

with the nominal stress tensor $\mathbf{s}{=}\mathbf{F}^{-1}\ \det(\mathbf{F})\boldsymbol{\sigma}$, the Cauchy stress $\boldsymbol{\sigma}$, the deformation gradient $\mathbf{F}$**,** and the displacement vector $\mathbf{u}$. Traction vectors are related to $\boldsymbol{\sigma}$ by $\mathbf{T}{=}\mathbf{n}\ \boldsymbol{\sigma}$. $\mathbf{T}_e$ is the vector of external tractions.

The mechanical model response is solved with the FE code ABAQUS. Cohesive elements are defined using an UEL subroutine. Computations were conducted with the Riks algorithm. The mesh employed four-node plane strain elements: 200×10 elements of size $(p/200) \cdot [(t/2)/10]$ nm^2 for the mineral, and 200×6 elements of size $(p/200)\ \cdot\ (d/6)$ nm^2 for the collagen domain. Cohesive interface elements possess four nodes and two integration points. Their length is $(p/200)$ nm for the collagen – collagen and the mineral – collagen interface parallel to the platelet face, and $[(t/2)/10]$ nm for the remaining interfaces.

The mineral is an elastic isotropic solid, $E^m = 100\,\mathrm{GPa}$, $\nu^m = 0.28$ (Katz and Ukraincik 1971, Viswanath *et al.* 2007). Each collagen domain represents a collagen triple helix in a wet environment. It is described as homogeneous elastic solid with $E^c = 5$ GPa and $\nu^c = 0.2$. Considering that a single collagen molecule would not exhibit shear deformation, the collagen subdomains are assigned a high shear modulus, $G^c = 50$ GPa, such that collagen domains deform mainly by stretch similar to the situation present in bead models of collagen (Bühler 2006).

Elastic model domains are connected across interfaces S_{int} described by cohesive law. Due to uncertainty in the exact potentials for bonds present in the MCF, a generic CZM is employed. The CZM relates tractions $\mathbf{T_{CZ}} = T_n\mathbf{n} + T_t\mathbf{t}$ to material separation $\Delta = \Delta_n\mathbf{n} + \Delta_t\mathbf{t}$, with $\mathbf{n}$ and $\mathbf{t}$ normal and tangential vectors to the cohesive surface. The cohesive constitutive relationship follows from the potential function ϕ of (Xu and Needleman 1994) and parameter choices of (Abdul-Baqi and van der Giessen 2001):

$$\phi(\Delta_n, \Delta_t) = \phi_0 - \phi_0 \exp\left(-\frac{\Delta_n}{\delta_0}\right)\left[\left(\frac{\Delta_n}{\delta_0}\right) + \exp\left(-\frac{\Delta_t^2}{\delta_0}\right)\right] \tag{3}$$

with tractions as derivatives of ϕ.

$$\begin{aligned} T_n &= -\frac{\partial\phi}{\partial\Delta_n} = -\sigma_{\max}\mathrm{e}\exp\left(-\frac{\Delta_n}{\delta_0}\right)\left[-1 + \left(\frac{\Delta_n}{\delta_0}\right) + \exp\left(-\frac{\Delta_t^2}{\delta_0^2}\right)\right] \\ T_t &= -\frac{\partial\phi}{\partial\Delta_t} = -2\sigma_{\max}\mathrm{e}\frac{\Delta_t}{\delta_0}\exp\left(-\frac{\Delta_n}{\delta_0}\right)\exp\left(-\tfrac{\Delta_t^2}{\delta_0^2}\right) \end{aligned} \tag{4}$$

The constitutive parameters are the cohesive strength $\sigma_{\max}$, the maximum traction, and the cohesive length δ_0, the material separation Δ_n required for

T_n to reach $\sigma_{\max}$ at $\Delta_t = 0$. The maximum of T_t at $\Delta_n = 0$ is $\tau_{\max} = \sqrt{2\mathrm{e}}\sigma_{\max} = 2.33\ \sigma_{\max}$. The cohesive energy is $\phi_0 = \sigma_{\max}\delta_0\mathrm{e}$. Values for $\sigma_{\max}, \delta_0, \phi_0$ emerge from considerations on the specific bond on each interface.

For the quantification of cohesion of the mineral-collagen interface $(\sigma_{\max}^{m-c}, \delta_0^{m-c}, \phi_0^{m-c})$ due to a structural water layer (Wilson *et al.* 2005) molecular interface bond energies [J/mole] are translated into the continuum framework with cohesive zone energies [J/m^2]. Considering d =1.5 nm, a rise of the collagen helix per turn of 0.3 nm, hydrogen bonds present at two of three turns of the collagen helix, and a bond energy of 20 kJ/mol for hydrogen bonds (Steiner 2002), and a projected area of the collagen helix onto the mineral surface $(d \cdot L)$ one obtains $\phi_0^{m-c} = 0.15\mathrm{J/m}^2$. The equilibrium bond length of hydrogen bonds determines the cohesive length δ_0^{m-c}=0.2 nm, consequently $\sigma_{\max}^{m-c} = 270\mathrm{MPa}$. For an estimation of weak and distributed interactions between collagen $(\sigma_{\max}^{c-c}, \delta_0^{c-c}, \phi_0^{c-c})$ the shear yield stress is associated with the tangential cohesive strength $\tau_{\max}^{c-c}$. With $\sigma_{\max}^{c-c} = 30\,\mathrm{MPa}$ it follows that $\tau_{\max}^{c-c} = \sigma_{\max}^{c-c}/2.33 \approx 12.9\,\mathrm{MPa}$, a value on the lower bound of the shear yield stress (10 to 19 MPa) of the collagen matrix in plexiform bone (Kotha and Guzelsu 2003). Based on the simulations in Bühler 2006, the cohesive length the collagen-collagen interaction is taken as δ_0^{c-c}=1 nm. Collagen cross-link $(\sigma_{\max}^{x}, \delta_0^{x}, \phi_0^{x})$ consist mainly of C-C and C-N bonds (Knott and Bailey 1998). The ultimate load at rupture of such bonds is obtained as several nano-Newton magnitude (Beyer 2000, Garnier *et al.* 2000). Here F_u=1.5 nN is employed. The ultimate load at rupture of a cross-link is translated into a value of $\sigma_{\max}^{x}$as $\sigma_{\max}^{x} = F_u/[(p/200) \cdot d] = 3000$ MPa. The elongation of C-C bonds to rupture is of the order 0.1 nm (Beyer 2000). In a collagen cross-link several C-C bonds exist in series. Assuming a sequence of 10 C-C bonds, we use δ_0^{x}=1 nm as the value of extension of such a chain up to rupture. The parameter values for mineral fracture $(\sigma_{\max}^{m}, \delta_0^{m}, \phi_0^{m})$ follow those of brittle ceramics with $\sigma_{\max}^{m}$ a fraction of the elastic modulus, $\sigma_{\max}^{m} = 3000\ \mathrm{MPa} = (3/100)E^m\mathrm{MPa}$. We employ $\phi_0^{m} = 0.73\ \mathrm{J/m}^2$, and consequently, $\delta_0^{m} = 0.09\mathrm{nm}$.

3 Results

Computations of uniaxial tensile loading are conducted for model MCFs considering enzymatic cross-linking, and additional non-enzymatic cross-linking present, and compared to the case of a de-mineralized fibril where a void space is located at the mineral position, and a MCF model where all building blocks interact via perfectly bonded interfaces. Stress-strain curves are depicted in Fig. 2. For the collagen-only model fibril, a near to linear stress-strain response is predicted. The modulus is slightly lower than approaches $E^c(1 - V_V^m)$ as the deformation response is enhanced by some sliding between collagen. For the model MCF with perfectly bonded

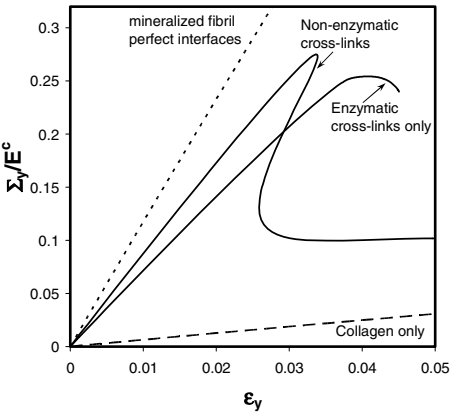

Fig. 2. Predicted overall stress-strain response

interfaces the stress-strain response is linear. The modulus is high and approaches the Voigt bound $E^c(1 - V_V^m) + E^m V_V^m$.

For the models accounting for the interface interactions, the predicted stress-strain response is linear only initially, $\varepsilon_y < 0.02$. The stiffness of both models accounting for the interfaces via the CZM is smaller than that of the model with perfectly bonded interfaces, but the reinforcing effect of the mineral phases raises the modulus significantly over that for the collagen-only fibril. Enzymatic cross-linking only leads to a lower initial modulus compared to the non-enzymatic case. The nonlinear response for the enzymatic and non-enzymatic case differs significantly. In the presence of enzymatic cross links only, a reduction in stiffness occurs at $\varepsilon \approx 0.02$. The peak load is reached at $\varepsilon_y = 0.04$, and subsequently a stable load drop is predicted. Such response can be qualified as ductile as the area under the stress-strain curve increases past the peak load. The model response for the model with non-enzymatic cross-links shows only a minor nonlinearity beyond $\varepsilon_y \approx 0.02$. The predicted strength higher than for the case with enzymatic cross-links only, and is reached at lower magnitude of applied strain, $\varepsilon_y = 0.035$. More significantly, the computed post peak response shows a pronounced snap-back. Such a snap-back behavior at failure would qualify as brittle as the area under the stress strain curve actually decreases. The finding that the presence of non-enzymatic cross-linking apparently embrittles the MCF is further investigated by studying the deformation response as well as the failure mechanism occurring of the fibril.

Figure 3 depicts predicted displacement fields for the models with enzymatic and non-enzymatic cross linking.

The contours of the displacement fields possess discontinuities at the interfaces, and the deformation emerging from the cohesive interfaces clearly contributes to the overall deformation response. In addition, Fig. 3 demonstrates that the failure modes differ between the conditions of enzymatic and non-enzymatic cross-linked collagen. In the presence of only enzymatic cross

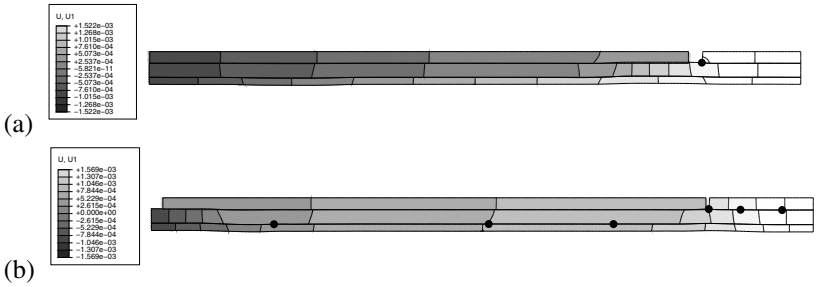

Fig. 3. Contour plots of displacement fields in the model MCF post failure load: (a) Enzymatic cross-links only; (b) Additional non-enzymatic cross-links. Cross-links are indicated as "•".Reprinted in part from J. Biomech. 41, Siegmund *et al.*, Failure of mineralized collagen fibrils: Modeling the role of collagen cross-linking, Copyright (2009), with permission from Elsevier.

linking, failure is due to debonding at the mineral-collagen interface. In the presence of the non-enzymatic cross-links failure is due to fracture of the mineral phase. The energy release processes of the two failure modes differ significantly. The stability of the failure processes, and a criterion for ductile failure, can be characterized by the elastically stored energy at fracture to the dissipation during formation of the fracture surface:

$$\phi_0(t \cdot \text{“1”}) > \frac{1}{2}\frac{\sigma_{\max}^2}{E}(pt \cdot \text{“1”}) \Rightarrow \frac{\phi_0 E}{2\sigma_{\max}^2} > p \tag{5}$$

Mineral fracture is characterized by a much higher value of cohesive strength than debonding at the mineral collagen interface, $\sigma_{\max}^m \approx 10\sigma_{\max}^{m-c}$. Consequently, the transition from debonding to mineral failure will lead to a ductile-to-brittle transition in the MCF failure.

The contribution of the interfaces to the model response can be quantified by considering the strain averages. The overall, applied, strain (here the strain component ε_y) can be related to the averages of respective strain components in mineral $\bar{\varepsilon}_y^m$, collagen $\bar{\varepsilon}_y^c$, and to the contribution from the interfaces $\bar{\varepsilon}_y^{int}$ as:

$$\varepsilon_y = V_V^m \bar{\varepsilon}_y^m + V_V^c \bar{\varepsilon}_y^c + \bar{\varepsilon}_y^{int} \tag{6}$$

Averages of strains $\bar{\varepsilon}_y^m$, $\bar{\varepsilon}_y^c$ are computed from the finite element simulations, and thus $\bar{\varepsilon}_y^{int}$ is obtained. For $\varepsilon_y = 0.03$ (i.e. during the nonlinear deformation regime preceding the peak load), the model predicts average strains as:

This result indicates that the deformation induced into the model through the cohesive zones affect the collagen little but shield the mineral from deformation and failure. *On average* non-enzymatic cross-linking does not suppress sliding between collagen as reflected in the minor change to $\bar{\varepsilon}_y^m$ with changes in cross-link state. The most significant changes occur for the mineral

Table 1. Average strains in collagen, mineral and the cohesive interfaces

	Enzymatic Cross-links, only	Non-enzymatic Cross-links	Perfect Bonds
$\bar{\varepsilon}_y^m$	0.0173	0.0188	0.0297
$\bar{\varepsilon}_y^c$	0.0311	0.0310	0.0301
$\bar{\varepsilon}_y^{int}$	0.0025	0.0023	0.0

phase where the increase in strain due to non-enzymatic cross-linking raises the estimated average stress (0.0188-0.0173)E^m=150 MPa. Moreover, local changes in the stress distribution occur with the additional non-enzymatic cross-linking. The stress distribution along the mineral and the center collagen fibril is shown in Fig. 4 for enzymatic and non-enzymatic cross-linking as well as for the perfectly bonded case. In all cases, the mineral carries significantly higher stresses than the collagen. The presence of the non-enzymatic cross-links introduces local perturbations into the collagen, but stresses remain at a low level compared to those in the mineral. For the mineral, the non-enzymatic cross-links elevate not only the average stress level but also alter the stress distribution such that stresses are elevated predominately at the mineral center-plane. It can be expected that as further non-enzymatic cross-links would be introduced the stress distribution would approach that of the case with perfect bonds assumed where stresses at the mineral center-plane are highly elevated over the mean value.

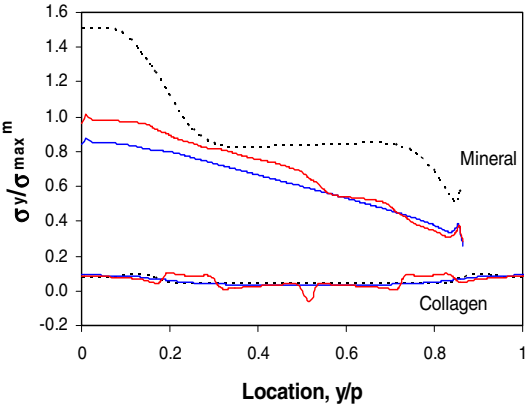

Fig. 4. Spatial distribution of stress component parallel to loading direction. Comparison of prediction for enzymatic, non-enzymatic cross-linking and a model with perfect bonding across all interfaces.

4 Discussion

Collagen cross-linking and its relationship to the energy absorption after yield has long been considered as a relevant parameter for bone fracture. Enzymatic cross-links accumulate in human bone up to the age of about 10-15 years (Garnero *et al.* 2006) and thereafter remain constant or may decline slightly (Eyre *et al.* 1988, Saito *et al.* 1997). Non-enzymatically mediated collagen cross-links form over a period of years (Monnier 1989), and collagen can accumulate these cross-links with age (Vasan et al. 2003, Odetti *et al.* 2005). Considering a macroscopic response of bone, enzymatic cross-linking has been linked to improved mechanical properties (Banse *et al.* 2002), such as an increased compressive strength and stiffness (Lees, *et al.* 1990, Bailey *et al.* 1992, Oxlund *et al.* 1995, Oxlund *et al.* 1996, Banse *et al.* 2002), but probably has no effect on toughness or ductility (Zioupos *et al.*1999, Wang *et al.* 2002, Keaveny *et al.* 2003, Hernandez *et al.* 2005). Non-enzymatic cross-linking prevents energy absorption by microdamage formation and may accelerate brittle fracture (Vashishth *et al.* 2001, Tang *et al.* 2007, Nyman *et al.* 2007, Vashishth *et al.* 2007), relates inversely to bone toughness (Wang *et al.* 2002), creep rate, and strain to failure (Vashishth *et al.* 2004, Vashishth 2007, Nyman *et al.* 2007, Tang *et al.* 2007). Increased pentosidine concentration in bone has been shown to reduce the ultimate strain (Hernandez *et al.* 2005), and the amount of post-yield deformation (Wang *et al.* 2002, Tang *et al.* 2007, Nyman *et al.* 2007). We present a mechanistic model for the analysis of the MCF, and model predictions reflect these experimentally observed trends.

The enhanced continuum model enabled by the CZM considers both deformation and failure mechanisms in detail as the outcome of deformation of collagen, the debonding of collagen from mineral interaction, and mineral fracture. The model introduces collagen as composed of several collagen domains (helix molecules) and their interaction. Sliding between individual collagen domains emerges as a relevant mode of deformation (Silver *et al.* 2003, Jäger 2005, Bühler 2006). Furthermore, it has been suggested that cross-linking may disturb sliding between collagen fibrils and alter mechanical properties (Silver *et al.* 2001). How this response of collagen translates into the response of the MCF has previously not been investigated. For the model MCF we predict that up to 10% of the overall deformation is due to the collagen sliding. This process is effective in shielding the mineral from load. Such findings are in good qualitative agreement with X-ray measurements (Gupta *et al.* 2006). We demonstrate that the mechanical response of the model MCF may significantly change with cross-linking of collagen. Model fibrils containing enzymatic cross-links only deform predominately by sliding between collagen molecules, and exhibit failure along the mineral-collagen interface leading to a stable softening, and a large toughness. With non-enzymatic cross-links present the strain contribution from the interfaces is reduced. This is found to lead to an increased level of *on-average* load transfer to the mineral, also apparent in the increased modulus. Non-enzymatic

cross-linking also appears to alter the stress distribution in the mineral such that a *local* increase in stresses towards the mineral center-plane is predicted which favors fracture of the mineral phase. The release of the large amount of elastically stored energy in the mineral phase causes unstable failure. These changes in the behavior of the MCF due to the cross-linking of collagen will subsequently relate to the decreased toughness and more brittle type of fracture of bone on the macroscale. How to exactly translate the response of the MCF into predictions of macro level bone failure through the hierarchical models requires further studies.

Acknowledgments. This work was in part supported by the Collaborative Biomedical Research Initiative of Purdue University and Indiana University.

References

1. Abdul-Baqi, A., van der Giessen, E.: Indentation-induced interface delamination of a strong film on a ductile substrate. Thin Solid Films 381, 143–154 (2001)
2. Allen, M.R., Gineyts, E., Leeming, D.J., Burr, D.B., Delmas, P.D.: Bisphosphonates alter trabecular bone collagen cross-linking and isomerization in beagle dog vertebra. Osteoporosis Int. 19, 329–337 (2008)
3. Allen, M.R., Burr, D.B.: Mineralization, microdamage, and matrix: How bisphosphonates influence material properties of bone. BoneKEy 4, 49–60 (2007)
4. Arnoux, P.J., Bonnoit, J., Chabrand, P., Jean, M., Pithioux, M.: Numerical damage models using a structural approach: Application in bones and ligaments. Eur. Phys. J. – Appl. Phys. 17, 65–73 (2002)
5. Bailey, A.J., Wotton, S.F., Sims, T.J., Thompson, P.W.: Post-translational modifications in the collagen of human osteoporotic femoral head. Biochem. Biophys. Res. Comm. 185, 801–805 (1992)
6. Bailey, A.J., Paul, R.G., Knott, L.: Mechanisms of maturation and ageing of collagen. Mech. Ageing Dev. 106, 1–56 (1998)
7. Banse, X., Sims, T.J., Bailey, A.J.: Mechanical properties of adult vertebral cancellous bone: correlation with collagen intermolecular cross-links. J. Bone Min. Res. 17, 1621–1628 (2002)
8. Beyer, M.K.: The mechanical strength of a covalent bond calculated by density function theory. J. Chem. Phys. 112, 7307–7312 (2000)
9. Boxberger, J., Vashishth, D.: Nonenzymatic glycation affects bone fracture by modifying creep and inelastic properties of collagen. Trans. Orthop Res. Soc. 29, 0491 (2004)
10. Bühler, M.J.: Atomistic and continuum modeling of mechanical properties of collagen: Elasticity, fracture, and self-assembly. J. Mat. Res. 21, 1947–1961 (2006)
11. Burr, D.B.: The contribution of the organic matrix to bone's material properties. Bone 31, 8–11 (2002)
12. Catanese, J., Bank, R., Tekoppele, J., Keaveny, T.: Increased cross-linking by non-enzymatic glycation reduces the ductility of bone and bone collagen. Proc. Am. Soc. Mech. Eng. Bioeng. Conf. 42, 267–268 (1999)

13. Currey, J.D.: Effects of differences in mineralization on the mechanical properties of bone. Phil. Trans. Royal Soc. London Series B, Bio. Sci. 304, 509–518 (1984)
14. Eyre, D.R., Dickson, I.R., Van Ness, K.: Collagen cross-linking in human bone and articular cartilage. Age-related changes in the content of mature hydroxypyridinium residues. Biochem. J. 252, 495–500 (1988)
15. Eyre, D.R., Wu, J.J.: Collagen cross-links. Top Curr. Chem. 247, 207–229 (2005)
16. Fritsch, A., Hellmich, C.: 'Universal' microstructural patterns in cortical and trabecular, extracellular bone materials, Micromechanics-based prediction of anisotropic elasticity. J. Theor. Bio. 244, 597–620 (2007)
17. Garnier, L., Gauthier-Manuel, B., van der Vegte, E.W., Snijders, J., Hadziioannou, G.: Covalent bond force profile and cleavage in a single polymer chain. J. Chem. Phys. 113, 2497–2503 (2000)
18. Garnero, P., Borel, O., Gineyts, E., Duboeuf, F., Solberg, H., Bouxsein, M.L., Christiansen, C., Delmas, P.D.: Extracellular post-translational modifications of collagen are major determinants of biomechanical properties of fetal bovine cortical bone. Bone 38, 300–309 (2006)
19. Gourrier, A., Wagermaier, W., Burghammer, M., Lammie, D., Gupta, H.S., Fratzl, P., Riekel, C., Wess, T.J., Paris, O.: Scanning X-ray imaging with small-angle scattering contrast. J. Appl. Crystal 40, S78-S82 (2007)
20. Gupta, H.S., Seto, J., Wagermaier, W., Zaslansky, P., Boesecke, P., Fratzl, P.: Cooperative deformation of mineral and collagen in bone at the nanoscale. Proc. Nat. Acad. Sci. USA 104, 17741–17746 (2006)
21. Hellmich, C., Barthélémy, J.F., Dormieux, L.: Mineral–collagen interactions in elasticity of bone ultrastructure – a continuum micromechanics approach. Eur. J. Mech. A 23, 783–810 (2004)
22. Hernandez, C.J., Tang, S.Y., Baumbach, B.M., Hwu, P.B., Sakkee, A.N., van der Ham, F., DeGroot, J., Bank, R.A., Keaveny, T.M.: Trabecular microfracture and the influence of pyridinium and non-enzymatic glycation-mediated collagen cross-links. Bone 37, 825–832 (2005)
23. Hutchinson, J.W., Evans, A.G.: Mechanics of materials: Top-down approaches to fracture. Acta. Mat. 48, 125–135 (2000)
24. Jäger, I., Fratzl, P.: Mineralized collagen fibrils: a mechanical model with a staggered arrangement of mineral particle. Biophys. J. 79, 1737–1746 (2000)
25. Jäger, I.: A model for the stability and creep of organic materials. J. Biomech. 38, 1459–1467 (2005)
26. Ji, B., Gao, H.: Mechanical properties of nanostructure of biological materials. J. Mech. Phys. Solids 52, 1963–1990 (2004)
27. Katz, J., Ukraincik, K.: On the anisotropic elastic properties of hyroxyapatite. J. Biomech. 4, 221–227 (1971)
28. Keaveny, T.M., Morris, G.E., Wong, E.K., Yu, M., Sakkee, A.N., Verzijl, N., Bank, R.A.: Collagen status and brittleness of human cortical bone in the elderly. J. Bone Mineral Res. 18(supp. l2), S307 (2003)
29. Knott, L., Bailey, A.J.: Collagen cross-links in mineralizing tissues: a review of their chemistry, function, and clinical relevance. Bone 22, 181–187 (1998)
30. Kotha, S.P., Guzelsu, N.: Effect of bone mineral content on the tensile properties of cortical bone: experiments and theory. J. Biomech. Eng. 125, 785–793 (2003)

31. Landis, W.J.: The strength of a calcified tissue depends in part on the molecular structure and organization of its constituent mineral crystal in their organic matrix. Bone 16, 533–544 (1995)
32. Lees, S.: Considerations regarding the structure of the mammalian mineralized osteoid from the viewpoint of the generalized packing model. Connect Tissue Res. 16, 281–303 (1987)
33. Lees, S., Eyre, D.R., Barnard, S.M.: BAPN dose dependence of mature crosslinking in bone matrix collagen of rabbit compact bone: Corresponding variation of sonic velocity and equatorial diffraction spacing. Connect Tissue Res. 24, 95–105 (1990)
34. Monnier, V.M.: Toward a Maillard reaction theory of aging. Prog. Clin. Bio. Res. 304, 1–22 (1989)
35. Needleman, A.: A continuum model for void nucleation by inclusion debonding. J. Appl. Mech. 54, 525–531 (1987)
36. Nyman, J.S., Roy, A., Tyler, J.H., Acuna, R.L., Gayle, H.J., Wang, X.: Age-related factors affecting the postyield energy dissipation of human cortical bone. J. Orthop. Res. 25, 646–655 (2007)
37. Odetti, P., Rossi, S., Monacelli, F., Poggi, A., Cirnigliaro, M., Federici, M., Federici, A.: Advanced glycation end products and bone loss during aging. Annals New York Acad. Sci. 1043, 710–717 (2005)
38. Oxlund, H., Barckmann, M., Ortoft, G., Ancreassen, T.T.: Reduced concentrations of collagen cross-links are associated with reduced strength of bone. Bone 17, 365S-371S (1995)
39. Oxlund, H., Mosekilde, L., Ortoft, G.: Reduced concentration of collagen reducible cross links in human trabecular bone with respect to age and osteoporosis. Bone 19, 479–484 (1996)
40. Petruska, J.A., Hodge, A.J.: A subunit model for the tropocollagen macromolecule. Proc. Nat. Acad. Sci. USA 51, 871–876 (1964)
41. Saito, M., Marumo, K., Fujii, K., Ishioka, N.: Single-column high performance liquid chromatographic fluorescence detection of immature, mature and senescent crosslinks of collagen. Annals. Biochem. 253, 26–32 (1997)
42. Silver, F.H., Christiansen, D.L., Snowhill, P.B., Chen, Y.: Transition from viscous to elastic-based dependency of mechanical properties of self-assembled type I collagen fibers. J. Appl. Polym. Sci. 79, 134–142 (2001)
43. Silver, F.H., Freeman, J.W., Seehra, G.P.: Collagen self-assembly and the development of tendon mechanical properties. J. Biomech. 36, 1529–1553 (2003)
44. Steiner, T.: The hydrogen bond in the solid state. Angewandte Chemie – Int. Ed 41, 48–76 (2002)
45. Tan, H., Jiang, L.Y., Huang, Y., Liu, B., Hwang, K.C.: The effect of van der Waals-based interface cohesive law on carbon nanotube-reinforced composite materials. Comp. Sci. Techn. 67, 2941–2946 (2007)
46. Tang, S., Bank, R., Tekoppele, J., Keaveny, T.: Nonenzymatic glycation causes loss of toughening mechanisms in human cancellous bone. Trans. Orthop. Res. Soc. 30 (2005)
47. Tang, S., Zeenath, U., Vashishth, D.: Effects of non-enzymatic glycation on cancellous bone fragility. Bone 40, 1144–1151 (2007)
48. Tvergaard, V.: Effect of fiber debonding in a whisker-reinforced metal. Mat. Sci. Eng. A 125, 203–213 (1990)
49. Vasan, S., Foiles, P., Founds, H.: Therapeutic potential of breakers of advanced glycation end product-protein crosslinks. Arch. Biochem. Biophys. 419, 89–96 (2003)

50. Vashishth, D., Gibson, G.J., Khoury, J.I., Schaffler, M.B., Mimura, J., Fyhrie, D.P.: Influence of non-enzymatic glycation on biomechanical properties of cortical bone. Bone 28, 195–201 (2001)
51. Vashishth, D., Wu, P., Gibson, G.: Age-related loss in bone toughness is explained by non-enzymatic glycation of collagen. Trans. Orthop. Res. Soc. 29 (2004)
52. Vashishth, D.: The role of collagen matrix in skeletal fragility. Curr. Osteoporos Rep. 5, 62–66 (2007)
53. Viguet-Carrin, S., Garnero, P., Delmas, D.P.: The role of collagen in bone strength. Osteoporos Int. 17, 319–336 (2006)
54. Viguet-Carrin, S., Roux, J.P., Arlot, M.E., Merabet, Z., Leeming, D.J., Byrjalsen, I., Delmas, P.D., Bouxsein, M.L.: Contribution of the advanced glycation end product pentosidine and of maturation of type I collagen to compressive biomechanical properties of human lumbar vertebrae. Bone 39, 1073–1079 (2006)
55. Viswanath, B., Raghavan, R., Ramamurty, U., Ravishankar, N.: Mechanical properties and anisotropy in hydroxyapatite single crystals. Scripta. Mat. 57, 361–364 (2007)
56. Wang, X., Shen, X., Li, X., Agarwal, C.M.: Age-related changes in the collagen network and toughness of bone. Bone 31, 1–7 (2002)
57. Wang, X., Li, X., Shen, X., Agrawal, C.M.: Age-related changes of noncalcified collagen in human cortical bone. Ann. Biomed Eng. 31, 1365–1371 (2003)
58. Wang, X., Qian, C.: Prediction of microdamage formation using a mineral-collagen composite model. J. Biomech. 39, 595–602 (2006)
59. Wilson, E.E., Awonusi, A., Morris, M.D., Kohn, D.H., Tecklenburg, M., Beck, L.W.: Highly ordered interstitial water observed in bone by nuclear magnetic resonance. J. Bone Min. Res. 20, 625–634 (2005)
60. Wu, P., Koharski, C., Nonnenmann, H., Vashishth, D.: Loading on non-enzymatically glycated and damaged bone results in an instantaneous fracture. Trans. Orthop Res. Soc. 28, 404 (2003)
61. Xu, X.P., Needleman, A.: Numerical simulation of fast crack growth in brittle solids. J. Mech. Phys. Solids 42, 1397–1415 (1994)
62. Zioupos, P., Currey, J.D., Hamer, A.J.: The role of collagen in the declining mechanical properties of aging human cortical bone. J. Biomed Mat. Res. 45, 108–116 (1999)

The Aerodynamics of Wind Turbines

J.N. Sørensen, R. Mikkelsen, N. Troldborg, V.L. Okulov, and W.Z. Shen

Department of Mechanical Engineering, Technical University of Denmark (DTU)
jns@mek.dtu.dk

In the paper we present state-of-the-art of research in wind turbine aerodynamics. We start be giving a brief historical review and a survey over aerodynamic research in wind energy. Next, we focus on some recent research results obtained by our wind energy group at Department of Mechanical Engineering at DTU. In particular, we show some new results on the classical problem of the ideal rotor and present a series of new results from an on-going research project dealing with the modelling and simulation of turbulent flow structures in the wake behind wind turbines.

1 Brief Historical Review

Windmills have existed for more than 3000 years and have greatly facilitated agricultural development. Even today, where other types of machinery have taken over the windmills jobs, the new machines are often called 'mills'. Except for propulsion of sailing ships, the windmill is the oldest device for exploiting the energy of the wind. Since the appearance of the ancient Persian vertical-axis windmills 3000 years ago, many different types of windmills have been invented. In the western part of Europe, the Dutch horizontal-axis windmill was for centuries the most popular type and formed the basis for the development of the modern wind turbine in the 20th century (note that a windmill is a machine intended for grinding grain and similar jobs, whereas the term wind turbine refers to an electricity producing machine). Today, the most popular turbine type is the 3-bladed horizontal-axis wind turbine, following the so-called 'Danish concept'.

The first electricity producing wind turbine was constructed by Charles F. Brush in the United States in 1887. Brush's machine was big and not very efficient. It had a 17 m diameter rotor, consisting of 144 blades, and a 12 kW generator. In the period 1891-1908, unaware of the work of Brush, basic wind turbine research was undertaken by Poul La Cour in Denmark. La Cour carried out systematic aerofoil studies using his own developed wind tunnel and the experimental wind turbines at Askov folk high school. Among

Fig. 1 Prof. Poul La Cour in front of his experimental wind turbines, 1899. Courtesy: The Poul La Cour Museum.

several important discoveries, he found that rather than being pushed by the wind, as was at that time generally believed to be the main aerodynamic principle, the driving force on the rotor blades is formed by suction. Further, La Cour demonstrated that fast rotating wind turbines with few rotor blades are most efficient for producing electricity. Based on his ideas the design of aerodynamically-efficient rotor blades soon advanced, and in 1918 about 3 % of the Danish electricity consumption was covered by wind turbines. However, in the following period fuel-based power became cheap and forced wind power out of the marked. Because of supply crises, renewed interest was paid to wind energy during World War II and during the Suez crisis. This lead to the construction of the Gedser turbine in 1957, that became the prototype for the new generation of wind turbines that was put into production after the oil crisis in 1973.

In many countries national programmes for investigating the potential of producing electricity from the wind were launched and big demonstration projects were carried out, e.g. in USA, Germany, Great Britain, Sweden, the Netherlands and Denmark. This together with the effort of a large number of small industries formed the basis for what is today an industry with a global annual turnover of more than 50 billion USD and an annual average growth rate of more than 20 %. Today, state-of-the-art wind turbines have rotor diameters of up to 120 m and 5 MW installed power, and these are

Fig. 2 Left figure: The 200 kW Gedser wind turbine erected in 1957; Right figure: Modern 2.5 MW wind turbine

often placed in large wind farms with a production size corresponding to a nuclear power plant. Although research in wind energy has taken place for more than a century now, there is no doubt that wind energy competitiveness can be further improved through further cost reductions, new innovative aerodynamic design and collaboration with complementary technologies.

In the following we will give an introduction to some of the most important aerodynamic research topics within the field of wind energy, and focus on some recent research projects carried out at the Technical University of Denmark. For more detailed reviews on wind turbine aerodynamics the reader is referred to the survey articles [1], [2], [3], [4], [5] and [6].

2 Aerodynamic Research in Wind Energy

The aerodynamics of wind turbines concerns, briefly speaking, modelling and prediction of the aerodynamic forces on the solid structures of a wind turbine and in particular on the turbine rotor blades. Aerodynamics is the most central discipline for predicting performance and loadings on wind turbines. The aerodynamic model is normally integrated with models for wind conditions and structural dynamics. The integrated aero-elastic model for predicting performance and structural deflections is a prerequisite for design, development and optimization of wind turbines. Aerodynamic modelling may also concern design of specific parts of wind turbines, such as rotor blade

geometry, or performance predictions of wind farms. Aerodynamics is the oldest science in wind energy. In 1915, using simple axial momentum and energy considerations, Lanchester [7] predicted that even an ideal wind turbine cannot exploit more than 59 % of the wind power passing through the rotor disk. A major break-trough was achieved by Betz [8] and Glauert [9] in 1920-30, who formulated the Blade Element Momentum (BEM) theory. This theory, which later was extended with many 'engineering rules, is today the basis for all rotor design codes in use by industry.

From an outsider's point of view, aerodynamics of wind turbines may seem simple as compared to aerodynamics of e.g. fixed-wing aircraft or helicopters. However, there are several added complexities. Most prominently, aerodynamic stall is always avoided for aircraft, whereas it is an intrinsic part of the wind turbines operational envelope. Stall occurs when the flow meets the wing at a too high angle of attack. The flow then cannot follow the wing surface and separates from the surface, leading to flow patterns far more complex than that of non-separated flow. This renders an adequate description very complicated and even for Navier-Stokes simulations it becomes necessary to model the turbulent small-scale structures in the flow, using Reynolds-averaging or large eddy simulations. Indeed, in spite of the wind turbine being one of the oldest devices for exploiting the energy of the wind, some of the most basic aerodynamic mechanisms are not yet fully understood. In order to avoid crashes during landing and takeoff, aircraft are always kept wide apart. This is also in deep contrast to the situation for wind turbines, which are often placed very close together in so-called wind farms. Hence, operation in the highly distorted wakes of other wind turbines is another added complexity, much akin to operation in the stochastic incoming wind. Wind turbines are subjected to atmospheric turbulence, wind shear from the ground effect, wind directions that change both in time and in space, and effects from the wake of neighbouring wind turbines. These effects together form the ordinary operating conditions experienced by the blades. As a consequence, the forces vary in time and space and a dynamical description is an intrinsic part of the aerodynamic analysis.

At high wind velocities, where a large part of the blade operates in deep stall, the power output is extremely difficult to determine within an acceptable accuracy. When boundary layer separation occurs, the centrifugal force tends to push the airflow at the blade towards the tip, resulting in the aerodynamic lift being higher than what it would be on a non-rotating blade. When the wind direction changes, misalignment with the rotational axis occurs, resulting in yaw error. Yaw error causes periodic variation in the angle of attack and invalidates the assumption of axisymmetric inflow conditions. Furthermore, it gives rise to radial flow components in the boundary layer. Thus, both the airfoil characteristics and the wake are subject to complicated 3-dimensional and unsteady flow behaviour.

When regarding wakes after wind turbines, a distinct division can be made between the near and far wake regions. The near wake is taken as the region

just behind the rotor. In this region, covering a few rotor diameters downstream, the presence of the rotor is apparent by the number of blades, blade aerodynamics, including stalled flow, 3-dimensional effects and the tip vortices. The far wake is the region downstream of the near wake, where the focus is put on the interference between wind turbines in park situations. The near wake research is centered on turbine performance and the physical process of power extraction, while the far wake research concerns the mutual influence when wind turbines are clustered in wind parks. In recent years, most aerodynamic research has focused on establishing detailed experimental data and on solving the incompressible Navier-Stokes equations for single rotors as well as for wind turbines located in complex terrain and for clusters of wind turbines Although such computations are so heavy that they cannot yet be integrated directly in the design process, they may aid the designer of wind turbines in understanding the basic physics and in establishing 'engineering rules' in combination with e.g. the BEM theory.

In the past two decades we have carried out research in most of the various topics related to wind turbine aerodynamics, and in the following sections we will show some of our recent results on the so-called ideal rotor and on CFD simulations of wind turbine wakes.

3 The Ideal Rotor

The determination of the ideal or theoretical maximum efficiency of a wind turbine rotor is today still a subject that has not been completely clarified. The most important upper limit was nearly a century ago derived by Betz [8] who, using axial momentum theory, showed that no more than 59 % of the kinetic energy contained in a stream tube having same cross area as the rotor can be converted into useful work. Using general momentum theory Glauert [9] developed a model for the optimum rotor that included rotational velocities. In this approach the rotor is treated as a rotating actuator disk, corresponding to a rotor with an infinite number of blades. The maximum efficiency was shown to be a function of tip speed ratio, with values ranging from zero efficiency at zero tip speed ratio to the aforementioned 59 % at high tip speed ratios. For a more realistic rotor with a finite number of blades, Betz [10] also showed that the ideal efficiency is obtained when the distribution of circulation along the blade produces a rigidly moving helicoid wake that moves backward (in the case of a propeller) or forward (in the case of a wind turbine) in the direction of its axis with a constant velocity (see Fig. 3).

Based on the criterion of Betz, a theory for lightly loaded propellers was developed by Goldstein [11] using infinite series of Bessel functions. The theory was later generalized by Theodorsen [12] to cover cases of heavily loaded propellers. Paradoxically, in his analysis Theodorsen correctly used the unsteady Bernoulli equation but neglected the time-dependent term in the momentum equation. Our interest in the subject was stimulated by the recent paper by

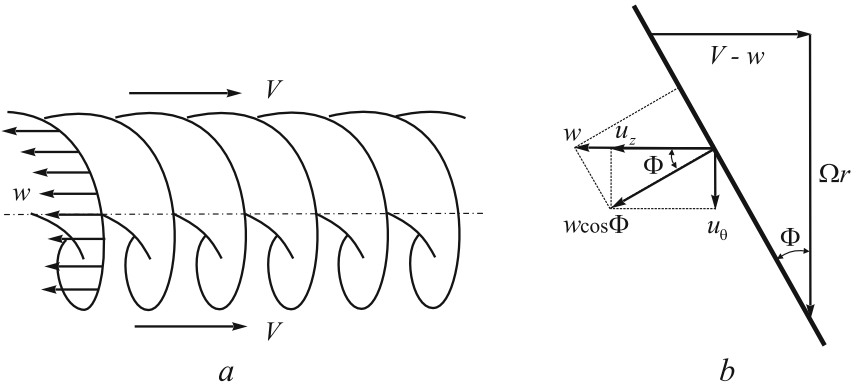

Fig. 3 (a) Sketch of helical surface representing the ideal far wake; (b) Definition of axial displacement velocity of the helical vortex sheet and velocity triangles determining pitch angle and geometry of the helical surface

Wald [13], who developed a complete set of Theodorsen's equations for determining the properties of an optimum heavily loaded propeller. However, when we tried to use the equations to analyze the optimum behaviour of a wind turbine the theory always predicted a much lower efficiency than expected and what is known from experiments. Further, when extending the theory to the case of a rotor with infinitely many blades, the results did not comply with Betz limit and the general momentum theory. Based on the analytical solution to the induction of helical vortex filament developed recently by Okulov [14] we analysed in detail the original formulation of Goldstein [11] and found that the model by a simple modification could be extended to handle heavily loaded rotors in a way that is in full accordance with the general momentum theory (Okulov and Sørensen [15], [16]).

Fig. 4a) presents the optimum power coefficient as a function of tip speed ratio for different number of blades, and in Fig. 4b) the corresponding thrust coefficient is depicted. From the figures it is evident that the optimum power coefficient has a strong dependency on the number of blades. Taking as an example a one-bladed rotor operating at a tip speed ratio of 5, only 38 % of the available power can be captured. For a three-bladed rotor operating at the same tip speed ratio about 50 % power can be captured, whereas an 'infinite-bladed' rotor with a value of 58 % is very close to the 'original' Betz limit. Another way of putting it is that a 3-bladed rotor obtains 50 % of the available power at a tip speed ratio of 5, whereas a 1-bladed rotor first obtains a 50 %-value at a tip speed ratio of 12. This means that a 1-bladed rotor in this case has to rotate more than double as fast as a 3-bladed rotor in order to produce the same power. The curves in Fig. 4a) are compared to C_p-values obtained from the general momentum theory. The comparison shows that the results

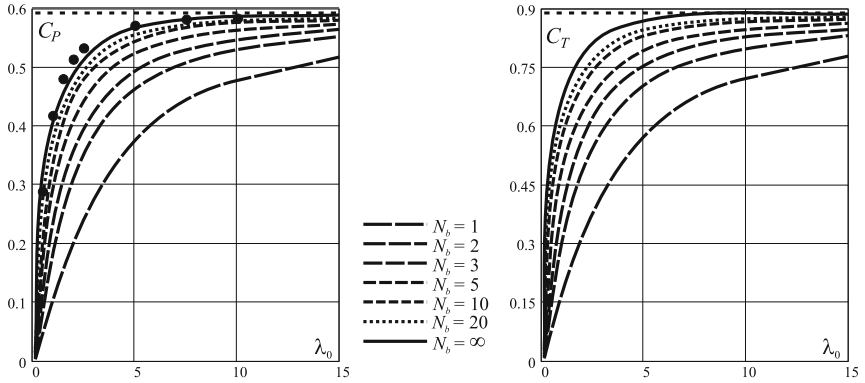

Fig. 4 (a) Power coefficient C_p and (b) thrust coefficient Ct, as function of tip speed ratio for different number of blades of an optimum rotor. Horizontal dashed lines: Original Betz limit; Points: General momentum theory; Dashed and solid lines: Present theory.

from the present theory for a rotor with infinite many blades are in excellent agreement with the values computed from general momentum theory.

4 Simulation and Modelling of Wakes

Modern wind turbines are often clustered in wind parks in order to reduce the overall installation and maintenance expenses. Because of the mutual interference between the wakes of the turbines the total power production of a park of wind turbines is reduced as compared to an equal number of stand-alone turbines. Thus, the total economic benefit of a wind park is a trade-off between the various expenses to erect and operate the park, the available wind resources at the site, and the reduced power production because of the mutual influence of the turbines. A further unwanted effect is that the turbulence intensity in the wake is increased because of the interaction from the wakes of the surrounding wind turbines. As a consequence, dynamic loadings are increased that may excite the structural parts of the individual wind turbine and enhance fatigue loadings. The turbulence created from wind turbine wakes is mainly due to the dynamics of the vortices originating from the rotor blades. The vortices are formed as a result of the rotor loading. To analyze the genesis of the wake, it is thus necessary to include descriptions of the aerodynamics of both the rotor and the wake. Although many wake studies have been performed over the last two decades, a lot of basic questions still need to be clarified in order to elucidate the dynamic behaviour of individual as well as multiple interactive wakes behind wind turbines. In a recent survey by Vermeer, Sørensen and Crespo [5] both near wake and far wake

aerodynamics are treated, whereas a survey focusing solely on far wake modelling was earlier given by Crespo, Hernandez and Frandsen [3].

In the past we have had an intensive effort on wind turbine wakes, with the main attention put on near wake modelling, wake interference and generation of turbulence in wakes. Although most wake research have been restricted to uniform, steady and parallel inflow conditions, thereby excluding wind shear, tower interference and dynamic inflow, our recent research activities deal with skewed and turbulent inflow conditions To simulate the flow field around the wind turbine rotor we employ the so-called actuator line technique developed by Sørensen and Shen [17]. In this model the three-dimensional Navier-Stokes equations are solved with body forces distributed along rotating lines representing the blades of the wind turbine. The flow field is thus determined by solving the three-dimensional Navier-Stokes equations using large eddy simulation, whereas the loading on each blade is computed by calculating the local angle of attack to determine the local forces from tabulated airfoil data. The method was originally formulated in vorticity-velocity variables, but was later reformulated in primitive variables (pressure-velocity) by Mikkelsen [18] and combined with the in-house *EllipSys* code (Michelsen [19] and Sørensen [20]). The technique enables to study wake dynamics without having to resolve in detail the viscous boundary layer of the rotor blades.

In the following we present some selected results on wake structures obtained using the actuator line model (see [21]-[24]). The computational results are analyzed for their content of organized anisotropic and coherent structures. Further, the computations form the background for the development of a low-dimensional wake turbulence model based on proper orthogonal decomposition.

4.1 Wake Behind a Single Turbine

In the following some of the results obtained from simulations of a standalone wind turbine are presented. The computations were carried out using airfoil data from the Tjaereborg wind turbine. The blade radius of this turbine is 30.56 m and it rotates at 22.1 RPM, corresponding to a tip speed of 70.7 m/s. The blade sections consist of NACA 44xx airfoils with a chord length of 0.9 m at the tip, increasing linearly to 3.3 m at hub radius 6 m. The blades are linearly twisted 1 degree per 3 m. Computations were carried out for the rotor operating at a tip-speed ratio of respectively 11.78, 7.07, 5.05 and 3.21 in order to study the effect on the wake when changing the thrust on the rotor. Fig. 5 show the contours of the instantaneous absolute vorticity in a meridional plane for each of the four cases and in Figure. 6 corresponding visualizations of the spatial structure of the vortex system are shown. In Fig. 5 regions of high vorticity appear as light colours. Note that the rotor is located to the left in the plots and that only the downstream development of the wake is shown. The bound vorticity of the blades is seen to be shed downstream from the rotor in individual vortex tubes. A closer inspection of the

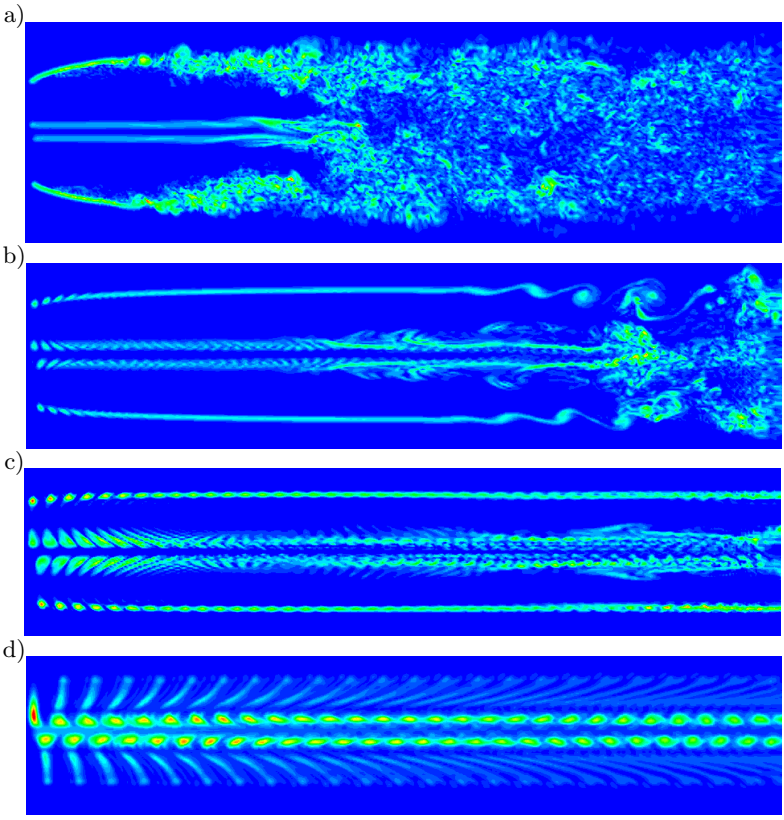

Fig. 5 Downstream development of the wake visualized using vorticity contours. The rotor is located to the left; a) $\lambda = 11.78$ ($V_\infty = 6\ m/s$); b) $\lambda = 7.07$ ($V_\infty = 10\ m/s$); c) $\lambda = 5.05$ ($V_\infty = 14\ m/s$); d) $\lambda = 3.21$ ($V_\infty = 22\ m/s$).

vorticity contours at Vo = 6 m/s shows that the distinct tip-vortex pattern is preserved about 0.5 rotor radii downstream, where after they smear into a continuous vorticity sheet. In the case where the free stream velocity is Vo = 10 m/s distinct tip vortices can be observed about 1.5 rotor radii downstream, whereas the tip vortices persist in the full flow domain at the higher wind speeds, i.e. at small tip speed ratios. For the rotor operating at the highest tip-speed ratio instability of the tip vortices is observed only 2 rotor radii downstream and 5 rotor radii downstream the entire wake completely breaks up. In the case where Vo = 10 m/s the tip vortices is observed to undergo a Kelvin-Helmholz instability approximately 7 rotor radii downstream. The root vortex also becomes unstable at this position. Further downstream the root and tip vortices interact, which causes the wake to become fully turbulent. Instability of the tip vortices is also observed for $V_o = 14$m/s, but as expected it takes place even further downstream (approximately 10 rotor

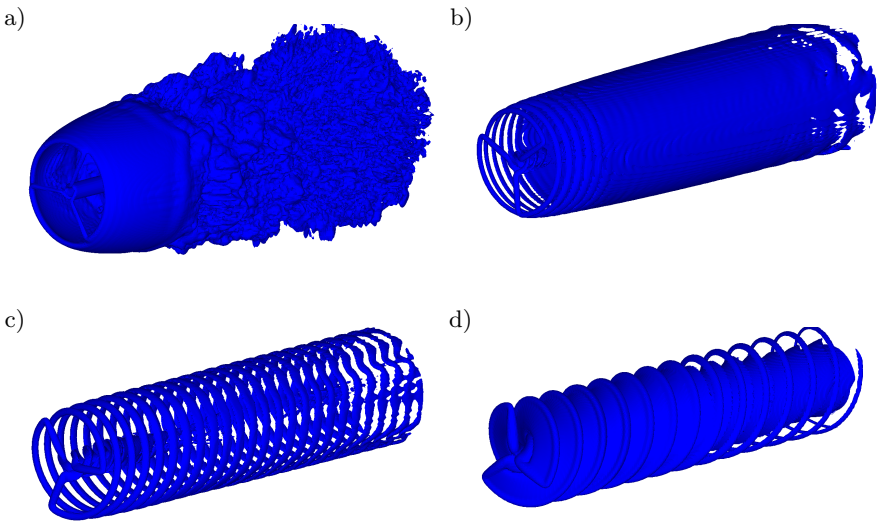

Fig. 6 Visualization of the downstream development of the wake using iso-surface plots of vorticity; a) $\lambda = 11.78$; b) $\lambda = 7.07$; c) $\lambda = 5.05$; d) $\lambda = 3.21$

radii downstream) and is not as strong due to the generally higher stability and persistence of the tip vortices, when the tip-speed ratio and thus also the trust is low. For $V_o = 22$m/s the wake seems to form a stable structure in the computational domain. Fig. 7 shows computed mean axial velocities as a function of downstream position for the four inflow velocities. Close to the rotor, the velocity distribution correlates directly with the load distribution of the rotor. In normal operation the highest loading is located at around 2/3 radius, while the loading close to the hub is low. Further downstream the velocity profile develops due to turbulent mixing and the influence of the pressure field behind the rotor. The figure clearly reveals that the wake development significantly depends on the loading of the rotor.

4.2 Three Turbines in a Row

The influence of mutual wake effects was studied for the case of three rotors located along a common axis with a distance of 6 rotor radii between the rotors. The rather close spacing was chosen as a compromise of on one hand being able to preserve the generated flow structures and on the other hand keeping the computer costs at a reasonably level. In Fig. 8 we show iso-vorticity contours in a cross-section along the axis of the rotors. In the upper figure the inflow is laminar whereas it is superposed by a turbulent flow field of intensity of about 0.1 in the lower figure. In the laminar case the wake behind the first turbine is seen to be dominated by organized tip and root vortices, whereas the flow is seen to undergo massive separation over the second rotor,

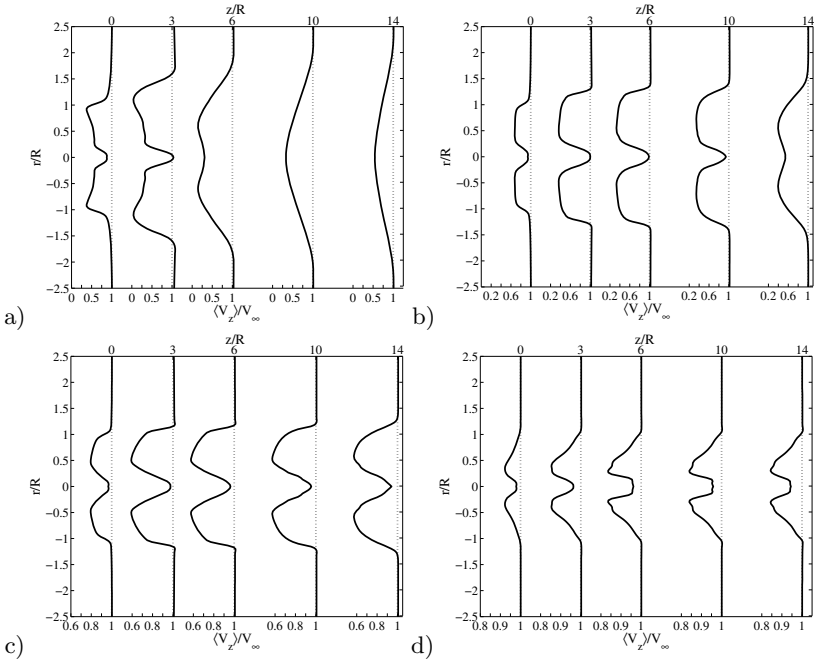

Fig. 7 Computed profiles of the time and circumferentially averaged axial velocity at different downstream positions; a) $\lambda = 11.78$; b) $\lambda = 7.07$; c) $\lambda = 5.05$; d) $\lambda = 3.21$

causing the third rotor to operate in a completely separated flow. It should be mentioned, however, that the highly separated flow partly is a result of the rotors being forced to operate at the same tip speed ratio, whereby the thrust coefficient gets very high for the downstream rotors. Comparing the two figures it is clearly seen that the ambient turbulence causes a dramatic effect on the stability of the wake structures. To quantify the structure of the flow field we compute the azimuthally averaged axial velocities in the wake behind the three rotors. The outcome is shown Fig. 9 that depicts the averaged axial velocity profiles as function of radius for laminar inflow (full line) and for turbulent inflow (dashed line). The difference in development of the velocity profiles is clearly seen in the wake after the first rotor, whereas the profiles are nearly identical after the second rotor, indicating that the rotors act like turbulent mixers. In both cases, between the second and the third rotor, the wake is seen to undergo a transition from organized vortex structures to be dominated by small-scale turbulence. Further downstream the velocity profile is seen to attain a Gaussian shape. At the moment we are quantifying the effect of the ambient turbulence on the performance of downstream located turbines.

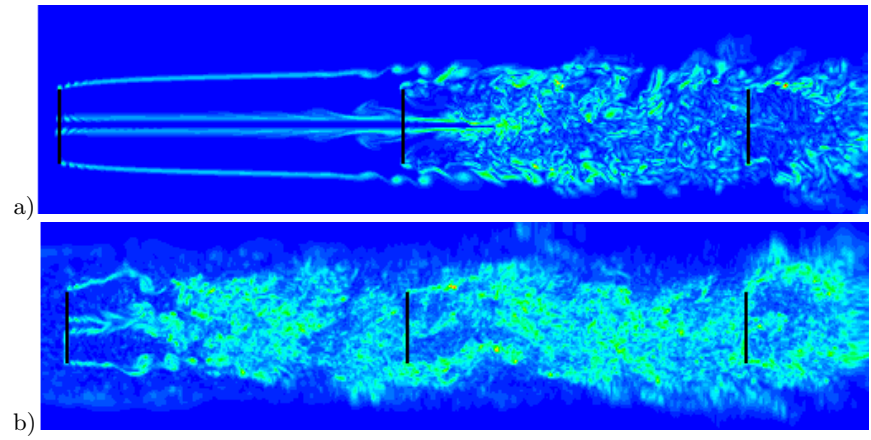

Fig. 8 Visualization of flow field between the rotors using vorticity contours. Regions of high vorticity appear as light colors. The rotors are indicated as black lines; a) Laminar inflow b) Turbulent inflow.

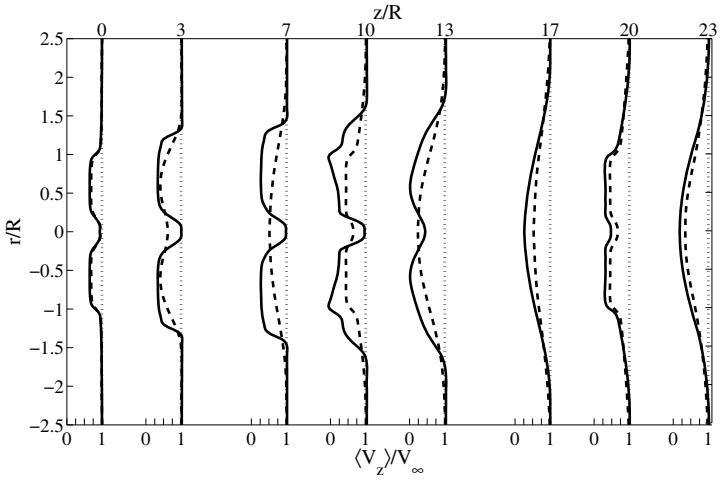

Fig. 9 Computed profiles of the averaged axial velocity at different downstream positions

4.3 Infinitely Many Turbines in a Row

To study the generation of turbulence in the interior of a wind farm we consider a row of turbines subject to periodic in- and outflow conditions. The introduction of periodic boundary conditions in the flow direction is a technique that has been largely used to study the generation of turbulence in boundary layers in channels. In the present case the turbulence is generated

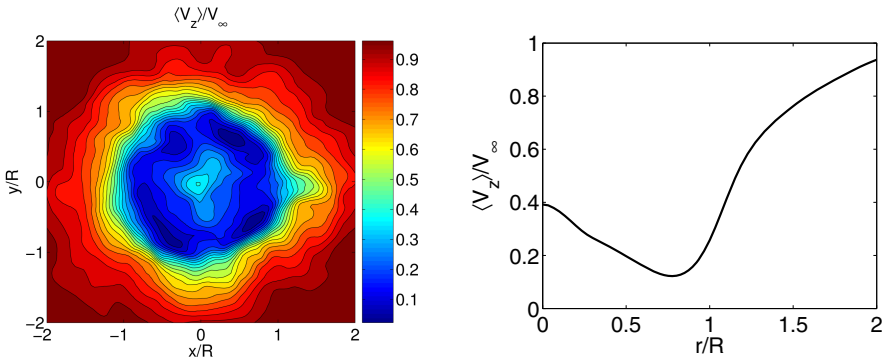

Fig. 10 Mean axial velocity $1R$ upstream from the rotor

by the 'mixing effect' of the rotor itself. In the following we will present some results from the simulations and demonstrate how they can be employed to derive low-dimensional turbulence models for later use in e.g. Blade-Element Momentum (BEM) codes. After the transients die out the flow becomes dominated by the development of turbulence. Due to the mixing of the rotor, turbulent kinetic energy is continuously added to the flow and statistics can be performed when the production of turbulence is in balance with the dissipation. When this happens the flow is statistically stationary and usual statistical tools can be applied. In the following we determine velocity profiles and compute Reynolds stresses and turbulence intensities in a cross-section located one radius upstream from the rotor. Fig. 10 depicts the mean axial velocity contours and the azimuthally averaged axial velocity one radius upstream from the rotor.

Reynolds Stresses

In Fig. 11 we show iso-surfaces of the Reynolds stresses. It is here seen that the normal stress in the main flow direction is the dominant component, attaining approximately double as big values as those in the plane perpendicular to the main flow direction. The shear stresses are even smaller, taking values in the order of 1 % for in-plane components and 4 % for the values correlating in- and out-plane shear stresses. It is also important to note that the shear stresses are very small inside the wake whereas big values are to be found in an annular domain surrounding the tips. This indicates that when the rotors are located on a common axis the main mechanism for generating turbulence is provided by the development of the tip vortices.

In Fig. 12 we show the radial distribution the circumferentially averaged Reynolds stresses obtained one radius upstream from the rotor. It is here clearly seen that the normal component is the most important and that most turbulence production takes place near the tips of the rotor.

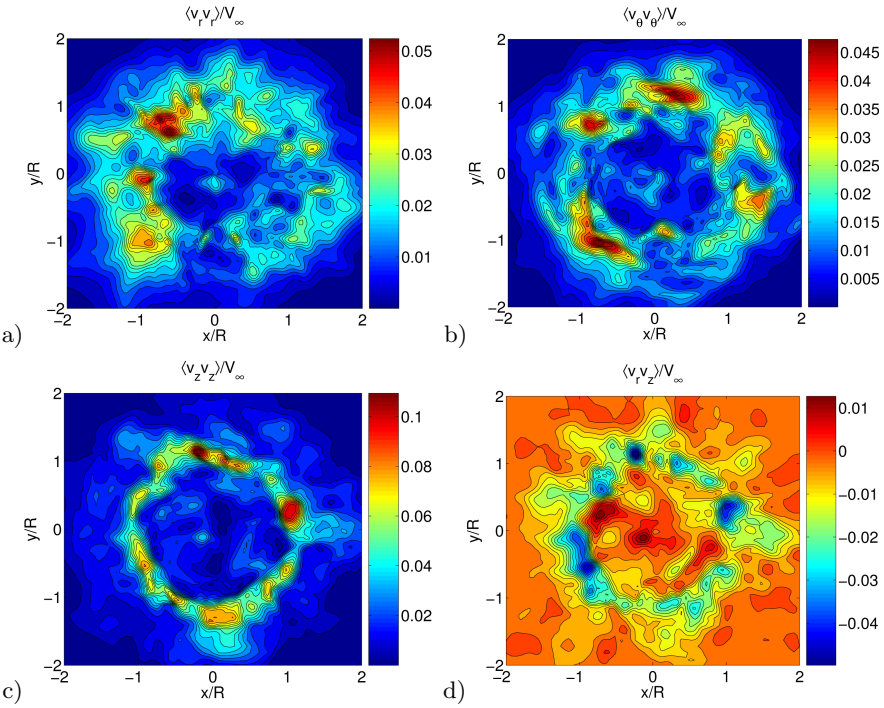

Fig. 11 Contours of the Reynolds stresses $1R$ upstream from the rotor

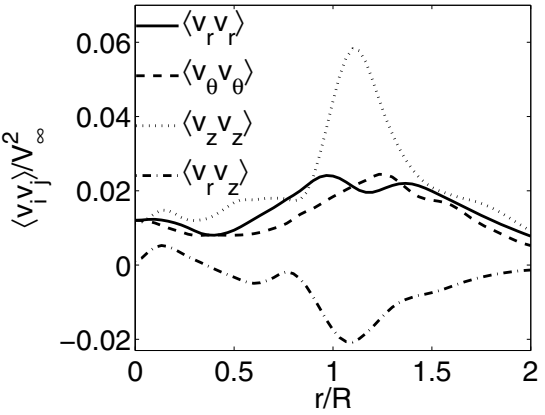

Fig. 12 Radial distribution of the circumferentially averaged Reynolds stresses $1R$ upstream from the rotor

Low-Dimensional Modelling

Most models for atmospheric turbulence are based on Fourier decomposition along with some simplifying hypotheses, such as isotropic or homogeneous

flow conditions combined with e.g. rapid distortion theory. Two popular turbulence models for determining stochastic inflow conditions for wind turbines based on the above assumptions are the model of Veers [25] and the Mann model [26]. When the turbulent flow is characterized by organized motions, however, the task of identifying and model the flow patterns cannot efficiently be accomplished by Fourier decomposition. As an alternative to Fourier decomposition, Proper Orthogonal Decomposition (POD) has in the past years gained increasing popularity as a technique for identifying the dominant coherent structures and for constructing low-dimensional models to describe the principal flow dynamics with a limited number of modes. POD is a transformation that produces a set of basis vectors which span the input data in such a way that the fraction of energy represented by any number of modes is the largest possible. Thus, the modes constitute a set of orthogonal basis functions of descending energy content. POD has mostly been used to analyze experimental data, but with the rapid development of computer technology, it is now also largely used to analyze numerical data. In the present work POD has been employed to analyze and model the dynamics of the dominant coherent structures in the wake ([22]). Several versions of the POD technique have been developed and in the present work the so-called

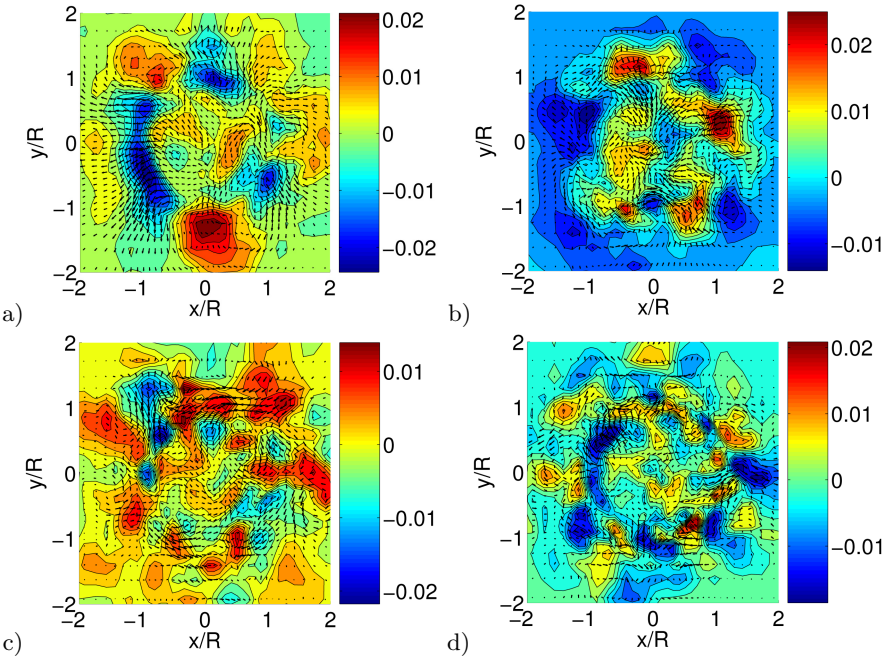

Fig. 13 From left to right: Velocity field associated with POD mode 1, 2, 3 and 8. The modes contain approximately 22%, 15%,10% and 4% of the total energy, respectively.

snapshot POD was applied. To illustrate the appearance of the POD modes we depict some representative samples in the following. In Fig. 13 we show the velocity fields of POD mode no. 1, 2, 3, and 8, respectively. These modes represent 22 %, 15 %, 10 %, and 4 % of the total turbulent energy, respectively. Using e.g. the first 10 modes, results in 90 % of the turbulent energy being captured, whereas 98 % is captured when increasing the number of modes to 20. This illustrates that only a relatively small number of POD modes are needed to reconstruct the computed turbulent flow field. A future application of this technique is to combine it with engineering BEM codes for obtaining turbulent inflow conditions to aeroelastic computations.

5 Conclusion and Future Perspectives

The aerodynamic research of wind turbines has contributed significantly to the success of modern wind energy. For most unsolved problems, engineering rules have been developed and verified. All of these rules, however, have a limited applicability, and, seen in the light of the rapid development of wind energy, the need to replace them by physical understanding and modelling based on computer simulations of the Navier-Stokes equations are increasing. Future research efforts are directed towards strong aero-elastic coupling between the flow field and the wind turbine. This demands the use of moving meshes and algorithms that combine structural-dynamics and aerodynamic loading. Applications range from analysis of specific parts of rotor blades, such as tip shapes, control mechanisms, vortex generators, etc, to detailed analyses of flow structures and stresses. Another important issue concerns the description of wake structures subject to atmospheric turbulence and optimization of wind turbines clustered in parks. Some of the 'classical' problems still remain, such as laminar-turbulent transition and boundary layer turbulence. These problems, however, are common for the fluid mechanics society in general.

References

1. Hansen, A.C., Butterfield, C.P.: Annual Review of Fluid Mechanics 25, 115–149 (1993)
2. Snel, H.: Wind Energy 1, 46–69 (1998)
3. Crespo, A., Hernandez, J., Frandsen, S.: Wind Energy 2, 1–24 (1998)
4. Leishman, J.G.: Wind Energy 5, 86–132 (2002)
5. Vermeer, L.J., Sørensen, J.N., Crespo, A.: Progress in Aerospace Sciences 39, 467–510 (2003)
6. Hansen, M.O.L., Sørensen, J.N., Voutsinas, S., Sørensen, N.N., Madsen, H.A.: Progress in Aerospace Sciences 42, 285–330 (2006)
7. Lanchester, F.W.: Transactions of the Institution of Naval Architects 57, 98 (1915)

8. Betz, A.: Zeitschrift fur das Gesamte Turbinenwesen 26, 307–309 (1920)
9. Glauert, H.: Airplane Propellers. In: Durand, W.F. (ed.) Aerodynamic Theory IV:L (1943)
10. Betz, A.: Schraubenpropeller mit Geringstem Energieverlust. Dissertation, Gottingen Nachrichten, Gottingen (1919)
11. Goldstein, S.: Proc R Soc London A 123, 440–465 (1929)
12. Theodorsen, T.: Theory of propellers. McGraw-Hill Book Company, New York (1948)
13. Wald, Q.R.: Progress in Aerospace Sciences 42, 85–128 (2006)
14. Okulov, V.L.: J. Fluid Mech. 521, 319–342 (2004)
15. Okulov, V.L., Sørensen, J.N.: J. of Fluid Mech. 576, 1–25 (2007)
16. Okulov, V.L., Sørensen, J.N.: Wind Energy 11, 415–426 (2008)
17. Sørensen, J.N., Shen, W.Z.: J. Fluids Engineering 124(2), 393–399 (2002)
18. Mikkelsen, R.: Actuator Disc Methods Applied to Wind Turbines. Dissertation, Technical University of Denmark, MEK-FM PHD 2003-02 (2003)
19. Michelsen, J.A.: Block structured multigrid solution of 2D and 3D elliptic PDE's. Report 94-06, Dept. of Fluid Mechanics, DTU (1994)
20. Sørensen, N.N.: General purpose flow solver applied to flow over hills. PhD dissertation, Ris-R-827(EN), Ris National Laboratory, Denmark (1995)
21. Troldborg, N., Sørensen, J.N., Mikkelsen, R.: Submitted to Wind Energy (2008)
22. Sørensen, J.N., Mikkelsen, R., Troldborg, N.: Submitted to Wind Energy (2008)
23. Troldborg, N., Sørensen, J.N., Mikkelsen, R.: Journal of Physics: Conference Series 75 (2007)
24. Mikkelsen, R., Sørensen, J.N., Troldborg, N.: Prescribed Wind Shear Modelling Combined with the Actuator Line Technique. In: Proc. 2007 EWEC Conference, Milan (2007)
25. Veers, P.S.: Three-dimensional wind simulation. SAND88-0152, Albuqueerque, NM, Sandia National Laboratories (1988)
26. Mann, J.: J. Fluid Mech. 273, 141–168 (1994)

Cohesive-Zone Modeling of Adhesive Joints

M.D. Thouless

Department of Mechanical Engineering, Department of Materials Science and Engineering, University of Michigan, Ann Arbor, MI 48109, USA
thouless@umich.edu

1 Introduction

Two distinct failure criteria have traditionally been used to model adhesive joints: a strength-based criterion using the cohesive strength of the adhesive, and an energy-based criterion using the toughness of the adhesive. In practice there are conditions under which the properties of a joint may be controlled by either one of these criteria, or by both. Cohesive-zone models have an advantage in that they incorporate both criteria simultaneously, automatically allowing whichever one is dominant to control fracture in a numerical analysis. Cohesive-zone models are particularly useful for problems involving adhesive joints in which the crack path is generally known; there is a natural convenience in being able to assign the entire deformation of the adhesive layer to the cohesive process, and to distinguish this deformation from that of the adherends. It is recognized that such an approach means that the cohesive law may be affected by details of the geometry, such as adhesive thickness [1], but similar limitations are accepted when using linear-elastic fracture mechanics to describe fracture.

Mixed-mode cohesive models can be developed by separately defining the mode-I and mode-II traction-separation laws, so each has a distinct toughness

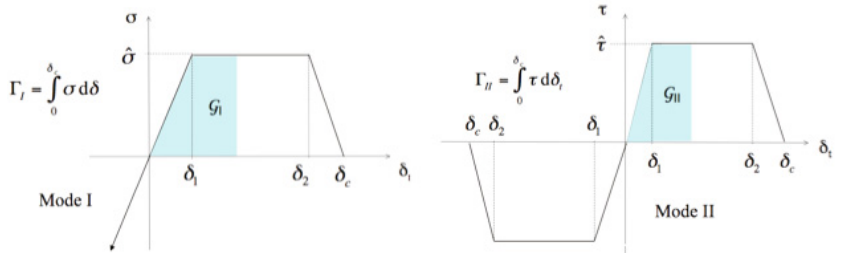

Fig. 1 Schematic mode-I and mode-II traction-separation laws, as described in [2]

(total area under the curve) and distinct strength, and coupling them through a mixed-mode failure criterion. Such an approach has been shown to work under linear-elastic conditions [2] and under conditions where the adherends deform in a plastic fashion [3]. A simple connection between the phase angle of linear-elasticity, and a more general definition that can be used in mixed-mode cohesive-zone models is given by [2, 3]

$$\psi = \tan^{-1}\left(\sqrt{\mathcal{G}_{II}/\mathcal{G}_I}\right), \tag{1}$$

where $\mathcal{G}_I$ and $\mathcal{G}_{II}$, the mode-I and mode-II energy-release rates, are the areas traced out under the mode-I and mode-II curves at any instant (Fig. 1). This definition has the feature that it can be used to define a phase angle at any point along an interface.

Mixed-mode linear-elastic fracture mechanics (LEFM) failure criteria are cast in terms of a phase-angle dependent toughness [4]. For example, one possible expression for a mode-dependent toughness that could be used in mixed-mode analyses is

$$\Gamma = \Gamma_I \frac{\lambda(1+\tan^2\psi^\infty)}{\lambda+\tan^2\psi^\infty}, \tag{2}$$

where $\lambda = \Gamma_{II}/\Gamma_I$, Γ_I and Γ_{II} are the values of the mode-I and mode-II toughnesses, and $\psi^\infty$is the nominal phase angle based on an LEFM analysis. In a cohesive-zone model, this particular mixed-mode fracture criterion is equivalent to [2, 3]

$$\mathcal{G}_I^*/\Gamma_I + \mathcal{G}_{II}^*/\Gamma_{II} = 1, \tag{3}$$

where $\mathcal{G}_I^*$ and $\mathcal{G}_{II}^*$ are the mode-I and mode-II energy-release rates at the crack tip. Other mixed-mode failure criteria can be expressed in a similar fashion, either in a form suitable for use in LEFM calculations, or in a form suitable to cohesive-zone analyses.

Many adhesive joints are in the form of laminates. Fracture of these laminates is driven by the effective axial force, N, moment, M, and transverse shear forces, V_s and V_u, as shown in Fig. 2. In LEFM, the energy-release rates, $\mathcal{G}_M$ and $\mathcal{G}_N$, and phase angles, ψ_M^∞ and ψ_N^∞, for loading by a moment and by an axial force are functions of the thickness of the laminates, h_1 and h_2, and α and β, which are the Dundurs parameters indicating the modulus mismatch [5]:

$$\mathcal{G}_M = f_M(\alpha,H)M{h_1}^{-3/2};\ \ \psi_M^\infty = g_M(\alpha,\beta,H) \tag{4}$$

$$\mathcal{G}_N = f_N(\alpha,H)N{h_1}^{-1/2};\ \ \psi_N^\infty = g_N(\alpha,H) + \psi_M^\infty \tag{5}$$

where $H = h_1/h_2$. The energy-release rates, $\mathcal{G}_{V_s}$ and $\mathcal{G}_{V_u}$, and phase angles, $\psi_{V_s}^\infty$ and $\psi_{V_u}^\infty$, for loading by symmetric and unsymmetric shear forces can be expressed as [6]:

$$\mathcal{G}_{V_s} = f_{V_s}(\alpha,\beta,H)V_s{h_1}^{-1/2};\ \ \psi_{V_s}^\infty = g_{V_s}(\alpha,\beta,H) \tag{6}$$

$$\mathcal{G}_{V_u} = f_{V_u}(\alpha,\beta,H)V_u{h_1}^{-1/2};\ \ \psi_{V_u}^\infty = g_{V_u}(\alpha,\beta,H) \tag{7}$$

In equations 4-7, all of the expressions that are not functions of β can be derived analytically from steady-state energy balance arguments. Conversely, expressions that are functions of β have to be derived numerically. The details of the crack-tip deformation are important for these terms.

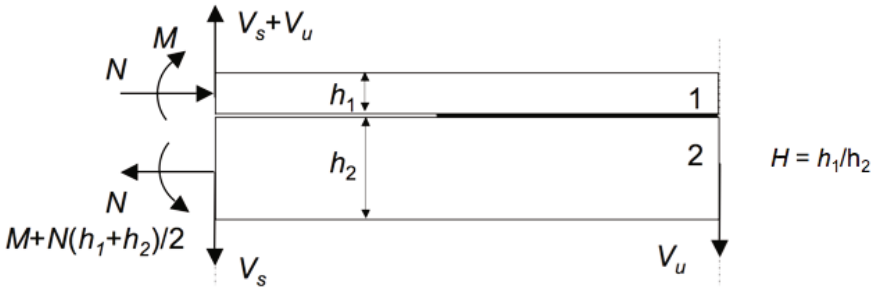

Fig. 2 Loads and moments acting on a laminated geometry [2, 6]

When these elastic laminated geometries are analyzed using mixed-mode cohesive-zone models, the properties of the traction-separation laws have no effect on the quantities that are not functions of β [2, 3]. In addition, the quantities that do depend on β can be accurately obtained by mixed-mode cohesive-zone analyses, provided the appropriate fracture-length scales, based on the cohesive parameters are not too large [2]. For example, Fig. 3 shows that the phase angle deduced from cohesive-zone analyses stabilizes at the value expected from LEFM results, even when the stress field along the interface shows no sign of a square-root-singularity [2]. Furthermore, it has also been shown that the length scale naturally introduced by a cohesive zone allows these models to produce useful values of phase angles, even under conditions when linear-elastic fracture mechanics would predict oscillatory stress fields [2].

2 Experimental Measurements of Cohesive-Zone Parameters

Two approaches are commonly used to deduce cohesive-zone parameters. One makes use of the J-integral, J [7-9]. If J can be determined from the remote loads and the geometry, and the crack opening displacement, u can be measured, then J can be plotted as a function of u, and the tractions across the interface can be deduced as

$$\sigma = dJ/du. \tag{8}$$

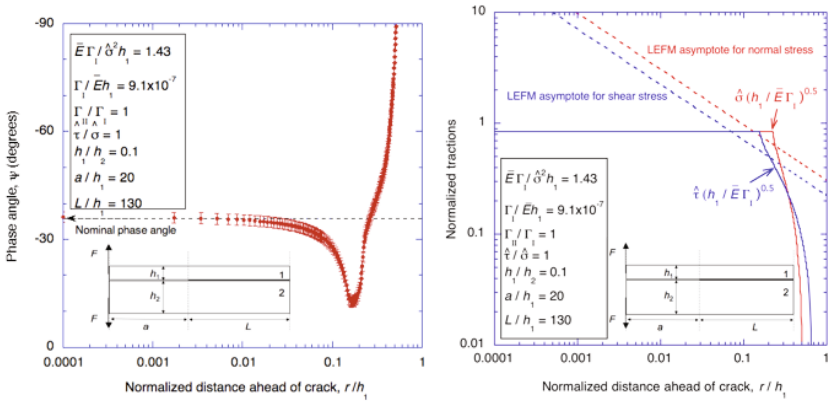

Fig. 3 (a) Phase angle plotted as function of distance ahead of an interface crack for a laminated geometry. **(b)** Normal and shear stresses along the interface under the same conditions. Both figures are reproduced from Ref. [2].

This enables a rigorous method to determine the traction-separation law up to the point of fracture. There are several potential problems. (i) It relies on the J-integral being valid for the test geometry. This may not be true if there is plasticity in the adherends, or if transverse shear forces are dominant in a laminated geometry and the cohesive-zone is too large [2]. (ii) While there seem to be situations where the results obtained from a geometry in which the J-integral is valid can be applied to other geometries, it is not obvious that this should always be true. Indeed, there is at least one published counter example where the change in constraint affects the failure mechanism of the adheisve layer, and, hence, the traction-separation law [10].

An alternative approach to determining cohesive parameters is an empirical one in which quantities such as load, displacement, crack advance and deformation are monitored experimentally, and then matched to numerical calculations in which the cohesive parameters are varied until a fit is made [11, 12]. Two potential problems with this approach are (i) the chosen geometry may have a lack of sensitivity to one of the cohesive parameters, and (ii) multiple pairs of parameters may provide equivalent fits to the experimental results. Care must always be taken to explore the sensitivity of the fits for the geometries and material parameters of interest.

The issue of multiple pairs of cohesive parameters providing fits to the data can be illustrated by a purely numerical example given in Yang *et al.* [11]. A bonded double-cantilever beam is loaded by a pure moment, and the constitutive properties of the adherends is described by a power-law hardening relationship: $\sigma = A\epsilon^n$. The critical moment to propagate a crack can be calculated if it is assumed that the cohesive strength plays no role in fracture. Under these conditions, the critical moment is given by [11]

$$\frac{M_f}{Ah^2} = \left(\frac{2}{\sqrt{3}}\right)\left(\frac{n+1}{4n}\right)^{n/(n+1)}\left[\frac{1}{2(n+2)}\right]^{1/(n+1)}\left(\frac{\Gamma_I}{Ah}\right)^{n/(n+1)} \tag{9}$$

where h is the thickness of the arms. As can be seen in Figure 4, this analytical prediction is valid when the cohesive strength is low. However, higher values of the cohesive strength can result in an increase in the critical moment. If one were to conceive of an experiment in which the critical moment were measured and then used to back out the corresponding cohesive parameters from the numerical fit, Figure 4 shows the ambiguity that might result.

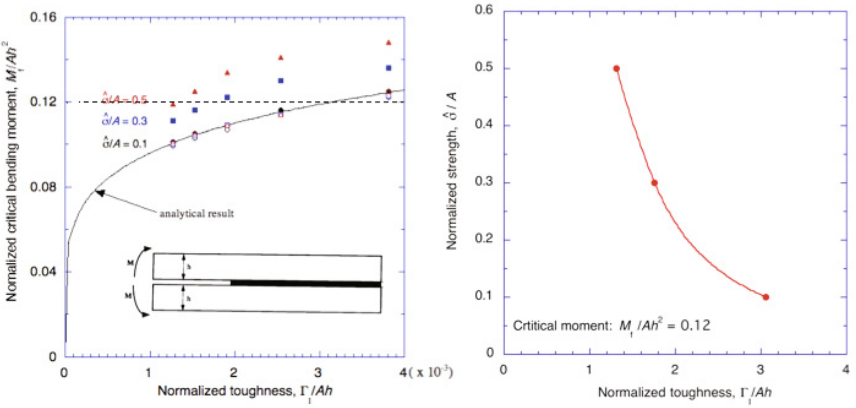

Fig. 4 (a) A plot of the critical bending moment required to fracture an adhesively-bonded double cantilever beam, showing the effect of cohesive strength. Reproduced from Ref. [11]. **(b)** A plot of the values of cohesive parameters that would provide a fit the critical bending moment of $M_f/Ah^2 = 0.12$.

A recent example by Sun *et al.* [13, 14] illustrates the issues and experimental procedures for determining the cohesive parameters in a system consisting of thin steel adherends (that deform plastically) and a commercial rubber-toughened epoxy. Under mode-I conditions, several experimental configurations can be used: a wedge test, a double-cantilever beam test, and a tensile test. In the wedge test, bonded coupons are driven over a wedge, so that fracture occurs. The arms of the specimen deform plastically during the process, and the residual radius of curvature can be used as an experimental observation that can be compared to numerical results. It is also possible to monitor the crack extension ahead of the wedge - this provides another experimental observation that can be compared to numerical results. As can be seen from Fig. 5, multiple pairs of cohesive parameters provided fits to each of these sets of observations, but the two sets of observations had different sensitivities to the two parameters. This resulted in an intersection between the fits for the two sets of data, so that a unique pair of a toughness and strength

could be defined within experimental limits. In a double-cantilever beam test for the same system, observations of the load-displacement plot and of the crack extension all gave the same information about the cohesive parameters - that the toughness was in the range of 3.9 to 4.5 kJm^{-2}. This was consistent with the results from the wedge test, but the numerical predictions for the double-cantilever test were insensitive to the cohesive strength. So, the cohesive strength could not be found from this geometry. A third geometry (a direct tension test) was devised that was sensitive to strength, but not to toughness [14]. The cohesive parameters deduced from numerical fits to the results of the double-cantilever and tension tests are illustrated in the second plot of Fig. 5. A comparison of the two pl! ots in Fig. 5 shows that all the tests gave very consistent values for the cohesive parameters of $\Gamma_1 = 4.2 \pm 0.3$ kJm^{-2} and $\hat{\sigma} = 24 \pm 3$ MPa.

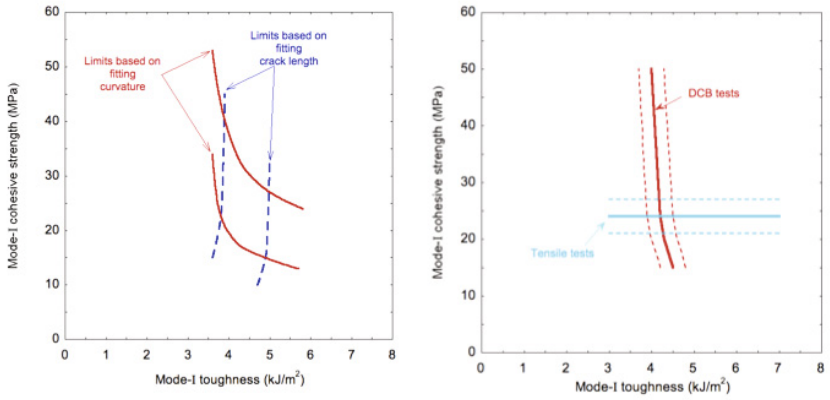

Fig. 5 Values of mode-I toughness and cohesive strength that provide fits to experimental observations for a wedge test, double-cantilever test, and tensile test using specimens made from a steel and a commercial adhesive. The spread of the two sets of lines corresponding to matching curvature and matching crack extension are a measure of experimental uncertainty. Both figures have been reproduced from Ref. [14].

3 Conclusions

Cohesive zones can be used to model mixed-mode fracture of elastic and plastic joints. The properties of these joints are determined by the strength or/and toughness of the adhesive layer, depending on the geometry and the properties of the adherends. The design of experiments to determine the cohesive properties of an adhesive layer must be done with an awareness of the different roles that toughness and strength may have on the behaviour of a joint. In a similar fashion, it should be noted that the question of whether

toughness or strength of an adhesive layer is the appropriate property to use for the design of a joint will depend on the geometry and on the material properties of the adhesive and adherends.

References

1. Kafkalidis, M.S., Thouless, M.D., Yang, Q.D., Ward, S.M.: J. Adhes. Sci. Technol. 14, 1593–1607 (2000)
2. Parmigiani, J.P., Thouless, M.D.: Eng. Frac. Mechs. 74, 2675–2699 (2007)
3. Yang, Q.D., Thouless, M.D.: Int. J. Fract. 110, 175–187 (2001)
4. Hutchinson, J.W., Suo, Z.: Adv. Appl. Mechs 29, 63–191 (1992)
5. Suo, Z., Hutchinson, J.W.: Int. J. Fract. 43, 1–18 (1990)
6. Li, S., Wang, J., Thouless, M.D.: J. Mech. Phys. Solids 52, 193–214 (2004)
7. Li, V.C., Chan, C.M., Leung, C.K.Y.: Cement and Concrete Research 17, 441–452 (1987)
8. Sørensen, B.F., Jacobsen, T.K.: Eng. Frac. Mechs 70, 1841–185 (2003)
9. Andersson, T., Stigh, U.: Int. J. Solids Structs 41, 413–434 (2004)
10. Cavalli, M.N., Thouless, M.D.: J. Adhesion 76, 75–92 (2001)
11. Yang, Q.D., Thouless, M.D., Ward, S.M.: J. Mech. Phys. Solids 47, 1337–1353 (1999)
12. Yang, Q.D., Thouless, M.D., Ward, S.M.: Int. J. Solids Struct. 38, 3251–3262 (2001)
13. Sun, C., Thouless, M.D., Waas, A.M., Schroeder, J.A., Zavattieri, P.D.: Int. J. Solids Structs 45, 3059–3073 (2008)
14. Sun, C., Thouless, M.D., Waas, A.M., Schroeder, J.A., Zavattieri, P.D.: Int. J. Solids Structs 45, 4725–4738 (2008)

Author Index

Allen, Matthew R. 217

Bigoni, Davide 1
Borkent, Bram 117
Burr, David B. 217

Carpinteri, Alberto 15
Chaboche, J.-L. 35

Davies, Matt 165

Fleck, Norman A. 57

Gottschald, Klaus 165
Gupta, N.K. 67

Hale, Alina 165
Hu, W.R. 85

Jensen, O.E. 101

Lohse, Detlef 117

Massabò, Roberta 135
Mikkelsen, R. 231
Moffatt, H.K. 155
Moresi, Louis 165
Mühlhaus, Hans-Bernd 165

Nicolas, Maxime 189

Okulov, V.L. 231

Paggi, Marco 15
Pailha, Mickael 189
Pouliquen, Olivier 189

Rudnicki, J.W. 199

Shen, W.Z. 231
Siegmund, Thomas 217
Sørensen, J.N. 231

Tang, Z.M. 85
Thouless, M.D. 249
Troldborg, N. 231

Author Index

The following pages contain a list of authors and co-authors of all the presentations at ICTAM2008. The extended summary of the presentations can be found on the associated CD. Additional material to this book can be downloaded from http://extra.springer.com. Each name is followed by a sequence of entries which are the presentation IDs. A bold-font indicates the presenting author.

Aage, Niels **12077**
Aarts, Annemarie 10713
Abarca, Marcelo 10084
Abderrahmane, Hamid **10391**
Abdi, Frank 10792
Abdul-Latif, Akrum **11086**
Abe, Masato 10781
Abelman, Herven **11776**
Abilez, Oscar 11345
Aboudi, Jacob 10893
Acartürk, Ayhan 10333
Achard, Jean-Luc 11376
Adachi, Taiji 11424
Adachi, Takashi 10691
Adam, Laurent 11764
Adler, Pierre **11161**
Aebi, Laurent 11001,11412,**11615**
Ahmed, Alauddin **11415**
Ahmedyanov, Ildar 10222
Ahmetolan, Semra 11373
Airiau, Christophe 11629
Aizikovich, Sergey **10667**
Ajdari, Armand 11445
Ajiro, Junji 11301
Akarapu, Sreekanth 11266

Akkermans, Rinie 10737
Aksel, Nuri 11314,11321,11482
Al-Salaymeh, Ahmed **11793**
Alaggio, Rocco 11411
Alain, Koenen 10900
Alam, Meheboob **10199**
Alastrue, Victor 12078
Alben, Silas **11133**
Alberding, Jonathan 11593
Alboussière, Thierry 11795,**11824**
Aldham, Ben 10159
Alekseenko, Sergey **12145**
Alexandrov, Viktor 10667
Alfaro, Iciar 10579,11326
Alfredsson, Henrik 11400
Alizard, Frédéric 10169
Allen, James 11746
Allix, Olivier **11245**
Almgren, Karin **11458**
Alon, McCormick 11410
Alonso, Ignacio **11319**
Alonso-Marroquin, Fernando **10861**
Altenbach, Holm **10195**
Amberg, Gustav 11252
Ambrósio, Jorge **10559**,11246
Amiroudine, Sakir **10505**,11201
An, Yi 11142
Andrade, Jose **11206**
Anrunachalakasi, Arockiarajan 11790
Antanovskii, Leonid **10450**
Antunes, José 11899
Araki, Keisuke **11738**
Aref, Hassan **10034**
Ariff, Fadiah 11633
Arimitsu, Yutaka **11095**
Ario, Ichiro **10460**
Ariza, Pilar **10886**
Arkhipov, Dmitry 10790
Arrate, Felipe 12071
Arratia, Paulo **11662**
Asai, Masahito 10368
Ashida, Fumihiro 10214,**11213**
Ashida, Kiwamu 10514
Ashton, Jesse 11109
Aspden, Jonathan 11337

Astafiev, Vladimir **10421**
Atkinson, Callum 12137
Atobe, Takashi **11538**
Aubry, Nadine **10531**,11619,11697
Auriault, Jean-Louis 11543
Ayas, Can 10556
Bühler, Stefan 11484
Ba, Jing **10590**
Bažant, Zdeněk 11525
Bachmayer, Mathias **10329**
Badiei, Arash 11317
Baek, Seung 11298
Baeten, André **10211**
Bagué, Anne 11848
Bai, Yilong **11169**
Bailey, Sean 10729
Bajer, Konrad 11323
Bakshi, Shamit 11874
Baleh, Rachid 11086
Balmforth, Neil 10520
Banerjee, Arun **10881**
Banerjee, Sanjoy 12199
Banerjee, Soumitro 11118
Barber, Jared 11593
Barber, Tracie 11294,11354,11529
Barbier, Gregory **10987**
Barenghi, Carlo **10152**
Barkley, Dwight 10291
Barnett, Matthew 11641
Barros, Marcelo **10863**
Barthès-Biesel, Dominique **11309**
Barton, David 11550
Bartout, Jean-Dominique 11205
Basack, Sudip **10406**
Baskaran, Raghuraman 11266
Bassom, Andrew 11508,11768
Basu, Sumit **12062**
Batra, Romesh **10541**
Bauwens, Luc **11090**
Bayandor, Javid **10792**,11912
Bazant, Martin 10528
Bedard-Tremblay, Laurie 11090
Bednarz, Tomasz **10773**
Bedrikovetsky, Pavel **10205**
Bedzinski, Romuald **11454**

Behrens, Bernd 10714
Beliakova, Tatiana 10619
Bellenger, Emmanuel 11377
Benedictus, Rinze 11033
Benning, Rainer **11845**
Berezovski, Arkadi 11079
Berg, Mats 10456
Bergeon, Alain 11490
Berloff, Natalia **10149**
Berloff, Pavel 11706
Bermejo-Moreno, Ivan 11414
Berrada, Kamal 11037
Berry, Joseph **11690**
Berthold, Fredrik 11458
Bertoldi, Katia **11399**
Bertram, Christopher **11719**
Bessho, Sadao 12181
Besuelle, Pierre 10659
Bevilacqua, Luiz 10863
Beysens, Daniel **11201**
Bhattacharjee, Joydip 10186
Bhattacharya, Kaushik **10555**,10799
Biagini, Paolo **10467**
Bielski, Jan **11188**
Bienvenu, Yves 11205
Bigoni, Davide **10014**
Bilger, Nicolas 11764
Binder, Ben 10481,**10661**
Binder, Kurt 10909
Binetruy, Christophe 10821
Binks, Bernard 10513
Birbaud, Anne-Laure 10485
Bivin, Yury 11479
Blackburn, Hugh **10291**
Blake, John **10517**
Blawzdziewicz, Jerzy 11418
Blazejczyk-Okolewska, Barbara 10574
Blonski, Slawomir **11606**
Bluemink, Johanna **11456**
Bo, Tianli 10784
Bobylev, Aleksey 12145
Bocciarelli, Massimiliano 10066
Bochud, Nicolas 11412
Bockstedte, Andreas 10928
Bode, Christiaan 11180

Bodenschatz, Eberhard **10532**,11402
Boeck, Thomas **10715**
Bogdanov, Igor 11161
Boguslawski, Andrzej 11124
Bohlius, Stefan 11803
Bohm, Josef 10993
Boiko, Andrey 11969
Boisse, Philippe 11235
Bolotnik, Nikolai 11225
Bolster, Diogo 11004
Bolzon, Gabriella **10066**
Bomer, Johan 11932
Bonnet, Guy 12175
Borgas, Michael **11178**
Borkent, Bram 11561
Bornert, Michel 10659
Borodulin, Vladimir 10626
Bottema, Murk 11317
Boulanger, Philippe 11110,**11111**
Bourdon, Christopher 10621
Boutin, Claude 11543
Boyce, Mary 10995,11399,11500,11657
Boyce, Russell **12031**
Boyle, Jonathan 10348
Bozhko, Alexandra **11362**
Brady, John **12131**
Brancher, Pierre 11632
Brand, Helmut 11803
Branger, Hubert 11622
Brassart, Laurence 11764
Bratukhin, Yury 11362
Brauer, Hartmut 11227
Braun, Stefan 10484
Bravo-Castillero, Julian 11885
Brear, Michael 10728
Brekelmans, Marcel 10562
Brennan, Michael 10908
Brethouwer, Geert 11282
Brinckmann, Steffen 10545
Brito, Daniel 11795
Broadbridge, Philip **10876**
Brogliato, Bernard 11070
Brons, Morten **10238**
Brotherton, Christopher 10621
Broutman, Dave 10504

Brouwer, Dannis 11310
Brown, Kevin 11931
Brownell, Cody 11840
Bruck, Angela 11673
Bruus, Henrik **10528**
Bryner, Juerg **11001**,11412,11615
Buckley, Marc 11808
Buckley, Paul 11613
Buffière, Jean-Yves 10336
Bui, Thanh 10506
Bukhanko, Anastasia **11318**
Burczynski, Tadeusz **11881**
Burteau, Anthony **11205**
Bush, John 10520
Busse, Friedrich 11260
Bustamante, Miguel 11159
Byrne, David 11520
Cain, Jason 10168
Caltagirone, Jean-Paul 10630
Camanho, Pedro 11943,12185
Candel, Sebastien **10485**
Cao, Yihua **10411**
Cao, Yu-Hui 11963
Carberry, Josie 11690,11702
Carey, Graham 11426,11871
Carpenter, Andrew 11771
Carpinteri, Alberto **10511**,10693
Carstensen, Carsten **11958**
Cartmell, Matthew **11240**
Case, Scott **10168**
Cassel, Kevin **10482**
Castro, Carlos **11500**
Cathalifaud, Patricia **11629**
Cavicchi, Andrea 11305
Ceccio, Steven 11599
Celina, Mathias 10621
Chaboche, Jean-Louis **11332**
Chabreyrie, Rodolphe **11619**
Chakrabarti, Anupam **11275**
Challis, Vivien **10326**
Chambart, Marion **11147**
Chan, Cho 10418
Chandrasekar, Srinivasan 11511
Chandre, Cristel 11619
Chang, Chien-Cheng **11071**,11396

Chang, Ching 10763
Chang, Hyun 11753
Chang, Min-Hsing **11571**
Chang, Wei-Tze 11441
Charpin, Jean 10519
Chateau, Xavier **10166**
Chattopadhyay, Amares **10218**
Chauhan, Kapil 10437,11041
Chaurasia, Hemant 12117
Chen, Chen-Shan 11441
Chen, Chih-Di 10940
Chen, Chih-Keng **11437**
Chen, Ching 11430
Chen, Chuan **10418**
Chen, Chuanyao 11856
Chen, Falin 11571
Chen, Hongxun 11536
Chen, Jeng-Tzong **11723**
Chen, Jian-Zhong 10811
Chen, Jie 10150
Chen, Jun 11963
Chen, Li-Qun **10384**
Chen, Nelson **11430**
Chen, Qi-Sheng **11733**
Chen, Sih-Li 11533
Chen, Taicong 11017
Chen, Ting-Yu **11176**
Chen, Weimin **10946**,10947
Chen, Weiqiu **10323**
Chen, Wen **11290**
Cheng, Chang-Jun 10811
Cheng, Che-Min 10946
Cheng, Gengdong **12088**
Cheng, Kai-Hung 11157
Cheng, Yang-Tse 10946
Cheng, Yi 11176
Cheong, Kwangyeil 11531
Cherepanova, Alexandra 10175
Chernoray, Valery 10303,**10383**
Chernousko, Felix **10538**
Cherubini, Stefania 10169
Cheung, Yin-Har 11401
Chevalier, Jérôme 11558
Chevy, Juliette 11181
Chhay, Marx **11143**

Chiarullo, Enzo 10066
Chiba, Akira 11284
Chin, Wilson 11524
Chinesta, Francisco **10579**,11326
Chng, Audrey **11212**
Choi, Geol **11363**
Choi, Sunghun 11535
Chomaz, Jean-Marc **10499**,11141
Chong, Min 11667,11746
Chotard-Ghodsnia, Roxana 11697
Chou, Ping-Chung 11902
Christensen, Ken 11518
Christodoulides, Paul **11146**
Chu, Chin-Chou **11396**
Chu, Haijian 11069
Chui, David **10909**
Chun, Ho 11969
Chung, Bong 11078
Chung, Chih-Ang **10940**
Chung, Peter 10502
Chuzel-Marmot, Yann **12097**
Cierpka, Christian **11600**
Cirak, Fehmi 11102
Clamond, Didier **11868**
Clarke, Richard **10446**
Clausen, Johan **11325**
Clayton, John **10502**
Cleary, Paul 10107
Clercx, Herman 10737
Cloots, Rudy 11371
Cocks, Alan **10568**
Cocou, Marius **10227**
Cole, David 11521
Colinet, Pierre 11955
Coman, Ciprian **11508**
Combescure, Alain 12097
Combescure, Didier 11147
Compton, Dale 11511
Cooker, Mark 10109,11786
Coorevits, Patrice 11813
Cormery, Fabrice 11937
Corona, Edmundo 10980
Costa, Josep 12185
Courtin, Stephan 10987
Cowin, Stephen **10572**

Cox, Brian **11727**
Cox, Stephen **10481**
Craig, Walter **11047**
Crowdy, Darren **11123**
Cueto, Elias 10579,**11326**
Curtin, William 11212
Czerwinska, Justyna 10046
Czolczynski, Krzysztof 10574
Dühring, Maria **11564**
Dabiri, John 10901,11087,11675,12129
Dahan, Marc **10988**
Dahl, Jonas **10725**
Dahlberg, Carl **11497**
Dai, Fulong 10942
Dai, Shiqiang 11536
Daivis, Peter 10794,10983,**11718**
Daly, Samantha **10799**
Daniel, Kroll 11410
Dankowicz, Harry **11065**
Dao, Trung-Kien 11437
Daraio, Chiara **11749**
Daros, Carlos **10405**
Das, Rajarshi **10107**
Dasgupta, Abhijit **12063**
Dauchot, Olivier 11203
Davies, Glyn 12134
Davis, Howard **11410**
Davis, Robert 11884
Deawwanich, Thana 11524
Debiève, Jean-François 11242
Deguen, Renaud **11795**
Delaere, Koen 11764
Delannay, Laurent 11764
Deleau, Fabrice **10900**
Delgado, Antonio 11845,11866
Dellinger, Nicolas **11376**
Delon, Giles 10513
Demekhin, Eugene 10518
Demirci, Ali **11373**
Dendy, Edward 10079
Denier, Jim **10028**,10446,11569
Denis, Mazuyer 10900
Denissenko, Petr 11375
Depouhon, Alexandre 11130
Deriaz, Erwan 10046

Deshpande, Vikram 11663
Desmorat, Rodrigue 10987,11147
Desrues, Jacques **10659**
Destrade, Michel 11110
Detournay, Emmanuel 10174,**11130**
Dewar, Robert **10491**
Dewar, William **11631**,11706
De Palma, Pietro 10169
DiCarlo, Antonio **10302**
Dias, Frederic 10661,11146,11451
Dieterich, James 11917
Dillon-Gibbons, Craig **12137**
Dinariev, Oleg 10205
Ding, Hu 10384
Ding, Jianping 11591
Diorio, James **11082**
Dmitrochenko, Oleg **10604**
Do-Quang, Minh **11252**
Doblare, Manuel 12078
Dobovsek, Igor **11163**
Dobriloff, Christoph **11757**
Doghri, Issam **11764**
Doig, Graham **11529**
Dollet, Benjamin 11548,11658
Domanski, Wlodzimierz **11406**
Dombovari, Zoltan 10580
Domhardt, Jan **11609**
Dominguez, Jaime 11224
Dong, Yu-Hong **11443**
Dong, Zhengzhu **10760**
Donnelly, Russell 11004
Doppler, Delphine 10338
Dorfman, Boris 10744
Dormieux, Luc 10921
Dorrell, Robert **11114**
Dovgal, Alexander **10746**
Drazen, David 10534
Dreiden, Galina 11385
Dreyer, Michael **11302**
Driscoll, James 11599
Drobniak, Stanislaw **11124**
Drugan, Walter 11409
Drzewiecki, Andrzej 10674
Du, Jianke **10860**
Dual, Jürg 10923,11001,11412,11615

Duan, Huiling 10666,11069
Dubois, Frédéric 10645
Ducruix, Sebastien 10485
Duggleby, Andrew **11635**
Duineveld, Paul **11812**
Dunaev, Igor **11276**
Dunaev, Vladislav **11276**
Duncan, James 11082
Duperray, Alain 11697
Dupont, Pierre 11242
Durairaj, Brindha 10264
Durox, Daniel 10485
Durrant-Whyte, Hugh **10013**
Durst, Franz 11793
Dussauge, Jean-Paul 11242,**12120**
Dutykh, Denys **10872**
Duval, Paul 11181
Dyskin, Arcady **10134**,11982
Dziedzic, Krzysztof 11077
Eberhard, Peter **10751**
Eckermann, Stephen 10504
Eggers, Jens 11514
Egner, Halina **10717**
Ehlers, Wolfgang **10333**,11320
Ehrenstein, Uwe 11226
Ehret, Alexander 11109
Eijkel, Jan 11932
Einav, Itai **10201**
Ejiri, Yoshihiro 10703
Ekiel-Jezewska, Maria **11682**,11890
Elad, David **10471**
Elfassi, Reut **10591**
Eloy, Christophe 10084,11817
Elsinga, Gerrit **11223**
El Omari, Kamal **11391**
Emmerich, Heike **10245**
Emran, Mohammad 11072
Engelbrecht, Juri **11079**
Enz, Stephanie **11821**
Epstein, Marcelo **12051**
Er, Guo 12104
Eremeev, Victor 10195
Eric, Vandre 11410
Ertunc, Özgür 11845
Eshuis, Peter 11476

Esler, Gavin 11513
Estevez, Rafael 11558
Estivalezes, Jean-Luc **10630**
Estrin, Yuri 10134
Evans, Anthony 11663
Evans, Peter **10962**
Facchini, Luca 10467
Falkovich, Gregory 11530
Fallenius, Bengt 11810
Falzon, Brian **12134**
Fan, Jing-yu 11193
Fan, Yang-Tsai 11533
Fang, Daining **11093**
Fang, Fei **11692**
Fang, Mingxia **11258**
Fang, Te-Hua 11270
Fang, Yihong **11699**
Fang, Zijun 11917
Farahmand, Bob 10792
Fareo, Gideon 11346
Fauci, Lisa **12106**
Faure, Thierry 11329
Favro, Lawrence 10856
Fayet, Michel 11235
Fazzalari, Nicola **11317**
Feld, Nicolas 11245
Feng, Kan 10892
Feng, Qi 11170,11258
Feng, Shihai 10652
Feng, Xi-Qiao **10933**,11419
Fernández-Nieves, Alberto 11445
Fernandes, Paulo **11390**
Ferreira, Elizabete **11110**
Fery, Andreas 11390
Festa, Gaetano 11918
Fialko, Yuri **11931**
Fidlin, Alexander **11806**
Fink, Rainer 11390
Finn, Matthew **10000**
Fischer, Franz **10629**
Fivel, Marc **11181**
Fleck, Norman **10316**,10568,10642,11319
Fleissner, Florian 10751
Flores, Paulo **11246**
Floryan, Jerzy **10368**

Fontelos, Marco 11636
Forbes, Larry **10772**
Forehand, David 11240
Forest, Samuel 11205
Forterre, Yoël 10849
Fortin, Jérôme 11377,11813
Foudras, Andreas 11702
Francois, Marianne **10079**
Fransson, Jens **11810**
Fraser, Barrie **10758**,11389
Friedman, Avner 10808
Friend, James 10648,**10671**,11175
Frohnapfel, Bettina **11064**
Fu, Liyun 10590
Fu, Song **10598**
Fuis, Vladimir **11297**,11488
Fujikawa, Shigeo **11372**
Fukagata, Koji 11063
Fukai, Jun 10764
Fukazawa, Yoshinari **10819**
Fukumoto, Yasuhide 10655,**11581**,11696
Fukuta, Masato 11481
Funakoshi, Mitsuaki **10775**,10819
Funakubo, Ami 11745
Furukawa, Tomonari 11427,11677
Fuster, Daniel 11848
Gäbel, Gunnar 10600
Gabi, Martin 11484
Gaffney, Eamonn 10517
Gai, Bing-zheng **10398**
Gai, Sudhir **11792**
Gailani, Gaffar 10572
Galeão, Augusto 10863
Gallaire, Francois **11226**
Gambarotta, Luigi **11305**
Gamezo, Vadim 10997
Gamstedt, Kristofer 11458
Gao, Bing 11113
Gao, Huajian 10933
Gao, Ling-Tian 10933
Gao, Peng 11435
Garbin, Valeria 11658
Garbowski, Tomasz 11191
Garcia, Andrew 11249
Gaskell, Philip 11321,11482,11851

Gatuingt, Fabrice 11147
Geers, Marc **10562**,11371
Geisler, Reinhard 11223
Gerbeth, Gunter 10869,11600,11858
Gersborg, Allan 12077
Gertsenstein, Semen 11839
Ghanem, Roger 12071
Ghosh, Susanta **11467**
Giannakopoulos, Antonios **11398**
Gibbesch, Andreas 11243
Giesecke, Andre **10869**
Giovannini, André 11632
Gitterman, Moshe **10730**
Givli, Sefi 10555
Goktepe, Serdar 11345
Goldhirsch, Isaac **11642**
Goldstein, Robert 11472
Golley, Bruce 11128
Gollub, Jerry 11662
Gonçalves, Paulo **11196**
Gondret, Philippe 10338
Gong, Kezhuang 10892
Goryacheva, Irina **10537**
Goto, Susumu **11889**
Goto, Tomonobu **11370**
Gouillart, Emmanuelle 11203
Gourjii, Alexandre **11003**,11004
Goutianos, Stergios 11985
Grah, Aleksander 11302
Graham, Alan **10652**
Gratecap, François 11326
Gray, William 11313
Green, Edward **10808**
Greer, Julia **10545**
Gregersen, Misha 10528
Gregory, James 11923
Greviskes, Brian **11672**
Griffith, Martin **11717**
Griffiths, Ross 11134,**11174**,11684
Grillet, Anne 10621
Grinfeld, Michael 10502
Groenwold, Albert 11825
Grosse, Sebastian **10656**
Gruber, Sebastian 11180
Grue, John **10576**

Guangwen, Jiang 10984
Gudemella, Raghukanth 10706
Gudmundson, Peter 11497
Guegan, Alan 12061
Guery, Ariane 11937
Guessasma, Mohamed **11813**
Guiamatsia, Irene 12134
Guilbaud, Daniel 11147
Guilleminot, Johann **10821**
Guimard, Jean-Mathieu 11245
Guinovart-Diaz, Raul 11885
Gundrum, Thomas 11858
Guo, Dawei 11699
Guo, Jiahong **11536**
Guo, Li-cheng **10608**
Guo, Mengqiu 10590
Guo, Ya-Fang **11020**
Gupta, Narinder **10317**
Gutmann, Sascha 10923
Guz, Igor **10620**
Guzanov, Vladimir 12145
Guzel, Bulgakova **10723**
Guzev, Mikhail **10847**
Haas, André **11321**
Hagiwara, Yoshimichi 11760,**11774**
Haines, Philip **11777**
Hajj, Muhammad **11925**
Haldar, Sandip 10145
Hall, Philip **11990**
Hall, Stephen 11719
Hallez, Yannick **11081**
Hamdouni, Aziz 11143
Hammerton, Paul **11768**
Hamza, Naseem 11855
Han, Xiaoyan 10856
Hanagud, Sathya **11630**
Hanazaki, Hideshi **10223**
Hansen, Anders **11279**
Hansen, Kurt 11049
Hansen, Rasmus 10034
Hao, Su **11292**
Harlen, Oliver **10365**
Harper, John **10954**
Hasagawa, Yosuke 11064
Hasegawa, Yosuke **11953**

Hashiguchi, Kazuhiro 11797
Hasimoto, Hidenori **10380**
Hassan, Eyad **11269**
Hattori, Yuji **11696**
Hayashi, Shunichi 10703
Hazel, Andrew 11777
He, Cunfu 11449
He, Xuefei 11688
Heath, Cynthia 10652
Hedrih, Katica **10135**
Heil, Matthias **10348**
Heining, Christian **11314**
Heller, Manfred 11291
Hendricks, Scott 10850
Henninger, Carole 11327
Henningson, Dan 11282
Herbold, Eric 11749
Hernandez-Garcia, Miguel 12071
Herwig, Heinz **11200**
Hewitt, Richard 10446,11777
Hicher, Pierre-Yves **10763**
Hicks, Peter **11596**
Hild, Francois **10336**
Hilgenfeldt, Sascha **10015**
Hill, James 10802
Hills, Christopher **11228**
Hirama, Mitsuru 11021
Hirose, Yuuki 11301
Hirouchi, Tomoyuki **11741**
Hiyama, Jun 11538
Hjärne, Johan 10383
Hlod, Andriy **10713**
Ho, Paul 11162
Hoepffner, Jerome **11063**
Hogan, John **11202**
Hogg, Andrew 11114,11174,11631,**11706**
Hogsberg, Jan 10899
Hole, Matthew 10491
Hollerbach, Rainer **11858**
Holzapfel, Gerhard 11386
Hong, Wei 11644
Hong, Yosun 11531
Hong, Yun **11298**
Horiuti, Kiyosi 11414
Hornung, Hans **10855**

Hoshi, Shintaro 10503
Hoshide, Toshihiko **10734**
Hosoi, Anette 11123
Houfek, Martin 11297,**11488**
Hourigan, Kerry 10122,10238,**10871**,11299,11352,11717
Howell, Richard 11217
Hrapko, Matej 11371
Hsieh, Cheng-Ta 11396
Hsieh, Shang-Hsien 11441
Hsu, Cheng-Kuei 11473
Hsu, Chin-Tsau 11905
Hsu, Hong-Jzen 11740,11743
Hsu, Jin-Chen 11099
Hsu, Shih-Ming 10020
Hu, Gengkai **11577**
Hu, Guo-Hui **11287**
Hu, Haiyan **11052**
Hu, Howard **11590**
Hu, Wenrui **10309**,11435
Hu, Wenwen 11055
Huang, Chi 10777
Huang, Chihyung **11923**
Huang, Li 10777
Huang, Ning **10261**
Huang, Rui **11162**
Huang, Siyuan 10598
Huang, Yyongli **11940**
Hudson, Stuart 10491
Huerre, Patrick 11554,**12061**
Hughes, Graham 11134,11174,**11684**
Huilgol, Raja 11353
Hultmark, Marcus 10729
Humphry, Katherine **11445**
Hunter, Peter 11109
Huo, Yongzhong **11542**
Huppert, Herbert 10874,11091,**11388**,11496
Hussain, Fazle **10310**
Hutchins, Nicholas **11667**,11734
Hutchinson, John **10307**
Huth, Robert 11958
Huyghe, Jacques **11951**
Hwang, Chi-Hung 11157
Iafrati, Alessandro **11809**
Ibrahim, Raouf 11736
Idiart, Martin **10642**

Iima, Makoto **11474**
Ikeda, Takashi **11736**
Illesinghe, Suhith 10159
Im, Seyoung **10130**,11753
Imbault, Didier 11376
Imberger, Jorg **10308**
Inacio, Octavio 11935
Ing, James 11118
Ingber, Marc 10652
Insperger, Tamás **11550**
Ishak, Anuar 11263
Itoh, Motoyuki 11374,**11752**
Itskov, Mikhail 11109
Iu, Vai 12104
Ivantsov, Andrey 11628
Iyengar, Narayana **10706**
Jabareen, Mahmood 10732
Jackson, Shaun 11690
Jacono, David **10684**
Jaiani, George **10023**
Jalmes, Arnaud 10513
Janajreh, Isam 11925
Jang, Bongkyun 10775
Jang, Wen-Yea **10971**
Janicek, Premysl 11297
Janjua, Mohammad 10531
Javadi, Mohsen **10714**
Jeffrey, Rob 11132
Jensen, Henrik 11325
Jensen, Oliver **10016**
Jenson, Ryan 11523
Jewell, Nathaniel 10028
Jeyakumaran, Jeku **10469**,11703
Ji, Jinchen **11129**
Jiang, Limei 11431
Jiang, Ye-Jian 11093
Jin, Qian 11697
Jin, Xiaoying 10860
Johansson, Arne 11282
Johnson, Ted 10090,**11513**
Jonker, Ben 11310
Jose, Antunes **11935**
Jun, Kabjin 11535
Jung, Sungpil 11019,**11440**,11531
Kachanov, Yury **10626**

Kadri, Usama **10385**
Kairn, Tanya 11718
Kaiser, Ingo **11198**
Kajka, Rafal 11865
Kajtar, Jules **11092**
Kala, Zdenek **10865**
Kalaidin, Eugene 10518
Kalliadasis, Serafim **10518**,11312
Kalt, Peter 11218,11782
Kamaltinova, Aygul 10723
Kamp, Leon 10737
Kaneda, Masayuki **10764**
Kang, Min 11162
Kano, Yoshio **10781**
Kapitaniak, Tomasz **10574**
Kaplanski, Felix **10655**
Karajan, Nils 10333,**11320**
Karcher, Christian 10493
Karihaloo, Bhushan **10666**,11069
Karimi, Nader **10728**,**10728**
Karmakar, Debabrata 10186
Karray, Mohamed 11327
Karuppiah, Kanaga 11673
Karyakin, Mikhail **10321**
Kasagi, Nobuhide 11064,11953
Kasai, Atsushi 10734
Kashtalyan, Maria 10620
Kashtanov, Arseny **11646**
Katija, Kakani **10901**
Kato, Katsuo 11752
Kato, Ryosuke 11436
Kawaguchi, Takashi 10781
Kawano, Hiroto 11095
Ke, Fujiu 11169
Keber, Marko 10567
Kecik, Krzysztof 11154
Keer, Leon 11292,**11651**
Kehoe, Timothy 11001
Keim, Nathan 11645
Kellermann, David 11427,**11677**
Kelly, Don **11677**
Kelso, Richard 11018,11269
Kere, Petri **10341**
Kerimbekov, Ruslan 10399
Kerr, Robert **11159**

Kerr, Ross **10891**
Ketterson, John 11292
Kevrekidis, Panayotis 11749
Khabakhpashev, Georgy **10790**
Khabakhpasheva, Tatiana **11778**
Kharlamov, Sergey 12145
Khelif, Abdelkrim 11564
Khromov, Alexander 11318
Khusnutdinova, Karima **11385**
Kienzler, Reinhold **10542**
Kiger, Ken **11078**
Kikuda, Masayuki 11370
Kim, Jeongbeom 11019
Kim, Ji-Hwan **10038**
Kim, Ju-Young 10545
Kim, Kijung 11535
Kim, Tongbeum **12210**
Kimbonguila, Adolphe 11813
Kimmoun, Olivier 10478,**11622**
Kimoto, Sayuri 11436
Kindelan, Ultano **11636**
Kireenkov, Alexey **10181**
Kirillov, Oleg **10157**
Kirkman-Brown, Jackson 10517
Kishimoto, Satoshi 10942
Kitsios, Vassili 10276
Klatte, Joerg 11302
Kleine, Harald 11180,11354,11792
Klika, Vaclav **11152**
Kluwick, Alfred **10484**,10889
Knowles, Philip 11078
Kobayashi, Masami **11691**
Kobayashi, Susumu **10691**
Kobayashi, Takeshi 10514
Koenig, Jens 10099
Kohr, Mirela 10793
Kok, Schalk **10894**,11825
Kolesnikov, Yurii 10493
Kondo, Djimédo 10821,**11880**,11937
Kondou, Masaki 10160
Kong, Ki-Jeong 11753
Konishi, Kazuhiro 10223
Konishi, Masaaki 11726
Kononova, Olga 10129
Korczyk, Piotr **11315**

Korzec, Maciek 10962
Kostin, Georgy **11464**
Kou, Kun 12104
Kovacs, Adam **10140**
Kovacs, Andras **10140**
Kovalyshen, Yevhen **10174**
Kowalewski, Tomasz **10046**,11315,11606
Kowalewski, Zbigniew **12118**
Kozlov, Victor **10303**,10746
Krämer, Ewald 11088
Kröger, Matthias 10600
Kraaijeveld, Famke 11951
Kraav, Tiina 11597
Krabbenhoft, Kristian **10358**
Kraige, Glenn **10850**
Krasnikovs, Andrejs **10129**
Krasnopolskaya, Tatyana **10968**
Krasnov, Dmitry 10715
Krason, Wieslaw 10124,**11865**
Kratochvil, Ctirad 11488
Kravtsov, Sergey 11706
Kraynik, Andrew **11492**
Krenev, Leonid 10667
Krenk, Steen **10899**
Krenn, Rainer 11243
Kreuzer, Edwin **10928**
Krittian, Sebastian **10844**,11109
Kroon, Martin **11386**
Kruszka, Leopold **10953**
Kuan, Chen-Chi **11818**
Kubair, Dhirendra **10145**
Kudela, Henryk **11232**
Kudela, Pawel 10242
Kuhl, Ellen **11345**
Kuhn, Günther 10507
Kulik, Victor 11969
Kumar, Pavan 11469
Kumar, Ranjeet 11189
Kumari, Pato 10218
Kuo, Wei-Chih 11099
Kuo, Wei-Ling **12070**
Kurnik, Wlodzimierz **11077**
Kuroda, Masaharu 10514
Kuroda, Mitsutoshi **11296**
Kuroda, Yuichiro 11370

Kurotaki, Takuji 11538
Kus, Waclaw 11881
Kwak, Byung 11363
Kyriakides, Stelios 10971,**10980**
Kyriakidis, Michalis 11470
Lü, Lefeng 11295
LaBarbera, Michael 11862
Ladeveze, Pierre **11098**
Lagrange, Romain **11817**
Lahellec, Noel 10279
Lammers, Peter 11064
Lammertink, Rob 11561
Lan, Jian 11045
Landolt, Andrin **10898**
Landor, Ivan 11152
Lang, Matthew 11500
Langevin, Dominique **10513**,11335
Langthjem, Mikael **10414**
Lanspeary, Peter **11218**,11269,11782
Lapuerta, Victoria 11621
Lapusta, Nadia **10548**,11522
Larsson, Fredrik 10596
Larsson, Ragnar 11193
Lau, Timothy **11018**
Laude, Vincent 11564
Lauga, Eric 11123
Laverón, Ana **11621**
Lavoie, Philippe **12158**
Lazauskas, Leo 11452
La Rizza, Patrick 11795
Le, Jia-Liang 11525
Le, Khanh **11844**
Le, Tu **10983**
Leal, Gary **10882**
Leblond, Jean-Baptiste **11334**
Leclerc, Eric 11309
Lee, Huei-Huang 11430
Lee, Hyeok 10871,**11299**
Lee, Inwon **11969**
Lee, Seung 12199
Lee, Sooho **11535**
Lee, Soon-Kong 11218,**11782**
Lee, Sungyon 11123
Lee, Yeaw **11851**
Lefebvre, Yannick 11309

Legarth, Brian **10902**
Leguillon, Dominique **10833**
Lei, Chengwang 10773,11694
Lellep, Jaan **11597**
Lemak, Mark 10881
Leming, Sarah 10621
Lemoyne, Luis 11848
Lenain, Luc 10534
Lenci, Stefano 10873
Lenoir, Nicolas 10659
Lentzen, Sven 11485
Leonardi, Eddie 11294,11354,11529,11906
Leontini, Justin **11539**
Lepenies, Ingolf 11164
Lesko, John 10168
Letellier, Christophe 11329
Leuckert, Janin 11609
Leung, Teresa **12121**
Leungvichcharoen, Sasikorn 11567
Levy, Benjamin **11632**
Levy, Florence 11309
Leweke, Thomas **10122**,**10122**,11352,11717
Lewis, Jennifer 11518
Le Dizès, Stéphane **11197**
Le Gac, Séverine 12209
Le Guer, Yves 11391
Li, Bin 11162
Li, Chongyin 12157
Li, Dan 11906
Li, Haiyan 10648,10671
Li, Hongliang **10796**
Li, Hongqi 11183
Li, Huaxiang **11613**
Li, Jiangyu **11676**
Li, Jianhua **11215**,11259
Li, Jie **11857**
Li, Keyu **11048**
Li, Longfei 11367
Li, Min 10946,**10947**
Li, Qiang 11282
Li, Shaofan **10595**
Li, Shuo 10072
Li, Zheng **10892**
Liang, Jun **11896**
Liao, Shijun **11104**

Liao, Yanguo 11940
Liberzon, Alexander 10591
Liberzon, Dan **11058**
Licht, Christian 11034
Liechti, Kenneth **10818**
Liew, Chin 11257
Liew, Jeffery 11524
Liffman, Kurt 10159
Lim, Jae 10130
Lim, Kian-Meng **11688**
Lim, Siak-Piang **11688**
Lin, Chien-Chang 11215
Lin, Jen-Fin 11270
Lin, Wang 11356
Ling, Jian **12157**
Liow, Jong-Leng **11521**
Litchfield, Andrew **11912**
Litewka, Przemyslaw **10700**
Liu, Bing 11037
Liu, Bo 11052
Liu, Caishan **11070**,11466
Liu, Diankui 10796
Liu, Jiong 10590
Liu, Johan 11193
Liu, Kuang-Chen **11175**
Liu, Lei 11020
Liu, Qingquan **11142**
Liu, Qixing 11725
Liu, Su 11449
Liu, Xinan 11082
Liu, Ya-Chao 11733
Liu, Yang 11896
Liu, Yi 10548
Liu, Ying **11220**
Liu, Ying-Hong 11071
Liu, Zenghua **11449**
Loefdahl, Lennart 10303
Loehnert, Stefan **11378**,11544
Lohse, Detlef **10311**,11476,11548,11561,11658
Loiseleux, Thomas **10338**
Lomakin, Evgeny **10619**
Longmire, Ellen **11668**
Lopez-Pamies, Oscar **10721**
Lopez-Realpozo, Juan 11885
Loureiro, Juliana **11617**

Lowrie, Robert 10079
Lu, Fei-Yau 11818
Lu, Tianjian 12210
Lu, Wei **10816**
Lu, Xia 11630
Lu, Xiao **11522**
Lucey, Anthony 10689,**11217**
Luding, Stefan 10861
Lukaschuk, Sergei **11375**
Lund, Erik 11279,11943
Lundell, Fredrik **11787**
Luo, Ying **11179**
Lusseyran, François **11329**
Lutz, Thorsten 11088
Luu, Li-Hua **10849**
Luxner, Mathias 11224
Lyly, Mikko 10341
Lyubimov, Dmitriy 10175,**11628**
Lyubimova, Tatyana **10175**,11628
Möller, Dirk 10923
Münch, Andreas 10962
Münch, Cécile 11379
Ma, Chien-Ching 11000
Ma, Haitao **11017**
Ma, Hongwei **10463**
Ma, Li **10633**
Ma, Xiang **11641**
Macaskill, Charlie 10758
Mace, Brian **10908**
Magagnato, Franco **11484**
Magnaudet, Jacques 11081
Mahajan, Dhiraj 12062
Mahaut, Fabien 10166
Mahesh, Krishnan **11879**
Maier, Giulio **11191**
Maiffredy, Lionel 11235
Makhovskaya, Yuliya 10537
Malachowski, Jerzy **10124**,11865
Malecha, Ziemowit 11232
Malinouskaya, Iryna 11161
Malinowski, Szymon 11315
Malley, Matthieu 11377
Man, Hou **11427**
Manasseh, Richard **10159**
Mangipudi, Kodanda 10059

Manneville, Paul **10880**
Mansour, John 11091
Mantell, Susan 11668
Manzhirov, Alexander **10470**
Mao, Weiguo 11725
Marie, Simon 11443
Markov, Vladimir 10222
Markovich, Dmitriy 12145
Marmonier, Frédéric 12109
Marsik, Frantisek **10158**,11144,11152
Martin, Eric 10833
Martin, Jerome 10372
Martinez, Alfredo 10513
Martinez, Miguel 12078
Martinoty, Philippe 11803
Marusic, Ivan 11667,11734
Maruszewski, Bogdan **10674**,**10674**
Maruyama, Shinichi 11234
Marze, Sebastien 11335
Mason, David **11346**,11776
Masri, Sami **12071**
Massabò, Roberta **10123**,11305
Masson, Jean-Paul 11795
Matar, Omar 11627
Mathis, Romain **11734**
Matsumoto, Yoichiro **11481**,11745,11797
Matsuo, Yousuke 10415
Mattner, Trent **10449**
Matveyenko, Valeriy **11384**
Maugin, Gerard 11079
Mazzilli, Carlos **10873**
Mazzino, Andrea 11915
McCue, Scott **10802**
McDonald, Nicholas **10090**
McGann, Mathew 10491
McMeeking, Robert **11663**
McNitt, Richard **11333**
McPhail, Yvette **11354**
McPhedran, Ross 11404
Meguizo-Gavilanes, Josue 11090
Meier, Alexander **11117**
Meijaard, Jacob **11310**
Meinhart, Carl 12199
Meinke, Peter 10099
Mejak, George **11208**

Meleshko, Viatcheslav 11000,11003,**11004**,11461
Melville, Kendall **10534**
Men, Shouqiang 11227
Menshykov, Olexandr 10620
Menzel, Andreas 11803,**12078**
Meriaux, Catherine 10891,11091,**11285**
Mesarovic, Sinisa **11266**
Mescheder, Ulrich 10140
Mestel, Jonathan **11807**
Meunier, Patrice 11817
Meyer, Georg **10889**
Mi, Jamie **10206**
Middelberg, Georg 11200
Mikkelsen, Lars **11985**
Mikkola, Aki 10604
Miklasz, Kevin 11862
Milani, Enrico 12144
Milani, Gabriele 12144
Miller, Madeline **12129**
Mills, Ruth 10491
Minchenya, Vitaly 10493
Mingzhi, Zhang 11692
Miroshnichenko, Andrey **10926**
Miroshnichenko, Elena 11238
Mitchell, Sarah 10515
Mitkin, Vladimir 10955,**12142**
Miura, Hideaki 11738
Miyamoto, Hitoshi **10963**
Miyao, Takehiro 10223
Miyazaki, Takeshi **10503**,10745
Mizerski, Krzysztof **11323**
Mizuno, Mamoru **10800**
Mizuta, Yo **10727**
Moase, William 10728
Moffatt, Keith **10736**,11323,11581
Mofrad, Mohammad **12000**
Moldenhauer, Patrick **10600**
Molin, Bernard **10478**
Monaghan, Joe **11091**,11092
Monchiet, Vincent 11880,**12175**
Mondy, Lisa **10621**
Monerie, Yann 11327
Monetto, Ilaria **11409**
Monkewitz, Peter 10437,**11041**,11400
Monteiro, Andre 11617

Monty, Jason 11667,**11746**
Moon, Kyungho 11535
Moore, Jeff 11518
Moresi, Louis 12133
Moret-Gabarro, Laia 11629
Morris, Don 10850
Morrison, Jonathan **10498**,12158
Moskovits, Martin 12199
Mosler, Joern **11102**
Mottet, Gérard 11334
Mourzenko, Valeri 11161
Mouton, Christopher 10855
Movchan, Alexander 11404
Movchan, Natasha **11404**
Muchatibaya, Gift 10515
Mudde, Robert 10385
Mudford, Neil 11354
Mueller, Andreas **10682**
Mueller, James 11808
Mueller-Hoeppe, Dana 11378,**11544**
Muhlhaus, Hans **12133**
Mullin, Tom 10446,**10578**
Mulmule, Aditya 11956
Muratore-Ginanneschi, Paolo **11915**
Mureithi, Eunice **11569**
Murthy, Haradanahalli **11855**
Murthy, Tejas **11511**
Musacchio, Stefano 11915
Muthuswamy, Maya 12159
Muto, Kota 11234
Myśliński, Andrzej **11775**
Myers, Tim **10515**
Nadal, François 11817
Nadolin, Konstantin **10970**
Nagai, Ken-ichi **11234**
Nagel, Sidney 11645
Nagib, Hassan **10437**,11041,11400
Naguib, Ahmed 10498,12158
Naha, Sayangdev 10486
Naito, Masato 10160
Nakagawa, Jun 10429
Nakahara, Akio **10415**
Nakai, Tonau 11370
Nakamura, Masanori 12181
Nakano, Masami 10414

Nakaryakova, Tatyana 11384
Nakatani, Akihiro **11450**
Nao-Aki, Noda **11350**
Narayanan, Ranga 10505
Narita, Fumio **10429**,11021,11576
Nasedkin, Andrey **11819**
Nash, Martyn 11109
Naumann, Dirk 11205
Naviaux, Pierre 11792
Nazar, Roslinda **11263**
Nazarenko, Sergey 11375
Nazarinia, Mehdi 10684
Neely, Andrew 11354,11529
Neild, Adrian 10923
Nemec, Tomas 10158
Neofytou, Panagiotis **11470**
Newaz, Golam **10856**
Ng, Chee-Loon 12142
Ng, Ching **11257**
Nguyen, Chuong **11702**
Nguyen, Dzuy **11524**
Nguyen, Franck 11205
Nguyen, Giang 10201
Nichols, Joseph 10499
Nicola, Lucia **11189**
Nielsen, Kim **10776**
Nikahd, Mousa 10436
Nikiforovich, Eugene 10968
Ning, Cao 10398
Niordson, Christian **11347**
Niroomandi, Siamak 10579
Nishimura, Masaomi **11686**
Nitsche, Wolfgang 11609,11757
Noda, Naotake 10608,11213
Nothwang, William 10502
Novati, Giorgio 11191
Nudurupati, Sai 10531
Nyirumulinga, Yohann **12109**
O'Brien, Stephen 10519
O'Byrne, Melanie **11134**
O'Byrne, Sean 11354
Oberti, Stefano **10923**
Obrecht, Hans **10996**
Obrist, Dominik **11125**
Odagiri, Nozomi 10800

Oertel, Herbert 10844
Ogawa, Takanobu 10997
Oguamanam, Donatus **11238**
Ohayon, Roger 12109
Ohl, Claus-Dieter 12209
Ok, Ali 10980
Oka, Fusao **11436**
Okamura, Makoto **10870**
Okawa, Teppei 11551
Okayasu, Mitsuhiro 10800
Olagnon, Christian 11558
Olhoff, Niels 11049
Oliemans, Rene 10385
Omishore, Abayomi 10865
Onck, Patrick **10059**
Onishi, Satomi **12201**
Ooi, Andrew 10159,10276
Ooshiro, Satoshi 11581
Oran, Elaine **10997**
Oristaglio, Michael 11215
Ortiz, Michael 10886,**12042**
Ortiz, Roland 12097
Osipov, Michael **10740**
Osipova, Lydia **10740**
Ostachowicz, Wieslaw **10242**
Ovarlez, Guillaume 10166
Overgaard, Lars **11943**
Oweis, Ghanem **11853**
Ozaki, Yoshihiko 11760
Ozawa, Hisashi 11357
Ozdemir, Izzet 10562
Paavola, Juha **10979**
Paggi, Marco 10511,**10693**
Pal, Prakash **10851**
Palaniappan, Devanayagam **11949**
Paletti, Ligieja **11033**
Palmer, Jeffrey **10995**
Palymsky, Igor 11839
Pan, Kuo-Long **11902**
Pandit, Mihir 11032
Pang, Chin 11906
Pang, Sze-Dai **11525**
Pangetsu, Joy 11726
Pao, Yih-Hsing 11264
Parau, Emilian **10109**,11786

Park, Chan 11753
Park, Chanseung 11440,**11531**
Park, Jong **11753**
Park, Noma 11879
Park, Seung **11113**
Park, Sungmoon 11440
Park, Taewon 11019,11440,11531,11535
Pasternak, Elena 10134,**11982**,**11982**
Pastur, Luc 11329
Pathak, Amit 11663
Patterson, John 10773,11694
Paul, Mark 11635
Pavlovskaia, Ekaterina **11118**
Peake, Nigel **10571**
Pedersen, Niels **11155**
Pedersen, Pauli **10750**
Pedley, Timothy **10330**
Peirson, William **11249**
Peletier, Mark 10713
Peltzer, Inken 11609
Peng, Cheng 11542
Peng, Hsin-Min 11264
Peng, Jifeng **11675**,12129
Peng, Wei-hong 10760
Pennathur, Sumita 11932
Pepe, Richard 10729
Peppin, Stephen 11388
Perales, Jose 11621
Pereira, Antonio **11312**
Perelmuter, Mikhail **10165**
Perlikowski, Przemyslaw 11563
Pesavento, Francesco 11313
Peters, Alisia 11561
Peters, Gerrit 11371
Petrolito, Joe **11128**
Petrov, Yuri 11646,**11756**
Petryk, Henryk **10509**
Pettermann, Heinz **11224**
Phillips, William **11168**
Pichler, Bernhard **10921**
Pinho, Fernando 11617
Piorek, Brian **12199**
Piponniau, Sébastien **11242**
Pirat, Christophe 11561
Pitman, Mark **10689**,11217

Pitti, Rostand **10645**
Pivovarov, Mikhail 11225
Pleiner, Harald **11803**
Plouraboué, Franck 11490
Pochiraju, Kishore **10950**
Podio-Guidugli, Paolo **10989**
Poelma, Christian 11223
Poitou, Arnaud 11326
Polikarpus, Julia 11597
Pombo, João 10559
Poncet, Raphael **11451**
Pop, Ioan 11263
Pop, Octavion 10645
Popescu, Mihail **11701**
Popinet, Stéphane **10397**,11848
Popov, Maxim 10740
Porter, Mason 11749
Post, Nathan 10168
Potapenko, Stanislav **10649**
Pouliquen, Olivier **10017**
Pradeep, Dhoorjaty 10310
Prakash, Jai 10793
Prasad, Raghu 10027,**11469**
Prastowo, Tjipto 11174
Prathap, Gangan 10252
Prochazka, Lukas **11387**
Prokunin, Alexander **10919**
Proppe, Carsten 11471
Prosperetti, Andrea 11456
Protas, Bartosz **11904**
Prunet-Foch, Bernard 11579
Prusak, Daniel **10756**
Puklicky, Libor 10865
Pullin, Dale **11414**
Pumir, Alain 10532
Punzmann, Horst **11066**,11520,11530
Pupurs, Andrejs 10129
Puri, Ishwar **10486**
Purohit, Prashant **10815**
Purvis, Richard 11596
Puscasu, Ruslan **10794**
Putin, Gennady 11362
Putot, Claude 10833
Putta, Jagadeesh **10742**
Qian, Yue-Hong **12112**

Qiao, Ni **11348**
Qifeng, Yu **10984**
Qin, Qian **11356**
Qin, Taiyan 10614
Qu, Guohui 11336
Qu, Shaoxing 11835
Quere, David **10315**
Quesada, Daniel 10833
Quinto Su, Pedro **12209**
Rösgen, Thomas 11117
Rüberg, Thomas 10257
Rüedi, Jean-Daniel **11400**
Réthoré, Julien 10336
Rabaud, Marc 10338
Rajagopalan, Raj 11660
Rajapakse, Nimal **10617**
Raka, Bumedijen 10987
Rakotomalala, Nicole 10372
Ralston, John 11701
Ramachandran, Arun 10882
Ramamurthi, Krishnaswami 11956
Ramasubramaniam, Ashwin 10886
Ramaswamy, Sriram **12125**
Rambely, Azmin **11633**
Ramdan, Raden **10948**
Randrüüt, Merle 11311
Ranganathan, Prabhakar **10524**
Rans, Calvin 11033
Rao, Rekha 10621
Raous, Michel 10227,**11327**
Rauh, Cornelia 11866
Ravi-Chandar, Krishnaswamy 10818,**11502**
Ravichandran, Guruswami 10799
Reardon, Patrick 10652
Rednikov, Alexey **11955**
Reed, Helen 11771
Rega, Giuseppe **11411**
Regardin, Clotilde 12109
Rego, Luiz 10205
Reinelt, Douglas 11492
Reinicke, Ulf 10996
Reizes, John 11906
Remmers, Joris 11951
Remy, Fabien 10478
Resagk, Christian 10834,**11227**

Resnyansky, Anatoly **11131**
Restrepo, Juan 11593
Ribeiro, Pedro **10366**
Richter, Mike 11164
Rio, Emmanuelle 10513
Ristenpart, Bill 11807
Robert, Maier 11410
Roberts, Anthony 10326
Robinet, Jean-Christophe **10169**
Robison, Rosalyn 11496
Rodríguez, Angel 11621
Rodriguez, Daniel 10276
Rodriguez-Ramos, Reinaldo 11885
Roesgen, Thomas 10170,**10898**,11387
Rogers, Eric 10399
Rohde, Andrew **11939**
Roisman, Ilia **11874**
Romain, Guibert **11490**
Rong, Bao 10999
Rosakis, Ares 11522
Roschektayev, Aleksej 10626
Ross, Shane **11127**
Rottman, James **10504**
Roux, Stéphane 10336
Roy, Clément 10122
Roy, Debasish 11467
Royer, Pascale **11543**
Rozhkov, Aleksey **10955**,11579
Ruban, Anatoly **11822**
Rubin, Miles **10732**
Rudiger, Gunther 11858
Rudnicki, John **10318**
Rui, Xiaoting **10999**
Rump, Owen 11513
Runesson, Kenneth **10596**
Ruo, An-Cheng 11571
Ruszinko, Endre **11073**
Ryvkin, Michael **10893**
Saberi, Shadi 11205
Sabina, Federico **11885**
Sadlej, Krzysztof **11890**
Sadovsky, Alexander **11126**
Sadus, Richard 11415
Sagar, Remalli **10027**
Sagaut, Pierre 11143,11443

Sahoo, Trilochan **10186**
Saif, Taher **11284**
Saint-Jalmes, Arnaud **11335**
Sakata, Sei-ichiro **10214**,11213
Sakurai, Katsutoshi 11774
Saldana, Christopher 11511
Salin, Dominique **10372**
Salonen, Eero-Matti 10979
Salupere, Andrus **11311**
Samson, Ophir 11123
Samsonov, Alexander 11385
San, Kuo-Ching **11740**
Sandel, Arnaud **11235**
Sano, Osamu **10523**,11729
Sansour, Carlo 11790
Sardesai, Chetan 10482
Sargsyan, Samvel **10679**
Saric, William **11771**
Sarkar, Arijit **11660**
Sasakawa, Akira 11374
Sattler, Rainer 11514
Saurin, Vasily 11464
Sauzay, Maxime **11392**
Savery, Mark 11524
Sayapin, Sergey **11555**
Sbragaglia, Mauro 11561
Scarano, Fulvio 11223
Schäfer, Bernd **11243**
Schöberl, Markus **11343**
Schanz, Martin **10257**
Scheider, Ingo **11328**
Schenkel, Torsten 10844
Schiehlen, Werner **10099**
Schlacher, Kurt 11343
Schlatter, Philipp **11282**
Schmauder, Siegfried **11683**
Schmid, Holger **11109**
Schmid, Peter 10499,11125,12061
Schmid, Sven **11088**
Schmidt, Laura 11645
Schmidt, Ruediger **11485**
Schoeppner, Greg 10950
Scholle, Markus 11321,**11482**
Schouveiler, Lionel **10084**
Schröder, Wolfgang **10506**,10656

Schrefler, Bernhard **11313**
Schroeder, Andreas 11223
Schryve, Mathieu 10227,11327
Schultz, Michael 10729
Schumacher, Joerg 10715,**11072**
Schwartz, Leonard **10519**
Scotti, Alberto 11078
Secomb, Timothy **11593**
Sedelnikov, Grigoriy 11628
Sedlar, Milan 11144
Segev, Reuven 12051
Sekhar, Raja **10793**
Sellier, Mathieu **10910**
Semenov, Ilya **10222**
Semenova, Irina 11385
Sengupta, Surajit 10909
Sermage, Jean-Philippe 10987
Serre, Eric 11141
Seuront, Laurent **12006**
Sevodina, Natalya 11384
Sfarni, Samir **11377**
Shabana, Yasser **10704**
Shang, Xiao-dong 10938
Shankar, Ravi 11511
Shanmugam, Saravanan **10264**
Shao, Jian-Fu 11880,**11937**
Shariff, Karim **10139**
Sharifulin, Albert 10183
Shats, Michael 11066,11520,**11530**
Shaw, Dein **10777**
Shaw, Stephen **11627**
She, Zhen-Su **11963**
Sheikh, Abdul 11032
Shemer, Lev **10744**,11058
Shen, Luming **10912**
Shen, Min **11183**
Shen, Yunian **11527**
Sheridan, John 10411,10684
Sherwin, Spencer 10291
Shi, Feng 10261
Shi, Hong-Hui **11136**
Shi, Jingyi 10914
Shi, San-Qiang **10897**
Shi, Yaolin 10614
Shibutani, Yoji 11463

Shifrin, Efim **11472**
Shiguo, Long **10355**
Shimizu, Kazuya **11797**
Shimokawa, Shinya **11357**
Shindo, Yasuhide 10429,**11021**,11576
Shobatake, Yasuyuki 11450
Shrivastava, Suresh **11037**
Shukla, Priyanka 10199
Shvets, Aleksandr 10968
Sibgatullin, Ilias **11839**
Siddiq, Amir 11683
Siechen, Scott 11284
Siegmund, Thomas **10081**
Sigmund, Ole 12077
Sihua, Fu 10984
Sika, Zbynek 11380
Silberstein, Meredith **11657**
Silva-Freire, Atila 11617
Simonov, Igor **11479**
Simonovic, Julijana **11575**
Singh, Bhrigu **11032**
Singh, Pushpendra 10531,11619,**11697**
Sinha, Koustav 12063
Siniov, Alexander 11555
Sirisup, Sirod **10462**
Skatulla, Sebastian **11790**
Skews, Beric **11180**
Skoczen, Blazej **10404**,10717,11188,11230
Slunyaev, Alexey 10744
Smith, David 10517
Smith, Wade **11703**
Smits, Alexander **10729**
Snook, Ian 11718
Soares, Renata 11196
Socha, John **11862**
Sogabe, Yuji 11095
Soh, Ai-Kah **10445**
Sohn, Dongwoo 10130
Sohn, Ki-Ju 10038
Soize, Christian 10821
Song, Taeckrim 11440
Song, Yicheng **10445**
Soria, Julio 10072,**10276**,12137
Sorokin, Alexander 10746
Sorokin, Sergey **10853**

Sottos, Nancy **10319**,11518
Speetjens, Michel **11461**
Spelt, Peter 11627
Srinil, Narakorn 10567
Stépán, Gábor 11550
Stampfl, Jürgen 11224
Stappenbelt, Brad **10231**
Starosta, Roman 10674
Stefani, Frank 10869,11858
Stefanski, Andrzej **11563**
Stegmeir, Matthew 11668
Steinberg, Adam **11599**
Steinberg, Ted **12008**
Steinmann, Paul 10507
Stepan, Gabor **10580**
Stepanyants, Yury **11140**
Stewart, Bronwyn **11352**
Stogner, Roy **11871**
Stokes, Yvonne **11426**
Stolk, Theo 11812
Stone, Howard 11445,11807,**12103**
Strakos, Petr **10993**
Stremler, Mark **10150**
Stupkiewicz, Stanislaw 10509
Su, Lester **11840**
Sudak, Leszek **11173**
Sugimoto, Takeshi **10078**
Sugimoto, Yoshiki 10703
Sulem, Catherine 11047
Sulem, Jean 11604
Sullivan, John 11923
Sumi, Takahiro 11538
Sumi, Yoichi **11551**
Sun, Chao 10007,**11401**,11548
Sun, Hongguang 11290
Sun, Jianhong **11905**
Sun, Lizhong 11214
Sun, Qicheng **10705**
Sun, Ren **10866**
Sundararajan, Sriram **11673**
Sung, Jie 11284
Suo, Zhigang **11644**
Suquet, Pierre **10279**
Suslov, Sergey **10183**
Sutalo, Ilija 10159

Suzuki, Tateyuki 10691
Svahn, Fredrik 11065
Sveda, Jiri **11380**
Svoboda, Jiri 10629
Szechenyi, Edmond 12109
Szelengowicz, Ivan 11749
Szeywerth, Rene 10484
Sznitman, Josue **10170**
Szumbarski, Jacek 11606
Szymczak, Tadeusz 12118
Sørensen, Jens **10312**
Sørensen, Kim 11325
Tachibana, Rie 11797
Tagawa, Toshio 10764
Tagawa, Yoshiyuki **11745**
Takagi, Daisuke **10874**
Takagi, Shu 11481,11745,11797
Takahashi, Naoya 10503,10734,**10745**
Takaki, Tomohiro **10636**,10948,11528,11741
Takashima, Kousuke 11774
Takeda, Tomo 11576
Takei, Ataka **11729**
Takeuchi, Shintaro 11797
Talamelli, Alessandro 11400
Tallaron, Christophe 11558
Talon, Laurent 10372
Tamano, Shinji **11374**,11752
Tamm, Kert 11311
Tanaka, Hiro **11463**
Tanaka, Martin 11127
Tandon, Gyaneswar 10950
Tang, Zhanfei 11336
Tanner, Roger **10230**
Tao, Jianjun **11260**
Tatsumi, Tomomasa **10716**
Tehrani, Parisa **10436**
Telin, Alexey 10723
Teymur, Mevlut 11373
Theofanous, Theo 10955,12142
Theofilis, Vassilis 10276
Thess, André **10493**,10834
Thiagarajan, Krish 10836
Thiele, Uwe 11312
Thiffeault, Jean-Luc 10000,**11203**
Thomas, Dirk **10456**

Thomas, Robert 10856
Thompson, Harvey 11321,11482,11851
Thompson, Mark 10122,10238,10684,10871,11299,11352,11539,11690,11717,**12117**
Thomsen, Jon 10725,11821
Thouless, Michael **12034**
Thovert, Jean-Francois 11161
Tian, Ali **10789**
Tian, Jiayong **10606**
Timchenko, Victoria **11906**,**11906**
Tinnes, Jean-Philippe 10336
Tirumkudulu, Mahesh 11660,**11956**
Tjan, Kuan-Khoon 11168
Tobushi, Hisaaki **10703**
Todd, Billy 10794,10983
Tokovyy, Yuriy **11000**
Tomita, Yoshihiro **10160**,10636,10948,11528,11686,11726,11741
Tomkratoke, Saifhon 10462
Tong, Jingwei 11183
Tong, Penger **10938**
Tonmukayakul, Peng 11524
Tordesillas, Antoinette **12159**
Torres, Clivia 11001
Tourabi, Ali 11376,11379
Tralli, Antonio **12144**
Trevelyan, Philip 11312
Trevino, Lydia **11087**
Triantafillou, Trent 11285
Trontin, Pierre 10630
Tropea, Cameron 11874
Trubchik, Irina 10667
Trumble, Kevin 11511
Truong, Nicholas 11719
Tsai, Ming 12070
Tsai, Peichun **11561**
Tsangaris, Sokrates 11470
Tsuji, Kinko 12209
Tuck, Ernest **11452**
Turon, Albert **12185**
Turteltaub, Sergio **10914**
Tutty, Owen **10399**
Tvergaard, Viggo 11296,11347
Tylikowski, Andrzej **10235**
Tyliszczaak, Artur 11124
Tzvetkov, George 11390
Uenishi, Koji **10628**

Uetani, Koji 11691
Uetsuji, Yasutomo **11444**
Uhl, Tadeusz 10756
Uhlherr, Alfred 10983
Ulbrich, Heinz 10329
Ulerich, Joe 11345
Utkin, Pavel 10222
Vainchtein, Dmitri 11619
Vaiyapuri, Senthilkumar **10252**
Valasek, Michael 10993,11380
Vallejo, Daniel 11224
Vanden-Broeck, Jean-Marc 10109,10661,**11786**
Vanierschot, Maarten **11237**
Vanneste, Jacques **11337**
Van Damme, Henri **12123**
Vardoulakis, Ioannis 10201,11398,11604
Varghese, Anoop 10541
Varghese, Joseph 12063
Varna, Janis 11458
Vasiliev, Aleksey 10926
Vatistas, Georgios 10391
Veidt, Martin 11257,11939
Veitch, Ben 10571
Vener, David 10520
Verdier, Claude 11697
Veron, Fabrice **11808**
Versluis, Michel 11548,**11658**
Veveakis, Emmanuil **11604**
Viaud, Bertrand **11141**,**11141**
Viba, Janis **10021**
Viel, Lisan 12199
Viggiani, Gioacchino 10659
Vignes-Adler, Michele **11579**
Vignoud, Lionel 11558
Vilotte, Jean-Pierre **11918**
Vincent, Debut **11899**
Vincent, Stephane 10630
Vlachos, Pavlos 11872
Vlaskin, Sergey 10518
Vogt, Jonathan **11294**
Vollmann, Jacqueline 11001,**11412**,11615
Wada, Shigeo **12181**
Wadhwa, Hemlata **10836**
Waeytens, Julien 11098
Wagner, Barbara 10962

Wagner, Christian **11514**
Wajnryb, Eligiusz **11418**,11890
Waki, Yoshiyuki 10908
Walkowiak, Marcel 10996
Walter, Johann 11309
Wan, Decheng **10213**
Wan, Frederic 11126
Wan, Shi-Xin 10803
Wan, Shu-Xiao 10811
Wand, Yikan 11109
Wang, An-Bang 11818
Wang, Chao 11896
Wang, Gang-Feng 11419
Wang, Guangqian 10705
Wang, Guoping 10999
Wang, Jane **10516**
Wang, Ji 10860
Wang, Jianxiang 10666,**11069**
Wang, Jinbin **11214**
Wang, Jun 11169
Wang, Li-Sheng **11264**
Wang, Ming-Chun 10947
Wang, Ping **11055**
Wang, Qian 11292
Wang, Qinghua 10942
Wang, Shibin 11183
Wang, Wei-Chung **11157**
Wang, Weifeng 11591
Wang, Xingzhe **11367**
Wang, Yue-Sheng **10687**,11045
Wang, Yuefang **11295**
Wang, Yun-Che **10172**
Wang, Zhengdao **10544**
Wang, Zhi-Yong 10633
Wang, Zhihua 10463
Wang, Ziping 11179
Warminski, Jerzy **11154**
Watanabe, Shinya **11576**
Watanabe, Tadashi **11526**
Watmuff, Jonathan **10722**
Watson, Andrew 10460
Weber, Wilhelm **10507**
Wei, Yang 11692
Wei, Yueguang **11330**
Wei, Yuqing 11368

Wei, Zhensong 11663
Weier, Tom 11600
Weihs, Daniel **11744**
Weiland, Chris **11872**
Weinberg, Eli 12000
Weiping, Zhu **10011**
Weir, Graham **10828**
Weislogel, Mark **11523**
Weitz, David 11445,**12122**
Weller, Thibaut **11034**
Wen, Jianming **11170**
Wessling, Matthias 11561
Westerweel, Jerry 11223
Wetzel, Christian **11471**
White, Scott **11518**
Wieckowski, Zdzislaw **11029**
Wiercigroch, Marian **10567**,11118
Wierschem, Andreas 11314
Wierzba, Ida 12121
Wijeyewickrema, Anil **11567**
Wilke, Daniel **11825**
Wilkins, Andy 10326
Wilson, Eddie 10580
Wilson, Marc 11321
Wilson, Mark 11482
Winther, Michael **11049**
Wismans, Jac 11371
Witelski, Tom 11807
Wong, Chong **10072**
Wong, Shaw **12001**
Worster, Grae 11388,**11496**
Wriggers, Peter **10061**,11378,11544
Wright, Callum 11291
Wroblewski, Adam **11230**
Wu, Bin 11449
Wu, Bisheng 10802
Wu, Cheng-Da **11270**
Wu, Lin-Zhi 10633
Wu, Qingyong 10966
Wu, Tsung-Tsong **11099**
Wu, Wen-Fang **11533**
Wu, Wen-Ping 11020
Wu, Xuesong **11554**
Wu, Zhiqiang 11095
Xia, Hua **11520**,11530

Xia, Ke-Qing **10007**,10938,11401
Xia, Mengfeng 11169
Xiao, Pan 11169
Xiao, Zhi-Wen 11571
Xiaolong, Jia 12157
Xie, Feng 11259
Xie, Ganquan 11215,**11259**
Xie, Huimin **10942**
Xie, Lee 11259
Xie, Zhoumin 10606
Xu, Ai-Jin 11287
Xu, Feng **11694**
Xu, Guanshui **11917**
Xu, Haitao 10532,**11402**
Xu, Hang 11104
Xu, Rui 11856
Xu, Shengli 12088
Yabuno, Hiroshi **10514**
Yagla, Jon 11872
Yaguchi, Hisao 11372
Yamagata, Toshio **11053**
Yamaguchi, Takao 11234
Yamanaka, Akinori **11528**
Yamaoka, Hidetaka **11424**
Yamashita, Kiyotaka 11301
Yamazaki, Shinya 11436
Yaminsky, Vassili 12201
Yan, Yan 11542
Yan, Zhi-Zhong 10687
Yang, Fan 11916
Yang, Fu-Ling **11441**
Yang, Guitong 10463
Yang, Guobiao **10662**
Yang, Huizhu 10590
Yang, Kyung-Soo 12147
Yang, Lei **11466**
Yang, Li **11725**
Yang, Lung-Jieh **11473**
Yang, Shang 10984
Yang, Shengyuan 11284
Yang, Wei **11916**
Yang, Xinhua **11856**
Yano, Takeru 11372
Yao, Shanshan 11577
Yarlanki, Srinivas 10365

Yashiro, Kisaragi 11686,**11726**
Ye, Yong 11856
Yen, Shun-Chang **11743**
Yeo, Leslie **10648**,10671,11175
Yeoh, Guan 11140
Yichun, Zhou 10355
Yin, Ching-Chung **10020**
Yin, Xiaochun 10789,11527
Yin, Zhaohua **11435**
Yokojima, Satoshi **11420**
Yokota, Kazuhiko 11374,11752
Yong, David 10134
Yong, Pan 10355
Yoon, Dong-Hyeog **12147**
Yoon, Jiwon **11019**
Yoshitake, Naoki **11760**
Yoshizawa, Masatsugu **11301**
You, Xiangchen 11104
You, Zhenjiang **11353**
Young, William **10520**
Yu, Gui-Lan **11045**
Yu, Shaohua 10614
Yu, Shou-Wen **11419**
Yu, Xiaobo **11291**
Yue, Chen 10617
Zaharieva, Rusi 11630
Zaleski, Stephane **11848**
Zanette, Jeronimo **11379**
Zannetti, Luca 11003
Zarins, Christopher 11345
Zastrau, Bernd **11164**
Zbib, Hussein 11266
Zeidis, Igor **11225**
Zeng, Xianwei **11591**
Zengsheng, Ma 10355
Zhang, Bin 12210
Zhang, Chuanzeng 10687
Zhang, Haitao 11502
Zhang, Hui 11760
Zhang, Ji-Qiao 11419
Zhang, Jinghong 11055
Zhang, Junqian **11368**
Zhang, Ke-Shi **10047**
Zhang, Neng-Hui **10811**
Zhang, Nong 10469,11703

Zhang, Qiang 10411
Zhang, Wendy **11645**
Zhang, Xi **11132**
Zhang, Xin-chun 11220
Zhang, Xinhua **11031**
Zhang, Yan **11193**
Zhang, Ying **11835**
Zhang, Yinong 11449
Zhang, Zhang 10662
Zhao, Haifeng 11330
Zhao, Hui-ming 10760
Zhao, Jian-Fu **10803**
Zhao, Longmao 10463
Zhao, Xuanhe 11644
Zhao, Zhen 11070
Zhe, Wang 11692
Zheng, Xiaojing 10261,**10784**,11014,11055
Zheng, Xuejun **10966**
Zhou, Gongcheng 11214
Zhou, Kun 11651
Zhou, Quan 10007
Zhou, Xia **11336**
Zhou, Xiaoming 11577
Zhou, Yichun 10966,11214,**11431**,11725,11940
Zhou, Zhe-Wei 11287
Zhu, BoJing **10614**
Zhu, Hai **12104**
Zhu, Linli **11014**
Zhu, Qizhi 11880
Zhu, Ting **11710**
Zhu, Yong 10818
Zhuang, Zhuo **12074**
Zhuo, Qi-Wei 11136
Zikanov, Oleg 10715,11628
Zilong, Zhang 11348
Zima, Patrik **11144**
Zima-Kulisiewicz, Bogumila **11866**
Zimmermann, Klaus 11225
Zinchenko, Alexander **11884**
Ziolskowski, Marek 11227
Zirpoli, Ada 11191
Zoueshtiagh, Farzam 10505
Zwaan, Ed 12209
d'Olce, Marguerite 10372
del Pino, Carlos 10446

de Borst, Rene 11951
de Jong, Nico 11658
de Sciarra, Francesco **10294**
de la Osa, Marc **11558**
du Puits, Ronald **10834**
du Tertre, Alban 10987
van Dommelen, Johannes **11371**
van Heijst, GertJan **10737**,11003
van Hoeve, Wim **11548**
van Wijngaarden, Leen 11456,11658
van den Berg, Albert 11932,12209
van den Bulck, Eric 11237
van der Giessen, Erik **10556**,10914,11189
van der Heijden, Gert 10366,**11389**
van der Meer, Devaraj **11476**
van der Weele, Ko **11476**
van der Wouden, Egbert **11932**
van de Ven, Fons 10713